TRW 07398-6017-R000

RADIO/OPTICAL/STRAPDOWN INERTIAL GUIDANCE STUDY FOR ADVANCED KICK STAGE APPLICATIONS

FINAL REPORT

Volume II - Detailed Study Results

30 JUNE 1967

Contract No. NAS 12-141

Prepared for
NATIONAL AERONAUTICS AND SPACE ADMINISTRATION
ELECTRONICS RESEARCH CENTER
Cambridge, Massachusetts

TRW SYSTEMS GROUP
ONE SPACE PARK - REDONDO BEACH, CALIFORNIA

FOREWORD

This report presents the results of a nine-month study of "Radio/Optical/Strapdown Inertial Guidance Systems" for future NASA unmanned space missions, conducted by TRW Systems for NASA/Electronics Research Center, Contract NAS 12-141.

The broad objectives of this study were to:

- Establish the guidance requirements for a selected group of future NASA unmanned space missions.
- Investigate possible guidance concepts based on the appropriate use of radio, strapdown inertial, and optical techniques, with the further objective of establishing the proper functional role, the capabilities, limitations, and constraints of each of these elements in the overall guidance system concept.
- Define feasible radio/optical/strapdown inertial guidance system design concepts and equipment configurations.
- Perform analyses to establish the feasibility (performance) of the selected design concepts.
- Indicate areas of technology where state-of-the-art advances are necessary.

Volume I summarizes the entire study, conclusions, and recommendations. Volume II describes the detailed findings that support these conclusions. Supplementary material is presented in Volume III (surveys of electro-optical sensors and of inertial instruments) and in Volume IV (classified sensor data).

CONTENTS

CONTENTS (Continued)

CONTENTS (Continued)

CONTENTS (Continued)

CONTENTS (Continued)

ILLUSTRATIONS

ILLUSTRATIONS (Continued)

ILLUSTRATIONS (Continued)

TABLES

TABLES (Continued)

TABLES (Continued)

TABLES (Continued)

1. INTRODUCTION

This report presents the results of a nine-month study of "Radio/Optical/Strapdown Inertial Guidance Systems" for future NASA unmanned space missions, conducted by TRW Systems for NASA/Electronics Research Center. This volume presents the detailed study results. Additional supplementary material is presented in Volumes III and IV.

1.1 STUDY OBJECTIVES

The broad objectives of this study were to:

- Establish the guidance requirements for a selected group of future NASA unmanned space missions.
- Investigate possible guidance concepts based on the appropriate use of radio, inertial, and optical techniques, with the further objective of establishing the proper functional role, the capabilities, limitations, and constraints, of each of these elements in the overall guidance system concept.
- Define feasible radio/optical/inertial guidance system design concepts and equipment configurations.
- Perform analyses to establish the feasibility (performance) of the selected design concepts.
- Indicate areas of technology where state-of-the-art advances are necessary.

The study constraints and scope of the work are defined as follows:

1) The representative missions to be studied were:
   - Synchronous earth orbit
   - Mars orbiter mission
   - Lunar orbiter mission
   - Solar probe mission using Jupiter Assist.
2) The choice of inertial systems was limited to strapdown systems.
3) Only existing NASA and DOD radio tracking systems were considered, i.e., no new equipment developments or facilities were considered.

4) The inertial instrument and optical sensor technology to be considered was limited to reasonable projections of the current state-of-the-art (to the early 1970's).

5) Initially the study was limited to upper stage guidance only. At ERC's request the study was expanded to include boost phase guidance.

1.2 STUDY IMPLEMENTATION

In accordance with the stated objectives, the study was carried out in the six major steps listed below.

1) Functional and performance requirements for the strapdown inertial guidance subsystem and the electro-optical sensors were defined by mission phase for each of the four generic missions studied.

2) A survey was accomplished of state-of-the-art electro-optical sensors and strapdown inertial components (gyros and accelerometers) that potentially could be used.

3) Based upon the results of 1) and 2), appropriate candidate sensors were selected and performance (error) models were developed for them.

4) A study of possible radio guidance concepts and the capabilities of existing NASA and DOD tracking systems was conducted to define candidate systems, their applicability, limitations, and performance capabilities for the four missions.

5) An overall radio/optical/strapdown inertial guidance system concept, equipment configurations, and operating sequences were developed for each of the four mission categories.

6) Performance analysis studies were conducted both to investigate the performance capabilities of the candidate radio/optical/strapdown inertial guidance configurations and to demonstrate their adequacy for the four missions.

The major emphasis in this study was placed on defining the configuration of the onboard optically aided strapdown inertial subsystem, and the definition and analysis of the functional and performance requirements for this equipment. Although the digital computer, the tracking transponder and data link, and the vehicle control system are essential elements of the

total guidance and control system, they have been considered only in a functional sense in defining the guidance concept and configuring the system; detailed study of these elements is outside the scope of this study.

1.3 ORGANIZATION OF THIS VOLUME

Section 2 of this volume develops the guidance system functional and performance requirements for the four missions. Mission and vehicle assumptions and ground rules are defined and the characteristics of the mission trajectories used for developing the performance requirements and analyzing the performance capabilities of the recommended system configurations are discussed.

Section 3 defines the recommended radio/optical/strapdown inertial guidance system in terms of a matrix of equipment configurations by mission. Functional block diagrams of the recommended configuration for each mission are presented.

Section 4 defines the candidate strapdown inertial guidance subsystems postulated for this study, presents appropriate preliminary design information, and develops performance (error) models for the candidate subsystems.

Section 5 defines candidate electro-optical sensors by mission and mission phase, develops error models for the sensors, and presents detailed information on sensor operating and design characteristics.

Section 6 covers the radio guidance studies, including a discussion of possible radio guidance concepts, presents description and performance characteristics of the available tracking systems, and discusses their utilization for the four missions studied.

Sections 7, 8, and 9 present the results of the mission performance analysis studies. Section 7 covers the powered flight regime, Sections 8 and 9 cover the navigation performance analysis studies for the interplanetary trajectory phases, including midcourse and planetary orbit insertion maneuvers. This includes a detailed study of Mars approach guidance using DSIF tracking plus an onboard optical/inertial system, incorporating a Mars approach guidance sensor.

2. MISSION CHARACTERISTICS, GUIDANCE SYSTEM FUNCTIONAL AND PERFORMANCE REQUIREMENTS

2.1 INTRODUCTION

This section presents a summary of the mission characteristics and requirements and the guidance system functional and performance requirements derived from these.

Under each mission heading, the mission and launch vehicle characteristics, trajectories, and mission performance accuracy requirements are summarized. Guidance system functional requirements and operating sequences derived from the mission requirements, vehicle characteristics, and guidance equipment capabilities are specified. Equipment configurations and functional interconnections are presented for each of the missions in Section 3.

2.2 STUDY ASSUMPTIONS AND DEFINITIONS

2.2.1 Mission Definitions and Requirements

It is assumed that the guidance requirements for the missions studied are representative of at least a major portion of the total requirements for NASA unmanned missions in the next decade. However, mission objectives are not precisely defined at the present time, and definitive payload characteristics are not available. Also, launch vehicle selections for the missions have not been firmly made, and definitive design data are not available on vehicle upper stage concepts currently in the planning and development stages. For these reasons, it was necessary to postulate somewhat arbitrarily a set of specific mission performance requirements, launch vehicle selections, vehicle and payload characteristics. These assumptions are detailed below.

For the same reasons as given above, it is not possible to present complete and definitive performance (accuracy) requirements for the guidance system. Consequently, some of the accuracy requirements presented in this report are based on mission requirements determined from past studies, and others are presented in parametric form. As more definitive trajectory data and mission objectives become available, these requirements can be updated.

The formulation of functional requirements and generic candidate guidance system configurations is also dependent on mission analysis although not to the extent to which the formulation of accuracy requirements is. The functional requirements and candidate configurations can therefore be discussed in terms general enough to be applicable to any reasonable contemplated mission plans.

2.2.2 Postulated Vehicle/Payload Combinations

For purposes of this study, specific launch vehicle/payload combinations were postulated for the four missions. Table 2-I shows these assumed combinations along with the interpretation of what constitutes the "kick" stage for each of the missions. For the purpose of this study, the "kick stage" has been defined to be the final propulsive stage. In some cases this may be an actual upper stage such as Centaur or HEUS (High Energy Upper Stage), and in other cases it may be a spacecraft such as Voyager. The portion of the mission to which the kick stage guidance is applicable also varies from mission to mission. The specific assumptions made as to the "guidance regime" are shown in Table 2-I.

2.2.3 Upper Stage Characteristics

Widely accepted quantitative values do not yet exist for the kick stage weights, mass ratios, propulsion capabilities (thrust, specific impulse), and ΔV (velocity increment) capabilities. Without these, it is impossible to define with any certainty the accuracy requirements for any mission phase or midcourse correction velocity limits. Lacking these data, it has been decided (1) to draw on results from other related studies as much as possible, or (2) to present the requirements in parametric form.

For the thrusting and ΔV capabilities, it will be assumed for the lunar and interplanetray missions, that the kick stage has two (or more) discrete thrust levels, the lowest thrust level suitable for corrective ΔV applications ranging from a few meters per second up to 100 m/sec. The highest thrust levels would be used for major orbital changes, with ΔV values up to several thousand m/sec. It is also assumed that the kick stage has complete three-axis attitude control capability.

The postulated separation of functions between the primary booster guidance and control (G and C) and the kick stage G and C are discussed under the individual mission headings.

Table 2-I. Vehicle Payload Combinations Postulated for Study Purposes

Generic Mission	Example Mission	Launch Vehicle	Kick Stage	Guidance Regime
Synchronous Earth Satellite	Advanced earth orbiting missions such as advanced meteorological or communication satellites	Atlas/Centaur	Centaur or HEUS†	Launch through snychronous orbit insertion (S/C payload assumes orbit trim and station keeping functions after insertion)
Mars Orbiter	Voyager	Saturn V	Voyager Interplanetary Spacecraft	Interplanetary orbit insertion through Mars orbit insertion and orbit trim
Lunar Orbiter	Advanced lunar orbiter photographic mission	Atlas/Centaur/HEUS†	Lunar Orbiter Spacecraft	Launch through lunar orbit insertion including orbital change maneuvers
Jupiter Flyby/ Swingby	• Solar probe with Jupiter assist • Jupiter flyby for scientific observation of planet	Atlas/Centaur/HEUS††	Interplanetary Spacecraft	Launch through injection into the interplanetary trajectory. Midcourse corrections and cruise attitude control provided by the spacecraft.†††

† A High Energy Upper Stage (HEUS) may or may not be required depending on the payload weight. It is assumed that the guidance equipment is located in the final stage but may provide guidance to the lower stages.

†† Other upper stages such as Burner II may be used depending on the mission requirements and payload weight.

††† It may be possible to locate the guidance equipment in the spacecraft and utilize it to provide the midcourse guidance and cruisé attitude control. The utility of this approach depends on the spacecraft concept (e. g., spinning or nonspinning spacecraft). The guidance systems studied here will provide the required capabilities for a fully attitude stabilized spacecraft.

2.2.4 Separation of Guidance Functions Between Kick Stage and the Mission Payload

It was necessary for some of the missions to postulate the existence of capabilities within the mission payload such as the capability for independent attitude control, propulsive maneuvers for small orbital corrections, communications, etc. At the time of separation of the payload spacecraft from the kick stage, these functions are activated and the kick stage functions terminated.

Since the payloads for the missions studied have not been defined in detail, reasonable assumptions have been made based on current spacecraft design trends. For example, for the synchronous orbit mission, the the payload spacecraft is assumed to have a capability for orbit trim and station keeping functions, as well as attitude stabilization and control, after insertion into orbit by the kick stage. Specific assumptions made for other missions are discussed in Section 3 of this volume.

2.2.5 Definition of Terms

Certain of the definitions pertaining to the missions, the launch vehicle, mission events, and trajectories used throughout this report are summarized below.

2.2.5.1 Missions

In general, the term "mission" is used in this report to encompass and describe the events which are associated with directing the launch vehicle or the spacecraft from the earth and which terminate with the accomplishment of the mission objectives. In the analysis of the various missions throughout this study, the following terms are used:

- Synchronous earth-orbit mission — In the synchronous earth-orbit mission, the launch vehicle is used to place the satellite payload into an earth-synchronous (24 hr period) equatorial orbit at a desired longitude. The injected payload (satellite) is assumed to have orbit trim and stationkeeping capability.

- Orbiter missions

  In an orbiter mission, approximately at the time when the spacecraft is closest to the target body (moon or planet), its trajectory is deliberately altered by a propulsive maneuver so that it remains in an orbit about the target body as a satellite.

- Solar probe mission

  In a solar probe mission the spacecraft is injected into a heliocentric orbit that passes within a specified distance of the sun. This is an untargeted mission requiring no trajectory alterations subsequent to injection.

- Flyby mission

  In a flyby mission the spacecraft passes close to the target planet. No propulsion forces are employed to alter the trajectory so as to remain in the vicinity of the target planet. The spacecraft departs from the region of the target planet. The spacecraft departs from the region of the target planet, although its trajectory will have been perturbed.

- Solar probe with planetary swingby

  In this mission the spacecraft passes close to a planet with the purpose of significantly altering the spacecraft trajectory. After departure from the target planet, the spacecraft continues on a heliocentric trajectory to within a prescribed distance from the sun. No propulsive forces are employed to alter the trajectory in the vicinity of the target planet. For a given distance of closest approach to the sun, this technique may be used to significantly reduce the launch vehicle ΔV requirements, usually at the expense of considerably longer mission durations.

2.2.5.2 Vehicle Terms

- Launch vehicle

  The launch vehicle includes the multistage boost vehicle which injects the spacecraft into the desired trajectory, all hardware up to the field joint where the spacecraft is mated, and the payload shroud which protects the spacecraft. Generically, the launch vehicle system also includes all appropriate ground support and test equipment.

- **Kick stage** — For the purposes of this study, "kick stage" refers to the final powered stage of the launch vehicle (the payload spacecraft is assumed to have only limited velocity capability for incremental orbit corrections). The kick stage is assumed to have complete three-axis guidance, navigation, and control capability for all launch vehicle stages except for the Mars orbiter mission.

- **High Energy Upper Stage (HEUS)** — This is a particular kick stage concept using an advanced propulsion system burning high-energy propellants such as H_2/F_2. Typical gross weight is 3200 kg. The thrust to weight ratio is approximately 1.

- **Spacecraft** — The spacecraft system encompasses the payload itself and all its component subsystems, the science payload, the adapter which is mounted to the kick stage, and limited propulsion capability for orbital corrections.

- **Launch operations system** — The launch operations system does not include any flight hardware, but constitutes the operational responsibility for supporting and conducting the launch of the combined launch vehicle and spacecraft through the separation of the spacecraft from the launch vehicle.

- **Mission operations systems** — Operational responsibility for supporting and conducting the mission after the spacecraft is separated from the launch vehicle is borne by the mission operations system.

2.2.5.3 Mission Events

In the analysis of the various missions throughout the study, the following terms are used:

- **Prelaunch** — Collectively, all events before liftoff.

- **Launch** — Collectively, all events from liftoff to injection.

• Liftoff and ascent	Departure of the combined launch vehicle-spacecraft from the ground and ascent to parking orbit of specified altitude (typically 185 km).
• Injection (synchronous earth-orbit mission)	Thrust termination of the kick stage, placing the kick stage/payload into a transfer trajectory to synchronous altitude from the parking orbit or, alternately, into the final synchronous earth orbit.
• Injection (lunar or interplanetary mission)	Thrust termination of the lower stages of the launch vehicle, placing the kick stage/payload into interplanetary or translunar trajectory, from the parking orbit.
• Separation (shroud)	Detachment of the nose fairing from the launch vehicle during ascent.
• Separation (spacecraft)	Detachment of the spacecraft from the spacecraft kick stage adapter after injection.
• Orientation maneuver	A programmed alteration of the kick stage attitude to cause it to assume a desired orientation.
• Reorientation maneuver	A programmed alteration of the kick-stage attitude to cause it to return to the cruise orientation.
• Midcourse trajectory correction maneuver	A propulsive maneuver performed to compensate for inaccuracies or pertubations so as to redirect the kick stage toward the intended aiming point. Generally, it requires orientation to a specific attitude, operation of the rocket engine, and reorientation to the cruise attitude. The time of this maneuver is during the interplanetary or translunar flight, but not necessarily at the midpoint.
• Encounter	Generally, encounter encompasses events occurring when the spacecraft is near the target planet. Specifically, it refers to the time when the kick stage is at its point of closest approach (periapsis).

- Orbital insertion — The propulsive braking maneuver by which the (orbiter) spacecraft trajectory at the target planet is changed from approach (hyperbolic) to orbital (elliptical).

2.2.5.4 Trajectory Terms

In discussing the trajectories possible for the various missions studied, the following terms are used:

- Direct trajectory — An interplanetary trajectory from the earth to a target planet, in which no intermediate planets (or satellites) are approached closely enough to significantly influence the trajectory.
- Swingby trajectory — An interplanetary trajectory from the earth to a target planet, in which an intermediate planet is passed sufficiently close to exploit the effect of its gravitational attraction. This exploitation may provide reduced mission duration, reduced launch energy, or an opportunity for scientific observations of the intermediate planet.
- Launch opportunity — The time during which trajectories to a target planet may be initiated from the earth, with reasonable launch energies. A launch opportunity is usually identified by the year in which it occurs and the target planet.
- Launch period — The space in arrival date-launch date coordinates in which earth-planet trajectories are possible in a given launch opportunity; specifically, the number of days from the earliest possible launch date to the latest.
- Launch window — The time in hours during which a launch is possible on a particular day.
- Geocentric (heliocentric; planetocentric) — Described or measured with respect to inertial coordinates centered with the earth (sun; planet). Pertaining to the portion of the flight in which the trajectory is dominated by the gravitation of the earth (sun; planet).

• C_3, launch energy, injection energy	Twice the geocentric energy per unit mass of the injected spacecraft. This is equivalent to the square of the geocentric asymptotic departure velocity.
• Asymptote	The line that is the limiting position which the tangent to a hyperbolic (escape) trajectory approaches at large distances from the attracting center.
• DLA	Declination of the outgoing geocentric launch asymptote.
• ZAL	Angle between the outgoing geocentric asymptote and the sun-earth vector.
• ZAP	Angle between the incoming planetocentric asymptote (at the target planet) and the planet-sun vector.
• ZAE	Angle between the incoming planetocentric asymptote (at the target planet) and the planet-earth vector.
• V_∞ or V_{HP}	Planetocentric asymptote approach velocity.
• Parking orbit	An unpowered, geocentric, approximately circular orbit, separating the powered portions of the launch injection sequence.

2.2.5.5 Coordinate Systems

The various coordinate systems used in specifying performance requirements and powered flight performance analysis results are defined here.

ECI (Earth-Centered-Inertial)	This is a right-handed coordinate system, in which Z lies along the earth's polar axis and X and Y lie in the earth's equatorial plane. The X-axis passes through the Greenwich meridian or in the direction of the Vernal Equinox at the time of launch, (specified in text).

RTN (Radial-Tangential-Normal)	A right-handed orthogonal coordinate system in which R lies in the direction of the nominal position vector from the center of the earth, and N lies in the direction of the orbital angular momentum. T forms a right-handed orthogonal set with R and N.
(X, Y, Z) Selenographic	Moon-Centered Inertial Coordinates. This is a right-handed orthogonal coordinate system in which Z lies along lunar polar axis, and X, Y lie in the lunar equatorial plane with X passing through zero lunar longitude (Sinus Medii).

2.3 SYNCHRONOUS EARTH SATELLITE MISSION

For this mission, a typical launch vehicle can be assumed to be the Atlas SLV3X-Centaur † with a variety of communication and meteorological satellites as the payload. It is assumed that the satellite payload itself has the capability of providing a ΔV for final orbit trim and stationkeeping. The ultimate functional and performance requirements imposed on the kick stage for this mission are to place a payload into a near synchronous earth orbit, at the desired longitude, with sufficient precision that final orbit trim corrections can be performed utilizing the limited propulsion capability of the payload. The kick stage guidance system accuracy requirements may be conveniently stated in terms of the payload ΔV required to correct the residual errors after final injection. Reasonable values lie in the range of 15-30 m/sec.

† The payload and coast duration capabilities of this vehicle are severely limited for this mission using the existing Centaur vehicle. For the purposes of this study, these problems are ignored. It is assumed that the Centaur vehicle may be modified to increase the payload capability, to extend the permissible coast duration, and to permit three-burn operation Another alternative, providing a large increase in payload capability, is to add an upper stage (such as HEUS) to the vehicle. The guidance requirements are not expected to be significantly different for either vehicle concept.

For purposes of this study, it is assumed that the kick stage guidance system provides the complete guidance and control of the launch vehicle from liftoff through parking orbit insertion, transfer injection, and synchronous orbit injection. Two extremes of ascent trajectories have been considered. In the first, the kick stage is injected into the transfer trajectory to synchronous altitude from a 185 km "parking orbit" at the first equatorial crossing from launch. In the second, the kick stage/payload may remain in the 185 km parking orbit for as long as 12 hr before transfer ignition. These are the extremes of the parking orbit coast period required to reach any desired final longitude for this mode of ascent.

2.3.1 Mission Characteristics

For the purposes of this study, the major events of the synchronous mission developed for the Atlas/Centaur (AC-8 configuration) have been adopted and modified. Following liftoff from the Atlantic Missile Range, a roll is introduced in the launch vehicle to obtain a launch azimuth of 90 deg. The Atlas booster is then controlled up to its cutoff (BECO) by a predetermined booster pitch program.

Injection into the parking orbit is accomplished by using two constant pitch rates selected to achieve the altitude and flight path angle for injection into the 185 km parking orbit. The first pitch rate occurs during the Atlas sustainer flight, lasting for ten sec after initiation of that phase, while the second rate occurs during the Centaur powered phase. After injection into the parking orbit, the Centaur coasts to the vicinity of the equator (first crossing) at which time the second burn (approximately 1.5 min) injects it into a Hohmann transfer ellipse. This burn is performed with a pitch rate that keeps the Centaur in a fixed attitude relative to the radius vector, and terminated on a predicted apogee altitude equal to that of the required synchronous circular orbit. During the coast in the Hohmann transfer, approximately 5 hr, the Centaur maintains a fixed inertial attitude.

Optimally, minimum energy requirements suggest dividing the orbit inclination plane change between perigee and apogee. For launch from AMR at 90 deg launch azimuth, the orbit inclination is 28.5 deg; approximately 2 deg should be removed at perigee and the remaining 26.5 deg at apogee. For this study, the gains from pursuing this approach do not

overcome the complexities introduced. Therefore, the method adopted for the third Centaur burn at apogee was to perform the total orbit plane change simultaneously with injection into the synchronous orbit.

Just prior to reaching apogee, instantaneous yaw and pitch attitude maneuvers were performed to establish an initial attitude for the final burn (approximately 39 sec) such that the Centaur would achieve the correct synchronous orbit. Characteristics of the actual synchronous orbit obtained are:

Altitude	=	35,850 km (19,326.5 nmi)
Longitude	=	102.7 deg
Velocity magnitude	=	3.08 km/sec (10,087.3 ft/sec)
Eccentricity	=	0
Inclination	=	0 deg
Period	=	1,436.1 min

After injection into the circular synchronous orbit, the payload separates from the Centaur. Any errors in the resulting spacecraft orbit are then corrected by the spacecraft itself.

Developing the nominal trajectory presented above was contingent on making the following simplifying assumptions:

a) A mission of this type requires a three-burn capability from the Centaur. Since presently only a two-burn capability is available,† the detailed sequence of events of the second burn was duplicated for a third burn.

b) Payload maximization could be obtained by optimizing several trajectory parameters such as launch azimuth, plane change philosophy, parking orbit altitude, vehicle attitude history, etc. However, for this guidance study, the exact maximum payload weight is irrelevant to the guidance scheme adopted. Hence, no payload maximization analysis was performed.

---

†A two-burn (Centaur stage) mission profile is also possible, using the technique as discussed under c) above. Although the three-burn capability and the extended coast capability required for either mission profile is not in the present Centaur design, these capabilities could be provided by an improved Centaur stage or an alternate stage having similar capabilities. It is beyond the scope of this study to assess the technical feasibility of these design changes.

c) Positioning a 24-hr synchronous spacecraft above a specified longitude may also be accomplished by injecting into an orbit offset from the required circular synchronous orbit. A drift rate results which allows the spacecraft to change its longitude. This drift rate is then removed, and the final orbital corrections made when the required longitude is reached. Since these corrections would be executed by the spacecraft and not the launch vehicle, guidance techniques for the Centaur would not be affected if such considerations were incorporated in this analysis. Consequently, the spacecraft was targeted directly into the 24-hr synchronous equatorial orbit, thus neglecting offset drift orbit considerations.

d) An eight-orbit phasing coast in 185 km parking orbit is simulated for certain runs by the analytical propagation of errors in the error analysis program (see Section 7). The remarks in b) above concerning Centaur capabilities apply here as well. The event times for the synchronous orbit missions are shown in Tables 2-II and 2-III for cases without and with an eight-orbit phasing coast, respectively.

2.3.2 Guidance System Operational Sequence

The guidance system operational sequence during each of the mission phases is summarized below:

a) Launch and boost to ~ 185 km parking orbit:[†] The strapdown inertial guidance subsystem is presumed to be providing the guidance function for this phase.[††]

b) Coast in parking orbit for a period t, with t depending on desired longitudinal positioning of satellite (15 min $\lesssim$ t $\lesssim$ 12 hr): During the coast period, the inertial guidance subsystem is required only to provide vehicle attitude control reference. The exact attitude profile to be followed during the coast phase will depend on the mechanization concept developed; however, at transfer ignition (at equatorial crossing) the kick stage attitude must be at that thrusting attitude required to place the kick stage/payload into the desired transfer

[†] This is a typical value assumed for this study and represents a reasonable lower limit for this type of mission. The parking orbit altitude is chosen as low as possible so as to maximize the injected payload weight. However, below about 185 km drag effects limit the orbital lifetime of the vehicle.

[††] Under certain conditions, radio guidance could also be used. See Section 6 for a discussion of this possibility.

Table 2-II. Event Times Without Phasing Coast – Earth Synchronous Orbit Mission

Time (sec)	Event
2.0	Start first powered phase (boost)
671.42822	Start first coast phase (circular)
1496.4282	Start second powered phase (perigee burn)
1630.0493	Start second coast phase (Hohmann transfer)
20,052.415	Apogee attitude update
20,652.415	Start third powered phase (apogee burn)
20,737.026	Start synchronous orbit

Table 2-III. Event Times With Phasing Coast – Earth Synchronous Orbit Mission

Time (sec)	Event
2.0	Start first powered phase (boost)
671.42822	Start first coast phase (circular)
43,381.5570	Perigee attitude update and time update
43,981.5570	Start second powered phase (perigee burn)
44,115.1781	Start second coast phase (Hohmann transfer)
62,537.5438	Apogee attitude update
63,137.5438	Start third powered phase (apogee burn)
63,222.1548	Start synchronous orbit

orbit. The attitude control during the period immediately prior to transfer ignition might be inertial only or optically aided inertial using earth (horizon) and sun sensors. Ground tracking might possibly be used, particularly for the multiorbit cases, for navigation updating of the transfer ignition burn time and of the required vector velocity increment. See Section 6 for a discussion of this possibility.

c) Transfer burn to apogee: This phase will be controlled autonomously by the strapdown inertial guidance subsystem.

d) Transfer coast: During the approximately 5 1/4-hr coast in the Hohmann transfer to the apogee at nominal synchronous altitude, the inertial guidance subsystem can again be relegated to the role of an attitude reference set. The kick stage/payload can possibly be ground tracked to determine the apogee burn requirements. (See Section 6). Five to fifteen min prior to apogee burn, absolute inertial attitude update can be provided by celestial sightings.

e) Apogee burn: The apogee burn is designed to circularize the orbit at synchronous altitude and is controlled by the strapdown inertial guidance subsystem. The use of the kick stage is presumably terminated at this time and the payload is separated from the kick stage.

2.3.3 Guidance System Performance Requirements

Because of (1) imperfect tracking or navigation during the transfer coast and (2) thrusting attitude and ΔV errors of the kick stage at apogee burn, the payload orbit will be imperfect in several respects:

a) The orbit is in general elliptical.

b) The orbital inclination is, in general, not zero.

c) The longitude of the subsatellite point is, in general, not the desired longitude.

The capability of the payload propulsion to correct for these errors dictates the final accuracy requirements of the kick stage apogee burn. An analysis of the relationship of trajectory errors to payload ΔV requirements is presented below.

The results of this analysis are a set of nonlinear expressions relating position and velocity errors at injection to the ΔV required to correct the errors. If ΔV_A represents the available payload propulsion capability, then the performance requirement for this mission may be stated as

$$\Delta V_{Total}\,(95\%) < \Delta V_A$$

where ΔV_{Total} is the value of ΔV required for 95 percent probability of successfully performing the correction. Reasonable values for ΔV_A lie in the range 15-30 m/sec. Results of a detailed performance analysis for this mission are presented in Section 7.

2.3.3.1 In-Plane Radius and Velocity Errors

The in-plane errors, exclusive of the longitude error, after the kick stage apogee burn are:

$$e_1 = \Delta r/r$$

$$e_2 = \Delta V/V$$

$$e_3 = \Delta \dot{r}/V$$

where

r = synchronous radius = 42165 km

V = synchronous velocity = 3.08 km/sec

Δr = error in r

ΔV = error in V

$\Delta \dot{r}$ = error in radial velocity (nominal $\dot{r}$ is zero)

$$e_1, e_2, e_3 \ll 1$$

For nominally circular orbits (nominal eccentricity e = 0), the actual eccentricity, semimajor axis, and perigee distance are

$$e = \left[(e_1 + 2e_2)^2 + e_3^2\right]^{1/2}$$

$$a = r(1 + 2e_1 + 2e_2)$$

$$r_p = a - er$$

Hohmann Transfer to Synchronous Altitude (Burn a). The semimajor axis of the Hohmann transfer ellipse and the required velocity at the beginning of the transfer will be

$$a_T = \frac{1}{2}(r_p + r)$$

$$= \frac{1}{2}(a + r(1 - e))$$

$$V_T = V\left[2\left(\frac{r}{r_p}\right) - \left(\frac{r}{a_T}\right)\right]^{1/2}$$

$$\cong V\left[1 - 3e_1 - 3e_2 + \frac{3}{2}\sqrt{(e_1 + 2e_2)^2 + e_3^2}\right]^{1/2} \qquad (2\text{-}1)$$

The actual velocity existing before the transfer burn is

$$V_p = V\left[2\left(\frac{r}{r_p}\right) - \left(\frac{r}{a}\right)\right]^{1/2}$$

$$\cong V\left[1 - 2e_1 - 2e_2 + 2\sqrt{(e_1 + 2e_2) + e_3^2}\right]^{1/2} \qquad (2\text{-}2)$$

Differencing Equations (2-1) and (2-2), the required ΔV for the Hohmann transfer is

$$\Delta V_a \cong -\frac{V}{2}\left[-e_1 + e_2 + \frac{1}{2}\sqrt{(e_1 + 2e_2)^2 + e_3^2}\right] \qquad (2\text{-}3)$$

Synchronization at Synchronous Altitude (Burn b). At the apogee of the transfer burn, the velocity is

$$V_a = V\left[2 - \left(\frac{r}{a_T}\right)\right]^{1/2}$$

$$\cong V\left[1 + e_1 + e_2 - \frac{1}{2}\sqrt{(e_1 + 2e_2)^2 + e_3^2}\right]^{1/2}$$

The required ΔV for synchronization is

$$\Delta V_b = V - V_a$$

$$\cong -\frac{V}{2}\left[e_1 + e_2 - \frac{1}{2}\sqrt{(e_1 + 2e_2)^2 + e_3^2}\right] \qquad (2\text{-}4)$$

Out-of-Plane Error (Burn c). The inclination error is

$$e_4 = \dot{W}/V \cong V\,\Delta i/V = \Delta i$$

where $\dot{W}$ is the component of velocity normal to the equatorial plane and Δi is the inclination error. The corrective ΔV required is then simply

$$\Delta V_c = V\,e_4 \qquad (2\text{-}5)$$

Longitude Error (Burn d). Following burns a, b and c above, the payload should be in a perfectly synchronized orbit but not necessarily at the desired longitude. To correct for this, an incremental velocity can be added to purposely desynchronize the orbit to change its orbital period, thus allowing the subsatellite point to drift under the payload. If the desynchronizing velocity increment is chosen properly, the desired subsatellite longitude should drift under the payload when the payload is at the correct apsis of its desynchronized orbit after n orbits. (If the payload is initially ahead of its desired location, the velocity increment required is positive and the "correct apsis" is the perigee.) At this time, an equal and opposite velocity increment is added to resynchronize the orbit. The total velocity increment required is

$$\Delta V_d = V\frac{\Delta L}{3\pi n} = V\,e_5 \qquad (2\text{-}6)$$

where ΔL is the longitude error and n is the number of whole orbits allowed for longitude correction.

2. 3. 3. 2 Total Velocity Requirement

The total velocity increment required from the payload is the sum of the absolute values from Equations (2-3), (2-4), (2-5) and (2-6), or

$$\Delta V_{Total} = |\Delta V_a| + |\Delta V_b| + |\Delta V_c| + |\Delta V_d|$$

$$= \frac{V}{2}\left\{\left| e_1 + e_2 + \frac{1}{2}\sqrt{(e_1 + 2e_2)^2 + e_3^2}\right| + \left|e_1 + e_2 - \frac{1}{2}\sqrt{(e_1 + 2e_2)^2 + e_3^2}\right| + 2|e_4| + 2|e_5|\right\} \quad (2\text{-}7)$$

Two possible cases can occur for Equation (2-7).

Case 1. If $|e_1 + e_2| > +\frac{1}{2}\sqrt{(e_1 + 2e_2)^2 + e_3^2}$

then $$\Delta V_{TOTAL} = (|e_1 + e_2| + |e_4| + |e_5|)\, V \quad (2\text{-}8)$$

Case 2. If $+\frac{1}{2}\sqrt{(e_1 + 2e_2)^2 + e_3^2} > |e_1 + e_2|$

then $$\Delta V_{TOTAL} = \left(+\frac{1}{2}\sqrt{(e_1 + 2e_2)^2 + e_3^2} + |e_4| + |e_5|\right) V \quad (2\text{-}9)$$

2. 3. 3. 3 Kick-Stage Apogee Burnout Error Allotment

From Equation (2-8) or (2-9), the allowable values of Δr, ΔV, $\Delta \dot{r}$, $\dot{W}$, and ΔL can be expressed as a function of the maximum available ΔV of the payload. Substituting for the e_i in (2-8) and (2-9), the requirements are

Case 1: $$\left|V\frac{\Delta r}{r} + \Delta V\right| + |\dot{W}| + \frac{V}{3\pi n}|\Delta L| \leq \Delta V_A \quad (2\text{-}10)$$

Case 2: $$\frac{1}{2}\sqrt{\left(\frac{V\Delta r}{r} + 2\Delta V\right)^2 + (\Delta \dot{r})^2} + |\dot{W}| + \frac{V}{3\pi n}|\Delta L| \leq \Delta V_A \quad (2\text{-}11)$$

where ΔV_A represents the available propulsion capability of the payload.

Typically, the total fuel capability of the payload may be on the order of 15 m/sec. Note that considerable flexibility in propulsion requirements for the longitude correction function is available by varying n.

2.4 MARS ORBITER MISSION

For this mission, it is assumed that the kick-stage guidance system[†] takes over after the Saturn V booster places the spacecraft[††] into the interplanetary transfer trajectory. The guidance system then is required for attitude referencing and control during the long coast phases, applying the midcourse ΔV corrections (based on ground-tracking data) and final insertion of the payload into the desired orbit about Mars.

The specification of the guidance system accuracy requirements, and hence the system configuration, is tentative due to the fact that definitive propulsion capabilities data and information regarding the desired final orbit characteristics and accuracy requirements are not available. Present studies on the planned Mars Voyager missions indicate that a sophisticated strapdown inertial guidance system for performing the midcourse and orbit insertion maneuvers may not be required although such a system has much to offer in the way of flexibility and growth potential to meet more demanding future Voyager mission requirements.[†††]

For purposes of this study the use of a complete three-axis inertial reference unit is postulated. A comparison of the capabilities of this type of system with simpler systems is made in Section 8. Use of an electro-optical approach guidance sensor to improve trajectory prediction accuracy

---

[†] Although the kick stage guidance system could conceivably be used to guide the Saturn V booster, that possibility is not considered in this study. It is assumed that ST-124 Inertial Guidance System located in the Saturn V Instrument Unit (IU) is used for the boost phase (launch through SIVB stage burnout including intermediate coast phases). A review of the performance capabilities of this guidance system shows that it is completely satisfactory for this mission phase.

[††] The interplanetary spacecraft (Voyager concept) includes the necessary propulsion capabilities for the midcourse corrections, Mars orbit insertion, and orbital trim maneuvers. For this mission, the "kick stage" and the interplanetary spacecraft are synonomous. The "payload" consists of a Mars landing capsule deployed from the spacecraft after insertion plus the scientific instrumentation aboard the main spacecraft.

[†††] These requirements are currently undefined. However, it is reasonable to expect, based on past experience, that as the missions become more sophisticated the mission accuracy requirements will become more demanding. Some possible advanced Voyager missions (1975 through 1984) are described in a TRW study performed for JPL, Ref 2-1.

near the target planet is also postulated although use of such a sensor appears to be necessary only if terminal mission accuracy requirements[†] are considerably more stringent than those imposed by the present Voyager mission.

2.4.1 Mission Characteristics

It is beyond the scope of this report to furnish effectively even a general comprehension of the complex mission analysis[††] which must be performed before the selection of representative Mars trajectories for guidance system evaluation is possible. For the purposes of this study, trajectories available from previous studies conducted at TRW were used.

For the purpose of generating guidance system functional and performance requirements, the current Voyager mission requirements were used as the starting point. Mission requirements and constraints were established from the "Performance and Design Requirements for the 1973 Voyager Mission," Ref 2-4. The principal mission requirements and constraints which directly concern the launch vehicle performance capabilities and guidance system accuracy are briefly discussed in the following paragraphs.

- Ascent Mode - The parking orbit ascent mode will be utilized for the 1973 mission. Parking orbit coast times will vary between 10 and 90 min.
- Transfer Trajectory - Type I transfer trajectories shall be used for the 1973 mission.
- Launch Energy - A maximum injection energy C_3 of 32.5 km^2/sec^2 will be assumed for the 1973 mission.
- Launch Window - A nominal launch period of 45 to 60 days and a minimum daily firing window of 2 hr, will be provided.

[†] The major source of error in the knowledge of the approach trajectory with respect to Mars is the uncertainty in the orbital position of Mars relative to the Earth (see Section 9, for further discussion).

[††] Some of the more basic mission analysis concepts, particularly those relating to launch vehicle and guidance system requirements, are discussed in Ref 2-2 and 2-3.

- Declination of Launch Asymptote - The absolute value of the declination of the launch asymptote (DLA) will not exceed the following values: $5 \text{ deg} \leq |\text{DLA}| \leq 36 \text{ deg}$. Declination of the launch asymptote is dependent on both liftoff and coast time. The injection errors attributable to the guidance hardware are also a strong function of this coast time.

- $V_{\infty_{Mars}}$ - To achieve a reasonable vehicle mass fraction into Mars orbit, the approach $V_{\infty_{Mars}}$ magnitude must not exceed a maximum of 3.25 km/sec.

- Injection Accuracy - The miss plus time-of-flight trajectory dispersions due to random errors arising from launch vehicle injection errors shall be correctable with a 1-σ midcourse trajectory correction velocity increment of 5 m/sec or less applied 2 days after injection.

- Mars Orbit Characteristics - The periapsis altitudes of the desired Mars satellite orbits lie between 500 and 1,500 km. The apoapsis altitudes lie between 10,000 and 20,000 km. These ranges apply both before and after orbit trim. No requirements have been set on either orbital inclination or the orientation of the line of apsides. Thus, the deboost velocity is assumed to be applied tangentially at the periares common to the hyperbolic approach trajectory and the elliptic orbit.

Since the launch phase guidance functions will be performed by the Saturn V guidance system, only the interplanetary trajectory is of interest here. The Earth-Mars trajectory chosen[†] has a launch date of 11 May 1971 and a trip time of 177 days. Characteristics of interest are shown in Figures 2-1, 2-2, and Table 2-IV (from Ref 2-5). Guidance system performance requirements based on the Voyager mission requirements are discussed in the following section. As a guideline for determining final approach and orbit accuracy requirements, equations for parametric evaluation of velocity requirements are also presented in Paragraph 2.4.3.

[†]Present Voyager planning calls for use of the Saturn V launch vehicle with the first mission scheduled for 1973. Trajectories for the 1973 launch opportunity were not available during this study. Since only post injection guidance is considered, the differences in boost phase trajectories are insignificant for the purposes of this study. The interplanetary trajectory used adheres to the mission constraints discussed above.

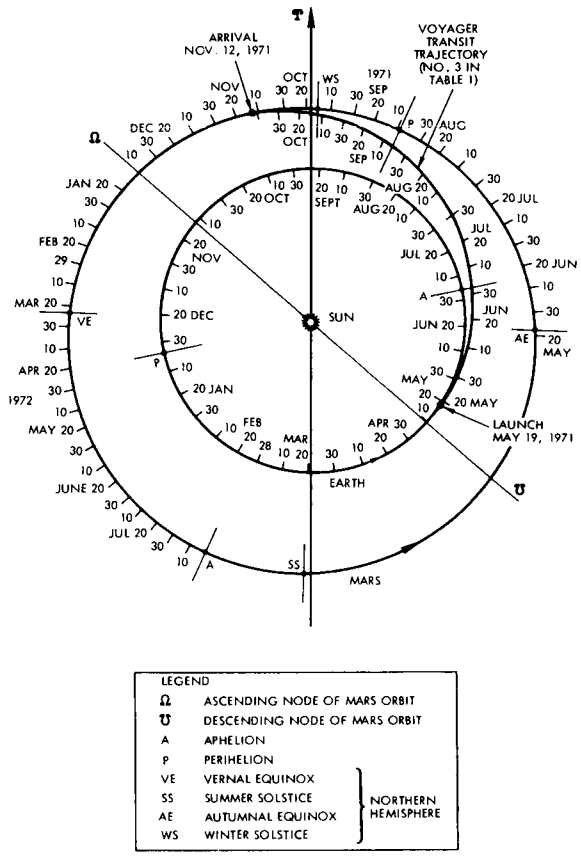

Figure 2-1. Voyager Sample Trajectory (from Ref 2-5)

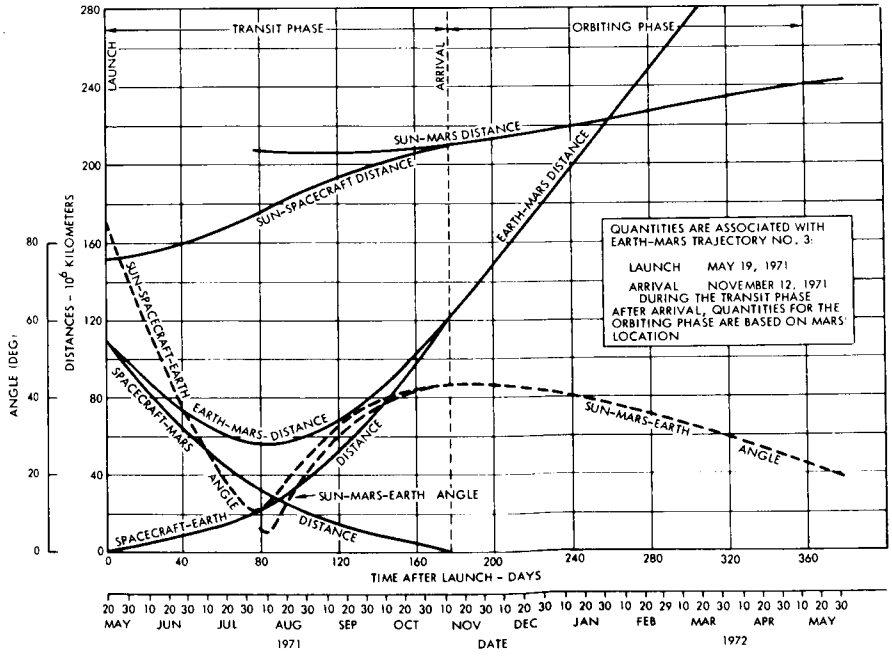

Figure 2-2. Geometrical Quantities Versus Time (from Ref 2-5)

Table 2-IV. Characteristics of 1971 Earth-Mars Trajectory (from Ref 2-5)

Launch date	May 19, 1971
Arrival date	November 12, 1971
Time of flight	177 days
Departure asymptote (from Earth)	
V_∞	2.92 km/sec
C_3	8.53 km^2/sec^2
Angle to ecliptic	-16 deg
Angle to Sun-Earth line	88 deg
Approach asymptote (to Mars)	
V_∞	3.25 km/sec
Angle to plane of Mars' orbit	-3 deg
Angle to Mars-Sun line	119 deg
Interplanetary Orbit	
True anomaly at arrival	142.5 deg
True anomaly at launch	4.5 deg
Heliocentric central angle	138 deg
Inclination to ecliptic	1.5 deg
Perihelion distance from Sun	151.2 x 10^6 km
Aphelion distance from Sun	220.5 x 10^6 km
Eccentricity	0.1853

2.4.2 Operational Sequences

The operational sequences for the Mars orbiter mission are assumed to be as outlined below:

a) Launch, parking orbit, and injection into interplanetary trajectory: These phases are presumed to be under the control of the primary Saturn guidance system. The kick-stage (spacecraft) guidance is in a semidormant state.

b) Separation from booster and first cruise phase: The kick-stage strapdown inertial subsystem used to provide rate damping signals to stabilize the separation induced tumbling transients. After the rate stabilization is accomplished, a celestial reference acquisition sequence is initiated. The celestial references will be the Sun and the star Canopus. The Sun and Canopus trackers will be body-fixed and will serve as the primary long-term inertial attitude references. After Sun/Canopus lockon is achieved, the gyros may be turned off (except for heaters) until required for the midcourse reorientation maneuver.

Deep Space Network (DSN) tracking will be used during this cruise phase for orbit determination and to compute the first midcourse velocity correction required to reduce the effects of injection errors. The midcourse thrust vector pointing and magnitude commands and time of execution command will be transmitted to the onboard guidance system for execution.

c) Midcourse execution: If the gyros were shutdown in the previous cruise phase, wheel power would be applied sufficiently early to ensure proper gyro operation during the following sequence. Ten to 30 min (the time will be dependent on available spacecraft slew rates and maximum required turn-through angles) prior to the time of execution of the midcourse correction burn, vehicle rotations will be commanded to orient the thrust vector in the required inertial direction. The attitude change sequence will depend on the type of inertial configuration chosen. Three basic inertial configurations can be considered:

Ia) A simple inertial configuration with a 3-axis gyro package and one longitudinal axis integrating accelerometer.

Ib) The above with the addition of two orthogonal lateral accelerometers (of the nonintegrating type).

II) A full strapdown inertial system, with a 3-axis gyro package and a 3-axis integrating accelerometer package, with full direction cosine computation capability.

For Configurations I, the orientation maneuver will be entirely open loop, using precomputed precision torquing signals applied sequentially to two out of the three gyros. For Configuration II, closed-loop control over final attitude can be exercised and simultaneous bi-axial attitude changes can be commanded.

When the proper attitude is achieved, and at the correct time, midcourse burn is initiated. Attitude control during burn is again dependent on the inertial configuration chosen:

Ia) For Configuration Ia, attitude will be maintained under control of the three rate-integrating gyros. Engine misalignments will be the largest source of burnout error in this case.

Ib) For Configuration Ib, attitude will again be maintained under control of the three rate-integrating gyros with the important modification that signals processed from the nonintegrating accelerometers can be used to provide attitude correction signals to largely compensate for engine misalignments.

II) For Configuration II, full 3-axis $\Delta\overline{V}$ control capability is provided and engine misalignments become unimportant. Further discussions will be limited to this configuration.

d) Subsequent cruise and midcourse correction phases: After completion of the first midcourse correction, the spacecraft will be "unwound" to the original Sun/Canopus reference attitude and continue in a cruise phase identical to the first. One or more further midcourse corrections will be made in a manner similar to the first. After the last midcourse correction, the trajectory will have been corrected such that terminal approach conditions meet mission requirements. (The midcourse correction requirements are defined in Paragraph 2.4.3.)

e) Approach phase: On the premise that a mission with terminal approach requirements is more stringent than those imposed on Mariner 1969 or Voyager, it is postulated that some form of approach navigation more accurate than available with DSN tracking will be required. To cover this possibility, this study includes considerations of an approach sensor. The sensor to be considered will be a planet tracker, with two degrees of electronic scan freedom relative to the kick stage. The sensor can provide:

1) Stadimetric ranging data

2) Clock and cone angles relative to the Sun/Canopus frame of reference (see Figure 9-1).

On the basis of approach measurements provided either via DSIF alone or in combination with the approach sensor, the approach trajectory will be determined and the following will be computed:

1) Magnitude and inertial direction of the deboost velocity to achieve the desired orbit about Mars.

2) Time of initiation of the deboost thrust.

DSIF orbit determination accuracy requirements are discussed in Section 6.

f) Deboost velocity application: The sequence of events and operations of this phase is the same as for the midcourse correction phase.

2.4.3 Guidance System Performance Requirements

2.4.3.1 Terminal Accuracy Requirements

Because of 1) midcourse errors, 2) imperfect approach trajectory estimation, and 3) execution errors at deboost burn, the final orbit will differ from the desired orbit. The Voyager mission requirements† shown in Table 2-V have been translated into system accuracy requirements for these three types of errors and are summarized in the following paragraphs.

Table 2-V. Voyager Mission Terminal Accuracy Requirements

Parameter	Allowable Dispersion (3σ)
Impact Parameter $\overline{B}$	500 km
Time of Encounter	3 min
Periapsis Altitude of Initial Oribt (prior to orbit trim maneuver)	30 percent
Orbital Inclination of Initial Orbit	5 deg

† The overall mission accuracy requirements have not been firmly established for the Voyager mission. The requirements stated in Table 2-V are based on preliminary Voyager requirements for the early missions.

2.4.3.2 Orbit Correction Requirements

The required precision with which the interplanetary spacecraft must execute the arrival date separation maneuver † and interplanetary trajectory corrections is a complicated function involving a number of considerations such as the final mission accuracy requirements, the orbit determination uncertainty as a function of time, the number of maneuvers to be performed, the amount of trajectory biasing necessary to satisfy the probability-of-impact constraint, the orbit trim philosophy, and several other considerations, all of which are vitally interwoven in the mission formulation. In order to achieve a rational balance among the various mission accuracy requirements, the maximum allowable maneuver errors during different phases of the flight were specified (Table 2-VI from Ref 2-4). The maximum allowable maneuver errors are defined by an error ellipsoid with an axis of symmetry parallel to the specified velocity increment.

2.4.3.3 Orbit Determination Accuracy Requirements

To meet the overall mission accuracy requirements given above, specification must also be placed on the orbit determination accuracy using the earth-based DSIF. Because of the trajectory geometry, tracking system characteristics, and the presence of trajectory disturbances, the orbit determination uncertainties vary throughout the mission. The allowable uncertainties (from Ref 2-4) are shown in Table 2-VII.

2.4.4 Analysis of Orbit Correction Requirements

Paragraph 2.4.3 indicates that the final orbit will differ from the desired orbit because of the effects of approach orbit estimation errors and maneuver execution errors. It is assumed that final orbit trim is to be accomplished by the interplanetary spacecraft. Limitations on spacecraft propulsion capability for orbit trim set constraints on the required precision of the initial orbit established. The final orbital requirements have not been established for the Voyager mission. The range of permissible orbit altitudes is given in Paragraph 2.4.3.1.

† This maneuver is intended to separate the arrival time of the two spacecraft launched by the Saturn V booster by at least 8 days. The maneuver is made in a similar manner, but prior to, the first midcourse correction.

Table 2-VI. Maximum Velocity Error Ellipsoids (from Ref 2-4)

Maneuver	Minimum Velocity Increments (m/sec)	Maximum Velocity Increments† (m/sec)	3σ Error Component Parallel to Specified Velocity Increment (meters/second or % of specified velocity increment)	3σ Error Component Normal to Specified Velocity Increment Along Any Two Orthogonal Axes (meters/second or % of specified velocity increment)
Interplanetary trajectory corrections	1.0 (0.3)	100 (200)	Larger of 0.1 m/sec or 3.0% (larger of 0.03 m/sec or 2.0%)	Larger of 0.1 m/sec or 3.0% (larger of 0.03 m/sec or 2.0%)
Mars orbit insertion	1.0 km/sec	2.0 km/sec	3.0% (1.5%)	5.0% (3.0%)
Mars orbit trim	5.0 (1.5)	150	Larger of 0.5 m/sec or 5.0% (larger of 0.2 m/sec or 3.0%)	Larger of 0.5 m/sec or 5.0% (larger of 0.2 m/sec or 3.0%)

Note: Numbers not in parentheses are maximum values.

Numbers in parentheses are design goals.

†For purpose of error calculations only.

Table 2-VII. Maximum Allowable 3σ Orbit Determination Uncertainties (from Ref 2-4)

Time at Which Orbit Estimate is Calculated	Magnitude and Time of Prior Orbit Corruptions†	Uncertainty in Magnitude of Impact Parameter Vector (km)	Uncertainty in Aiming Plane Normal to Nominal Impact Parameter Vector (km)	Uncertainty in Time of Encounter (min)
Injection +2 days	Planetary vehicle injection	2000 (1000)	2000 (1000)	15 (7)
Injection +30 days	150 m/sec arrival date adjustment and interplanetary trajectory correction at I +5 days	1000 (500)	1500 (750)	10 (5)
Encounter -30 days	5 m/sec interplanetary trajectory correction at I +30 days	500 (300)	750 (500)	4 (3)
Encounter -2 days	1 m/sec interplanetary trajectory correction at E -30	400 (150)	500 (200)	3 (1)
Encounter -4 hr	Same as above	300 (100)	500 (150)	2 (0.5)
Orbit insertion +4 returns to orbit periapsis	2.2 km/sec orbit insertion maneuver	10 (1)	10^{-4} (10^{-5})	5 (0.1)
Orbit trim +3 returns to orbit periapsis	Orbit trim maneuver of 100 m/sec	10 (1)	10^{-4} (10^{-5})	5 (0.1)

†For purposes of error analysis only. Numbers not in parentheses are maximum allowable uncertainties.
Numbers in parentheses are design goals.

The orbit trim profile is assumed to consist of four separate burns as follows:

a) Perform a Hohmann transfer from the perigee of the imperfect orbit to the desired apoares distance.

b) Perform a Hohmann transfer from this new apoares distance to the desired periares distance.

c) Execute a burn to rotate the line of apsides.

d) Perform the desired inclination correction.

The above profile is not optimum but does provide a simple means for establishing a conservative estimate of the precision with which the spacecraft must be placed in orbit.

2.4.4.1 In-Plane Errors

The in-plane errors after the orbit insertion burn are

$$\Delta r_a = r_a - R_a$$

$$\Delta r_p = r_p - R_p$$

$$\Delta\psi = \psi - \Psi$$

where

r_a, r_p = apoares and periares, respectively, of orbit established by the orbit insertion burn.

R_a, R_p = apoares and periares, respectively, of the desired orbit

ψ, Ψ = angles defining actual and desired lines of apsides

Hohmann Transfer to Desired Apoares (Burn a). The velocity existing at the periares of the orbit established by the spacecraft is

$$V_p = \left[2\mu \frac{r_a/r_p}{r_a + r_p}\right]^{1/2}$$

$$\cong \sqrt{2\mu \frac{R_a/R_p}{R_a + R_p}} \left[1 + \frac{R_p/R_a}{R_a + R_p}\Delta r_a - \frac{2 + R_a/R_p}{R_a + R_p}\Delta r_p\right]^{1/2} \quad (2\text{-}12)$$

The velocity at this periares required to reach apoares R_a is

$$V_{p_{req'd}} = \left[2\mu \frac{R_a/r_p}{R_a + r_p}\right]^{1/2}$$

$$\cong \sqrt{2\mu \frac{R_a/R_p}{R_a + R_p}} \left[1 - \frac{1}{R_a + R_p} \Delta r_a - \frac{2 + R_a/R_p}{R_a + R_p} \Delta r_p\right]^{1/2} \tag{2-13}$$

Differencing Equations (2-12) and (2-13), the required ΔV for the Hohmann transfer is

$$\Delta V_a = V_p - V_{p_{req'd}}$$

$$\cong \sqrt{2\mu \frac{R_a/R_p}{R_a + R_p}} \left[\frac{\Delta r_a}{2 R_a}\right] \tag{2-14}$$

Hohmann Transfer to Desired Periares (Burn b). The apoares velocity following Burn a is

$$V_a = \left[2\mu \frac{r_p/R_a}{R_a + r_p}\right]^{1/2}$$

$$\cong \sqrt{2\mu \frac{R_p/R_a}{R_a + R_p}} \left[1 + \frac{R_a/R_p}{R_a + R_p} \Delta r_p\right]^{1/2} \tag{2-15}$$

The apoares velocity required to reach periares R_p is

$$V_{a_{req'd}} = \sqrt{2\mu \frac{R_p/R_a}{R_a + R_p}} \tag{2-16}$$

Differencing Equations (2-15) and (2-16), the required ΔV for the Hohmann transfer is

$$\Delta V_b = V_a - V_{a_{req'd}}$$

$$\cong \sqrt{2\mu \frac{R_p/R_a}{R_a + R_p}} \left[\frac{R_a/R_p}{2 (R_a + R_p)} \Delta r_p\right] \tag{2-17}$$

Rotation of Line of Apsides (Burn c). After the correct apsis distances have been established, the line of apsides can be rotated by applying a radial ΔV increment at

$$f = \frac{\Delta\psi}{2} \text{ or } \pi + \frac{\Delta\psi}{2}$$

where f is the true anomaly measured from the newly established periares.

The required velocity increment at either f is

$$\Delta V_c = (1 - R_p/R_a) \sqrt{2\mu \frac{R_a/R_p}{R_a + R_p}} \sin \frac{\Delta\psi}{2} \qquad (2\text{-}18)$$

Inclination Error (Burn d). The corrective ΔV required for inclination change is

$$\Delta V_d = V \sqrt{1 - \cos \Delta i}$$

where V is the velocity at the true anomaly angle f_e, at the node, and Δi is the desired change in inclination. The maximum for the above expression for ΔV_d occurs at $f_e = 0^o$ and is

$$\Delta V_{d_{max}} = \sqrt{2\mu \frac{R_a/R_p}{R_a + R_p}} \sqrt{1 - \cos \Delta i} \qquad (2\text{-}19)$$

2.4.4.2 Total Corrective Velocity Requirement

The total velocity increment required from the payload is the sum of the absolute values from Equations (2-14), (2-17), (2-18) and (2-19), or

$$\Delta V_{Total} = |\Delta V_a| + |\Delta V_b| + |\Delta V_c| + |\Delta V_d|$$

$$= \sqrt{2\mu \frac{R_a/R_p}{R_a + R_p}} \left\{ \frac{|\Delta r_a|}{2R_a} + \frac{|\Delta r_p|}{2(R_a + R_p)} + (1 - R_p/R_a) \sin \frac{|\Delta\psi|}{2} + \sqrt{1 - \cos \Delta i} \right\} \qquad (2\text{-}20)$$

2.4.5 Analysis of Approach Guidance Requirements

The velocity increment ΔV required to place the interplanetary spacecraft into the desired aerocentric orbit is determined on the basis of approach trajectory parameters determined by DSN tracking, by the use of optical sightings, or a combination of both. If on the basis of approach trajectory estimation it is determined that the expected periapsis distance will be in error, two alternative guidance techniques are available.

a) At some time T before encounter, apply a corrective velocity increment ΔV_c normal to the approach trajectory to achieve the correct periares distance R_p. At periares, apply the orbit insertion retrovelocity ΔV_p to achieve the desired apoares distance, R_a. The total velocity increment required to insert the kick stage/payload into the nominally desired aerocentric orbit is then $\Delta V_T = |\Delta V_c| + |\Delta V_p|$. This technique is illustrated in Figure 2-3.

b) On the basis of approach orbit parameter estimations, apply a ΔV_p at encounter (i.e., at T = 0) to achieve the desired apoares distance R_a. At apoares, apply a corrective velocity increment ΔV_a to achieve the desired R_p. The total velocity increment is $\Delta V_T = |\Delta V_a| + |\Delta V_p|$. This technique is illustrated in Figure 2-4.

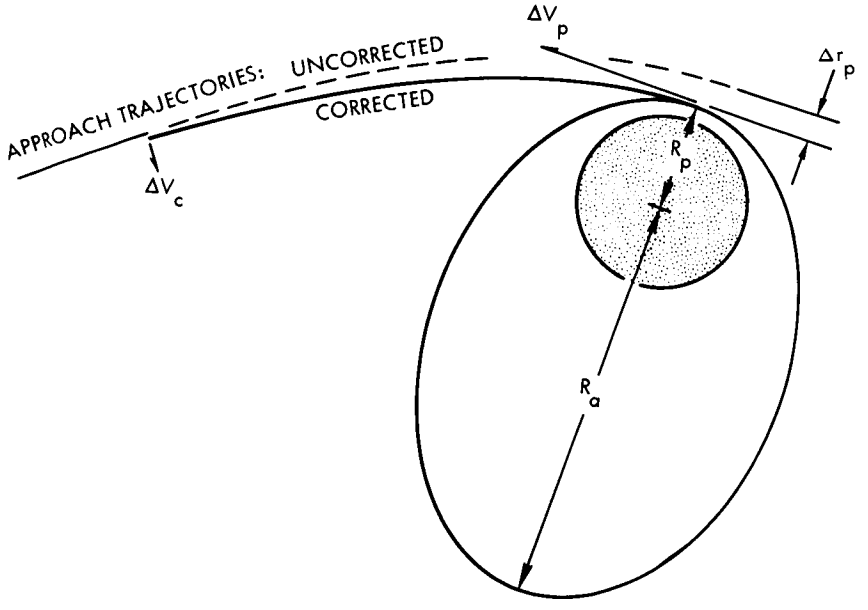

Figure 2-3. Method of Achieving Desired R_p and R_a by Combination of Approach Orbit Correction and Retro ΔV_p

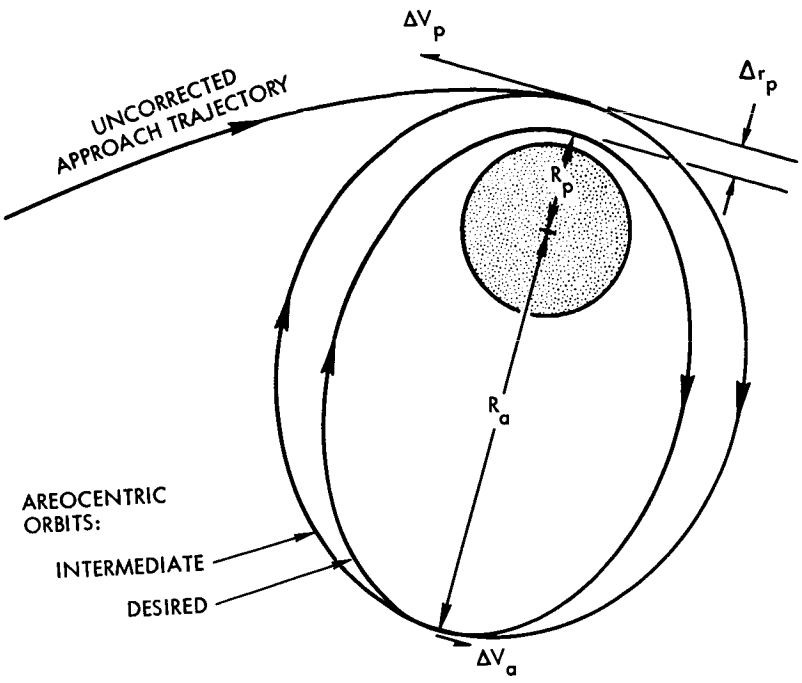

Figure 2-4. Method of Achieving Desired R_p and R_a by Applying Required Velocity Increments at Two Apsides

The above sequences assume no requirements on the orientation of the line of apsides and have been chosen primarily to provide an insight as to when reliable approach trajectory parameters must be established to perform meaningful and efficient approach trajectory corrections. That is, if approach trajectory estimation data are not expected to be accurate until two days before encounter (T = 2), then it would be meaningless to apply a corrective ΔV_c at any time before this.

The results of a parametric study for Technique (a) above are presented in Figure 2-5. The desired areocentric orbit was assumed to have periapsis and apoapsis altitudes of 1,000 and 10,000 km, respectively. The approach velocity was taken to be V_∞ = 3 km/sec, and approach periares errors of -500 to +500 km were covered. For $\Delta\gamma_p$ = 500 km, approximately 1.5 percent more ΔV is required by waiting until T = 0.25 days as compared to T = 4 days. This is a negligible penalty to pay for the added orbit estimation accuracy obtainable by the 3.75 days of additional tracking.

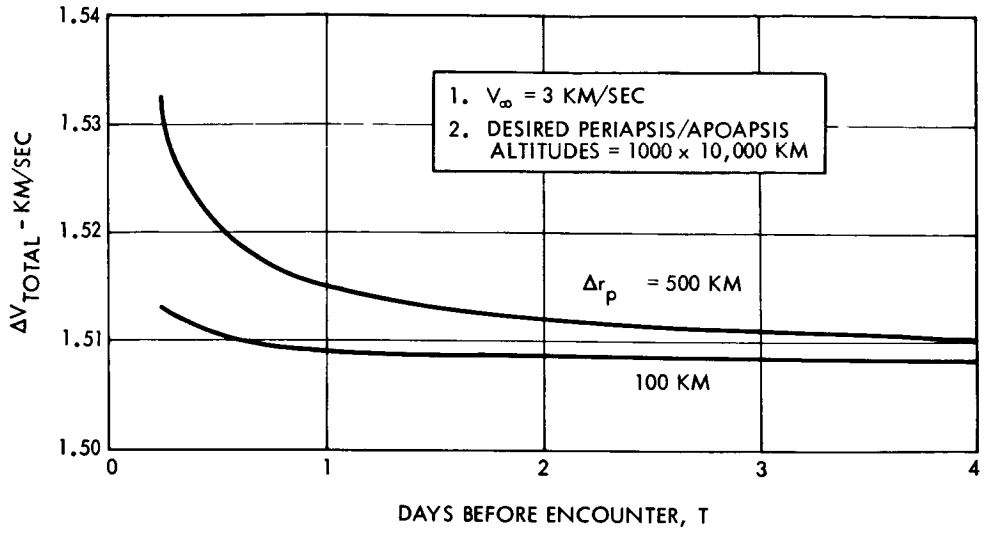

Figure 2-5. Total Velocity Increment Required for Approach Trajectory Correction and Orbit Insertion Versus Time of Correction Application

The trend of the curves in Figure 2-5 would seem to indicate that if one were to wait until T = 0, the ΔV would become excessive. Fortunately this is not so as evidenced by the plots in Figures 2-6, 2-7, and 2-8. It is true (at least for $\Delta r_p > 0$) that the ΔV_{TOTAL} for Technique (b) is larger than for Technique (a); however, the increase is only on the order of 7 percent, worst case. Technique (b) offers a reasonable compromise between fuel requirements and approach trajectory orbit determination accuracy and is recommended as the procedure to follow. Tracking, either DSIF alone or in combination with optical aids, will be continued until about 1 or 2 hr prior to encounter. By this time, the approach trajectory position estimation errors will have been reduced to the order of 10 to 100 km and a reasonably accurate computation of ΔV_p to be applied at encounter can be computed.

2.5 LUNAR ORBITER MISSION

The booster/payload combination for this mission is assumed to be the Atlas SLV3X/Centaur/HEUS/lunar orbiter. Based on past experience, e.g, Surveyor and Lunar Orbiter, the need for a sophisticated inertial guidance system on the spacecraft is questionable for the translunar and lunar operations phases of this mission. However, for this study, it is assumed that the kick stage guidance system is to be used not only for these

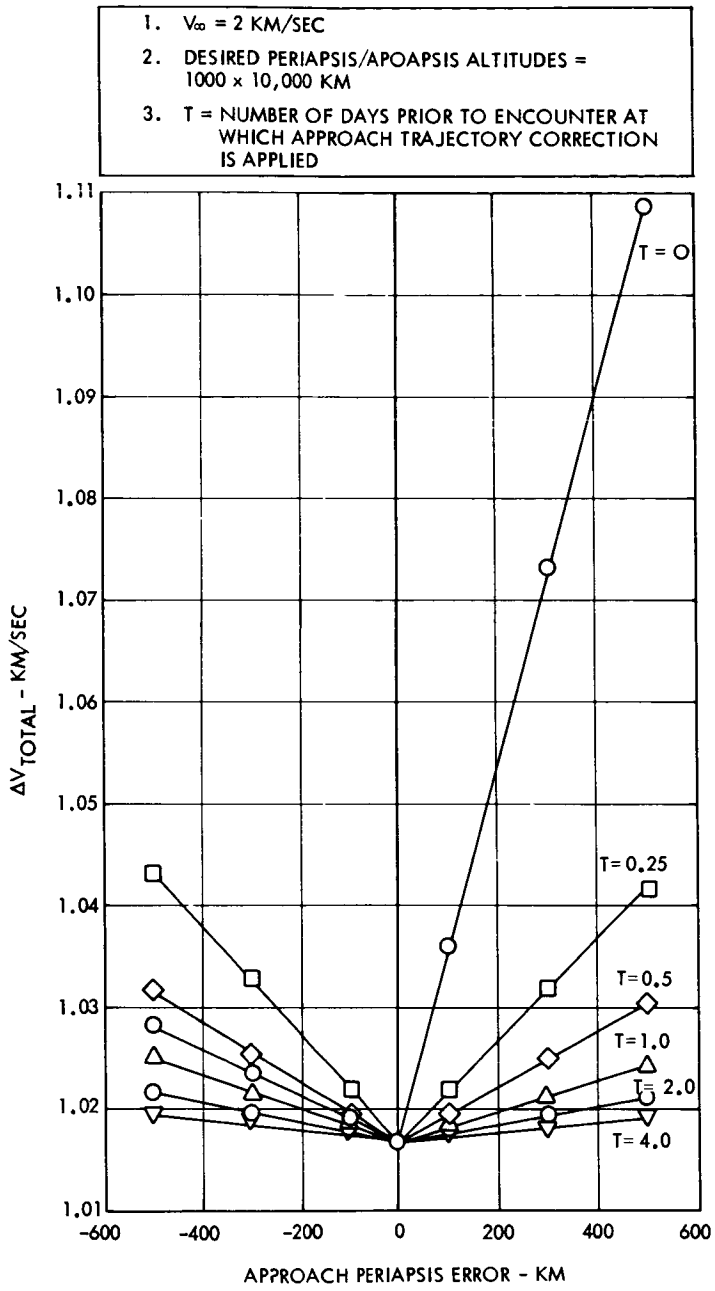

Figure 2-6. Total Velocity Increment Required for Approach Trajectory Correction and Orbit Insertion, V_∞ = 2 km/sec

phases but also for primary guidance and control of the lower booster stages. The operational sequences and functional requirements are summarized below.

2.5.1 Mission Characteristics

This mission is operationally very similar to the Mars Orbiter Mission discussed in Subsection 2.4. The primary difference to be noted is

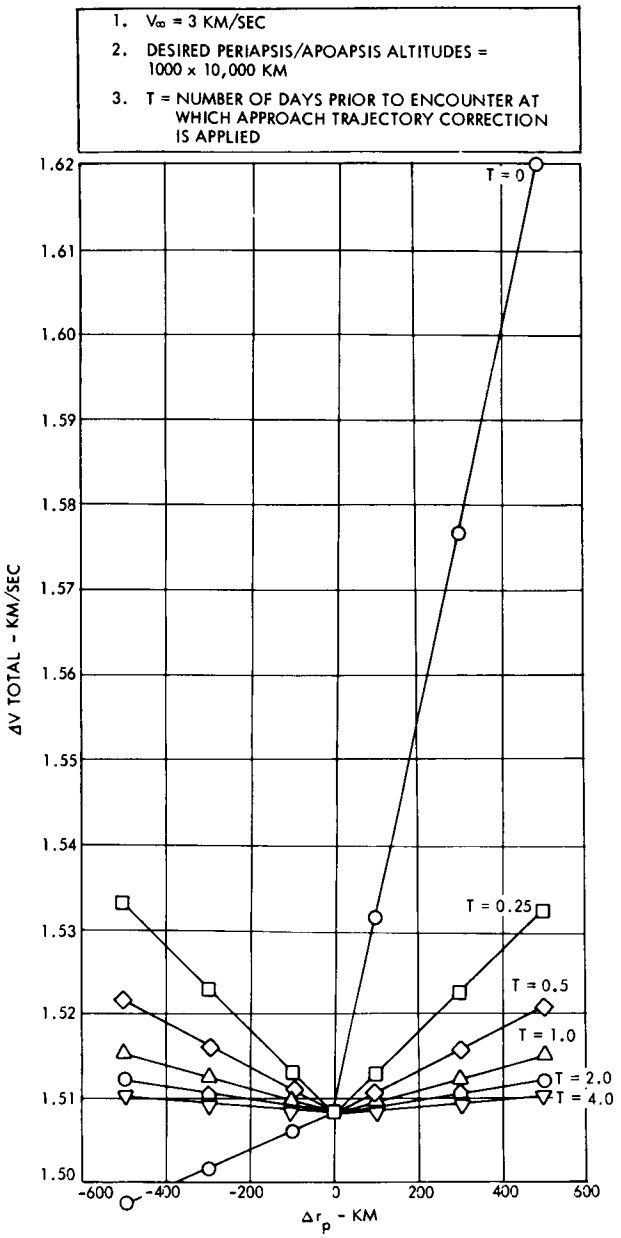

Figure 2-7. Total Velocity Increment Required for Approach Trajectory Correction and Orbit Insertion, V_∞ = 3 km/sec

that USBS/DSIF tracking and orbit estimation accuracy will probably be sufficient to obviate the need for an approach sensor.

A parking orbit ascent trajectory with a coast time of approximately 14 min was selected for this study. The rationale for this selection was based on the fact that the largest figure-of-merit is obtained for parking orbit missions having coast times in this range.

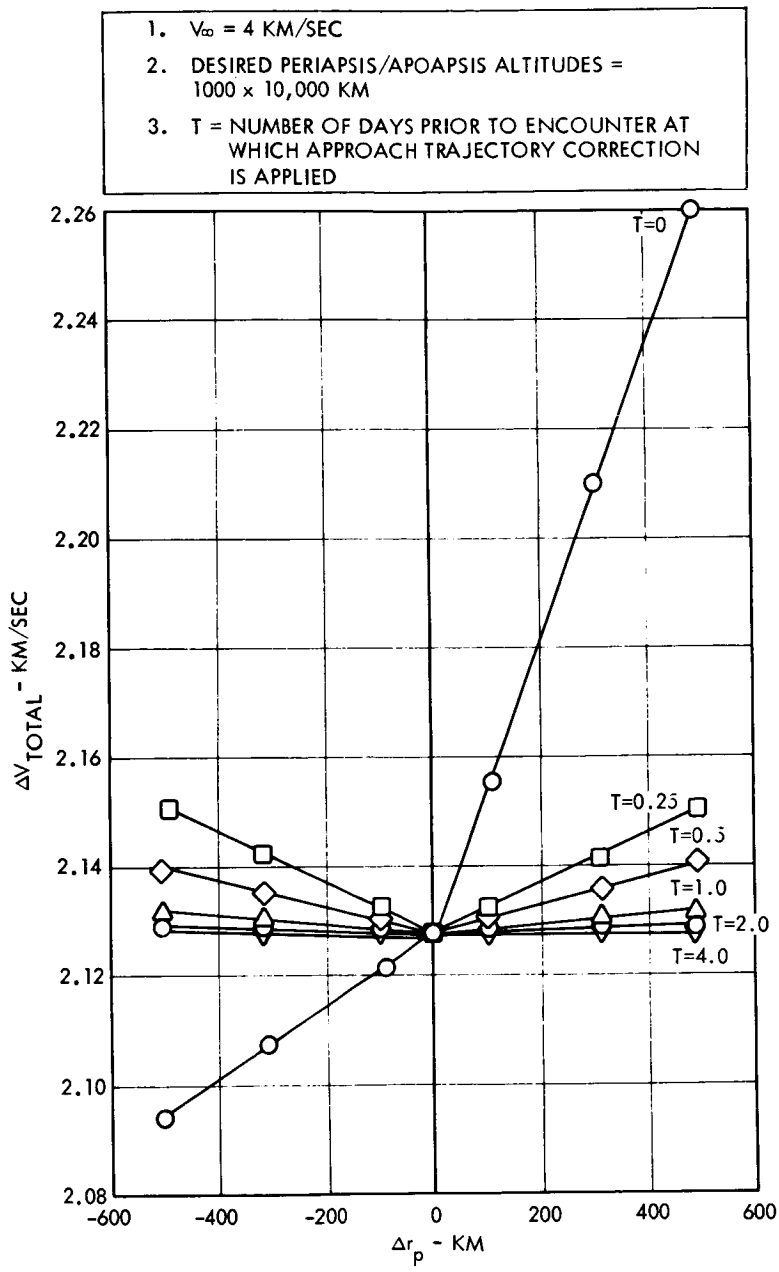

Figure 2-8. Total Velocity Increment Required for Approach Trajectory Correction and Orbit Insertion, V_∞ = 4 km/sec

The lunar mission reference trajectory used for error analysis purposes was a closed-loop targeted trajectory for the Atlas Centaur (AC-12 Configuration) launch vehicle. The trajectory profile is shaped by a predetermined pitch steering program from launch to booster cutoff (BECO). After BECO the sustainer is ignited and closed loop guidance is initiated. The guidance system continues to steer the vehicle through sustainer cutoff (SECO) and Centaur first-burn ignition until parking

orbit is reached. The first-burn duration (launch to parking orbit injection) is approximately 585 sec and injects the vehicle into a 167 km perigee, 173 km apogee orbit. The Centaur stage coasts in this orbit for 845 sec, whereupon it reignites and burns for another 106 sec, injecting the payload into a highly elliptical (e = 0.97167) transfer orbit. The transfer time is approximately 65 hr. The event times for the launch through injection phase are shown in Table 2-VIII.

Table 2-VIII. Event Times for Lunar Mission (Launch Through Injection)

Time (sec)	Event
0.	Start first powered phase (boost)
585.04952	Start first coast phase (circular)
1426.8700	Start second powered phase (injection)
1603.2040	End second powered phase

Two midcourse corrections are assumed for this mission, the first at 15 to 20 hr after injection and the second a few hours prior to lunar intercept.

Deboost is made into an intermediate orbit with approximate apsis distances of 3590 and 1990 km. The deboost velocity increment required is 745 m/sec. After accurate determination of the orbit has been made, a final orbit adjust maneuver is made to place the vehicle into a 3589 by 1784 km orbit.

2.5.2 Guidance System Operational Sequence

The guidance system operational sequence for the various phases of the lunar orbiter mission studied at TRW is described below:

a) Launch and boost to ~167 km parking orbit: The kick stage strapdown inertial guidance subsystem will provide the guidance function for this phase.

b) Coast in parking orbit: The kick stage and payload will coast in the parking orbit until translunar injection, which occurs approximately 14 min after entering the parking orbit. The inertial guidance subsystem will be relegated to the role of an attitude reference during this phase.

c) Translunar injection: The kick stage will be ignited to inject the kick stage/payload into the translunar trajectory. Attitude and burn control will be provided by the strapdown inertial guidance subsystem.

d) Coast until first midcourse correction: Following the injection burn, a celestial reference acquisition sequence is initiated and the kick stage/payload will be attitude fixed to the sun and the star Canopus via body-fixed sun and star sensors. The strapdown accelerometers can be turned off (except for heaters) and the flight computer algorithm for updating the direction cosines can be placed in a standby mode.

Deep-Space Network (DSIF) tracking will be used during this coast phase for orbit determination and to compute the midcourse velocity correction required to reduce the effects of injection errors. The midcourse thrust vector pointing and magnitude commands and time of execution command will be transmitted to the kick-stage system.

e) First midcourse correction: Approximately 15 to 20 hr from translunar injection, the first midcourse correction will be executed. Ten to 30 min prior to the time of execution, the accelerometers will be turned on, the direction cosine solution algorithm will be initialized, and vehicle rotations will be commanded to orient the thrust vector in the required inertial direction. When the proper attitude is achieved, and at the correct time, midcourse burn is initiated.

f) Second coast phase and second midcourse correction: After completion of the first midcourse correction, the kick stage/payload will be "unwound" to the original Sun/Canopus reference attitude and continue in a cruise phase identical to the first. The second midcourse burn will occur a few hours prior to translunar injection and is designed to null selected miss components at lunar intercept.

g) Coast until deboost maneuver into intermediate lunar orbit: This phase will be identical to the other coast phases.

h) Deboost into intermediate lunar orbit: Based on the tracking data obtained, the kick stage/payload will be injected into an intermediate orbit with approximate apsis distances of 3590 and 1990 km. The deboost velocity increment required is approximately 745 m/sec.

i) Coast in intermediate orbit: The amount of coast time in the intermediate orbit will be chosen such that the orbit is properly phased with respect to the preselected target. The kick stage/payload will be tracked by DSIF stations to determine orbital parameters and the retromaneuver required to place the kick stage/payload into the final orbit.

j) Retro into final orbit: Based upon the orbital estimates obtained from DSIF tracking data, and controlled by the strapdown inertial guidance system, the spacecraft will be injected into the final orbit. The desired final orbit will nominally have an apocynthion and pericynthion of 3589 km and 1784 km, respectively.

2.5.3 Performance Requirements

2.5.3.1 Translunar Injection

The kick/payload must be injected into a translunar trajectory such that the desired lunar orbit can be achieved by the kick stage propulsive capability. A set of deviations† of the kick stage/payload position and velocity from the nominal trajectory which will permit the meeting of the requirements of the final orbit is listed in Table 2-IX.

Table 2-IX. Guidance Requirements for Translunar Injection and Translunar Coast Phases (1σ Values)

Parameter	Translunar Injection	Coast until First Midcourse Correction	Coast until Second Midcourse Correction	Coast until Deboost into Intermediate Lunar Orbit
Δx	14.9 km	685 km	160 km	81 km
Δy	18.4 km	996 km	358 km	47 km
Δz	19.5 km	680 km	262 km	16.7 km
$\Delta \dot{x}$	21.4 m/sec	18.8 m/sec	2.1 m/sec	15.3 m/sec
$\Delta \dot{y}$	19.5 m/sec	10.8 m/sec	4.6 m/sec	30 m/sec
$\Delta \dot{z}$	32.4 m/sec	12.0 m/sec	3.0 m/sec	14.1 m/sec
Coordinate System	ECI	ECI	ECI	Selenographic

†The position and velocity errors are stated either in an earth-centered inertial (ECI) vernal-equinox, equatorial coordinate system or in selenographic coordinates. Note that these errors are stated as deviations from the a priori nominal trajectory.

2.5.3.2 Translunar Coast Phases

Prior to the first (second) midocurse corrections, the deviations of position and velocity from the nominal trajectory must be within certain limits. These limits are determined by the correction capability of the midcourse correction system. A set of injection deviations from the nominal trajectory propagated to the point of the first midcourse correction which satsify the midcourse correction capability are listed in Table 2-IX. Prior to the second midcourse maneuver, the deviations must be such that the correction of miss components at the target are within the capability of the second midcourse maneuver. A set which satisfies these requirements is shown in Table 2-IX.

During each phase, the position and velocity of the kick stage/payload will be determined by earth-based tracking stations. At the end of the final coast phase, as a result of the midcourse corrections, the position and velocity of the kick stage/payload must be within the limits shown in the last column of Table 2-IX.

2.5.3.3 Midcourse Correction Maneuvers

Approximately 15 hr after translunar injection, the first midcourse correction will be commanded. The requirements on the maneuver execution errors are shown in Table 2-X. The guidance law assumed is directed to nulling the errors in the impact plane and error in the time of flight or the impact plane error only.† Hence, these controlled quantities will be reduced by the midcourse maneuver.

The second midcourse maneuver will be executed a few hours prior to translunar injection. The requirements on the maneuver execution errors are in Table 2-X.

---

† The performance analysis results are presented in Section 8 for both guidance laws. Detailed mission payload requirementd dictate the choice for a given mission.

Table 2-X. Guidance and Control Requirements for First and Second Midcourse Corrections

Parameter	First Midcourse Correction	Second Midcourse Correction
Pointing error	0.4 deg (1σ)	0.4 deg (1σ)
Error proportional to ΔV	0.04% (1σ)	0.04% (1σ)
Velocity cutoff Resolution error	0.02 m/sec (1σ)	0.02 m/sec (1σ)
Velocity increment required (not to be exceeded more than 1% of the time)	64 m/sec	3 m/sec

2.5.3.4 Deboost Into Lunar Orbit

Based upon tracking data, the following quantities will be determined for injection into the intermediate orbit:

a) Thrust initiation time

b) Body attitude

c) Velocity increment.

These quantities will be computed to null the deviations from nominal of the apocynthion, inclination, longitude of the ascending mode, and the argument of pericynthion. A set of required accuracies of position and velocity at the end of this phase which will meet the orbital requirements is given in Table 2-XI.

2.5.3.5 Coast in Intermediate Orbit and Final Orbit Insertion

There are no active guidance requirements during the intermediate orbiting phase. However, the position and velocity must be within certain limits at the end of this phase. A set of position and velocity accuracies which (in combination with the expected execution errors) will not violate the orbit accuracies required is indicated in Table 2-XII.

Table 2-XI. Guidance and Control Requirements for Deboost Into Intermediate and Final Lunar Orbit

Parameter	Deboost Into Intermediate Orbit (1σ values)†	Deboost Into Final Orbit (1σ values)†
Δx	80.4 km	14.2 km
Δy	24.2 km	18.9 km
Δz	9.7 km	13 km
$\Delta \dot{x}$	2.7 m/sec	13 m/sec
$\Delta \dot{y}$	47 m/sec	3.3 m/sec
$\Delta \dot{z}$	11.5 m/sec	0.7 m/sec
Pointing error	0.4 deg	0.4 deg
Error proportional to ΔV	0.04%	0.04%
Velocity cutoff	0.02 m/sec	0.02 m/sec
Velocity increment required (not be exceeded more than 1% of the time)	758 m/sec (2485 ft/sec)	33 m/sec (110 ft/sec)
Coordinate System	Selenographic	Selenographic

† Except for required velocity increment.

Table 2-XII. Guidance Requirements for Coast in Intermediate Orbit

Parameter	Specification (1σ Values)
Δx	14.4 km
Δy	19 km
Δz	13 km
$\Delta \dot{x}$	0.6 m/sec
$\Delta \dot{y}$	3.6 m/sec
$\Delta \dot{z}$	1.5 m/sec
Coordinate System	Selenographic

The required maneuver for final adjustment of the orbit will be calculated using previous estimates of position and velocity. The maneuver (pitch attitude, yaw attitude, velocity magnitude) will be calculated so as to null the deviations at the pericynthion after retrothrusting at apocynthion to give a specified pericynthion inclination and argument of pericynthion.

At the completion of the maneuver, the position and velocity must be within prescribed limits so that the desired lunar orbit can be achieved. The final lunar orbital requirements are given in Table 2-XIII.

Table 2-XIII. Lunar Orbital Phase Accuracy Requirements

Parameter	Specification (1σ Values)
Error in semimajor axis	7.24 km
Error in pericynthion altitude	0.2 km
Inclination error	0.01 deg
Error in ascending node at first target pass	
• Selenographic latitude	0.1 deg
• Selenographic longitude	0.1 deg
Error in argument of periapsis at first target pass	0.01 deg

2.6 SOLAR PROBE WITH JUPITER ASSIST

Prior to planetary encounter this mission is similar to the Jupiter flyby mission studied in Ref 2-6. For the solar probe mission, the spacecraft trajectory passes in close proximity to Jupiter (a few radii is typical). The trajectory is altered by the gravitational field of Jupiter so that after encounter the spacecraft is in a heliocentric trajectory passing close to the Sun (not necessarily in the ecliptic plane). The flyby mission is similar in that the encounter is made again at a few radii with the purpose of making scientific measurements during the encounter phase.

The Atlas SLV3X/Centaur/HEUS can be considered as a typical booster for this mission. The kick stage (HEUS) guidance system is

assumed to provide the primary guidance and control functions for all booster stages and until completion of the final midcourse correction maneuver. After the midcourse correction is completed, the system will be used only to control vehicle attitude. No further trajectory corrections are required.

2.6.1 Mission Characteristics

2.6.1.1 Post Encounter Trajectories

It has been indicated (Ref 2-7) that spacecraft passing close to the planet Jupiter can make use of the gravitational energy added to or subtracted from the orbital energy expressed in heliocentric coordinates to achieve a number of missions subsequent to encounter. Among these missions are those leading to the far reaches of the solar system (exploration of the outer planets and interplanetary space beyond Jupiter, even to the extent of achieving trajectories which escape from the solar system), those in which heliocentric energy is decreased and the spacecraft returns to the Earth or even substantially closer to the Sun, and those employing orbits highly inclined to the ecliptic. Not all of these options are possible from the Earth-Jupiter trajectories associated with the relatively low launch energies and 20- to 30-day launch periods. Some of the options which are available include trajectories which lead to trans-Jupiter regions of the solar system (achievable by eastward equatorial passages), trajectories which return closer to the Sun (perihelion distances 4 to 0.6 AU, achievable by westward equatorial passages), and 20- to 40-deg inclinations of subsequent heliocentric orbits to the ecliptic (achievable by polar passages). Some of the general characteristics of these post encounter trajectories are tabulated in Table 2-XIV.

2.6.1.2 Preencounter Trajectory

The particular preencounter trajectory selected for this study is a sample from the 1972 Jupiter launch opportunity. The general nature of the trajectory is illustrated in Figure 2-9 and 2-10. Some significant mission parameters for the particular trajectory selected are given in Table 2-XV. The variation in spacecraft distances to the Earth, Sun, and Jupiter during the interplanetary phase is indicated in Figure 2-11.

Table 2-XIV. General Characteristics of Trajectory Subsequent to Jupiter Encounter (from Ref 2-6)

Launch Energy Required (C_3) (km^2/sec^2)	Flight Time (days)	V_{HP} ‡ (km/sec)	ZAP‡ (deg)	Characteristics of Heliocentric Trajectory after Jupiter Encounter†		
				Eastward (Equatorial)	Westward (Equatorial)	Polar
100 (Type I)	500	11	150	In ecliptic, approximately tangential to Jupiter's orbit, velocity 1.3 times solar escape velocity	In ecliptic, returning inward to perihelion as close as 0.6 AU	Inclined up to 43 deg to ecliptic
82 (minimum, Type I)	750	7	120	In ecliptic, tangential or outward from Jupiter's orbit, velocity 1.1 times solar escape velocity	In ecliptic, inward to perihelion 0.9 to 4 AU depending on closeness of approach to Jupiter	Inclined up to 31 deg to ecliptic
95 (Type I or II)	950	6	90	In ecliptic, outward from tangential, velocity up to 0.95 times solar escape velocity	In ecliptic, inward from tangential, velocity up to 0.95 times solar escape	Inclined up to 27 deg to ecliptic
90 (Type II)	1250	7	60	In ecliptic, outward from tangential, velocity up to 0.9 times solar escape velocity	In ecliptic, tangential or inward from Jupiter's orbit, velocity up to 1.05 times solar escape velocity	Inclined up to 31 deg to ecliptic

†All heliocentric orbits subsequent to encounter are posigrade.

‡See glossary of terms, Paragraph 1.4.

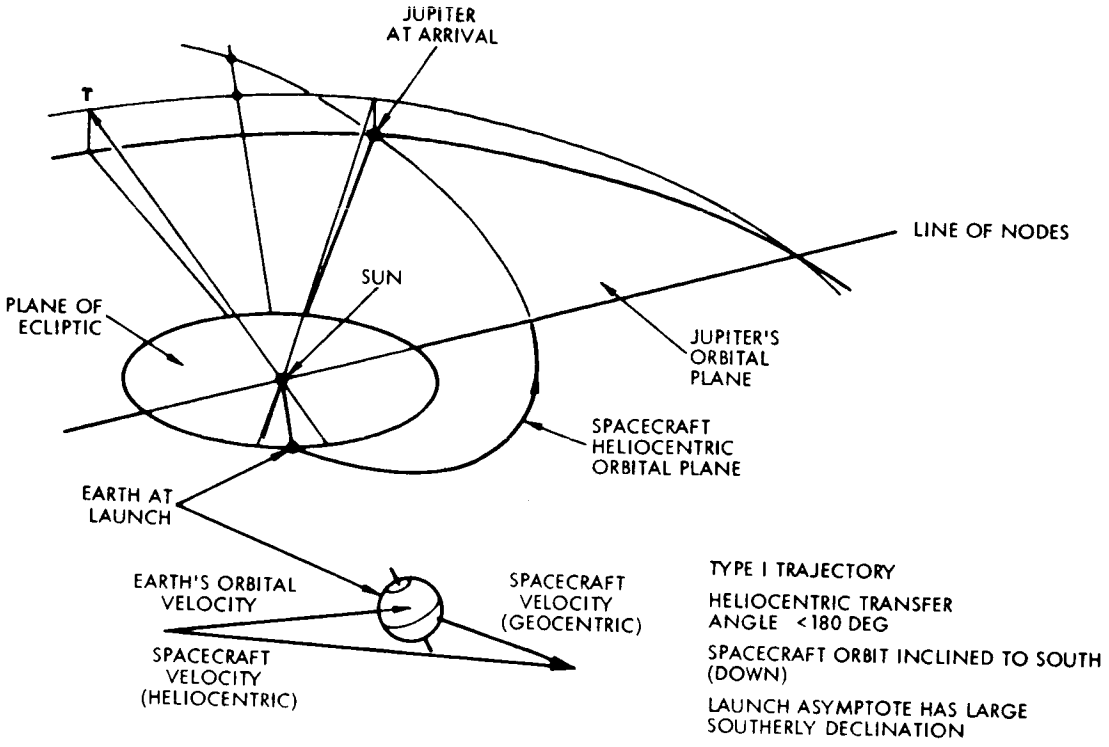

Figure 2-9. Typical Type I Trajectory Earth-Jupiter

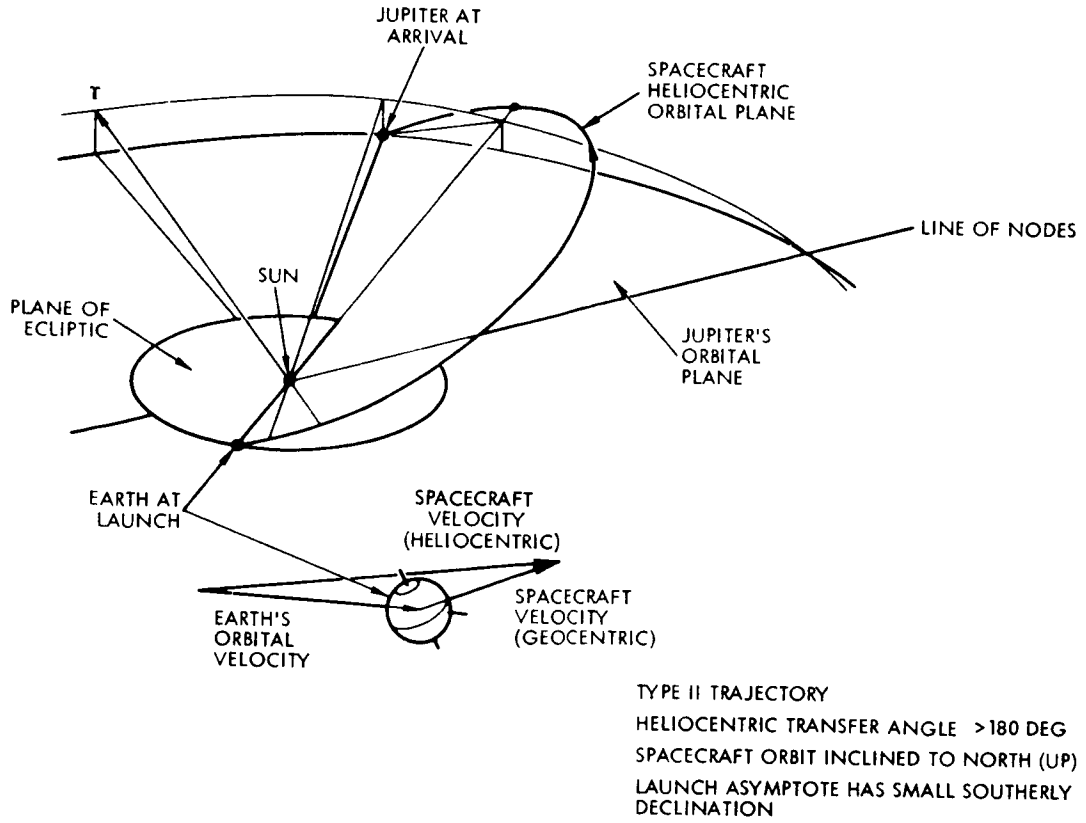

Figure 2-10. Typical Type II Trajectory Earth-Jupiter

Table 2-XV. Characteristics of 1972 Earth-Jupiter Trajectory (from Ref 2-6)

Launch date	March 14, 1972
†C_3, km^2/sec^2	86.24
Arrival date	March 26, 1974
Flight time, days	742
Heliocentric transfer angle, deg.	156.63
†DLA, deg.	-30.2
†V_{HP}, km/sec	7.00
†ZAP, deg.	122
†ZAE, deg.	116
†ZAL, deg.	70
Jupiter-Earth distance at encounter, AU	5.83
Inclination of spacecraft orbit plane to ecliptic, deg.	2.30

†See glossary of terms Paragraph 2.2.5 for definition of symbols.

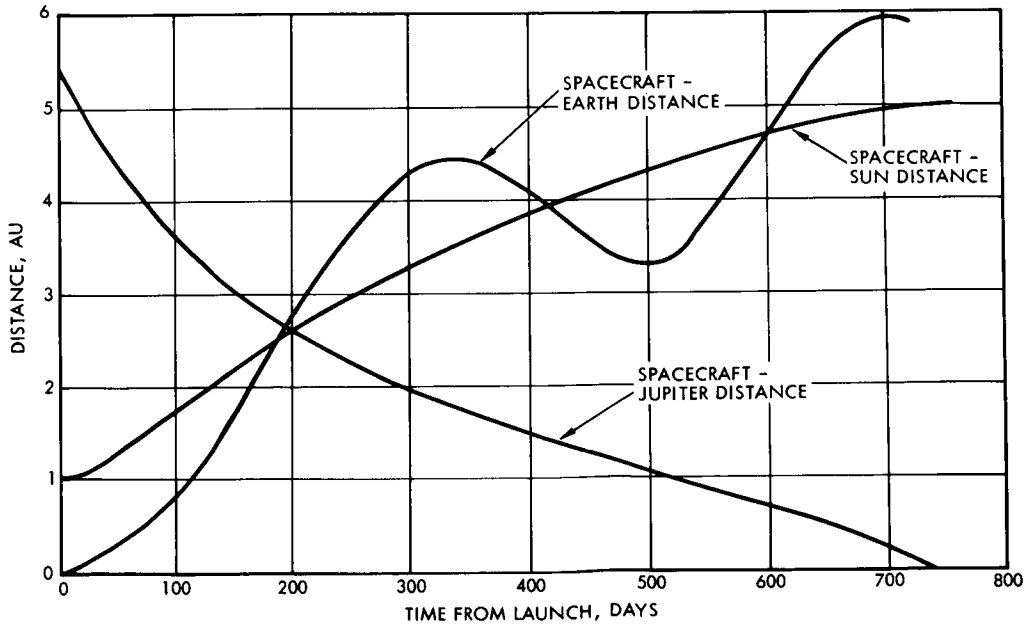

Figure 2-11. Distances from Spacecraft to Earth, Sun, and Jupiter (from Ref 2-6)

2.6.1.3 Encounter Geometry

The geometrical characteristics of the spacecraft trajectory in the near vicinity of Jupiter are determined by 1) the large gravitational influence of the planet, 2) the choice of interplanetary trajectory, and 3) the choice of the input parameter $\overline{B}$. While the first influence is not subject to control, the other two are.

For a given interplanetary trajectory, the choice of the inpact parameter vector $\overline{B}$ specifies in which direction from Jupiter and what distance the approach asymptote lies. $\overline{B}$ is commonly expressed in components $\overline{B} \cdot \overline{R}$ and $\overline{B} \cdot \overline{T}$, where $\overline{R}$, $\overline{S}$, $\overline{T}$ are a right-hand set of mutually orthogonal unit vectors aligned as follows: $\overline{S}$ is parallel to the planetocentric approach asymptote, $\overline{T}$ is parallel to the plane of the ecliptic and positive eastward, and $\overline{R}$ completes the set and has a positive southerly component. The magnitude of $\overline{B}$ determines the distance of closest approach to Jupiter,

$$\theta = \tan^{-1} \frac{\overline{B} \cdot \overline{R}}{\overline{B} \cdot \overline{T}}$$

and the angle specifies the orientation of the Jupiter-centered orbit plane as a rotation about the S axis. These definitions are illustrated in Figure 2-12.

The effects of Jupiter's gravitational field are to increase the spacecraft velocity to a maximum, at the point of closest approach to the planet, and to focus and bend the trajectory. The closer the distance from Jupiter a periapsis, the greater these effects are. Figure 2-13 indicates how some of these quantities vary with R_p, the distance from the planet center at periapsis, for two different values of the asymptotic approach velocity. All quantities in the figure are expressed in planet-centered coordinates.

Sample encounter trajectories have been generated and plotted for eastward equatorial passages following the interplanetary trajectory discussed above. The planet-centered trajectory is not exactly in the plane of the equator, but can be within about 5 deg of the equatorial

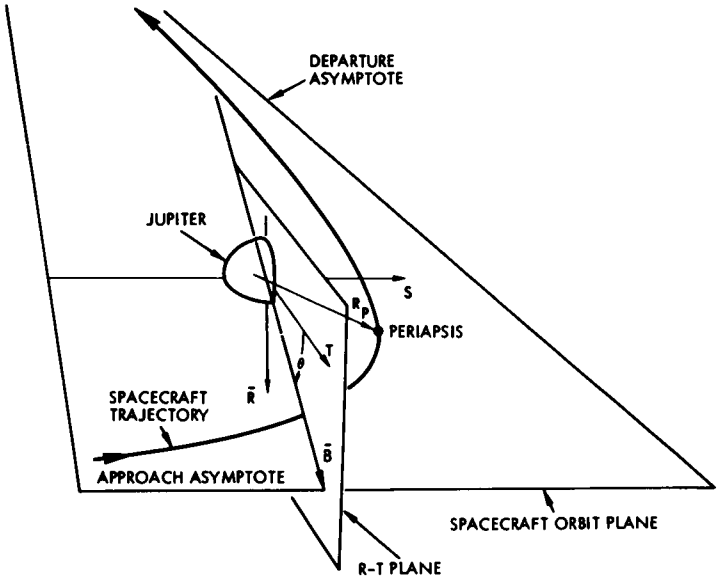

Figure 2-12. Encounter Geometry

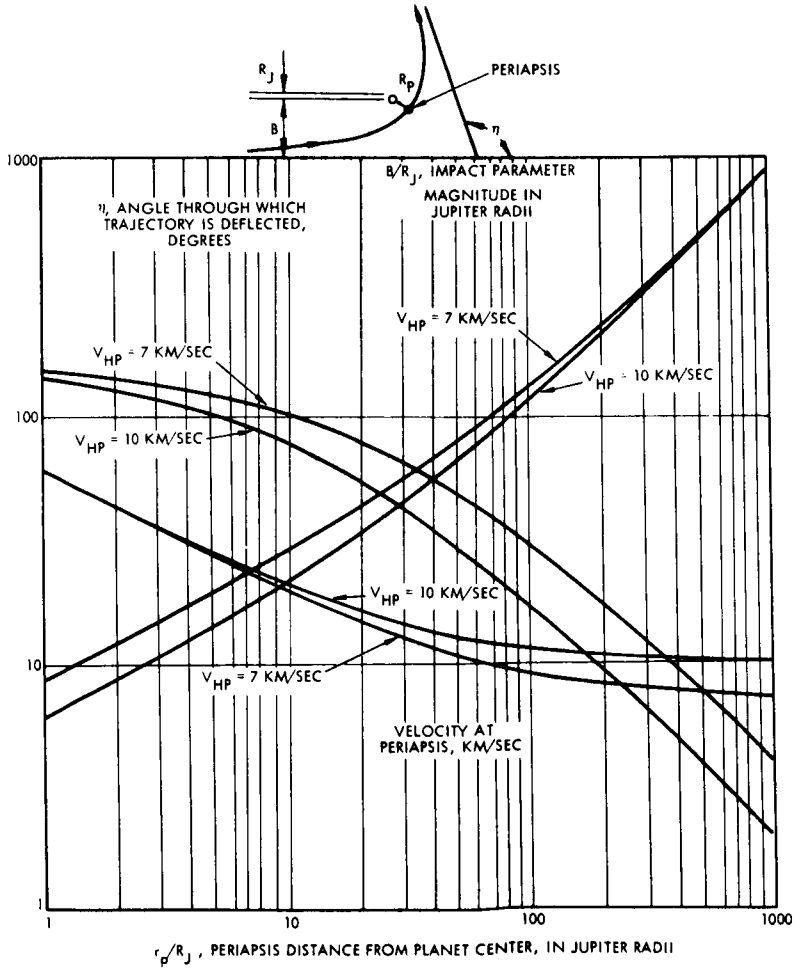

Figure 2-13. Jupiter Gravitational Effects Versus Periapsis Distance (from Ref 2-6)

plane. Values of R_P, the periapsis distance from the planet's center, of 1.5 to 3 R_J (Jupiter radii), are used. Figure 2-14 shows the path within 100 R_J of Jupiter, with R_P equal to 1.5 R_J. Figure 2-15 shows the same trajectory at an enlarged scale, within 6 R_J of the planet.

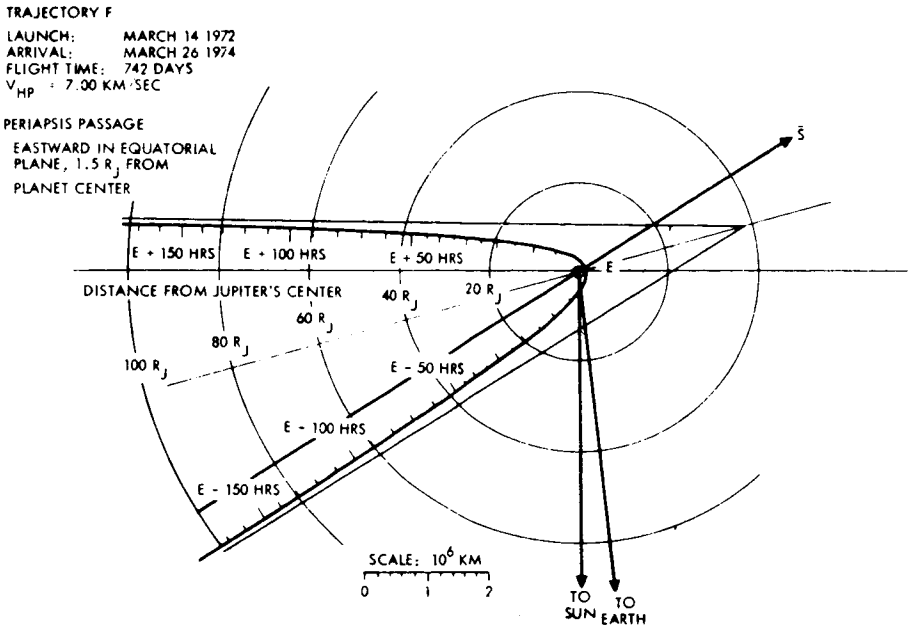

Figure 2-14. Encounter Geometry at Jupiter, R_P = 1.5 R_J (from Ref 2-6)

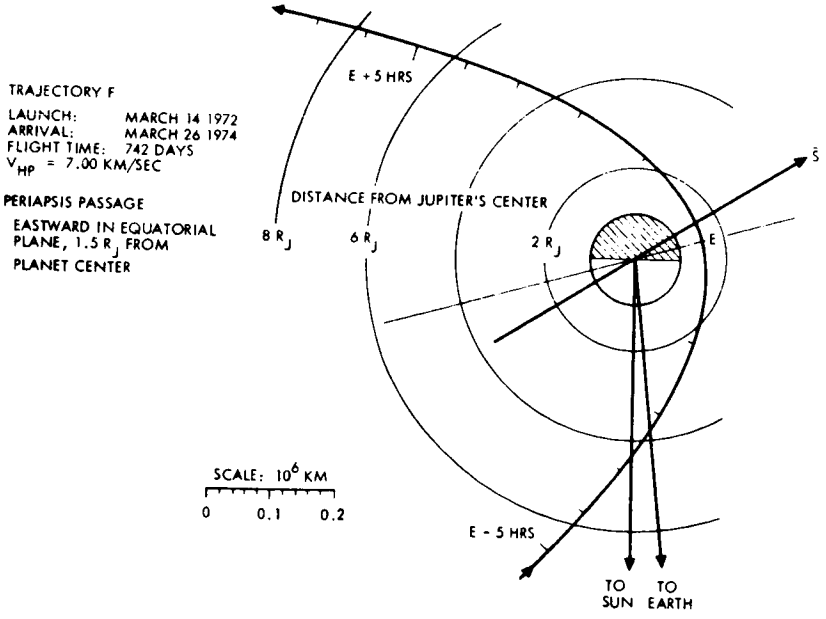

Figure 2-15. Encounter Geometry at Jupiter, R_P = 1.5 R_J (from Ref 2-6)

2.6.2 Guidance System Operational Sequence

Independent of the specific mission trajectory chosen, the various mission profiles do not differ significantly from one another in the mission phases and required guidance system functions. The typical trajectory will contain the following phases with the indicated guidance system functions required:

a) Launch and boost to ~ 185 km parking orbit: The kick The kick-stage strapdown inertial guidance system will provide the guidance function for this phase.

b) Coast in parking orbit: Following injection into the parking orbit, the kick stage/payload will coast until the interplanetary orbit injection maneuver.

The inertial guidance will perform attitude reference and control functions during this phase.

c) Heliocentric orbit injection: For the injection energy assumed, a velocity increment of approximately 7.0 km/sec is needed. This will be divided between the Centaur second burn and the kick stage. The kick-stage inertial guidance system will provide the attitude and burn control for both stages.

d) Coast in heliocentric transfer ellipse and midcourse correction: These phases are similar to the corresponding phases for the Mars and Lunar orbiter missions. The midcourse correction will occur 5 to 20 days from injection.

e) Coast to Jupiter encounter: The strapdown system will perform only attitude control functions during this phase, with the primary attitude reference being obtained from the body-fixed Sun and Canopus sensors.

2.6.3 Guidance System Performance Requirements

2.6.3.1 Overall Mission Accuracy Requirements

For both the solar probe mission with Jupiter swingby and Jupiter flyby mission to observe the planet requires that the vehicle pass the planet at a prescribed point defined by the impact vector $\bar{B}$. Another major mission requirement is the midcourse correction capability of the spacecraft. The tolerances shown in Table 2-XVI are typical values and have been used as requirements in this study.

Table 2-XVI. Assumed Jupiter Mission Requirements

Parameter	Value or Tolerance
Encounter distance	142, 800 km ±40, 800 km (3σ) $2R_j^{\dagger}$ ±0.6R_j (3σ)
Maximum allowable ΔV for midcourse corrections (not to be exceeded more than 1 percent of the time)	100 m/sec
†R_j denotes the radius of Jupiter.	

2.6.3.2 Interplanetary Trajectory Injection

The ascent guidance phase will include the atmospheric and exo-atmospheric ascent, the injection into a parking orbit, and the final injection into the heliocentric elliptic transfer orbit. The accuracy of the injection conditons can be traded off with the midcourse correction requirements. The requirements shown in Table 2-XVII are based on typical midcourse correction capabilities.

Table 2-XVII. Injection Guidance Requirements for the Jupiter Mission

Parameter	Specification (1σ values)
Error in velocity magnitude at injection	9.5 m/sec
Total velocity error perpendicular to the velocity direction	34.7 m/sec

2.6.3.3 Midcourse Corrections

Midcourse corrections are required to remove the terminal errors resulting from injection inaccuracies. The number and timing of these corrections are functions of the correction philosophy, the tracking system accuracy, and the trajectory or spacecraft constraints on the maneuver.

For the purpose of this study, a particular correction philosophy, trajectory, spacecraft configuration, and a single midcourse correction are assumed (see Section 8). The midcourse correction removes either terminal errors in two mutually perpendicular directions and the time-of-flight error or terminal errors only.

The requirements for execution of the midcourse maneuver are presented in Table 2-XVIII.

Table 2-XVIII. Guidance Requirements for Midcourse Correction

Parameter	Specification (1σ Values)
Proportional error	0.75 percent
Pointing error	2/3 deg
Velocity cutoff resolution error	0.0188 m/sec

REFERENCES FOR SECTION 2

2-1 "Voyager Support Study, Advanced Mission Definition, Final Report," TRW Document No. 04480-6001-R000, November 1966.

2-2 "Design Parameters for Ballistic Interplanetary Trajectories, Part I. One-Way Transfer to Mars and Venus," JPL Technical Report No. 32-77, 16 January 1963.

2-3 "Trajectory Selection Considerations for Voyager Mission to Mars During the 1971-1977 Time Period," JPL Document EPD-281, 15 September 1965.

2-4 "Performance and Design Requirements for the 1973 Voyager Mission, General Specifications for," JPL Document SE 002BB-001-1 B21, (Draft) 1 January 1967.

2-5 "Phase 1A Study Report, Voyager Spacecraft," TRW Systems Report 5410-0004-RU-001, 30 July 1965.

2-6 "Advanced Planetary Probe Study, Final Technical Report," TRW Systems Report 6547-6004-R000, 27 July 1966.

2-7 "Utilizing Large Planetary Perturbations for the Design of Deep-Space Solar Probe and Out-of-Ecliptic Trajectories," JPL Report TR 32-849, 15 December 1965.

3. RECOMMENDED RADIO/OPTICAL/STRAPDOWN INERTIAL GUIDANCE SYSTEM

3.1 EQUIPMENT CONFIGURATION BY MISSION

A block diagram of the total guidance system suitable for any of the missions is shown in Figure 3-1, together with a matrix showing the specific equipment utilization by mission. The recommended configuration is that of a basic "core" system used for all the missions, with auxiliary sensors added in a modular or building block fashion to configure the system to a particular mission. The auxiliary sensors interface with the core system through the digital computer. If the computer input/output design is such as to accommodate any set of auxiliary sensors without any required redesign, then the mission dependent changes can be accomplished with a minimum of effort by suitably changing the stored computer programs (software).

While the implementation of the "core" inertial guidance system is identical in each of the missions, its role varies significantly from mission to mission. For example, in the synchronous earth orbit mission, the strapdown subsystem (supplemented by appropriate electro-optical sensors) can essentially provide complete, autonomous guidance and navigation. In the lunar orbit mission, it provides precise guidance during midcourse and orbit insertion maneuvers, with primary translunar navigation provided by ground tracking during the coasting phases. The inertial subsystem provides primary attitude reference information for the earth synchronous orbit mission, while in the other missions, primary attitude reference information during heliocentric orbit phases is provided by the sun and star sensors.

The inertial measurement unit shown in Figure 3-1 is a strapdown configuration. Outputs of the three orthogonal body-mounted gyros are in the form of pulses, each quantized pulse representing an incremental attitude change about the gyro's sensitive axis. The computer accepts this information and can generate body angular rate information and/or total body attitude information. The output pulses of the three body-mounted accelerometers represent velocity increment information, which is combined with the gyro data to provide total velocity change information in

EQUIPMENT CONFIGURATION

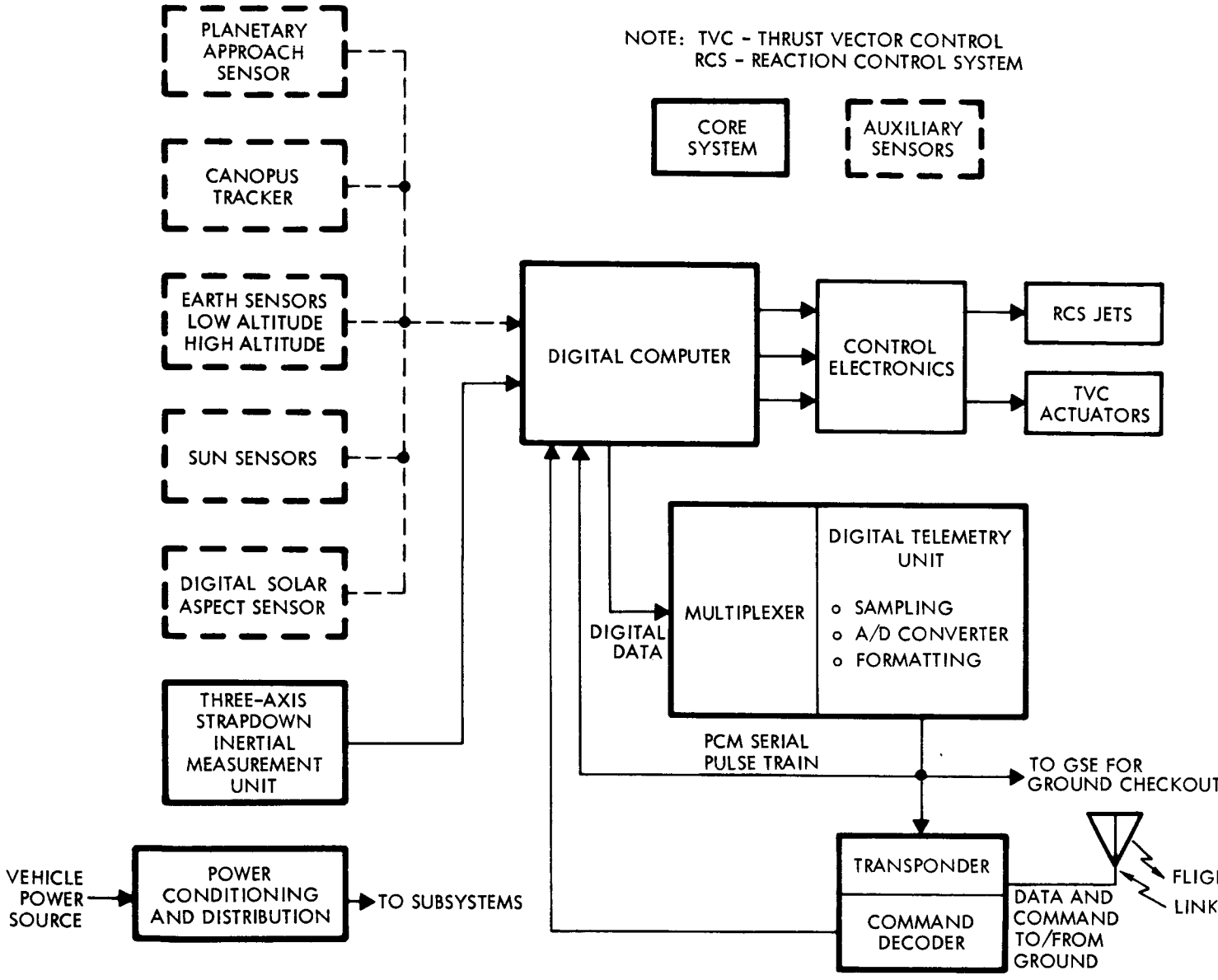

COMMAND LINK USED FOR FLIGHT AND GROUND SEQUENCING, MODE CONTROL, ETC.
TELEMETRY LINK (HARD WIRE AND/OR RF) USED FOR GROUND CHECKOUT

EQUIPMENT UTILIZATION

EQUIPMENT		EARTH SYNCHRONOUS ORBIT	LUNAR ORBIT	SOLAR PROBE (JUPITER SWING-BY)	MARS ORBITER
CORE SYSTEM	3-AXIS STRAPDOWN INERTIAL MEASUREMENT UNIT	▲	▲	▲	▲
	DIGITAL COMPUTER	▲	▲	▲	▲
	S-BAND TRACKING TRANSPONDER & COMMAND LINK	▲ NOTE 1	▲	▲	▲
	AUXILIARY EQUIP. POWER CONDITIONING & DISTRIBUTION, TELEMETRY, ETC.	▲	▲	▲	▲
AUXILIARY SENSORS	STAR (CANOPUS) TRACKER (ATTITUDE REFERENCE)		▲	▲	▲
	EARTH SENSOR (HORIZON SCANNER) (LOCAL VERTICAL REFERENCE) • LOW ALTITUDE • HIGH ALTITUDE	▲			
	SUN SENSOR (CRUISE ATTITUDE REFERENCE)		▲	▲	▲
	SUN SENSOR SOLAR ASPECT SENSOR FOR ATTITUDE REFERENCE & NAVIGATION FIX (OPTIONAL)	▲ NOTE 1			
	PLANETARY APPROACH SENSOR				▲ NOTE 2

NOTE 1: THE NAVIGATION UPDATE REQUIRED PRIOR TO THE FINAL ORBIT INSERTION MAY BE MADE EITHER BY GROUND-BASED RADIO TRACKING OR BY AN ON-BOARD TECHNIQUE UTILIZING THE SUN SENSOR (SEE SECTION 3.2.4).

NOTE 2: THIS SENSOR MAY BE ADDED IF IMPROVED APPROACH GUIDANCE AND ORBIT INSERTION IS REQUIRED (THIS REQUIREMENT IS NOT FIRMLY ESTABLISHED FOR THE MARS MISSION CONSIDERED IN THIS STUDY). (SEE SECTION 3.3.3.) THIS SENSOR, TOGETHER WITH A PRECISION CANOPUS TRACKER AND SUN SENSOR, CAN BE USED TO REDUCE THE UNCERTAINTY IN THE SPACECRAFT TRAJECTORY WITH RESPECT TO MARS DURING THE APPROACH PHASE (SEE SECTION 4.3).

Figure 3-1. Equipment Configuration and Utilization

some chosen set of inertial reference axes. A detailed description of the strapdown inertial subsystem is present in Section 4.

The auxiliary sensors in this study have been limited to electro-optical sensors, used primarily for attitude referencing. These sensors include earth horizon scanners, sun sensors, star trackers, and planetary approach sensors. The application of these sensors by missions and by mission phases are explained in detail in Section 3. Detailed discussions of individual sensors are presented in Section 5.

The interface areas involving the control subsystem, the power subsystem, and the tracking, telemetry and control subsystems are not discussed in this report.

The recommended system configurations for each mission are discussed in the remainder of this section.

3.2 CANDIDATE SYSTEM CONFIGURATIONS FOR SPECIFIC MISSIONS

3.2.1 Earth-Synchronous Orbit Mission

A functional block diagram of the candidate system configuration for this mission is indicated in Figure 3-2. The evolution of this configuration is discussed in the following paragraphs.

The core configuration for this mission consists of the three-axis strapdown inertial guidance subsystem, with three single-degree-of-freedom pulse-torqued gyros, three accelerometers body-mounted in an orthogonal triad, and a digital computer. This core configuration has been analyzed† for the minimum parking orbit case, using the two different sets of strapdown inertial components (see Section 4). Applying the criteria defined in Paragraph 2.3.3, this configuration was found to be marginal in performance, requiring 35 to 73 m/sec ΔV capability from the payload for orbit error correction (Runs 1, 3 and 5 in Table 3-I). The primary source of this poor performance is the approximately five and one-half hours over which the effects of gyro bias drift will act, resulting in misapplication in the direction of the apogee burn.

†See Subsection 7.3 (Table 3-I was extracted from this discussion).

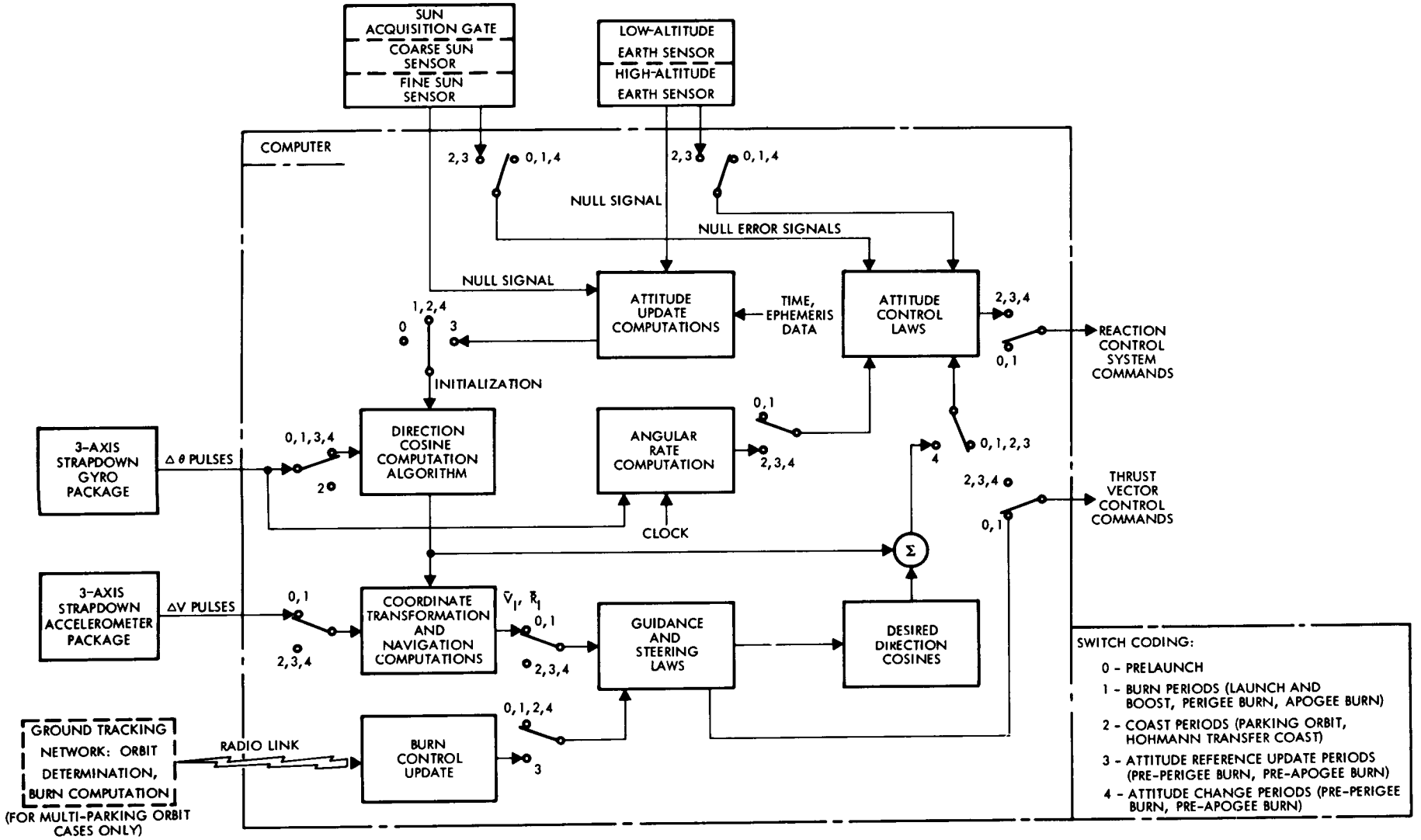

Figure 3-2. Guidance System Functional Block Diagram for Earth-Synchronous Mission

Table 3-I. Summary of Synchronous Mission Performance Analysis Results

Run No.	Coast Orbits	System No.	Prelaunch Calibration	Time Update	Attitude Update		95% ΔV (m/sec) Required by Payload for Orbit Trim
					Perigee	Apogee	
1	0	166	No	No	No	No	73
2	0	166	No	No	No	Yes	13
3	0	166	Yes	No	No	No	75
4	0	166	Yes	No	No	Yes	9
5	0	266	No	No	No	No	35
6	0	266	No	No	No	Yes	8
7	8	166	No	No	Yes	Yes	163
8	8	166	No	Yes	Yes	Yes	22
9	8	166	Yes	No	Yes	Yes	109
10	8	166	Yes	Yes	Yes	Yes	19
11	8	266	No	No	Yes	Yes	83
12	8	266	No	Yes	Yes	Yes	19

The obvious solution to this problem is to provide a means for attitude updating a short time prior to apogee burn. Several alternative techniques for providing this function of attitude updating, or more precisely, of attitude referencing during the long transfer coast period are as follows:

a) Use an earth horizon sensor to provide kick stage attitude reference about two vehicle axes and "gyrocompassing" about the third axis. This scheme has the natural disadvantage that attitude control about the third axis is still imprecise because of the gyro drift effects. This technique has not been investigated in this study.

b) Use both an earth horizon sensor and a sun sensor for complete three-axis attitude referencing. The sensors may be body-fixed or gimbaled relative to the body. In the first case, the kick stage attitude will be fixed relative to the local vertical/sun line frame and will have to be altered prior to the apogee burn. In the second case, the complexities of mechanical gimbaling and angular readout requirements are added and no distinct total system advantage is expected.

   In either case, it would be preferable if the launch time/mission profile is constrained so that the sun is at a zenith angle between 45 deg and 135 deg for a period of five to 15 minutes before apogee burn time. The zenith angle constraint is introduced for pointing accuracy considerations (note that for a zenith angle of 0 degrees the combination of sun and earth sightings does not give complete three-axis attitude information). The time constraint is introduced to minimize the time over which attitude must be remembered and maintained inertially.

c) Replace the sun sensor with a star tracker to obtain greater flexibility in the launch time/mission profile constraint. A suitable star can be selected prior to launch. One possible problem with this equipment configuration is that associated with the inflight identification and acquisition of the chosen star. This problem must be investigated further.

The performance of the system using earth and sun sightings to improve attitude information prior to apogee burn was investigated. The results indicate a six- to eight-fold improvement in performance over the core configuration (Runs 2, 4, and 6 in Table 3-I), at least for the missions in which transfer ignition occurs at the first equatorial crossing.

For missions in which the kick stage remains in several parking orbits before transfer ignition, attitude updating would be required prior to the transfer ignition to minimize the effects of gyro drift during the long parking orbit coast periods. This attitude updating, or referencing, can be provided by the same earth horizon sensor/sun sensor combination. The launch time/mission profile constraint imposed by this technique is that the sun should be at a zenith angle of 45 deg to 90 deg for a period 5 to 15 min prior to the transfer, or perigee, burn for the following reasons:

- Use of the lower zenith limit is necessary for accuracy considerations.
- Use of the 90 deg limit is required to minimize the effects of atmospheric refraction.

Note that the zenith angle constraint can be met for both perigee and apogee burns with proper selection of the launch time (see Figure 3-3).

The approximate kick stage positions prior to the apogee burn are:

Minutes before apogee burn	θ_a (deg)
15	2
10	1.5
5	1

The approximate kick stage positions prior to the perigee burn are:

Minutes before perigee burn	θ_i (deg)
15	60
10	40
5	20

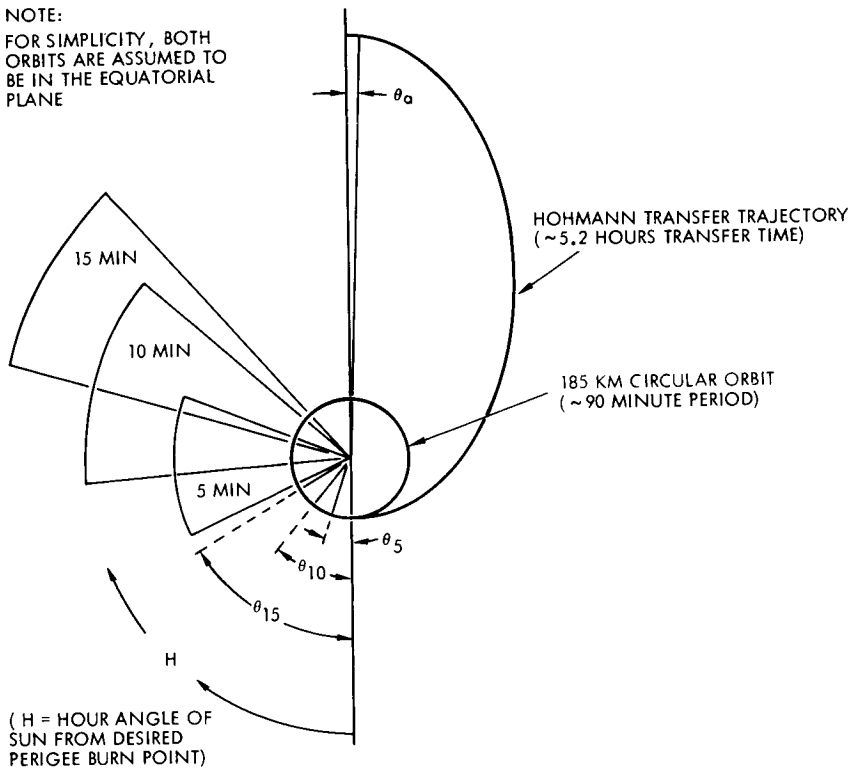

Figure 3-3. Acceptable Sun Locations for Perigee and Apogee Burns

- Zenith angle constraints:

  $45^{\circ} \leq \xi \leq 90^{\circ}$ in 185 km orbit;
  $45^{\circ} \leq \xi \leq 135^{\circ}$ near apogee of
  Hohmann transfer

- To meet above constraints at T minutes before both perigee and apogee burns, the sun must be within the H limits indicated on Figure 3-3 by the fan-shaped regions:

$$\begin{aligned} 105^{\circ} \leq H \leq 137^{\circ}, \quad T &= 15 \\ 85^{\circ} \leq H \leq 130^{\circ}, \quad T &= 10 \\ 65^{\circ} \leq H \leq 110^{\circ}, \quad T &= 5 \\ 45^{\circ} \leq H \leq 90^{\circ}, \quad T &= 0 \end{aligned}$$

- For 5 minutes of continuous visibility before both perigee and apogee burns the H limits should be:

$$\begin{aligned} 105^{\circ} \leq H \leq 130^{\circ}, \quad 10 \leq T \leq 15 \\ 85^{\circ} \leq H \leq 110^{\circ}, \quad 5 \leq T \leq 10 \\ 65^{\circ} \leq H \leq 90^{\circ}, \quad 0 \leq T \leq 5 \end{aligned}$$

Even with attitude updating prior to both the perigee and the apogee burns, the system performance is poor for the multi-parking orbit case (Runs 7, 9, and 11 in Table 3-I). This poor performance is attributable to parking orbit injection errors which propagate into errors in transfer burn ignition time. The effects of this error source can be minimized by properly updating the ignition time. The significant improvements (five to eight fold) in system performance obtainable with the addition of this updating procedure can be seen in Table 3-I (Runs 8, 10, and 12).

Several techniques for ignition time update are possible.

a) Complete parking orbit determination via ground tracking

b) Complete parking orbit determination via earth, sun and star sensor readings

c) A combination of a) and b)

d) Simple prediction of equatorial crossing time (and hence proper time for transfer burn ignition) via earth and sun sensor readings.

Parking orbit determination via ground tracking is a proven technique. However, there may be several shortcomings to this technique for this particular application. The primary disadvantage is that, depending on mission objectives, the kick stage may be required to remain at the parking altitude for fewer than two complete orbits. In this situation, the accuracy of the orbit determination may be degraded sufficiently that no performance advantage is gained (Section 6 discusses the problems of tracking in the low altitude earth orbit).

Parking orbit determination by a series of multiple celestial sightings has the same limitations as that by ground tracking. Further complications arise from the fact that the sun will be eclipsed for half of each parking orbit. Also, to ensure sufficient sun sightings while the sun is visible, the kick stage may have to be continually maneuvered during the daylight portion of the orbit to achieve favorable sun line-of-sight angles relative to the kick stage.

Technique d) is a "one-shot" open-loop prediction technique and is, under the best conditions, the least accurate of those listed; but it may

prove to be adequate and is attractive from several standpoints. It does not require ground tracking and can be implemented with a body-fixed earth horizon tracker and a body-fixed sun aspect sensor. Detailed analyses of this technique have not been conducted as yet but are recommended as an area for further study. The basic concepts for this technique are outlined as follows:

a) The angle subtense between the earth and sun lines-of-sight from the vehicle can be expressed as

$$A = \pi - \zeta = \cos^{-1} [(\cos \Omega \cos t - \sin \Omega \sin t \cos i_e) \cos E - ((\sin \Omega \cos t + \cos \Omega \sin t \cos i_e) \cos i_s + \sin t \sin i_e \sin i_s) \sin E]$$

where ζ = zenith angle

Ω = longitude of the ascending node

t = sun angle measured in ecliptic plane from vernal equinox

i_e = inclination of equatorial and ecliptic planes (23.4 deg).

i_s = orbital inclination

E = $\omega + v$

ω = argument of perigee

v = true anomaly

b) For an error-free injection, nominal values of Ω, i_s and the time of equatorial crossing (i.e., the time when $E = 0$) are predeterminable; for the nominal time of equatorial crossing, t is also predeterminable.

c) Transfer burn ignition occurs at equatorial crossing, or when $E = 0$; then

$$A_o = \cos^{-1} (\cos \Omega \cos t - \sin \Omega \sin t \cos i_e)$$

d) Since the nominal values of Ω and t are known, a nominal value of A, A_o, at which transfer ignition should nominally occur, is precomputable.

e) During the parking orbit coast, the vehicle attitude can be controlled to that predetermined inertial attitude required for the nominal transfer ignition burn attitude.

f) From 5 to 15 minutes before ignition time (depending on sun visibility conditions), begin tracking of the sun with the body-fixed sun aspect sensor. When $A = A_o$, ignite engine for transfer burn.

Note that besides those errors due to attitude errors and to electro-optical sensor errors, technique d) is subject to errors arising from nominal injection. That is, because Ω and t would in fact be non-standard, the value of A_0 used would not be that value which would actually exist at the time of equatorial crossing on the non-standard trajectory. However, it is important to note that this additional error is effectively no worse after several orbits than it would be if the transfer ignition were to occur at the first equatorial crossing.

Because of the relative simplicity of the concept outlined above, further investigation is recommended. The sun visibility requirements, sun sensor field of view and accuracy requirements, and expected performance accuracy should be determined.

3.2.2 Mars Orbiter Mission

A matrix of possible system elements by mission phase is listed in Table 3-II. The onboard core guidance configuration includes the three-axis strapdown inertial guidance subsystem, a body-fixed Sun sensor assembly, a body-fixed Canopus tracker assembly, and a digital computer. Midcourse and orbit insertion $\Delta\overline{V}$ commands will be generated on the basis of DSIF tracking data and executed under control of the strapdown inertial system. For improved approach guidance and Mars orbit insertion, a planetary approach sensor can be added. The functional block diagram for this configuration is illustrated in Figure 3-4.

In this configuration, the primary attitude reference is established by the spacecraft-Sun line and the spacecraft-Canopus line. The Sun/Canopus acquisition sequence will be completely automatic. The acquisition sequence is functionally the same as used on past lunar and planetary space shots:

a) Null error signals from the coarse sun sensor, and then the fine sun sensor, will be used to control the appropriate reaction control jet thrusters until the sun sensor optical axis is aligned to the sun.

G AND C MODES OF OPERATION / EQUIPMENT USAGE	INJECTION			CRUISE AND MIDCOURS			
	LAUNCH THROUGH PARKING ORBIT INJECTION	PARKING ORBIT	INTERPLANETARY ORBIT INJECTION BURN	CRUISE			MIDCOU
	LAUNCH GUIDANCE	INERTIAL ATTITUDE HOLD RE-ORIENTATION	POWERED FLIGHT GUIDANCE	SUN ACQ	STAR ACQ	CRUISE ATTITUDE CONTROL	REORIENT REORIENT-ATION MANEUVER
MAJOR FUNCTIONAL REQUIREMENTS/ CONSTRAINTS	GUIDANCE AND NAVIGATION THROUGH BOOST PHASE ACCOMPLISHED BY SATURN V GUIDANCE	MAX-PARKING ORBIT 90 MIN	INJECTION ACCURACY REQT 5 M/SEC (1σ) (MID-COURSE ΔV)	ACQUIRE SUN AND CANOPUS 3-AXIS ATTITUDE CONTROL			M/C CORR BY ON BO DSIF/DSN CORRECTI 100 KM, 1 2 CORRECT 30 DAYS A ΔV AVAIL
STRAPDOWN SENSOR PACKAGE	▲	▲	▲	▲	▲	▲	▲
DIGITAL COMPUTER	▲	▲	▲	▲	▲	▲	▲
BOOSTER THRUST VECTOR CONTROL (TVC)	▲		▲				
BOOSTER ATTITUDE CONTROL (RCS)		▲					
SPACECRAFT TVC							
SPACECRAFT RCS HIGH T LOW T				▲	▲	▲	(TWO LEV ▲
SUN SENSOR(S) COARSE FINE				▲		▲	
STAR TRACKER (CANOPUS)					▲	▲	
PLANET APPROACH TRACKER							
USBS TRACKING	▲	▲	▲				
DSIF/DSN TRACKING AND ORBIT PREDICTION						▲	
EARTH-SPACECRAFT COMMAND/DATA LINK					▲	▲	▲

Table 3-II. Mars Orbiter Mission

SE CORRECTION(S)		CRUISE	APPROACH AND ORBITAL OPNS										
			MARS APPROACH	MARS ORBIT INJECTION		ORBITAL ATTITUDE CONTROL		ORBIT TRIM MANEUVER	ORBIT ATTITUDE CONTROL	CAPSULE DEPLOY		ORBITAL OPNS
BURN	REORIENT			REORIENT	BURN	REORIENT	HOLD			REORIENT	DEPLOY	
OWERED HASE GUIDANCE	REACQ SUN AND CANOPUS	CRUISE ATTITUDE CONTROL										
CTION EXECUTED RD SYSTEM USING NAVIGATION N ACCURACY (3σ) MIN ($\bar{R}$, $\bar{T}$ PLANE) ONS AT 5 DAYS AND TER INJECTION BLE 100M/SEC		3-AXIS ATTITUDE CONTROL	•APPROACH ORBIT DETERMINATION USING DSIF/DSN 500 KM (3σ) 3 MIN ($\bar{R}$, $\bar{T}$ PLANE) •ON-BOARD APPROACH SENSOR (OPTIONAL) (MEASURE SUN/MARS CANOPUS/MARS ∠'S)	NORMAL ORBIT 500-1500 KM PERIAPSIS 10,000-20,000 KM APOAPSIS V_∞<3.25 KM/SEC TOLERANCES (3σ) ±30% PERIAPSIS ALT ±5 DEG INCLINATION		3-AXIS ATTITUDE CONTROL		ΔV = 100 M/SEC	3-AXIS ATTITUDE CONTROL			ANTENNA POINTING FOR DATA RELAY SCIENTIFIC EXPERIMENTS
L SYSTEM ASSUMED)												
			(START 5 HRS PRIOR TO ENCOUNTER)									

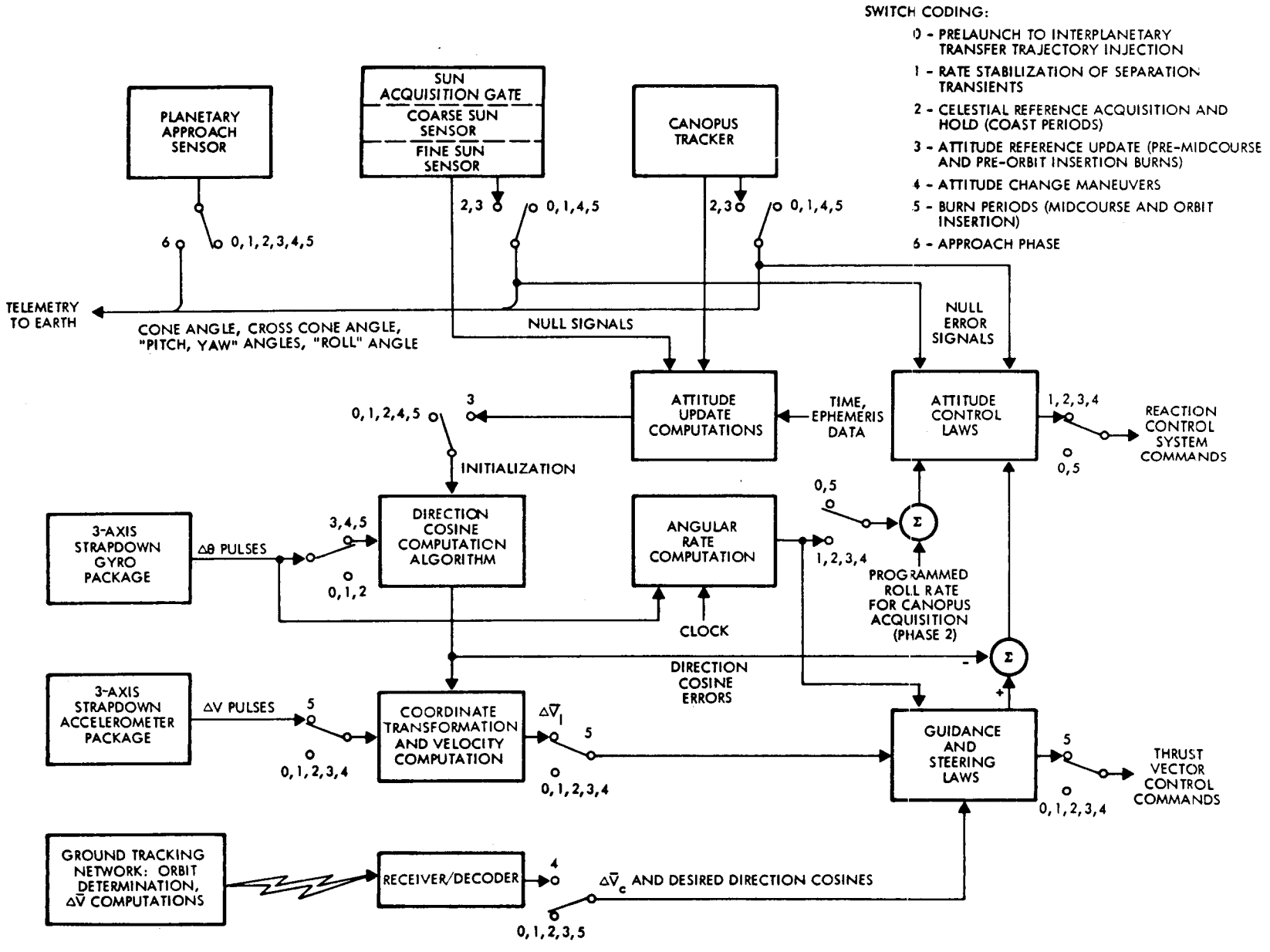

Figure 3-4. Guidance System Functional Block Diagram for Mars Orbiter Mission (Configuration II)

b) Programmed body rate signals are then used to rotate the spacecraft about the just established Sun line to locate Canopus. (The Canopus tracker, 1 x 16 deg instantaneous field of view, is mounted such that 1) its long view dimension and the Sun sensor optical axis are coplanar, and 2) its null axis is chosen such that Canopus will be in the field of view throughout the interplanetary trajectory.) Canopus discrimination can be accomplished by utilizing both minimum and maximum signal threshold detection.

c) When the Canopus image is nulled in the narrow view dimension, complete three-axis inertial attitude reference for the spacecraft has been established. Initial values for the direction cosines relating spacecraft orientation to a reference inertial coordinate frame are thus established.

The desired spacecraft attitude for all periods of thrust application (i.e., for the midcourse corrections and for the aerocentric orbit injection) can be expressed in terms of desired direction cosine values. The attitude change maneuvers required to achieve the proper thrusting directions can be controlled by differencing the proper three elements of the desired and computed direction cosine matrices. The burn time will be controlled on the basis of the desired ΔV magnitudes and the outputs of the accelerometers, which can be turned on only for the thrusting periods.

The body-fixed approach sensor will be designed to have a 15 by 15 deg total field of view and will have its null axis prealigned such that the target plane will be in its field of view from 6-1/2 days to one day before encounter. The geometrical relationships between the three electro-optical sensors and their fields-of-view are illustrated in Figure 3-5.

The approach sensor is sensitive in the visible light spectrum and, as a consequence, the planet image may be gibbous or crescent depending on approach conditions. Several algorithms suitable for determining planet apparent diameter and centroid location within the total field-of-view have been tested. One algorithm uses a simple three-point fix-scheme and requires several complete scans of the image to minimize the effects of instrument errors. Another algorithm uses all available data points obtained in one scan.

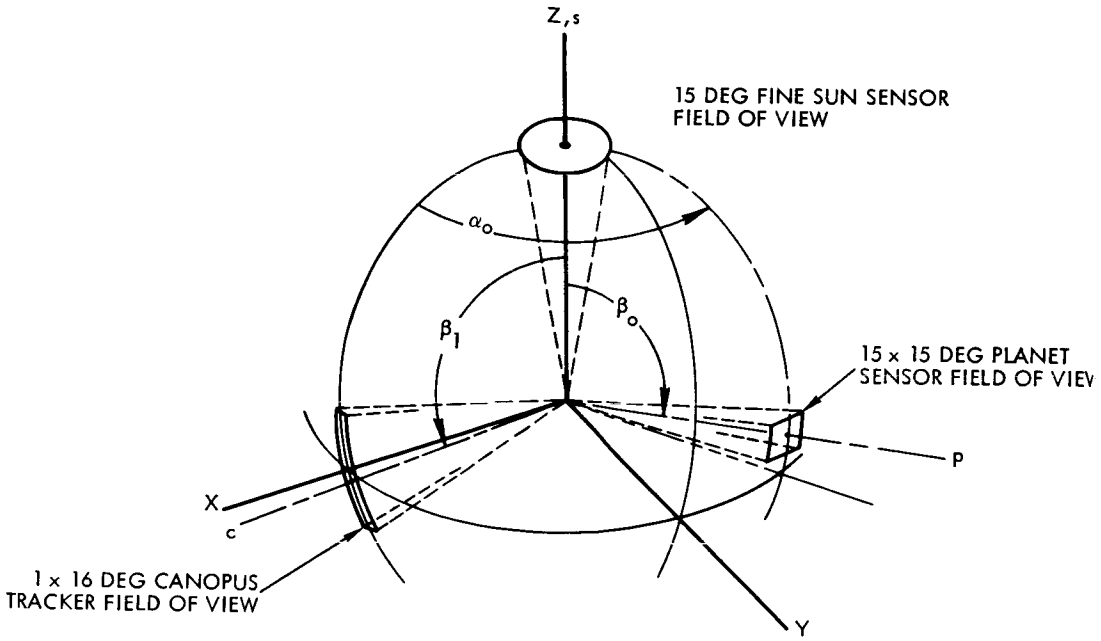

X, Y, Z - VEHICLE FIXED REFERENCE COORDINATE SET

s - SUN SENSOR OPTICAL AXIS

c - CANOPUS TRACKER OPTICAL AXIS

p - PLANET SENSOR OPTICAL AXIS

α_o, β_o - AVERAGE CLOCK AND CONE ANGLES RESPECTIVELY FOR GIVEN TRAJECTORY

β_1 - AVERAGE SUN - CANOPUS CONE ANGLE FOR GIVEN TRAJECTORY

Figure 3-5. Electro-Optical Sensor Field of View Geometry

In the three-point solution, the basic equation defining the circle offset from the center of the scan field is used:

$$r^2 = (x_i - x_c)^2 + (y_i - y_c)^2 \qquad (3-1)$$

where:

r is the radius,

x_i, y_i are the coordinates of a point on the circle

x_c, y_c are the offset coordinates of the center of the circle

$i = 1, 2, 3$

The solution equations, after three fixes are obtained, are

$$\begin{pmatrix} x_c \\ y_c \end{pmatrix} = \frac{1}{2}\begin{pmatrix} x_2 - x_1 & y_2 - y_1 \\ x_3 - x_2 & y_3 - y_2 \end{pmatrix}^{-1} \begin{pmatrix} x_2^2 + y_2^2 - x_1^2 - y_1^2 \\ x_3^2 + y_3^2 - x_2^2 - y_x^2 \end{pmatrix} \qquad (3\text{-}2)$$

$$r = \left[(x_i - x_c)^2 + (y_i - y_c)^2\right]^{1/2} \qquad (3\text{-}3)$$

When using all available data points, a least squares error (LSE) technique can be used. Equation (3-1) is first linearized by assuming a priori values x_{co}, y_{co}, and r_o for x_c, y_c, and r, and

$$\Delta x_c = x_c - x_{co}$$

$$\Delta y_c = y_c - y_{co}$$

$$\Delta r = r - r_o$$

The LSE estimates of the parameters Δx_c, Δy_c and Δr are

$$\begin{pmatrix} \Delta\hat{x}_c \\ \Delta\hat{y}_c \\ \Delta\hat{r} \end{pmatrix}_{LSE} = (M^T M)^{-1} M^T \begin{pmatrix} \Delta x \\ \Delta y \\ \Delta r \end{pmatrix} \qquad (3\text{-}4)$$

where:

$$M = \begin{bmatrix} 1 & \frac{y_{co} - y_1}{E_1} & \frac{r_o}{E_1} \\ 1 & \frac{y_{co} - y_2}{E_2} & \frac{r_o}{E_2} \\ 1 & \frac{y_{co} - y_n}{E_n} & \frac{r_o}{E_n} \end{bmatrix}$$

$$E_i = \left[r_o^2 - (y_i - y_{co})^2\right]^{1/2}$$

The assumed a priori values are then updated with the new estimates found in (3-4):

$$x_{c1} = x_{co} + \Delta\hat{x}_c$$

$$y_{c1} = y_{co} + \Delta\hat{y}_c$$

$$r_1 = r_o + \Delta\hat{r}$$

The iteration process is continued until the magnitudes of $\Delta\hat{x}_c$, $\Delta\hat{y}_c$, and $\Delta\hat{r}$ conform to some pre-established smallness criterion. Analysis has shown that no more than 3 iterations are required to reduce the final error to a level well below the level of random error due to input noise.

Both schemes were analyzed by means of simulation in which uniformly distributed random noise with zero mean was superimposed in each data point. Linear scanning of the 15 x 15 deg square raster was assumed with a scan resolution of 0.015 deg (1000 lines across the aperture). The results showed that the errors were approximately linear with input noise level. The comparative results are therefore plotted normalized to the input noise level and the normalized errors are plotted against disk size. Figure 3-6 shows that the errors are comparable. Intuitively however, the LSE may seem to be a more desirable choice because of its comparative insensitivity to occasional peak noise inputs.

3.2.3 Lunar Orbiter Mission

Inasmuch as the guidance system for this mission will probably be used to control the launch and ascent phases, as well as the translunar and lunar phases, the complete three-axis strapdown inertial guidance subsystem will be required. The system block diagram and operational features are similar to those for the Mars orbiter mission (less the approach sensor) and will not be repeated.

3.2.4 Jupiter Flyby Mission

The comments for the lunar orbiter mission apply to this mission, and no further discussion will be made.

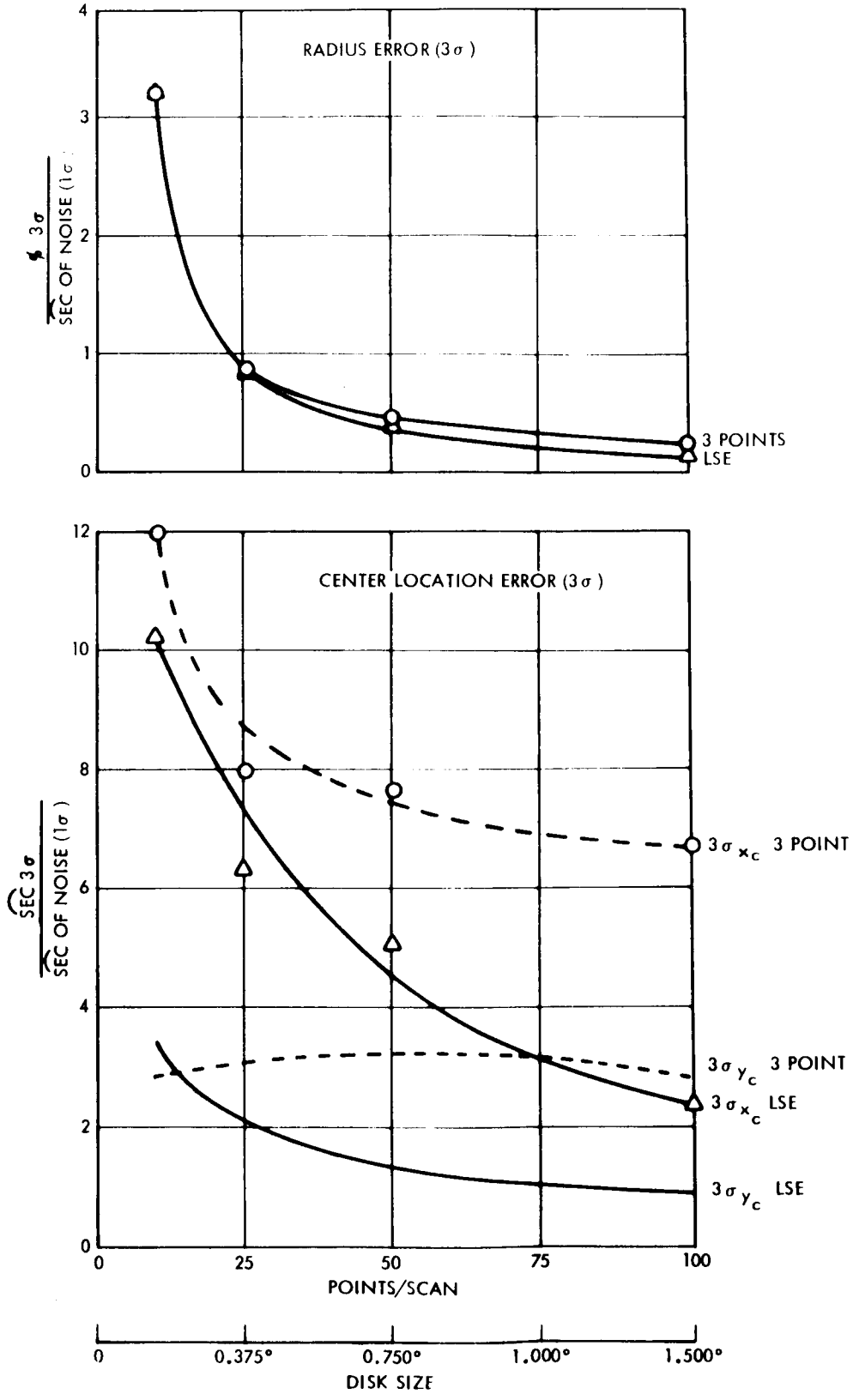

Figure 3-6. Comparison of Methods for Determining Planet Apparent Diameter and Centroid Location

4. STRAPDOWN INERTIAL GUIDANCE SUBSYSTEM

4.1 SUBSYSTEM CONFIGURATION AND INSTRUMENT SELECTION

Based upon the inertial equipment survey presented in Volume III (Part II), two representative strapdown Inertial Reference Units (IRU) were configured for purposes of this study. These IRU mechanizations, denoted by TG-166 and TG-266, were based on presently available inertial instruments and represent a range of readily achievable performance capabilities. The selected IRU configurations are shown in Table 4-I. The TG-166 represents an IRU subsystem with reasonable accuracy and available at moderate cost. The TG-266 represents a higher performance IRU subsystem available at a higher cost.

Table 4-I. Inertial Instrument Selection and Physical Characteristics of TG-166 and TG-266 IRU Subsystems

IRU Model Number	Gyros	Accelerometers	Volume (cm^3)	Weight (kg)	Power (w)
TG-166	Nortronics GIK7	Kearfoot Model C 702401-005	8,200	8.7	72
TG-266	Honeywell GG334	See Volume IV for selected accelerometer †	11,000	13.0	83

† In order to permit an unclassified presentation of performance data in this section, the identification of the TG-266 accelerometer is made in Volume IV.

The strapdown configuration for both candidate IRU subsystems consists of three single-degree-of-freedom gyros and three accelerometers mounted in an orthogonal triad. A functional block diagram of both the TG-166 and TG-266 IRU mechanizations is shown in Figure 4-1. Pulse torqued gyro loops are assumed in both mechanizations. The accelerometer rebalance loops are assumed analog with analog-to-digital conversion at the output as shown in Figure 4-1. Appendix A discusses pulse torquing

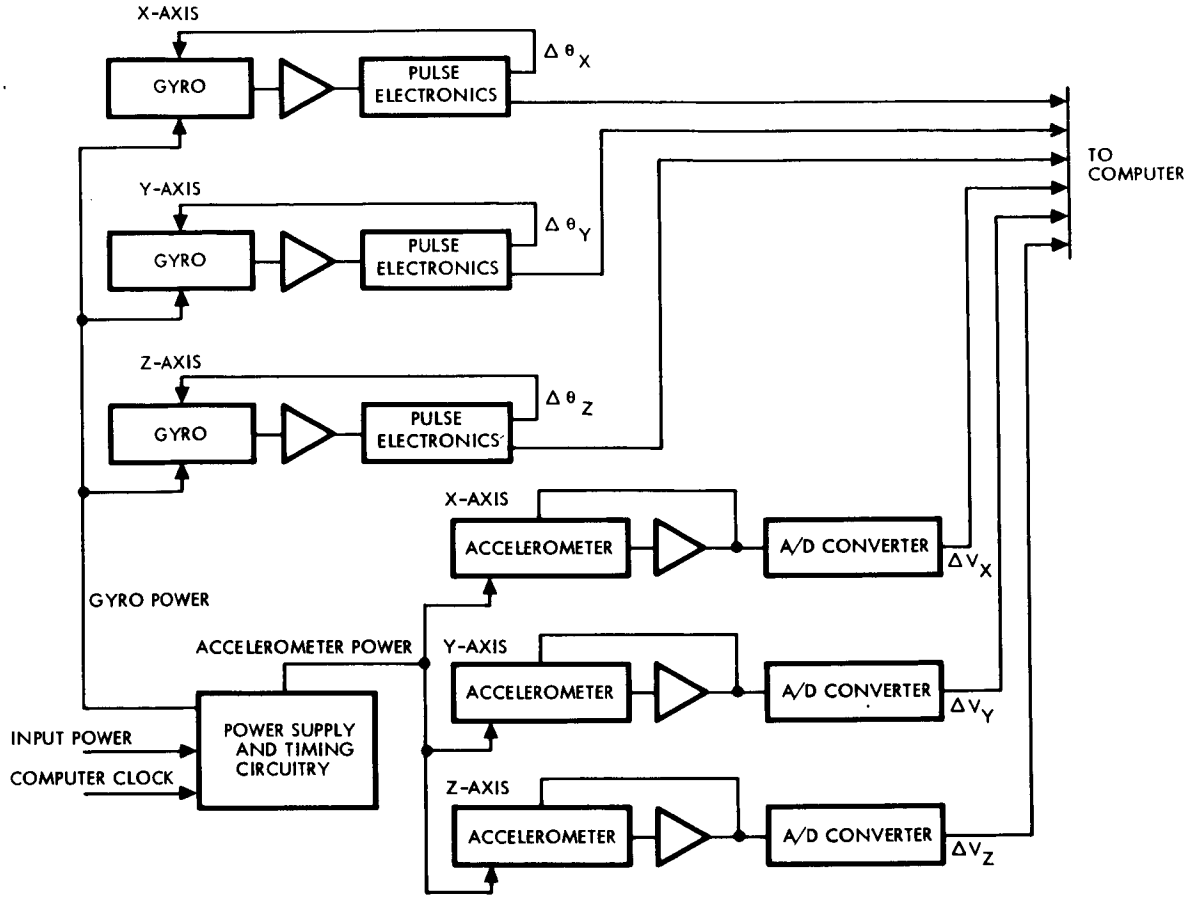

Figure 4-1. TG-166 and TG-266 System Block Diagram

techniques applicable to these mechanizations. The actual system and configurations in the two candidate subsystems are the same except that the TG-266 accelerometer loop utilizes a servo position amplifier instead of a force-to-balance loop.

4.2 SUBSYSTEM ERROR MODELS

Error models for the two IRU subsystem configurations are given in this subsection. These error models will be used as the basis for the mission performance analyses presented in Section 7.

The error model coefficients were derived from the hardware sensitivities given in Subsection 4.3. Each of the error model coefficients represents a number of individual error sources. When error sources could be represented by terms of the same form and where the resulting errors were statistically independent, these errors were combined by

computing the root sum square of the individual error magnitudes. Those errors which were not statistically independent were combined in an algebraic fashion.

The hardware sensitivities are shown in Tables 4-II and 4-III. These sensitivities were derived from actual test data (information obtained from the instrument manufacturers and TRW circuit design studies). In those cases where data were not available, the error sensitivity terms were conservatively estimated. Although several terms of the error model had to be estimated, the sensitivities are generally insignificant in practice.

Two error models are presented for each configuration, one in which a calibration update is performed just prior to launch and one without an update. This correction or updating would be made within a few hours of launch to the thrust axis accelerometer bias and scale factor and the roll axis gyro fixed drift and mass unbalance along the spin axis. The calibration update is derived from a measurement of the output of the thrust accelerometer and roll gyro immediately before or after the system is installed in the launch vehicle and a second measurement just prior to flight. It will be shown in Subsection 4.7 that the system statistical figure of merit can thereby be improved.

4.2.1 Instrument Error Model Equations

The reference coordinate system used is shown in Figure 4-2. The X axis corresponds to the local vertical at lift-off or the roll axis of the launch vehicle, while the Y and Z axes coincide with the two level axes and the pitch and yaw axes of the vehicle, respectively.

4.2.1.1 Accelerometer

The error in sensed acceleration due to uncompensated error characteristics and due to errors or changes in measured, compensated error characteristics can be expressed by the following equation:†

† The adequacy of a given error model (the form, choice of terms and the effects modeled) depends on the instrument characteristics, and on the particular application. For the purposes of this study, an error model of this form with $K_3 = 0$ adequately represents the instrument characteristics of the accelerometers chosen provided that proper account is taken of the calibration errors including the correlations introduced by the calibration process (see Test and Tables 4-IV and 4-V).

Table 4-II. TG-166 IRU 60-Day Error Model Sensitivities

Accelerometer Loops	
Accelerometer Loop Bias	
Sensor and electronics uncertainty	9.0 μg
Sensor stability	12.5 μg
Electronics stability	8.0 μg
Sensor temperature sensitivity	6.0 μg/°F
Electronics temperature sensitivity	1.0 μg/°F
Sensor voltage sensitivity	3.0 μg/%
Electronics voltage sensitivity	10.0 μg/%
Sensor vibration sensitivity	5.0 μg
Sensor frequency sensitivity	0.1 μg/cps
Compensation error	1.0 μg
Accelerometer Loop Scale Factor	
Sensor and electronics uncertainty	12.0 ppm
Uncorrected sensor stability uncertainty	51.3 ppm
Electronics stability	41.0 ppm
Sensor temperature sensitivity	20.0 ppm/°F
Electronics temperature sensitivity	7.0 ppm/°F
Sensor voltage sensitivity	5.0 ppm/%
Electronics voltage sensitivity	1.0 ppm/%
Sensor vibration sensitivity	10.0 ppm/g
Electronics nonlinearity	25.0 ppm
Sensor frequency sensitivity	0.1 ppm/cps
Clock rate error	5.0 ppm
Compensation error	1.0 ppm
Vibropendulous Coefficient	10 $\mu g/g^2$
Sensor Cross Axis Sensitivity (Pendulous Axis)	15 μg/g
Sensor Cross Axis Sensitivity (Output Axis)	1 μg/g
Sensor Cross Coupling Coefficient (Pendulous Axis)	50 $\mu g/g^2$
Sensor Cross Coupling Coefficient (Output Axis)	5 $\mu g/g^2$

Table 4-II. TG-166 IRU 60-Day Error Model Sensitivities (Continued)

Accelerometer Input Axis Inflight Alignment	
Y_m accelerometer to X_m	0.2 arc sec/g
Z_m accelerometer to X_m	0.2 arc sec/g
Compensation error	
X_m accelerometer misalignment	0.01 arc sec
Y_m accelerometer misalignment	0.01 arc sec
Z_m accelerometer misalignment	0.01 arc sec
Gyro Loops	
Gyro Non-g Sensitive Bias	
Sensor and electronics uncertainty	0.05 deg/hr
Sensor stability	0.15 deg/hr
Electronics stability	0.02 deg/hr
Electronics voltage sensitivity	0.006 deg/hr/%
Sensor temperature sensitivity	0.012 deg/hr/^{o}F
Electronics temperature sensitivity	0.002 deg/hr/^{o}F
Sensor vibration sensitivity	0.10 deg/hr/g
Spin motor frequency error	0.00007 deg/hr
Compensation error	5×10^{-5} deg/hr
Gyro Mass Unbalance Along the IA (MUIA)	
Sensor uncertainty	0.05 deg/hr/g
Sensor stability	0.55 deg/hr/g
Sensor temperature sensitivity	0.017 deg/hr/g/^{o}F
Sensor vibration sensitivity	0.30 deg/hr/g
Compensation error	0.0000 deg/hr/g
Gyro Mass Unbalance Along the SPA (MUSRA)	
Sensor uncertainty	0.05 deg/hr/g
Sensor stability	0.55 deg/hr/g
Sensor temperature sensitivity	0.015 deg/hr/g/^{o}F
Sensor vibration sensitivity	0.30 deg/hr/g
Compensation error	0.00002 deg/hr/g
Gyro OA Acceleration Drift	0.02 deg/hr/g
Gyro Anisoelastic Coefficient	0.04 deg/hr/g^2

Table 4-II. TG-166 IRU 60-Day Error Model Sensitivities (Continued)

Gyro Torquer Scale Factor (Low Range)	
Sensor and electronics uncertainty	6 ppm
Uncorrected sensor stability	48 ppm
Electronics stability	20 ppm
Sensor temperature sensitivity	12.5 ppm/^{o}F
Electronics temperature sensitivity	12.0 ppm/^{o}F
Electronics voltage sensitivity	10.0 ppm/%
Sensor vibration sensitivity	10.0 ppm/g
Electronics nonlinearity	3.0 ppm
Sensor nonlinearity	5.0 ppm
Spin motor frequency error	0.5 ppm
Compensation error	4.0 ppm
Gyro Torquer Scale Factor (High Range)	
Sensor nonlinearity	100 ppm
Electronics nonlinearity	330 ppm
Remainder of errors	56 ppm
Gyro Input Axis Alignment	
Stability	
X gyro to Y_m	10 arc sec
Y gyro to Z_m	10 arc sec
Z gyro to Y_m	10 arc sec
X gyro to Z_m	10 arc sec
Compensation error	
X_m gyro misalignment	0.01 arc sec
Y_m gyro misalignment	0.01 arc sec
Z_m gyro misalignment	0.01 arc sec

Table 4-III. TG-266 IRU 60-Day Error Model Sensitivities

Accelerometer Loops	
Accelerometer Loop Bias	
Sensor and electronics uncertainty	6 μg
Sensor stability	8 μg
Sensor temperature sensitivity	17 μg/°F
Electronics temperature sensitivity	1 μg/°F
Sensor voltage sensitivity	1 μg/%
Electronics voltage sensitivity	1 μg/%
Compensation error	1 μg
Accelerometer Loop Scale Factor	
Sensor and electronics uncertainty	8.0 ppm
Sensor stability	7.0 ppm
Electronics stability	1.0 ppm
Sensor temperature sensitivity	1.4 ppm/°F
Electronics temperature sensitivity	1.0 ppm/°F
Sensor voltage sensitivity	1.0 ppm/%
Electronics voltage sensitivity	1.0 ppm/%
Sensor vibration sensitivity	21.0 ppm/g
Clock rate error	5.0 ppm
Compensation error	1.0 ppm
Vibropendulous Coefficient	10 $\mu g/g^2$
Sensor Cross Axis Sensitivity (Pendulous Axis)	10 μg/g
Sensor Cross Axis Sensitivity (Output Axis)	1 μg/g
Sensor Cross Coupling Coefficient (Pendulous Axis)	30 μg/g
Sensor Cross Coupling Coefficient (Output Axis)	15 $\mu g/g^2$
Accelerometer Input Axis Inflight Alignment	
Y_m accelerometer to X_m	0.2 arc sec/g
Z_m accelerometer to X_m	0.2 arc sec/g

Table 4-III. TG-266 IRU 60-Day Error Model Sensitivities (Continued)

Compensation error	
X_m accelerometer misalignment	0.01 arc sec
Y_m accelerometer misalignment	0.01 arc sec
Z_m accelerometer misalignment	0.01 arc sec
Gyro Loops	
Gyro Non-g Sensitive Bias	
Sensor and electronics uncertainty	0.004 deg/hr
Sensor stability	0.060 deg/hr
Electronics stability	0.020 deg/hr
Electronics voltage sensitivity	0.006 deg/hr/%
Sensor temperature sensitivity	0.012 deg/hr/^{o}F
Electronics temperature sensitivity	0.002 deg/hr/^{o}F
Sensor vibration sensitivity	0.07 deg/hr/g
Gyro Mass Unbalance Along the IA (MUIA)	
Sensor uncertainty	0.004 deg/hr/g
Sensor stability	0.06 deg/hr/g
Sensor temperature sensitivity	0.01 deg/hr/g/^{o}F
Sensor vibration sensitivity	0.15 deg/hr/g
Gyro Mass Unbalance Along the SRA (MUSRA)	
Sensor uncertainty	0.004 deg/hr/g
Sensor stability	0.084 deg/hr/g
Sensor temperature sensitivity	0.015 deg/hr/g/^{o}F
Sensor vibration sensitivity	0.15 deg/hr/g
Compensation error	0.001 deg/hr/g
Gyro Anisoelastic Coefficient	0.02 deg/hr/g^2
Gyro Torquer Scale Factor	
Sensor and electronics uncertainty	6 ppm
Uncorrected sensor stability	10 ppm
Electronics stability	20 ppm
Sensor temperature sensitivity	13 ppm/^{o}F

Table 4-III. TG-266 IRU 60-Day Error Model Sensitivities (Continued)

Electronics voltage sensitivity	10 ppm/%
Electronics nonlinearity	3 ppm
Sensor nonlinearity	5 ppm
Compensation error	4 ppm
Gyro Input Axis Alignment	
Stability	
X gyro to Y_m	10 arc sec
Y gyro to Z_m	10 arc sec
Z gyro to Y_m	10 arc sec
X gyro to Z_m	10 arc sec
Compensation	
X_m gyro misalignment	0.01 arc sec
Y_m gyro misalignment	0.01 arc sec
Z_m gyro misalignment	0.01 arc sec

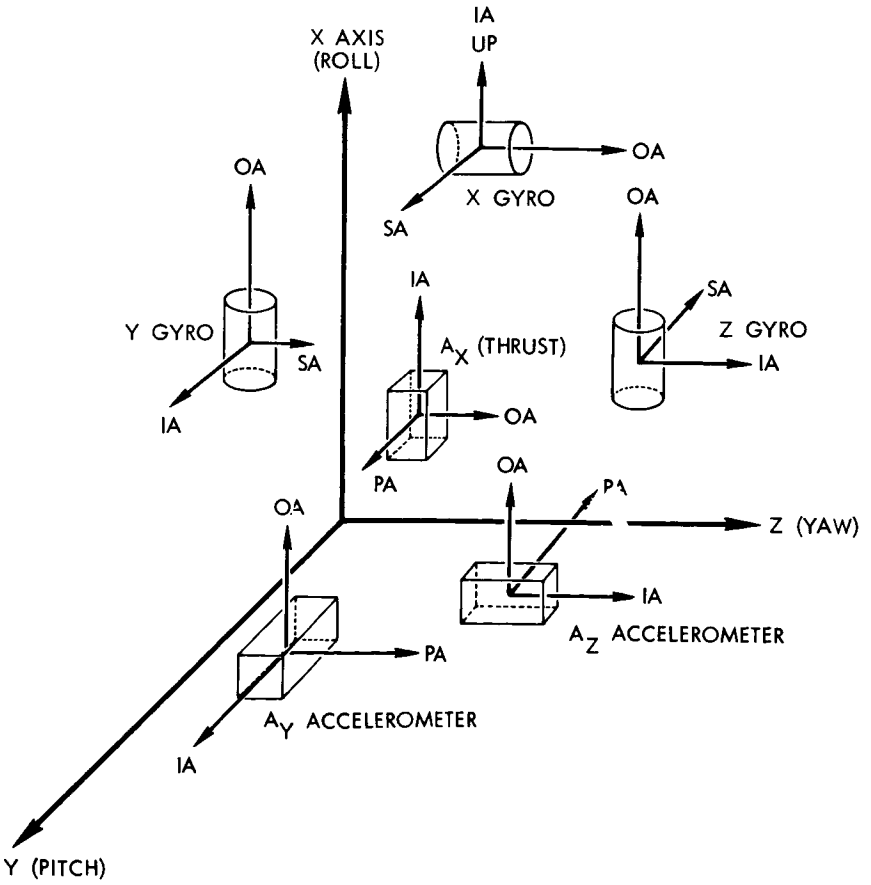

Figure 4-2. Strapdown Coordinate Axis (Pad Orientation)

Table 4-IVA. TG-166 IRU Error Model (No Update)

	1σ Value		
Accelerometer Error Source	X	Y	Z
Bias uncorrelated (μg)	21.0	21.0	21.0
Bias correlated (μg)			
Scale factor (ppm)	75.0	75.0	75.0
Alignment (mrad)	Y-X 0.06	Z-Y 0.06	
Gyro Error Source			
Fixed drift uncorrelated (deg/hr)	0.187	0.187	0.187
Fixed drift correlated (deg/hr)			
MUSA (deg/hr/g)	0.627	0.627	0.627
MUIA (deg/hr/g)	0.627	0.627	0.627
Scale factor (ppm)	57.0	57.0	57.0
Alignment (mrad)	0.05	0.05	0.05
IRU Error Source			
Alignment (mrad)	0.10	0.10	0.10

Table 4-IVB. TG-166 IRU Error Model (Update)

	1σ Value		
Accelerometer Error Source	X	Y	Z
Bias uncorrelated (μg)	13.0	21.0	21.0
Bias correlated (μg)	18.0		
Scale factor (ppm)	29.0	75.0	75.0
Alignment (mrad)	X-Y 0.06	Z-Y 0.06	
Gyro Error Source			
Fixed drift uncorrelated (deg/hr)	0.12	0.187	0.187
Fixed drift correlated (deg/hr)	0.16		
MUSA (deg/hr/g)	0.31	0.63	0.63
MUIA (deg/hr/g)	0.63	0.63	0.63
Scale factor (ppm)	57.0	57.0	57.0
Alignment (mrad)	0.05	0.05	0.05
IRU Error Source			
Alignment (mrad)	0.10	0.10	0.10

Table 4-VA. TG-266 IRU Error Model (No Update)

	1σ Value		
Accelerometer Error Source	X	Y	Z
Bias uncorrelated (μg)	14.0	14.0	14.0
Bias correlated (μg)			
Scale factor (ppm)	24.0	24.0	24.0
Alignment (mrad)	Y-X 0.05	Y-Z 0.05	
Gyro Error Source			
Fixed drift uncorrelated (deg/hr)	0.09	0.09	0.09
Fixed drift correlated (deg/hr)			
MUSA (deg/hr/g)	0.16	0.16	0.16
MUIA (deg/hr/g)	0.16	0.16	0.16
Scale factor (ppm)	26.0	26.0	26.0
Alignment (mrad)	0.05	0.05	0.05
IRU Error Source			
Alignment (mrad)	0.10	0.10	0.10

Table 4-VB. TG-266 IRU Error Model (Update)

	1σ Value		
Accelerometer Error Source	X	Y	Z
Bias uncorrelated (μg)	10.0	14.0	14.0
Bias correlated (μg)	13.0		
Scale factor (ppm)	23.0	24.0	24.0
Alignment (mrad)	Y-X 0.05	Y-Z 0.05	
Gyro Error Source			
Fixed drift uncorrelated (deg/hr)	0.07	0.09	0.09
Fixed drift correlated (deg/hr)	0.06		
MUSA (deg/hr/g)	0.09	0.16	0.16
MUIA (deg/hr/g)	0.16	0.16	0.16
Scale factor (ppm)	26.0	26.0	26.0
Alignment (mrad)	0.05	0.05	0.05
IRU Error Source			
Alignment (mrad)	0.10	0.10	0.10

$$\Delta a_j = K_0 + K_1 a_{i_j} + K_2 a_{i_j}^2 + K_3 a_{i_j} a_{0_j}$$

where subscripts i and 0 refer, respectively, to the input and output axes of each accelerometer, and the subscript j refers to the X, Y, and Z accelerometer. The coefficients have the following definition:

Δa_j = error in sensed acceleration along the X, Y, and Z axes

K_0 = bias uncertainty

K_1 = linear scale factor uncertainty

K_2 = sensitivity to the square of the acceleration along the input axis

K_3 = sensitivity to the product of the acceleration along the input axis and acceleration along the output axis

The error in sensed acceleration due to the uncompensated misalignment of the input axis of each accelerometer, with respect to the reference coordinate system, is expressed as follows:

$$\Delta a_i = \beta_{i_j} a_j + \beta_{i_k} a_k$$

where

Δa_i = error in sensed acceleration along the i axis

β_{i_j} = misalignment of the i accelerometer input axis toward the j axis

β_{i_k} = misalignment of the i accelerometer input axis toward the k axis

4.2.1.2 Gyro

The gyro drift rate due to uncompensated error characteristics or due to errors of changes in measured, compensated error characteristics can be expressed as follows:†

$$\dot{\Phi}_j = C_0 + C_1 a_{i_j} + C_2 a_{s_j} + C_3 a_{i_j} a_{s_j}$$

† Additional error sources, not strictly instrument dependent but significant in this application, are included in Tables 4-IV and 4-V. The most significant of these are gyro scale factor and gyro misalignment errors.

where the subscripts i and s refer to the input and spin axes of the gyro, respectively.

C_0 = fixed drift rate uncertainty

C_1 = spin axis mass unbalance uncertainty

C_2 = input axis mass unbalance uncertainty

C_3 = anisoelastic coefficient

The resulting coordinate angular misalignment due to gyro errors is given by:

$$\Phi_j = \Phi_{j_0} + \int_0^t \dot{\Phi}_j \, dt \; \dagger$$

Φ_{j_0} = initial uncompensated misalignment of the gyro coordinate system about the j axis

$\dot{\Phi}_j$ = drift rate about the j axis as determined from error model

4.2.2 Error Model Summary

The error model equations used to evaluate the system performance are discussed above. The coefficient of each term in the equation is listed in Tables 4-IV and 4-V. The magnitude of each coefficient has been computed from the characteristics of the hardware, the manner in which it will be calibrated or updated prior to flight, and the expected flight environment.

4.3 ERROR SENSITIVITIES

The performance sensitivities of the guidance hardware are shown in Tables 4-II and 4-III. The IRU error models in Tables 4-IV and 4-V were derived from these sensitivities and the expected flight environment.

---

†It should be noted that the drift rates must be transformed into inertial coordinates before this integration is performed.

The gyros, accelerometers, rebalance electronics, and related equipment are acted on by disturbances during the period from calibration to launch and during flight. The sensitivities of each component to each significant disturbance has been based on a short-term duration of 8 hr and long-term duration of 60 days.

The sensitivities, wherever possible, were derived from data taken from instrument and breadboard level tests which were performed to measure the performance characteristics.

The sensitivities are essentially the ratios of the change of a performance parameter per change in a disturbance. An example would be the change in non "g" sensitive drift rate for a change in temperature.

$$\dot{\theta}_T = \frac{\Delta\dot{\theta}}{\Delta T}$$

where

$\dot{\theta}_T$ = sensitivity to temperature

$\Delta\dot{\theta}$ = change in drift rate between two temperatures

ΔT = change in temperature

Sensitivities for both the TG-166 and TG-266 IRU subsystems were derived in Tables 4-II and 4-III, respectively. Since both subsystems have the same configuration and even the same generic type of inertial components, the major difference will be seen in the magnitude of the error sources, not the kinds of error sources themselves. In the case of the

gyro, both instruments are floated, integrating rate, single-degree-of-freedom devices and have approximately the same types of error sources. The individual error values are quite different, however, in some cases.

The electronic sensitivities appearing in Tables 4-II and 4-III were derived by assuming that the electronics design maximum tolerances were 3σ values. Present circuit development and laboratory tests indicate that most of the circuits will meet the design maximum tolerance under stress. (In the case of the TG-266 IRU, the electronic errors are considerably smaller since the susceptibility to electronic variation in the servo loops can be minimized at increased cost.)

The TG-166 IRU subsystem error model has a great deal of test data to substantiate the magnitude of the error terms appearing in Table 4-IV. It appears, however, that the vendor's test data on the drift rate terms both g and non-g sensitive could have relatively large measurement errors. This occurred because the test data were compiled on an earlier program which did not require the accuracy associated with a strapdown guidance application. Therefore, the drift rate measurement tests were not designed for accuracy beyond the requirements of the earlier program. It would be expected that the GIK-7 gyro drift rate terms would be somewhat reduced when more accurate data are available. This also assures that the sensitivities in Table 4-II are conservative.

The error model developed for the TG-266 IRU subsystem is somewhat lacking in test data in support of the Honeywell GG-334A gyro. Some data were available, but not as much as for the GIK-7 gyro. A great many more of the sensitivities were obtained directly from the vendor without test data verification, but all of the values obtained appear to be within reasonable ranges considering the type and design of the instrument.

4.4 DISTURBANCES

The disturbances which affect strapdown guidance system accuracy fall into four categories. These disturbances can also be subdivided into prelaunch and inflight. The types of disturbances in this error model are listed below.

a) Electrical power disturbances

b) Thermal disturbances

c) Magnetic disturbances

d) Inflight vibration disturbances.

4.4.1 Electrical Power Disturbances

The prime power for the guidance system is +28 vdc power provided from the missile power system. The expected power disturbances are listed below.

+28 vdc	$1\sigma = \pm 3.3$ percent
constant power spectral density from 100 cps to 100 kc	$1\sigma = 0.2$ v rms

The 3.3 percent tolerance refers to the voltage set point and the 0.2 v rms refers to the noise characteristics. In addition, it should be noted that the error model does not account for any power transients which may occur. The IRU power supply should be designed to eliminate or minimize these power transients.

4.4.2 Thermal Disturbances

The thermal disturbances which will affect the guidance accuracy are listed below.

a) Change in ambient temperature during laboratory test and calibration

b) Change in ambient temperature from laboratory to launch

c) Change in ambient temperature during flight.

In the case of the laboratory environment, the temperature variation was assumed to be $\pm 5^{\circ}$F about a mean temperature of 72°F.

In estimating the change in temperature from laboratory and launch, it is assumed that the IMU is in a shaded air-conditioned compartment. Therefore, expected temperature variation would be similar to the laboratory environment of $72^{\circ}F \pm 5^{\circ}F$.

The estimate of ambient temperature during flight was derived from knowledge of Atlas-Centaur flight data and thermal analysis. The data and analysis indicate that the temperature can be considered a ramp function as measured at the skin of the units comprising the subsystem.

Two heating cases would exist, the maximum heating rate and the minimum heating rate. In the case of the maximum heating rate, the following assumptions should be made: continuous direct solar radiation, maximum earth thermal and albedo radiation. The minimum heating rate assumes no direct solar radiation and minimum earth thermal and albedo radiation. Table 4-VI lists the analytical results of the thermal analysis and flight data for the Atlas-Centaur and an estimate for the TG-166 and TG-266 IRU subsystems.

Table 4-VI. Temperature Rate ($^{\circ}F$/Min)

System	Unit	Maximum Heating	Minimum Heating	Flight Data	Estimate
Atlas/ Centaur (powered flight)	Platform	0.96	0.00	0.90	
	Platform electronics	0.80	-0.32	0.70	
TG-166	IRU				0.70
TG-266	IRU				0.70

4.4.3 Vibration

During flight the guidance system will experience vibration inputs both linear and rotational in nature. An estimate from data accumulated in several missile programs has been made and is shown in Figures 4-3 through 4-6.

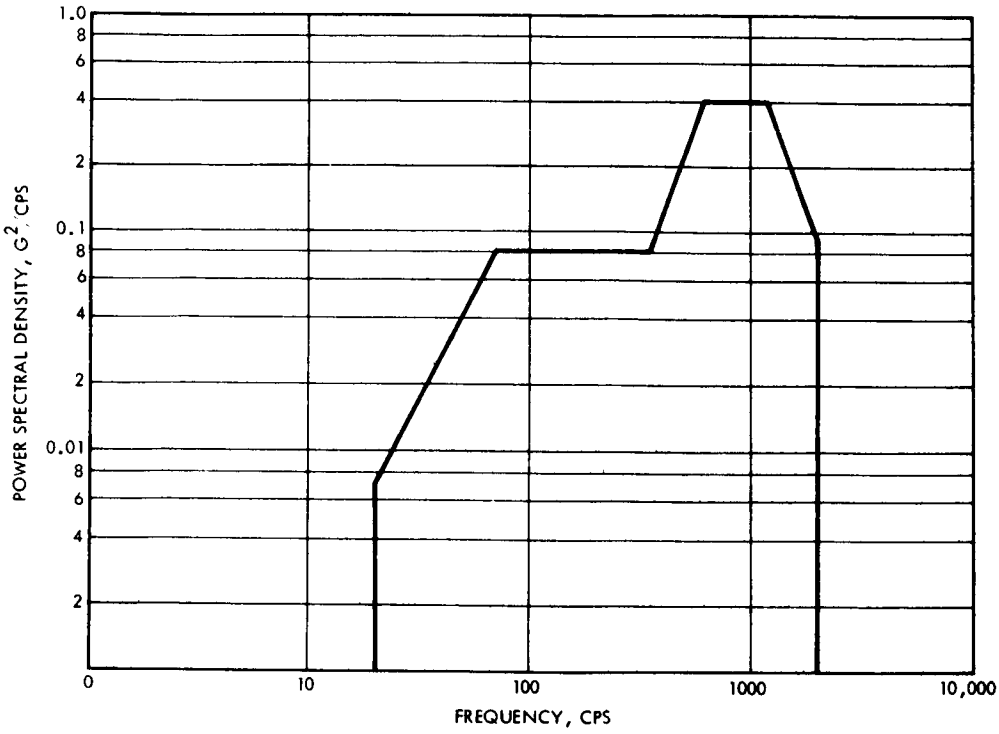

Figure 4-3. Predicted Spectrum for Typical Space Booster Linear Vibration

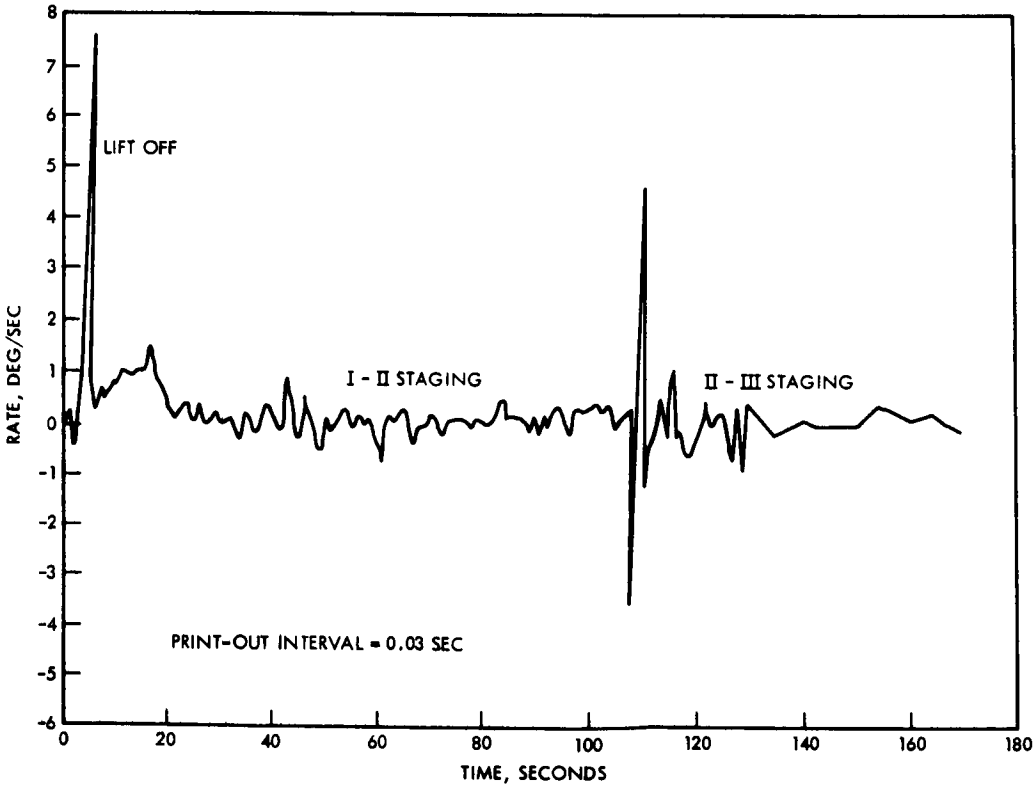

Figure 4-4. Pitch Rate Versus Time

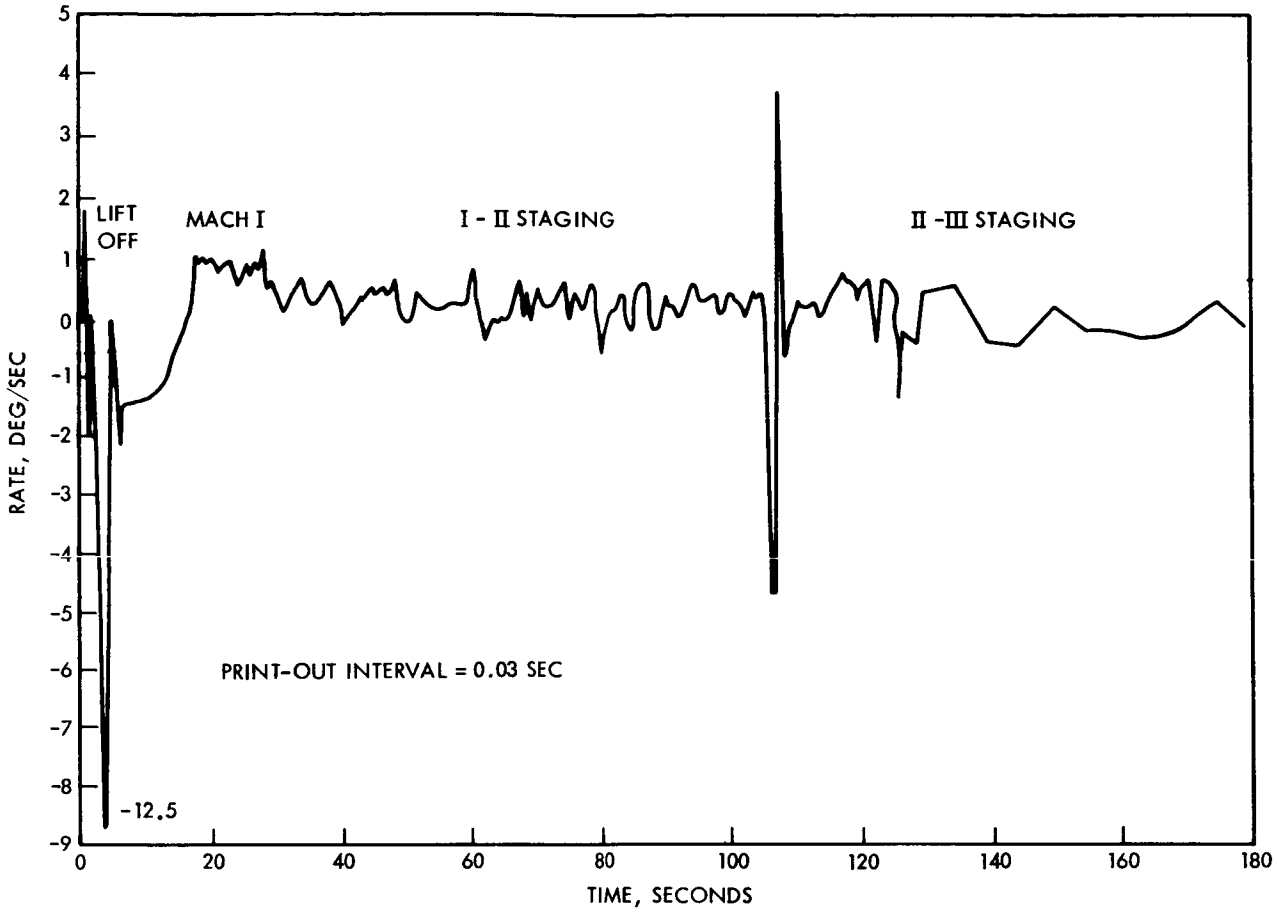

Figure 4-5. Yaw Rate Versus Time

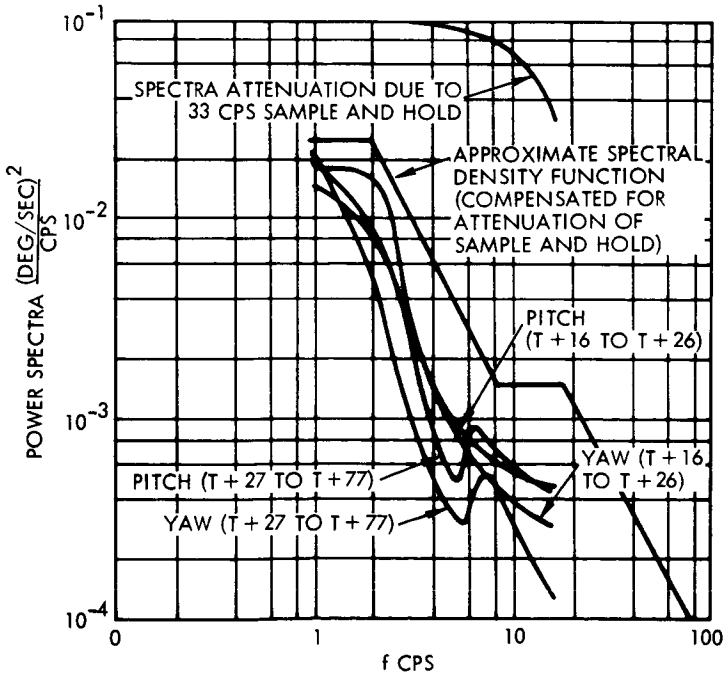

Figure 4-6. Rotational Power Spectral Density

4.4.3.1 Linear Vibration

A great deal of flight test data is available on several types of missiles. The power spectral density shown in Figure 4-3 was derived from the combination of the Atlas/Mercury, Atlas/Agena, Titan, Polaris, Thor-Able, and Minuteman vibration data. The envelope of this spectrum was developed from representative magnitudes for all significant flight events.

4.4.3.2 Rotational Vibration

The ability to derive an estimate of the rotational vibration experienced during the missile flight is considerably impaired by the lack of rate information at information frequencies in excess of 2 or 3 cps. Data for several different types of vehicles were examined but due to the low bandwidth of both the rate information and the telemetry channels, little could be derived. The best information available was data from Minuteman II flights where a data bandwidth of 30 cps was available.

The plots in Figures 4-4 and 4-5 represent the rate information plotted with 3- to 4-sec smoothing. The plots also show missile flight events.

The Minuteman flight data have been analyzed and a power spectral density function computed for both the pitch and yaw data. This set of data was considered representative of the typical Minuteman rotational vibration.

The straight line approximation of this power spectral density is shown in Figure 4-6. The flight times analyzed were from T + 16 to T + 26 which includes transition through Mach I and T + 27 to T + 77 which includes maximum "q", staging of first and second stages, and one-half second stage burn. The combination of all of these events will result in a high estimate of the total environment over the flight. However, this was done to obtain a conservative approach for design purposes.

4.4.4 Magnetic Fields

Changes in the magnetic field experienced by the system originate from two sources:

a) Rotation of the IMU with reference to the earth's magnetic field

b) Magnetic field variations internal and external to the system

With proper design no significant change should be caused by b). Therefore, only the earth's magnetic effect need be considered in the IRU calibration.

4.5 ERRORS DUE TO RANDOM VIBRATION INPUTS

TRW has developed a series of digital computer programs to determine the equivalent drift rate errors resulting from IRU exposure to an environment of random rotational vibration. From previous analyses two of these rectification error sources are the largest, first, the "fictitious coning" and second, the spin-input rectification. Although several other sources exist, they are relatively small.

4.5.1 Fictitious Coning

A coning motion can be induced into the IRU subsystem by simultaneous out-of-phase sinusoidal or random inputs about two orthogonal axes. The rotational rate resulting from this input will be computed by the airborne computer and used to update the direction cosines. An error in the coning drift rate will result if the rate sensor loops supplying the computer with vehicle rotational rates have different phase characteristics. The difference between the phase shifts experienced through each loop will cause vehicle input rates to change phase relationship at the input to the computer. The computer will then calculate the coning drift rate on the basis of these rates. Since the rate is dependent on the phase between the two input rates and the phase relationship of the sensor outputs is in error with respect to the true vehicle rate, an erroneous coning rate will be computed which results in an equivalent net drift rate.

4.5.2 Spin-Input Rectification

The spin-input rectification error is the result of angular vibration excitation acting simultaneously about the input and spin axes of the gyro.

The error is introduced when the input axis of the gyro is allowed to have an offset angle due to the rate on the input axis. If there exists a rate of appropriate phasing and frequency about the spin axis 90 deg from the null position of the input axis, an error rate will be rectified by the gyro.

Appendix B presents the general solution for the mean drift rate caused by rectification errors in a strapdown IRU subjected to random vibrations. A computer program exists at TRW for performing the necessary integrations. An approximate analytical solution is also presented in Appendix B for the mean drift rate for the special case of a single input where both the transfer functions and input power spectral density are rational functions of frequency. A particularly simple result is obtained when the spectrum is approximated by that of a first-order Gauss-Markov process. The answer is obtained without the necessity for numerical integration and thus verifies the computer solutions.

4.5.3 Results

The results of the calculation of fictitious coning and spin-input rectification based upon the rotational vibration environment given in Figure 4-6 are listed in Table 4-VII below.

These error magnitudes are negligible with respect to the other subsystem hardware errors. Therefore, they do not appear as an error source in the error models presented earlier.

Table 4-VII. Strapdown Inertial Component Errors Due to Random Rotational Environment

Fictitious Coning	0.00104 deg/hr
Spin-Input Rectification	0.00076 deg/hr

4.6 LABORATORY CALIBRATION

Laboratory calibration involves a sequence of measurements which may contain errors. See Table 4-VIII for the error model. The laboratory calibration terms for the accelerometers and gyro will be derived from measurements taken during the six IRU calibration orientations shown in Figure 4-7.

Table 4-VIII. Error Models of Calibration Measurement Uncertainties

Error Source	Measurement Uncertainties (1σ)	
	TG-166	TG-266
Accelerometer Bias		
Sensor threshold	1	1
Sensor short term stability	5	3
Test equipment accuracy	5	5
Voltage measurement	3	–
A/D Converter short-term stability or servo loop	5	1
	13 μg	6 μg
Accelerometer Scale Factor		
Bias uncertainty	13	6
Scale factor short term stability	10	5
A/D converter short-term stability or servo loop	5	1
Timing	1	1
	17 ppm	8 ppm
Gyro Non-g Sensitive Bias		
Sensor random drift	0.050	0.0037
Electronics random drift	0.001	0.001
Reading granularity	0.0001	0.0001
	0.05 deg/hr	0.004 deg/hr
Gyro g Sensitive Bias		
Sensor random drift	0.050	0.0037
Alignment	0.005	0.005
Electronics	0.001	0.001
Readability	0.0001	0.0001
	0.05 deg/hr	0.0066 deg/hr

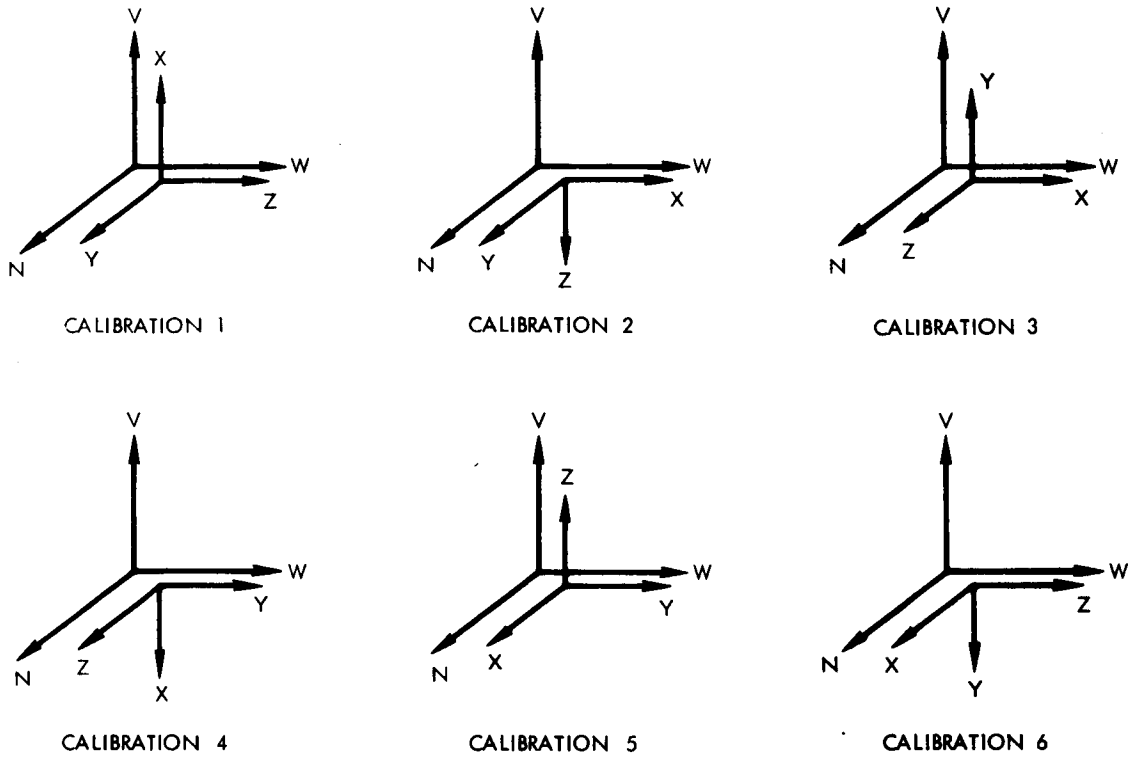

Figure 4-7. Six Calibration Positions

Table 4-IX shows the measurement terms to be used to determine instrument calibration. The accelerometer bias and scale terms can be obtained from the A_{up} and A_{down} measurements taken in positions (1, 4), (3, 6), and (2, 4), respectively. The bias and scale factor can be computed using the expression below.

$$\text{Bias} = \frac{\Sigma\Delta V_U + \Sigma\Delta V_D}{2(T)}$$

where

Bias = accelerometer bias

$\Sigma\Delta V_U$ = summation of the ΔV pulses taken with the IA up

$\Sigma\Delta V_D$ = summation of the ΔV pulses taken with the IA down

T = duration of measurement period

$$SF = \frac{\Sigma\Delta V_U - \Sigma\Delta V_D}{2T(g)}$$

Table 4-IX. Instrument Calibration Measurement Terms

Instrument	Calibration Position					
	1	2	3	4	5	6
X accelerometer	A_{UP}			A_{DOWN}		
Y accelerometer			A_{UP}			A_{DOWN}
Z accelerometer		A_{DOWN}			A_{UP}	
X gyro	$CT + MUSA(g) + \Omega_V$	$CT + \rho_x \Omega_H$	$CT + \rho_x \Omega_H + MUIA(g)$	$CT - MUSA(g) - \Omega_V$	$CT + \Omega_H$	$CT + MUIA(g) + \Omega_H$
Y gyro	$CT + \Omega_H$	$CT - MUIA(g) + \Omega_H$	$CT + MUSA(g) + \Omega_V$	$CT + \rho_y \Omega_H$	$CT + MUIA(g) + \rho_g \Omega_H$	$CT + MUSA(g) - \Omega_V$
Z gyro	$CT + \Omega_H \rho_z$	$CT - MUSA(g) - \Omega_V$	$CT - MUIA(g) + \Omega_H$	$CT + \Omega_H$	$CT + MUSA(g) + \Omega_V$	$CT + MUIA(g) + \rho_z \Omega_H$

CT = Constant torque (gyro bias)

Ω_H = Local horizontal earth's rate

Ω_V = Local vertical earth's rate

ρ = Misalignment angle

where

SF = accelerometer scale factor

g = gravitational acceleration

The computation of gyro drift terms, while more involved, requires merely a series of simple arithmetic operations using data taken during the six calibration positions.

4.7 PRELAUNCH CALIBRATION

This subsection presents the results of a prelaunch calibration study for the inertial sensors in a strapdown configuration. A Saturn vehicle ground environment is assumed. The study indicates that it is feasible to perform a prelaunch calibration on the strapdown guidance system after it has been installed in the launch vehicle (or spacecraft) in the launch configuration.

The results show that vehicle sway is the dominant error source. Furthermore, the measurement uncertainty of a gyro with its axis vertical and with use of the proper filtering technique could reduce a 20-min measurement period to 0.003 deg/hr (1σ). However, uncertainty for the gyros with their axes horizontal was far greater. The vertical accelerometer measurement uncertainty would remain about the same as laboratory conditions (9μg); but greater degrees of uncertainty occur in the horizontal accelerometer measurements, which render them virtually useless. Therefore, only the roll axis gyro and accelerometer are considered for prelaunch calibration.

4.7.1 Procedure

The individual error sources are calibrated on the bench about 60 days before launch. About 8 hr before launch, the roll axis gyro and accelerometer are recalibrated by measurements taken in the launch configuration, i.e., roll axis nominally vertical. The significant errors are gyro bias drift and mass unbalance along the spin axis drift, and accelerometer bias and scale factor.

4.7.2 Notation

Since both the gyro and accelerometer have fixed and g-sensitive terms, a single derivation is adequate. By having B represent the sensor

bias error and G the sensor g-sensitive error, the sensor errors can be divided into Equations (4-1) and (4-2):

$$B = B_1 + B_2 + B_3 + B_4 \tag{4-1}$$

and

$$G = G_1 + G_2 + G_3 + G_4 \tag{4-2}$$

where

B_1, G_1	have correlation times longer than 60 days
B_2, G_2	have correlation times between 8 hr and 60 days
B_3, G_3	have correlation times shorter than 8 hr
B_4, G_4	exist only in the presence of the launch and flight vibration environment

The total sensor error is given by

$$E = B + aG \tag{4-3}$$

where a is the roll axis acceleration. The B_i and G_i and all measurement errors are assumed to be independent random variables with zero mean.

4.7.3 Bench Calibration

At time t_1, bench calibration is performed and the calibrated bias, B_c, and g-sensitive, G_c, errors are obtained. If the calibration is performed over about a period of a day, the error sources with correlation times shorter than 8 hr (B_3 and G_3) will average out fairly well. If ϵ_B and ϵ_G represent the measurement error, including any residual error caused by the presence of B_3 and G_3, then

$$B_c(t_1) = B_1(t_1) + B_2(t_1) + \epsilon_B(t_1) \tag{4-4}$$

$$G_c(t_1) = G_1(t_1) + G_2(t_1) + \epsilon_G(t_1) \tag{4-5}$$

4.7.4 Prelaunch Calibration

At time t_2, 60 days later and 8 hr before launch, a measurement

of the total sensor error is performed, using the calibration obtained at time t_1.

$$E(t_2) = B(t_2) - B_c(t_1) + g\left[G(t_2) - G_c(t_1)\right] + \epsilon(t_2) \tag{4-6}$$

where ϵ is the measurement error and a has been replaced by g under the assumption that the gyro is in a one-g field. Because of the assumptions made about the correlation times,

$$B_1(t_2) \cong B_1(t_1) \tag{4-7}$$

$$G_1(t_2) \cong G_1(t_1) \tag{4-8}$$

and from Equations (4-1), (4-2), (4-4) through (4-8)

$$E(t_2) = B_2(t_2) - B_2(t_1) + B_3(t_2) - \epsilon_B(t_1)$$

$$+ g\left[G_2(t_2) - G_2(t_1) + G_3(t_2) - \epsilon_G(t_1)\right] + \epsilon(t_2) \tag{4-9}$$

This measurement is now used to correct both the bias and g-sensitive calibrations.

$$B_c(t_2) = B_c(t_1) + k_B E(t_2) \tag{4-10}$$

$$G_c(t_2) = G_c(t_1) + k_G E(t_2)/g \tag{4-11}$$

The gains k_B and k_G are chosen to minimize the variance of $B'(t_3)$ and $G'(t_3)$, the residual bias and g-sensitive errors at launch time, where

$$B'(t_3) = B(t_3) - B_c(t_2) \tag{4-12}$$

$$G'(t_3) = G(t_3) - G_c(t_2) \tag{4-13}$$

Note that at time t_3 and throughout the flight, the B_4 and M_4 terms are present because of the vibration environment. Because of the assumptions about correlation times,

$$B_1(t_3) \cong B_1(t_1) \tag{4-14}$$

$$G_1(t_3) \cong G_1(t_1) \tag{4-15}$$

$$B_2(t_3) \cong B_2(t_2) \tag{4-16}$$

$$G_2(t_3) \cong G_2(t_2) \tag{4-17}$$

Combining the above equations gives

$$\begin{aligned} B'(t_3) = {} & \left[B_2(t_2) - B_2(t_1) - \epsilon_B(t_1)\right](1 - k_B) + B_3(t_3) + B_4(t_3) \\ & - k_B\left[B_3(t_2) + g\left[G_2(t_2) - G_2(t_1) + G_3(t_2)\right.\right. \\ & \left.\left. - \epsilon_G(t_1)\right] + \epsilon(t_2)\right] \end{aligned} \tag{4-18}$$

$$\begin{aligned} G'(t_3) = {} & \left[G_2(t_2) - G_2(t_1) - \epsilon_G(t_1)\right](1 - k_G) + G_3(t_3) + G_4(t_4) \\ & - k_G\left\{G_3(t_2) + \left[B_2(t_2) - B_2(t_1) + B_3(t_2) - \epsilon_B(t_1)\right]\Big/g \right. \\ & \left. + \frac{\epsilon(t_2)}{g}\right\} \end{aligned} \tag{4-19}$$

Calculating the variance by squaring Equations (4-18) and (4-19) and finding the expectation gives

$$\begin{aligned} \sigma^2_{B'} = {} & \left[2\sigma^2_{B_2} + \sigma^2_{\epsilon_B}\right](1 - k_B)^2 + \sigma^2_{B_3} + \sigma^2_{B_4} \\ & + k_B^2\left\{\sigma^2_{B_3} + g^2\left[2\sigma^2_{G_2} + \sigma^2_{G_3} + \sigma^2_{\epsilon_G}\right] + \sigma^2_{\epsilon}\right\} \end{aligned} \tag{4-20}$$

$$\begin{aligned} \sigma^2_{G'} = {} & \left[2\sigma^2_{G_2} + \sigma^2_{\epsilon_G}\right](1 - k_G)^2 + \sigma^2_{G_3} + \sigma^2_{G_4} \\ & + k_G^2\left\{\sigma^2_{G_3} + \left[2\sigma^2_{B_2} + \sigma^2_{B_3} + \sigma^2_{\epsilon_B}\right]\Big/g^2 \right. \\ & \left. + \frac{\sigma^2_{\epsilon}}{g^2}\right\} \end{aligned} \tag{4-21}$$

Let

$$\sigma_{BL}^2 = 2\sigma_{B_2}^2 + \sigma_{\epsilon_B}^2 \tag{4-22}$$

$$\sigma_{GL}^2 = 2\sigma_{G_2}^2 + \sigma_{\epsilon_G}^2 \tag{4-23}$$

$$\sigma_E^2 = \sigma_{B_3}^2 + g^2\sigma_{G_3}^2 + \sigma_\epsilon^2 \tag{4-24}$$

Then

$$\sigma_{B'}^2 = \sigma_{BL}^2(1 - k_B)^2 + \sigma_{B_3}^2 + \sigma_{B_4}^2 + k_B^2\left(g^2\sigma_{GL}^2 + \sigma_E^2\right) \tag{4-25}$$

$$\sigma_{G'}^2 = \sigma_{GL}^2(1 - k_G)^2 + \sigma_{G_3}^2 + \sigma_{G_4}^2 + k_G^2\left(\sigma_{BL}^2/g^2 + \sigma_E^2/g^2\right) \tag{4-26}$$

Let the partial derivatives of the variances with respect to the gains be set equal to zero.

$$\frac{\partial\sigma_{B'}^2}{\partial k_B} = -2(1 - k_B)\sigma_{BL}^2 + 2k_B\left(g^2\sigma_{GL}^2 + \sigma_E^2\right) = 0 \tag{4-27}$$

$$\frac{\partial\sigma_{B'}^2}{\partial k_G} = -2(1 - k_G)\sigma_{GL}^2 + 2k_G\left(G_{BL}^2/g^2 + \sigma_E^2/g^2\right) = 0 \tag{4-28}$$

Then

$$k_B = \frac{\sigma_{BL}^2}{\sigma_{BL}^2 + g^2\sigma_{GL}^2 + \sigma_E^2} \tag{4-29}$$

and

$$k_G = \frac{g^2\sigma_{GL}^2}{\sigma_{BL}^2 + g^2\sigma_{GL}^2 + \sigma_E^2} \tag{4-30}$$

are the optimal gains. Note that the optimal gains do not depend upon the $B_3(t_3)$ and $B_4(t_3)$ errors or the $G_3(t_3)$ and $G_4(t_3)$ errors. Thus the optimal calibration procedure gives the best estimate of $B_c(t_2)$ and $G_c(t_2)$ without regard to the errors that are expected to arise later. Therefore it would be erroneous to lump the errors arising from $B_3(t_3)$, $B_4(t_3)$, $G_3(t_3)$, and $G_4(t_3)$ in with the errors at time t_2 that contribute to σ_E^2. This circumstance is not surprising, since the error terms under consideration at t_3 are assumed to be uncorrelated with those at t_2.

4.7.5 Inputs for the Error Analysis Program

The error analysis program requires the standard deviations $\sigma_{B'}$ and $\sigma_{G'}$ which may be obtained by taking the square roots of Equations (4-25) and (4-26). In addition, the correlation between $B'(t_3)$ and $B'(t_3)$ is required. It is defined by

$$\rho_{B'G'} = \frac{\langle B'(t_3)G'(t_3)\rangle}{\sigma_{B'}\sigma_{G'}} \tag{4-31}$$

where $\langle x\rangle$ is the expected value of x. From Equations (4-18) and (4-19)

$$\begin{aligned}\langle B'(t_3)\, G'(t_3)\rangle = &-\left(2\sigma_{B_2}^2 + \sigma_{\epsilon_B}^2\right)/g\, k_G(1 - k_B) \\ &- \left(2\sigma_{G_2}^2 + \sigma_{\epsilon_G}^2\right) g\, k_B(1 - k_G) \\ &+ \left(\sigma_{B_3}^2/g + g\,\sigma_{G_3}^2 + \sigma_\epsilon^2/g\right) k_G k_B\end{aligned} \tag{4-32}$$

From Equations (4-22) through (4-24) and (4-31)

$$\rho_{B'G'} = \frac{-\frac{\sigma_{BL}^2}{g} k_G(1 - k_B) - \sigma_{GL}^2\, g\, k_B(1 - k_G) + \frac{\sigma_E^2}{g} k_G k_B}{\sigma_{B'}\sigma_{G'}} \tag{4-33}$$

4.7.6 Errors in the Absence of Calibration

To form a basis of comparison, we find the errors that would exist if the prelaunch calibration were omitted, by setting k_B and k_G equal to zero.

$$\sigma_B^2 = \sigma_{BL}^2 + \sigma_{B_3}^2 + \sigma_{B_4}^2 \tag{4-34}$$

$$\sigma_G^2 = \sigma_{GL}^2 + \sigma_{G_3}^2 + \sigma_{G_4}^2 \tag{4-35}$$

$$\rho_{BG} = 0 \tag{4-36}$$

4.7.7 Note on the Determination of σ_{BL} and σ_{GL}

Equations (4-22) and (4-23) show that a coefficient of two appears before $\sigma_{B_2}^2$ and $\sigma_{G_2}^2$. It is important to recognize that the coefficient of two would also appear in the results of a physical measurement made to determine σ_{B_2}. In fact, the results of such a measurement would be

$$\sigma_{BM}^2 = 2\sigma_{B_2}^2 + 2\sigma_{\epsilon_B}^2 \tag{4-37}$$

$$\sigma_{GM}^2 = 2\sigma_{G_2}^2 + 2\sigma_{\epsilon_G}^2 \tag{4-38}$$

since measurement errors occur both at the beginning and the end of the 60-day period. Therefore

$$\sigma_{BL}^2 = \sigma_{BM}^2 - \sigma_{\epsilon_B}^2 \tag{4-39}$$

$$\sigma_{GL}^2 = \sigma_{GM}^2 - \sigma_{\epsilon_G}^2 \tag{4-40}$$

although in practice $\sigma_{\epsilon_B}^2$ and $\sigma_{\epsilon_G}^2$ should be small enough so that Equations (4-39) and (4-40) may be approximated by

$$\sigma_{BL}^2 \cong \sigma_{BM}^2 \tag{4-41}$$

$$\sigma_{GL}^2 \cong \sigma_{GM}^2 \tag{4-42}$$

4.7.8 Numerical Results

Table 4-X is obtained from Tables 4-II and 4-IV.

Table 4-X. Prelaunch Calibration Errors for the TG-166 IRU Subsystem

	Gyro		Accelerometer	
σ_{BL}	0.180	deg/hr	20.4	μg
σ_{B3}	0.050	deg/hr	5.0	μg
σ_{B4}	0	deg/hr	0	μg
σ_{GL}	0.549	deg/hr/g	74.5	μg/g
σ_{G3}	0.050	deg/hr/g	10.0	μg/g
σ_{G4}	0.300	deg/hr/g	0	μg/g
σ_{ϵ}	0.033	deg/hr	13.0	μg

With the above choice of units, g equals 1. The results are presented in Table 4-XI for the uncalibrated case, the optimal case, and the basic case where $k_B = 0$, $k_G = 1$, that is, where all of the correction is applied to the g-sensitive error. The basic method is used because the improvement obtained by using the optimal method is only 5 percent at best and because the basic method is simpler. The modified error sources are presented in Table 4-XII.

Table 4-XI. Comparison of Optimal and Basic Prelaunch Calibration Errors with the Uncalibrated Case for the TG-166 System

Uncalibrated Case

	Gyro		Accelerometer	
k_B	0		0	
k_G	0		0	
σ_B	0.187	deg/hr	21.0	μg
σ_G	0.627	deg/hr/g	75.0	μg/g
$\rho_{B'G'}$	0		0	

Optimal Case

	Gyro		Accelerometer	
k_B	0.0953		0.0666	
k_G	0.887		0.886	
$\sigma_{B'}$	0.178	deg/hr	20.3	μg
$\sigma_{G'}$	0.356	deg/hr/g	27.0	μg/g
$\rho_{B'G'}$	-0.453		-0.672	

Basic Case

	Gyro	Accelerometer
k_B	0	0
k_G	1	1
$\sigma_{B'}$	0.187	21.0
$\sigma_{G'}$	0.362	28.5
$\rho_{B'G'}$	-0.479	-0.696

Table 4-XII. Modified Error Sources for the TG-166 System

Error Source†	Description	Value	Units
73	Accelerometer scale factor	28.5	μg/g
263	Gyro input axis g-sensitive drift	0.362	deg/hr/g

$\rho_{40,73} = -0.696$

$\rho_{230,263} = -0.479$

†See Table 7-I for the definition of error source numbers.

4.7.9 Percentage of Improvement

It is of interest to determine the percentage of cases in which the use of the optimal or basic calibration technique leads to improvement over the uncalibrated system. The injections error can be expressed as

$$\Delta V_i = \frac{\partial V_i}{\partial B} B'(t_3) + \frac{\partial V_i}{\partial G} G'(t_3) \qquad (4\text{-}43)$$

The partial derivatives are available from the Error Analysis Program. A Monte-Carlo technique was used to generate random shifts in the gyro bias, mass unbalance and measurement errors and compute the resultant injection velocity. The random shifts and measurement errors were generated from gaussian pseudorandom numbers.

The errors for both the updated and non-updated configuration were computed and compared. The percentage of cases of increased injection error for the updated system were computed and printed out.

The results of the computer runs are summarized in Table 4-XIII.

Table 4-XIII. Statistical Improvement Due to Prelaunch Calibration

Run	Number of Samples	No Improvement	Improvement	Percent of Systems Improved
1	590	51	539	91.4
2	530	43	487	91.9
3	500	45	455	91.0
4	500	47	463	92.7

Runs 1 and 2 are for gyro mass unbalance calibration while Runs 3 and 4 are for accelerometer scale factor calibrations. In Runs 1 and 3 the basic calibration technique was used while in Runs 2 and 4 the optimal calibration technique was used. The advantage of the optimal method over the basic method is not marked.

5. ELECTRO-OPTICAL SENSORS

5.1 INTRODUCTION AND SUMMARY

The objective of Task II of the Radio/Optical Strapdown Inertial Guidance Study is to recommend a preliminary design and to analyze the performance of an optically-aided inertial guidance system to be used in future unmanned space flights. The approach to this portion of the study has been to:

1) Identify the functional and performance requirements for electro-optical sensors by mission phase for each of the four generic missions studied.

2) Survey the state-of-the-art of electro-optical devices that potentially might be used, including body-fixed star mappers for three-axis altitude determination, planetary horizon sensors, and sun sensors.

3) Using the results of 1) and 2), select appropriate candidate sensors.

4) Develop performance models for the sensors and analyze their performance in conjunction with other elements of the system for each of the four missions.

The method of implementation which has been considered in this study is that of a strapdown inertial guidance system in which the electro-optical sensors are used to update system alignment and bound the errors due to gyro drift. In addition, the electro-optical sensors may be used for regaining control of spacecraft attitude after a complete power shut-down during an interplanetary coast phase, or after recovery from a complete power failure.

The candidate electro-optical sensors which have been selected are based upon those defined in a state-of-the-art survey presented in Volume III, (Part I), of this report. Information in this survey was obtained directly from manufacturers and research laboratories, and defines both the current state-of-the-art and projected advancements in the near future. In addition, applicable information compiled under the

USAF Standardized Space Guidance System Study (Ref 4-1) was included. This survey included the following types of optical sensors:

- Sun sensors, including both nulling devices and solar aspect sensors.
- Earth sensors, including both horizon sensors for use in earth orbit and long-range earth sensors for use in interplanetary flight.
- Star trackers, including both gimbaled and strapdown subsystems, using both mechanical and electronic scanning, and photoelectric or solid-state optical radiation detectors.
- Star field sensors, using photoelectric and solid-state detectors, with either mechanical or electronic scanning techniques.
- Planet sensors, for terminal approach or planetary orbit, employing both mechanical and electronic scanning.

It was determined that the four specified missions could be accomplished utilizing various combinations of sun sensors, earth sensors, a Canopus sensor, and a planetary approach sensor. Only in the case of the Mars orbiter mission was it determined that state-of-the-art equipment was not applicable. In this case it was determined that, in order to obtain a higher degree of accuracy[†], higher precision would be required for both the Canopus sensor and the planetary approach sensor. A preliminary design concept of instruments for both of these applications is defined.

This section discusses the selection of the electro-optical sensors, provides descriptive preliminary design information, and develops performance (error) models for the selected sensors. Mission performance results are given in Sections 7 and 8.

[†]This type of mission can be performed with reasonable accuracy without the use of an approach guidance sensor. More specifically, the early Voyager missions can be accomplished using a combination of on-board optical inertial system (without the approach sensor) plus precision earth-based tracking, if the projected improvements in the DSIF can be achieved (see Section 6). Nevertheless, the accuracy improvement due to use of the approach guidance sensor may be useful for advanced orbiter missions.

5.2 MISSION PROFILE AND ELECTRO-OPTICAL SENSOR OPERATIONAL SEQUENCES

In the following paragraphs the operational sequence of utilization of the selected electro-optical sensors is discussed for the several phases of the specified missions. The sensors which have been selected for the various missions are defined in Table 5-I.

5.2.1 Earth Synchronous Orbiter

During launch, injection into the parking orbit, coast in parking orbit, injection into the transfer orbit, and injection into synchronous orbit, the primary attitude reference will be the inertial elements of the guidance system.

Launch and injection into the parking orbit will be accomplished using only the strapdown inertial guidance system. The duration of the parking orbit will vary between 15 min and 18 hr, depending upon the longitude desired for boost into the transfer orbit. If the duration of the parking orbit is sufficiently long to require correction of the inertial reference system prior to boost into the transfer orbit, optical sightings will be utilized at this time. A low-altitude earth horizon sensor will be used to obtain a measurement of the vertical, in conjunction with sun sensors to obtain yaw alignment. Two choices of sun sensor configurations are apparent. Using a combination of coarse and fine sun sensors, vehicle maneuvers will be required in order to obtain a solar sighting, after which the vehicle will be returned to the earth-referenced attitude. Alternately, the use of a digital solar aspect sensor will permit a solar sighting to be obtained simultaneously with measurement of the vertical by the earth horizon sensor, without requiring vehicle maneuvers. The latter choice is recommended.

After approximately five hours in the transfer orbit, correction of the inertial reference system alignment will again be required prior to injection into the earth-synchronous orbit. Again, the sun will be used as a reference for correcting the vehicle attitude in yaw, and the earth will be used as a reference for correction of the vertical.

Table 5-I. Recommended Electro-Optical Sensors for Various Missions

TYPE OF SENSOR	RECOMMENDED SENSOR	MISSION AND PHASE: EARTH SYNCHRONOUS ORBITER — Low Altitude Parking Orbit	EARTH SYNCHRONOUS ORBITER — Transfer Orbit	LUNAR ORBITER — Lunar Transfer Orbit	LUNAR ORBITER — Midcourse Correction Maneuver	MARS ORBITER — Interplanetary Transfer Orbit	MARS ORBITER — Midcourse Correction Maneuver	MARS ORBITER — Planetary Approach	SOLAR PROBE WITH JUPITER ASSIST — Interplanetary Transfer Orbit	SOLAR PROBE WITH JUPITER ASSIST — Midcourse Correction Maneuver
SUN SENSORS										
Coarse	TRW Systems – VASP Sun Sensors (Modified)	▲	▲	●	●	●	●	●	●	●
Fine	Ball Bros. Research Corp. Fine Eye No. FE-5A	▲	▲	●	●	●	●	●	●	●
Digital Aspect	Adcole Corporation Aspect Sensor No. 1402	●	●							
EARTH SENSORS										
Low Altitude	Advanced Technology Division American Standard Advanced OGO Earth Sensor	●								
High Altitude	Advanced Technology Division American Standard Modified OGO		●							
CANOPUS TRACKER										
Contemporary	ITT Federal Laboratories Lunar Orbiter Canopus Tracker			●	●		●		●	●
High Accuracy	Vidissector Tracker (New Design)							●		
PLANETARY APPROACH SENSOR										
High Accuracy	Digitally Scanned Image Tube (New Design)							●		

● = Primary Choice

▲ = Alternate Choice

The same choice of sun sensors pertains, and the digital solar aspect sensor is again recommended. Due to the reduced angular subtense of the earth at synchronous altitude, a high-altitude earth sensor must be used.

5.2.2 Lunar Orbiter

As in the case of the earth-synchronous orbiter, the inertial elements of the guidance system will be utilized as the primary attitude reference for launch, injection into parking orbit, and for coast in parking orbit. The duration of the parking orbit may vary between 0 and 20 min. For this short coast phase, no attitude update of the inertial system is required.

After injection into the lunar transfer orbit, the primary attitude references will be the Sun and Canopus. The coarse and fine sun sensors, in conjunction with a single-axis Canopus tracker, will be used during this phase of the mission. The precision available from these sensors together with the onboard inertial system and ground radio tracking aids (see Section 6) is adequate to perform the midcourse correction maneuver and deboost into lunar orbit without the use of additional electro-optical sensors for approach guidance.

5.2.3 Mars Orbiter

Injection into interplanetary transfer orbit will normally require parking orbit coasts not exceeding 30 min. Thus, no optical sensors are required during this phase of the mission. After injection into the interplanetary transfer orbit, coarse and fine sun sensors in conjunction with a Canopus tracker will be used. However, the Canopus tracker is also used for approach guidance to Mars. To achieve any significant improvement in approach trajectory estimation over that available with earth-based DSIF tracking (Section 6), very high precision is required during this phase of the mission. Therefore, a Canopus sensor with higher tracking accuracy than that available in state-of-the-art equipment is required for this mission. A preliminary design concept for such a sensor is presented in Paragraph 5.3.4.

Precise sensing of the line-of-sight to the Sun is required during approach guidance, which may be performed with an available fine sun

sensor. With the reference frame established by lines-of-sight to the Sun and Canopus, a planetary approach sensor will be used to define spacecraft position data with respect to the planet by: a) defining the direction to the center of Mars, and b) establishing the apparent angular subtense of the planet to permit stadimetric ranging. A preliminary design concept of a high-precision planet sensor, utilizing a high-resolution electronically-scanned image tube, for this phase of the Mars mission is presented in Paragraph 5.3.5.

5.2.4 Solar Probe With Jupiter Assist

Again, no electro-optical sensors are required prior to injection into the interplanetary transfer orbit. For the interplanetary cruise phase and for midcourse corrections the sensor used will be identical to those used for the Mars mission. The use of a planetary approach sensor in approach to Jupiter is not required for guidance purposes since no trajectory corrections are made subsequent to the midcourse maneuver.

5.3 DESCRIPTION OF SELECTED ELECTRO-OPTICAL SENSORS

In the following paragraphs, the electro-optical sensors selected for the various missions are described in detail, and justification for their selection is provided. Wherever feasible, state-of-the-art equipment was selected, based upon the survey defined in Volume III (Part I).

5.3.1 Coarse and Fine Sun Sensors

The coarse and fine sun sensor combination will be utilized in all of the four missions under consideration for determination of vehicle attitude prior to midcourse correction maneuvers and for vehicle reorientation during recovery from complete power shutdown or failure. In addition, this sensor combination will be used for determination of vehicle attitude during approach to the planet Mars. Although a digital aspect sensor is recommended for use as a primary reference prior to injection into the earth-synchronous or interplanetary transfer orbits, the coarse and fine sun sensor combination is recommended as a backup in case of power failure.

The candidate sun sensor system consists of two coarse sun sensor units having a 4π steradian total field-of-view and sufficient environmental

resistance to be mounted outboard the spacecraft, and a narrow-field fine sensor to be mounted inboard, integrated with the other fine optical sensors. The coarse sun sensor is a design proposed by TRW for the Voyager program, and is based on a sun sensor developed for the VASP spacecraft. Each coarse sun sensor unit consists of two silicon solar cells, mounted back-to-back and in optical contact with a plano-convex lens. The cell outputs are connected in opposing polarities across a low resistance. The voltage measured across the resistance is proportional to the sun elevation above the common plane of the two solar cells and, hence, provides a one-axis error signal. Figure 5-1 illustrates the coarse sun sensor concept, its measured transfer characteristic, and system arrangement.

The fine sun sensor is the FE-5A "fine eye" developed by the Ball Brothers Research Corporation. Two pairs of "fine eyes" are required to track the sun, one pair for each axis. Each of the "fine-eye" sensors consists of an objective lens, knife-edge reticle, filter, and silicon solar cell. The output current from a single cell is linearly proportional to the displacement of the sun angle from the optical axis. A pair of sensors provides a total linear error-sensing range of ±5 deg from the null plane. Two such pairs define an image null angle. The fine-eye unit is very simple, mechanically rigid, and electrically stable. The performance specification indicates a null shift of ±1 min or less, over a temperature range of -20 to +85°C. This fine sun sensor system has been successfully used on the Lunar Orbiter and OSO-1 spacecraft.

Selection of the particular sun sensor design described above is based on two considerations:

1) Use of separate units permits coverage of a full 4-π steradian field with good linearity and stability about null.

2) The silicon solar cell has been thoroughly proven in space applications and requires no power input.

The scale factors for the coarse and fine sun sensors are designed to be nearly equal between 4 and 5 deg from null. The attitude control system is switched from the coarse sun sensor to the fine sun sensor

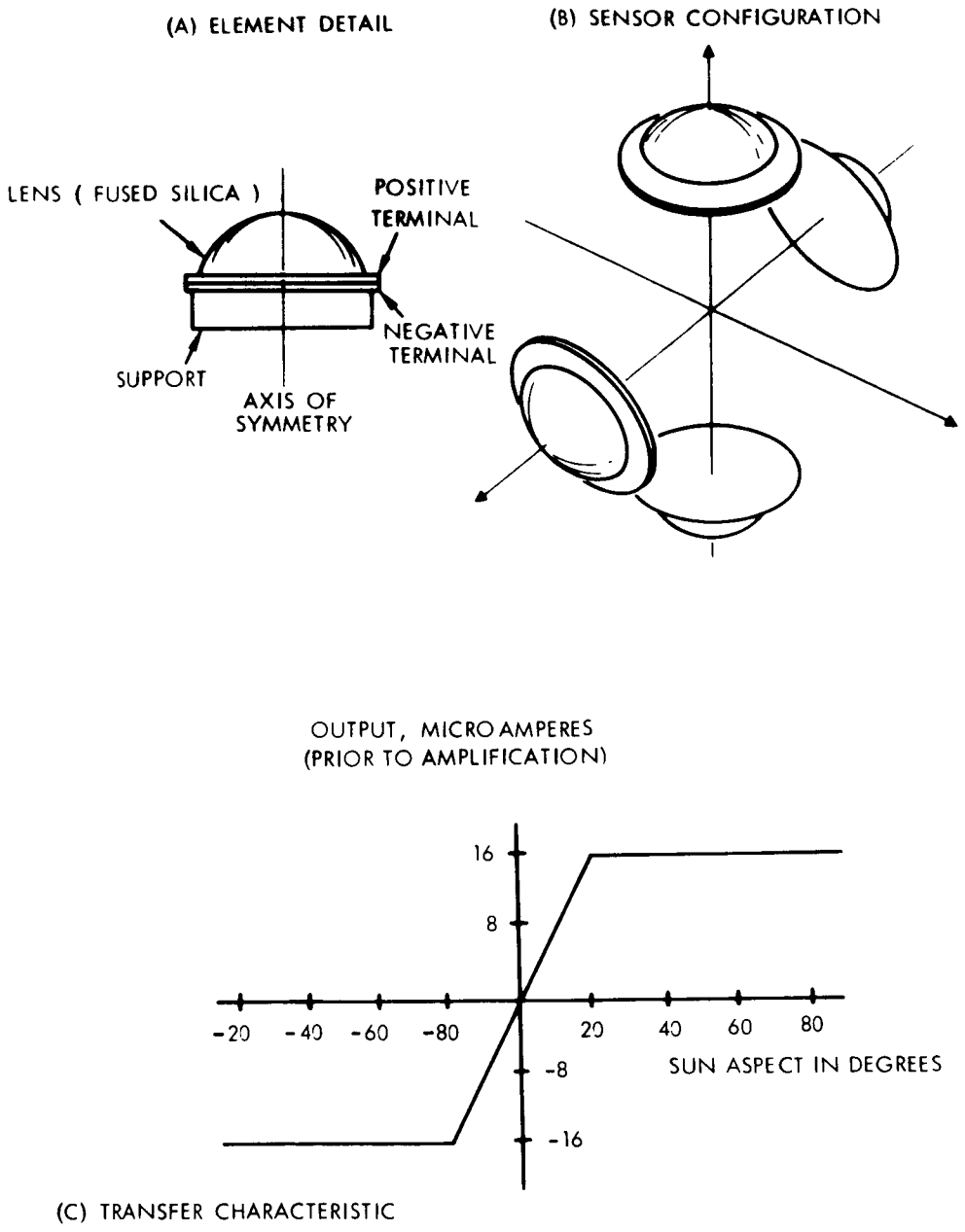

Figure 5-1. Coarse Sun Sensors

within the 4- to 5-deg band, so that the transition will not produce a discontinuity in the signal. The electronic configuration of the sun sensor configuration is illustrated in Figure 5-2. Detailed specifications are defined in Table 5-II.

5. 3. 2 Digital Solar Aspect Sensor

The digital solar aspect sensor is recommended as the primary reference for correction of vehicle attitude in yaw for the following missions and phases:

a) Earth-synchronous orbiter

1) Prior to injection into the transfer orbit from parking orbit.

2) Prior to injection into the synchronous orbit from the transfer orbit.

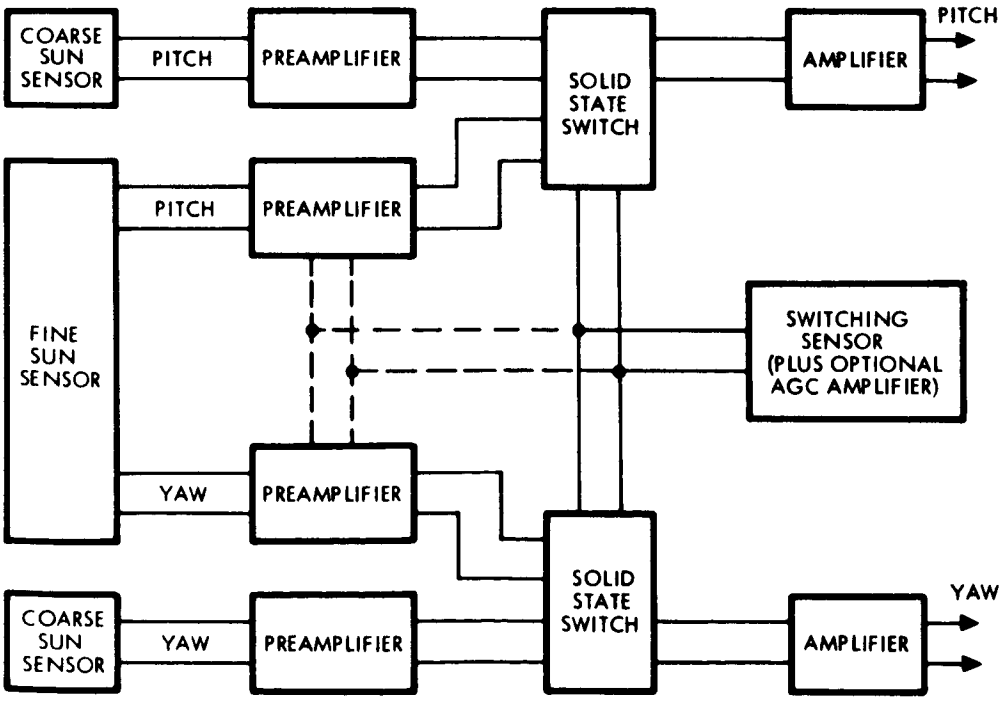

Figure 5-2. Sun Sensor Electronic Configuration

Table 5-II. Coarse and Fine Sun Sensor Specifications

Fine Sensor Assembly†	
Accuracy (fine eye pair at null)	± arc min
Peak output (short-circuit current in direct sunlight)	1.5 ma nominal
Angular range (fine eye pair)	±15 deg nominal
Angular sensitivity (front edge)	5 μamp/arc min
Spectral response	0.70 to 1.1 μ; 0.81 μ peak
Response time (rise time from 10 to 90 percent of peak value)	20 μsec or less
Resolution	Virtually infinite
Temperature operating range	-20°C to + 85°C
Weight: FE-5A fine eye	6.0 gm
Eye assembly retainer	3.5 gm
Coarse Sensor Assembly	
Field of view	4π ster
Null accuracy (each axis)	±1 deg
Linearity (over ±20 deg each axis)	±10 percent
Physical Characteristics (Includes Electronics)	
Size	330 cm^3
Weight	0.34 kg
Power	700 mw

†Manufacturer's specifications.

b) Lunar orbiter, Mars orbiter, and solar probe with Jupiter assist

1) Prior to injection into interplanetary transfer orbit from earth parking orbit.

This device, designed and developed by the Adcole Corporation of Waltham, Massachusetts, measures two orthogonal components of the sun's offset from the instrument reference axis in terms of two 12-bit digital words. The total field-of-view is 64 x 64 deg for both acquisition and fine measurement.

The digital solar aspect sensor consists of two single-axis units in a single assembly. Each single-axis detector lead consists of a gray-coded reticle, silicon photo cell array, and a housing. The gray-coded reticle is a small oblong block of fused quartz with a slit centered along the top surface and a gray-coded pattern on the bottom surface. Sunlight passing through the slit is screened by the pattern to either illuminate

or not illuminate the photo cells below. The outputs of the photo cells comprise a digital word, representative of the solar aspect about one axis. An additional photo cell is usually included, which is always "ON", when the sun is within field-of-view of the detector head. The output of this cell is used as an AGC signal to compensate for the photo cell output variation as a function of solar angle. This permits accurate angular determination of the transition between resolution elements. The characteristics of the digital solar aspect sensor are defined in Table 5-III.

Table 5-III. Digital Solar Aspect Sensor Specifications†

Model	Adcole type 1402
Field-of-view	64 x 64 deg
Resolution	1/64 deg
Accuracy	2 arc min
Output	Two 12-bit words
Operating temperature range	-70 to 100°C
Size	1.3 x 1.3 x 2.1 cm
Weight	0.15 kg
Power	None required

†Manufacturer's specification.

5.3.3 Earth Sensors

The performance requirements for the earth sensors have been based primarily upon the constraints determined by the synchronous earth-orbit mission. The pre-injection phases of the lunar and interplanetary missions are assumed to have the same alignment accuracy requirements.

In the parking orbit of the earth-synchronous mission, the half-angle subtended by the earth is approximately 75 deg; and at synchronous altitude, this half-angle is 8.7 deg. The present status of earth sensor technology precludes precise determination of the vertical over this wide angular range with one instrument. Therefore, two earth horizon sensors are recommended, one for use in the earth parking orbit and the other for use at synchronous altitude.

The low-altitude earth sensor is the advanced OGO horizon tracker developed by the Advanced Technology Division of American Standard for the OGO spacecraft. This instrument consists of four sensors, arranged at 90-deg intervals in yaw, utilizing linear scanning and edge-tracking of the horizon.

The high-altitude earth sensor is the modified OGO horizon tracker, also developed by the Advanced Technology Division of American Standard. The scanning mechanism is the same as that used in the OGO horizon tracker, but only two sensors are utilized, arranged at 90-deg intervals in yaw, with linear scanning across the earth's disc in two orthogonal planes. From the survey presented in Volume III (Part I), the selection of these horizon sensors was based upon the following considerations:

a) For use in a nonspinning vehicle, edge-tracking, radiance-balance, horizon-sector, and conical scanners may be considered. The radiance balance technique was rejected due to low accuracy. The latter two were rejected from the standpoint of reliability, as rotating mechanisms are required for scan generation.

b) The edge-tracking sensor has the advantage of utilizing a scanning mechanism utilizing flexural pivots of high reliability.

c) The edge-tracking technique inherently has a higher signal-to-noise ratio than the conical scanning method. (See Appendix A.)

d) The spectral bandpass utilizing the 14- to 16-μ CO_2 absorption band provides improved definition of the infrared horizon of the earth, in comparison to previous sensors utilizing infrared wavelengths shorter than 14 μ, in which inaccuracies have resulted due to discontinuities in the infrared horizon.

The selected sensors are described in the following paragraphs.

5.3.3.1 Low-Altitude Earth Sensor

The advanced horizon sensor system for OGO utilizes four infrared search-track units to track the earth's horizon in four planes separated in vehicle azimuth by 90 deg, as illustrated in Figure 5-3. These search-track units, referred to as trackers, generate analog signals representing the angular elevation of the horizon in each plane from the

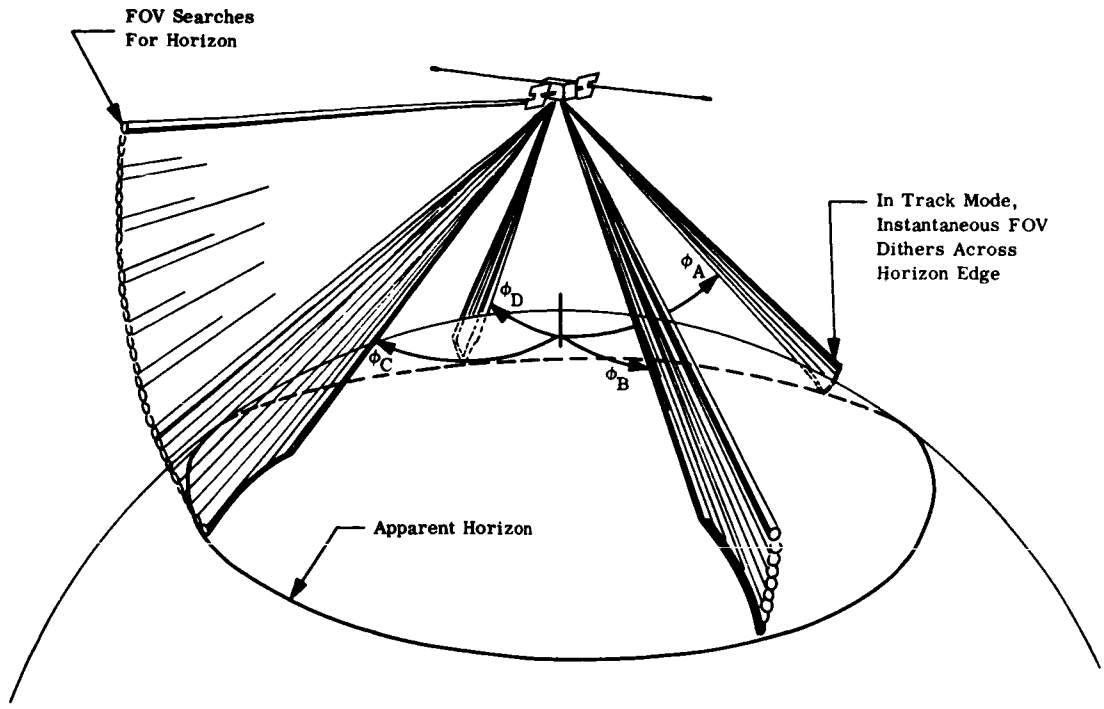

Figure 5-3. A-OGO Horizon Edge Tracker

nominal vertical of the spacecraft. The four trackers (designated A, B, C, and D) thus measure the angles θ_A, θ_B, θ_C, and θ_D, respectively (as shown in Figure 5-3).

These elevation analog signals are fed to a switching matrix, depicted in the system block diagram in Figure 5-4, where logic supplied by the OGO spacecraft determines the appropriate position signals for local-vertical (nadir) computation. The spacecraft logic bases this selection, in part, on sun-presence and track-check (earth-presence) information from each tracker. Presence of the sun in the field-of-view of a tracker or absence of a track-check signal from any tracker will cause the logic to omit that signal from its computations. Any three angular output signals are then fed via the matrix to two summing amplifiers, which read out vehicle attitude in terms of pitch and roll. The system is redundant in that the outputs from any three trackers are sufficient to provide attitude information (only two orthogonal trackers are required if altitude is known). In the event of failure of one of the

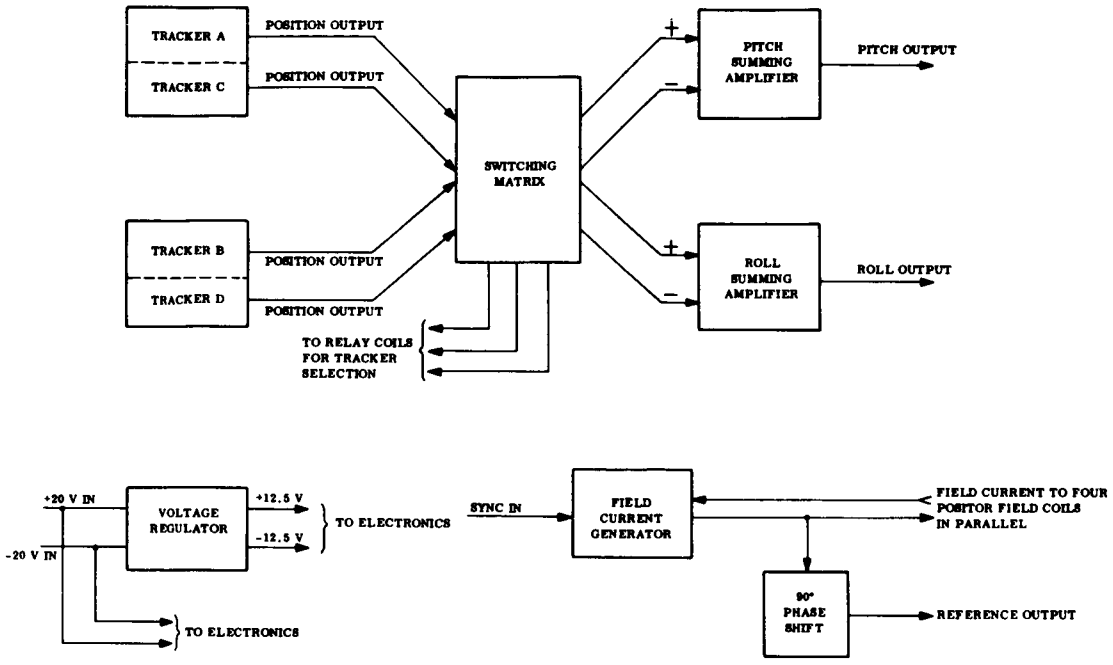

Figure 5-4. A-OGO Horizon Sensor System Block Diagram

three active trackers, the remaining tracker signal is then utilized to provide continuous pitch-and-roll information. Upon command, the fourth tracker can also be switched in if four-tracker logic is desired.

Attitude information is normally obtained from the A-OGO sensor by performing simple analog computations with any three of the four elevation signals. If, for example, the spacecraft is moving so that tracker A is looking forward, then θ_B and θ_D are the horizon elevation angles in the roll plane. Assuming that the switching matrix is in a state that ignores the elevation signal from tracker C, then the elevation signal from tracker A represents the horizon elevation, θ_A, in the pitch plane of the spacecraft. In analog notation, the symbols θ_A, θ_B, and θ_D represent the horizon elevation signals from each of these three trackers.

If a reference signal, R, proportional to the radius angle of the earth were available, the vehicle pitch would be $(R - \theta_A)$. The A-OGO

system uses the mean of θ_B and θ_D to represent R. Thus, for this particular switching-matrix state, the pitch analog signal is

$$\text{Pitch} = 1/2(\theta_B + \theta_D) - \theta_A.$$

The roll calculation requires only the horizon elevation signals from trackers B and D. Thus, in the same switching state, the roll analog signal is

$$\text{Roll} = 1/2(\theta_B - \theta_D)$$

The detailed design of each tracker and its associated tracking loop are described below.

Electronics. The servo circuit of each tracker includes those elements necessary to perform the search and track functions. (Refer to Figure 5-5.) These are the telescope, the thermistor bolometer, the signal preamplifier, the signal amplifier, the Schmitt trigger, the Positor drive amplifier, and the Positor itself.

The servo tracking loop is intentionally made to oscillate at a controlled dither frequency (20 cps) and with a controlled amplitude (2.5 deg peak-to-peak nominal) when the earth's horizon is being tracked. This oscillation, manifested by motion of the Positor mirror, causes the field-of-view of the telescope to continually cross and recross the horizon. If the horizon is centered on this oscillation of the field-of-view, the output waveform from the signal amplifier will be symmetrical and therefore the zero crossings will be equally spaced in time. The Schmitt-trigger output switches to positive or negative, according to whether the input voltage is above or below zero; therefore, under these conditions, the Schmitt output will be positive for the same length of time it is negative, resulting in a zero dc component in the output. If the horizon is displaced from the center of the oscillation, the output waveform from the signal amplifier will be asymmetrical, resulting in unequal positive and negative output from the Schmitt, and thus a dc component. This dc component is amplified by the drive amplifier and drives the Positor mirror drive coils to recenter the oscillating field-of-view on the horizon. The dc drive thus is seen to be the error signal of a closed-loop servo.

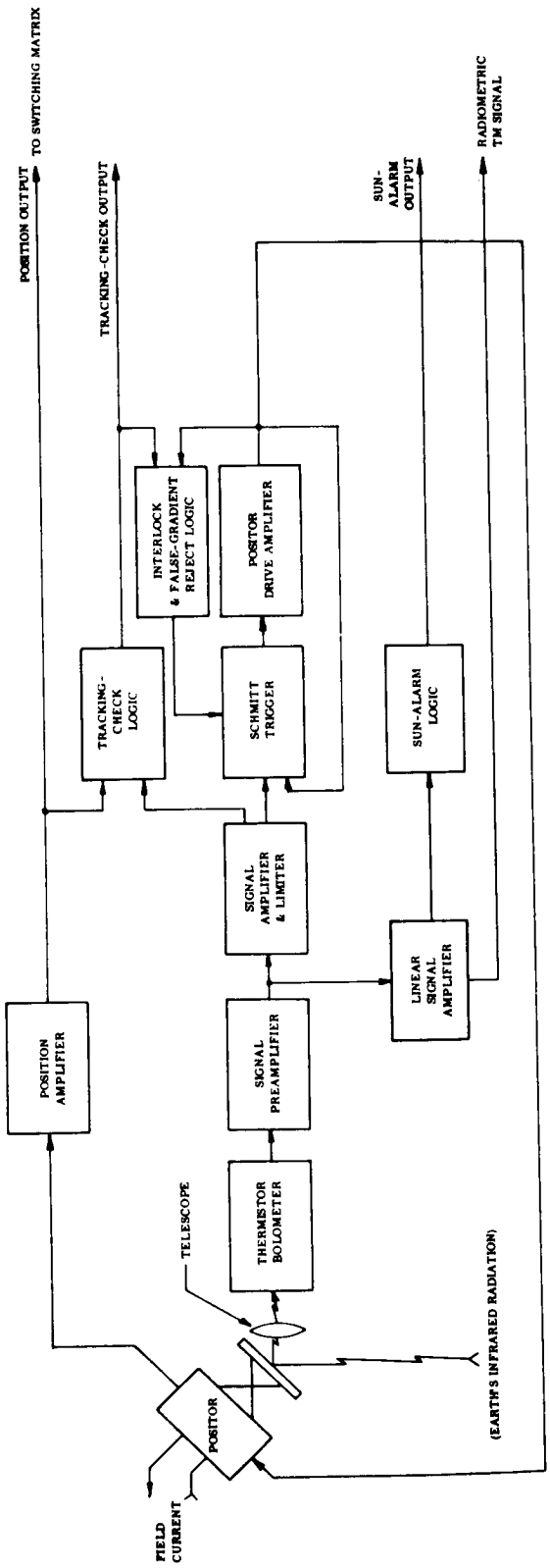

Figure 5-5. A-OGO Tracker Block Diagram

The drive-amplifier output voltage is fed back to the Schmitt trigger and interlock circuits. When, during the search, the earth is located, the tracking action discussed above takes place. If the earth is not in the field-of-view during the search, the Positor mirror moves to its stops, where the drive voltage reaches a level high enough to switch the Schmitt. The Positor mirror is then returned to the space stop[†], where the search action is repeated. Search rate is 90 deg/sec, and each of the four trackers covers a 90-deg field-of-view.

The readout circuits include the field current generator, individual position amplifiers for each tracker, a switching matrix, and two summing amplifiers. (Refer to Figure 5-6.) The field current generator supplies a 2461-cps current to the field coils of all the Positors in parallel; 2461-cps voltages proportional to the Positor angular position are induced in the drive coils. These voltages are amplified by the position amplifiers for each tracker and then combined in the switching matrix and summing amplifiers into redundant pitch and roll outputs.

The logic circuits are one of the major improvements of the A-OGO sensor. Salient features are as follows:

1) A tracker will acquire only on the space-to-earth sweep of the Positor.

2) Should a weak gradient (ghost from sun, window, or atmospheric gradient) appear during the space-to-earth sweep, the Schmitt will track it momentarily if it is above the equivalent energy of a blackbody temperature of approximately 165°K. However, the logic will then reject it and the tracker will continue on, seeking the true earth horizon.

3) If, while tracking a normal gradient, the system drifts to a weak gradient, the logic will drive the Positor to the space stop and reacquisition will begin.

4) If the system encounters a reverse gradient in its search, reject circuitry will continue the Positor through the reverse gradient in search of the true horizon.

[†]An interlock is used to prevent tracking during the earth-to-space search. This design absolutely prevents acquisition of a gradient within the earth.

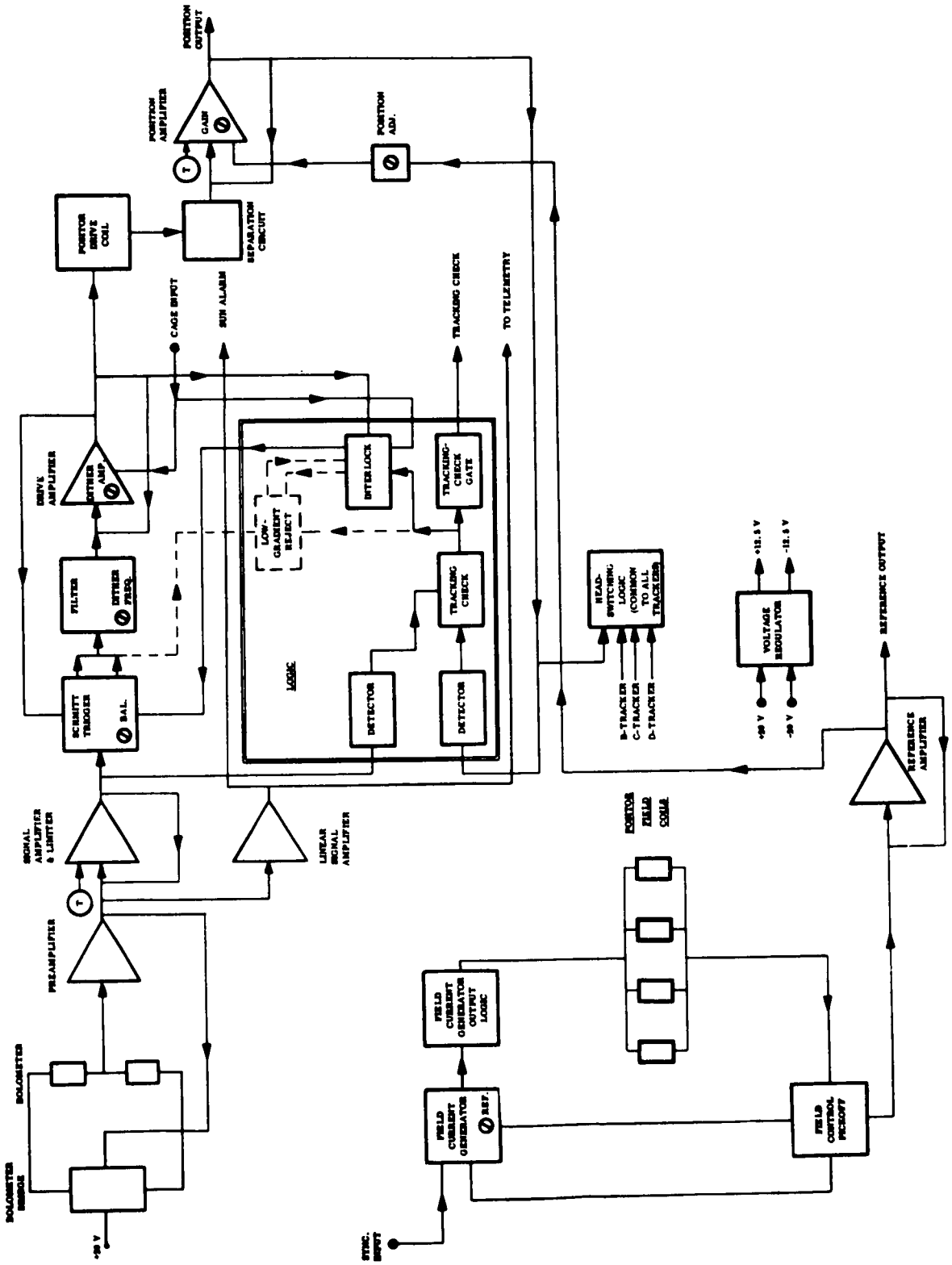

Figure 5-6. A-OGO Tracker Electronics

5) If some unusual gradient is detected and tracked, logic has been incorporated that will prevent the tracking point from following this false horizon into earth. "Space bias" has been introduced as added insurance against problems experienced by earlier wideband sensor designs. This bias references the system to space by making the dither slightly asymmetrical with regard to the gradient tracking point.

Other logic circuits are the track-check circuits, which furnish output signals indicating whether the trackers are actually tracking the earth's horizon, and the sun-alarm circuits, which furnish a logical output signal when the sun is being tracked.

Three special circuits are included: (1) the radiometric channel, (2) field-coil circuitry, and (3) the voltage regulator.

A wideband amplifier, referred to as a linear signal amplifier, is utilized to measure the level of the infrared radiation seen by the sensor (and also to provide the sun-alarm logic). As indicated (Ref Figure 5-6) this channel may be telemetered to the ground, where sensor input data can be gathered for studying sensor performance and scientific information can be provided regarding gradient uniformity within the CO_2 layer.

In the original OGO sensor, the field coils of all four Positors were in series; if any one coil failed to open, the system failed. The Positor field coils on the A-OGO sensor have been designed in parallel to provide the redundancy not available in the earlier system. Should any one coil open, system performance will be affected only when the sun comes into the field-of-view of one of the three remaining trackers (three trackers are required unless altitude is known). Through this configuration, system reliability has been improved significantly.

In addition to the circuits discussed above, a voltage regulator is required to further regulate the ±20-vdc vehicle power supply. This circuit supplies ±15 vdc with an output impedance of less than 1 ohm. An added advantage of the regulator is that, because of its low-output impedance, individual decoupling of many of the circuits is unnecessary, thereby simplifying circuit design.

Optics. The optical path and optical components of the A-OGO sensor are depicted in Figure 5-7. The pivoted Positor mirror used to

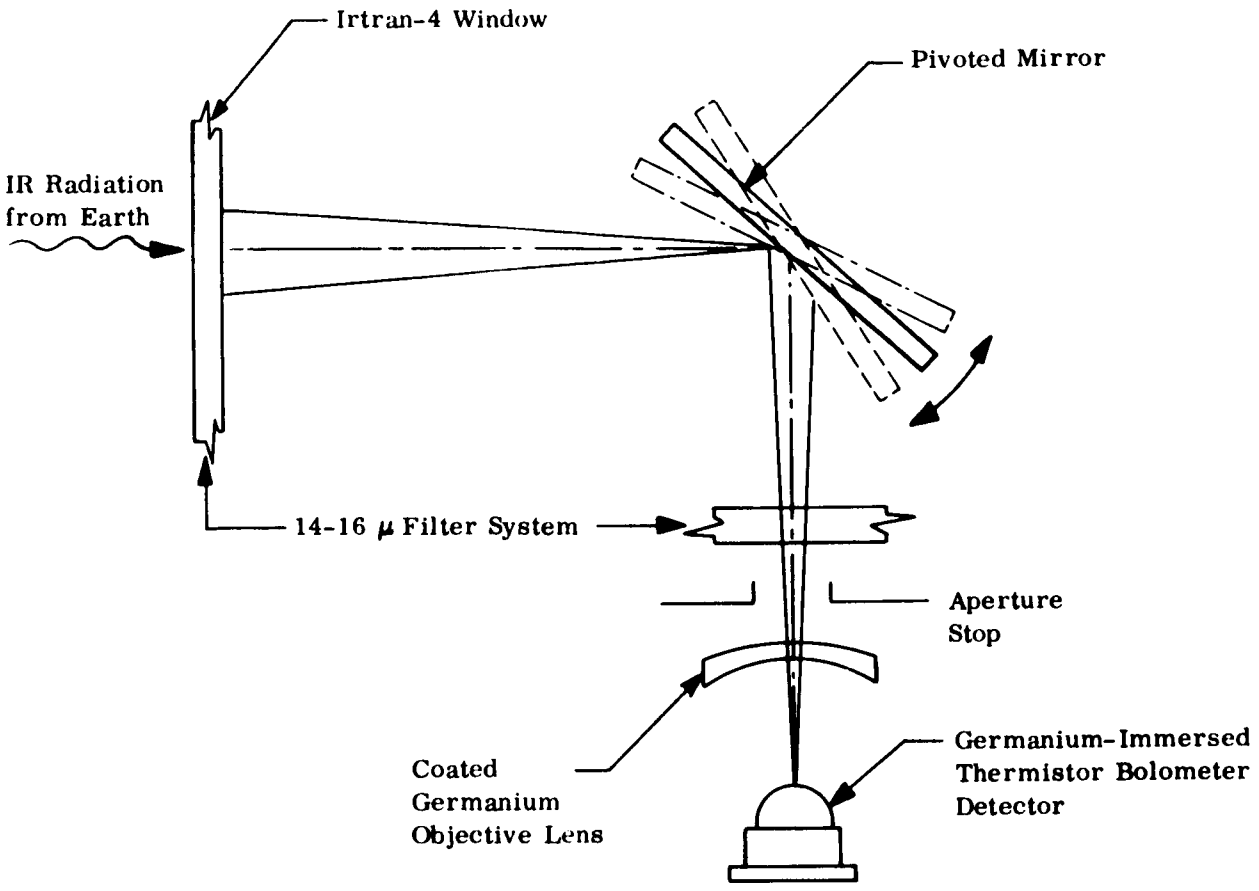

Figure 5-7. Optical Path and Components, A-OGO Horizon Sensor System

direct the optical beam is made of beryllium. Its surface, which is polished to an overall flatness of less than 4 fringes of Hg green light, has a minimum reflectance of 95 percent in the 14- to 16-μ bandpass. The telescope contains a filter, an objective lens, and a thermistor bolometer detector.

The A-OGO filter system consists of three elements: the Irtran-4 window, the long-wavelength bandpass filter, and the narrow-bandpass filter. The latter two are interference-filter coatings deposited on germanium substrates. The long-wavelength bandpass filter rejects the short wavelengths of the narrow-bandpass sideband. The Irtran-4 window is also interference-coated for antireflection at 15 μ, and rejects the long wavelengths of the 21-μ narrow-bandpass sideband.

The objective lens of the telescope is a germanium meniscus lens with an effective focal length of 19.9 mm. This lens is also antireflection-coated and is stopped down to a clear aperture of 2.3 cm^2.

The telescope detector is a germanium hemispherically immersed thermistor bolometer. The active bolometer-flake area is 0.1 x 0.1 mm, but the effective area (virtual image) is 0.4 x 0.4 mm, due to the germanium hemisphere. The resulting field-of-view, when combined with the objective lens, subtends a solid angle equal to 4.0×10^{-4} ster.

Mechanical Configuration. The central electronic unit (CEU) provides the interface electronics to and from the OGO spacecraft and all test points used in ground checkout of the sensor system. Also housed in the CEU is the electronic circuitry required to drive both heads. The CEU is 19 x 14 x 10 cm high, with four 3.2 cm circular connectors mounted on the top surface.

A single dual-tracker head is illustrated in Figure 5-8. The cutaway view depicts placement of the major components of the head. The configuration is approximately triangular with a base of 16.5 cm, an altitude of 15 cm, and a thickness of 7.4 cm. A complete system has two dual-tracker heads.

The detailed system characteristics of the A-OGO sensor are presented on Table 5-IV.

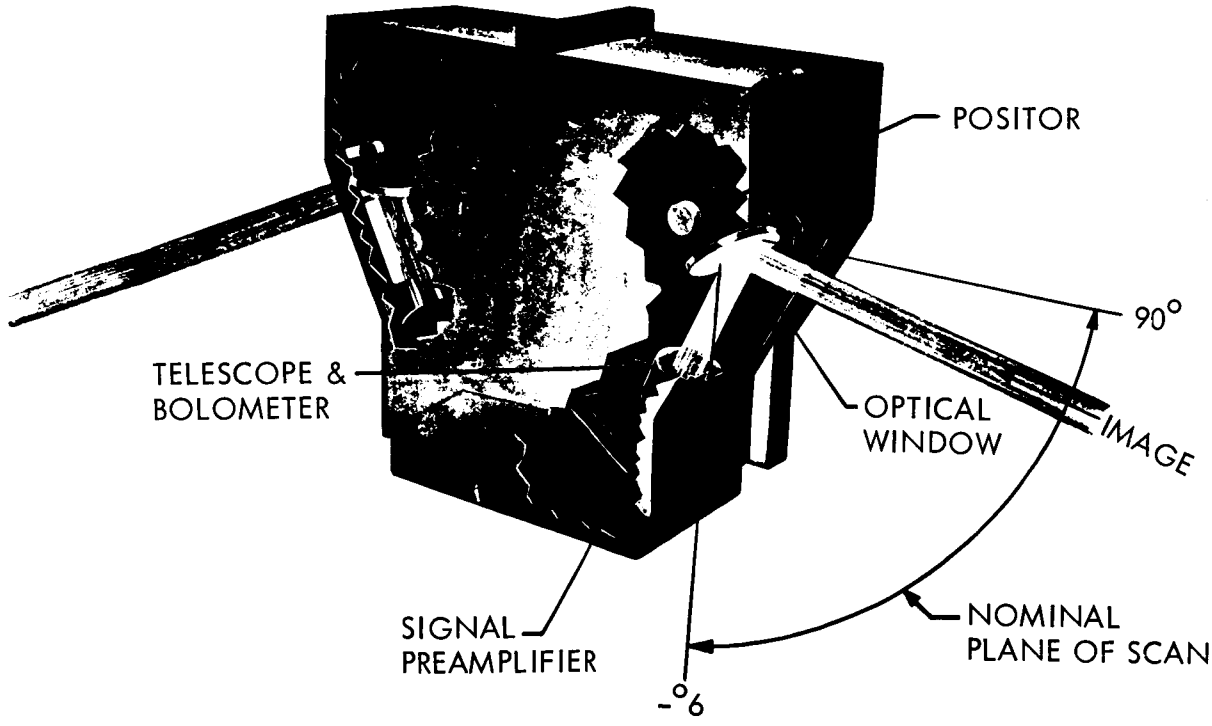

Figure 5-8. A-OGO Dual Tracker Head

Table 5-IV. A-OGO Horizon Sensor System Specifications[†]

Physical Characteristics	
(a) Size	
Tracking head (each)	1100 cm^3 (2 per system)
Central electronic unit	2700 cm^3
Total volume (per system)	5000 cm^3 (max)
(b) Weight	
Tracking head (each)	2.5 kg
Central electronic unit	2.3 kg
Total weight (per system)	7.6 kg
(c) Power required	<10 w (nominal) <12 w (max)
Optical Characteristics	
(a) IR detector	Immersed thermistor bolometer
(b) IR spectral bandpass	14.0 to 16.0 μ
(c) Telescope field-of-view	1.2 deg at half-response contour
Sensor Outputs	
(a) Pitch/roll	2461-cps signal with amplitude proportional to roll and/or pitch attitude error
(b) Other	Position, sun alarm, track check, radiance-level monitor (TM) — all of these from each of the four trackers.

[†]Manufacturer's specifications.

Table 5-IV. A-OGO Horizon Sensor System Specifications[†] (Continued)

Performance	
(a) Tracking range (each of 4 trackers)	-2 to +85 deg (min)
(b) Tracking rate	>15 deg/sec
(c) Operational range	±30 deg (±45 deg from nominal)
(d) Altitude range	220 to 150,000 km or 90 to 110,000 km
(e) Accuracy[††]	≤0.05 deg (3σ)
Null	
±10 deg[†††]	≤0.10 deg (bias) + 0.05 deg (3σ)
(f) Reliability (for 3 or 4 trackers operating)	0.95 for 1 year (present parts) 0.98 for 1 year (highest reliability parts available)
(g) Operational life	≥1 year
(h) Storage life	3 years
(i) Pitch and roll scale factors	0.4 v rms/deg
(j) Position-output scale factor	0.1 v rms/deg
(k) Noise	±0.02 deg peak-to-peak at 0.6 Hz bandwidth
Environmental Levels	
(a) Shock	50 g for 2.2 ms in all axes
(b) Acoustic noise	Not tested (design goal: SPL of 145 db overall from 51.5 to 9500 Hz)

[†]Manufacturer's specifications.

[††]Excluding geometric cross-coupling errors (which can be calibrated out) and errors due to horizon anomalies and earth oblateness.

[†††]Simultaneous roll and pitch.

Table 5-IV. A-OGO Horizon Sensor System Specifications† (Continued)

Environmental Levels (Cont'd)	
(c) Vibration	
Random	20 to 2000 Hz, 0.1 g^2/Hz with roll-off at 12 db/octave above 1000 Hz for 12 min in each of three axes
Sinusoidal	At 1/2 octave/min in each of three axes: 5 to 250 Hz — 4.9 (peak)†† 250 to 400 Hz — 9.1 g (peak) 400 to 3000 Hz — 20.5 g (peak)
(d) Thermal vacuum (system operating)	
Vacuum	Space vacuum
Temperature	
Electronics	$-35^{\circ}F$††† to $+160^{\circ}F$
Bolometer	$0^{\circ}F$††† to $+113^{\circ}F$
(e) Acceleration	18 g in any direction for 3 min in each of three mutually perpendicular axes
(f) Relative humidity	95 percent R.H. at $100^{\circ}F$ for 50 hr
(g) Fungus	Uses non-nutrient parts and materials
(h) RFI	Meets MIL-I-26600 paragraphs: Conducted audio — 50 to 15 kHz Conducted RF — 0.1 to 920 mHz Radiated RF — 0.1 to 920 mHz Meets lower frequencies as follows: Laboratory test — 1 to 50 Hz Conducted — Threshold of susceptibility 0.3 v rms at 3 Hz

†Manufacturer's specifications.

††DA limited to 0.5 in.

†††Through use of heaters, system can be subjected to $-60^{\circ}F$.

5.3.3.2 High-Altitude Earth Sensor

The function of each earth sensor assembly (ESA) is to sense one component of the angle between the spacecraft reference yaw axis (U axis) and the local vertical. This information is used for attitude control and attitude determination.

Two identical earth sensors oriented at 90-deg intervals in yaw are used. They perform equivalent functions in parallel. They are both mounted on the -U end of the spacecraft where they view nominally along the -U axis as shown in Figure 5-9.

The ESA scans a small field-of-view (0.6 by 0.6 deg) back and forth through an angle of ±14.5 deg from the null optical axis which is aligned with the U axis of the spacecraft. Each ESA consists of two units, the sensor head unit and the sensor electronics unit.

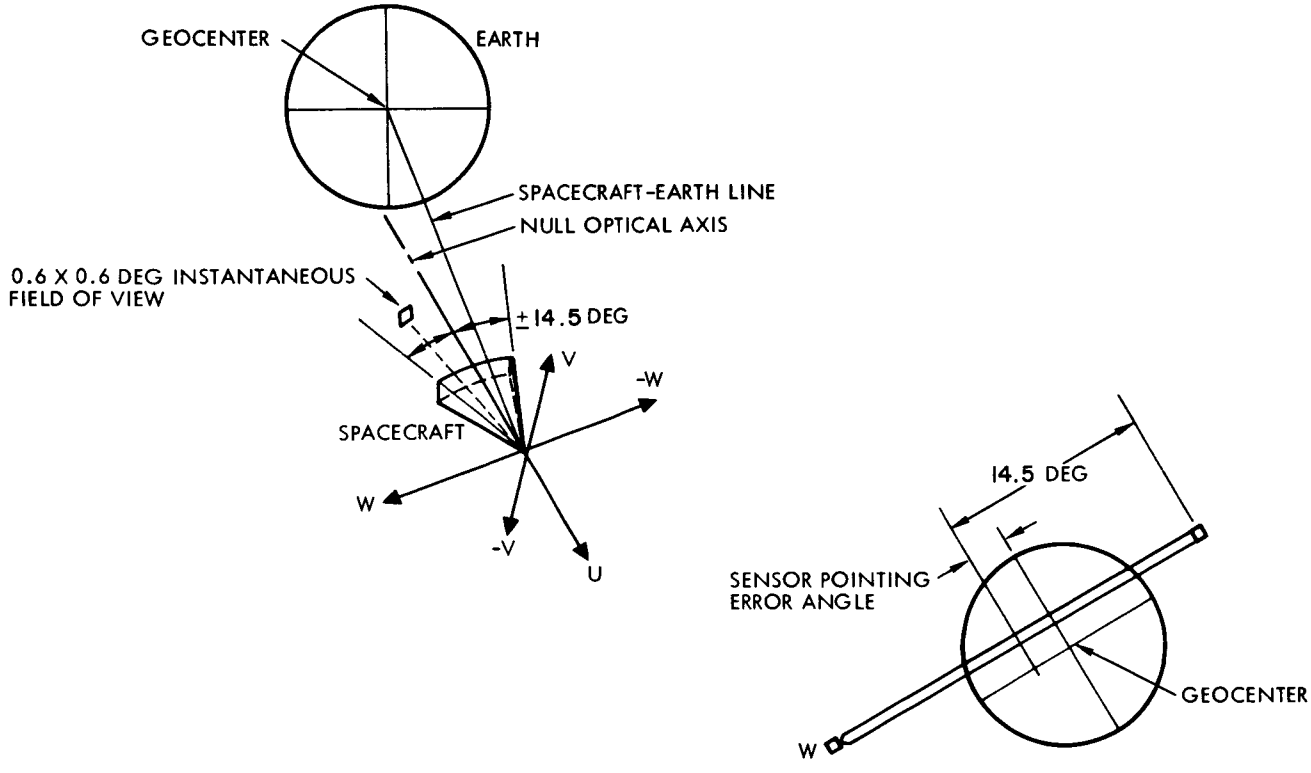

Figure 5-9. ESA Scan Geometry

Operational Description. The ESA is an infrared electro-optical device with a mechanical scanning element. Infrared radiation in the 13.5- to 25-μ region is focused on a thermistor bolometer by a germanium telescope. The bolometer and its associated electronics detect the

earth's radiation when it is present in the instantaneous field-of-view. The output of each sensor is a sequence of discrete logic pulses from which earth pointing error can be computed.

Referring to the block diagram and waveforms of Figure 5-10, the radiation reaches the telescope by reflection from a plane mirror, which is caused to oscillate rotationally by an electromagnetic drive mechanism. The mirror, its flexure spring suspension, and the drive and readout coils comprise a unit called a Positor. The cyclic motion of the Positor causes the field-of-view seen by the telescope to scan in the UW plane at approximately 5 cps. The scan is a sawtooth wave having constant angular rates in both directions. It is generated by a Positor position servo loop driven by a digital counter which counts pulses from a reference clock.

A quantized analog sawtooth wave is formed by the reversible counter and D to A converter. This is the Positor position command. It has an amplitude of ±14.5 optical scan deg. The 4.8-kc clock rate with a quantization of 0.05 deg produces a constant scan velocity of 240 deg/sec.

The Positor position command is summed with the demodulated Positor position signal in the drive amplifier to form a position error signal. The drive amplifier applies current to the drive coil which produces torque to accelerate the positor in response to the position error signal. Positor position feedback is obtained by sensing the modulated reference current in the readout coil, which is subsequently amplified and demodulated. Servo loop compensation is obtained with Positor current feedback and a lead-lag filter in the position feedback.

As the instantaneous field-of-view is caused to scan back and forth by the Positor, the field-of-view sweeps from cold space through the earth's warm disc to cold space on the other side and then reverses. This infrared energy from the earth focused on the bolometer produces a series of electrical pulses at the bolometer output, the leading and trailing edges of which, when properly time correlated and synchronized, define the edges and the center of the earth.

The primary output of the sensor then, is the radiance logic signal which is produced by amplifying, filtering, and level detecting the bolometer output in the preamplifier, signal amplifier, filters, space clamp,

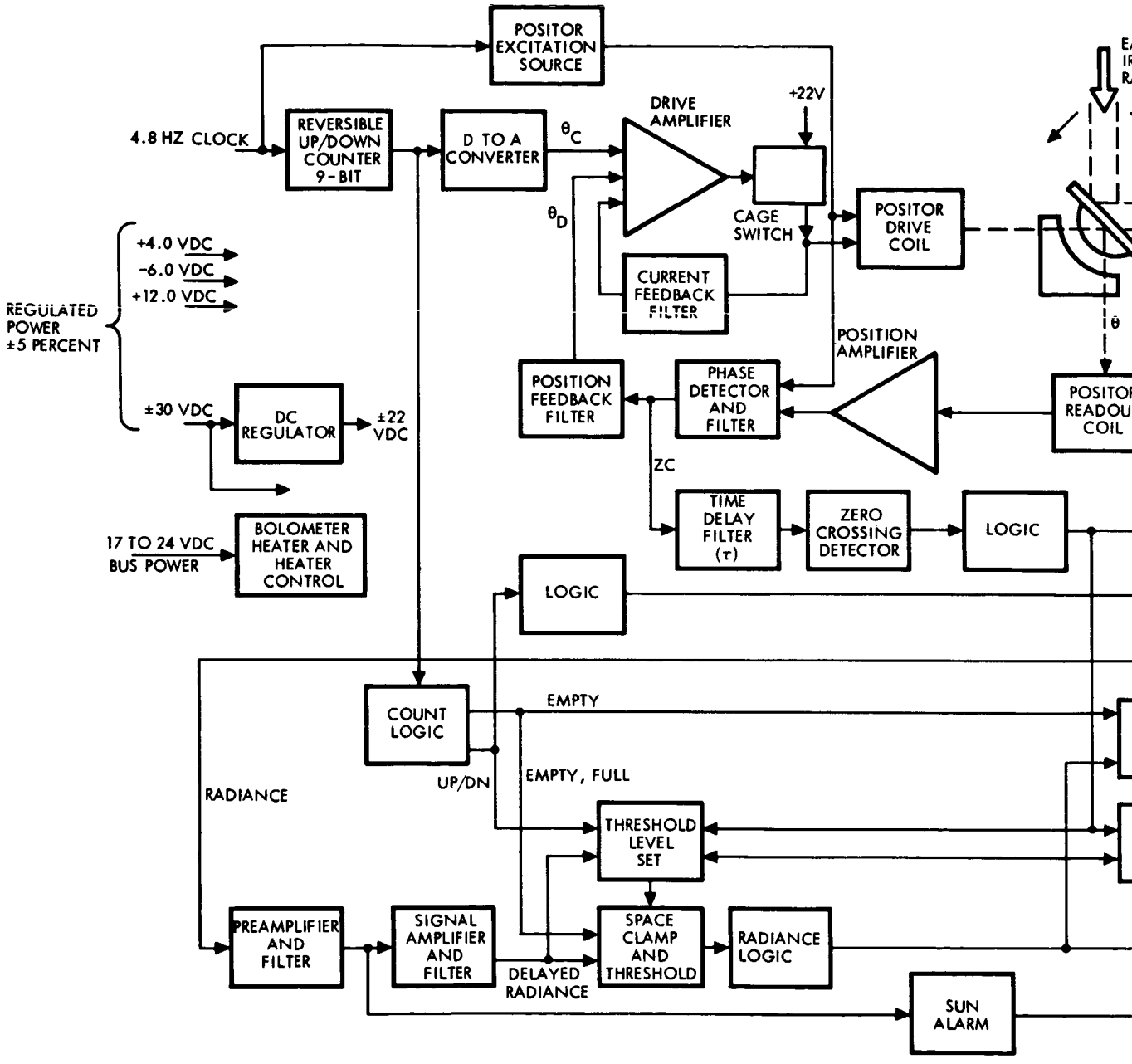
POSITOR EXCITATION SOURCE
4.8 HZ CLOCK
REVERSIBLE UP/DOWN COUNTER 9-BIT
D TO A CONVERTER
θ_C
DRIVE AMPLIFIER
+22V
θ_D
CAGE SWITCH
POSITOR DRIVE COIL
CURRENT FEEDBACK FILTER
+4.0 VDC
-6.0 VDC
+12.0 VDC
REGULATED POWER ±5 PERCENT
±30 VDC
DC REGULATOR
±22 VDC
POSITION AMPLIFIER
POSITION FEEDBACK FILTER
PHASE DETECTOR AND FILTER
POSITOR READOUT COIL
θ
ZC
TIME DELAY FILTER (τ)
ZERO CROSSING DETECTOR
LOGIC
17 TO 24 VDC BUS POWER
BOLOMETER HEATER AND HEATER CONTROL
LOGIC
COUNT LOGIC
EMPTY
UP/DN
EMPTY, FULL
RADIANCE
THRESHOLD LEVEL SET
PREAMPLIFIER AND FILTER
SIGNAL AMPLIFIER AND FILTER
SPACE CLAMP AND THRESHOLD
RADIANCE LOGIC
DELAYED RADIANCE
SUN ALARM

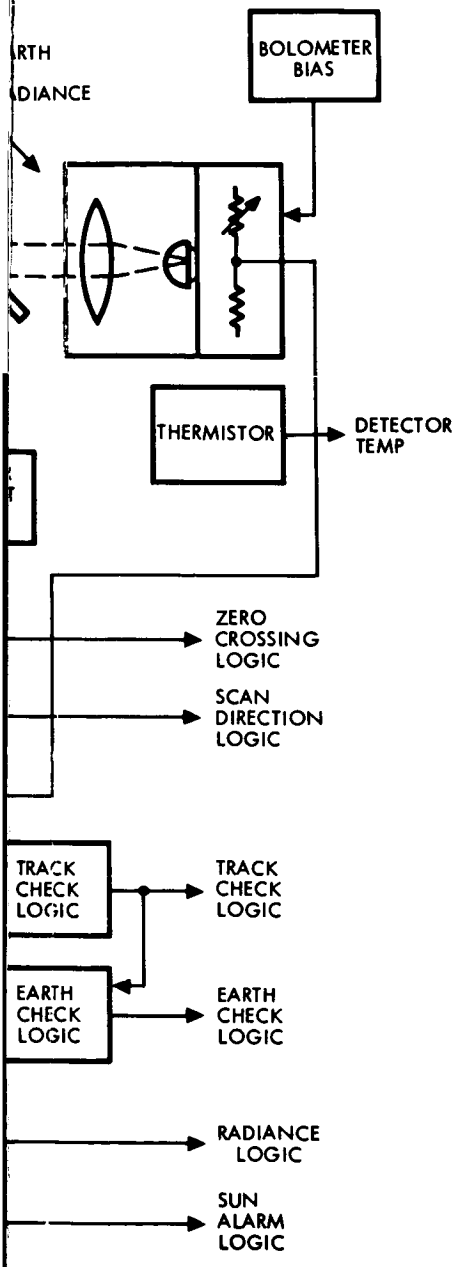

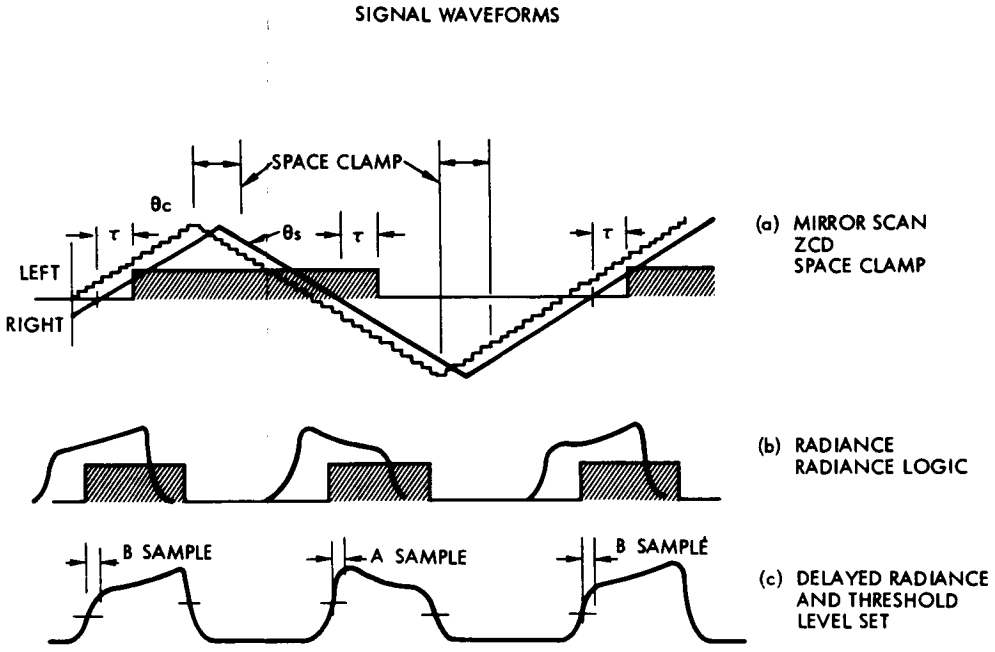

Figure 5-10. ESA Block Diagram

and threshold circuits. The radiance signal is filtered to minimize errors due to noise and clamped to space radiance twice per scan cycle to minimize errors due to long-term level shifts. The radiance threshold levels on each side of the earth are independently regulated to minimize errors due to unequal temperatures on opposite edges of the earth.

A discrete logic signal is produced by the zero crossing detector when the Positor crosses through the center line of the instrument. This signal is delayed for a time equal to the radiance signal delay, and defines the null optical axis of the instrument. A scan direction signal is logically derived from the reversible counter.

The radiance logic signal, zero crossing signal, and scan direction signal together with the reference clock signal are sufficient to compute the earth pointing error angle component being scanned. This is done by accumulating clock pulses in a digital register during the period that the bolometer sees the earth, and the field-of-view is to one side of the null optical axis. Pulses are subtracted from the counter when the earth is in view on the other side of the null optical axis. After one complete cycle, the residual count in the digital register corresponds to four times the pointing angle from the center of the earth's chord being scanned. This procedure is shown in Figure 5-11.

In addition to the basic logic signals formed by the sensor for purposes of error computation, several other logical checks are generated. These indicate:

a) When the earth's chord being scanned exceeds 1.4 deg

b) When the sensor null optical axis is directed within the earth's disc

c) When the sun is present in the field-of-view.

The first listed logic discrete is called track check and is generated by comparing the duration of the earth radiance logic pulse to the duration of a reference one-shot flip-flop. It is used during the acquisition sequence to prevent an attempt to acquire the edge of the earth. The second logic signal is called earth check. It is formed by noting that the sensor null optical axis is crossed by the Positor scan while the earth

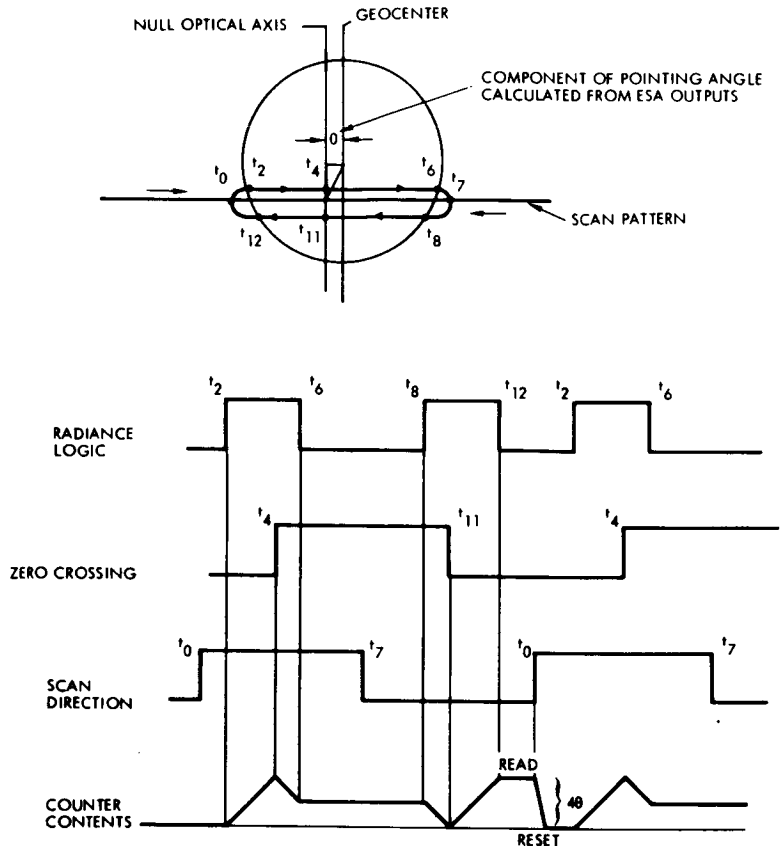

Figure 5-11. Pointing Angle Calculation

signal is present and track check is true. The third logic output determines, by means of an intensity threshold, that the sun is being viewed by the bolometer. It is called the sun alarm. The sun alarm is used to prevent control action based on error signals obtained when the sun is present.

The ESA's are powered by +4.0, +12.0, -6.0, and ±30 v from dc converters. In addition, bus power is applied to both of ESA's heaters. Converter power is only supplied to one ESA at a time. Both are turned off when the ACS power is turned off, but heater power from the bus is always present. Thermostatically controlled 2-w heaters in each ESA prevent the unit temperature from falling to levels which may result in bolometer damage. They turn full on at temperatures below $+20^{\circ}F$. A thermistor temperature sensor for telemetry is situated at the back of the telescope of each ESA.

The flexure springs supporting the Positor mirror of the ESA are designed for long life and low scanning drive power and can be damaged by harsh treatment. They are mechanically resonant with very little inherent damping and, as such, must be protected from severe vibration levels. The Positors are protected from the otherwise dangerous vibration environments of the boost and injection phases by electrical caging devices in each unit. These are merely semiconductor switches which short circuit the drive windings of the Positors, providing damping due to back emf as in a galvanometer. The short circuit is closed when ESA power is off and open when power is turned on.

Design. The ESA spectral passband includes the 14- to 16-μ CO_2 absorption band which is generally considered the most stable spectral region for an earth sensor. However, because of the relatively low amount of radiant power available to the sensor in this spectral region, the energy from 16 μ to the cutoff wavelength determined by the lens material is also utilized. This results in a less uniform earth radiance but considerably more signal out of the ESA.

The telescope consists of a germanium lens and a bolometer immersed in a hemispherical germanium lens. The telescope barrel is aluminum with the lens bonded in with epoxy. The germanium lens is coated with a multilayer interference filter designed to provide a transmission cuton wavelength of 13.5 μ. The transmission of the germanium in the lens and in the bolometer immersion lens determines the long wavelength cutoff of the telescope. Figure 5-12 is a typical transmission versus wavelength curve for the lens. Figure 5-13 shows the relative response in the 14- to 16-μ region. The bolometer peak responsivity is specified to be greater than 235 v/w incident on the bolometer. By multiplying the ordinate of Figure 5-13 by this responsivity, the spectral response of the telescope and bolometer combination can be obtained. The optical parameters of the telescope are given below:

Instantaneous field-of-view	0.6 by 0.6 deg
Optical speed	f/0.318
Aperture	5.07 cm diameter

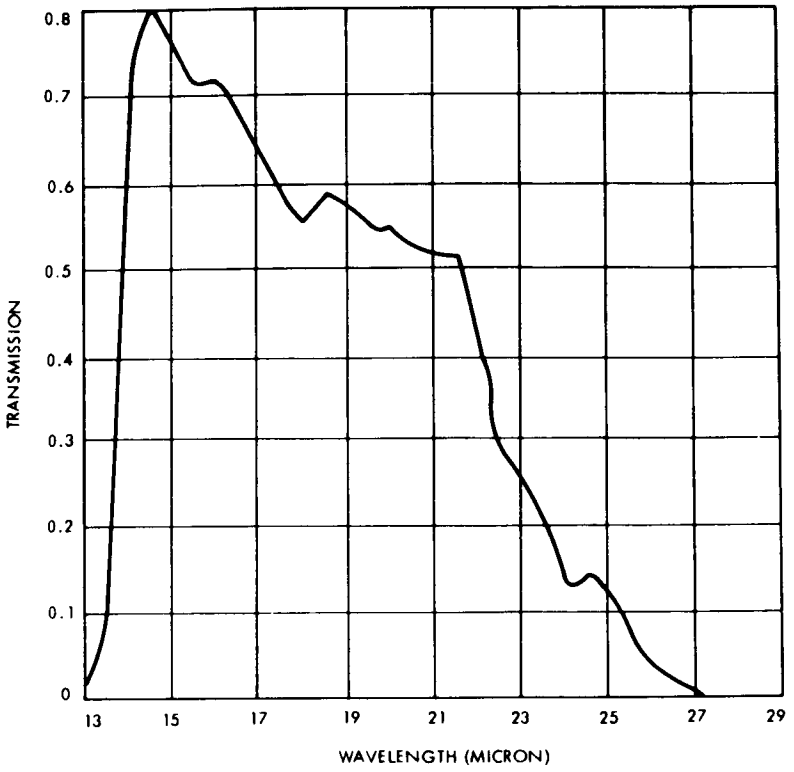

Figure 5-12. Lens Transmission

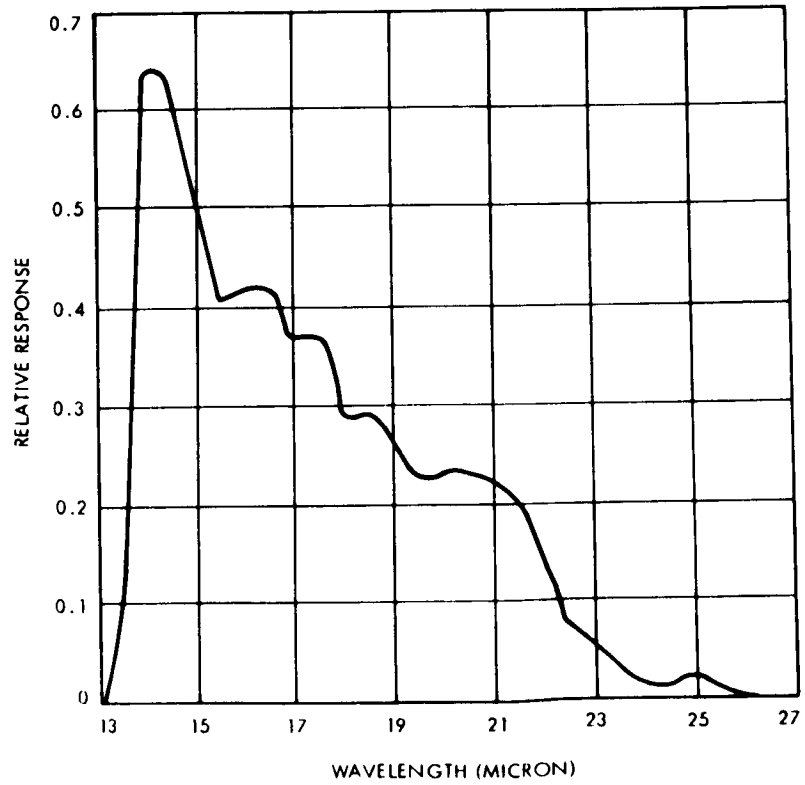

Figure 5-13. System Spectral Response

Focal length	3.98 cm
Bolometer flake size	0.01 by 0.01 cm

The Positor is an electromechanical device for rotation of a mirror and readout of its angular position with no bearings or sliding surfaces. The Positor was initially developed by the Advanced Technology Division of American Standard (ATD) for the OGO horizon scanner. The Positor structure is shown in Figure 5-14, and a schematic diagram is shown in Figure 5-15.

The mirror is connected to the rotor of a permanent magnet torquer. Two coils which are free to rotate in a cylindrical air gap are also connected to the rotor and form the drive coils which are connected in series. A pair of flexure pivots are used to connect the rotor to the base structure. Electrical connection to the rotor is made through the flex-springs. A current through the drive coils causes a torque which rotates the rotor against the constraint of the flex-springs. A high frequency (4.8 kc) carrier is added to the drive signal which results in an ac flux field linking the drive coils and the readout coil. A suppressed carrier, amplitude modulated voltage output is developed in the readout coil, the amplitude of which is linearly proportional to the rotor rotation from its null position and the phase indicates the rotational direction.

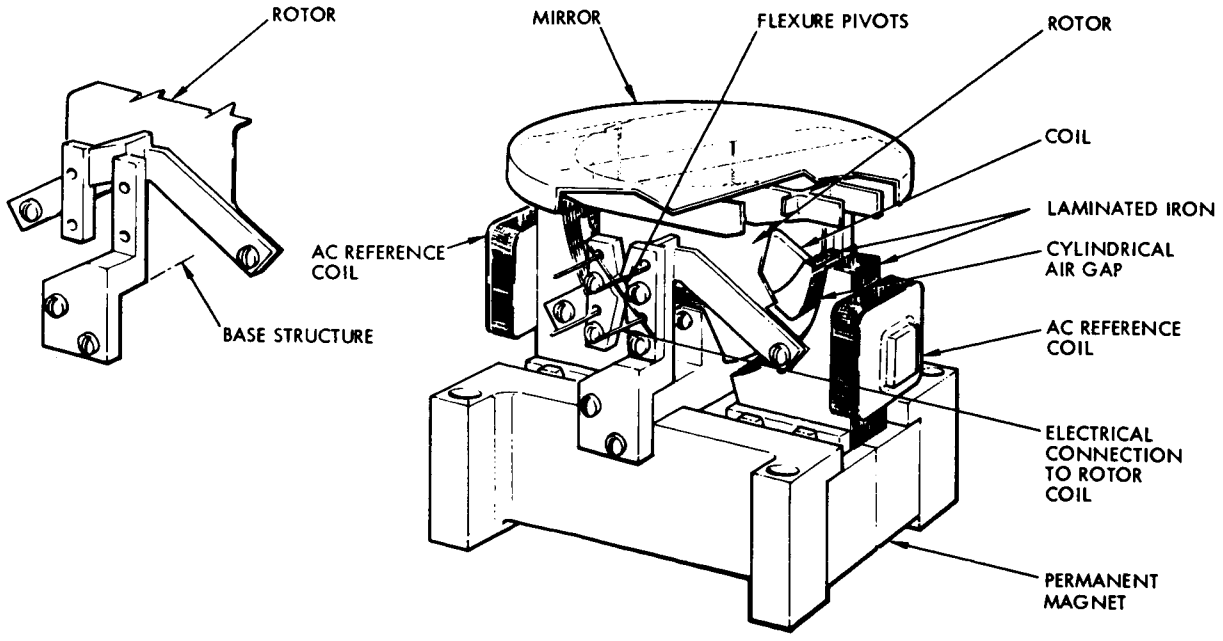

Figure 5-14. ATD Positor

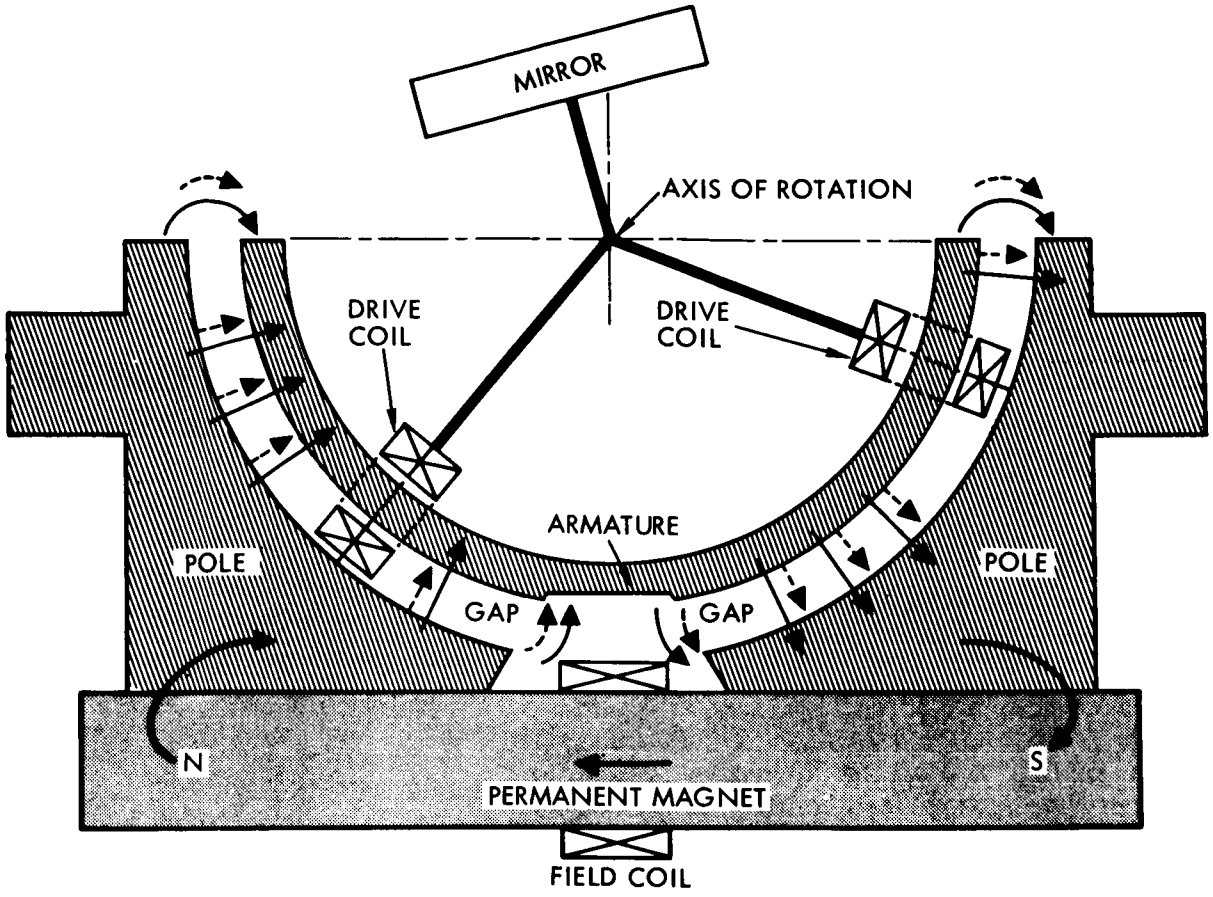

Figure 5-15. Positor Schematic Diagram

The armature and mirror moment of inertia and flexure spring constant produce a Positor resonant frequency of 16 to 18 cps. Oscillations are damped by currents induced by armature motion. The Positor characteristics are

Positor mechanical damping	$2 \times 10^{-7} \frac{\text{ntms}}{\text{rad}}$
Positor spring constant	$9.8 \times 10^{-3} \frac{\text{ntm}}{\text{rad}}$
Positor moment of inertia	7.7×10^{-7} kgm^2
Positor torque constant	$6 \times 10^{-2} \frac{\text{ntm}}{\text{amp}}$
Armature copper resistance	68 ohms
Armature inductance	13 mh
Feedback gain constant	$12.3 \frac{\text{v}}{\text{rad}}$

The detailed characterisitcs of the MOGO sensor are presented in Table 5-V.

Table 5-V. MOGO Horizon Sensor System Specifications†

Parameter	MOGO (single axis)
Altitude range	Synchronous to 130,000 km
Total error	Total: 0.06 deg - (0.04 deg for 3σ noise, including anomalies) (0.02 deg for gradient, scale factor, and alignment) (over entire ±2.5 deg range; 93,000 km altitude)
Operational range	±4.5 deg (for 9 deg earth)
Linear range	±2.5 deg
Alignment error	±0.01 deg
Output noise	0.013 deg rms
Scale factor	Digital output (0.003125 deg per bit for 19.2 kc clock)
Accuracy (at large pitch and roll angles)	Not specified beyond 2.5 deg
Type	Chord scanner
Scan angle	29 deg total
System time constant	208 ms
Scan frequency	4.8 cps (240 deg/sec)
Dither frequency	Not applicable
Optics field-of-view (instantaneous)	0.5 deg (to half-power points)
IR detector	Ge- immersed thermistor bolometer (mylar-backed)

†Manufacturer's specifications

Table 5-V. MOGO Horizon Sensor System Specifications (Continued)

Parameter	MOGO (single axis)
IR bandwidth	13.5 to 22 μ (germanium roll-off); (half of power in 14-16 μ band)
Earth acquisition signal (track check)	Yes
Redundant	No
Power	2.5 w (no heater) 0 to 2 w (for heater from +20 deg to -45 deg F)
Size	3300 cm^3
Weight	2.9 kg
Operating lifetime	18 months in orbit
Storage life	> 1 year
Reliability	0.902 (for 18 months) 0.990 (for 18 months with parallel redundancy)
Shock	80 ±8 g for minimum duration of 6 ± 0.5 ms (sawtooth)
Acoustic noise	See random vibration
Vibration	a) Random: (3 axes) 20-300 cps - 0.03 g^2/cps 300-2,000 cps - 0.12 g^2/cps Minimum duration - 17 min/axis b) Sinusoidal: (3 axes) 5 - 300 cps - 3.5 g rms 300 - 2,000 cps - 5.0 g rms (random and sinusoidal applied simultaneously)
Temperature	Operating: -45 deg to +120 deg F Nonoperating: -45 deg to +140 deg F

5.3.4 Canopus Trackers

The Canopus tracker which is recommended for the lunar orbiter mission is the instrument developed by ITT Federal Laboratories for the lunar orbiter program, with a specified accuracy of 50 arc sec rms.

Two other instruments were also considered, based upon the survey conducted in Ref 5-1. The first was the instrument developed by NASA-JPL and the Barnes Engineering Co., for use in the Mariner programs, with a specified accuracy of ± 0.1 deg. Although the performance of this instrument has been proven in the Mariner program, the ITT instrument is preferred from the standpoint of higher accuracy.

The second instrument considered was the Canopus tracker developed by Hughes Aircraft Co. (Santa Barbara Research Corporation) for the Surveyor program. A detailed description of this equipment is contained in Ref 5-2. Although this instrument has been successfully employed in the Surveyor program, the ITT Federal Laboratories tracker is preferred, primarily from the standpoint of reliability, and secondly from the standpoint of higher accuracy. The SBRC instrument uses several mechanisms which may be objectionable from the standpoint of long lifetime, i.e., a single-axis cam-driven scanning mirror, and a rotating reticle for modulation of the incident star radiation. The specified accuracy of the SBRC instrument is 6 arc min.

For the interplanetary missions, where computer simulation of the mission has indicated the requirement for very high accuracy, development of an instrument with higher accuracy than that available in currently available equipment is recommended. Specifications for the recommended instrument are defined in this section.

5.3.4.1 Canopus Tracker for Lunar Orbit

For the lunar orbiter mission, the ITT Federal Laboratories lunar orbiter Canopus tracker is recommended. Detailed engineering design data is considered proprietary by the manufacturer. However, a brief description and summary specification follows.

The tracker is contained in a single package, consisting of optics, an ITT FW 143 multiplier phototube detector, and electronics. The electronics comprise signal detection circuits, scanning logic, deflection

circuits, and power supplies. The tracker provides an analog output signal which is proportional to the angular displacement of the line of sight to Canopus about one axis.

A simplified block diagram is illustrated in Figure 5-16. The star image is focused by the optical system on the photocathode of the ITT FW 143 multiplier phototube, an image dissector. The optical radiation incident on the photocathode causes emission of photoelectrons, which are then accelerated within the image section of the photomultiplier toward an electrode at higher potential at the opposite end of the image section. This electrode contains a narrow slit which permits acceptance of only a portion of the electron image from the photocathode, thus defining the instantaneous field-of-view. By application of scanning waveforms to a magnetic deflection coil around the image section, the electron image may be made to scan across the narrow slit in the electrode, thus providing spatial modulation of the electronic star image. When the electrons pass across the slit aperture, amplification of this current is accomplished by a series of multiplier dynodes. The amplified signal pulse, collected by the anode of the photomultiplier tube, comprises the star signal.

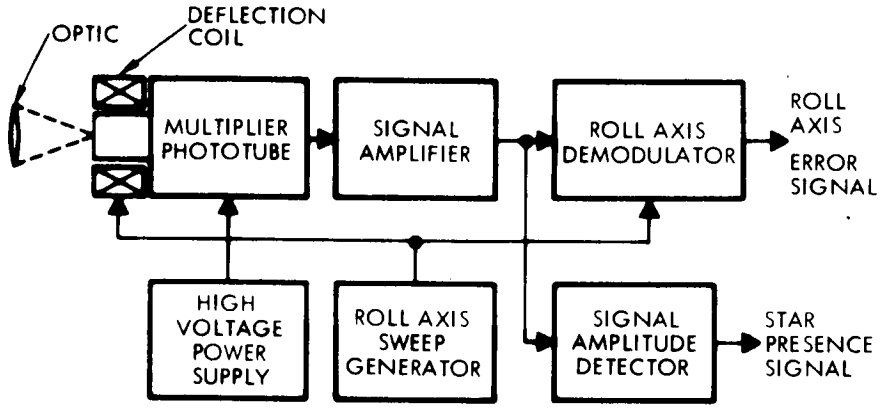

Figure 5-16. ITT Federal Laboratories' Canopus Sensor Simplified Functional Diagram

Scanning is performed on one axis only, orthogonal to the direction of the slit in the accelerating electrode of the image section, which corresponds to the roll axis of the spacecraft. The field-of-view in the yaw

axis (along the slit of the accelerating electrode) is sufficiently large to accommodate the apparent change in the position of Canopus during the mission. In addition, provision is made for prelaunch mechanical adjustment of the instrument along the yaw axis to accommodate the position of Canopus for a specific launch date. Specifications and physical characteristics of the ITT instrument are given in Table 5-VI.

Table 5-VI. ITT Canopus Tracker Specifications †

Stellar sensitivity (as set by threshold gates)	-1.92 to 0.08 m
Total FOV	8.2†† x 16 deg
Instantaneous FOV	1 x 16 deg
Null stability	50 arc sec rms
Equivalent angular noise	15 arc sec rms
Error bandwidth	10 cps
Error gradient (over 2 deg)	1 v/deg
Optics	20 mm f/1.0
Signal-to-noise	24 at 0.1 deg
TM outputs	(1) Canopus recognition
	(2) Star magnitude
Power input	3.1 w at 21 vdc
	4.95 w at 31 vdc
Weight	3.2 kg
Size	10 x 14 x 30.5 cm
Environment	Space qualified

†Manufacturer's specifications.
††Axis of control

5.3.4.2 Canopus Tracker for Mars Mission

Results of computer simulation for advanced Mars orbiter missions have determined that the precise approach guidance may be obtained through utilization of an approach guidance sensor in conjunction with a fine sun sensor and Canopus tracker. A high degree of accuracy is required in all three sensors. The accuracy of the Canopus tracker is beyond that of state-of-the-art equipment. The composite error due to bias calibration, bias stability, and alignment must be in the order of 0.5 arc min.

For purposes of comparison, the physical and performance specifications of the Mariner IV and Lunar Orbiter Canopus sensors are compared to the specifications for the proposed Voyager Canopus sensor in Table 5-VII.

The primary reason for not considering either the Mariner or Lunar Orbiter Canopus sensors for use in the approach guidance phase of the advanced Mars mission is that of inadequate accuracy (6 arc min and 50 arc sec, respectively).

In considering improvements which can be made to obtain increased accuracy, as well as increasing performance and producibility, the following are apparent (although other instrumentation approaches may even prove superior):

a) The use of a refractive optical system (in comparison to the wide-angle Cassegrain used in the Mariner instrument) will give improved optical image resolution.

b) The use of the recently developed high-resolution ITT F4012 vidissector will have the following advantages over the CBS CL1147 and ITT FW143 image dissectors:

   1) The use of a flat photocathode simplifies the design of the optical system eliminating the use of corrector elements, improving optical resolution.

   2) No fiber-optic faceplate is required (as in the CBS CL1147 Reconnatron), resulting in increased producibility and reduced cost of the detector.

   3) The ITT FW 143 has extreme off-axis pincushion distortion, defocusing of the electron

Table 5-VII. Specifications — Contemporary and Proposed Canopus Sensors

ITEM	MARINER IV CANOPUS SENSOR	LUNAR ORBITER CANOPUS SENSOR	HIGH ACCURACY CANOPUS SENSOR (NEW DESIGN)
1. Manufacturer	NASA – JPL/Barnes Engineering Company	ITT Federal Laboratories	
2. Application	Mariner IV	Lunar Orbiter	Mars Orbiter (Voyager)
3. Optical System	Semi-solid Cassegrain Schmidt 0.8 in f.l. f/0.6 t/1.0	Refractive – 7 elements + corrector 20 mm f/1.0	Refractive 25 mm f/1.0
4. Detector	CBS Type CL 1147 Image Dissector	ITT Type FW 143 photomultiplier	ITT FW 4012 Vidissector
Spectral Response	S-11	S-20	S-11
Aperture Dimensions	0.012 x 0.160 in.	0.024 x 0.435 cm	0.044 x 0.64 cm
5. Instrument Field of View			
Roll (total)	4°	8.2° (±6° after acquisition)	8°
Pitch (total)	30°	18°	30°
Instantaneous	0.85° (roll) x 11° (cone)	1° (roll x 18° (cone)	1° (roll) x 16° (cone)
6. Gimbaling	Electronic	Mechanical adjustment for launch window	Electronic
7. Scanning			
Roll (search)	+2° sinusoidal at 1 kHz	±4.1° triangular at 14 Hz	±4° at 10 to 20 Hz
Roll (track)	+2° sinusoidal at 1 kHz	±1.5° triangular at 800 Hz + dc bias	±1.5° triangular at 1 kHz
Pitch	5 programmed and 3 optional increments (4.6° ea)	None	Six (maximum) programmed increments
8. Stellar Sensitivity	-2.4 to +0.6 Mag		
(threshold)	+0.85°	-1.92 to + 0.08 m	Between 1/4 and 4x Canopus Mag.
9. Linear Range		±6°	±1°
10. Electronic Bandwidth	0.312 Hz	0.75 Hz	1.0 Hz
11. Time Constant	0.5 sec (roll axis)	0.2 sec (roll axis)	<0.5 sec (roll axis)
12. Acquisition Rate	0.116°/sec	Not spec	0.1°/sec
13. Error Gradient (at null)	8 v/deg	1 v/deg	8 v dc/deg
14. Signal to Noise		24 at 0.1 deg	
15. Accuracy			
At Null			
Noise	0.114° (6.85 arc min) Pk-Pk	15 arc sec rms	0.003° (10 arc-sec) rms 1-sigma
Bias	0.1° (6 arc min)	50 arc sec rms (stability)	±0.008° (± 29 arc-sec)
Alignment	Not Spec	Not spec	±0.004° (± 15 arc-sec)
Off-Axis			(4° off-axis)
Noise	Not Spec	Not spec	0.003° (10 arc-sec) rms 1-sigma
Bias	Not Spec	Not spec	±0.008° (± 29 arc-sec)
Alignment	Not Spec	Not spec	±0.004° (± 15 arc-sec)
Major Error Source	Deflection nonlinearity, compensation/mech alignment	I.D. and aperture alignment and edge irregularities	Bias calibration and stability, alignment
16. Sun Protection	CdS sensor – 1000 FT-C threshold Photoconductive sensor	CDS sensor – 100 FT-C threshold	Required – 1000 FT-C threshold
17. Weight	2.3 kg	3.2 kg (7 lb)	2.7 kg (6 lb)
18. Volume	10.2 x 12.7 x 28.0 cm	10.2 x 14.0 x 30.5 cm (4 x 5.5 x 12 in)	10.2 x 12.7 x 30.5 in (4 x 5 x 12 in)
19. Power	1.5 w. (av)	3.1 w at 21 vdc, 4.95 w at 31 vdc	6 w plus 2 w for sun shutter

image, and shading due to reduced collection efficiency. The ITT F4012 is extremely linear and resolution is maintained over the entire photocathode area.

4) Photocathode sensitivity, more uniform than either the CBS CL1147 and the ITT FW143, will permit more precise photometric calibration of the sensor.

One disadvantage, however, is that the ITT 4012 vidissector utilizes magnetic focus and deflection, requiring an addition 1.7 w of power above that required by the CL1147 Reconnatron.

A complete preliminary design is not defined, as the electronic circuit design approach is not unique, and would be similar to that of the Mariner and Lunar orbiter instruments. However, particular features which are recommended in the design are:

a) Utilization of a low-frequency search scan over a field of ±4 deg in roll, upon which a high frequency scan of ±1.5 deg is superimposed for star acquisition.

b) After star acquisition tracking may be maintained over a field of ±4 deg.

c) Programmed increments of cone angle adjustment during the course of the mission, accomplished by application of a dc bias to the imaging section of the vidissector.

A proposed specification for the Voyager Canopus sensor is defined in Table 5-VII, with a number of the specified parameters resulting from previous studies of the Voyager spacecraft configuration by TRW Systems for the NASA Jet Propulsion Laboratory. The accuracy requirements, however, have been developed in this study as a result of computer simulation of advanced Mars orbiter missions. The accuracy requirements are particularly stringent, and as defined in Paragraph 3.2.4 for the proposed planetary approach sensor, will require particular attention to the following:

a) Measurement and calibration of nonlinearities in the image tube angular deflection versus deflection current transfer function.

b) Consideration of the effects of component aging and the resultant changes in bias level throughout the course of the mission.

c) Consideration of the effects of spacecraft thermal stress, which may result in changes in bias level throughout the course of the mission.

d) Precision in initial alignment of the sensor reference axis with respect to the spacecraft coordinate system, requiring very small angular tolerances in both mechanical alignment and optical simulation equipment.

5.3.5 Planet Approach Sensor

Results of computer simulation of the Mars mission have determined that the accuracy of approach guidance may be improved over that obtainable with radio-inertial guidance by the use of an optical planetary approach sensor, providing that the approach sensor has the capability of determining the relative angular position of the geometrical centroid of the planet to an accuracy of one arc min. This accuracy will be determined primarily by bias errors and long-term stability of the sensor.

In this section, the preliminary design concept of a planetary approach sensor is defined, which in addition to having the capability of determining the clock and cone angle to the geometrical centroid of the planet, also has the capability of measuring the apparent angular subtense of the planet, permitting stadimetric ranging.

A high-resolution, electronically scanned image tube is chosen as the radiation sensor, primarily from the standpoint of reliability, permitting electronic gimbaling in clock and cone angle during planetary approach. This type of design has been selected in preference to the more conventional alternative approach, that of using a single-element point detector with mechanical scanning and gimbaling.

The configuration selected utilizes both deflection voltages and error signals in digital form, from which clock angle, cone angle, and apparent planetary angular subtense may be computed with high precision. (See Paragraph 3.3.2.) This computation can either be computed on board the spacecraft by the guidance system computer, or may be telemetered to earth for use in ground-data processing.

5.3.5.1 Optical Field-of-View Requirements

Utilizing the trajectory selected for the Mars mission in this study, the variations in clock and cone angle to the planet centroid during planetary approach have been determined, as well as the variation in apparent angular subtense of the planet. The planet approach sensor would be used during the approach phase from approximately ten days to one-half day before encounter. The variations in clock angle, cone angle, and apparent angular subtense of the planet over this time interval are indicated in Figure 5-17. Using these values as nominal, the optical total field-of-view required for the approach sensor will be 13 x 13 deg, centered at a clock angle of 263 deg and a cone angle of 127 deg. In order to permit reasonable variations in vehicle attitude, a slightly large field-of-view has been selected, 15 x 15 deg.

5.3.5.2 Planetary Radiance, Luminance, and Detector Selection

The selection of a suitable detector for utilization in the planet approach sensor is based upon two considerations: (1) the radiance and luminance characteristics of the planet Mars, and (2) the corresponding types of detectors which are available for sensing this radiation. Studies previously performed by TRW Systems (Ref 5-3) have determined

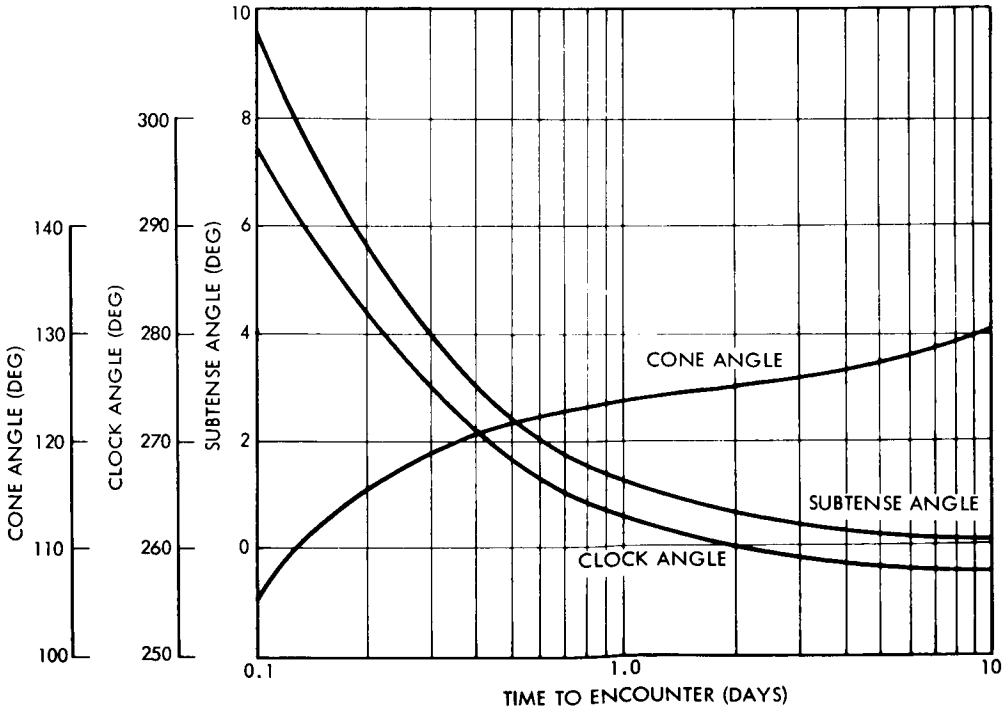

Figure 5-17. Measurement Angles Versus Time to Encounter

that two ranges in the infrared range of the spectrum may be considered for use in determining the local vertical to the planet Mars. Due to the extremely high concentration of CO_2 in the Martian atmosphere, one range which may be considered is the CO_2 absorption band centered at 15 μ. However, the precise range of the temperature variations in the atmospheric structure and the corresponding variations in atmospheric radiance are not well defined at this time, preventing estimation of the variations in the effective apparent height of the atmosphere in the infrared range. For this reason, it is not recommended that this spectral range be considered for use at this time. The more suitable spectral range in the infrared spectrum is that at wavelengths longer than 20 μ, where radiance from the planetary disc may be observed.

Considering the available detectors, thermistor bolometers would be the most suitable for use in this spectral range, based upon extensive experience which has been gained by utilization in earth-horizon sensors. However, inasmuch as these devices are single-element or "point" detectors, scanning and pointing must be accomplished by using mechanical devices with either flexure pivots or rotating bearings. Unfortunately, no suitable infrared image tubes are suitable for use in this spectral range, based upon considerations of both detectivity and reliability.

With the recommended configuration of the approach sensor being based upon the use of an electronically scanned and electronically gimbaled image tube, the near-visual range of the spectrum must be utilized, as numerous imaging sensors of adequate sensitivity and reliability are available for use in this spectral range.

Two types of image tubes have been considered — photoelectric image dissectors and vidicons, both of which are currently in use in various satellite and spacecraft programs. Several tradeoffs in performance are immediately apparent. The vidicon sensors have the distinct advantage of high sensitivity, due to the integrating characteristics of the photoconductive target, permitting storage of the radiation-induced electronic pattern of photoelectrons. This permits extremely short exposure times of the target in the order of a few milliseconds, followed by slow-scan readout of the raster to determine the apparent position of the planet.

This feature would be of considerable value in preventing distortion of the image of the planet during the exposure interval in the presence of random spacecraft motion within the range of the limit cycle of the control system. A second advantage is that of the very high signal-to-noise ratio resulting from the integrating characteristics of the photoconductive target. A disadvantage, however, is the lower level of reliability of a vidicon sensor, compared to that of an image dissector. The primary failure mode of vidicons is wear-out of the thermionic filament. This problem is not present in image dissectors which do not utilize an electron gun. Although data from the Tiros program has indicated that an MTBF of approximately 1 year may be anticipated from vidicons in continuous operation in a space environment (Ref 5-4), data obtained from a manufacturer of image dissector tubes has indicated a considerably higher MTBF for this type of detector. Data obtained from the ITT Industrial Laboratories, based upon information utilization of approximately 400 image dissectors with a total accumulated operating time of 400,000 hr, have determined that only one failure has been reported. These data were accumulated under conditions of aging, burn-in, shock, vibration, high and low temperatures, and exposure to controlled levels of light. Based upon this data, the estimate of the failure rate is one failure per 400,000 hr. Shelf life is in excess of 5 years.

Primarily from the standpoint of reliability, the image dissector has been selected for utilization in the approach sensor. A second advantage is that of simplicity in subsystem design; since continuous scanning may be utilized, in contrast to the expose-readout-neutralize cycle which would be employed with a vidicon. Although the image dissector requires utilization of a longer exposure interval (frame time) in order to obtain an adequate signal-to-noise ratio, the amount of spacecraft motion during a frame time has been found to be extremely small, resulting in negligible distortion of the observed optical image. An analysis of signal-to-noise ratio, based upon the mean value of luminance of Mars and the anticipated sensor resolution, scanning rates, and detection bandwidth, has determined that performance will be adequate for this application.

A detailed calculation of the signal-to-noise ratio of the recommended planetary approach subsystem is contained in Subsection 5.4, and anticipated performance is summarized in Paragraph 5.3.5.4.

The type of image dissector which has been selected for use in this subsystem is the type 4011 vidissector, a high resolution image dissector recently developed by the ITT Federal Laboratories. Figure 5-18 illustrates the resolution which has been obtained with this sensor, utilizing dynamic focusing. Although both electromagnetic focusing and deflection are utilized, the power consumption of the tube is only 1.5 w. This dissector is available with several types of photocathodes: S-20, S-11, and S-1. Although the S-20 is the most sensitive, this surface has a limitation in allowable photocathode current density of 1 $\mu amp/cm^2$, based upon fatigue considerations. The S-11 photosurface has been selected, having a higher photocathode current density limitation of 10 $\mu amp/cm^2$, permitting the use of an optical system of lower f-number, and resulting in a higher signal-to-noise ratio. The S-1 photosurface was not considered due to its inherently low absolute sensitivity.

5.3.5.3 Subsystem Mechanization

During the approach phase, the planet Mars will normally appear as an illuminated crescent in the visible range of the spectrum. Within the optical field-of-view of 15 x 15 deg, the image of the planet, varying in apparent diameter from 0.1 to 2.5 deg, will be focused on the image dissector photocathode. Rectilinear sweep voltages will be generated in digital form, using a 1000-line raster. Referring to Figure 5-19, both the apparent angular offset (x_c, y_c) of the geometrical center and the apparent angular radius (r) of the planet image may be determined by solution of the following equation, defining the location of the points on the periphery of a circle offset from the origin of the coordinate system:

$$(x_i - x_c)^2 - (y_i - y_c)^2 = r^2$$

As the image of the planet is scanned, the signal waveform is differentiated (Figure 5-19). The resultant signal is then processed by an

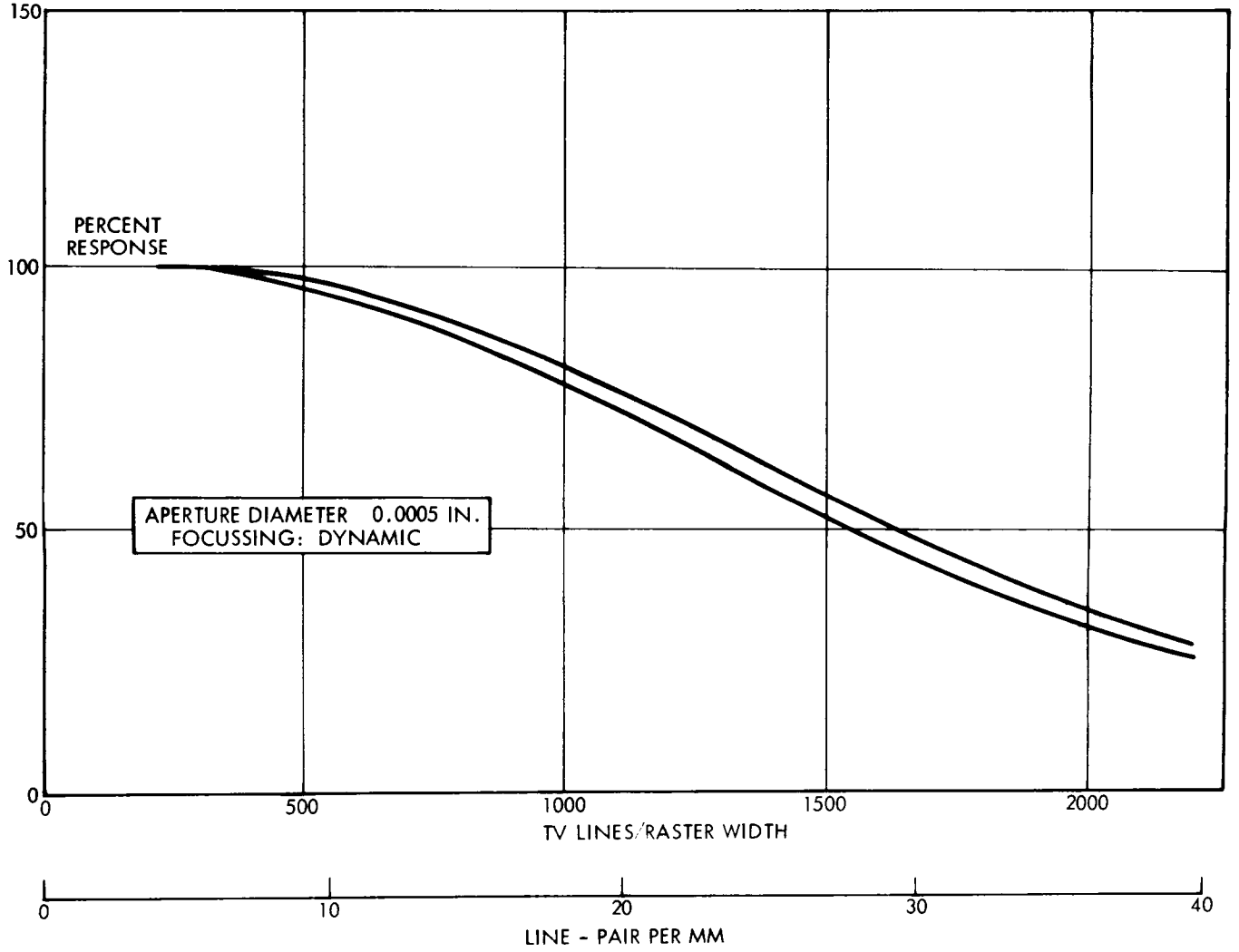

Figure 5-18. ITT Type 4011 Vidissector Modulation Transfer Function

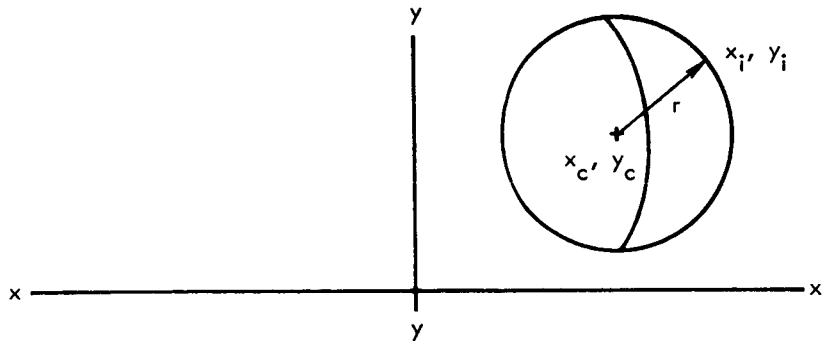

a) SCANNING GEOMETRY

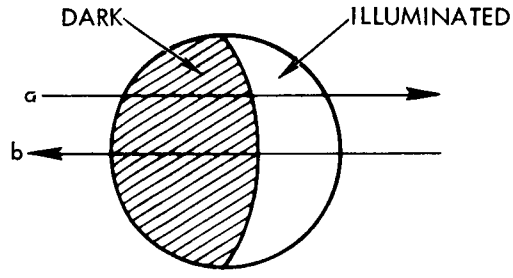

b) METHOD OF SCANNING

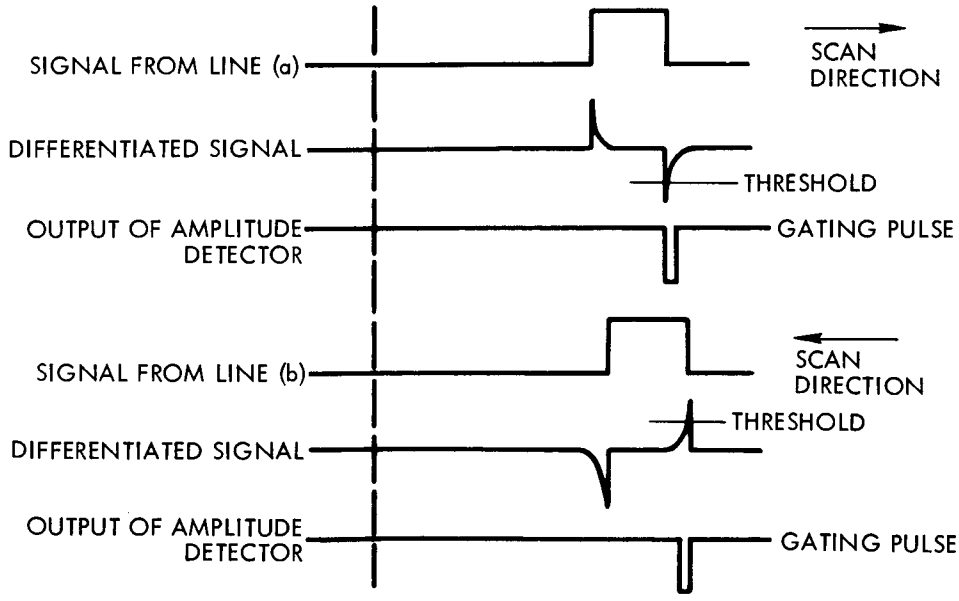

c) WAVEFORMS

Figure 5-19. Planet Scanning Technique

amplitude detector, the output of which enables gates, and thus permits measurement of the outputs of counters defining the values of the sweep voltages at the instant that the edge of the planet image is scanned.

Two measurements of x_i and y_i will enable solution of the above equation to determine the coordinates of the geometric center of the planet image, if the value of apparent angular radius, r, is known. If the value of the radius is not known, three sets of data points will enable solution of the equation for the coordinates of the geometric center, x_i and y_i, as well as the apparent angular radius, r. The accuracy of the computation can be improved by sequential processing of a number of data points from successive scans. The accuracy and noise levels which may be anticipated are defined in Subsection 5.4.

Optical System. A suitable optical system for the planetary approach sensor would be the Farrand Super Farron refracting optic, with a speed of f-0.87 and t-1.0, a focal length of 76 mm, and with resolution of 100 lpm[†] on-axis and 50 lpm off-axis. Using a 15 x 15 deg field-of-view, the size of the field on the photocathode of the ITT 4011 vidissector would be 13 cm^3.

Electronic Configuration. The function diagram of the proposed planet approach sensor is illustrated in Figure 5-20, and the scanning waveforms are defined in Figure 5-21.

Signal Amplification and Detection Circuits. The signal amplification and detection circuits consist of a preamplifier, high-frequency compensation network, signal amplification and passband filters, automatic threshold control, and amplitude detector.

The signal from the vidissector is amplified by a preamplifier, followed by a high-frequency compensation network. With a vidissector load resistor of approximately one megohm, the frequency response at the output of the vidissector would normally be in the order of 5 kHz. The high-frequency compensation network accentuates the higher frequencies, providing an overall signal bandwidth of 62.5 kHz. The automatic threshold control network provides a bias to the amplitude detector proportional to the luminance of the planet image, enabling detection of the

[†]Lines per millimeter.

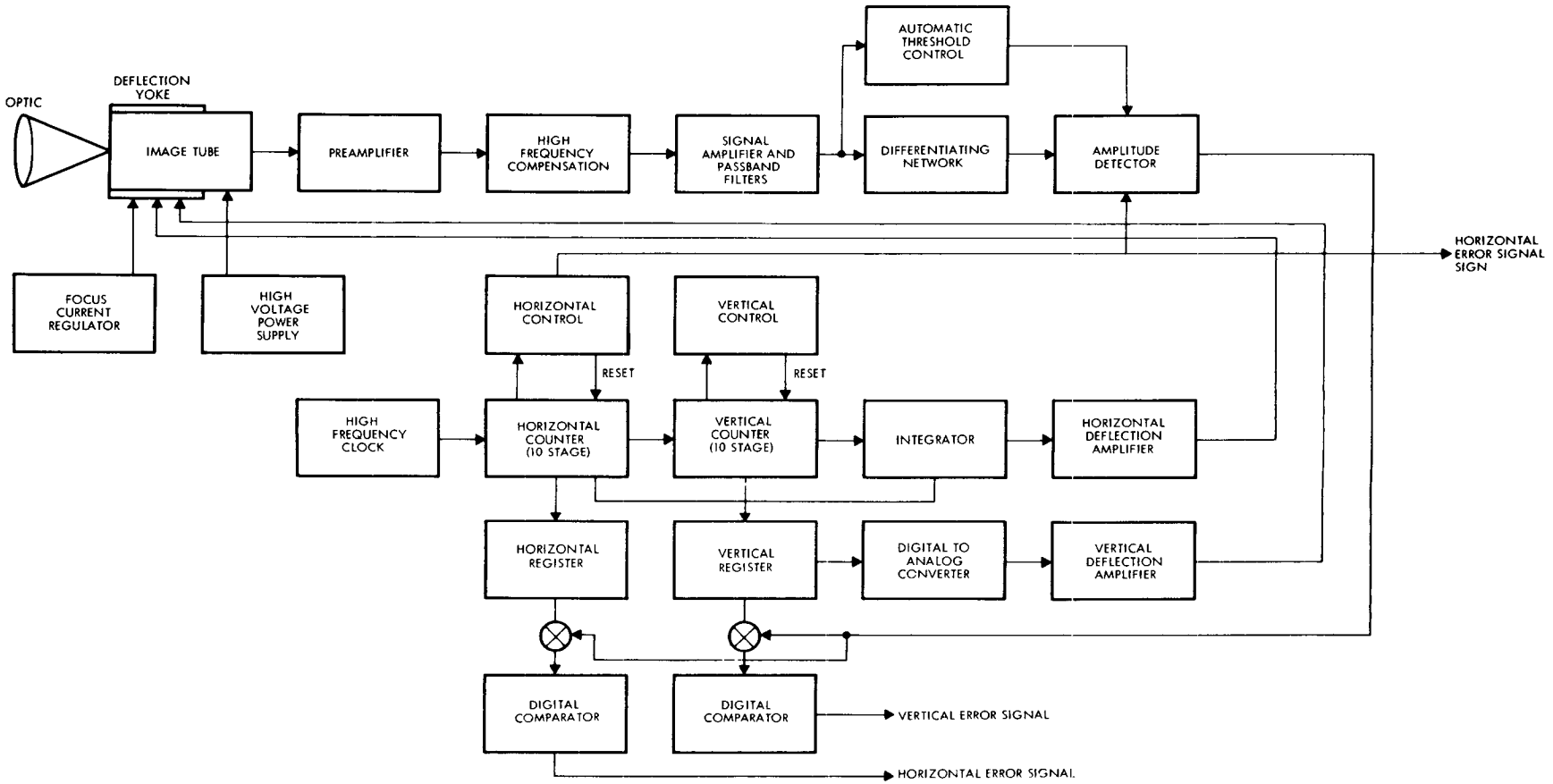

Figure 5-20. Functional Diagram – Approach Guidance Sensor

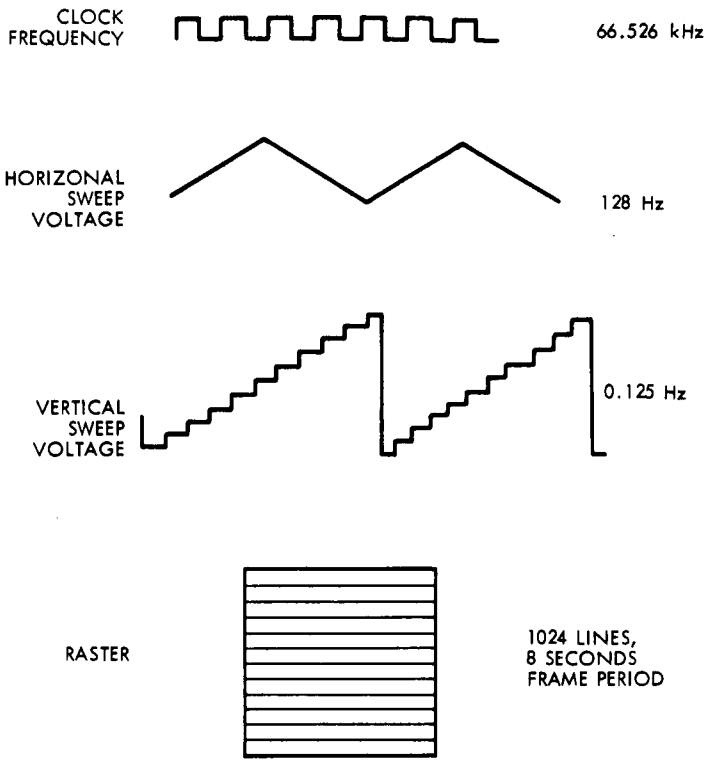

Figure 5-21. Planet Approach Sensor Scanning Waveforms

differentiated signal at approximately 1/3 of the peak signal amplitude, thus minimizing the error of detection of the location of planetary edge with variations in planet luminance. Both positive and negative amplitude detection would be provided, depending upon the direction of x-axis scanning voltage, as determined by the horizontal control circuit.

Deflection and Auxiliary Circuits. A high-voltage supply circuit would be utilized to supply -2400 v to the vidissector, and the intermediate voltages for the drift tube element and dynodes. A focus regulator would provide constant current, compensating for variations in temperature of the focus coil.

Assuming a scanning period of 8 sec, the reference for generation of sweep voltages would be high-frequency clock operating at a frequency of 66.526 kHz. The 10-stage horizontal counter, in conjunction with an integrator, would provide a triangular horizontal sweep voltage at a frequency of 128 Hz. The output of the 10-stage vertical counter, driven by the horizontal counter, would be accumulated in a register and then converted to a staircase waveform by a digital-to-analog converter, providing

a vertical sweep voltage at the frequency of 0.125 Hz. The combination of horizontal and vertical sweep voltages would then provide a raster of 1024 lines per frame. The horizontal counter would be reset at the end of each line by the horizontal control circuit, and the vertical counter would be reset at the end of each frame by the vertical control circuit.

Determination of the horizontal and vertical location of the planetary edge would be determined by gating the output of the horizontal and vertical register with the gating pulse from the amplitude detector at the instant of scanning the planetary edge. These binary numbers would be compared in the digital comparator circuits to a reference binary number corresponding to the center of the raster (optical axis) in x and y coordinates. The outputs of the two comparator circuits would comprise the error signals in binary form. One additional signal, indicating the sign of the horizontal error signal, would be provided by the horizontal control circuit, accommodating the bidirectional scanning of the horizontal waveform.

5.3.5.4 Proposed Specification

A proposed specification for the planet approach sensors is defined in Table 5-VIII. This specification should be considered as a design objective. Discussion of the specified values of noise, bias, and alignment errors is contained in Section 4.

5.4 SENSOR ERROR MODELS

The purpose of this section is to specify the error contributions expected from the electro-optical sensors chosen for use in the Radio/Optical/Inertial Guidance Study. This information was generated for use in the digital computer guidance simulations perfomed during the study. The section contains sensor performance data, a discussion of the interpretation of the data, justification for the figures quoted, and a discussion of means for achieving performance improvments needed as indicated by the results of the guidance simulations. The performance data relate only to instrument errors and do not include attitude computation errors, spacecraft flexure stress relative to the sensor, etc.

Table 5-VIII. Proposed Specification – Mars Approach Sensor

Function:	The planetary approach sensor will be used for approach guidance of an unmanned spacecraft to the planet Mars. The sensor will scan the optical image of the planet and will provide information defining the relative angular displacement of multiple points on the planetary limb with respect to the spacecraft coordinate system. From these data, the relative angular displacement of the geometric center and apparent angular subtense of the planet will be determined by the spacecraft guidance computer.
Specifications:	
Acquisition field of view	15 x 15 deg
Variation in apparent angular subtense of planet	From 0.1 to 2.5 deg
Variation in clock angle	11 deg
Variation in cone angle	8 deg
Gimbaling of clock and cone angles	Electronic
Mode of scanning	Continuous
Optical system	Farrand Super Farron 76 mm/f-0.87/t-1.0
Detector	ITT type 4011 1-1/2 in. Vidissector
Scan pattern	Rectilinear raster, 1024 lines per frame, noninterlaced
Scanning rate	8 sec per field
Form of output signals	Digital, binary; one 10-bit word on each of two axes defining points on the planet limb
Equivalent angular noise At null Off axis	 10 arc sec rms (1σ) 10 arc sec rms (1σ)
Fixed bias error	10 arc sec (1σ) (assumes calibration of repeatable nonlinearity)
Long-term bias error (long-term stability)	10 arc sec (1σ)

Table 5-VIII. Proposed Specification – Mars Approach Sensor (Continued)

Specifications (Continued):	
Alignment	Provision for alignment of optical axis with respect to mounting surfaces to an accuracy of 10 arc sec.
Weight	3.2 kg
Volume	12 x 12 x 30 cm
Power	8 w
Environment	Qualified for operation in space environment. Specific environmental levels to be determined.

5.4.1 Sensor Performance Summary

Table 5-IX is a list of all optical sensors chosen for the various strapdown guidance system configurations and a specification of the errors which they may be expected to contribute. The instruments listed have previously been described in detail and rationale has been provided for their selection.

The figures quoted in the accuracy column of Table 5-IX represent the uncertainty in a given optical measurement made by the particular sensors. As stated previously, this uncertainty does not include the effect of computational approximations except for the earth sensors; nor, does it include uncertainties in apparent target location, i.e., due to velocity aberration, parallax, etc. The quoted figure includes errors in alignment of the sensor to a stable, plane mounting surface.

The interpretation of the error magnitude tabulated may be best described by an idealized experiment. Assume that an ideal mounting surface is placed on a dividing table and precisely aligned and leveled relative to an exactly realistic target simulator. Further assume that the sensor is mounted, aligned as it would be in the operational case and a large number of target position readings taken at a known target angle θ_o. The judgement of what comprises a large number of readings is part of the

Table 5-IX. Summary of Electro-Optical Sensor Errors

Sensor	Type	Null Accuracy			Offset Accuracy (1)			
		Noise (rms) (deg)	Bias Instability (deg)	Alignment Error (deg)	Offset (deg)	Noise (deg)	Bias Instability (deg)	Alignment Error (deg)
Sun Sensors								
Coarse	TRW Voyager	(2)	±1.0	±1.0	20	(2)	±1.0	±1.0
Fine	BBRC/FE 5A	(2)	±0.022	±0.004	5	(2)	±0.022	±0.004
Digital Aspect	ADCOLE 1402	0.006	±0.04	±0.004	32	0.006	±0.04	±0.004
Earth Sensors								
Low Altitude	A-OGO	0.03	±0.09(3)	±0.016	10	0.03	±0.14	±0.016
High Altitude	M-OGO	0.04	±0.10	±0.016	2.5	0.04	±0.10	±0.016
Canopus Sensor								
Lunar Mission	ITT Lunar Orbiter	0.02	±0.014	±0.016	4	0.02	±0.05	±0.016
Interplanetary	Vidissector Tracker	0.002	±0.008	±0.004	4	0.002	±0.008	±0.004
Planet Approach								
Sensors (4)	Digitally Scanned Image Tube	0.003	±0.008	±0.004	6.75	0.003	±0.008	±0.004

NOTES:

(1) For two-axis measurement system, Figures given include sum of error in both axes.
(2) Negligible, i.e., < 1 arc sec.
(3) Oblateness error and horizon altitude error included as sources of bias error.
(4) 1.5 deg planet subtense.

test planning, and the number will be assumed to be sufficient to produce an accurate sample mean measured angle $\bar{\theta}_m$. The quantity termed bias is then $\Delta\theta$, where:

$$\Delta\theta = \bar{\theta}_m - \theta_o$$

The quantity labeled noise is defined in terms of the standard deviation of the set of measured angles from the sample mean. The computation of this parameter is done by means of the following equation, i.e., sample variance.

$$\sigma^2 = \frac{1}{N-1}\left[\sum_{i=1}^{N} \theta_i^2 - N\bar{\theta}_m^2\right]$$

where

θ_i = a single target angle measurement

N = total number of measurements

In the ideal experiment, and throughout this document, the power spectrum of the noise is assumed to be uniform prior to the bandwidth limiting filter.

The noise and bias are obviously functions of the sensor environment, notably of temperature; and the figures quoted in the tables correspond to realistic extremes for orbtial environments. It is assumed that the component of bias which is stationary over the mission period and measurable by means similar to those described above prior to launch, will be compensated for in data processing.

5.4.2 Derivation of Sensor Accuracy

5.4.2.1 Sun Sensors

Coarse Sun Sensor. The candidate coarse sun sensor is that which has been proposed by TRW for the Voyager spacecraft. This sensor consists of two units, one for each sensitive axis. The sensor unit is composed of two solar cells, mounted back-to-back, each immersed in a plano-convex lens. The two solar cells are connected across a low resistance with opposing polarity. The sensor provides a sun present signal over the entire 4-π ster field. The signal polarity indicates in which hemisphere

the sun is located; and near the null plane the signal amplitude is linearly proportional to the sun's angular displacement. Laboratory experience with this device indicates that a null stability of between one-half and one deg may be attained, depending upon the thermal and geometric characteristics of the mounting structure. The linearity of the signal output is within 10 percent in the region ±20 deg from the null plane. Due to the high level of the sun signal relative to solar cell and amplifier noise, the angular effect of noise may generally be taken as negligible. The coarse sun sensor is not a critical item since measurements are not made with the device for use in fine guidance.

Fine Sun Sensor. On-Axis Analog Sun Sensor. The Ball Brothers FE-5A "Fine Eye" sun sensors have a specified accuracy of ±1 min of arc per measurement axis over a linear range of ±5 deg and a temperature range of -20 to +85°C. These sensors were tested by Boeing to this specification during the Lunar Orbiter Program and this specification was found to be valid. As with the coarse sun sensor, very little random noise component is expected in the total error figure. The major expected error contributors are uncompensated sensitivity drifts in the silicon cell, particularly due to temperature variations, and mechanical variations in the structure and knife edge reticle, again predominantly due to thermal fluctuations. The ±1 min is thus in the form of a bias slowly varying bias correlated manner with sensor temperature variations. A partial compensation of this effect might be accomplished by measuring the bias error as a function of temperature prior to launch and making onboard corrections in the digital computer from cell and structure temperature inputs. It is estimated that an initial alignment accuracy of ±15 arc sec can be achieved.

Off-Axis Digital Sensor. In order to make a precise measurement of spacecraft attitude using a single fine sensor system as described above, it is necessary to maneuver the spacecraft attitude until the sun falls within the sensors 20-deg field. If it is desirable to avoid the maneuvering requirement, the nulling sun sensors described above might be replaced by one or more digital solar aspect sensors of the type manufactured by the Adcole Corporation. These devices consist of a gray-coded reticle, silicon photo cells and a housing. The gray-coded reticle is a small oblong block of fused quartz with a slit centered along the top surface and

a gray-coded pattern on the bottom surface. A single-axis device encoder solar aspect into a 12-bit word and has a 64-deg field. The resulting angular resolution is 1/64 deg which is equivalent to an rms quantization error and is equivalent to an rms noise level of approximately 0.004 deg per axis.

The manufacturer specifies that the accuracy of the measured solar aspect is 0.03 deg per axis defined at the transition between encoder quanta where there is no resolution error. Two such devices are supplied in a single package to provide two axis sensitivity. As with the analog fine sun sensor, a 15-arc sec initial alignment accuracy is estimated.

5.4.2.2 Earth Sensor

The earth sensor system described below is composed of two separate sensor assemblies, one for low altitude another for high. Since the scanning mechanism is identical for the two assemblies, it is feasible to consider an operational system composed of a single assembly of operation in two modes.

Low-Altitude Earth Sensor Errors. The candidate low-altitude sensor is the advanced OGO earth sensor system developed for NASA/Goddard by Advanced Technology Laboratories. The system consists of four edge-tracking infrared telescopes oriented by pairs in and perpendicular to the orbital plane. For purposes of error analysis the earth is assumed to be a perfect sphere with a fixed horizon at constant radiance. Deviations of the real earth from the ideal model are then treated as sources of error in measurement of the ideal horizon angle.

The following error sources are significant for the low-altitude earth sensors:

a) Earth oblateness

b) Horizon altitude and radiance variations

c) Detector and preamplifier noise

d) Angle transducer nonlinearities

e) Misalignment.

These factors will be treated separately below.

Earth Oblateness Error. At low altitudes the deviation of the earth from a sphere contributes a significant error in determination of attitude relative to the geocentric line. This error is completely determinate, of course, and can be eliminated by computed corrections using navigation and attitude data is available. This effect is discussed in detail in Ref 5 and 6 where the true shape is assumed to be an ellipsoid of revolution. The ellipsoid and relevant angles are illustrated in Figure 5-22. In Ref 6 the following equation is derived for the deviation, $\Delta\theta$, of the true horizon angle from an average circle centered about the geocentric line.

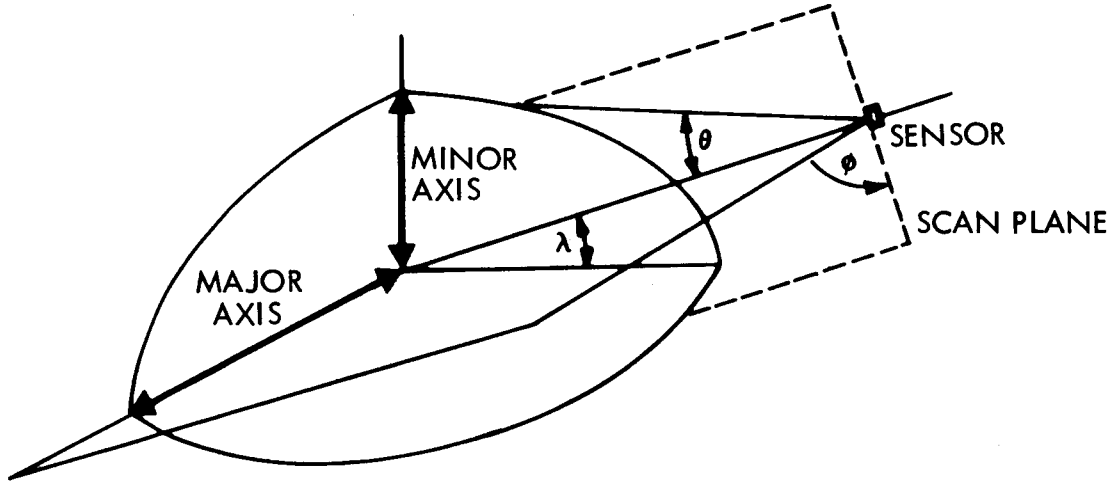

ϵ = eccentricity of the earth ellipsoid

α = earth equatorial radius

ρ = satellite - geocenter distance

λ = subpoint latitude

ϕ = azimuth angle of scan plane relative to plane defined by geocentric line and major axis of ellipsoid

Figure 5-22. Geometry for Oblateness Error

The quantity $1/2\ [\Delta\theta\ (\phi) - \Delta\theta\ (\phi + 180^{\circ})]$ is the oblateness error in the single-axis attitude measurement by a scanner pair of the sensor system. For a spacecraft altitude of 185 km, subpoint latitude of 45 deg and sensor azimuth angle of 90 deg, the attitude measurement error is 0.18 deg. The error in the other axis is zero since the horizon angle measurement

errors are symmetrical. If the sensor system is oriented such that the scan planes are at azimuth angles of 45, 135, 225 and 315 deg from the equator the single-axis error is reduced by $1/\sqrt{2}$. If the orbit is such that all subpoint latitudes from 0 to 45 deg are experienced for equal times, the rms value of $\Delta\theta$ is $1/\sqrt{2}$ times the peak and:

$$\Delta\theta = 0.18 \text{ deg } \sqrt{2} \cdot \sqrt{2}$$

$$\Delta\theta = 0.09 \text{ deg rms, per axis}$$

The error in each axis is equal, and the magnitude of the vector pointing error is 0.13 deg.

Horizon Altitude and Radiance Variations. To the extent that the altitude and radiance of the earth's horizon are a known function of position and season, this error source is also determinate. A practical system, however, will tolerate rather than attempt to analytically compensate for horizon errors. McArthur (Ref 5) has used meteorological data to compute the variance of the earth horizon altitude in the 14- to 16-μ CO_2 absorption band. His results indicate a standard deviation of 0.88 km in the horizon location at the 80 percent point in the horizon radiance profile. From Figure 5-23 it can be seen that a horizon tracking telescope will experience a horizon angle measurement error $\Delta\theta$, where:

$$\Delta\theta = \frac{0.88 \text{ km}}{\left[R^2 - (R + h)^2\right]^{1/2}} = \frac{0.88 \text{ km}}{\left(2Rh + h^2\right)^{1/2}}$$

$$\Delta\theta = 0.0063 \text{ rad} = 0.035 \text{ deg, rms}$$

If the horizon altitude errors at the four track points are assumed to be uncorrelated, the net two axis error is $\Delta\theta = 0.05$ deg, rms.

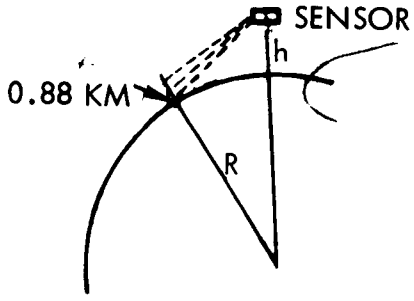

Figure 5-23. Horizon Altitude Error

The earth sensor system for low altitude use consists of horizon tracking telescopes. Variation of the horizon radiance does not affect such a device as severely since it will tend to track at a point corresponding to a fixed fraction of the limb radiance, regardless of its absolute value.

Detector and Preamplifier Noise. Using the definition of detectivity (D^*) as the reciprocal of noise equivalent power normalized to unity bandwidth and one square centimeter detector area, the sensor signal-to-noise ratio is given by:

$$S/N = N_{\Delta\lambda} A_t \Omega_t \eta D^* (A_a B_\eta)^{-1/2} k^{-1}$$

Where the symbols and numerical values are the following:

Telescope clear aperture area, $A_t = 2.3\ cm^2$

Telescope field-of-view, $\Omega_t = 4 \times 10^{-4}$ ster

Telescope transmission, $\eta = 0.25$ (assumed)

Detector area, $= 10^{-4}\ cm^2$

Detector detectivity, $D^* = 3 \times 10^8 \frac{cm\text{-}cps^{1/2}}{w}$ (assumed)

Noise bandwidth, $B_n = 50$ cps

Spectral bandpass, $\Delta\lambda = 2\mu$ (14μ-16μ)

Minimum earth radiance, $N_{\Delta\lambda} = 365 \frac{\mu w}{cm^2\ ster}$

Preamplifier noise figure, $k = 2$ (6 db assumed)

The resulting signal-to-noise value, using these values is:

$$S/N = 177$$

This ratio is of peak earth signal-to-rms-noise in the sensor band. Except where noted the numerical values used are from manufacturer's specifications. The two assumed values are reasonable sensor parameters and the minimum earth radiance is from the model atmospheres of Wark (Ref 5-8).

In order to relate this figure to angular tracking error, it is necessary to consider briefly the operating principle of the horizon tracker. The telescope mirror scans the horizon in a small amplitude linear "dither." Reference to Figure 5-24 shows that a small displacement of the center of

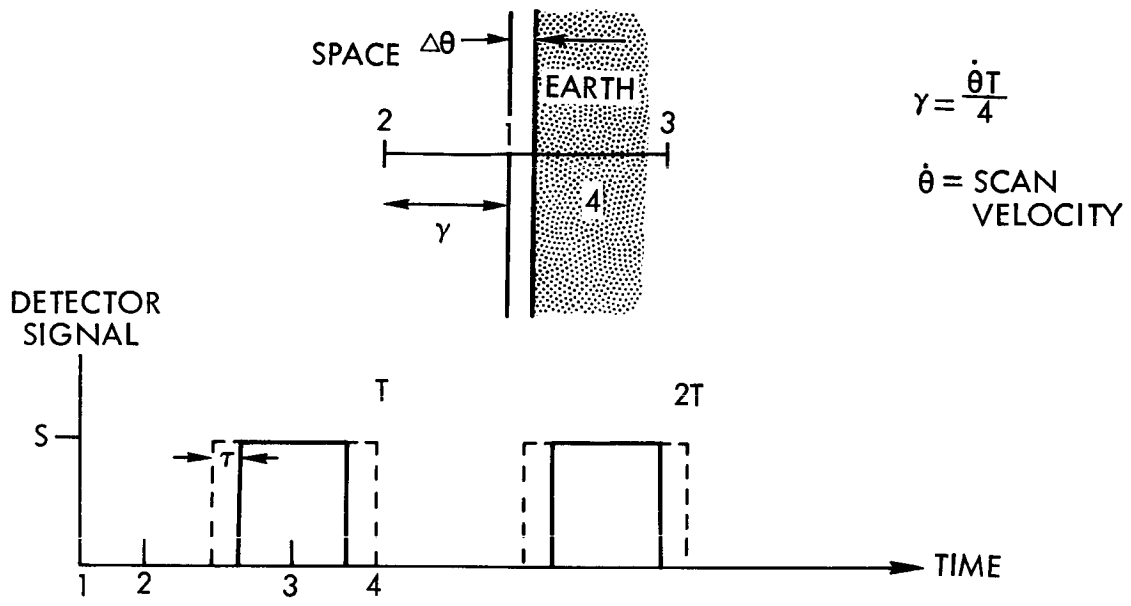

Figure 5-24. Sensor Scan and Detector Output Waveform with Attitude Offset

the scan creates an asymmetry in the signal. Tracking is accomplished by detecting the second harmonic content of the signal. For a small displacement $\beta\theta$, the amplitude of the second harmonic of the signal shown in Figure 5-23 is:

$$C_2 = \frac{4S\tau}{T}$$

If the second harmonic is filtered and full-wave rectified, the dc error signal is:

$$E_{\Delta\theta} = \frac{2}{\pi}\left(\frac{4S\tau}{T}\right)$$

From the figure it can be seen that:

$$\frac{\tau}{T} = \frac{\Delta\theta}{4\gamma}$$

so

$$E_{\Delta\theta} = \frac{2S}{\pi\gamma}\,\Delta\theta$$

Therefore, when $E_{\Delta\theta}$ equals the noise N, the noise induced error near null is:

$$\Delta\theta_n = \frac{\pi\gamma}{2} \left(\frac{1}{S/N}\right)$$

For a scan amplitude $\gamma = 2$ deg the error in earth horizon measurement is:

$$\Delta\theta_n = 0.018 \text{ deg}$$

The net sensor noise contribution, assuming that all four horizon angle measurements are combined is 0.036 deg. This brief analysis neglects the finite size of the sensor field-of-view and the finite width of the horizon.

Angle Transducer Nonlinearity. The tracking telescopes of the candidate earth sensor system are equipped with induction coil angle transducers. At or near the nominal spacecraft attitude (null), the linearity and scale factor characteristics of the four transducers can be balanced to eliminate transducer bias errors. When attitude offsets or orbital altitude variations cause significant angular displacement of the tracking point from null, an angle measurement error is experienced. The manufacturer specifies that the effect is equivalent to a total attitude measurement error of 0.10 deg or less at 10 deg displacement from null.

Misalignment. The two tracking telescopes required for measurement of a given attitude displacement component would be packaged in a single assembly. The relative alignment between the two may, therefore, be kept to a precise tolerance. It is difficult to assess the accuracy of alignment expected between the unit and the spacecraft reference surface over long periods in orbital environment. From experience reported in the instrument description section of Ref 5-6, however, it is reasonable to quote a figure of 1 arc min for initial alignment error and 1 arc min for null drift during the mission.

The measurement errors computed above are summarized in Table 5-X. Sensor noise, bias instability, and initial alignment errors are listed separately. The general source of bias instability are combined in an rss manner, even though there is some correlation among them, particularly the dependence of both horizon altitude error and oblateness error upon spacecraft altitude.

Table 5-X. Summary of Errors, Low-Altitude Earth Sensor

	Measurement Errors, 1σ (deg)	
	Null	±10 deg
Sensor Noise	0.036	0.036
Horizon altitude variation	0.05	0.05
Earth oblateness	0.13	0.13
Transducer	0	0.10
Alignment drift	0.016	0.016
Total Bias Instability (RSS Above)	0.14	0.17
Initial Alignment Error	0.16	0.16

High-Altitude Earth Sensor. There are two significant differences between the earth sensor systems proposed for high- and low-altitude applications:

1) The effects of the earth's oblateness and of horizon altitude variations is greatly reduced at synchronous altitude.

2) The high-altitude sensor scans a small optical field through the earth's disc and computes single-axis attitude by measuring the time separation between signal threshold crossings and a reference pulse.

Since the errors experienced by the high-altitude sensor are primarily due to the instrument rather than the earth, and since TRW is currently acceptance testing the device, it is convenient to simply use the test specification figures for an error model. This specification limits the single-axis sensor error to 0.03-deg rms in noise or uncorrelated error an 0.09 deg in bias of which 1 arc min is assumed to be misalignment. The magnitude of the vector attitude measurement is 0.42 deg due to sensor noise and 0.10 deg due to bias instability.

5.4.2.3 Canopus Sensors for Lunar and Mars Missions

The Canopus sensor recommended for use in the optical sensor package is the device built by ITT for the Lunar Orbiter spacecraft. This device is specified to have a bias stability of ±0.014 deg at null and an rms angular noise of ±0.005 deg. The field-of-view of this Canopus sensor is

±4 deg in the sensitive axis and 16 deg in the non-sensitive axis. This field-of-view is adequate for lunar missions but must be modified to 30 deg in the nonsensitive axis for the Mars mission. The bias stability away from null is degraded to ±0.05 deg maximum error over the entire field.

Guidance simulation indicated that the bias stability and noise of the Canopus sensor must be reduced from the Lunar Orbiter performance level for the Mars mission. The net error contribution due to bias instability and alignment error must be in the order of ±1/2 arc min. The design steps required to improve stability are similar to those required for the approach guidance sensor and are discussed in the next section. The design changes required to reduce the angular noise contribution are described below.

Computation of Canopus Sensor Error Due to Noise. In order to derive the design changes necessary to reduce the angular noise jitter from the level expected in the Lunar Orbiter Canopus sensor, it is necessary to briefly consider its principle of operation. Figure 5-25 illustrates the scanning pattern generated on the image dissector photocathode and the resulting waveform.

The null noise error in a device of this type will be computed; and the parameter changes required to reduce this noise to the desired level will be derived.

It can be seen that an angular displacment of angle ϵ will result in a dc error signal given by:

$$i_{\epsilon} = I_s \frac{2\tau}{T}$$

and since

$$\tau = \frac{\epsilon}{4\phi} T,$$

then

$$i_{\epsilon} = \frac{\epsilon}{2\phi} I_s$$

where I_s is the peak star signal current and the angular error at a signal-to-noise (S/N) is:

$$\epsilon_n = 2\phi/(S/N) \qquad \epsilon_n = 3(S/N)^{-1} \text{ deg}$$

For the image dissector, the noise level is determined by shot noise in the average current due to the presence of Canopus, therefore:

$$S/N = \left(\frac{3 E_s A_o T_o k}{2e \Delta f a \left(\frac{g}{g - 1} \right)} \right)^{1/2}$$

where:

E_s = illumination due to Canopus, lumens/cm^2

A_o = area of Lunar Orbiter sensor aperture, 3.14 cm^2

T_o = transmission of optics, 0.75

k = photocathode responsivity, amps/lumen

e = charge on the electron, 1.6×10^{-19} coulombs

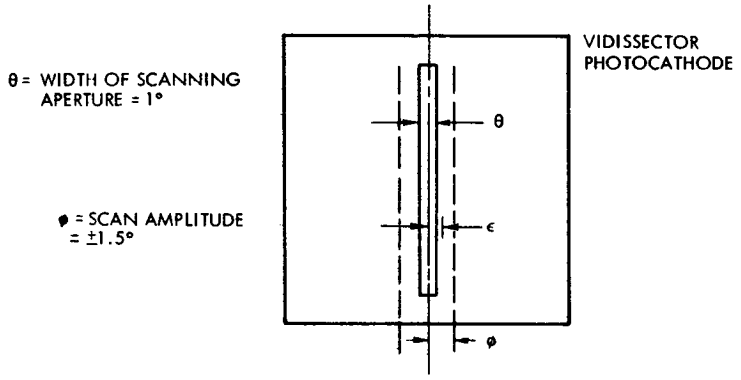

(A) IMAGE DISSECTOR SCANNING GEOMETRY

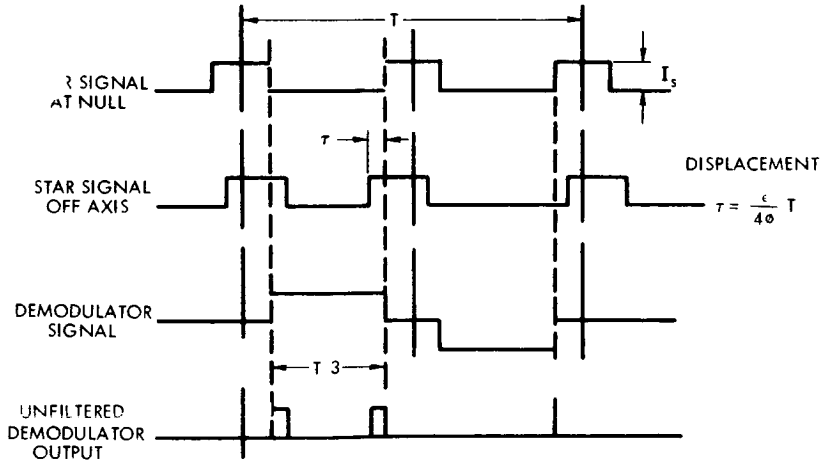

(B) SIGNAL WAVEFORMS

Figure 5-25. Canopus Tracker Scanning Geometry and Waveforms

Δf = noise bandwidth, 15.7 Hz

g = dynode gain per stage, 2.5

α = star signal duty cycle = 1/3

The visual magnitude of Canopus is -0.72; and the illumination outside the earth's atmosphere due to a zero magnitude star is 2.65×10^{-10} lumens/cm^2 (Ref 7). Therefore:

$$E_s = 2.65 \times 10^{-10} (2.51)^{0.72}$$

$$E_s = 5.2 \times 10^{-10} \text{ lumens/cm}^2$$

The minimum cathode luminous sensitivity specified by ITT for their S-20 cathode to a calibrated 2879°K source is 80 μamps/lumen. Spectral convolution indicates that an S-20 surface has a response 1.35 times greater to Canopus than to an equally luminous 2870°K source, therefore:

$$k = 8 \times 10^{-5} \times 1.35$$

$$k = 1.1 \times 10^{-4} \text{ amp/lumen}$$

Inserting the above values into the signal-to-noise equation yields:

$$S/N = \left\{ \frac{(3)(5.2 \times 10^{-10})(3.14)(0.75)(1.1 \times 10^{-4})}{(2)(1.6 \times 10^{-19})(15.7)(2.5/1.5)(1/3)} \right\}^{1/2} = 224$$

The resulting angular null error is:

$$\epsilon_n = 3(224)^{-1} = 0.0135 \text{ deg, rms or 48 arc sec}$$

Modifications Required to Reduce Noise Error. This noise error is excessive for use during the terminal guidance mode of the Mars mission. The figure can be reduced by increasing the size of the entrance aperture and narrowing the electrical bandwidth. If a one-inch diameter ITT vidissector image tube is considered, the modulating slit may have a length of 0.28 in., and hence a 16-deg field-of-view in the nonsensitive axis will correspond to a focal length of 9.0 in. The full 30-deg coverage required during the mission will be provided by electronically gimbaling the aperture in the nonsensitive direction as the mission progresses. With f/1.0 lens speed:

$$A_o = \pi(0.5 \times 2.54)^2$$

$$A_o = 5.1 \text{ cm}^2$$

To reduce the noise error to 10-arc sec rms, a value consistent with the accuracy requirements for the Mars mission, the electrical bandpass may then be reduced to:

$$\Delta_f = 15.7 \left(\frac{10}{12}\right)^2 \left(\frac{5.10}{3.14}\right)$$

$$\Delta_f = 1.1 \text{ Hz}$$

which is sufficiently wide in view of the 10-arc sec/sec maximum drift rate discussed below.

In summary, the modifications necessary to the ITT Lunar Orbiter Canopus sensor to make it suitable for use in the Mars mission are the following:

1) Use of a vidissector image tube with a large modulating slit so that a larger optical entrance aperture and field-of-view may be used

2) Increase of the entrance aperture area from 0.5 cm^2 to 7.3 cm^2 at f/1.0

3) Decrease of the electrical noise bandwidth from 15.7 cps to 2.3 cps

4) Implementation of those design guides discussed in Paragraph 3.2.4 for the reduction of null drift and misalignment in a scanned image tube.

5.4.2.4 Planetary Approach Sensor

The configuration of the planetary approach guidance sensor has been defined in Paragraph 5.3.5. The alternatives considered were closed-loop analog tracking devices versus digital scanners with computer processing, and mechanically solar versus electronically gimbaled scanners. As a result of comparing these options it was decided to recommend an electronically scanned digital image tube. The cone and clock angle to the center of the planet and the apparent angular radius of the planet will be computed in the spacecraft digital computer from the sensor digital output signals. The accuracy of the data obtained in this approach is limited by several factors:

1) Random noise in the planet edge position indications due to noise in the analog signal prior to threshold detection

2) Distortion in the deflection system

3) Photosurface and planet brightness nonuniformity and nonuniformity in planet brightness

4) Uncertainty in the initial alignment of the reference axis to the spacecraft reference coordinate system

5) Drift of the reference axis relative to its initial aligned position due to thermal stress and component aging during the mission period preceeding operation

6) Spacecraft limit cycle motion.

Error Due to Random Noise. Errors of the first type are readily subject to analysis assuming a valid model for the noise source. An analysis has been performed based upon the assumption of band-limited white, gaussian noise with zero mean (see Paragraph 3.3.2).

In order to convert the data in Paragraph 3.3.2 to meaningful angular noise values, it is necessary to know the actual noise level in the digital edge indications.

The limiting noise ratio in the output of the image dissector is shot noise in the signal, hence:

$$S/N = \left(\frac{BA_a k}{8T^2 \, e\Delta f \frac{g}{g-1}} \right)^{1/2}$$

where

B = average planet brightness, lamberts

A_a = area of the image dissector scan aperture, cm^2

k = responsitivity of photocathode, amps/lumen

T = "T" number of optical system (effective f-number)

e = the charge on the electron, 1.6×10^{-19} coulombs

Δf = sensor output noise bandwidth, Hz

g = image dissector multiplier gain per stage, 2.5

In order to evaluate the given expression it is necessary to assign values to the various parameters. The average brightness of the planetary surface is given by:

$$B = \frac{E_o (2.51)^{-V}}{\omega^2}$$

where

E_o = illumination outside the earth's atmosphere due to a zero magnitude star, $2.65 \times 10^{-10} \frac{\text{lumen}}{\text{cm}^2}$

V = apparent visual magnitude of Mars

ω = angular semidiameter of Mars, rad

Ref (5-10) gives the visual magnitude of Mars in terms of its range to the sun (r) and to the earth (Δ):

$$V = -1.41 + 5 \log r\Delta$$

The mean sun planet distance is $r = 1.524$ Au[†] and the planet earth distance at opposition is $\Delta = 0.523$ Au. Therefore:

$$V = -1.41 + 5 \log (0.798)$$

or

$$V = -1.90$$

The equatorial semidiameter of Mars at 1 Au is given in Ref (5-11) as 8.80 sec, so at $\Delta + 0.523$ Au:

$$\omega = 8.80 \times \frac{1}{0.523}$$

$$\omega = 16.8 \text{ arc sec} = 8.15 \times 10^{-5} \text{ rad}$$

and

$$B = \frac{2.65 \times 10^{-10} (2.51) + 1.90}{(8.15 \times 10^{-5})^2}$$

$$= 0.229 \text{ lamberts or } 213 \text{ ft lamberts}$$

[†] The variation is solar illumination at Mars over the Martian year is approximately ±15 percent.

The aperture chosen for the ITT 4011 vidissector has a diameter of 0.0008 in. and hence an area:

$$A_a = \frac{\pi}{4}(0.0008 \times 2.54)^2$$

$$A_a = 3.24 \times 10^{-6} \text{ cm}^2$$

The responsitivity of the S-11 photocathode to the planet image may be computed from the calibrated responsitivity stated by ITT of 50 μa/lumen of radiation from a 2870°K source, the color index of the planet from Ref (5-10), B-V + +1.41 and spectral convolutions which indicate a correction of 1.25 times between 2870°K and an equally luminous source of color index +1.41. Therefore:

$$k = 5 \times 10^{-4} \times 1.25$$

$$k = 6.3 \times 10^{-4} \text{ amps/lumen}$$

The planetary approach sensor has been conceptually configured to use the Super Farron optical system which has a 3-in. focal length and an effective speed of T/1.0. The scan period is 8 sec so for a raster of 10^6 resolution elements

$$\Delta f_s = \frac{1}{2t}$$

where τ is the dwell time of the scanning aperture on the resolution element:

$$\tau = \frac{8}{10^6} = 8 \times 10^{-6}$$

so

$$\Delta f_s = \frac{1}{2 \times 8 \times 10^{-6}} = 6.25 \times 10^4 \text{ Hz}$$

and for an RC noise roll-off at the image dissection output, the noise bandwidth is:

$$\Delta f_n = \pi/2 \, \Delta f_s$$

$$\Delta f_n = 9.80 \times 10^4 \text{ Hz}$$

Finally, evaluating the signal-to-noise expression:

$$S/N = \left\{ \frac{(0.229)(3.24\times10^{-6})(6.3\times10^{-4})}{8(1.0)^2(1.6\times10^{-19})(9.8\times10^{4})(2.5/1.5)} \right\}^{1/2}$$

$$S/N = 18.5$$

To compute angular noise on the edge crossing indications, it is necessary to find the slope on the planet edge signal. This slope is determined primarily by the frequency response of the image dissector scan mechanism and its output circuit. Measurements made by the manufacturer indicate that the spatial frequency response of the tube is 0.71 at 850 TV lines per horizontal scan line and that the device may be approximated by an RC circuit with:

$$\tau_d = \frac{8}{1000}\,\frac{2}{850} = 1,85 \times 10^{-5} \text{ sec}$$

The output time constant τ_o, was previously specified as:

$$\tau_o = 8 \times 10^{-6} \text{ sec}$$

For purposes of this discussion τ_o will be neglected and the planet signal input will be represented by a step function, so that the planet crossing output signal is given by:

$$i_o(t) = S(1-e^{-t/\tau_d})$$

and

$$\frac{\Delta i_o}{\Delta t} = \frac{S}{\tau_d}\, e^{-t/\tau_d}$$

As shown in Figure 5-26 the time jitter on the threshold crossing is computed by dividing the noise current by the slope:

$$\Delta t_n = N\,\frac{\Delta t}{\Delta i_o}$$

And this jitter may be converted to angular noise by multiplying by the angular horizontal scan rate, $\dot{\theta}$:

$$\dot{\theta} = \frac{15 \text{ deg}}{8/1000} = 1880 \text{ deg/sec}$$

so that

$$\Delta\theta_n = \dot{\theta} N \frac{\tau_d}{S} e^{t/\tau_d}$$

$$\Delta\theta_n = \dot{\theta}(S/N)^{-1} \tau_d e^{t/\tau_d}$$

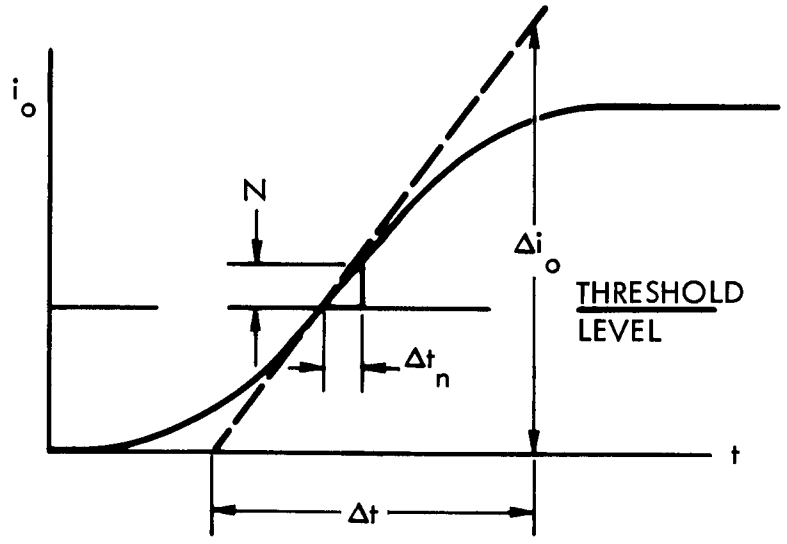

Figure 5-26. Planet Edge Signal Slope and Noise Level

Considering t as the time of threshold, it can be seen that the noise error can be minimized by setting the threshold level at the minimum value tolerable from a false alarm standpoint. Assuming a gaussian distribution of noise amplitude in the ratio of 5.25 to 1 between threshold level and rms noise will reduce false crossings to a mean rate of one per 10 data frames. From the computed peak signal-to-noise ratio of 18.5 and the above expression for the filtered signal, it is found that:

$$t_{threshold} = 0.386 \tau_d$$

$$t_{threshold} = 7.7 \times 10^{-6} \text{ sec}$$

and

$$\Delta\theta_n = \dot{\theta}(S/N)^{-1}\ \tau_d\ e^{t/\tau_d}$$

$$= (1880)(18.5)^{-1}(1.85 \times 10^{-5})\ (1.47)$$

$$\Delta\theta_n = 2.75 \times 10^{-3}\ \text{deg}$$

or

$$\Delta\theta_n = 10.0\ \text{arc sec}$$

The figure is only approximate in that a detailed sensor design was not carried out and all frequency response factors were not considered in conversion to noise equivalent angle. Table 5-XI summarizes the effect of the computed angular noise of the planet centroid and radius determination (refer to Figure 5-26).

Table 5-XI. Summary of Planet Approach Sensor Noise Error in Determination of Centroid and Radius by "3 Point" and Least Squares Estimates (LSE) Methods

Planet Disk Size (deg)	3-Point Method Error, 3σ			LSE Error, 3σ		
	x_c arc-sec	y_c arc-sec	radius percent	x_c arc-sec	y_c arc-sec	radius percent
0.15	120	28	32	102	35	32
0.375	87	31	8	74	22	8
0.75	75	32	5	46	13	3
1.5	67	27	2.5	24	9	1.5

Error Due to Image Tube Distortion. The second type of error source mentioned at the beginning of the section is image tube distortion. The assumption of an ideal rectangular raster scan of the field-of-view depends upon a linear relationship between deflection voltage and displacement of the scanning beam on the tube face. In practice the curve expressing this relationship tends to have a slight "S" shape with the maximum

deviation from linearity being in the order of 1 percent for current devices, projected to 0.1 percent for deflection systems under development. The effect of this factor may be eliminated by measuring the distortion error as a function of raster coordinates and making corrections in the computer prior to computation of planet centroid and radius. This procedure will eliminate distortion error to the extent that distortion is independent of thermal aging effects and measurable.

Error Due to Nonuniformities in Photosurface Response and Planet Brightness. The third source of error for the approach guidance sensor is the nonuniformity of the photosensitive surface and planet brightness. If the planet edge is sensed by a fixed threshold on the video output signal as previously postulated, angular error will be introduced by deviation of the photocurrent above or below the expected level due to variations in the surface sensitivity and illumination. This error source may be greatly reduced by incorporating a proportional threshold with the threshold level for a given scan line controlled by a sample of the planet signal from the previous line.

Error Due to Spacecraft Limit Cycle Motion. The motion of the spacecraft attitude during the approach phase will cause motion of the planet image on the photocathode during the scan. The computed centroid of the planet will tend to reflect the average planet position during the scan which is the desired information. The planet radius measurement, however, will be in error due to this motion. The magnitude of this attitude drift rate is assumed to be 10-arc sec/sec which is the peak value predicted in the TRW Voyager spacecraft study. The time required to scan the planet disc is maximum when the planet subtends 2.5 deg. Under these conditions an image motion of 13 arc sec will occur during the scan. Under the postulated data processing conditions a good average measure of the radius error is one-half this value, or 6.5 arc sec.

Error Due to Alignment. The initial alignment of the sensor reference axis to the spacecraft is limited to a finite accuracy, constrained in principle only by the degree of patience taken to average noise errors and compensate for all known sources of bias. In practice this accuracy is also limited by the quality and sophistication of the optical planet simulator and angle measurement equipment used. It is reasonable to expect that

this source of error can be limited to slightly in excess of the noise angular error in the centroid location at the maximum planet disk size or approximately 15 arc sec.

Error Due to Thermal Stress and Component Aging. The effect of thermal stress and component aging upon the stability of the sensor axis alignment over the mission period is quite significant when an overall accuracy in the order of one arc min is desired. The following design steps must be taken if the bias drift is to be kept below one arc min.

1) Careful design of the power supply to eliminate output voltage drift;

2) Selection of components for all critical circuits which are resistant to value drift with temperature and age;

3) Design of a mounting structure which is mechanically very stable with time and serves as an integral mounting structure housing for the entire optical sensor system package.

REFERENCES FOR SECTION 5

5-1 "Standardized Space Guidance System, Final Report for Phase 1a," TRW Space Technology Laboratories Report, SSD-TDR-64-132, Vol. III, dated 29 May 1964.

5-2 Sochely A. H., and E. W. Peterson, "The Surveyor Canopus Sensor," Proceedings of the Infrared Information Symposium, Vol. 8, No. 3, Santa Barbara Research Corporation, Goleta, California, August 1963, pp 5 through 9.

5-3 Burkic, J. W., "Radiometric Model of Mars," TRW Memo No. 9354.3-427, 21 June 1965.

5-4 Schnapf A., "The TIROS Wheel Satellite," RCA Review Vol. XXVII, No. 1, March 1966, pp 3 through 40.

5-5 Hales, K. A., "The Deterministic Error in Earth Sensor Readings Caused by the Earth's Oblateness," TRW IOC 66.7231.8-71, 3 August 1966.

5-6 Duncan, J., W. Wolfe, G. Oppel, and J. Burn, "Infrared Horizon Sensors," published by the Institute of Science and Technology, University of Michigan, April 1965.

5-7 McArthur, W. G., "Horizon Sensor Navigation Errors Resulting from Statistical Variations in the CO_2 14-16 Micron Radiation Band," Transactions of the 9th Symposium on Ballistic Missile and Space Technology, Vol. 1, August 1964.

5-8 Wark, D. Q., J. Alishouse, and G. Yamamoto, "Calculations of the Earth's Spectral Radiance for Large Zenith Angles," Weather Bureau Meteorological Satellite Laboratory Report No. 21, October 1963.

5-9 H. P. Westimar, Editor, Reference Data for Radio Engineers, International Telephone and Telegraph Corporation, New York, Fourth Edition, 1961, p 421.

5-10 Allen, C. W., Astrophysical Quantities, University of London The Athlone Press, 1963.

6. RADIO GUIDANCE

6.1 INTRODUCTION AND SUMMARY

One objective of the Radio/Optical/Strapdown Inertial Guidance Study is to study the role of radio command in the guidance of unmanned launch vehicles employing the advanced kick stage design. The approach to this portion of the study has been to:

1) Identify (by mission phase) where radio guidance can be most usefully employed for the four mission categories discussed in Section 2

2) Identify limitations and constraints on the vehicle and mission profile (trajectory and sequence of operations)

3) Identify candidate radio guidance systems

4) Develop error models for the candidate systems and analyze their performance capabilities for selected mission phases.

On the basis of these results, use of the radio tracking instrument and its interface with the onboard guidance system is recommended.

6.1.1 Assumptions and Ground Rules

The following assumptions have been made and ground rules established for conducting this study:

1) Only existing NASA and DOD radio tracking systems are considered; i.e., no new systems are postulated nor has relocation of existing equipment been considered. The tracking systems considered are those shown in Table 6-I. These systems are described in Subsection 6.2.

2) Those tracking systems that cannot be used for near real-time trajectory or orbit determination without major additions of equipment such as ground links, ground computational facilities, ground/vehicle data links, etc., are not considered. Generally, this eliminates the range instrumentation systems such as MISTRAM,† AZUSA, UDOP, GLOTRAC, etc.

† MISTRAM has limited real time capability. (It is used for range safety.) It's uncertain future makes it questionable for this application.

Table 6-I. Radio Tracking Systems Considered in Study

System	Location
DOD Systems • GE Mod III • BTL	Eastern and Western Test Ranges (Cape Kennedy and Vandenberg AFB)
NASA Systems • STADAN • C-band Radars† • Unified S-band System (USBS) • DSIF	World-wide deployment. See Tables 6-IV and 6-V for station locations.

† DOD C-Band trackers are also considered

6.1.2 Conclusions

The following general conclusions result from this study:

1) Use of the C-band radars is limited to low earth-orbit tracking only. Station locations, coverage, data communication constraints, and system accuracy limitations are such as to eliminate these systems from consideration as useful radio guidance systems for the missions considered. However, tracking and orbit determination of spacecraft in low-altitude earth-parking orbits are possible to reasonable accuracies (as were done on the Gemini program).

2) The GE Mod III and BTL radio/inertial systems may be used for accurate guidance during the launch-phase from both ETR and WTR. These systems are currently in use for Atlas/Agena and Thor/Delta launches. A limitation is reached when the elevation angle of the vehicle as seen from the radar site drops below 5 deg. This condition is reached prior to orbit insertion for most vehicles employing upper stages such as Centaur, Agena, and Delta (final stage). Nevertheless, it is possible to use these systems to guide the lower stages of certain multistage vehicles and "turn over" the guidance to the onboard systems at the appropriate time during the mission.

3) The use of the NASA STADAN net is useful for long-term tracking of spacecraft in earth orbit. Its use is suggested for the synchronous earth orbit mission (after final orbit insertion) for long-term orbit determination and station-keeping. The vehicle equipment required is normally associated with the mission payload and not considered to be part of the launch vehicle guidance.

4) The NASA Unified S-band and DSIF nets provide excellent coverage and orbit determination capabilities for the lunar and interplanetary missions. These systems require extensive ground communications and computational facilities. The USBS is generally limited to near-earth and lunar missions. The DSIF net extends this capability to interplanetary distances.

5) The use of the DSIF for tracking and orbit determination is virtually a necessity for the interplanetary missions. Although completely autonomous onboard optical/inertial systems may be conceived for these missions the required performance is considerably beyond the present state-of-the-art for most missions. An accurate onboard system is required, in any case, for controlling accurately powered maneuvers such as midcourse corrections and orbit insertion maneuvers.

6.2 RADIO GUIDANCE SYSTEM CONCEPTS AND TRADEOFFS

The methods of implementing radio command guidance which were considered in this study are:

1) A ground-based computer, receiving information from a radar or radar net during powered flight, computes engine on-off commands and transmits turning rate commands to an onboard attitude control system.

   An example of this type of system is the radio-guided Atlas (GE Mod III System). It requires a minimum of onboard inertial equipment but is satisfactory only for near-earth operations because of transit time delays. It also has the disadvantage of constraining the maneuver times because of incomplete coverage. A second example of such a system is the BTL radio/inertial system used for Thor/Delta and other vehicles. In both systems a radar is used to track during powered flight, and a filter is used to estimate the position, velocity, and acceleration components. Because the acceleration components are estimated by the filter, only a minimum of inertial equipment (an autopilot) is required. The system errors are the result of an optimum weighting between the radar noise and the vehicle uncertainties (thrust, I_{sp}, mass) and autopilot gyro drifts.

2) A ground-based computer, receiving information from a radar net during free flight, computes the time of initiation, direction, and magnitude of a desired velocity increment. The required onboard equipment includes a sequencer to start and control the burn, an attitude reference system including optical alignment devices, and an integrating accelerometer. This type of system was used for the Ranger/Mariner midcourse corrections. It is satisfactory mainly for small burns.

   The errors in this type of system occur in determining the desired velocity increment and in the execution of the burn. The errors in determining the desired velocity increment occur as the result of errors introduced during free flight tracking by radar noise and biases. Execution errors are the result of inertial and optical instrument errors and vehicle dispersions. The vehicle dispersions cause errors in three ways:

   a) Engine misalignments and center of gravity offsets introduce directional errors. It is possible to use three accelerometers to sense and correct these errors.

   b) Thrust, weight, and I_{sp} dispersions cause the burnout position to deviate from nominal. Without onboard computing capability, the velocity increment cannot be modified to compensate for these errors.

   c) Thrust tailoff impulse dispersions cannot be corrected for by guidance unless vernier engines are provided.

3) Ground tracking during free flight provides a position and velocity estimate which is used to update a complete inertial guidance system on board the spacecraft. The Apollo mission will utilize guidance of this type.

   The errors in this system are caused by radar noise and biases during free flight tracking and inertial and optical instrument errors as well as thrust tailoff impulse.

4) Inertial guidance without radio aid. Although this type of guidance is conceivable for a synchronous satellite mission, it is totally unfeasible for a lunar or interplanetary mission unless some sort of terminal navigation sensor is used. Depending on the mission requirements, this may be beyond the current state-of-the-art.

The candidate radio/inertial systems considered in this study are shown in Table 6-II and include systems of all four types. The radio tracking portions of these candidate systems are described in Subsection 6.3, and performance models are given in Subsection 6.4. Limitations, constraints, and performance capabilities are discussed in Subsection 6.5.

6.3 DESCRIPTIONS OF CANDIDATE TRACKING SYSTEMS

6.3.1 BTL Radio/Inertial Guidance System

This is the Radio/Inertial Guidance System developed by the Bell Telephone Laboratories for Titan I. Vehicle position (range, elevation, and azimuth) is continuously determined by a precise, ground-based, single-antenna, automatic tracking radar. A high-level radar transponded pulse is returned by a vehicle-borne transmitter in response to each ground radar pulse group. A ground-based digital data processing unit accepts the position data in suitable form and derives vehicle velocity (in both range and crosswise directions) by noting the change in position as a function of time. The vehicle position and velocity data so obtained are compared automatically with calculated values representing the desired trajectory, and steering orders are derived. Coded steering commands are communicated to the vehicle over the radar beam. Thrust cutoff commands are sent to the vehicle when the ground-based computer determines that necessary conditions for the desired free-flight trajectory have been met.

The performance of the system depends critically upon accurate determination of velocity in order to permit thrust cutoff at the appropriate velocity. The techniques used in this system include "smoothing" of radar data and inertial "updating." The smoothing techniques, in effect, filter out the high-frequency pulse-to-pulse radar jitter while retaining the more slowly changing characteristics of the desired data. This smoothing operation results in some delay in the computed velocity. That is to say, the value of smoothed velocity at any instant is that which the missile experienced several seconds earlier in its flight.

Table 6-II. Candidate Systems — Radio/Inertial Guidance System Combinations

Type	Ground Based System	Vehicle Subsystems	Tracking System	Limitations
1	Tracking radar computer, data link to vehicle Cutoff and steering commands generated in ground computer on the basis of tracking information and transmitted to vehicle	Transponder/decoder Autopilot Gyros torqued by turning rate commands	GE-Mod III (Atlas) BTL (Titan I, Thor, Thor, Delta)	Existing systems limited to launch guidance only Minimum elevation angle 5 deg
2	Tracking radar(s), ground communication net, computer, data link to vehicle	Partial inertial system (e.g., Ranger/Mariner) • Attitude reference (optically aided) • Single accelerometer	C-band radars	• USBS limited to near earth and lunar missions • Appreciable time required for gathering data and computing trajectory
3	Tracking data used to compute orbit. Orbital data transmitted to vehicle over data link	Complete inertial system • Attitude reference (optically aided) • 3-axis IRU • Computer	S-band radars (USBS) DSIF	• C-band systems limited to low altitude earth coverage limited
4		Complete inertial system (IRU and computer) with optical aids (as required)	None	Adequate for synchronous orbit injection, lunar/planetary orbit injection

This delayed velocity information is updated by the addition of a velocity increment based upon the inertial properties of the vehicle and the propulsion and control subsystems. The velocity increment is derived from the computer's estimate of vehicle acceleration acting over the known period of time delay occasioned by the smoothing operation. The accuracy of velocity determination is enhanced by the choice of an optimum smoothing time. This choice is determined by two factors, radar jitter and the inertial characteristics of the vehicle. The effect of radar jitter diminishes with increased smoothing time as a result of averaging the position measurements over a longer time interval. In contrast, uncertainties in the inertial characteristics of the missile, such as autopilot gyro drift and thrust variations, increase the velocity updating error as smoothing time is increased. There is, then, a smoothing interval for which the two sources of error contribute equally, and intervals shorter or longer than this "optimum" correspond to greater error.

The combined use of smoothed radar position data and inertial updating of velocity is an essential element in the guidance accuracy that has been achieved. The method has led to the term "radio-inertial" guidance.

The functions of vehicle position measurement and command signaling are accomplished by the system radar. The antenna consists of a 4-ft parabolic dish with a Cassegrain subreflector and multimode feed in a two-axis (elevation and azimuth) mount. Digital code wheels are fixed directly on the two-axis mount for elevation and azimuth angle readouts. The radar is based on generally conventional monopulse principles. Operation is at X-band.

6.3.2 GE Mod III Radio/Inertial Guidance System

The GE Mod III radio/inertial guidance system is used to guide the Atlas missile on both weapon system and space missions. It is composed of position pulse tracking and CW interferometer rate subsystems plus a fairly large digital computer (manufactured by the Burroughs Corporation). The major difference between this system and the BTL system is in the addition of the interferometer rate measuring system. The rate data is used to determine vehicle velocity to a high degree of accuracy without the elaborate smoothing and updating techniques required by the

BTL system. For most missions, the GE system is inherently more accurate and less susceptible to atmospheric disturbances and vehicle perturbations (propulsion, weight, etc.) than is the BTL system.

The system operates at X-band. The airborne units consist of pulse and rate subsystem beacons, a decoder, and antennas. The decoder can provide pitch and yaw attitude rate commands to the vehicle control system as well as number of discrete signals.

Table 6-III gives the weight and power characteristics of the airborne portions of the two guidance systems previously described. These data, especially the weights data, should be taken with a good deal of caution before attempting to draw any system conclusions. The weights shown are only for the airborne guidance equipment and do not take into account any structural weight necessary to mount the units or vehicle modifications required for interface compatibility. There are other less obvious items, such as weight penalties due to trajectory shaping constraints, injection altitude increase required for maintaining adequate elevation angles (greater than 5 deg) and acceptable vehicle antenna look angles.

Table 6-III. Vehicle Borne Equipment Data

	GE	BTL
Model	III-G	Series 600
Weight (kg)	25	20.5
Power (w)	180	25

6.3.3 The NASA STADAN System

Space Tracking and Data Acquisition Network (STADAN) is a complete spacecraft tracking system designed to handle long term tracking and data acquisition simultaneously for a number of unmanned spacecraft in earth orbit, and for probes extending as far out as the moon. The system consists essentially of the Minitrack network, first used on the Vanguard program, supplemented by range and range-rate measurement equipment at selected stations, a ground communications system, and computational

facilities. The network is under operational control of Goddard Space Flight Center. A detailed description of the STADAN system is given in Ref 6-1.

The following description of the tracking systems is quoted from Ref 6-2:

> "Minitrack uses radio interferometers which measure two of the three direction cosines of a line from the system center to a transmitting satellite, as a function of time, while the satellite passes through the beam pattern of the receiving antennas. The reference lines for these measurements are orthogonal in the plane of the ground antennas. The third direction cosine is thus implicitly defined, and the angular position of the satellite is determined. From a series of independent angle measurements made at various ground stations, satellite orbits can be determined to a great accuracy by computer methods.
>
> "Minitrack performs its angular position measurements by phase comparison techniques to measure the difference in arrival time of the wavefront from a satellite source at each antenna of a pair of antennas separated by known distances in wavelengths. Measurement of this radio path difference is accomplished by a comparison of the phase angle of the signal received at one antenna to that received at another. Antenna pairs are aligned along east-west and north-south baselines to form a convenient coordinate system.
>
> "Since the accuracy of the measurement of the angles increases, two pairs of antennas are aligned along orthogonal baselines many wavelengths long to obtain good angular resolution. As a radio source travels through the antenna pattern, the relative phase will cycle from zero to 360 electrical degrees for each wavelength added to the radio path difference. Because the phase meters repeat their readings every wavelength, a number of different space angles produce identical phase readings during a satellite transit. This ambiguity is resolved by employing several progressively shorter baselines which produce fewer integral numbers of wavelength changes while the satellite moves through the antenna beam.
>
> "While the Minitrack system functions extremely well with conventional earth satellite orbits, spacecraft with highly eccentric orbits do not lend themselves well to tracking by an angle-measuring system. An eccentric orbit can mean an orbital period of many hours. Such relatively slow angular motion at or near apogee, effectively degrades the precision of the basic angular measurements by radio interferometers. Satellite orbital parameters must be determined as rapidly as possible in order to extract maximum usable data from the

spacecraft. Range and range-rate systems can provide more direct and meaningful measurements than space angle measurements when working with highly elliptical orbits. Accordingly, a range and range-rate measurement system has been developed and is operational. The range and range-rate system functions as a high precision spacecraft tracking system capable of accurately determining the range and radial velocity of a spacecraft from near earth orbits out to cislunar distances.

"Each range and range-rate station employs two distinct systems: an S-band system and a VHF system. For use with the S-band system, a three-channel ranging transponder is installed in the spacecraft. This permits tracking computations from data supplied by a single ranging station, or computations from data supplied simultaneously by a complex of two or three stations. The VHF system is used primarily for acquisition, but is also used for ranging when the spacecraft cannot carry the S-band, three-channel transponder. In this case, a VHF transponder is used which functions as a command receiver, telemetry transmitter, and a single-channel ranging transponder. Thus the tracking configuration may be either that of a single range and range-rate station operating simultaneously.

"Each ranging station can measure spacecraft range with a resolution of ±15 meters, and range rate with a resolution of 0.1 meter per sec."

6.3.4 C-Band and S-Band (USBS) Tracking Systems

The C-band and S-band (USBS) tracking stations are intended for tracking manned and unmanned spacecraft in earth orbit. The S-band systems may be used out to cislunar distances and beyond. The descriptions of these systems given below are extracted from Ref 6-2.

6.3.4.1 Station Locations

The station locations and the site status are given in Table 6-IV.

6.3.4.2 C-Band Radars

The C-band radars measure range, azimuth, and elevation. All radars use azimuth-elevation antenna mounts.

Table 6-IV. Station Locations and Site Status C- and S-Band Trackers

Call Letters	Station	Site	Site Status	Operational Date	Geodetic Coordinates			Geocentric Rectangular Coordinates		
					Latitude	Longitude	Height above ellipsoid(m)	U(m)	V(m)	W(m)
CNV	Cape Kennedy	FPS-16	Operational	Now	28°28'54.36"±1.0"	- 80°34'35.45"±1.2"	14 ±40	918 608±32	-5 534 781±38	3 023 564±34
MLA	Merritt Island	TPQ-18	Operational	Now	28°25'29.5"±1.0"	- 80°39'51.9"±1.2"	12 ± 40	910 604±32	-5 539 146±38	3 018 018±34
MIL		USBS 30' MSFN	Test Phase	Feb 1967	28°30'29.78"±1.0"	- 80°41'36.3"±1.2"	10 ± 40	907 086±32	-5 535 257±38	3 026 143±34
PAFB	Patrick Air Force Base	FPQ-6	Operational	Now	28°13'35.59"±1.0"	- 80°35'57.45"±1.2"	15 ± 40	918 602±32	-5 548 399±38	2 998 673±34
GBI	Grand Bahama Island	TPQ-18	Operational	Now	26°38'10.86"±1.0"	- 78°16'03.8"±1.2"	12 ± 41	1 160 070±32	-5 585 912±39	2 842 277±34
GBM		USBS 30' MSFN	Planned	Sept 1967	26°37'58.29"1.0"	- 78°14'15.59"±1.2	5 ± 41	1 163 032.7±32	-5 585 466.3±39	2 841 928.2±34
SSI	San Salvador Island	FPS-16	Operational	Now	24°07'07.77"±1.0"	- 74°30'14.89"±1.2"	5 ± 42	1 556 154±33	-5 612 886±40	2 590 317±34
GTI	Grand Turk Island	TPQ-18	Operational	Now	21°27'46.40"±1.0"	- 71°07'55.61"±1.2"	28 ± 42	1 920 453±33	-5 619 460±40	2 319 190±34
ANT	Antigua Island	FPQ-6	Operational	Now	17°08'38.51"±1.1"	- 61°47'34.29"±1.2"	58 ± 42	2 881 618±35	-5 372 588±40	1 868 098±34
ANG		USBS 30' MSFN	Planned	Feb 1968	17°01'14"±1.1"(1)	- 61°44'58"±1.2"(1)	28 ± 42	2 887 573±35	-5 373 920±40	1 855 014±34
BDA	Bermuda	FPS-16	Operational	Now	32°20'53.17"±1.2"	- 64°39'13.68"±1.4"	18 ± 43	2 308 904±39	-4 874 347±41	3 393 132±39
		FPQ-6	Test Phase	Oct 1966	32°20'52.67"±1.2"	- 64°39'13.47"±1.4"	19 ± 43	2 308 912±39	-4 874 354±41	3 393 120±39
		USBS 30' MSFN	Test Phase	Dec 1966	32°21'04.63"±1.2"	- 64°39'29.45"±1.4"	21 ± 43	2 308 451±34	-4 874 356±41	3 393 432±39
CYI	Grand Canary Island	MPS-26	Operational	Now	27°44'41.5"±4.6"	- 15°36'07.2"±5.1"	36 ± 32	5 440 847±77	-1 519 317±138	2 951 544±127
		USBS 30' MSFN	Planned	Jan 1968	27°44'24"±4.6"	- 15°36'11"±5.1"	40 ± 32	5 441 070±77	-1 519 482±138	2 951 062±127
ASC	Ascension Island	TPQ-18	Operational	Now	-07°58'21.94"±3.4"	- 14°24'06.10"±3.5"	143 ± 32	6 118 555±43	-1 571 172±103	- 878 821±105
ACN		USBS 30' MSFN (Dual)	Test Phase	May 1967	-07°57'18.20"±3.4"	- 14°19'39.28"±3.5"	562 ± 32	6 121 247±43	-1 563 425±103	- 876 940±105
PRE	Pretoria, South Africa	MPS-25	Considered	Now	-25°56'37.44"±1.4"	28°21'30.56"±1.5"	1626 ± 43	5 051 635±43	-2 726 681±43	-2 774 184±43
CRO	Carnarvon, Australia	FPQ-6	Operational	Now	-24°53'50.65"±1.9"	113°42'57.88"±2.2"	62 ± 66	-2 328 319±60	5 300 017±64	-2 668 811±60
		USBS 30' MSFN (Dual)	Test Phase	Dec 1966	-24°54'27.33"±1.9'	113°43'27.29"±2.2"	58 ± 66	-2 328 882±60	5 299 247±64	-2 669 833±60
GWM	Guam	USBS 30' MSFN (Dual)	Test Phase	Dec 1966	13°18'33.28"±6.4"	144°44'03.89"±6.6"	127 ± 32	-5 068 804±125	3 584 345±163	1 458 757±193
HAW	Hawaii	FPS-16	Operational	Now	22°07'30.96"±1.4"	159°40'03.43"±1.6"	1142 ± 43	-5 543 977±53	-2 054 341±74	2 387 711±73
		USBS 30' MSFN (Dual)	Test Phase	Feb 1967	22°07'41.06"±1.4"	-159°40'02.02"±1.6"	1137 ± 43	-5 543 848±53	-2 054 337±74	2 387 997±73
CAL	Pt. Arguello, California	FPS-16	Operational	Now	34°34'53.45"±1.0"	-120°33'40.14"±1.2"	646 ± 40	-2 673 158±33	-4 527 065±36	3 600 253±34
GYM	Guaymas, Mexico	USBS 30'	Test Phase	Feb 1967	27°57'47.54"±1.0"	-110°43'15.06"±1.2"	19 ± 41	-1 994 696±32	-5 273 004±38	2 972 930±33
WHS	White Sands, Nex Mexico	FPS-16	Operational	Now	32°21'29.60"±1.0"	-106°22'10.43"±1.2"	1232 ± 40	-1 520 192±31	-5 175 317±37	3 394 730±33
TEX	Corpus Christi, Texas	USBS 30' MSFN (Dual)	Test Phase	Mar 1967	27°39'13.50"±1.0"	- 97°22'42.49"±1.1"	10 ± 40	- 726 061±30	-5 606 849±38	2 942 592±32
EGL	Eglin Air Force Base	FPS-16	Operational	Now	30°25'18.36"±1.0"	- 86°47'53.21"±1.2"	28 ± 40	307 465±31	-5 496 185±38	3 210 810±33
MAD	Madrid, Spain	USBS 85' MSFN (Dual)	Test Phase	Sept 1967	40°27'19.29"(2)	- 4°10'2.62"(2)	825	4 847 850	- 353 231	4 117 146
RID		USBS 85' DSIF (Dual)	Test Phase	Dec 1967						
BRA	Canberra, Australia	USBS 85' MSFN (Dual)	Test Phase	July 1967	-35°35'50.0"±1.9"	148°58'45.0"±2.2"	1097 ± 66	-4 450 343±63	2 676 239±60	-3 692 602±61
NBE		USBS 85' DSIF (Dual)	Planned	Oct 1967						
GDS	Goldstone, California	USBS 85' MSFN (Dual)	Test Phase	July 1967	35°20'30.10"±1.1"	-116°52'23.84"±1.2"	965 ± 40	-2 354 748±34	-4 646 829±37	3 669 433±35
GLD		USBS 85' DSIF (Dual)	Test Phase	July 1967	35°23'22.81"±1.1"	-116°50'56.62±1.2"	1029 ± 40	-2 351 415±34	-4 645 122±37	3 673 811±35

(1) Approximate
(2) Uncertainties not available
See also ref. 36.

Dual indicates a common antenna and two receivers and transmitters Geogetic coordinates referenced to the Fischer Ellipsoid of 1960. The Geocentric Rectangular Coordinate system consists of a u-axis at the intersection of the earth's equitorial plane with the Greenwich meridian, a v-axis along the earth's rotational axis, and a w-axis such to complete a right-handed coordinate system.

Table 6-IV presents the range performance when the radars are operating in conjunction with the 0.5-kw and 2.5-kw beacons. Three range limits are given:

a) The maximum range for the tracking accuracy listed in the table

b) The maximum range for acquisition and tracking with degraded accuracy

c) The maximum unambiguous range.†

6.3.4.3 Unified S-Band System (USBS) Radars

The USBS tracking radars measure range, range rate, and two angles. The stations are equipped with either 85-ft or 30-ft antennas. There are always two 85-ft stations located close together; one is a MSFN, and the other is a DSIF station. The 85-ft antennas have dual capability. Two receivers and transmitters are connected to each antenna. The transmitters operate on different frequencies so that one 85-ft antenna can track (and communicate with) two spacecraft simultaneously, provided both craft are within the antenna beam. Accurate angle data are obtained only for the spacecraft onto which the antenna is locked. Some of the 30-ft antennas also have dual capability.

6.3.4.4 Range-Rate Measurements

The S-band tracking systems are capable of precision range-rate ($\dot{r}$) measurements by measuring a change in range Δ_r during finite time interval T.

$$\dot{r} = \frac{\Delta r}{T}$$

The change in range Δr during the time interval T is measured by counting doppler cycles plus the cycles of a superimposed bias frequency. Two counting methods are available.

† This range is not a fundamental limitation. It may be changed by adjusting the radar pulse rate. Range ambiguities may also be easily detected and resolved in data processing.

1) Destructive N Count: The time is measured for a predetermined and constant number of doppler plus bias cycles. Due to the superimposed bias frequency, the measured time (integration time) is approximately 0.8 sec and varies only slightly with the doppler frequency. For this method no continuous doppler count is obtained over a longer time period than 0.8 sec, and the quantization errors are negligible. The highest sampling rate with 0.8-sec integration time is 1 measurement per sec. The destructive N-count can also be used with 0.8 sec integration time, yielding a highest sampling rate of 10 measurements per sec.

2) Nondestructive T Count: Doppler plus bias cycles are counted continuously, and the counter is read out at constant time intervals T without destroying the information in the counter. The doppler counter may be read out one or ten times per sec. As the readout is nondestructive, lower sampling rates are obtained by discarding intermediate readouts. The counter can count 35 binary digits before overflowing. This gives a total count time of 9 to 10 hrs before overflow. The exact value depends on the range rate. The 35 binary digits remain correct during overflow so that the only effect of overflow is an ambiguity. Both the low- and the high-speed data formats have the capability to transmit the 35 binary range rate digits.

   For this method, a continuous doppler count over longer time periods is obtained, and the quantization errors are not negligible and are negatively correlated.

6.3.4.5 Two- and Three-Way Doppler

Two basic modes of operation are available, the two-way and the three-way mode (Figure 6-1). In the two-way mode, one station both transmits and receives the signal. The received signal is compared with the same oscillator that generated the transmitted signal.

In the three-way mode, only the primary station transmits the signal, and the secondary station receives the signal. The received signal is compared to a different oscillator than the one which was used for generation of the signal. A frequency difference between the two oscillators shows up a bias in the three-way doppler.

The two-way doppler count is proportional to $2\dot{r}_1$, and the three-way doppler is proportional to $(\dot{r}_1 + \dot{r}_2)$. Three-way doppler may be obtained from more than one secondary station simultaneously. A primary station can simultaneously obtain two-way doppler.

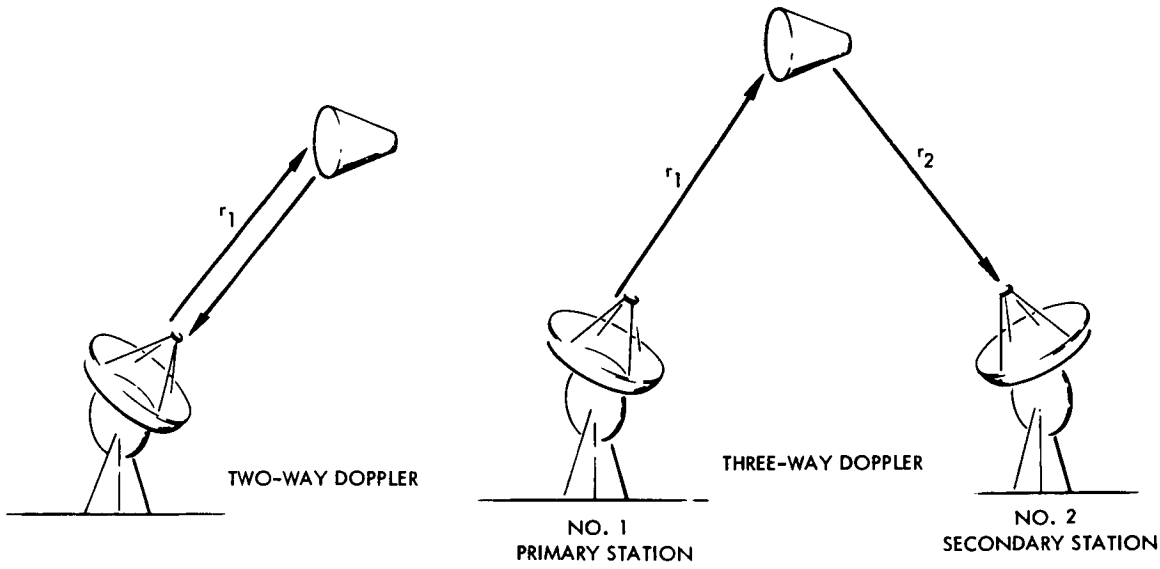

Figure 6-1. Two-Way and Three-Way Doppler

6.3.5 Description of the DSIF Networks

Ref 6-5 and 6-6 contain a detailed description of the DSIF tracking system and the associated ground communication network and other facilities. The following summary description is extracted from Ref 6-6. The DSIF is a precision tracking and communications system capable of communicating with a spacecraft via command and telemetry for control and data acquisition purposes, respectively, and of tracking a spacecraft in angle, doppler, and range for orbit determination purposes.

The DSIF, at present, comprises two complete tracking networks of three 85-ft-diameter antenna aperture configurations each. These stations are located at approximately 120 deg intervals in longitude and between 40°N and 40°S latitude. There are two tracking stations for each latitude. There are several other single DSIF stations for special support purposes which include the Spacecraft Monitoring Station at Cape Kennedy, the Spacecraft Command Station on Ascension Island, and the R and D stations at Goldstone. Two basic networks provide continuous surveillance for spacecraft above nominally 18,000 km altitude. Tracking periods per station are from 8 to 12 hrs depending on overlap coverage.

A third tracking network comprised of three 210-ft diameter alt-azimuth supported antenna reflectors is planned for in 1971. The present plan is to situate two antennas overseas at the Madrid and Canberra

Table 6-V. DSIF Station Locations[a]

Location	Antenna diameter, ft	Station identification number	Geodetic latitude	Geodetic longitude	Height above mean sea level, meters[b]	Geocentric latitude	Geocentric longitude	Geocentric radius, km
Goldstone, Calif. (Pioneer)	85	11	35.38950N	243.15175E	1037.5	35.20805N	243.15080E	6372.0639
Goldstone, Calif. (Echo)	85	12	35.29986N	243.19539E	989.5	35.11861N	243.19445E	6372.0449
Goldstone, Calif. (Mars [c,d])	210	13	35.24772N	243.20599E	1213.5	35.06662N	243.20505E	6372.2869
Goldstone, Calif. (Venus [e])	85	14	35.42528N	243.12222E	1160	35.24376N	243.12127E	6372.1594
Woomera, Australia	85	41	31.38314S	136.88614E	144.8	31.21236S	136.88614E	6372.5481
Canberra, Australia [c,d]	85	42	35.40111S	148.98027E	654	35.21962S	148.98027E	6371.6816
Johannesburg, S. Africa	85	51	25.88921S	27.68570E	1409.1	25.73876S	27.68558E	6375.5504
Madrid, Spain [c,d]	85	61	40.429 N	355.751 E	800	40.334 N	355.751 E	6374.37
Spacecraft monitoring, Cape Kennedy, Fla. [f]		71	28.48713N	279.42315E	4.0	28.32648N	279.42315E	6373.2874

[a]The parameters are referenced to the NASA Earth Model Spheroid with an equatorial radius of 6378.165 km and a flattening of 1/298.3.

[b]Measured to the point of intersection of the hour angle axis with the plane of the declination gear on polar mount antennas.

[c]Under construction with estimated completion as follows: Goldstone Mars, January 1966; Canberra, December 1964; Madrid, June 1965.

[d]Tentative location; definite location to be determined after antenna erection.

[e]This station is used normally for engineering and development; on special assignment it may be used in operations.

[f]Temporary location of present L-band station.

(Tidbinbilla) locations. The third 210-ft antenna located at Goldstone recently became operational. The location of all prime tracking stations and of support stations are shown in Table 6-V.

6.4 TRACKING SYSTEM ERROR MODELS

This subsection is concerned with the measurement accuracy of ground-based tracking systems used for determining the vehicle position and velocity. Ref 6-2 and 6-7 have been used as the major source of information. The errors quoted are considered conservative and are not to be construed as specifications.

In both the USBS and DSIF systems, the primary measurement of interest is a precision measurement of range rate between the spacecraft and the station. For near-earth and lunar missions ranging data are also available and in general will be used to improve the overall trajectory estimation.

6.4.1 Error Models for the GE-Mod III and BTL Radio/Inertial Systems

Error models for these systems are classified secret and are not given here. Detailed information may be found in Ref 6-8.

6.4.2 Error Models for the C- and S-Band (USBS) Tracking Systems

The significant error sources associated with ground-based tracking systems may be described by a statistical error model in which the errors are classified as bias or noise.

Bias Errors are errors which are essentially time invariant during the time of observation. Typical biases are station location, time tagging errors, and measurement biases.

Noise Errors are errors which vary appreciably during the time of observation and have an average value of zero. A typical source for gaussian distribution noise is the thermal noise in electronic systems. The quantization error[†] in the doppler cycle counter is nongaussian distributed noise In some cases the correlation between measurements is not negligible.

[†] Only whole cycles are counted which comprises the quantization error.

The error models for the C- and S-band (USBS) tracking systems are given in Tables 6-VI thru 6-XI, with the exception of station location, uncertainties in the velocity of light, and time tagging errors. Station location errors are given in Table 6-IV. Timing uncertainties in synchronization at a station to Universal Time Corrected (UTC)[†] are quoted (Ref 6-2) to be 5.4 msec. The uncertainty of synchronization between stations is 4.2 msec.

Since the range-rate data is of primary interest, the errors associated with measurement are discussed in detail below (taken from Ref 6-2).

Range Rate Uncertainties:[††] Three classes of noise contributing to range rate uncertainties are recognized: quantization noise, white phase noise, and random walk noise.

For the two-way doppler operating in the nondestructive T-count mode, the total one-sigma noise $\sigma(\dot{r}_1)$ for $\dot{r}_1$ is

$$\left[\sigma(\dot{r}_1)\right]^2 = \left(\frac{0.09}{T}\right)^2 + \left(\frac{0.08}{T}\right)^2 \quad (\text{ft/sec})^2$$

for land-based USBS trackers, where

$\left(\frac{0.09}{T}\right)^2$ = the term due to the quantization error. The correlation coefficient $\sigma = -0.5$ for adjacent measurements and $\rho = 0$ for nonadjacent measurements.

$\left(\frac{0.08}{T}\right)^2$ = the term due to random phase walk and white noise. The correlation coefficient $\rho = -0.5$ for adjacent measurements and $\rho = 0$ for nonadjacent measurements.

T = the count or integration time in seconds.

[†]Station clocks are synchronized by timing signals received from radio station WWV which broadcasts time signals derived from the United States Frequency Standard.

[††]Atmospheric refraction effects, although significant, are neglected in the following analysis.

Table 6-VI. C-Band Radar Tracking Accuracies and Limitations (from Ref 6-2)

Station	C-Band Radar Type	Angular Tracking Limits				Tracking Accuracies and Maximum Range								Maximum Range for Acquisition and Tracking At Degraded Accuracy		Maximum Unambiguous (nmi)
		Azimuth		Elevation		Azimuth		Elevation		Range		Maximum Range				
		Angle Limit (Ang deg)	Max. Angular Rate (Ang deg)	Angle Limit (Ang deg)	Max. Angular Rate (Ang deg)	Noise (mrad)	Bias (mrad)	Noise (mrad)	Bias (mrad)	Noise (ft)	Bias (ft)	(nmi) Note 1	(nmi) Note 2	(nmi) Note 1	(nmi) Note 2	
CNV	FPS-16	360	40	-10 to +190	30	0.2	0.4	0.2	0.4	30	60	2,600	1,200	13,000	5,800	1,000
MLA	TPQ-18	360	28	-2 to 85	28	0.2	0.4	0.2	0.4	30	60	16,000	7,200	80,000	36,000	32,000
PAT	FPQ-6	360	28	-2 to 85	28	0.15	0.3	0.15	0.3	20	40	16,000	7,200	80,000	36,000	32,000
GBI	FPS-16	360	40	-10 to 190	30	0.2	0.4	0.2	0.4	30	60					
SSI	FPS-16	360	40	-10 to 190	30	0.2	0.4	0.2	0.4	30	60	2,600	1,200	13,000	5,800	1,000
GTK	TPQ-18	360	28	-2 to 85	28	0.2	0.4	0.2	0.4	30	60	16,000	7,200	80,000	36,000	32,000
ANT	FPQ-6	360	28	-2 to 85	28	0.15	0.3	0.15	0.3	20	40	16,000	7,200	80,000	36,000	32,000
BDA	FPS-16	360	40	-10 to 190		0.2	0.4	0.2	0.4	30	60	6,000	2,700	30,000	13,000	32,000
	FPQ-6	360	28	-2 to 85	28	0.15	0.3	0.15	0.3	20	40					
CYI	MPS-26	360	56	-2 to 898	28	1.0	2.0	1.0	2.0	60	120	2,300	1,000	11,500	5,100	2,500
ASC	TPQ-18	360	28	-2 to 85	28	0.2	0.4	0.2	0.4	30	60	16,000	7,200	80,000	36,000	32,000
	FPS-16	360	40	-10 to 190	30	0.2	0.4	0.2	0.4	30	60					
PRE	MPS-25	360	40	-10 to 190	30	1.0	2.0	1.0	2.0	60	120	2,600	1,200	13,000	5,800	1,000
CRO	FPQ-6	360	28	-2 to 85	28	0.15	0.3	0.15	0.3	20	40	16,000	7,200	80,000	36,000	32,000
HAW	FPS-16	360	40	-10 to 190	30	0.2	0.4	0.2	0.4	30	60	2,600	1,200	13,000	5,800	32,000
CAL	FPS-16	360	40	-10 to 190	30	0.2	0.4	0.2	0.4	30	60	6,000	2,700	30,000	13,000	500
WHS	FPS-16	360	40	-10 to 190	30	0.2	0.4	0.2	0.4	30	60	6,000	2,700	30,000	13,000	1,000
EGL	FPS-16	360	40	-10 to 190	30	0.2	0.4	0.2	0.4	30	60	2,600	1,200	13,000	5,800	1,000

NOTE 1: Assumes 2.5 kw C-Band Beacon

NOTE 2: Assumes 0.5 kw C-Band Beacon

Table 6-VII. USBS Angle Tracking Accuracy (from Ref 6-2)

	Noise, 1σ (mrad)	Bias, 1σ (mrad)
Land-based X-Y mount	0.8	1.6

Table 6-VIII. USBS Range-Rate Measurement Accuracy (Two-Way Doppler, Nondestructive T Count)(from Ref 6-2)

Sampling Rate	Noise, 1σ					Bias, 1σ
	Quantization		White Noise and Random Phase Walk		Total Noise $\sigma(\dot{r}_1)$ $\sigma^2 = \sigma_q^2 + \sigma_w^2$ (ft/sec)	$\sigma(\dot{r}_1)$ (ft/sec)
	$\sigma_q(\dot{r}_1)$ (ft/sec)	Correlation	$\sigma_w(\dot{r}_1)$ (ft/sec)	Correlation		
1 per sec	0.09	-0.5	0.08	-0.5	0.12	0.03 This bias accounts for various model errors and must not be solved for.
1 per 6 sec	0.015	-0.5	0.013	-0.5	0.02	
1 per 60 sec	0.0015	-0.5	0.0013	-0.5	0.002	

Table 6-IX. USBS Range-Rate Measurement Accuracies (Two-Way Doppler, Destructive N Count)(from Ref 6-2)

Sampling Rate	Count Time (sec)	Noise, 1σ		Bias, 1σ
		$\sigma(\dot{r}_1)$ (ft/sec)	Correlation	$\sigma(\dot{r}_1)$ (ft/sec)
10 per sec and lower	0.08	1.0	0	0.03 This bias accounts for various model errors and must not be solved for.
1 per sec and lower	0.8	0.1	0	

Table 6-X. USBS Range-Rate Measurement Accuracy (Three-Way Doppler, Nondestructive T Count) (from Ref 6-2)

Sampling Rate	Noise, 1σ							Bias, 1σ
	Quantization		White Noise		Random Phase Walk		Total Noise $\sigma(\dot{r}_1 + \dot{r}_2)$ $\sigma^2 = \sigma_q^2 + \sigma_w^2 + \sigma_r^2$ (ft/sec)	$\sigma(\dot{r}_1 + \dot{r}_2)$ (ft/sec)
	$\sigma_q(\dot{r}_1 + \dot{r}_2)$ (ft/sec)	Correlation	$\sigma_w(\dot{r}_1 + \dot{r}_2)$ (ft/sec)	Correlation	$\sigma_r(\dot{r}_1 + \dot{r}_2)$ (ft/sec)	Correlation		
1 per sec	0.18	-0.5	0.13	-0.5	0.017	0	0.22	0.2 If the 3-way bias is solved for, the bias must not be reduced below 0.06 ft/sec.
1 per 6 sec	0.030	-0.5	0.022	-0.5	0.0069	0	0.038	
1 per 60 sec	0.0030	-0.5	0.0022	-0.5	0.0022	0	0.0042	

Table 6-XI. USBS Range Measurements (from Ref 6-2)

	Noise 1σ (ft)	Bias, 1σ (ft)
Measurement Accuracy	30	60
Tracking Range	Lunar distance with 30-ft or 85-ft ground antennas and high gain antennas on spacecraft and 20 w transmitted from spacecraft	

For the three-way doppler mode the one-sigma noise $\sigma(\dot{r}_1 + \dot{r}_2)$ for $(\dot{r}_1 + \dot{r}_2)$ is given by:

$$\left[\sigma(\dot{r}_1 + \dot{r}_2)\right]^2 = \left(\frac{0.18}{T}\right)^2 + \left(\frac{0.13}{T}\right)^2 + \frac{(0.017)^2}{T} \quad (\text{ft/sec})^2$$

$\left(\frac{0.18}{T}\right)^2$ = the term due to quantization. The correlation coefficient is $\rho = -0.5$ for adjacent measurements and $\rho = 0$ for nonadjacent measurements.

$\left(\frac{0.13}{T}\right)^2$ = is due to white noise. The correlation coefficient is $\rho = -0.5$ for adjacent measurements and $\rho = 0$ for nonadjacent measurements.

$\frac{(0.017)^2}{T}$ = the term due to random phase walk. The correlation coefficient for all measurements is $\rho = 0$.

T = is the count or integration time.

Destructive N Count: Quantization errors are negligible in this mode. "White" noise and random walk errors are the same as for non-destructive read out. Independent of sampling rate, the count time is approximately 0.08 or 0.8 sec. From the previous equations for the two-way doppler mode, we obtain:

$$\sigma(\dot{r}_1) = 0.10 \text{ ft/sec for } T = 0.8 \text{ sec}$$

$$\sigma(\dot{r}_1) = 1.0 \text{ ft/sec for } T = 0.08 \text{ sec}$$

and for the three-way mode

$$\sigma(\dot{r}_1 + \dot{r}_2) = 0.16 \text{ ft/sec for } T = 0.8 \text{ sec}$$

$$\sigma(\dot{r}_1 + \dot{r}_2) = 1.6 \text{ ft/sec for } T = 0.08 \text{ sec}$$

Because of the gap (approximately 0.2 sec for a sampling rate of 1 per sec) between measurements, the correlation coefficient for adjacent measurements is practically zero.

Bias Errors: A conservative upper bound for the bias in the two-way doppler mode is 0.03 ft/sec (1 cm/sec).

In the three-way doppler mode the dominating bias source is the frequency difference between the oscillators in the primary and secondary station. A conservative estimate of the relative difference in oscillator frequency is 2×10^{-10} and the bias in $(\dot{r}_1 + \dot{r}_2)$ is then 0.2 ft/sec (6 cm/sec).

6.4.3 Error Model for DSIF

Ref 6-7 gives the present and projected future (1970's) error models for DSIF. These errors are range-rate measurement errors shown in Table 6-XII for 2-way doppler tracking (nondestructive T-count).

Table 6-XII. DSIF Error Model
(from Ref 6-7)

	Range-Rate Measurement Errors	
	Present Mariner Mars	1970's
Guaranteed Accuracy at 1 AU	0.5 Hz (0.030 m/sec)	0.015 Hz 0.001 m/sec
Probably accuracy under same conditions	0.010 Hz 0.0006 m/sec	0.003 Hz 0.0002 m/sec

For purposes of the analyses discussed in Section 9, a conservative value intermediate between the guaranteed and probable accuracies for the 1970 time period has been selected (essentially equivalent to the present probable accuracy). In addition, a range-rate bias error is assumed, uncorrelated from station to station. These errors are shown in Table 6-XIII.

Table 6-XIII. DSIF Range-Rate Errors Assumed for Analysis Purposes

Error Source	RMS Error
Uncorrelated noise on doppler rate	0.732×10^{-2} m/sec (equivalent to 0.12 fps per 1 sec sample, 25 measurements averaged) (also equivalent to 0.0006 m/sec uncorrelated RMS error a 1 sample/min)
Range-rate bias	10^{-2} m/sec (0.0328 ft/sec)

For purposes of the Mars mission analysis, a simple, single-station approximation to the three-station DSIF net tracking the vehicle was made by assuming the range-rate bias to be exponentially correlated noise with a time constant of 1/3 day (see Section 9 for additional details).

6.5 LIMITATIONS, CONSTRAINTS, AND PERFORMANCE CAPABILITIES

Radio guidance performance capabilities, limitations, and constraints for the earth orbit, lunar, and interplanetary missions are discussed in this subsection. Rather than analyze each mission independently, it is more convenient and meaningful to analyze the requirements, tracking system performance capabilities, and constraints by major mission phase (see Table 6-XIV).

Table 6-XIV. Mission Phases for Lunar and Interplanetary Missions

Mission	Launch Through Parking Orbit Trajectory	Parking Orbit Coast	Translunar Or Interplanetary Orbit Insertion Burn	Midcourse Correction	Terminal Burn for Orbit Insertion
Lunar	X	X	X	X	X
Mars	X	X	X	X	X
Jupiter	X	X	X	X	

Mission phases for a synchronous earth orbit mission are:

- Launch through parking orbit injection
- Coast in low-altitude parking orbit
- Transfer burn
- Transfer orbit coast
- Final injection burn at synchronous altitude.

Paragraph 6. 5. 1 discusses the use of radio guidance during launch through orbit insertion (parking orbit, translunar, or interplanetary). Tracking and orbit determination capabilities are discussed in Paragraph 6. 5. 2 for earth parking orbits and synchronous orbits and in Paragraph 6. 5. 3 for the translunar and interplanetary phases. Section 9 presents detailed results for DSIF tracking, with and without an approach guidance sensor for the Mars mission.

6. 5. 1 Use of Radio Guidance — Launch Through Orbit Insertion

Radio guidance is currently in use for several NASA launch vehicles (Atlas/Agena, Thor/Delta, Titan II/Gemini) and AF launch vehicles (Titan III, Atlas/Agena, Thor/Delta). Launch phase radio guidance is provided for these vehicles using either the GE Mod III or BTL radio/inertial guidance systems. In all cases the tracking radar is located in the vicinity of the launch site and tracks the vehicle to the lower elevation angle limit (5 to 10 deg depending on the mission accuracy requirements). By suitably shaping the launch trajectory to maintain acceptable elevation and vehicle antenna look-angles, accurate guidance can be provided through the first two, and portions of the third, stages of powered flight. For Atlas/Agena, guidance is assumed by a simple onboard inertial system (attitude reference, programmer, and a single, axially mounted accelerometer for thrust cutoff) during the Agena burn. The radio guidance serves to initialize the inertial system.

A number of difficulties are encountered in extending the use of radio guidance to vehicles employing high performance upper stages (Atlas/Centaur) or requiring additional stages to meet the requirements of higher energy missions. As indicated in the following paragraphs, the best available tracking radars suitably located at downrange sites will meet the launch phase guidance requirements for many lunar and interplanetary

missions. However, there are severe siting and related problems such as acquisition and vehicle antenna coverage. Some payload (weight) penalties and launch azimuth (and consequently launch window) constraints are incurred due to tracking system geometrical constraints. Trajectories are, in general, limited to direct ascent types. The approach of using radio guidance with parking orbit trajectories appears impractical.

The analysis of radio guidance feasibility and performance during the launch through injection phases has been based on a lunar mission, and an Atlas/Centaur trajectory has been assumed. Performance results are presented in terms of the midcourse ΔV correction required to correct the miss and time of flight errors at the moon due to the launch guidance errors. Typical Figure of Merit (FOM) values for this mission are 10 m/sec (1σ).

6.5.1.1 Siting Considerations

For complete radio guidance, one consideration is conditions near the final vehicle burnout point. Figure 6-2 shows the locus of these points for direct ascent trajectories and Figure 6-3 shows the region of possible burnout points for parking orbit missions. Also shown on these figures are the geometrical viewing limits from appropriate ground locations for both a 5 and 10 deg minimum elevation angle above the local horizontal. It has been assumed that burnout always occurs at a 110 nmi altitude† for direct ascent cases and 90 nmi for parking orbits.

Direct Ascent. As can be seen from Figure 6-2, direct ascent trajectories launched at azimuths greater than 90 deg (97 deg) burn out in view from Antigua if the minimum acceptable elevation angle is 5 deg (10 deg). However, a particular trajectory which is just visible at burnout will not be visible at the time it passes through its minimum altitude of 90 nmi. This might occur quite early in flight and thus be of no interest for radio guidance of the terminal phase. The detailed altitude versus time history of the limiting trajectories will determine exactly when acquisition can occur and, therefore, determine the time available for guidance. This aspect of the problem has not been explored.

The accuracy analysis of Subsection 6.5.1.2 assumes sufficient time is available to implement optimum filtering and thus realize the full accuracy potential of the system. If such is not the case, the trajectories would

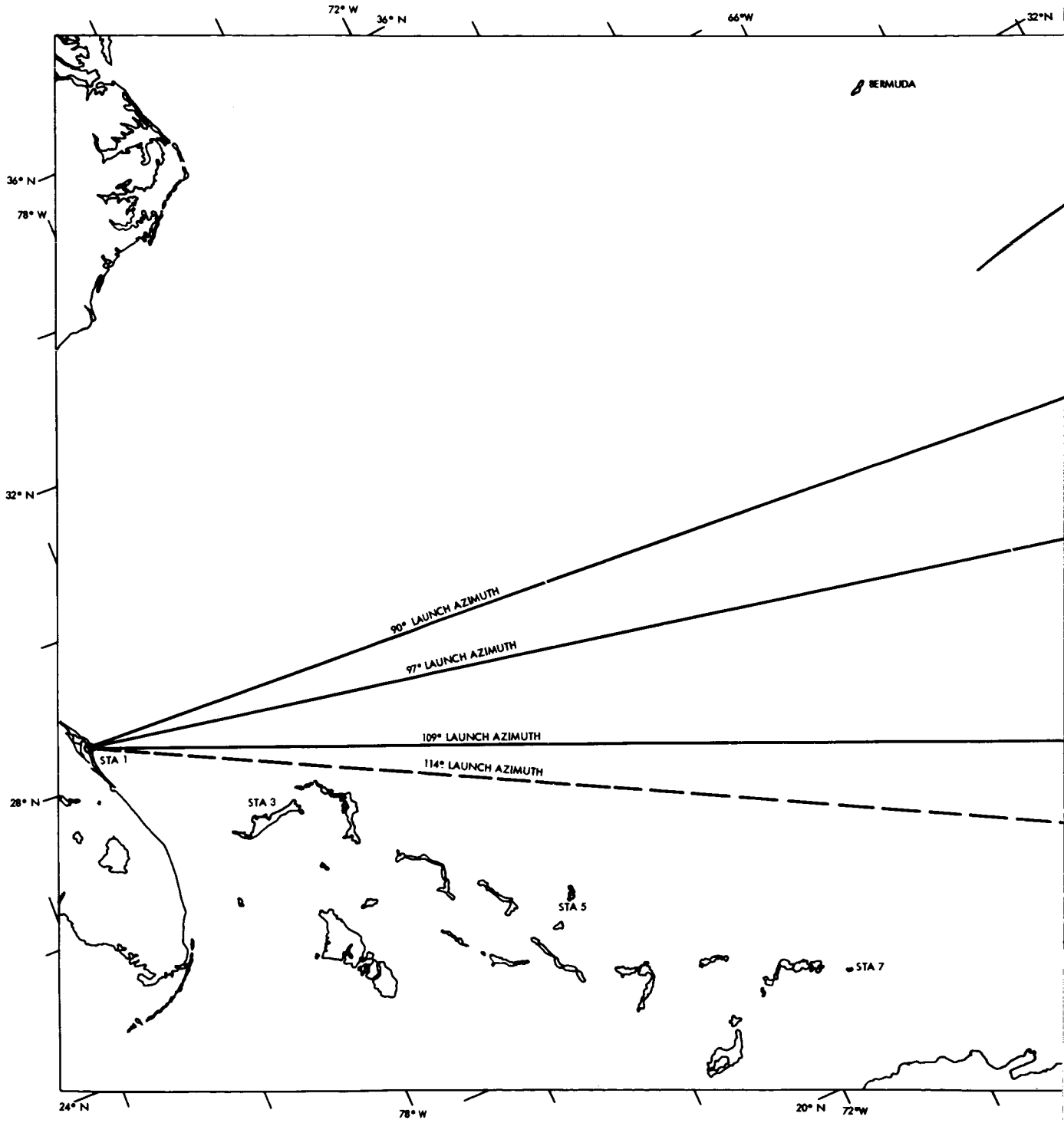
72° W
36° N
66°W
32°N
BERMUDA
36° N
78° W
32° N
90° LAUNCH AZIMUTH
97° LAUNCH AZIMUTH
109° LAUNCH AZIMUTH
114° LAUNCH AZIMUTH
STA 1
28° N
STA 3
STA 5
STA 7
24° N
78° W
20° N
72°W

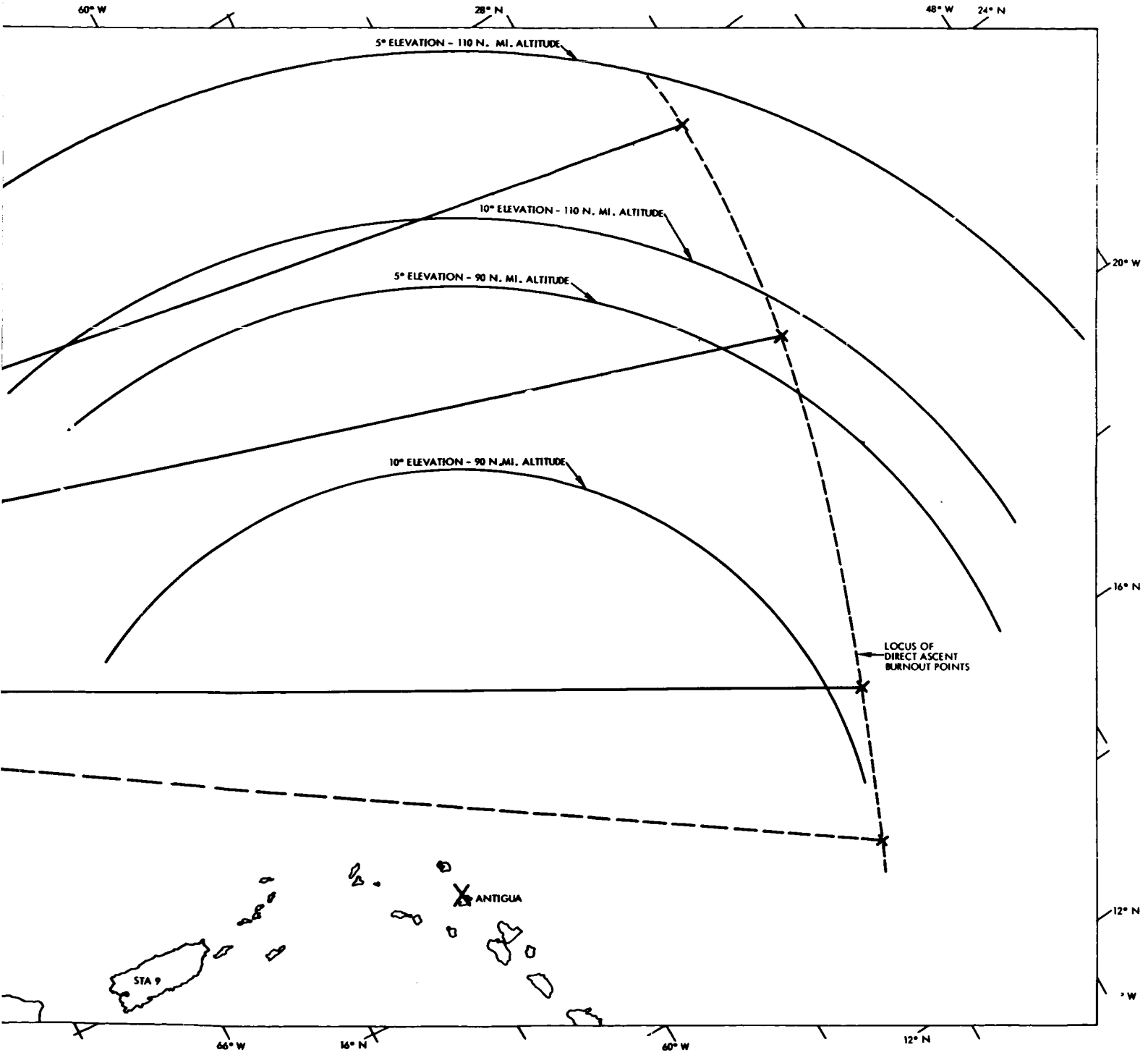

Figure 6-2. Atlas/Centaur Direct Ascent—Antigua Viewing Limits

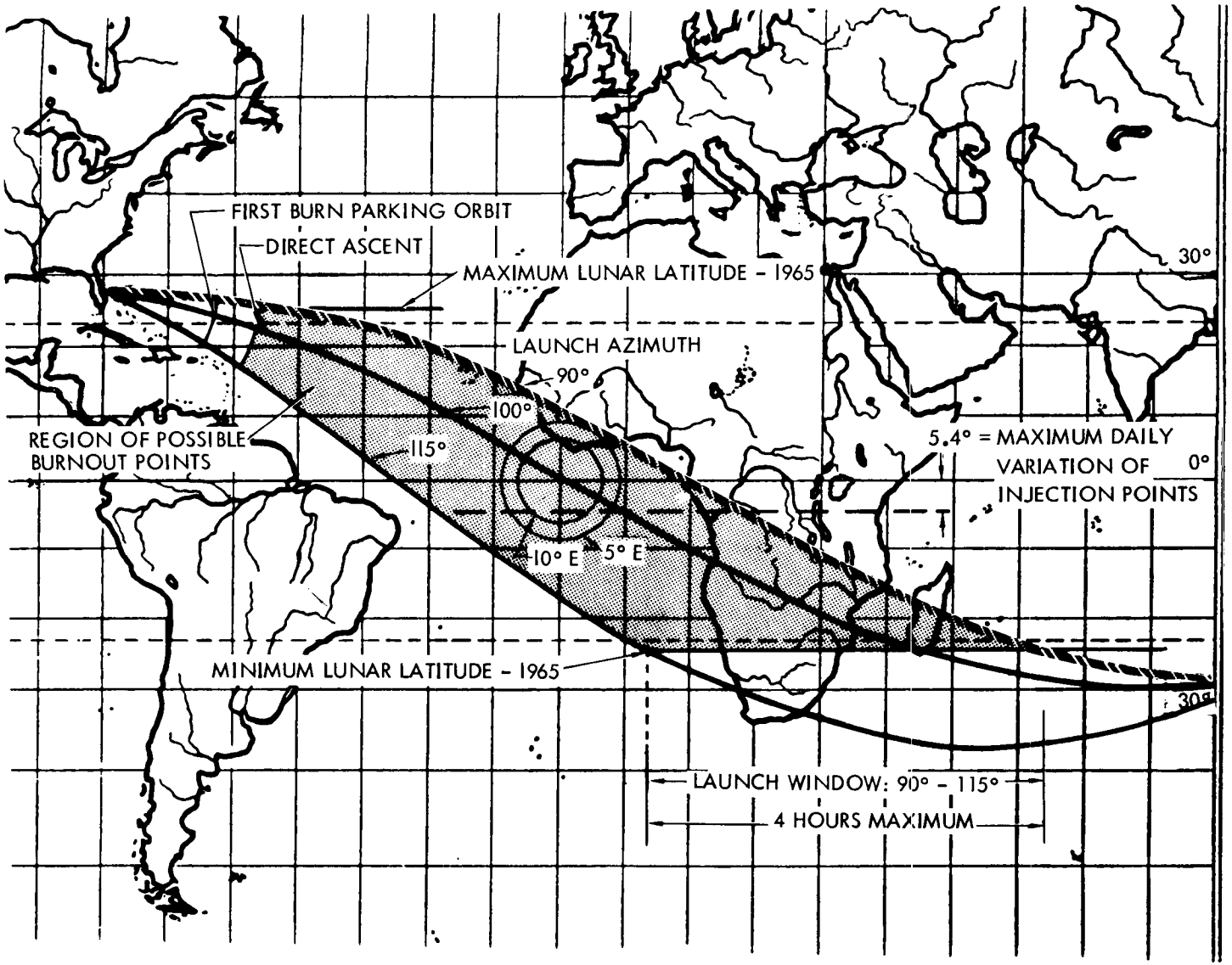

Figure 6-3. Parking Orbit Mission Burnout Points

have to be reshaped at some expense in payload performance. Note that the radio guidance airborne equipment may be lighter than the inertial guidance equipment so it is possible that no net payload loss would be involved.

In conclusion, from purely a burnout geometry point of view, one radio guidance station at Antigua can handle direct ascent trajectories suitably shaped (90 to 114 deg) over the launch azimuth region. There is no payload penalty over an inertial guidance approach if a 5-deg elevation angle results in acceptable accuracy. The question of acquisition probability has not been evaluated.

Parking Orbit. As seen in Figure 6-3, the possible parking orbit burnout points cover an appreciable expanse, mostly ocean. A single ground station cannot view a very large section of this region regardless of where it is located. For an equatorial station the launch window coverage on the proper day is either 20 min at 10-deg elevation angle limits or 44 min at 5 deg. Depending on the time of the year, there is considerable movement of the burnout point locus from day to day so that if a ship were used, it would have to rapidly change positions. There are techniques for enlarging the launch window by varying the injection true anomaly at the expense of payload loss; however, the whole approach of using radio guidance with parking orbit trajectories appears impractical.

Airborne Antenna Coverage. Another primarily geometrical area not explored relates to airborne antenna coverage. The use of radio guidance assumes that adequate signal strength exists at the various receiver inputs. Since transmitter power and ground antenna gain are essentially fixed for any existing radar system (to change these characteristics involves long lead time development), the airborne antenna design is the only variable. A detailed study of the problem of obtaining an antenna with the proper combination of gain and angular coverage (they are related as their product must equal one) has not been performed, but an initial examination indicates that there probably will be no severe problem for direct ascent trajectories. In these cases, the antenna is at least only looking south.

---

†The direct ascent trajectories are shaped to have a minimum altitude of 90 nmi but this occurs before burnout. For the three cases studied, burnout actually occurred between 112 and 114 nmi.

The parking orbit missions are more critical since a hemispherical airborne antenna is needed.

6.5.1.2 Accuracy Analysis

An analysis of the accuracy attainable at Centaur final burnout using a tracking radar has been performed using, as a typical trajectory, a lofted (+8.56 deg true anomaly) direct ascent case. While this was the only trajectory studied and injection error to midcourse correction transformations are trajectory dependent, it is felt that the results obtained are indicative of the accuracy obtainable with radio guidance.

Four geometrical conditions were investigated involving elevation angles at burnout of 5 and 10 deg and yaw angles measured from the trajectory plane of 0 and 60 deg. Also, two tracking radars, the FPS-16 and the BTL, are included. The results are shown in Table 6-XV. Assuming a typical FOM requirement of 10 m/sec (1σ), the BTL radar† is acceptable for low yaw angles (i.e., the radar located close to the trajectory plane) but becomes marginal at high yaw angles. The FPS-16 goes from marginal to unacceptable as the yaw angle increases. Elevation angle variations from 10 to 5 deg cause only a small change in the final result.

Table 6-XV. Radio Guidance FOM, m/sec (1σ) for Lunar Mission (Lofted Direct Ascent Trajectory) Miss and Time of Flight Corrected at Midcourse

Guidance System	5 Deg Elevation Angle		10-Deg Elevation Angle	
	0 Deg Yaw Angle	±60 Deg Yaw Angle	0 Deg Yaw Angle	±60 Deg Yaw Angle
FPS-16	11	29	10.5	27
BTL	7	13.5	6.5	13

Errors arise from three general sources: site location uncertainties, radar biases, and radar noise in combination with missile acceleration uncertainties. For the case investigated, the midcourse correction required for a 1000-ft site (position) uncertainty in each of two orthogonal

directions on the earth's surface is 0.166 m/sec, thus this source is negligible even if a ship were involved and its location was uncertain to 1 nmi. Radar angular bias errors (azimuth and elevation) are normally in the vicinity of 0.1 m (1σ) and these require a midcourse correction of 0.81 m/sec. They are also negligible. If a ship were utilized, a 1.0 mrad error in pitch, yaw, and roll would require 13 m/sec midcourse correction. This term may or may not be negligible depending on how accurately the ship's orientation is known.

The remaining source of error which contributes to almost all of the midcourse correction shown in Table 6-XV is due to radar noise. Here the problem of determining a signal, the vehicle position and velocity components in the presence of noise is involved. While the detailed analysis leading to the results of Table 6-XV is too lengthy to give here, consider the problem of determining a vehicle's speed when it is directed along the radar line of sight using position data corrupted by white noise. Note that the determination must be made before burnout while the velocity is changing. If a filter were designed which minimizes the effect of white position noise and which at the same time gives zero error in the absence of noise if the velocity is changing linearly with time (constant acceleration) the noise error is given by

$$\sigma_{noise} = \sqrt{\frac{96}{T^3} S_o}$$

where

S_o = the position noise's one-sided spectral density in ft^2/cps

T = the smoothing time

However, if constant thrust is assumed, the velocity is not changing linearly with time. It has a nonzero second derivative, called jerk, equal to

$$\text{jerk at burnout} = J = \frac{\text{mass rate x thrust}}{(\text{mass})^2}$$

---

†The GE Mod III system has approximately the same FOM for the higher (±60 deg) yaw angles although it is somewhat better at low yaw angles.

The filter error (sometimes termed lag error) is

$$\epsilon_j = 0.1\ JT^2$$

Some of the jerk error at burnout can be eliminated because its nominal value is known. The remaining uncertainty due to mass rate, I_{sp}, and final mass variations represents only a fraction, say its 1σ value is k, of the nominal amount. Thus the uncorrectable error is

$$\sigma_j = 0.1\ kJT^2$$

The total velocity error is

$$\sigma_T = \sqrt{\sigma_n^2 + \sigma_j^2}$$

and for the optimum value of smoothing time is

$$\sigma_{T_{opt}} = 2.72\ S_o^{2/7}\ (kJ)^{3/7}\ \text{ft/sec}$$

Therefore, in this example, the form of the filter must be selected, the spectral density of the position noise at zero frequency, and the jerk uncertainty must be known in order to determine the optimum filtering time and resulting error. A similar situation arises when determing errors normal to the radar line of sight. Here other missile unknowns, such as autopilot gyro drift and programmer/torquer scale factor errors, enter into the analysis. The analysis results indicated below consider all of those factors, and the actual geometry other than white noise models.

The results of the FPS-16 accuracy analysis are based on the use of an optimum filter with the assumed error model as follows:

Radar Noise	1σ Value	Time Constant†
Range	10 ft	1.7 sec
Azimuth	0.1 mrad	1.7 sec
Elevation	0.1 mrad	1.7 sec

†Assumed to have an exponential correlation function.

Vehicle Parameters	1σ Value	Time Constant†
Equivalent gyro drift	10 deg/hr	50 sec
ΔI_{sp}	1/3 percent	∞
Δ Propellant flow rate	2/3 percent	∞

The coordinate system chosen is a right handed Cartesian system at the vehicle where

a) The X axis is locally horizontal in the desired pitch plane

b) The Y axis is locally horizontal normal to the pitch plane

c) The Z axis is locally vertical.

The 1σ position and velocity uncertainties at injection resulting from optimum filtering are given in Table 6-XVI together with the required midcourse correction assuming the lofted direct ascent trajectory.

Table 6-XVI. FPS-16 Filtering Errors and Midcourse FOM for Lunar Mission

Coordinate	5-Deg Elevation Angle		10-Deg Elevation Angle	
	0 Deg Yaw Angle	±60 Deg Yaw Angle	0 Deg Yaw Angle	±60 Deg Yaw Angle
$\dot{X}$ (m/sec)	1.3	3.7	1.3	3.5
$\dot{Y}$ (m/sec)	3.4	2.2	3.3	2.1
$\dot{Z}$ (m/sec	3.4	3.4	3.3	3.3
X (m)	18.0	64.0	16.0	52.0
Y (m)	65.0	37.0	51.0	30.0
Z (m)	65.0	65.0	51.0	51.0
FOM (m/sec) (1σ)	10.5	28.2	10.2	26.7

As previously shown in Table 6-XV, the BTL radar is significantly more accurate than FPS-16; however, to avoid security classification problems, its detailed characteristics are not given here. An initial analysis of the GE Mod III system indicates that it is not appreciably better than

†Assumed to have an exponential correction function.

the BTL system especially at the limits of yaw angle studied. Accuracy data on both of these systems are contained in Ref 6-8.

6.5.2 Orbit Determination Accuracy During Earth Orbit Coast

Numerous studies have been made of orbit determination accuracies for spacecraft in low and high altitude earth orbits in support of Mercury, Gemini, Apollo, and other NASA and DOD space programs. Some results from these studies that are particularly pertinent to the present study are summarized here. Use of all available NASA C-band and USBS tracking stations is assumed, as is the availability of appropriate computing facilities for near-real-time orbit computation.

Figures 6-4 and 6-5 present some typical results from Ref 6-3, showing the orbit determination accuracies for a vehicle in a low altitude (185 km) earth orbit. The C- and S-band stations and their tracking periods are shown along the bottom of the figures. The dashed lines show the degradation in the vehicle position and velocity uncertainties if tracking is terminated at the points indicated. The need for multiple stations is evident.

For lunar and planetary missions utilizing relatively short parking orbit ascent trajectories and for extended duration low-altitude earth orbits, the conclusion is drawn that the use of radio guidance is not practical for the missions and vehicles covered in this study. This is due to a combination tracking system coverage limitation, tracking system performance limitation, and time delays inherent in gathering the data, transmitting it to a central computing facility, reducing the data, computing vehicle commands, and transmitting these commands via data link to the orbiting vehicle.

For the synchronous orbit mission, it is shown in Section 7 that a navigation update[†] is required prior to synchronous orbit injection for missions that involve long parking orbit coast times. This correction can be made by either of two methods:

[†] This is in addition to the required attitude updates required prior to the transfer burn and final orbit insertion. The errors to be corrected are primarily the accumulated position errors.

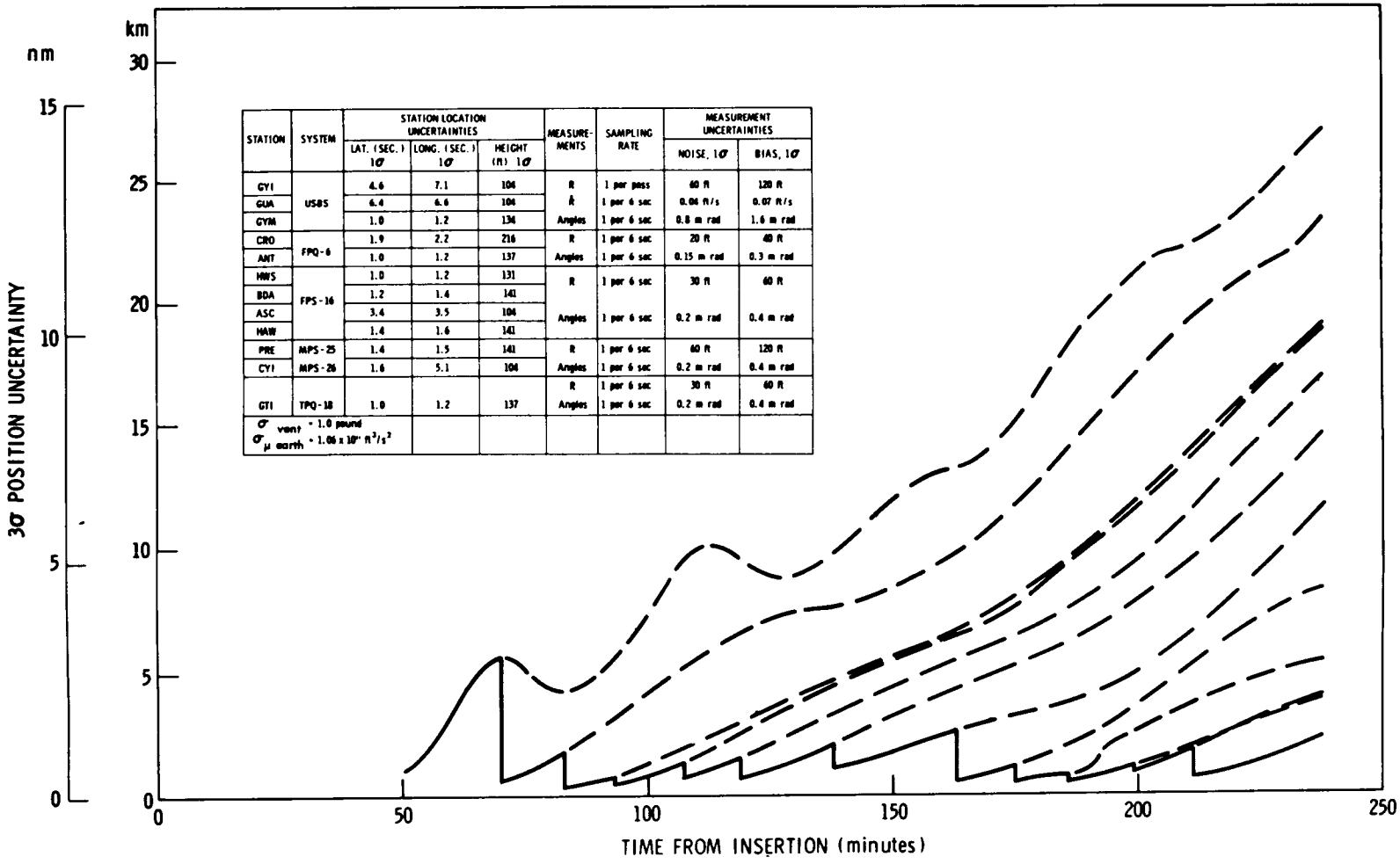

STATION	SYSTEM	STATION LOCATION UNCERTAINTIES			MEASUREMENTS	SAMPLING RATE	MEASUREMENT UNCERTAINTIES	
		LAT. (SEC.) 1σ	LONG. (SEC.) 1σ	HEIGHT (ft) 1σ			NOISE, 1σ	BIAS, 1σ
GYI	USBS	4.6	7.1	104	R	1 per pass	60 ft	120 ft
GUA		6.4	6.6	104	Ṙ	1 per 6 sec	0.04 ft/s	0.07 ft/s
GYM		1.0	1.2	134	Angles	1 per 6 sec	0.8 m rad	1.6 m rad
CRO	FPQ-6	1.9	2.2	216	R	1 per 6 sec	20 ft	40 ft
ANT		1.0	1.2	137	Angles	1 per 6 sec	0.15 m rad	0.3 m rad
WHS	FPS-16	1.0	1.2	131	R	1 per 6 sec	30 ft	60 ft
BDA		1.2	1.4	141				
ASC		3.4	3.5	104	Angles	1 per 6 sec	0.2 m rad	0.4 m rad
HAW		1.4	1.6	141				
PRE	MPS-25	1.4	1.5	141	R	1 per 6 sec	60 ft	120 ft
CYI	MPS-26	1.6	5.1	104	Angles	1 per 6 sec	0.2 m rad	0.4 m rad
GTI	TPQ-18	1.0	1.2	137	R	1 per 6 sec	30 ft	60 ft
					Angles	1 per 6 sec	0.2 m rad	0.4 m rad
σ_{vent} = 1.0 pound $\sigma_{\mu\ earth}$ = 1.06 x 10^{16} ft^3/s^2								

CRO FPQ-6 HAW FPS-16 ANT FPQ-6 WHS FPS-16 ASC FPS-16 PRE MPS-25 CRO FPQ-6 HAW FPS-16 ANT FPQ-6 WHS FPS-16 ASC FPS-16 PRE MPS-25

Figure 6-4. 3-σ Position Uncertainty for a 90-deg Launch Azimuth Earth Parking Orbit (from Ref 6-3)

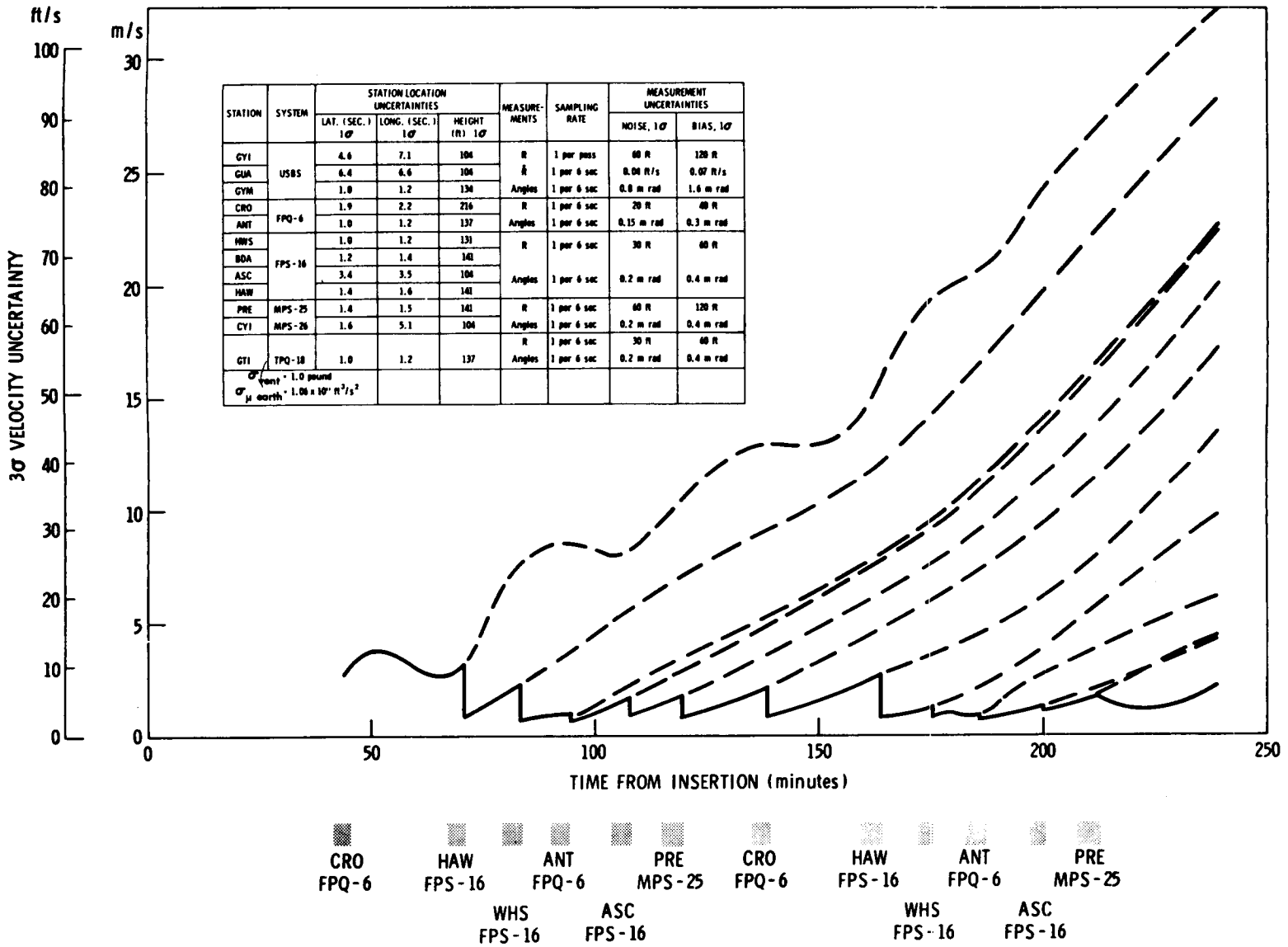

STATION	SYSTEM	STATION LOCATION UNCERTAINTIES			MEASUREMENTS	SAMPLING RATE	MEASUREMENT UNCERTAINTIES	
		LAT. (SEC.) 1σ	LONG. (SEC.) 1σ	HEIGHT (ft) 1σ			NOISE, 1σ	BIAS, 1σ
GYI	USBS	4.6	7.1	104	R	1 per pass	60 ft	120 ft
GUA		6.4	6.6	104	Ṙ	1 per 6 sec	0.06 ft/s	0.07 ft/s
GYM		1.0	1.2	134	Angles	1 per 6 sec	0.8 m rad	1.6 m rad
CRO	FPQ-6	1.9	2.2	216	R	1 per 6 sec	20 ft	40 ft
ANT		1.0	1.2	137	Angles	1 per 6 sec	0.15 m rad	0.3 m rad
WHS	FPS-16	1.0	1.2	131	R	1 per 6 sec	30 ft	60 ft
BDA		1.2	1.4	141				
ASC		3.4	3.5	104	Angles	1 per 6 sec	0.2 m rad	0.4 m rad
HAW		1.4	1.6	141				
PRE	MPS-25	1.4	1.5	141	R	1 per 6 sec	60 ft	120 ft
CYI	MPS-26	1.6	5.1	104	Angles	1 per 6 sec	0.2 m rad	0.4 m rad
GTI	TPQ-18	1.0	1.2	137	R	1 per 6 sec	30 ft	60 ft
					Angles	1 per 6 sec	0.2 m rad	0.4 m rad
σ_{thrust} = 1.0 pound $\sigma_{\mu\ earth}$ = 1.06 x 10⁷ ft³/s²								

Figure 6-5. 3-σ Velocity Uncertainty for a 90-deg Launch Azimuth Earth Parking Orbit (from Ref 6-3)

1) Radio tracking during the transfer orbit coast to determine the position error. The major part of the error can be removed by proper adjustment of the time of initiation of the final orbit insertion burn.

2) Use of an onboard electro-optical sensor (e. g., a sun sensor) to establish a "line-of-position" fix at some point during the transfer orbit coast. The position error is removed as in 1) above.

The feasibility of method 1) depends on the availability of suitably located tracking stations. A desirable location depends on the choice of longitude of the satellite after injection into the final synchronous orbit. Although it may be possible to select suitable tracking stations for most final longitudes of interest, some operational and trajectory constraints are evident.† The use of the second method, which can be implemented entirely within the onboard system, appears very attractive. Further study of this technique is recommended.

For tracking a spacecraft after injection into the final synchronous orbit, the use of ground-based tracking is somewhat more useful. Such a capability is useful for long-time stationkeeping which requires periodic orbit prediction and adjustment. Such a capability can be easily implemented with either the S-band systems or the NASA STADAN net. The latter system is recommended for this purpose.

6. 5. 3 Orbit Determination Accuracy During Translunar and Interplanetary Trajectory Phases

Extensive studies have been made of orbit determination accuracies for lunar missions in support of the Apollo, (Ref 6-10), Lunar Orbiter, and other programs. Similar, but less comprehensive studies have been made for various interplanetary missions. Some results from these studies particularly pertinent to the present study are summarized here. Additional study conclusions for the Jupiter Mars missions are presented in Sections 8 and 9.

†It is also possible to use different modes of ascent from the one studied here. One commonly used technique is to inject the satellite into an equatorial orbit whose period is substantially different from 24 hr and let the satellite "drift" to the required longitude, at which point the orbital period is corrected.

The results of tracking accuracy studies are normally computed in the form of state-vector uncertainties as a function of time from injection. The quantities used here to represent the uncertainties are the square root of the sum of the variances of the three position components and the velocity components.

6.5.3.1 Translunar Orbit Determination Using the S-Band Tracking Systems

The results presented in Ref 6-10 and summarized below indicate that launch azimuth, earth orbital coast type, flight time, and date of launch have effects on DSIF tracking during the early portion of the flight, largely due to their effects on coverage. In the latter portion of the trajectory the accumulated accuracy of DSIF tracking is to a large extent independent of the trajectory. Flight time is the only trajectory parameter having an appreciable effect on the latter portion of the trajectory. C-band radar is found to be useful in reducing uncertainties in the early part of the flight, but it is limited to tracking the first 1.5 hr of the trajectory. The addition of range information to this network gives a marked improvement in tracking accuracy.

The USBS/DSIF network assumed to be tracking the spacecraft during the translunar trajectory consists of Goldstone, Canberra, and Madrid. The locations of these stations are listed in Table 6-IV. Each station is assumed to be capable of simultaneous measurements of range, range rate, azimuth, and elevation; but the case where range information is absent is also considered.

All errors are assumed to be random with zero mean and zero correlation between stations and between data types. All systematic errors, such as tracking station location uncertainty, uncertainty due to atmospheric refraction, and uncertainties in physical constants, such as the speed of light and gravitational parameters of the earth and the moon are not included.

This study assumed that when the vehicle is visible to two DSIF stations simultaneous sightings are taken. Since range and range-rate measurements involve transmission from the spacecraft, it is implied that there are two transponders on the spacecraft or that the two tracking stations are synchronized.

In order to have a basis of comparison as data are acquired along the trajectory, all matrices are propagated to closest approach to the moon. For convenience, the matrix is summarized by the quantity "root-semitrace." This is defined to be the square root of the sum of half of the elements on the diagonal of an even order square matrix and is designated symbolically as "RST." The RST's of the matrix at the moon are

$$\text{Position RST} = \text{RST(R)} = \sqrt{\sum_{i=1}^{3} \sigma_i^2}$$

$$\text{Velocity RST} = \text{RST(V)} = \sqrt{\sum_{i=4}^{6} \sigma_i^2}$$

where σ_i^2 respresents the variance of the i^{th} coordinate. These quantities serve to indicate the bounds of the 1σ three-dimensional uncertainty ellipsoids of position and velocity respectively.

The a priori information assumed at orbit insertion consisted of uncorrelated 1-σ uncertainties of 10 km in position and 10 m/sec in velocity, in each inertial direction. The nominal trajectory to be used has a launch azimuth of 90 deg, a 70-hr flight time, a launch date of January 22, 1968, and a selenographic inclination of the approach hyperbola of 130 deg. Plots of RST(R) and RST(V) as a function of time from injection are presented in Figures 6-6 and 6-7. It is of interest to note that both of these quantities behave similarly. At the bottom of the figure are plotted the periods when two DSIF stations are able to track the spacecraft. Associated with these periods of overlapping coverage are dramatic drops in RST(R) and RST(V) over the period of one hour.

The results of this study indicate the tracking capability during the translunar trajectory with earth based radar. Certain generalizations are now made, keeping in mind the assumptions of this study.

The position and velocity uncertainties associated with radar tracking only may be characterized by the following properties:

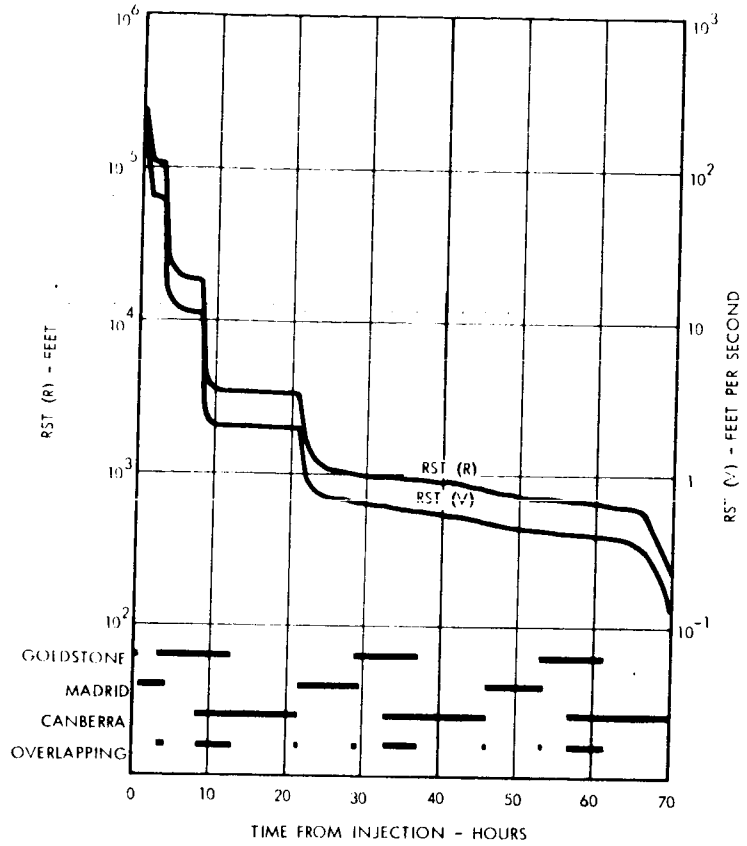

Figure 6-6. Tracking Uncertainties Using Range, Range Rate, and Angular Data (90-deg Launch Azimuth, 70-Hour Flight Time, 22 January 1968 Launch, Approach Hyperbola Inclination of 130 deg)(from Ref 6-10)

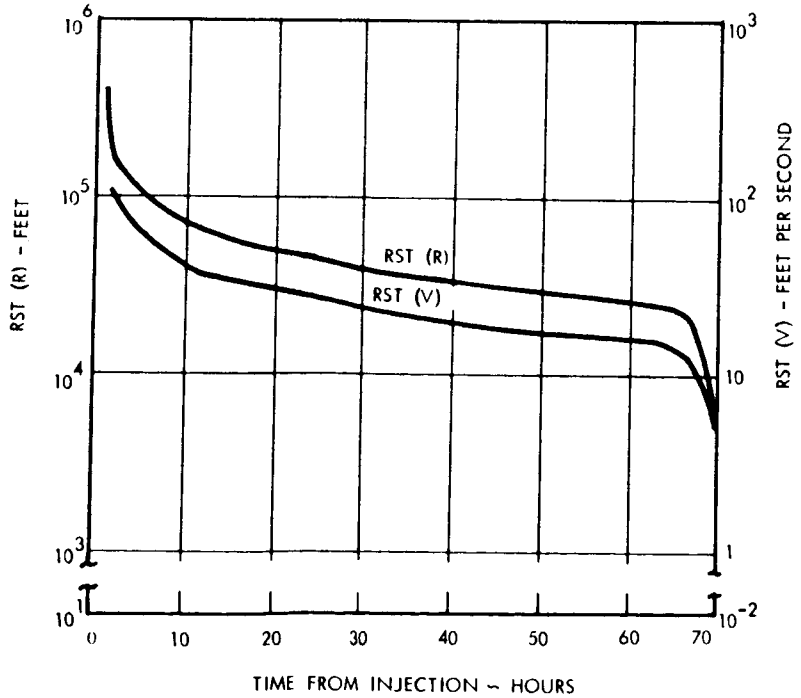

Figure 6-7. Tracking Uncertainties with No Range Data (from Ref 6-10)

a) Sensitivity over the early portion of the trajectory to launch azimuth, type of coast, flight time, and date of launch due to changes in tracking coverage

b) Insensitivity over the latter portion of the trajectory to the trajectory parameters

c) Largest uncertainties are in the downrange direction (measured in orbit plane coordinates)

d) Sudden drops occur in the overall uncertainties at the start of periods of simultaneous or near simultaneous tracking by two stations when range data are used.

In general, it can be said that DSIF tracking is greatly improved by the addition of range information, particularly if simultaneous or near simultaneous tracking by two stations is possible. There are periods during the flight when there is relatively little improvement in the tracking uncertainties. During these periods, which in some cases may last for ten hours or more, it would be possible to reduce the sampling frequency considerably without seriously affecting the tracking accuracy. Table 6-XVII presents RST(R) and RST(V) measured at pericynthion without and with the simulation of midcourse correction effects, for the various types of tracking systems.

Table 6-XVII. Translunar Tracking Accuracy

Data Type	Midcourse Correction Effects Not Included		Midcourse Correction Effects Included	
	1 σ Position Uncertainty (km)	1 σ Velocity Uncertainty (km/sec)	1 σ Position Uncertainty (km)	1 σ Velocity Uncertainty (km/sec)
DSIF (range, range rate, angle data)	0.1	0.06	0.8	0.46
DSIF (no range)	2.1	1.5	3.7	2.9
C-band radar	1.9	0.37	—	—

6.5.3.2 Interplanetary Orbit Determination Accuracy Using DSIF

The use of DSIF for tracking and orbit determination is virtually a necessity for the interplanetary missions considered in this study. As is shown in Section 9, for the Mars orbiter mission, a completely autonomous onboard optical inertial system cannot meet the desired mission accuracy requirements within the present (or near future) state-of-the-art. However, use of the onboard optical/inertial system in conjunction with DSIF is extremely attractive both in terms of accuracy and operational utility. In this mode of operation, DSIF is used as the primary source of accurate position and velocity data (with respect to the earth) and the onboard system is used to accurately control the midcourse, orbit insertion and orbit trim maneuvers. Use of onboard sensors is also useful in determining the spacecraft orbit relative to a planet whose position with respect to the earth is uncertain to a significant degree. See Section 9, for a more detailed discussion.

The orbit determination accuracies attainable with DSIF depend on the mission trajectory and will also change significantly throughout the mission. Detailed results are presented in Section 9 for the Mars-orbiter mission using the trajectory described in Section 2. Table 6-XVIII presents some approximate results for Mars mission for present and future tracking system capabilities. A comparison is also made with the expected errors at encounter in the absence of tracking data for a typical launch injection guidance error of 10 m/sec.

Table 6-XVIII. Approximate Trajectory Determination Accuracies for a Mars Mission

	Error At Encounter
Launch Injection Guidance Only	
10 m/sec	90,000 - 200,000 km
Earth Based Tracking Using DSIF	
Present (Mariner 4 Results)	
• 5 days after injection	2400 km
• All data including post encounter tracking	500 km
Future (1971)	
• Injection - 5 days	1000 km
• 5 - 120 days	150 km
• After 120 days	100 km

REFERENCES FOR SECTION 6

6-1 "Space Tracking and Data Acquisition Network Facilities Report (STADAN)," Goddard Space Flight Center, Greenbelt, Maryland, Report No. X-530-66-33, December 1965.

6-2 Harold L. Hoff, "Tracking, Command, Control and Data-Acquisition of NASA Flight Programs," (NASA-Goddard Space Flight Center, Greenbelt, Maryland), published in Annals New York Academy of Sciences, Vol. 134, 22 November 1965, p. 475.

6-3 "Apollo Mission and Navigation Systems Characteristics," MSC-GSFC Apollo Navigation Working Group Technical Report No. 66-AN-1.1, 1966.

6-4 "Apollo Navigation, Ground and On-Board Capabilities," MSC-GSFC Apollo Navigation Working Group Technical Report No. 65-AN-2.0, 1 September 1965.

6-5 J. H. Painter and G. Hondros, "Unified S-Band Telecommunications Techniques for Apollo," NASA Technical Note TN D-2208, Volume 1 — Functional Description, NASA/MSC, March 1965.

6-6 "Description of Deep Space Network Operational Capabilities as of 1 January 1966," NASA Technical Memorandum 33-225, Jet Propulsion Laboratory, 1 July 1966.

6-7 "Planned Capabilities of the DSN for Voyager," Engineering Planning Document No. 283, Jet Propulsion Laboratory, 15 September 1965.

6-8 N. A. Renzetti, et al., "Projected NASA/JPL Deep Space Network Capabilities in the 1970's," Jet Propulsion Laboratory, March 1966, presented at AIAA/AAS Stepping Stones to Mars Meeting, Baltimore, Maryland, 28-30 March 1966.

6-9 "Accuracies of Air Force Ballistic Missiles, Twelfth Quarterly CEP Status Report (U)," BSD-TRD-62-226 (STL Report No. 6101-7664-RA-000), August 1962. (S)

6-10 "Analysis of Apollo Orbit Determination Accuracy with Random Errors in Ground Based Radar and Outboard Optical Observations," Volume 3, The Translunar Trajectory, TRW Systems Document 8408-6042-RC-000, 4 May 1964. (C)

7. PERFORMANCE ANALYSIS OF CANDIDATE OPTICAL/INERTIAL SYSTEMS FOR BOOST FLIGHT, SYNCHRONOUS ORBIT INJECTION, AND MAJOR POWERED MANEUVERS

7.1 INTRODUCTION AND SUMMARY

The navigational errors of the inertial guidance subsystem, as augmented by the optical sensor subsystem, were determined in this study by means of an inertial guidance error analysis program which calculates the effect of each error source on the position, velocity, and orientation errors by integrating the first order perturbation equations along a nominal trajectory.

Three missions were analyzed. The results for the synchronous orbit mission are described in Subsection 7.3. For this mission the errors at injection into synchronous orbit were first calculated and the results used to compute (by a Monte Carlo technique) the delta-velocity required to achieve the desired orbit. Twelve different runs were made with different candidate systems.

The results for translunar orbit injection are described in Subsection 7.4. In this analysis the errors at injection into translunar orbit were first calculated and the results used to determine the delta-velocity required to perform the midcourse correction maneuver. Four different error analysis runs are made, three with different candidate strapdown systems and for comparison one with the Centaur gimbaled platform.

The analysis of the midcourse correction and planetary orbit insertion maneuvers is described in Subsection 7.5. The navigational errors produced by these maneuvers were determined for application to the studies of midcourse guidance. (See Section 8.)

7.2 TRAJECTORIES USED FOR PERFORMANCE ANALYSES

Powered flight performance analyses of the TG-166 and TG-266 strapdown guidance systems (augmented by electro-optical sensors as discussed below) were performed for three missions: the Lunar (parking orbit ascent) mission, the earth synchronous mission, and the Mars orbiter mission. In each case a nominal trajectory (launch through injection) was generated which was representative of the mission desired, and subsequently an error analysis tape containing a position, acceleration, and

attitude history for powered flight was produced for use in analyzing the guidance system performance requirements.

The general characteristics of these powered flight trajectories, as well as the characteristics of the trajectories during the translunar, interplanetary approach, and orbiting phases, are given in Subsections 2.3, 2.4, 2.5, and 2.6.

7.3 ERROR ANALYSIS FOR SYNCHRONOUS SATELLITE MISSION

The synchronous orbit mission involves extended flight times so that a pure inertial system can cause unacceptable injection errors. Both optical attitude updates using onboard sensors, and a time of perigee burn update using ground tracking or an autonomous navigator are considered as solutions to the problem.

7.3.1 Error Models

The error models for the two strapdown systems, TG-166 and TG-266 (see Section 4), are presented in Table 7-I. The different types of error sources are discussed below.

7.3.1.1 Initial Conditions

The initial velocity errors were taken as zero relative to the earth. The initial orientation errors include, in addition to the 20 arc sec shown in Table 7-I, the effects of accelerometer errors. These effects are introduced because it is assumed that the accelerometers are used in a leveling mode to initialize the direction cosine matrix. The initialization of the direction cosine matrix in azimuth is assumed to be accomplished optically.

7.3.1.2 Optical Attitude Update Measurement Errors

In the synchronous orbit mission, optical attitude updates are required. It is assumed that a measurement may be made in the 185 km coasting orbit 10 min before perigee burn and in the Hohmann transfer orbit 10 min before apogee burn. The earth sensor errors are assumed to be 1080 arc sec per axis in 185 km orbit and 540 arc sec per axis in synchronous orbit. The sun sensor errors are assumed to be 120 arc sec per axis. It is assumed that the sun lies approximately in the direction of the vehicle roll axis during the apogee measurement, and fairly near the horizontal plane in the perigee measurement. The sun sensor is used for pitch and yaw

Table 7-I. Error Models Used for Strapdown Inertial Guidance Performance Analysis

Number	TG-166	TG-266	Units	Type	Description
1	3	3	m	Initial	Vertical position
2, 3	15	15	m	Initial	East, north position
7, 8, 9	20	20	arc sec	Initial	Orientation
10	540	540	arc sec	Optical	Roll axis at apogee (earth)
20, 30	120	120	arc sec	Optical	Yaw, pitch axes at apogee (sun)
11, 31	1080	1080	arc sec	Optical	Roll, pitch axes at perigee (earth)
21	120	120	arc sec	Optical	Yaw axis at perigee (sun)
39	0.238	0.238	arc sec	Tracker	Update time
40, 51, 62	21	14	μg	Accelerometer	Bias
73, 77, 81	75	24	$\mu g/g$	Accelerometer	Scale factor
74	12	10	arc sec	Accelerometer	X accelerometer input axis rotation toward y axis
75	12	10	arc sec	Accelerometer	X accelerometer input axis rotation toward z axis
78	12	10	arc sec	Accelerometer	Y accelerometer input axis rotation toward z axis
82, 83, 84	15	10	$\mu g/g$	Accelerometer	Pendulous axis g sensitivity
85, 86, 87	1	1	$\mu g/g$	Accelerometer	Output axis g sensitivity
91, 97, 103	50	30	$\mu g/g^2$	Accelerometer	Input-pendulous g product sensitivity
92, 98, 104	0.5	0.5	$\mu g/g^2$	Accelerometer	Input-output g product sensitivity
230, 241, 252	0.187	0.09	deg/hr	Gyro	Bias drift
263, 266, 269	0.627	0.16	deg/hr/g	Gyro	Input axis g sensitive drift
264, 267, 270	0.627	0.16	deg/hr/g	Gyro	Spin axis g sensitive drift
265, 268, 271	0.02	0	deg/hr/g	Gyro	Output axis g sensitive drift
275, 281, 287	0.04	0.04	$deg/hr/g^2$	Gyro	Anisoelastic drift
290, 294, 298	57	26	ppm	Gyro	Scale factor
291, 292, 293	10	10	arc sec	Gyro	Gyro input axis rotations toward each of other two axes
295, 296, 297	10	10	arc sec	Gyro	Gyro input axis rotations toward each of other two axes

angles in the apogee measurement and for the yaw angle in the perigee measurement, with the earth sensor being used for the remaining angles. See Subsection 5.3 for details.

7.3.2 Method of Analysis

7.3.2.1 Error Analysis Program

The error analysis program (Ref 7-1) used for these analyses is capable of analyzing either strapdown or gimbaled inertial guidance systems in space or missile applications. The primary function of the program is to integrate the error differential equation for each error source, thus giving rise to a 9 x 1 error sensitivity vector for each error source. The first three components of the sensitivity vector represent the partial derivatives of position error with respect to the error source. The next three components represent the partial derivatives of velocity error with respect to the error source. The last three components represent the partial derivatives of orientation error with respect to the error source. The sensitivity vectors can be considered collectively to constitute the columns of a 9 x n sensitivity matrix.

Statistical data concerning system operation can be derived from the sensitivity matrix by various operations. System errors in various coordinate systems can also be computed by transforming the individual columns of the sensitivity matrix to the desired coordinate system. The initial value of the sensitivity matrix corresponds to various initial alignment schemes or to previous runs made with the error analysis program. Thus, the computation and manipulation of the sensitivity matrix is the central problem in the error analysis of an inertial guidance system. The program accounts for error source correlation for several initial alignment modes such as self-leveling using inertial system accelerometers, gyrocompassing, or external optical alignment. Also, nonorthogonal instrument input axis orientations are optional; and single-axis platform or pendulous integrating gyro accelerometer strapdown modes are available.

In all types of inertial guidance systems the gyros provide an angular reference for measurements made by the accelerometers. The angular reference may be physical (in the case of a gimbaled platform system) or analytic (in the case of a strapdown system). For a strapdown inertial

system, the accelerometer outputs are transformed to the computational coordinates by multiplication by the direction cosine matrix. It is assumed in the error analysis program that the navigation system computer makes no computational errors (roundoff or truncation) and that there are no gravity modeling errors.

7.3.2.2 Sensitivity Matrix Generation

The general procedure for the calculation of an error sensitivity matrix is described in Section 7.3.2.1. This section describes the special techniques used to accomplish the 185 km coast period, the optical attitude updates, and the time update.

First Crossing Burn—No Updates. The mission in which the perigee burn occurs at the first equatorial crossing and in which no attitude updates are made is run first. The sensitivity matrix is calculated 10 min before the perigee burn and 10 min before the apogee burn for use in the later missions.

Introducing Coast Orbits. The sensitivity matrix calculated 10 min before the perigee burn is taken as the starting point. The sensitivities are then propagated analytically through an integral number of coast orbits and used as initial values for the rest of the mission.

Introducing Attitude Updates. The perigee and apogee optical attitude updates are introduced by zeroing all of the attitude errors in the appropriate sensitivity matrix followed by the insertion of three attitude error sources in body coordinates to represent the optical sensor errors. The sensitivities are then propagated in the normal manner to the next update time or to the end of the mission.

Introducing Time Updates. The synchronous orbit mission may remain in a 185 km orbit up to eight revolutions to facilitate longitude synchronization. During this time, the position and velocity errors build up excessively, requiring some kind of update. A full position and velocity update would reduce the final errors in synchronous orbit caused by position and velocity errors at the end of coast to very small levels, where they will be dominated by the effects of attitude errors.

Under these circumstances, it seems more interesting to investigate a modified update which has the advantage of onboard computational simplicity. The rationale for the modified update lies in the fact that, to first

order, the deviation of the actual coast orbit from the nominal coast orbit remains constant during the eight-orbit period. The growth of position and velocity errors during this period arises only from displacement of the actual vehicle from its nominal location along the orbit because of the error in the period of the actual orbit. Therefore, if the perigee burn initiation time is modified in such a manner that the along track position error between the actual vehicle at the actual burn time and its nominal location at the nominal burn time is zero, the final error in synchronous orbit caused by position and velocity errors in the coast phase should be no worse than in the case where perigee burn occurs at the first equatorial crossing.

If such a time-only reset were to be implemented, it only would be necessary to initiate position and velocity to their nominal values at the start of perigee burn. The nominal optical sensor angles might require modification to account for the time shift.

Derivation of Time Updates. Let $\bar{x}$ represent the state vector of the vehicle comprising position and velocity with components in an earth-centered inertial coordinate system.

$$\bar{x} = \begin{pmatrix} \bar{r} \\ \bar{v} \end{pmatrix} \tag{7-1}$$

If $\bar{x}_o$ is the nominal state vector and $\Delta\bar{x}$ is the perturbation state vector, then at nominal perigee burn time, t_o,

$$\bar{x}(t_o) = \bar{x}_o(t_o) + \Delta\bar{x}(t_o) \tag{7-2}$$

If Δt is the time correction, then the actual perigee burn time, t, is

$$t = t_o + \Delta t \tag{7-3}$$

and

$$\bar{x}(t) = \bar{x}_o(t) + \Delta\bar{x}(t) \tag{7-4}$$

The perturbation state vector after the time update is the actual state vector at the actual burn time minus the nominal state vector at the nominal burn time.

$$\Delta\bar{x}^*(t) \quad \bar{x}(t) - \bar{x}_o(t_o) \tag{7-5}$$

Introducing (7-4) into (7-5) gives

$$\Delta\bar{x}^*(t) = \bar{x}_o(t) - \bar{x}_o(t_o) + \Delta\bar{x}(t) \qquad (7-6)$$

Since Δt and $\Delta\bar{x}$ are first order quantities, the difference between $\Delta\bar{x}(t_o + \Delta t)$ and $\Delta\bar{x}(t_o)$ is second order. Therefore, to first order, (7-6) becomes

$$\Delta\bar{x}^* = \bar{x}(t) - \bar{x}(t_o) + \Delta\bar{x} \qquad (7-7)$$

where the zero subscripts are dropped from the nominal state vector and the time arguments are dropped from the perturbation vectors and are assumed to be t_o.

For a circular orbit, the desired change in the firing time is given by the negative of the downrange component of position error divided by the vehicle velocity.

$$\Delta t_d = - \frac{\bar{r} \cdot \left(\frac{\bar{v}}{v}\right)}{v} \qquad (7-8)$$

The actual change in the firing time is given by the desired change plus any error introduced by the updating procedure.

$$\Delta t = \Delta t_d + \Delta t_e \qquad (7-9)$$

Expressed in matrix form,

$$\Delta t = \left[- \frac{v_x}{v^2} - \frac{v_y}{v^2} - \frac{v_z}{v^2} \right] \begin{Bmatrix} \Delta r_x \\ \Delta r_y \\ \Delta r_z \end{Bmatrix} + \Delta t_e \qquad (7-10)$$

The nominal position and velocity at the actual burn time are

$$\bar{r}(t) = \bar{r}(t_o) + \bar{v}(t_o)\Delta t \qquad (7-11)$$

$$\bar{v}(t) = \bar{v}(t_o) - \bar{r}(t_o)\omega^2 \Delta t \qquad (7-12)$$

where ω is the orbital angular velocity

$$\omega = v/r \qquad (7-13)$$

From (7-1), (7-7), (7-11), and (7-12)

$$\Delta\bar{r}^* = \bar{v}(t_o)\,\Delta t + \Delta\bar{r} \tag{7-14}$$

$$\Delta\bar{v}^* = -\bar{r}(t_o)\omega^2\Delta t + \Delta\bar{v} \tag{7-15}$$

In matrix form,

$$\Delta\bar{r}^* = \begin{Bmatrix} v_x \\ v_y \\ v_z \end{Bmatrix} \left[-\frac{v_x}{v^2} \; -\frac{v_y}{v^2} \; -\frac{v_z}{v^2} \right] \begin{Bmatrix} \Delta r_x \\ \Delta r_y \\ \Delta r_z \end{Bmatrix} + \begin{Bmatrix} v_x \\ v_y \\ v_z \end{Bmatrix} \Delta t_e + \begin{Bmatrix} \Delta r_x \\ \Delta r_y \\ \Delta r_z \end{Bmatrix} \tag{7-16}$$

$$\Delta\bar{v}^* = \begin{Bmatrix} r_x \\ r_y \\ r_z \end{Bmatrix} \left[\frac{v_x}{r^2} \; \frac{v_y}{r^2} \; \frac{v_z}{r^2} \right] \begin{Bmatrix} \Delta r_x \\ \Delta r_y \\ \Delta r_z \end{Bmatrix} - \begin{Bmatrix} r_x \\ r_y \\ r_z \end{Bmatrix} \omega^2 \Delta t_e + \begin{Bmatrix} \Delta v_x \\ \Delta v_y \\ \Delta v_z \end{Bmatrix} \tag{7-17}$$

Expanding and combining (7-16) and (7-17) gives

$$\Delta\bar{x}^* = \begin{bmatrix} 1 - \frac{v_x^2}{v^2} & -\frac{v_x v_y}{v^2} & -\frac{v_x v_z}{v^2} & 0 & 0 & 0 \\ -\frac{v_y v_x}{v^2} & 1 - \frac{v_y^2}{v^2} & -\frac{v_y v_z}{v^2} & 0 & 0 & 0 \\ -\frac{v_z v_x}{v^2} & -\frac{v_z v_y}{v^2} & 1 - \frac{v_z^2}{v^2} & 0 & 0 & 0 \\ \frac{r_x v_x}{r^2} & \frac{r_x v_y}{r^2} & \frac{r_x v_z}{r^2} & 1 & 0 & 0 \\ \frac{r_y v_x}{r^2} & \frac{r_y v_y}{r^2} & \frac{r_y v_z}{r^2} & 0 & 1 & 0 \\ \frac{r_z v_x}{r^2} & \frac{r_z v_y}{r^2} & \frac{r_z v_z}{r^2} & 0 & 0 & 1 \end{bmatrix} \Delta\bar{x} + \begin{Bmatrix} v_x \\ v_y \\ v_z \\ -r_x\omega^2 \\ -r_y\omega^2 \\ -r_z\omega^2 \end{Bmatrix} \Delta t_e \tag{7-18}$$

In the error analysis program, the perturbation state vector is given by

$$\Delta\bar{x}' = \sum_{i=1}^{n} \bar{s}_i' \epsilon_i \tag{7-19}$$

where the $\bar{s}_i'$ are sensitivity vectors and the ϵ_i are the individual error sources. The vectors are shown primed because in the error analysis program they are 9-vectors, the last three states comprising the three orientation perturbations. Since attitude will be updated at the same time as time, these states can be ignored. Let $\Delta\bar{x}$ represent the first six states of $\Delta\bar{x}'$ and $\bar{s}_i$ the first six components of $\bar{s}_i'$. Then

$$\Delta\bar{x} = \sum_{i=1}^{n} \bar{s}_i \epsilon_i \tag{7-20}$$

Rewrite (7-18) as

$$\Delta\bar{x}^* = [M]\,\Delta\bar{x} + \bar{s}^*_{n+1}\,\epsilon_{n+1} \tag{7-21}$$

where:

$[M]$ is the matrix

$\bar{s}^*_{n+1}$ is the column vector and

ϵ_{n+1} equals Δt_e.

Substitution of (7-20) in (7-21) gives

$$\Delta\bar{x}^* = [M] \sum_{i=1}^{n} \bar{s}_i \epsilon_i + \bar{s}^*_{n+1}\,\epsilon_{n+1} \tag{7-22}$$

which becomes

$$\Delta\bar{x}^* = \sum_{i=1}^{n} [M]\,\bar{s}_i \epsilon_i + \bar{s}^*_{n+1}\,\epsilon_{n+1} \tag{7-23}$$

If we let

$$\bar{s}_i^* = [M]\,\bar{s}_i \qquad i = 1, 2 \cdots n \tag{7-24}$$

then

$$\Delta\bar{x}^* = \sum_{i=1}^{n+1} \bar{s}_i^* \epsilon_i \tag{7-25}$$

which is in the form of (7-20). Thus to accomplish the time update, each sensitivity vector must be multiplied by the matrix [M] and a single additional sensitivity vector must be added.

Circularization of Orbit. The position and velocity at injection do not correspond precisely to those required for a circular orbit because of the oblateness effects in the trajectory program. Since the above calculations assume a circular orbit, it is necessary to calculate an equivalent circular orbit before commencing them.

The semimajor axis of the actual orbit is given by

$$\frac{1}{a} = \frac{2}{r} - \frac{v^2}{\mu} \tag{7-26}$$

The new orbit is to have the same period as the old orbit. Therefore

$$r' = a \tag{7-27}$$

The initial position vector of the two orbits must have the same direction

$$\bar{r}' = \frac{a\bar{r}}{r} \tag{7-28}$$

The velocity in a circular orbit is given by

$$v' = \sqrt{\mu/a} \tag{7-29}$$

And its direction must lie in the orbital plane, perpendicular to $\underline{r}$.

$$\bar{v}' = v' \frac{(\bar{r} \times \bar{v}) \times \bar{r}}{|(\bar{r} \times \bar{v}) \times \bar{r}|} \tag{7-30}$$

The $\bar{r}'$ and $\bar{v}'$ thus obtained are used in the time reset calculations.

Coast—Time Reset Theorem. The time reset calculations require the subtraction of nearly equal quantities. This situation can cause difficulties because of roundoff and because the subtraction process enhances the errors in the state transition matrix used for the propagation of errors through the coast phase. These errors exist because of the secant method

used to obtain the state transition matrix, and because the position and velocity in the error analysis program do not exactly correspond to a circular orbit.

This cause of computational error is reduced by proving that the errors following a time reset at the end of an n-orbit circular coast are the same as the errors following a time reset at the beginning of the coast. Thus the necessity for the propagation of errors through the eight-orbit coast period is eliminated for the cases where a time reset is made.

The derivation is simplest if an RTN inertial coordinate system is used. For this case [M] of Equation (7-21) becomes

$$[M] = \begin{bmatrix} 1 & 0 & 0 & 0 & 0 & 0 \\ 0 & 0 & 0 & 0 & 0 & 0 \\ 0 & 0 & 1 & 0 & 0 & 0 \\ 0 & \omega & 0 & 1 & 0 & 0 \\ 0 & 0 & 0 & 0 & 1 & 0 \\ 0 & 0 & 0 & 0 & 0 & 1 \end{bmatrix} \tag{7-31}$$

The state transition matrix for a circular orbit for n periods, in RTN inertial coordinates is

$$[\Phi] = \begin{bmatrix} 1 & 0 & 0 & 0 & 0 & 0 \\ -6\pi n & 1 & 0 & 0 & -6\pi n/\omega & 0 \\ 0 & 0 & 1 & 0 & 0 & 0 \\ 6\pi n\omega & 0 & 0 & 1 & 6\pi n & 0 \\ 0 & 0 & 0 & 0 & 1 & 0 \\ 0 & 0 & 0 & 0 & 0 & 1 \end{bmatrix} \tag{7-32}$$

Direct calculation shows that

$$[M][\Phi] = [M] \tag{7-33}$$

Thus if a time reset is performed, the state transition matrix for n orbits can simply be ignored with a resultant saving in computational accuracy. Fortunately an orientation reset is accomplished at the same time, so that all of the orientation errors are set equal to zero. Therefore, they need not be propagated through the n orbits either.

Time Reset Errors. It is assumed that the vehicle position along its orbit at the update time can be established to one nautical mile. The corresponding time error is then 0.238 sec. This assumption is conservative, but may not be as conservative as it first appears because it allows for the following factors:

- Relatively poor tracking coverage at 185 km altitude
- Air density variations
- Uncertainty in ballistic coefficient
- Possibility of no coverage during one or more orbits preceding burn
- Possibility burn may occur 180 deg from part of orbit where most recent tracking data has been obtained.

If an on board navigation system were used the coverage problems would be eliminated and replaced by problems such as the inherent accuracy of onboard techniques. For this case one nautical mile is not so conservative.

7.3.2.3 Synchronization Velocity Requirement

The delta-velocity required to synchronize the orbit is calculated by a Monte Carlo technique for a 95 percent probability of successful synchronization.

Generation of Normalized Error Quantities. The three components in RTN coordinates of position error and the three components of velocity error (in the order: altitude, downrange, crossrange) are normalized by dividing them by their nominal values. Let

$$\{\Delta x\} = \begin{bmatrix} \Delta r_x \\ \Delta r_y \\ \Delta r_z \\ \Delta v_x \\ \Delta v_y \\ \Delta v_z \end{bmatrix} \qquad (7\text{-}34)$$

and

$$[A] = \begin{bmatrix} \frac{1}{r} & 0 & 0 & 0 & 0 & 0 \\ 0 & \frac{1}{r} & 0 & 0 & 0 & 0 \\ 0 & 0 & \frac{1}{r} & 0 & 0 & 0 \\ 0 & 0 & 0 & \frac{1}{v} & 0 & 0 \\ 0 & 0 & 0 & 0 & \frac{1}{v} & 0 \\ 0 & 0 & 0 & 0 & 0 & \frac{1}{v} \end{bmatrix} \tag{7-35}$$

where r and v are the nominal values of position and velocity magnitude. Then the normalized errors are

$$\{\epsilon\} = [A]\{\Delta x\} \tag{7-36}$$

If $[C]$ is the covariance matrix of $\{\Delta x\}$ as obtained from the error analysis program and $[D]$ is the covariance matrix of the normalized errors, then

$$[D] = [A][C][A^T] \tag{7-37}$$

The vector $\{\epsilon\}$ must be generated by pseudo random numbers with the covariance matrix $[D]$. First find the orthogonal matrix $[E]$ such that

$$[D] = [E][F][E^T] \tag{7-38}$$

where $[F]$ is diagonal. Then let

$$[B] = [E]\left[F^{1/2}\right] \tag{7-39}$$

We then have

$$[D] = [B][I][B^T] \tag{7-40}$$

If $\{y\}$ is a vector of independent Gaussian random numbers of zero mean and unit standard deviation, then the covariance matrix of $\{y\}$ is the identity matrix. If we let

$$\{\epsilon\} = [B]\{y\} \tag{7-41}$$

then the covariance matrix of $\{\epsilon\}$ is given by Equation (7-40) as required.

Calculation of Delta-Velocity Requirement. In order to calculate a figure of merit for each different system configuration, it is assumed that the payload thruster is used to correct the orbit so that it is circular, synchronous, and has zero inclination, and so that the vehicle is at the proper longitude. The correction profile is assumed to be as suggested in Section 2.3.2:

1) Perform a Hohmann transfer from the perigee of the imperfect orbit to synchronous altitude

2) Circularize when synchronous altitude is reached

3) Change the inclination to zero where the orbit intersects the equatorial plane

4) Synchronize to the correct longitude.

The above profile is not necessarily optimum, but permits the use of the following simple calculations.

The individual velocity increments for each of these burns were derived in Section 2.3.2. Using the notation of this section, the v_i are rewritten as

$$\Delta v_1 \cong -v\left\{0.5\epsilon_1 + 0.5\epsilon_5 + 0.25\left[(\epsilon_1 + 2\epsilon_5)^2 + \epsilon_4^2\right]^{1/2}\right\} \tag{7-42}$$

$$\Delta v_2 \cong -v\left\{0.5\epsilon_1 + 0.5\epsilon_5 - 0.25\left[(\epsilon_1 + 2\epsilon_5)^2 + \epsilon_4^2\right]^{1/2}\right\} \tag{7-43}$$

$$\Delta v_3 \cong v\left(\epsilon_3^2 + \epsilon_6^2\right)^{1/2} \tag{7-44}$$

$$\Delta v_4 \cong \frac{\epsilon_2}{3\pi n} \tag{7-45}$$

where n is the number of orbits allowed for resynchronization. The total Δv is given by

$$\Delta V = \sum_{i=1}^{4} \left|\Delta v_i\right| \tag{7-46}$$

Monte Carlo Technique. One thousand sets of 6 random numbers are generated for each case. For each set (7-41) through (7-46) are performed.

The number of times ΔV falls within each 1.5 m/sec band from 0 to 150 m/sec is counted. The cumulative distribution is then calculated and interpolated to obtain the 95 percent ΔV. The number of synchronization periods, n, is taken as one.

7.3.3 Results and Conclusions

Table 7-II presents the twelve runs made. It gives the run number, the number of extra complete 185 km coasting orbits inserted before the perigee update, the strapdown system used, and whether or not prelaunch calibration, perigee attitude update, apogee attitude update and time update were performed.

Table 7-IIIA presents the results of these runs. One sigma position, velocity, and orientation errors at injection into synchronous orbit are presented in TRN (radial, tangential, normal) coordinates along with the ΔV required for 95 percent probability of successful synchronization. The same results are presented in ECI (earth centered inertial)(coordinates) in Table 7-IIIB.

For each component of position, velocity, and orientation the error sources are scanned to determine which one makes the largest contribution. The number of this error source is entered in Table 7-IV. The amount of the contribution is then normalized and substituted into an Equation (7-46) with the other ϵ_i taken as zero. The results for all six components of position and velocity are compared, and the number of the error source in the column corresponding to the component giving the largest ΔV is underlined. Thus, the error sources given in Table 7-IV, especially the underlined ones, are those most in need of improvement, if the performance of a particular run is considered inadequate. See Table 7-I for an identification of the error sources by number. The contributions of the individual error sources to position, velocity, and orientation errors are shown in Tables 7-V through 7-VIII for the most interesting cases; that is for the even numbered cases which exhibit significantly smaller ΔV requirements. Error sources contributing less than 0.15 m/sec to the velocity errors were dropped out of the table.

Table 7-II. Synchronous Mission Runs

Run Number	Coast Orbits	System Number	Prelaunch Calibration	Time Update	Attitude Update	
					Perigee	Apogee
1	0	166	No	No	No	No
2	0	166	No	No	No	Yes
3	0	166	Yes	No	No	No
4	0	166	Yes	No	No	Yes
5	0	266	No	No	No	No
6	0	266	No	No	No	Yes
7	8	166	No	No	Yes	Yes
8	8	166	No	Yes	Yes	Yes
9	8	166	Yes	No	Yes	Yes
10	8	166	Yes	Yes	Yes	Yes
11	8	266	No	No	Yes	Yes
12	8	266	No	Yes	Yes	Yes

Table 7-IIIA. Error Analysis Results for the Synchronous Mission (RTN Coordinates)

Run No.	Position (km)			Velocity (m/sec)			Orientation (arc sec)			95% ΔV (m/sec)
	R	T	N	R	T	N	Yaw	Roll	Pitch	
1	56.5	41.8	35.7	26.7	11.2	23.4	2900	3110	3670	73
2	56.7	41.8	35.7	7.4	1.9	1.9	176	505	308	13
3	49.7	20.8	19.8	26.4	11.0	23.6	2930	3090	3670	75
4	50.0	20.8	19.9	6.2	1.8	1.6	176	490	307	9
5	30.2	20.3	14.0	13.0	5.2	11.1	1380	1500	1760	35
6	30.3	20.3	14.1	5.2	1.1	1.2	136	482	285	8
7	513	793	430	83.5	14.5	8.1	176	505	308	163
8	59.1	128	73.8	9.9	2.0	2.1	176	505	308	22
9	354	534	290	56.7	10.2	5.8	176	490	307	109
10	52.8	122	68	9.1	1.9	2.1	176	490	307	19
11	259	408	222	42.7	7.4	4.4	136	482	285	83
12	33.2	121	66	8.0	1.3	1.8	136	482	285	19

Table 7-IIIB. Error Analysis Results for the Synchronous Mission (ECI Coordinates)

Run No.	Position (km)			Velocity (m/sec)			Orientation (arc sec)			95% ΔV (m/sec)
	X	Y	Z	X	Y	Z	X	Y	Z	
1	60.1	36.0	35.4	26.3	11.6	23.3	2900	3100	3670	73
2	60.4	36.0	35.7	7.5	1.3	1.9	187	501	308	13
3	51.2	18.4	19.8	26.1	11.6	27.5	2920	3090	3670	75
4	51.5	18.4	19.9	6.3	1.3	1.6	186	487	307	9
5	32.3	16.8	14.1	12.7	5.5	11.0	1380	1490	1760	35
6	32.3	16.8	14.1	5.2	0.9	1.2	148	479	285	8
7	634	701	430	84.8	1.6	8.1	187	501	308	163
8	71.3	121	73.8	10.0	1.5	2.1	187	501	308	22
9	436	472	289	57.6	1.6	5.8	186	487	307	109
10	64.0	117	68.0	9.1	1.5	2.1	186	487	307	19
11	314	357	218	42.4	1.3	4.3	148	479	285	83
12	46.3	116	65.9	8.0	1.3	1.8	148	479	285	19

Table 7-IV. Identification of Largest Error Contributors For Each Run

Run Number	Position			Velocity			Orientation		
	R	T	N	R	T	N	Yaw	Roll	Pitch
1	241	73	263	230	252	252	252	230	241
2	241	73	263	73	241	20	252	10	10
3	241	9	263	230	252	252	252	230	241
4	241	9	263	10	241	20	252	10	10
5	241	9	9	230	252	252	252	230	241
6	241	9	9	10	241	20	20	10	10
7	73	73	73	73	73	73	252	10	10
8	241	31	31	31	241	20	252	10	10
9	241	241	241	241	241	241	252	10	10
10	241	31	31	31	241	20	252	10	10
11	241	9	9	9	9	9	20	10	10
12	241	31	31	31	241	20	20	10	10

Table 7-V. Summary of Position, Velocity, and Orientation Errors — Synchronous Orbit Injection Runs 2 and 4

Error Source	Position (km)			Velocity (m/sec)			Orientation (arc sec)		
	R	T	N	R	T	N	Yaw	Roll	Pitch
9	-19.1	15.2	8.2	-2.4	0.6	0.3	0	0	0
10	0.1	0	0	3.8	-0.1	0	14	475	257
20	0	0	0	0	-0.5	-1.0	120	-3	-2
30	0	0	0	-0.6	0	0	0	57	-106
40	5.4	-7.0	-3.8	0.8	-0.1	-0.1	0	0	0
62	-1.1	1.0	0.5	-0.2	0	0	0	0	0
73†	27.1	-34.8	-18.8	4.2	-0.6	-0.4	0	0	0
73††	10.3	-13.2	-7.2	1.6	-0.2	-0.2	0	0	0
230	-1.1	-1.5	4.6	0.7	-0.2	0.4	2	113	47
241	42.8	-2.1	-1.1	3.4	-1.4	-0.8	0	47	-113
252	0.4	3.9	-8.3	0.1	0.5	0.9	-128	2	1
263†	-2.7	-11.6	26.3	-0.3	-0.4	0.9	2	107	-48
263††	-1.6	-6.7	15.2	-0.2	-0.2	0.5	1	62	-28
268	8.3	-4.1	-2.3	1.0	-0.3	-0.2	0	-2	-3
294	-13.3	8.3	4.5	-1.6	0.4	0.2	0	0	0

†Run 2 ††Run 4

Table 7-VI. Summary of Error Analysis Results — Synchronous Orbit Injection Run 6

Error Source	Position (km)			Velocity (m/sec)			Orientation (arc sec)		
	R	T	N	R	T	N	Yaw	Roll	Pitch
9	-19.1	15.2	8.2	-2.4	0.6	0.3	0	0	0
10	0.1	0	0	3.8	-0.1	0	14	475	257
20	0	0	0	0	-0.5	-1.0	120	-3	-2
30	0	0	0	-0.6	0	0	0	57	-106
40	3.6	-4.6	-2.5	0.6	-0.1	-0.1	0	0	0
73	8.7	-11.1	-6.0	1.3	-0.2	-0.2	0	0	0
230	-0.5	-0.7	2.2	0.3	-0.1	-0.2	1	54	23
241	20.6	-1.0	-0.5	1.6	-0.7	-0.4	0	23	-54
252	0.2	1.9	-4.0	0	0.2	0.4	-62	1	0
263	-0.7	-3.0	6.7	-0.1	-0.2	-0.2	1	27	-12
294	-6.1	3.8	2.0	-0.7	0.2	0.1	0	0	0

Table 7-VII. Summary of Error Analysis Results — Synchronous Orbit Injection Runs 8 and 10

Error Source	Position (km)			Velocity (m/sec)			Orientation (arc sec)		
	R	T	N	R	T	N	Yaw	Roll	Pitch
9	-19.2	18.3	9.9	-2.6	0.6	0.3	0	0	0
10	0.1	0	0	3.8	-0.1	0	14	475	257
11	-3.7	2.1	1.9	-0.5	-0.6	1.4	0	0	0
20	0	0	0	0	-0.5	-1.0	120	-3	-2
30	0	0	0	-0.6	0	0	0	57	-106
31	-12.1	117.6	63.7	-5.9	0.3	0.2	0	0	0
39	0.3	4.4	2.4	-0.2	0	0	0	0	0
40	5.4	-7.0	-3.8	0.8	-0.1	-0.1	0	0	0
62	-1.1	1.5	0.8	-0.2	0	0	0	0	0
73†	27.1	-35.1	-19.0	4.2	-0.6	-0.4	0	0	0
73††	10.3	-13.3	-7.2	1.6	-0.2	-0.2	0	0	0
230	-0.3	-2.0	4.2	0.8	-0.1	-0.1	2	113	47
241	44.2	-22.0	-11.9	4.3	-1.4	-0.8	0	47	-113
252	0.5	3.9	-8.3	0.1	0.5	0.8	-128	2	1
268	8.4	-6.5	-3.5	1.0	-0.3	-0.2	0	-2	-3
294	-13.3	10.2	5.5	-1.7	0.4	0.2	0	0	0

† Run 8 †† Run 10

The following conclusions were reached for the synchronous orbit mission:

- Prelaunch calibration is desirable
- Apogee attitude update is necessary for all missions
- Perigee attitude update and time update are necessary for missions with a long 185 km coast period
- The performance of the TG-166 system for long coasts and of the more accurate TG-266 system for both short and long coasts is limited by the horizon tracker errors
- Time update errors of the magnitude used are not significant compared to other error sources
- A full position and velocity update would not provide significant improvement unless the attitude update errors were reduced.

Table 7-VIII. Summary of Error Analysis Results — Synchronous Orbit Injection Run 12

Error Source	Position (km)			Velocity (m/sec)			Orientation (arc sec)		
	R	T	N	R	T	N	Yaw	Roll	Pitch
9	-19.2	18.3	9.9	-2.6	0.6	0.3	0	0	0
10	0.1	0	0	3.8	-0.1	0	14	475	257
11	-3.7	2.1	1.9	-0.5	-0.6	1.4	0	0	0
20	0	0	0	0	-0.5	-1.0	120	-3	-2
30	0	0	0	-0.6	0	0	0	57	-106
31	-12.1	117.6	63.7	-5.9	0.3	0.2	0	0	0
39	0.3	4.4	2.4	-0.2	0	0	0	0	0
40	3.6	-4.7	-2.5	0.5	-0.1	-0.1	0	0	0
73	8.7	-11.2	-6.1	1.3	-0.2	-0.2	0	0	0
230	-0.2	-1.0	2.0	0.4	0	0.1	1	54	23
241	21.3	-10.6	-5.7	2.1	-0.7	-0.4	0	23	-54
252	0.2	1.9	-4.0	0	0.3	0.4	-62	1	0
294	-6.1	4.7	2.5	-0.8	0.2	0.1	0	0	0

7.4 ERROR ANALYSIS FOR TRANSLUNAR ORBIT INJECTION

The lunar mission is analyzed from liftoff to injection into the earth-moon transfer orbit. The performance of the TG-166 and TG-266 system is compared with that of a Centaur gimbaled inertial guidance system. The ΔV required for a 95 percent probability of successfully performing the midcourse correction is taken as a figure of merit.

7.4.1 Error Models

The error models for the TG-166 and TG-266 systems are presented in Table 7-I. Table 7-IX presents the error model for the Centaur AC-10 gimbaled IMU as obtained from Ref 7-2. Figure 7-1 shows the Centaur gyro and accelerometer orientation at launch.

7.4.2 Method of Analysis

The error analysis program was used to calculate both the errors at injection into translunar orbit and the delta velocity required for the midcourse correction.

Table 7-IX. Error Model for the Centaur IMU

Error Source	Value	Units	Type	For Centaur IMU (from Ref 7-2) Description
1	3	m	Initial	Vertical position
2, 3	15.3	m	Initial	East, north position
7	18.6	sec	Initial	Azimuth error
8, 9	11.1	sec	Initial	Level errors
40, 51, 62	42	μg	Accelerometer	Bias
41	24	μg	Accelerometer	u accelerometer in-flight bias
52	26	μg	Accelerometer	v accelerometer in-flight bias
63	29	μg	Accelerometer	w accelerometer in-flight bias
73, 77, 81	51	μg/g	Accelerometer	Scale factor
76	10.3	sec	Accelerometer	v accelerometer input axis rotation toward u axis
79	10.3	sec	Accelerometer	w accelerometer input axis rotation toward u axis
80	11.3	sec	Accelerometer	w accelerometer input axis rotation toward v axis
88, 94, 100	9.4	$\mu g/g^2$	Accelerometer	Scale factor g proportional nonlinearity
90, 96, 102	9	$\mu g/g^2$	Accelerometer	Output axis g^2 sensitivity
91, 97, 103	13	$\mu g/g^2$	Accelerometer	Input-pendulous g product sensitivity
92, 98, 104	12	$\mu g/g^2$	Accelerometer	Input-output g product sensivitity
93, 99, 105	8	$\mu g/g^2$	Accelerometer	Pendulous-output g product sensitivity
230	0.084	deg/hr	Gyro	u gyro bias drift
241	0.094	deg/hr	Gyro	w gyro bias drift
252	0.093	deg/hr	Gyro	v gyro bias drift
263	0.106	deg/hr/g	Gyro	u gyro input g sensitive drift
266	0.114	deg/hr/g	Gyro	w gyro input g sensitive drift
269	0.101	deg/hr/g	Gyro	v gyro input g sensitive drift
264	0.173	deg/hr/g	Gyro	u gyro spin g sensitive drift
267	0.177	deg/hr/g	Gyro	w gyro spin g sensitive drift
270	0.190	deg/hr/g	Gyro	v gyro spin g sensitive drift
275, 281, 287	0.009	$deg/hr/g^2$	Gyro	Input-spin g product drift

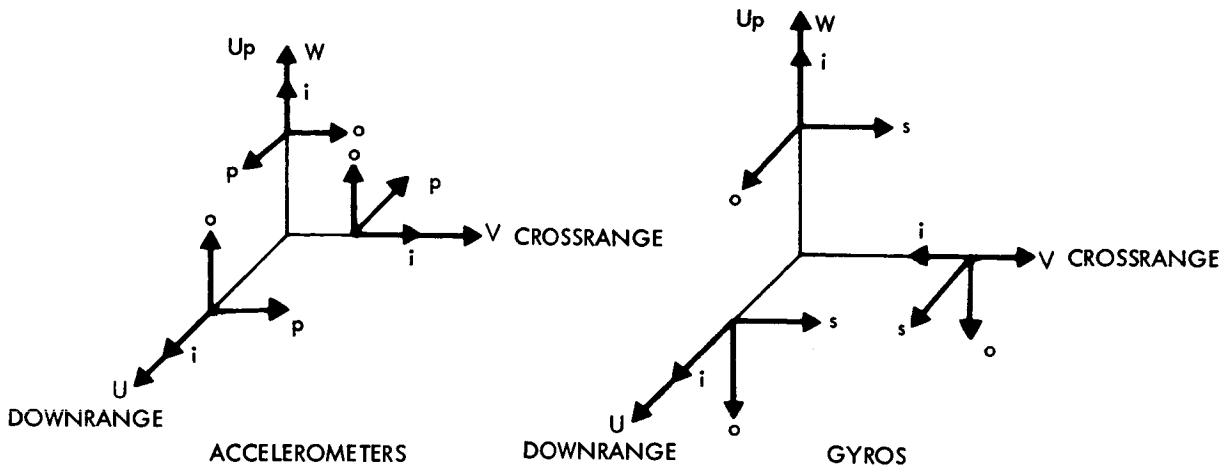

Figure 7-1. Centaur Sensor Orientation

7.4.3 Results and Conclusions

Table 7-X identifies the four runs made. It gives the inertial subsystem error model used and whether or not prelaunch calibration is performed. Table 7-XI summarizes the one-sigma position, velocity and the orientation errors at injection into earth-moon transfer orbit, and the ΔV required for 95 percent probability of successfully performing the midcourse correction. The errors are presented in RTN (radial, tangential, normal) coordinates. The ΔV requirement is given for the two cases of variable time of arrival guidance and fixed time of arrival guidance.

Table 7-X. Lunar Orbit Injection Error Analysis Runs

Run Number	Guidance System	Prelaunch Calibration
1	TG 166	No
2	TG 166	Yes
3	TG 266	No
4	AC 10	No

For each component of position, velocity, and orientation, and for the two cases of ΔV, the error sources are scanned to determine which one makes the largest contribution. The number of this error source is entered in Table 7-XII. See Tables 7-I and 7-IX for an identification of

Table 7-XIA. Error Analysis Results for the Lunar Mission (RTN Coordinates)

Run No.	System No.	Pre-launch Cal.	Position (km)			Velocity (m/sec)			Orientation (arc sec)			95% ΔV (m/sec)	
			R	T	N	R	T	N	Yaw	Roll	Pitch	Variable Time	Fixed Time
1	TG-166	No	1.8	3.5	5.6	7.5	2.9	9.0	568	233	304	50	62
2	TG-166	Yes	1.4	3.4	3.3	7.2	2.8	4.8	291	233	304	49	60
3	TG-266	No	0.8	1.9	1.8	3.6	1.4	2.8	175	114	147	25	31
4	A/C-10	No	1.5	3.4	1.5	5.0	2.4	2.4	161	152	150	37	48

Table 7-XIB. Error Analysis Results for the Lunar Mission (ECI Coordinates)

Run No.	System No.	Pre-launch Cal.	Position (km)			Velocity (m/sec)			Orientation (arc sec)		
			X	Y	Z	X	Y	Z	X	Y	Z
1	TG-166	No	2.7	3.9	5.0	8.1	4.8	7.7	550	253	319
2	TG-166	Yes	2.1	3.2	3.0	7.5	3.0	4.1	299	249	283
3	TG-266	No	1.2	1.8	1.7	3.8	1.7	2.3	172	123	143
4	A/C-10	No	2.0	2.9	1.8	5.2	2.1	2.1	160	152	152

the error sources by number. The error contribution of the individual error sources to position, velocity and delta velocity errors for the runs are shown in Tables 7-XIII through 7-XV. Error sources contributing less than 0.3 m/sec to the velocity errors were dropped out of the tables.

The following conclusions were reached for the translunar orbit injection mission:

- Prelaunch calibration is desirable
- The most significant error sources are pitch gyro bias and roll gyro mass unbalance for the strapdown systems and v-gyro mass unbalance for the gimbaled system
- All resulting errors are well within the requirements summarized in Paragraph 2.5.2.

Table 7-XII. Most Significant Error Sources†

Run Number	System Number	Prelaunch Calibration	Position (km)			Velocity (m/sec)			Orientation (arc sec)			95 Percent ΔV (m/sec)	
			R	T	N	R	T	N	Yaw	Roll	Pitch	Variable Time	Fixed Time
1	166	No	241	241	263	241	241	263	263	252	241	241	241
2	166	Yes	241	241	263	241	241	263	263	252	241	241	241
3	266	No	241	241	263	241	241	263	263	252	241	241	241
4	AC10	No	62	270	241	252	270	230	230	241	252	270	270

†See Table 7-I for Identification of Error Sources

Table 7-XIII. Error Analysis Results – Lunar Injection Runs 1 and 2

Error Source	Position (km)			Velocity (m/sec)			Delta Velocity (m/sec)					
	R	T	N	R	T	N	Variable Time			Fixed Time		
7	0	0	-0.6	0	0	-0.1	0.8	0.2	0.8	1.3	-0.2	0.5
8	0	-0.3	0.2	0.3	-0.2	-0.3	0.7	0.2	0.7	1.3	-0.3	0.3
9	0.1	-1.0	-0.1	0.9	-0.5	0.1	3.6	1.0	3.5	6.1	-1.2	1.5
40	0.3	-0.1	0	0.5	-0.1	0	-0.3	0	-0.4	-0.6	0.3	-0.2
51	0	0	-0.2	0	0	-0.2	0.1	0	0.2	0.2	0	0.1
62	-0.1	0	0	-0.1	0.1	0	-0.2	-0.1	-0.2	-0.3	0	-0.1
73†	-1.2	-0.9	0	2.1	-0.7	0	1.3	0.7	1.0	0.2	0	0.5
73††	0.5	-0.3	0	0.8	-0.3	0	0.5	0.2	0.4	0.8	0	0.2
230	0	0	-1.0	-0.1	0	-2.8	0.4	0.2	0.7	0.6	-0.3	0.5
241	-1.3	3.0	0	-6.9	2.7	0	-15.3	-5.3	-13.8	-25.6	3.7	-5.8
252	0	0.1	1.7	-0.1	0	2.1	-2.0	-0.4	-2.1	-3.0	0.6	-1.3
263†	-0.2	0.3	-5.2	-0.5	0.2	-8.4	3.5	0.2	4.4	5.3	-1.4	3.1
263††	-0.1	0.2	-3.0	-0.3	0.2	-4.8	2.0	0.1	2.6	3.0	-0.8	1.8
267	0	-0.1	0	0.1	0	0	0.2	0.1	0.2	0.3	-0.1	0.1
268	-0.2	0.5	0	-0.8	0.4	0	-2.2	-0.7	-2.1	-3.7	0.6	-0.9
271	0	0	0.3	0	0	0	-0.4	-0.1	-0.4	-0.6	0.1	-0.2
291	0	0	0.3	0	0	0.3	-0.2	0	-0.3	-0.4	0.1	-0.2
294	0.2	-0.9	0	1.3	-0.6	0	3.4	1.1	3.2	5.7	-1.0	1.4
295	0	0	0	0	0	0	0.1	0	0	0.1	0	0
297	0	0	-0.3	0	0	0	0.5	0.1	0.5	0.8	0.1	0.3

†Run 1

††Run 2

Table 7-XIV. Error Analysis Results – Lunar Injection Run 3

Error Source	Position (km)			Velocity (m/sec)			Delta Velocity (m/sec)					
	R	T	N	R	T	N	Variable Time			Fixed Time		
7	0	0	-0.6	0	0	-0.1	0.8	0.2	0.8	1.3	-0.2	0.5
8	0	-0.3	0.2	-0.3	-0.2	-0.3	0.7	0.2	0.7	1.3	-0.3	0.3
9	0.1	-1.0	-0.1	0.9	-0.5	0.1	3.6	1.0	3.5	6.1	-1.2	1.5
40	0.2	-0.1	0	0.4	0	0	-0.2	0	-0.3	-0.4	0.2	-0.1
51	0	0	-0.1	0	0	-0.2	0.1	0	0.1	0.1	0	0.1
62	-0.1	0	0	-0.1	0.1	0	-0.1	-0.1	-0.1	-0.2	0	0
73	0.4	-0.3	0	0.7	-0.2	0	0.4	0.2	0.3	0.7	0	0.2
230	0	0	-0.5	0	0	-1.3	0.2	-0.1	0.3	0.3	-0.2	0.2
241	-0.6	1.5	0	-3.3	1.3	0	-7.0	-2.6	-6.6	-12.3	1.8	-2.8
252	0	0	0.8	-0.1	0	1.0	-0.9	-0.2	-1.0	-1.5	0.3	-0.6
263	0	0.1	-1.3	-0.1	0.1	-2.1	0.9	0	1.1	1.3	-0.4	0.8
267	0	0	0	0	0	0	0.1	0	0.1	0.1	0	0
291	0	0	0.3	0	0	0	-0.2	0	-0.3	-0.4	0.1	-0.2
294	0.1	-0.4	0	0.6	-0.3	0	1.6	0.5	1.5	2.1	-0.5	-0.6
295	0	0	0	0	0	0	0.1	0	0	0.1	0	0
297	0	0	-0.3	0	0	0	0.5	0.1	0.5	0.8	-0.1	0.3

Table 7-XV. Error Analysis Results – Lunar Injection Run 4

Error Source	Position (km)			Velocity (m/sec)			Delta Velocity (m/sec)					
							Variable Time			Fixed Time		
	R	T	N	R	T	N						
7	0	0	-0.6	0	0	-0.1	0.8	0.2	0.8	1.2	-0.2	0.5
8	0	-0.2	0.1	0.2	-0.1	-0.2	0.4	0.1	0.4	0.7	-0.2	0.2
9	0.1	-0.5	0	0.5	-0.3	0.1	2.0	0.6	1.9	3.4	-0.6	0.9
40	0	0	0.3	0.1	0	0.5	-0.2	0	-0.3	-0.3	0.1	-0.2
41	0	0	0.2	0	0	0.2	-0.2	0	-0.3	-0.4	0.1	-0.2
51	0.2	-0.6	0	0.5	-0.6	0	3.1	0.9	3.1	5.4	-1.1	1.4
52	0.1	-0.4	0	0.3	-0.4	0	2.0	0.5	1.9	3.3	-0.7	0.9
62	0.7	-0.7	0	1.6	-0.6	0	2.1	0.8	1.8	3.4	-0.3	0.8
63	0.4	-0.2	0	0.9	-0.2	0	0.4	0.2	0.2	0.5	0.1	0.1
77	0.2	-0.3	0	0.4	0.1	0	0.2	0.1	0.2	0.3	0	0.1
80	0.3	-0.7	0	0.8	-0.5	0	2.3	0.7	2.3	4.0	-0.8	1.0
81	0.6	-0.2	0	1.0	-0.4	0	0.7	0.4	0.5	1.1	0	0.2
94	0.1	-0.1	0	0.1	-0.2	0	0.7	0.2	0.7	1.2	-0.2	1.0
96	0.1	-0.2	0	0.3	-0.2	0	0.7	0.2	0.7	1.2	-0.2	0.3
98	0.1	-0.1	0	0.2	-0.1	0	0.3	0.1	0.3	0.5	-0.1	0.1
100	0.2	-0.1	0	0.3	-0.2	0	0.3	0.1	0.2	0.4	0	0.1
102	0.1	-0.1	0	0.3	-0.1	0	0.5	0.2	0.4	0.8	-0.1	0.2
104	0.1	-0.1	0	0.2	-0.1	0	0.2	0.1	0.1	0.2	0	0.1
230	0	0.1	-0.2	0.1	0.1	-1.9	-0.8	-0.4	-0.5	-1.2	0	-0.2
241	0	0	-0.9	0	0	-0.5	1.1	0.3	1.2	1.7	-0.2	0.7
252	-0.7	1.5	0	-34.0	1.3	0.1	-7.6	-2.6	-6.8	-12.7	1.9	-2.9
263	0	0.1	-0.1	-0.1	0.1	-1.3	-0.7	-0.3	-0.6	-1.2	0	-0.2
264	0	0	0	0	0	0.1	0	0	0	0	0	0
266	0	0	-0.9	0	0	-0.1	1.2	0.3	1.2	1.9	-0.2	0.7
269	0	0	0	0.1	0	0	0.2	0.1	0.2	0.3	-0.1	0.1
270	-0.7	2.6	0	2.6	1.5	0	-8.8	-2.5	-8.6	-15.0	2.9	-3.8

REFERENCES FOR SECTION 7

7-1 D.F. McAllister and J.C. Wilcox, "Digital Computer Program for a Generalized Inertial Guidance System Error Analysis, Version II (GEAP II)," TRW Document No. 08768-6009-T000, 11 May 1967.

7-2 D. Strawther, "Centaur Guidance System Accuracy Report, AC-10 Accuracy Analysis," GD/C-BTD 64-013-11, 1 April 1966.

8. PERFORMANCE ANALYSES FOR THE MIDCOURSE PHASE

8.1 INTRODUCTION

Midcourse trajectory corrections generally are required to meet the terminal accuracy requirements of lunar and interplanetary missions. This is due to the fact that for many missions the injection errors, propagated to the target planet or to the moon, exceed the desired errors at encounter. The injection errors depend somewhat on the launch vehicle characteristics, but primarily on the accuracy of the booster guidance system. The state-of-the-art of boost phase guidance is quite advanced; however, even for the best available guidance systems, the errors at injection are considerably in excess of those desired for most targeted interplanetary or lunar missions.

The capabilities of ground-based radio tracking and orbit determination techniques (see Section 6) have advanced to the point where midcourse trajectory corrections can be made with sufficient accuracy to meet the mission terminal objectives with a reasonably small expenditure of spacecraft propellants.

The midcourse correction problem is analyzed in this section primarily for the Jupiter mission.† The analysis applies either to a flyby mission or to a solar probe with a Jupiter swingby. A fully attitude-stabilized spacecraft with suitable propulsion for making the necessary maneuvers is assumed. The analysis calls heavily on the results contained in Ref 8-1, 8-2, and 8-3.

The guidance concept (see also Subsections 2.4, 2.5 and 2.6) is similar to that employed in Ranger, Mariner, Surveyor, Lunar Orbiter, and other missions:

1) Use of the DSIF (S-band) tracking systems and ground computational facilities is assumed for orbit determination from injection through encounter with the target planet (see Section 6).

†Analysis of the Lunar mission or Mars mission is similar and will not be presented here.

2) Based on this determination of the spacecraft position and velocity, corrective maneuvers are computed and transmitted to the spacecraft onboard guidance equipment for execution.

The midcourse maneuver is defined by the impulsive velocity correction, ΔV, necessary to correct the target errors and (optionally) the time of flight.

There are many tradeoffs associated with:

1) Single versus multiple midcourse maneuvers and the points at which the corrections are applied

2) Allowable spacecraft $\overline{\Delta V}$ capability (this ultimately becomes a tradeoff with payload weight)

3) Ranges of possible injection guidance errors (these depend on the booster guidance system and on the launch through injection trajectory)

4) Tracking system accuracies attainable (these are a function of the trajectory geometry, tracking radar capabilities and utilization, and ground data reduction capabilities)

5) Midcourse maneuver execution errors (these depend on the sophistication of the onboard optical/inertial system (see Paragraph 8.4.4).

Analysis of these tradeoffs is beyond the scope of this study.

8.2 MIDCOURSE GUIDANCE TECHNIQUES

Midcourse guidance is performed by pointing the spacecraft thrust in a direction so that a single velocity increment removes the target errors. This technique, "arbitrary pointing," was used with Ranger, Mariner, and Surveyor, and allows a single correction to remove all target errors or to remove two components of miss at the target (critical plane correction) and not correct time-of-flight errors.

Target errors are conveniently specified in terms of the components of the impact parameter vector $\overline{B}$ in the R-T plane and the time of flight t_f. See Figure 8-1.

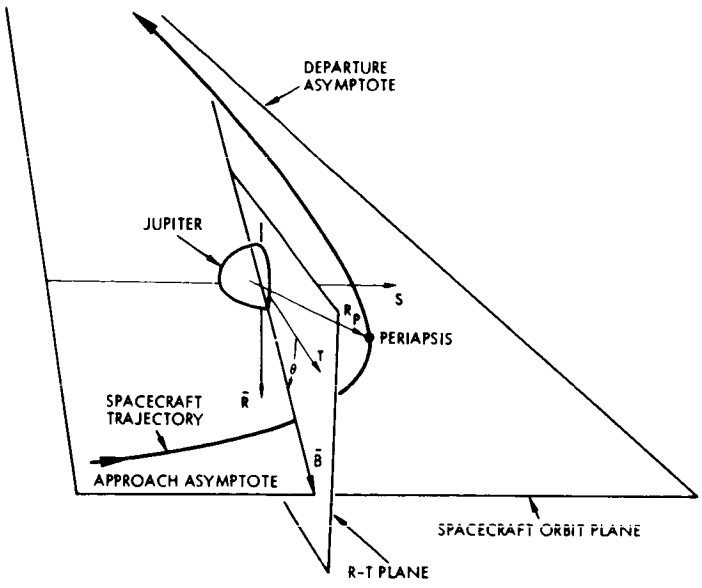

Figure 8-1. Encounter Geometry

For a given interplanetary trajectory, the choice of the impact parameter vector $\overline{B}$ specifies in which direction from the planet and at what distance the approach asymtote lies. $\overline{B}$ is commonly expressed in components $\overline{B} \cdot \overline{R}$ and $\overline{B} \cdot \overline{T}$, where $\overline{R}$, $\overline{S}$, and $\overline{T}$ are a right-hand set of mutually orthogonal unit vectors aligned as follows: $\overline{S}$ is parallel to the planetocentric approach asymptote, $\overline{T}$ is parallel to the plane of the ecliptic and positive eastward, and $\overline{R}$ completes the set and has a positive southerly component. The magnitude of $\overline{B}$ determines the distance of closest approach to the planet and the angle

$$\theta = \tan^{-1} \frac{\overline{B} \cdot \overline{R}}{\overline{B} \cdot \overline{T}}$$

specifies the orientation of the planet centered orbit plane as a rotation about the $\overline{S}$ axis. These definitions are illustrated in Figure 8-1. The velocity injection errors ΔV_I are statistically represented by a covariance matrix Σ_I

$$\Sigma_I = E \left[\Delta V_I \, \Delta V_I^T \right]$$

where E indicates expected value. It is assumed for this study that each component of ΔV_I is normally distributed and that errors in position at injection have negligible effect on the miss at the target.

Because the injection errors are linearly related to the components of miss at the target $\overline{B} \cdot \overline{T}$ and $\overline{B} \cdot \overline{R}$, the uncorrected target miss is statistically represented as

$$\Sigma_T = C_I \Sigma_I C_I^T$$

where C is the matrix of partial derivatives of the target coordinates with respect to the components of velocity:

$$C = \begin{bmatrix} \frac{\partial(\overline{B} \cdot \overline{T})}{\partial \dot{x}} & \frac{\partial(\overline{B} \cdot \overline{T})}{\partial \dot{y}} & \frac{\partial(\overline{B} \cdot \overline{T})}{\partial \dot{z}} \\ \frac{\partial(\overline{B} \cdot \overline{R})}{\partial \dot{x}} & \frac{\partial(\overline{B} \cdot \overline{R})}{\partial \dot{y}} & \frac{\partial(\overline{B} \cdot \overline{R})}{\partial \dot{z}} \end{bmatrix}$$

and the subscript I refers to the time of injection. Thus, Σ_T is the covariance matrix of the two dimensional normal distribution for the two components of miss at the target. Σ_T is a symmetrical matrix of the form

$$\Sigma_T = \begin{bmatrix} a & x \\ x & b \end{bmatrix}$$

Then

$$\Sigma_T^{-1} = \frac{1}{ab - x^2} \begin{bmatrix} b & -x \\ -x & a \end{bmatrix}$$

and the two dimensional probability density function is

$$p[(\overline{B} \cdot \overline{T}), (\overline{B} \cdot \overline{R})] = \frac{1}{2\pi(ab - x^2)^{1/2}}$$

$$\exp\left\{ - \frac{1}{2(ab - x^2)} \left[b(\overline{B} \cdot \overline{T})^2 - 2x(\overline{B} \cdot \overline{T})(\overline{B} \cdot \overline{R}) + a(\overline{B} \cdot \overline{R})^2 \right] \right\}$$

Contours of constant probability p are ellipses in the $\overline{B} \cdot \overline{T}$, $\overline{B} \cdot \overline{R}$ plane and are described by

$$b(\overline{B} \cdot \overline{T})^2 - 2x(\overline{B} \cdot \overline{T})(\overline{B} \cdot \overline{R}) + a(\overline{B} \cdot \overline{R})^2 = \text{constant}$$

The square roots of the eigenvalues of the matrix Σ_T are the size of the semimajor and semiminor axes of the ellipse which contains a certain probability. The numerical value of the probability is dependent upon the relative sizes of the eigenvalues. Standard tables (Ref 8-4) have been prepared indicating the factor by which the square roots of the eigenvalues must be multiplied so that the resulting ellipse contains a certain percentage of possible situations.

8.3 MIDCOURSE CORRECTION ΔV REQUIREMENTS FOR THE JUPITER MISSION

8.3.1 Injection Errors

The launch vehicle configuration assumed for study of the Jupiter mission is the Atlas/Centaur/HEUS configuration (see Paragraph 2.2.6). The permissible injection errors are based on the performance requirements established in Subsection 2.6 for this mission, and represent a reasonable upper bound of the errors attainable with the present Centaur guidance system.† See Table 8-I.

The trajectory used represents a sample from the Jupiter 1972 launch opportunity, and is representative of midcourse guidance analysis. Detailed trajectory characteristics are as follows:

Launch date	March 14, 1972
Flight time	742 days
Trajectory type	I
Injection energy	86.244389 $(km/sec)^2$
Heliocentric transfer angle	156.62839 deg

Additional trajectory data are given in Paragraph 2.6.1.

†Section 7 of this report presents the injection errors for the TG-166 and TG-266 strapdown inertial guidance systems for two of the four missions studied. Although not computed specifically for the Jupiter mission, the injection errors for the TG-266 system are expected to meet the requirements established in Table 8-I.

Table 8-I. Allowable Injection Guidance Errors for Jupiter Mission

Parameter	Specification (1σ)
Uncertainty in injection velocity magnitude	9.5 m/sec
Uncertainty in velocity perpendicular to the velocity vector	34.7 m/sec

For the trajectory described above, and consistent with the injection errors specified in Table 8-I,

$$\Sigma_I = \begin{bmatrix} 541.87 & -446.00 & -315.18 \\ -446.00 & 902.13 & -212.90 \\ -315.18 & -212.90 & 1052.2 \end{bmatrix} (\text{m/sec})^2$$

in the geocentric equatorial coordinate system.

The numerical value of Σ_T is

$$\Sigma_T = \begin{bmatrix} 90.811076 & 10.241762 \\ 10.241762 & 15.161822 \end{bmatrix} \times 10^{10}\ \text{km}^2$$

The square roots of the eigenvalues of this matrix multiplied by an appropriate factor (Ref 8-4) indicate the size of the 99 percent probability miss ellipse at the target. The 99 percent semimajor and minor axes are 2,208,138 and 854,404 km, respectively. This miss ellipse is illustrated in Figure 8-2.

Note that these uncorrected injection errors propagated to the planet are extremely large. For comparison, the diameter of Jupiter is approximately 1.4×10^5 km.

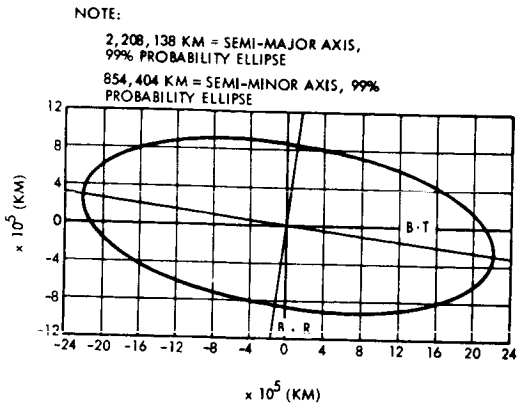

Figure 8-2. 99 Percent Probability Miss Ellipse

8.3.2 Velocity Requirements to Remove Target Errors

The velocity requirements to remove target errors, including time of flight deviations and the requirements to remove miss-only errors, are presented in Figure 8-3. The numbers represent 99 percent velocity loading, i.e., the velocity required to remove 99 percent of all possible injection errors. The least velocity requirement for control of all target errors is 85 m/sec and occurs 20 days after injection. The least velocity requirement for control of miss only is 43 m/sec and occurs 300 days after injection. In order to perform a correction early, for example at 10 days after injection, between 82 and 87 m/sec are required.

The numbers were computed from

$$\Sigma_V = C\Sigma_T C^T$$

where C is evaluated at the time of the midcourse correction, for a critical plane correction 10 days past injection.

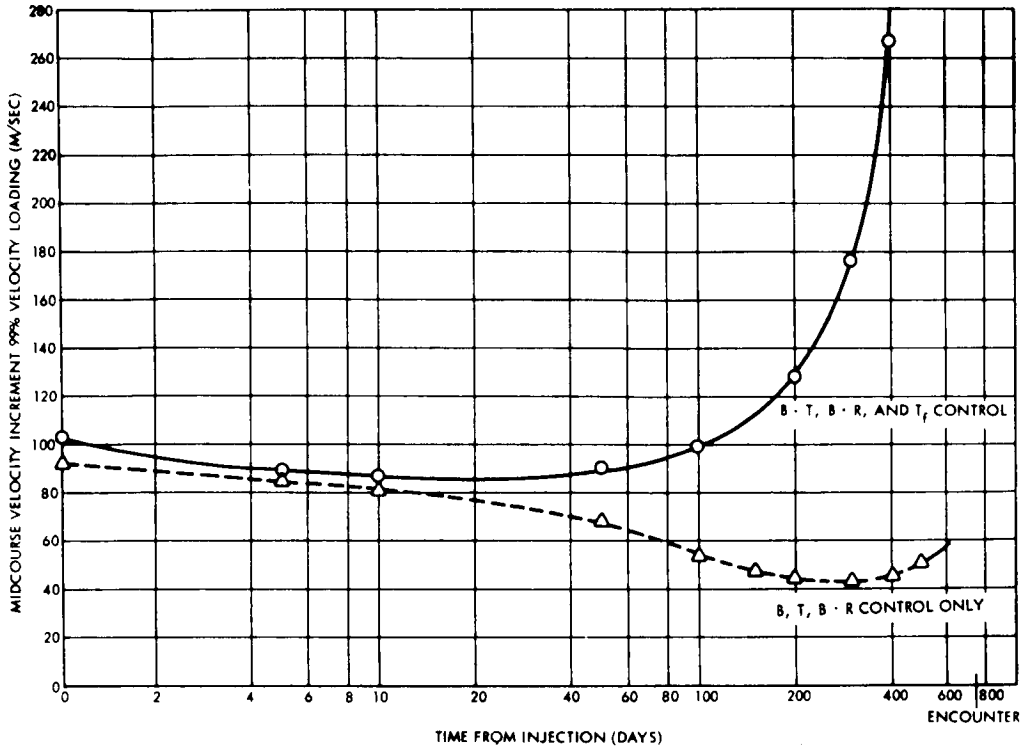

Figure 8-3. Midcourse Correction Requirement, 99 Percent Velocity Loading

8.4 POST MIDCOURSE TRAJECTORY ACCURACY ANALYSIS

Estimates for the uncertainty of control of the interplanetary trajectory subsequent to the midcourse correction maneuver are presented in the following paragraphs. The contributions to this uncertainty are the error in execution of the midcourse trajectory correction, the uncertainty in tracking the spacecraft from injection to midcourse correction, ephemeris and astronomical unit errors, and certain identifiable but unpredictable trajectory perturbations acting after the midcourse correction. The midcourse guidance technique, described in Subsection 8.2, is assumed for this analysis. It consists of a single midcourse correction about 10 days after launch, with the thrust vector directed essentially parallel to the critical plane so as to reduce $\overline{B} \cdot \overline{T}$ and $\overline{B} \cdot \overline{R}$ errors.

The rms and percentage contributions to the target coordinates $\overline{B} \cdot \overline{T}$ and $\overline{B} \cdot \overline{R}$ are listed in Table 8-II. The development of each error source is presented in the following sections. The percentage contribution of the total deviation in $\overline{B} \cdot \overline{T}$ and $\overline{B} \cdot \overline{R}$ is computed by assuming that the mean square error contributions are additive.

Table 8-II. Post-Midcourse Trajectory Errors

Error Source	RMS $\bar{B} \cdot \bar{T}$ Error (km)	RMS $\bar{B} \cdot \bar{R}$ Error (km)	Percent of Total $\bar{B} \cdot \bar{T}$ Variance	Percent of Total $\bar{B} \cdot \bar{R}$ Variance
Injection errors	951,000	388,000	†	†
Midcourse execution errors††	8,850	10,600	93.0	99.4
Pre-midcourse tracking errors	2,050	625	5.0	0.3
Nongravitation perturbations (unpredictable portions)	1,067	217	1.4	-
Ephemeris errors	500	500	0.3	0.2
Astronomical Unit conversion factor uncertainty	303	303	0.2	0.1
Total rss	9,150	10,650	100.0	100.0

Total 99 percent miss ellipse:

Semimajor axis = 26,300 km

Semiminor axis = 17,400 km

† Does not directly affect post-midcourse target errors.

†† Arbitrary pointing critical plane correction at 10 days past injection.

The midcourse execution errors are calculated for a Mariner-type midcourse guidance system (Configuration Ia described in Paragraph 2.4.1.3) and represent the largest error contribution, as might be expected.

More accurate control of the trajectory, if required, could be obtained by improving the precision of the midcourse maneuver either by using a full strapdown guidance system or by increasing the number of maneuvers. Of the remaining errors, the greatest is the pre-midcourse tracking uncertainty which causes the estimated position of the spacecraft to be in error. This error is based on present state-of-the-art tracking accuracies attainable by the DSIF (see Section 6). Presumably by 1972, greater accuracy can be attained. Likewise ephemeris errors and uncertainty in the AU are based on present state-of-the-art and by 1972 will be appreciably reduced.

8.4.1 Tracking Errors

This paragraph describes the results of an analysis of pre-midcourse tracking performed to calculate the state vector uncertainties due to radar tracking. The dispersion ellipse at Jupiter was computed from these state vector uncertainties.

Range-rate observations at the rate of one every 10 min for a period of 10 days from a single ground radar constituted the tracking configuration assumed. The radar was located on the equator at the Greenwich meridian and was assumed capable of observing the spacecraft continuously. The a priori standard deviation assigned to the range-rate observations was 10^{-2} m/sec. Although this may depart from the design values of the mission, linear scaling applies to the resultant uncertainties. For example, if the a priori standard deviation is halved, the state vector uncertainties are halved at any given time.

The covariance matrix given in Subsection 8.3 was propagated from injection to the $\overline{B} \cdot \overline{T}$, $\overline{B} \cdot \overline{R}$ target coordinate system. This matrix is

$$\begin{bmatrix} 4.228 & -0.4521 \\ -0.4521 & 0.3905 \end{bmatrix} \times 10^{6}(\text{km})^{2}$$

The square roots of the eigenvalues of this matrix multiplied by an appropriate factor (see Subsection 8.2) give the semimajor and semiminor axes of the 99 percent probability dispersion ellipse. The 99 percent semimajor and minor axes are 5110 and 1450 km, respectively. The dispersion ellipse is plotted in Figure 8-4. For comparison purposes, it is noted that the radius of Jupiter is approximately 71,400 km.

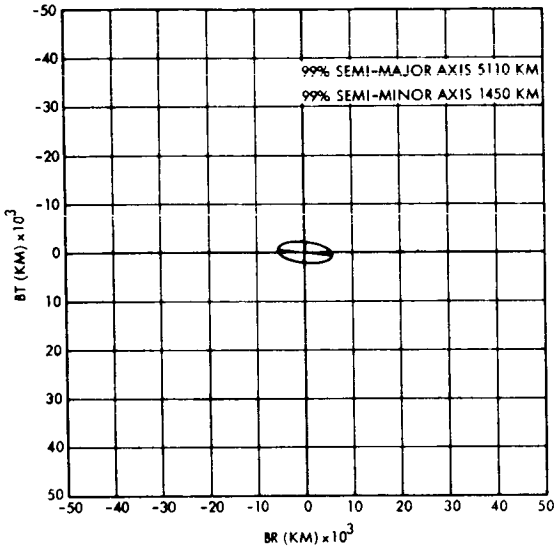

Figure 8-4. Tracking Uncertainty Ellipse Tracking from Injection to 10 Days — One Point Every 10 Min

8.4.2 Midcourse Correction Execution Errors for a Mariner-Type Simplified Strapdown Inertial Guidance System

Orientation and execution errors introduced by the midcourse correction subsystem are evaluated in this section for a Mariner-type strapdown guidance system. This is a simplified inertial configuration with a 3-axis gyro package and one longitudinal axis accelerometer. Cruise attitude reference is provided in a Sun sensor/Canopus sensor combination. Reorientation maneuvers are made by open-loop gyro torquing. The corresponding errors for a full strapdown configuration are presented in the following section.

8.4.2.1 Thrust Magnitude Errors

The thrust magnitude errors characteristic of a timed motor burn are analyzed in Appendix H of Ref 8-1. The proportional errors are a function of burn time and vary between 0.66 and 0.95 percent (1σ).

A value equal to 0.75 percent is selected for this analysis. The resolution errors, primarily due to the motor ignition and shutdown transients, are equal to 0.0188 m/sec (1σ), if both transient errors are root-sum squared.

8.4.2.2 Pointing Errors

Pointing errors include contributions from the following sources: Canopus and Sun sensor resolution, stability and mounting tolerances of these sensors with respect to the vehicle centerline, attitude errors due to open-loop gyro torquing through the required reorientation angles, thrust misalignment errors, and vehicle attitude control errors during the thrusting period. It is beyond the scope of this report to analyze these error sources in detail for the Mariner-type system. However, a reasonable value for the composite pointing error for this type of system is 2/3 deg (1σ). This value is used in the subsequent analysis.

8.4.2.3 Midcourse Correction Covariance Matrix

To accurately compute the effects of the pointing and velocity execution errors, a Monte Carlo simulation should be employed.

An alternate second moment error analysis can be employed enabling an estimate of the execution errors to be simply computed. Thus, the covariance matrix of execution errors Σ_e is (Ref 8-4)

$$\Sigma_e = \left(\sigma_s^2 - \sigma_p^2\right)\Sigma_v + \left(\sigma_r^2 - \sigma_a^2\right)\Sigma_{|v|} + \left(\sigma_p^2\,|\bar{v}|^2 + \sigma_a^2\right)I$$

where

σ_s^2 = variance of the proportional velocity error

σ_p^2 = variance of the pointing error (includes thrust misalignment error)

σ_r^2 = variance of the resolution error (nonproportional component of velocity magnitude error)

σ_a^2 = variance of the vehicle attitude error due to imperfect vehicle control system performance

v = midcourse correction velocity increment

$|\bar{v}|$ = expected value of v squared

Σ_v = midcourse correction velocity covariance matrix

$\Sigma_{|v|}$ = normalized midcourse correction velocity covariance matrix

I = unit matrix

Because the distribution of the error sources will not generally be normal, Σ_e will not represent the covariance of a multidimensional normal distribution. However, it will be assumed that all error sources are zero mean normal so that Σ_e may be propagated to the target and compared with other error effects which are normal.

The previous paragraphs indicate that reasonable 1-σ error estimates are

$\sigma_s = 0.0075$ (0.75 percent)

$\sigma_p = 0.0116$ rad (2/3 deg)

$\sigma_r = 0.0188$ m/sec

For a critical plane midcourse correction at 10 days

$$\Sigma_v = \begin{bmatrix} 1001.6947 & -52.702607 & -98.524102 \\ & 73.535761 & 102.51410 \\ \text{symmetric} & & 143.56311 \end{bmatrix} (\text{m/sec})^2$$

$$|v|^2 = T_r \Sigma_v = 1218.79357\ (\text{m/sec})^2$$

in the geocentric equatorial coordinate system. Therefore for these values,

$$\Sigma_e = \begin{bmatrix} 0.085 & 0.0042 & 0.0078 \\ & 0.158 & -0.008 \\ \text{symmetric} & & 0.165 \end{bmatrix} (\text{m/sec})^2$$

in this same coordinate system. Propagating this to the target coordinate plane using the matrix C (defined in Subsection 8.2) gives the post-midcourse correction target covariance matrix

$$\Sigma_{TM} = C \Sigma_e C^T$$

which is numerically equal to

$$\Sigma_{TM} = \begin{bmatrix} 0.7845 & 0.2681 \\ 0.2681 & 1.128 \end{bmatrix} \times 10^8 \text{ km}^2$$

The square roots of the eigenvalues of this matrix multiplied by an appropriate factor which is a function of the ratio of the eigenvalues gives the 99 percent semimajor and minor axes of the post-correction miss ellipse. Selection of the appropriate factor is made assuming that the errors are multidimensional normal. For nonnormal distributions, the determination of such a factor is complicated. It is anticipated that this factor does not differ significantly (more than 10 to 20 percent for other continuous distributions). The semimajor axis is 24,480 km, and the semiminor axis is 17,300 km. The miss ellipse is plotted in Figure 8-5. Although it is not intended here to control the day of arrival, the time of day of arrival can be controlled to 3.6309 hr, 1σ, by the single-correction program.

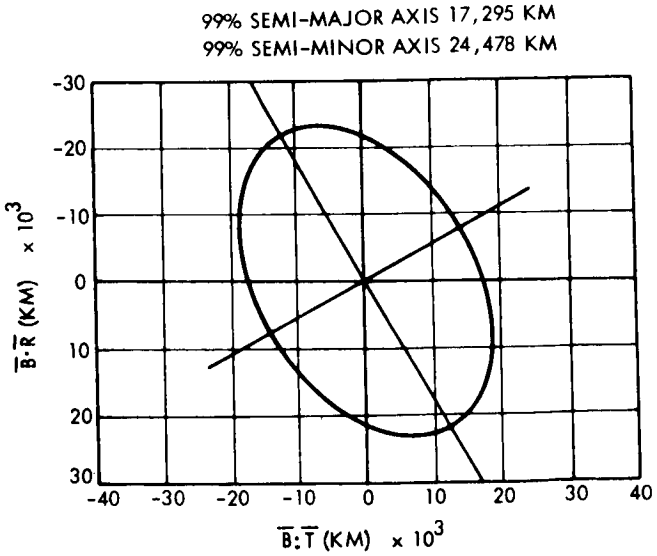

Figure 8-5. Critical Plane Correction at 10 Days, 99 Percent Post-Correction Miss Ellipse

8.4.3 Midcourse Covariance Matrix for a Full Strapdown Inertial Guidance System

Midcourse maneuver and execution errors were investigated using the GEAP II error analysis program (see Section 7) for the TG-166 strapdown inertial guidance subsystem. A simple relationship was found to hold between errors and delta velocity. Covariance matrices were calculated to represent the errors of a range of possible midcourse corrections with a large and small value of delta velocity and reorientation angle. Six runs were made using the TG-166 error model and the parameters shown in Table 8-III.

Table 8-III. Midcourse Correction Delta Velocity and Reorientation Angles

Run Number	ΔV (m/sec)	$\Delta\theta$(deg)
1	6	0
2	60	0
3	6	90
4	60	90
5	6	180
6	60	180

For all runs, the parameters given in Table 8-IV were used.

Table 8-IV. Parameters Used for Midcourse Maneuver Error Analysis

Acceleration	0.5 m/sec^2	Along X axis
Rotation rate	0.5 deg/sec	About axis midway between Y and X axes
Optical initialization	3 arc min	Per axis

The optical initialization was accomplished first, followed by the rotation and then the burn. The covariance matrices obtained are shown in Table 8-V. The elements below the diagonal of the covariance matrices

Table 8-V. Error Covariance Matrices for Midcourse Corrections

Run 1

2.87 E-3	0	0	4.60 E-4	0	0
0	1.47 E-2	0	0	2.35 E-3	0
0	0	1.47 E-2	0	0	2.35 E-3
1	0	0	7.36 E-5	0	0
0	1	0	0	3.76 E-4	0
0	0	1	0	0	3.76 E-4

Run 2

2.87 E-1	0	0	4.60 E-1	0	0
0	1.47 E-2	0	0	2.36 E-0	0
0	0	1.47 E-2	0	0	2.36 E-0
1	0	0	7.36 E-3	0	0
0	1	0	0	3.77 E-2	0
0	0	1	0	0	3.77 E-2

Run 3

2.87 E-3	0	0	4.60 E-4	0	0
0	1.52 E-2	-5.67 E-5	0	2.43 E-3	-9.21 E-3
0	-0.004	1.52 E-2	0	-9.21 E-3	2.43 E-3
1	0	0	7.36 E-5	0	0
0	1	-0.003	0	3.89 E-4	-1.49 E-6
0	-0.003	1	0	-0.004	3.89 E-4

Run 4

2.87 E-1	0	0	4.50 E-1	0	0
0	1.53 E-2	-8.81 E-1	0	2.46 E-0	-1.55 E-2
0	-0.006	1.53 E-2	0	-1.55 E-2	2.46 E-0
1	0	0	7.36 E-3	0	0
0	1	-0.006	0	3.95 E-2	-2.70 E-4
0	-0.006	1	0	-0.007	3.95 E-2

Run 5

2.87 E-3	0	0	4.60 E-4	0	0
0	1.62 E-2	-0.657 E-4	0	2.59 E-3	-1.06 E-4
0	-0.004	1.62 E-2	0	-1.06 E-4	2.59 E-3
1	0	0	7.36 E-5	0	0
0	1	-0.041	0	4.14 E-4	-1.71 E-3
0	-0.041	1	0	-0.041	4.14 E-4

Run 6

2.87 E-1	0	0	4.60 E-1	0	0
0	1.64 E-2	-8.30 E-0	0	2.63 E-0	-1.41 E-1
0	-0.051	1.64 E-2	0	-1.41 E-1	2.63 E-0
1	0	0	7.36 E-3	0	0
0	1	-0.053	0	4.22 E-2	-2.37 E-3
0	-0.053	1	0	-0.056	4.22 E-2

have been replaced by the correlations. The first three states are position and the last three are velocity.

It is apparent from the results that position errors are very nearly proportional to the square of the delta velocity and that velocity errors are very nearly directly proportional to the delta velocity. It is also apparent that the magnitudes of the position errors are insignificant and only velocity errors need be considered. From Table 8-V, the velocity error along the thrust direction can be computed to be

$$\epsilon(\Delta v) \cong 0.43 \times 10^{-3} \Delta v$$

or

$$\frac{\epsilon(\Delta v)}{\Delta v} \cong 0.043 \text{ percent}$$

Also, from Table 8-V, the cross axis velocity errors are

$$\epsilon(\Delta v_{\text{cross axis}}) \cong 10^{-3} \Delta v.$$

The pointing errors are thus 10^{-3} rad, or 0.06 deg.

8.4.4 Comparison of Mariner-Type System with a Full Strapdown System

The results obtained in the last two sections for the equivalent proportional velocity errors and pointing errors for midcourse maneuver execution are compared in Table 8-VI. It is evident that at least an order of magnitude improvement is available by using the more sophisticated strapdown inertial system. Optical sensor accuracies are comparable in the two systems (3 arc min inertial accuracy in each axis is assumed for the latter system).

The significant improvement noted for the full strapdown system is due primarily to two effects:

- reduction in the attitude errors incurred during the reorientation maneuver by measuring the attitude change using the strapdown gyros
- reduction in the vehicle attitude control errors during the thrusting period (the strapdown mechanization permits closed loop steering control based on sensed velocities during the burn).

Table 8-VI. Comparison of Midcourse Execution Errors for Two Types of Inertial Guidance Subsystem Mechanizations

	Mariner-Type Simplified Strapdown Guidance System	TG-166 Full Strapdown Guidance System†
Proportional velocity error	0.75 percent (1σ)	0.043 percent (1σ)
Pointing error	0.67 deg (1σ) (11.6 x 10^{-3} rad)	0.06 deg (1σ) (10^{-3} rad)
Resolution error	0.0188 m/sec	(Negligible)
ΔV error in performing a maximum 100 m/sec maneuver	0.75 m/sec (1σ) (parallel component)	0.04 m/sec (1σ)
	1.2 m/sec (1σ) (lateral component)	0.1 m/sec (1σ)

†See Paragraph 3.3.1.2 for error model.

8.4.5 Extrapolation of Results to Other Mission and to Orbit Insertion Maneuvers

The errors presented in Table 8-VI for the two types of optical/inertial systems may be applied directly to the analysis of the midcourse correction requirements for other missions and to other maneuvers such as orbit insertion. The resultant mission errors will, of course, be different than those given above for the Jupiter mission.

The TG-166 performance satisfies all of the midcourse correction and orbit insertion ΔV requirements summarized in Paragraph 2.4.2.2 Table 2-VI. The TG-266 system, which has better accelerometer performance, also satisfies these requirements.

REFERENCES FOR SECTION 8

8-1 "Advanced Planetary Probe Study, Final Technical Report," TRW Systems Report No. 6547-6004-R000, 27 July 1966.

8-2 "Phase 1A Study Report, Voyager Spacecraft," TRW Systems Report No. 5410-0004-RU-001, 30 July 1965.

8-3 "Phase 1A Task B Final Technical Report, Voyager Spacecraft," TRW Systems Report No. 5410-6001-R0V01, 17 January 1966.

8-4 "Distribution of Quadratic Forms," H. Solomon, Stanford University Technical Report 45, January 1960.

8-5 "A Simplified Model of Midcourse Maneuver Execution Errors," JPL TR 32-504, 15 November 1963.

9. NAVIGATION PERFORMANCE ANALYSES FOR INTERPLANETARY AND PLANET APPROACH PHASES

9.1 INTRODUCTION

The radio/optical/inertial tracking and navigation error analyses were conducted using the SVEAD† computer program. The results of the study are discussed in this section. Briefly, this error analysis was concerned with the comparative performance of DSIF tracking (earth-based doppler) and onboard optical navigation. Optical instruments considered were: star sensor, planet (Mars) sensor, Sun sensor. The planet sensor is used in conjunction with the other sensors to make measurements of the cone and clock angles (defined below) and to make an angular subtense (range measurement) of Mars. Major error sources considered were: slowly drifting biases in the optical equipment, uncertainty in the diameter of Mars, Mars ephemeris errors, doppler bias error (slowly drifting), and uncertainty in the dynamic model of the solar system (that is, errors in solar radiation forces on the spacecraft, gravitational constants, planet oblateness, etc.).

The principal purpose of the optical measurements is to locate the position of the planet (Mars) relative to the spacecraft. The lines of sight to two known stars may be used to provide a known coordinate system, in which Mars may be located. For this study, one star was taken to be Canopus, and the other was taken to be the Sun. Mars is then located by a cone angle ψ and a clock angle θ, as shown in Figure 9-1. The angle ϕ, shown in Figure 9-1, is the Sun-Canopus angle. The subtense angle α, not shown, is an angular diameter measurement which can be used to determine the distance to Mars. A time history of these angles is shown in Figure 9-2. Useful optical measurements for the trajectory considered in this study could actually be made only over the period from ten days to 0.5 day prior to Mars encounter (Mars perifocus). Some of the limitations are due to fixed axis trackers (no gimbals), limited field of view (about 15 deg), and finite image size of Mars. However, for the error analysis

†SVEAD is a state variable estimation and accuracy determination program. See Ref 9-1. The equations for the error analysis program are discussed in detail in Appendix D.

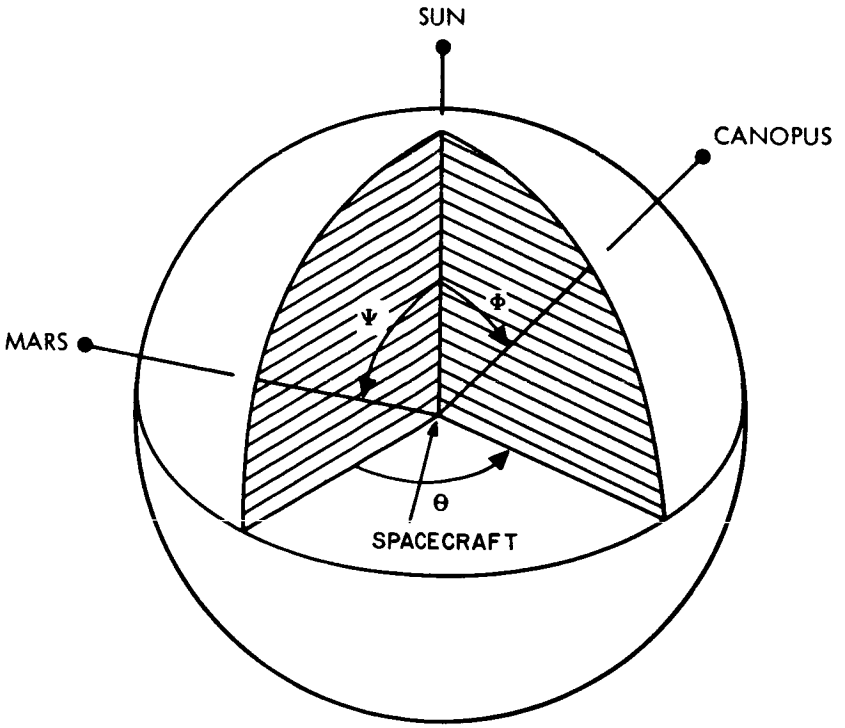

Figure 9-1. Optical Angle Measurements

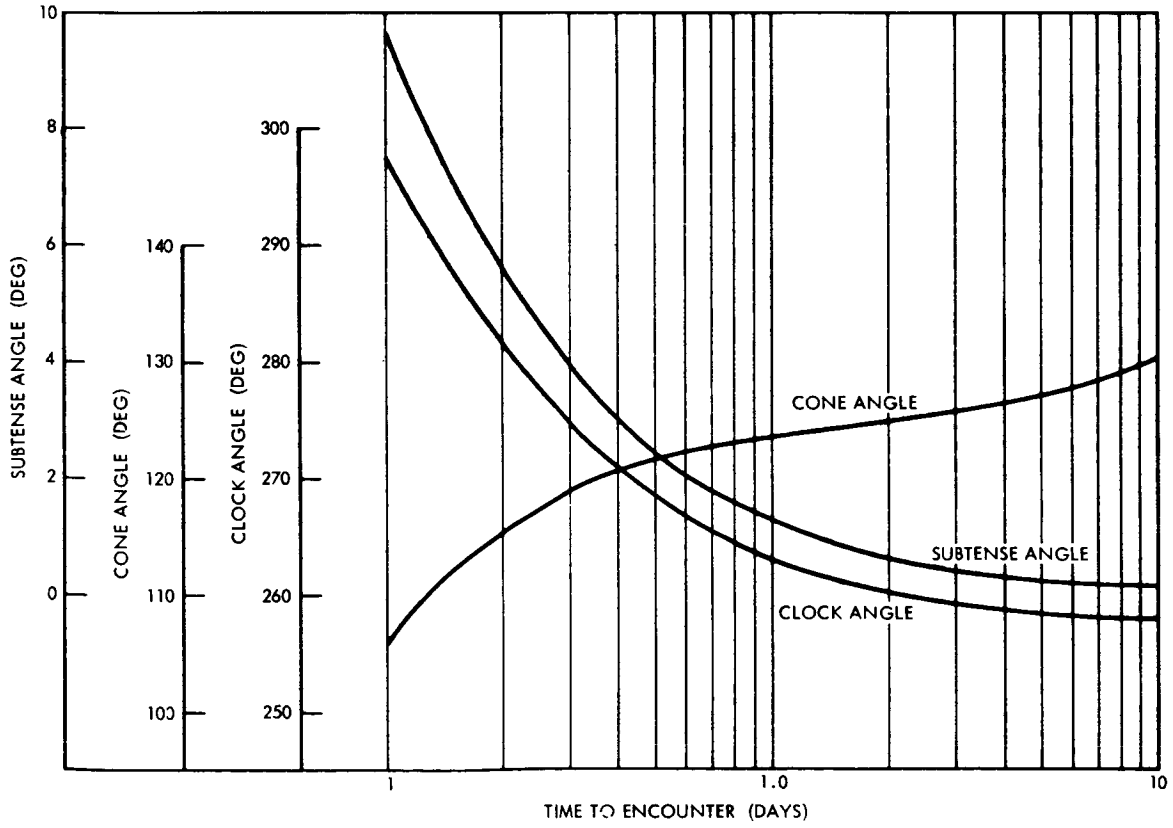

Figure 9-2. Measurement Angles Versus Time to Encounter

runs, the optical sensors were assumed to work all the way from the earth to Mars perifocus.

Rather than arbitrarily specify the time interval between measurements, ΔT was automatically controlled by the program. This was done by inputing a position accuracy requirement to the trajectory integrator equations. The integrator then chose a small ΔT during times of rapid trajectory changes, and a large ΔT when the character of the trajectory was slowly changing. Thus, in the vicinity of the earth $\Delta T \approx 6$ sec; in deep space $\Delta T \approx 12$ hr; and $\Delta T \approx 111$ sec at Mars perifocus. A time history of ΔT is shown in Figure 9-3.

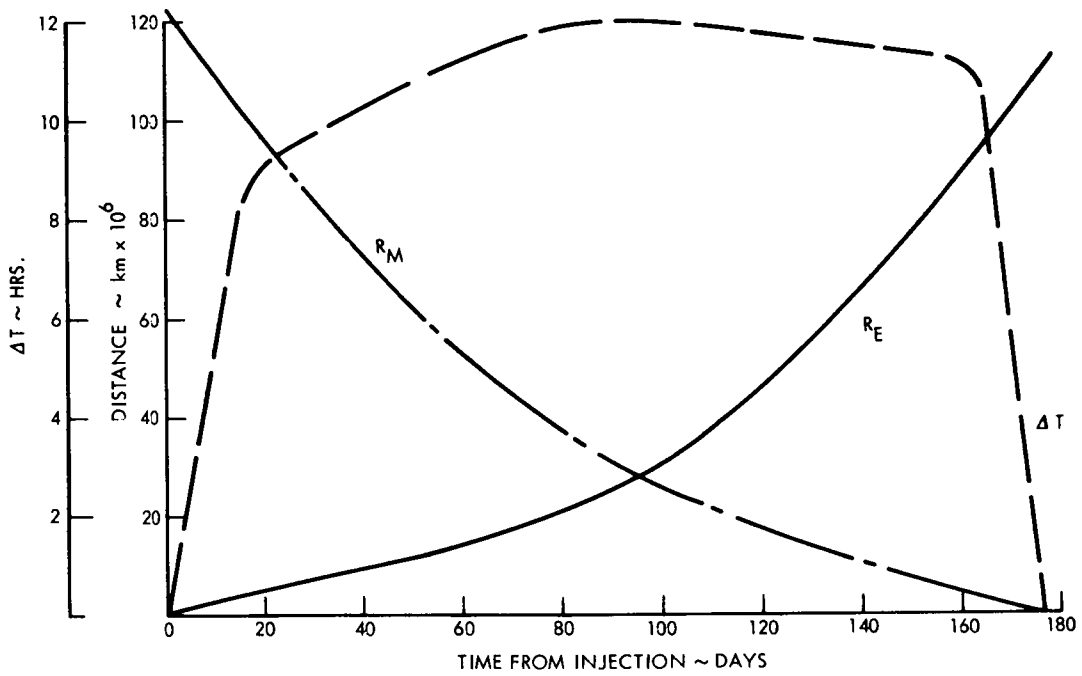

Figure 9-3. Integration Step Size and Relative Distances of Vehicle From Earth and Mars Versus Flight Time

9.2 TRAJECTORY USED FOR NAVIGATION ERROR ANALYSIS

The interplanetary trajectory used in this study is described in Paragraph 2.4.1.

The total time of flight from earth to Mars, for this study, was 15.228×10^6 sec or 176.25 days. The tracking and navigation error analysis started at 3 hr out from earth. The X, Y, Z coordinates mentioned below, are of no special significance. They are nonrotating, cartesian coordinates with the Z axis parallel to the earth's axis of rotation, and the X axis parallel to the earth's orbit plane of the ecliptic).

9.3 ERROR MODEL SUMMARY

All "biases" in the error models were assumed to be slowly drifting random variables, exponentially correlated in time. Thus, each bias error has a standard deviation and a time constant associated with it; the larger the time constant the more nearly constant is the bias.

A list of pertinent inputs is given in Tables 9-I, 9-II, and 9-III. Two different error models for the electro-optical sensors were used in order to investigate the possible improvements in orbit determination accuracies practicable by using the Mars approach sensor.

9.4 SUMMARY OF RESULTS AND CONCLUSIONS

Five different doppler tracking and optical navigation cases were considered:

1) Doppler only
2) Doppler plus optical
3) Doppler plus improved optics
4) Optical only
5) Improved optics only.

As mentioned previously, the optical equipment can actually work only in the range of 10 days from Mars perifocus to 1/2 day from perifocus. However, for the error analysis study, all equipment was assumed to be operating 3 hr out from earth to Mars encounter.

A summary of the results of the error analysis study is shown in Table 9-IV. It appears from this table that the value of optical measurements is marginal, if Doppler information is available up to perifocus.†

† No consideration was given to the problem of Mars eclipsing the vehicle. This problem would be very mission dependent.

Table 9-I. Radio/Optical/Inertial Error Model Mars Mission

Error	(Variance)$^{1/2}$	Time Constant
Random Acceleration Acting on Spacecraft† (Models uncertainty in the dynamic model of the solar system, i.e., errors in solar pressure forces, gravitational constants, etc.)	0.531×10^{-8} m/sec^2 (0.174×10^{-7} ft/sec^2) (causes a 200 km position error in 176 days)	1 week
Tracking System Errors		
• Range rate bias	10^{-2} m/sec (0.0328 ft/sec)	1/3 day
• Uncorrelated noise on doppler rate	0.732×10^{-2} m/sec (0.024 ft/sec) (equivalent to 0.12 ft/sec per 1 sec sample, 25 meas. averaged)	
Vehicle Errors at Injection (3 hr)		
• Position	2 km (6560 ft)	
• Velocity	2 m/sec (6.56 ft/sec)	
Mars Ephemeris Error (Relative to Earth)		
• Position	220 km (7.22×10^{-5} ft)	
• Velocity	0.05 m/sec (0.164 ft/sec)	
Radius of Mars	20 km (6.56×10^{4} ft)	1 day

†Equivalent error averaged over 25 measurements

Table 9-II. Optical Error Model A

Error	(Variance)$^{1/2}$		Time Constant
Sun Sensor Bias	1.746×10^{-3} rad	(6 arc min)	1/2 week
Sun Sensor Uncorrelated Noise	0.349×10^{-4} rad† (0.1746×10^{-3} rad††)	(0.12 arc min)	
Mars Sensor Bias	1.92×10^{-3} rad	(6.6 arc min)	1/2 week
Canopus Sensor Bias	0.873×10^{-3} rad	(3 arc min)	1/2 week
Mars Sensor Uncorrelated Noise	0.349×10^{-4} rad† (0.1746×10^{-3} rad)††		
Canopus Sensor Uncorrelated Noise	0.1746×10^{-4} rad† (0.873×10^{-4} rad)††		
Mars Subtense Measurement			
• Lower limit on (variance)$^{1/2}$ of bias	0.873×10^{-3} rad	(3 arc min)	1/2 week
• Error proportional to subtense angle †††	1%		1/2 week
• Uncorrelated noise	0.1746×10^{-4} rad† (0.873×10^{-4} rad)††	0.06 arc min (0.3 arc min)††	

†Equivalent error of 25 measurements averaged. This value was used in the error analysis.

††Single measurement error

†††Percent of subtense angle (α) contributing to the standard deviation of the bias error adding to subtense angle, i.e., $\sigma_\alpha^2 = (0.873 \times 10^{-3})^2 + (0.01\alpha)^2$

Table 9-III. Optical Error Model B (Improved Optics)

Error	(Variance)$^{1/2}$		Time Constant
Sun Sensor Bias	0.407×10^{-3} rad	(1.4 arc min)	1/2 week
Sun Sensor Uncorrelated Noise	0.349×10^{-4} rad† (0.1746×10^{-3} rad)††	(0.12 arc min)	
Mars Sensor Bias	0.391×10^{-3} rad	(1.35 arc min)	1/2 week
Canopus Sensor Bias	0.391×10^{-3} rad	(1.35 arc min)	1/2 week
Mars Sensor Uncorrelated Noise	0.349×10^{-4} rad† (0.1746×10^{-3} rad)††		
Canopus Sensor Uncorrelated Noise	0.1746×10^{-4} rad† (0.873×10^{-4} rad)††		
Mars Subtense Measurement			
• Lower limit on (variance)$^{1/2}$ of bias	0.485×10^{-4} rad	(0.17 arc min)	1/2 week
• Error proportional to subtense angle†††	0%		
• Uncorrelated noise	0.1745×10^{-4} rad† (0.873×10^{-4} rad)††	0.06 arc min (0.3 arc min)††	

†Equivalent error of 25 measurements averaged. This value was used in the error analysis.

††Single measurement error.

†††See note on previous table.

Had the optical measurements been cutoff at 1/2 day to encounter, then the optical performance would have been worse than shown.

The results given in Table 9-IV are shown graphically, and in more detail, in Figures 9-4 through 9-8. It is interesting to note the very sharp shoulders, at 0.1 days to encounter, on the Doppler only curves (Figure 9-4.). These sharp shoulders may be caused by too slow a sampling rate (see Figure 9-9) for the doppler information around this time. It is suspected that had the sample rate been increased by, say, a factor of 10, starting at about 2 days to encounter, then the doppler-only tracking might have shown a significant improvement between 1 day and 0.05 days to encounter. It is also suspected that an increased sample rate would not much improve the performance of the optical equipment. Thus, based on the data available, it appears that optical tracking may offer a significant improvement in tracking accuracy only during the brief time range of 1.5 days to 0.05 days from encounter, the maximum improvement occurring at 0.1 days. Bear in mind, though, that the optical instruments under consideration in this study can be used to closer than 0.5 days to encounter.

Position and velocity error curves for the entire earth to Mars mission are shown in Figure 9-10 through 9-15. Care must be exercised in drawing conclusions from these curves. Since they are plotted on a log-log scale, their shapes are distorted and they tend to overemphasize that part of the mission where the optical measurements give improved performance. One may deduce, with the aid of these curves, that the principal

Table 9-IV. Standard Deviations of Position Errors

	2.5 Days to Encounter			At Mars Perifocus		
	σ_x km	σ_y km	σ_z km	σ_x km	σ_y km	σ_z km
Case 1	570	500	450	4.3	7.5	1.4
Case 2	570	500	440	4.0	7.0	1.35
Case 3	500	450	375	2.4	4.1	0.9
Case 4	32,000	28,000	15,500	24	21	15.5
Case 5	4200	3750	2150	5.4	5.4	4.0

error source, prior to 6 days from encounter, is due to the Mars ephemeris error when doppler or doppler plus optical tracking is employed. The principal error source in optical tracking alone, prior to 6 days from encounter, is the initial position and velocity error of the spacecraft with respect to the earth. It is also seen from these curves that a good position fix with respect to Mars occurs sometime after one day to encounter, irrespective of the measurements employed. In fact, doppler-only tracking does not obtain a good position and velocity fix until sometime after 2000 sec (0.02 days) to encounter. However, as mentioned earlier, this might be improved by increasing the doppler sampling rate. It is of interest to note here that it takes about 370 sec for light to travel between earth and Mars at the time of encounter. Thus, position and velocity updates, radioed from the earth to the vehicle, would be based on data that was 740 sec old. This problem could be eliminated if the vehicle carried its own ultrastable oscillator and processed the doppler data onboard. However, in this case the range-rate bias errors would probably be larger than those considered here.

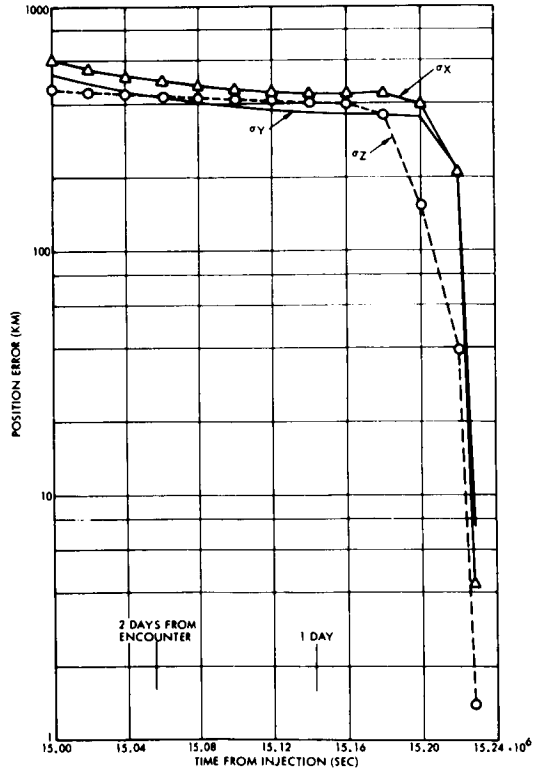

Figure 9-4. Doppler Only Tracking

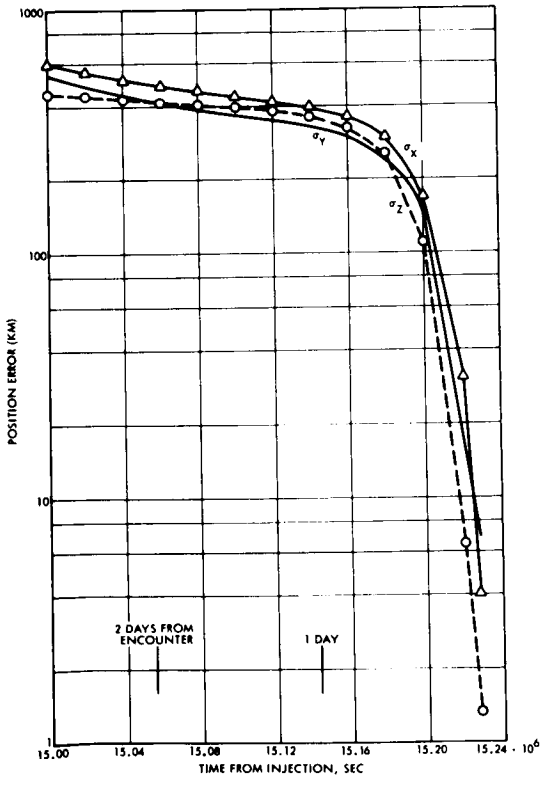

Figure 9-5. Doppler Plus Optical Tracking

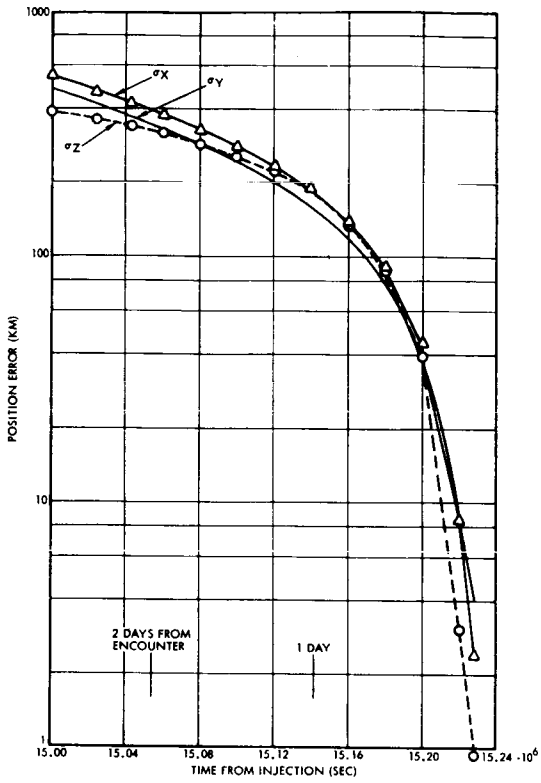

Figure 9-6. Doppler Plus Improved Optical Tracking

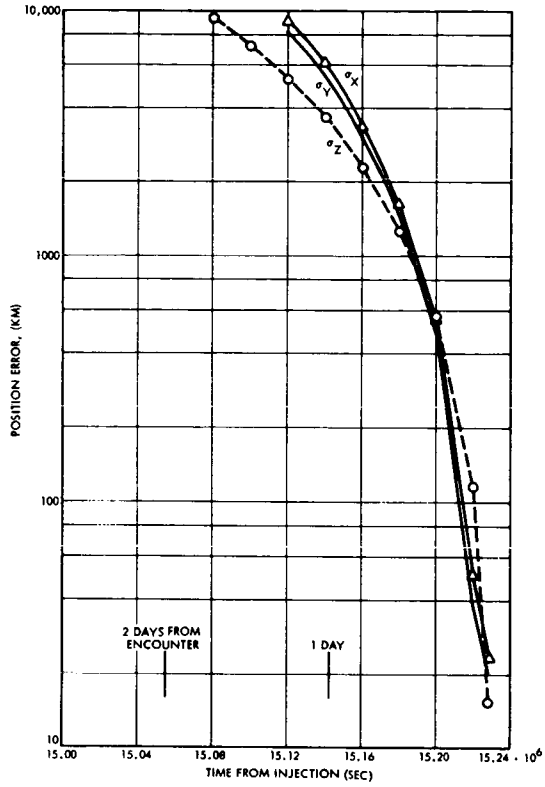

Figure 9-7. Optical-Only Tracking

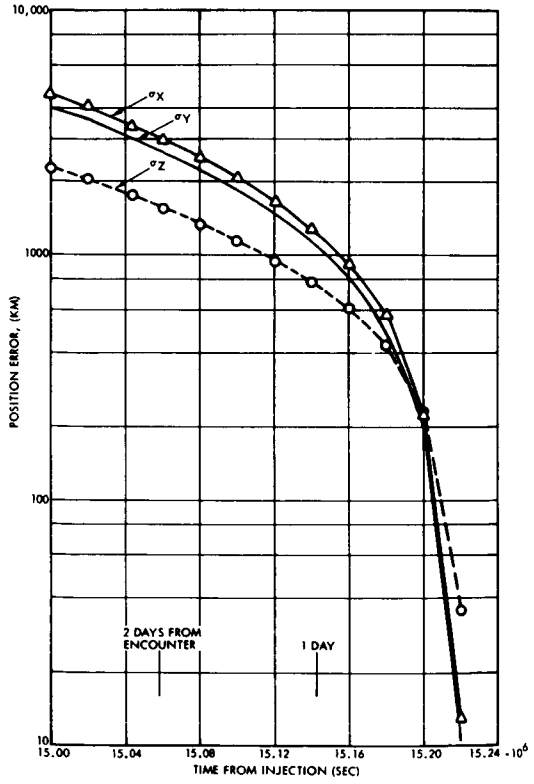

Figure 9-8. Improved Optical-Only Tracking

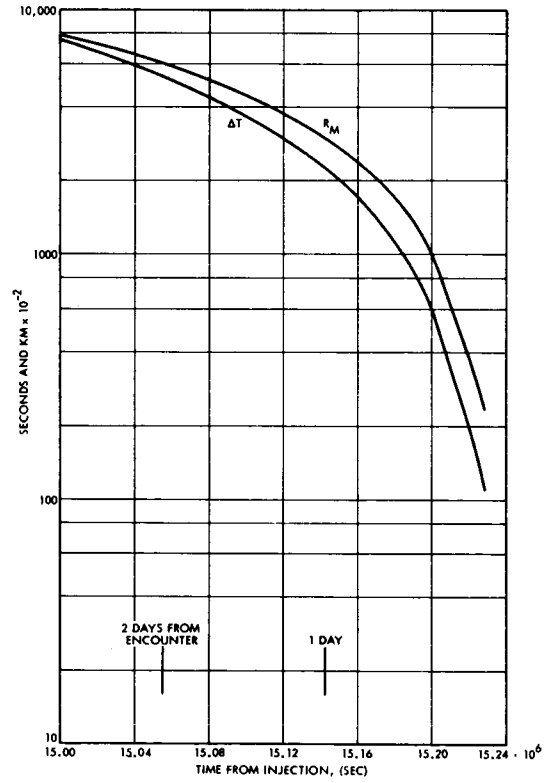

Figure 9-9. Integration (Measurement) Interval and Distance From Mars

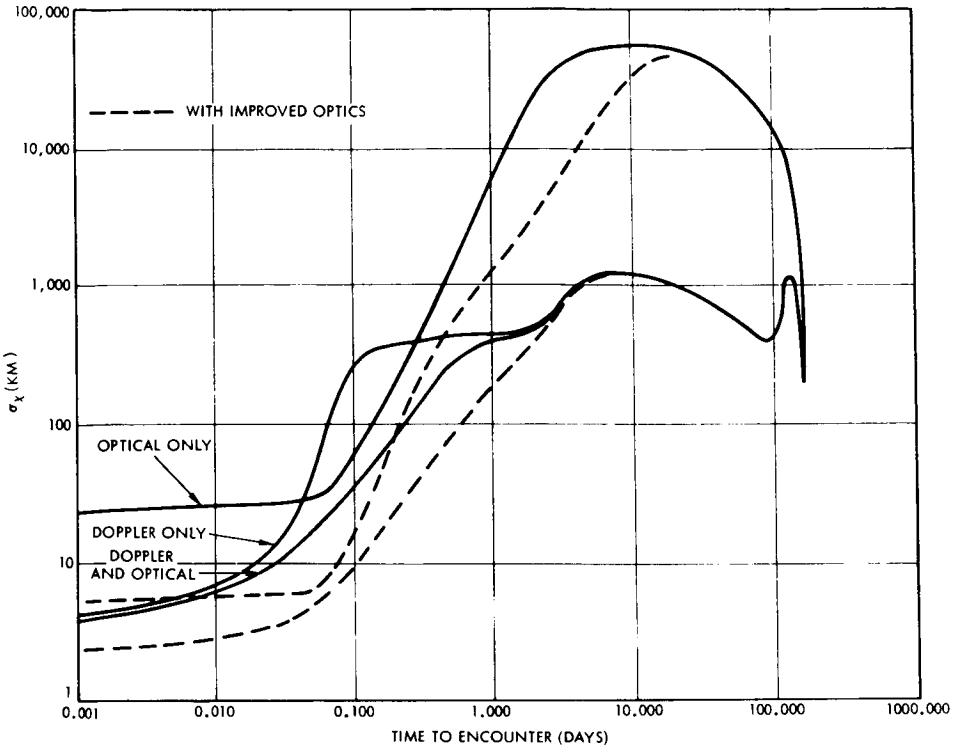

Figure 9-10. Mars/Vehicle Position Standard Deviation

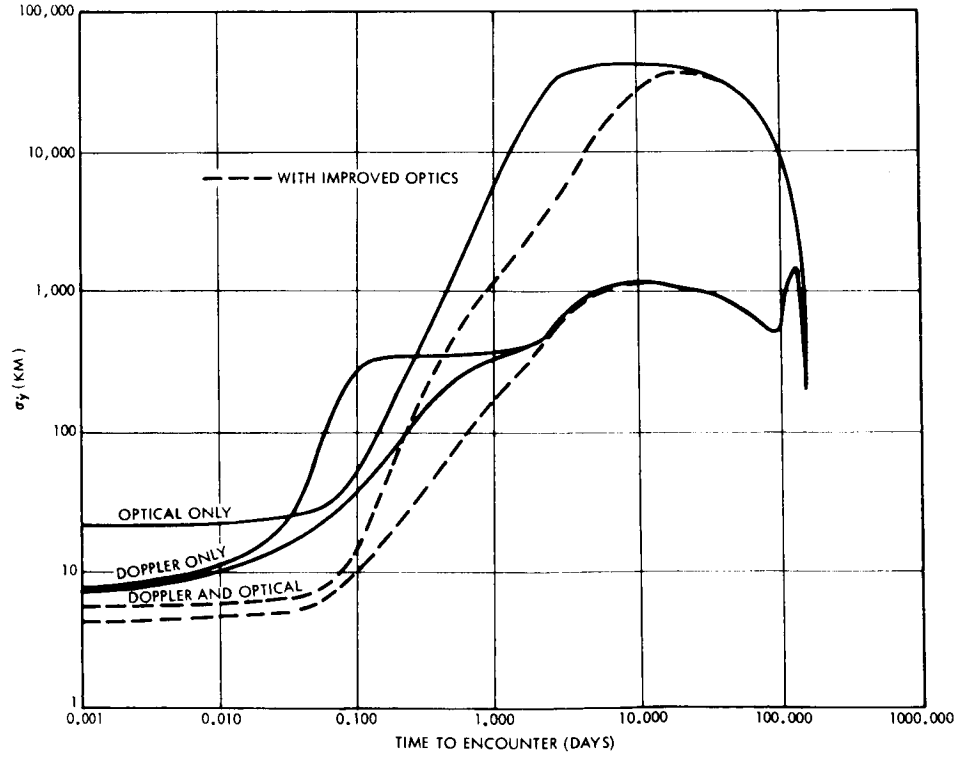

Figure 9-11. Mars/Vehicle Position Standard Deviation

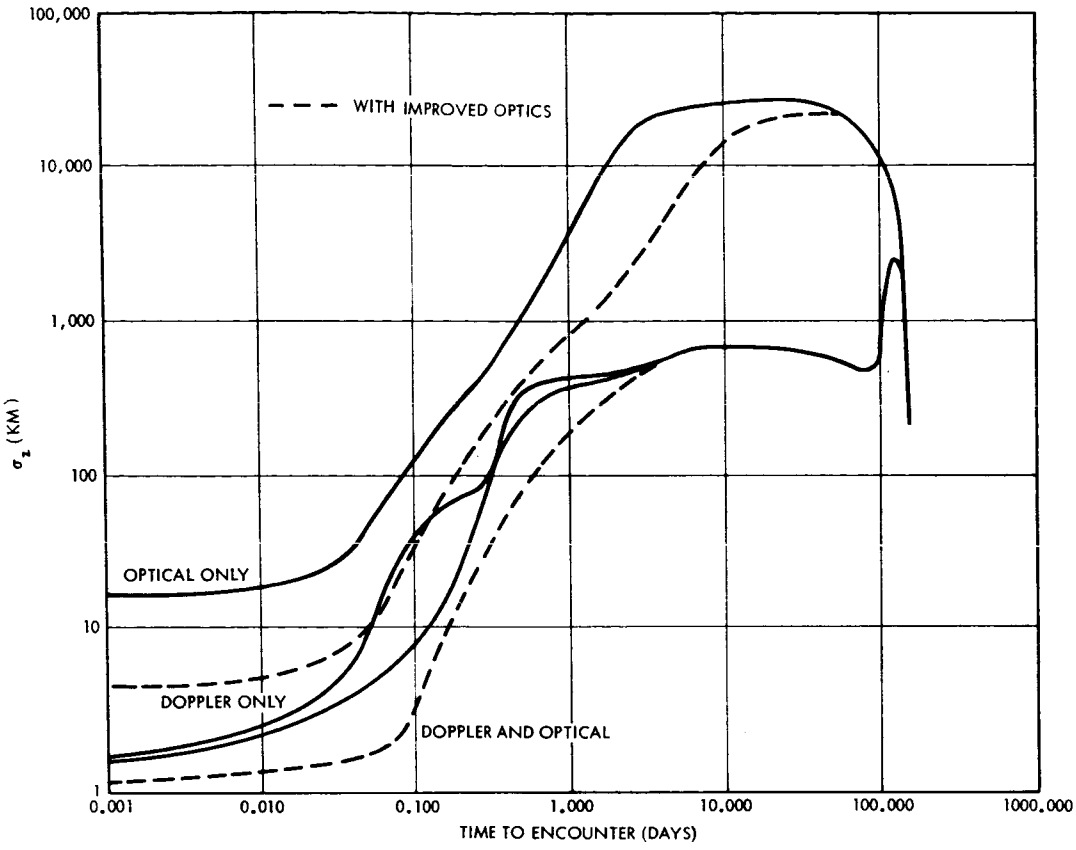

Figure 9-12. Mars/Vehicle Position Standard Deviation

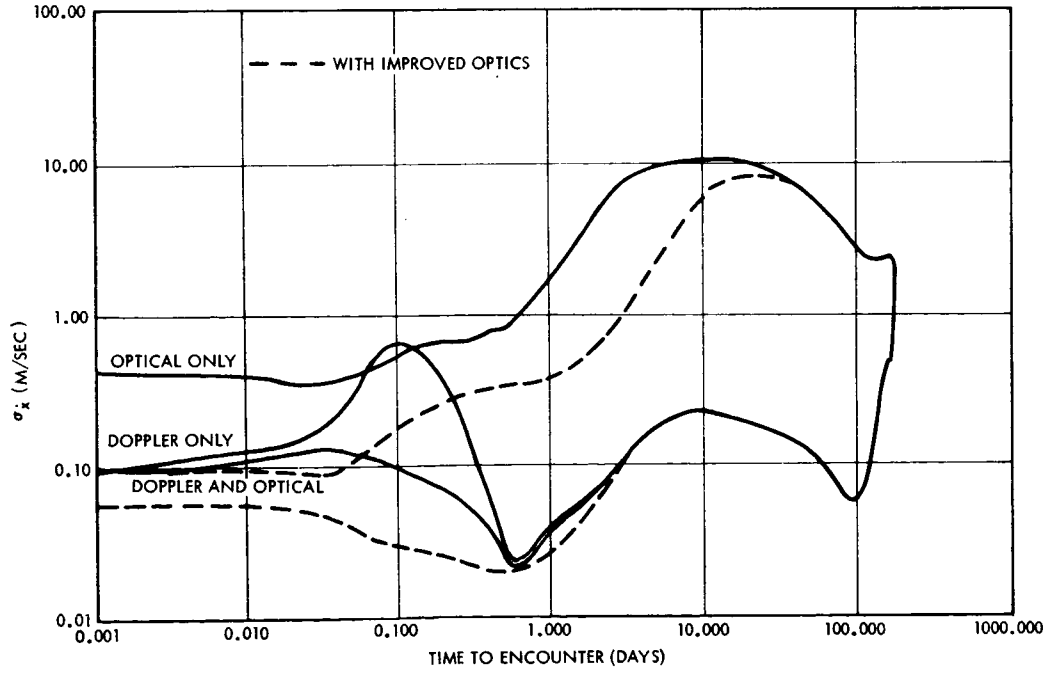

Figure 9-13. Mars/Vehicle Velocity Standard Deviation

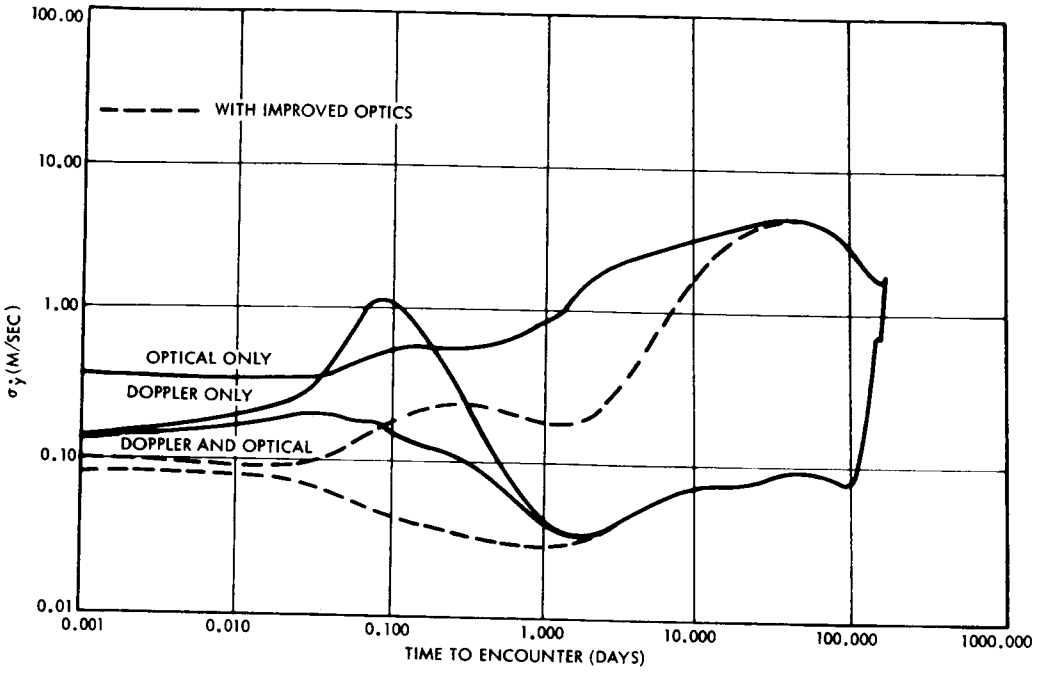

Figure 9-14. Mars/Vehicle Velocity Standard Deviation

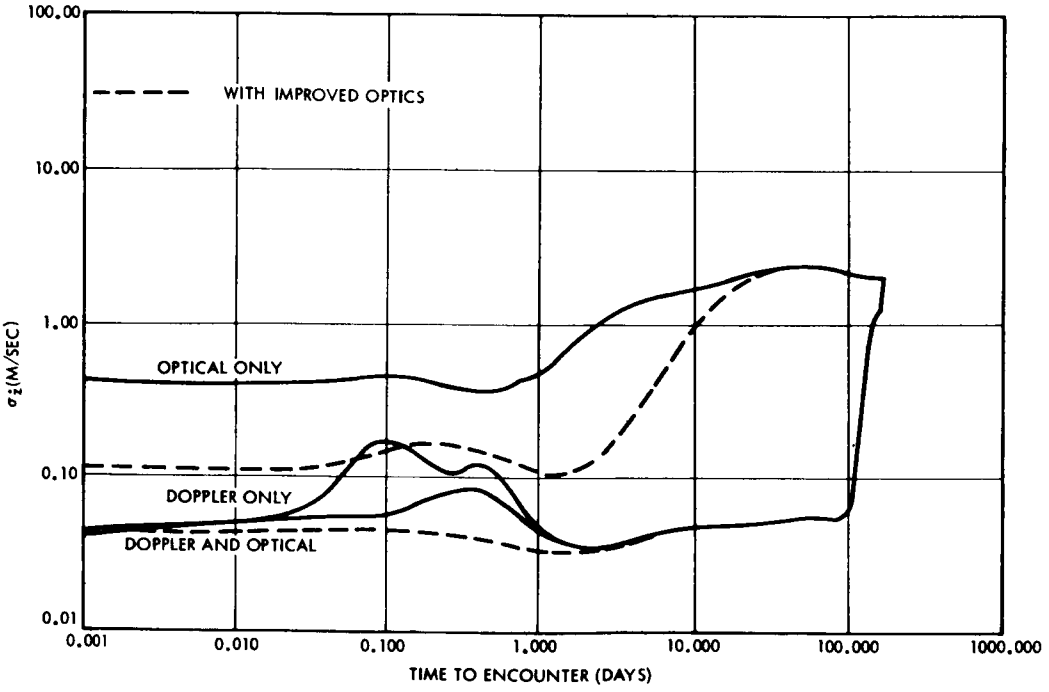

Figure 9-15. Mars/Vehicle Velocity Standard Deviation

REFERENCES FOR SECTION 9

9-1 "SVEAD Users Manual," TRW Systems Report No. 7221.11-10, W. M. Lear, 28 April 1967.

APPENDIX A

PULSE-TORQUING TECHNIQUES

1. INTRODUCTION

Precision pulse torquing of inertial instruments has certain attactive features which have led to a rather wide application of the technique to current guidance system design. While the design details of the various systems are widely different, there is much that all of these systems have in common. This presentation will develop a general description of the pulse-torquing concept and will then discuss some of the electrical error sources for two generic categories.

In order to avoid needless abstraction while maintaining a general analysis, the development has been related to a specific piece of hardware, the SDF, rate integrating gyro. From the electrical design point of view, the analysis carries over to other instruments which lend themselves to precision pulse torquing.

2. TORQUING TECHNIQUES

A number of pulse-torqued mechanizations have been proposed and used. While the specific details and refinements vary widely, most techniques may be categorized as:

a) Constant power, or

b) Variable power, (includes pulse on demand).

This breakdown will be used in the discussion to follow.

2.1 Constant Power

Constant power systems are characterized by constant amplitude, constant duty cycle electrical torquing with a quantized approximation to continuous proportional control being accomplished by modulating the ratio of positive to negative pulses. This system is commonly mechanized with a 100-percent duty cycle, i.e., current flows into the torquer continuously and is allowed to reverse sign only at precisely spaced clock-pulse times. Pulsing is thus quantized to the fixed pulse amplitude – clock period product. A symbolic representation of the essentials is presented in Figure A-1. While other techniques have been used for current reversal, the bridge switch is typical and is usually constructed around switching

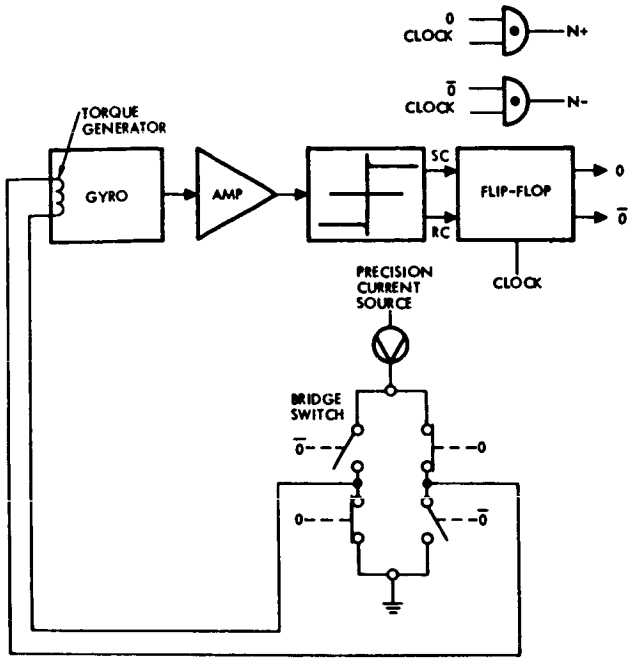

Figure A-1. Constant Power-Pulse-Torque Representation

transistors. Center-tapped torque generator windings and reverse-polarity current sources have also been used in this application. In any event, the problem is the same: the inherent difficulty in maintaining the current pulses constant and balanced plus to minus. The effects of these imperfections will result in both errors in bias and scale factor.

$$E_R = \left\{ \left[1 - \frac{\Delta_1 + \Delta_2}{2A} \right] \frac{H}{A} \int_0^T \omega dt - CT \frac{\Delta_1 - \Delta_2}{2A} \right\}_{\text{Indicated}} - \left\{ \frac{H}{A} \int_0^T \omega dt \right\}_{\text{Actual}} \qquad \text{(A-1)}$$

where

E_R = accumulated angle error

Δ_1 = difference between ideal pulse weight and actual pulse weight for positive pulse

Δ_2 = difference between ideal pulse weight and actual pulse weight for negative pulse

A = area of the ideal torquer pulse

H = angular momentum of gyro

ω = input rate

CT = fixed drift

Review of the error equation above shows that for a constant power mechanization a change in pulse area, (the amplitude – time integral), results in clearly separable scale factor and bias errors. This derived relationship agrees with intuition. If the positive and negative pulse areas increase the same amount, ($\Delta_1 = \Delta_2$), a scale-factor change will result, but the bias term will be zero. On the other hand, if the positive and negative pulse change so that $\Delta_1 = -\Delta_2$ the error will appear as a pure bias term.

2.2 Variable Power

The variable power mechanization, (most commonly referred to as pulse-on-demand), is distinguished by a three-state torquing system as opposed to the binary (positive or negative) levels of the constant power approach. A nominal zero rebalance torque level is added so that the system can call up a positive, a negative, or no rebalance pulse depending upon the state of the gyro output axis. A small dead band is established around the gyro output axis null so that no pulse is called for when the output state is within this dead band. The continuous limit cycling of the binary system is eliminated. A very-much-simplified symbolic representation of the variable power (pulse-on-demand) mechanization is shown in Figure A-2. Again, techniques other than the bridge switch and the precision current source have been used to generate the reversible polarity pulses. Magnetic core and capacitor storage discharge have been used, but the problem remains in maintaining the constant and balanced current pulses. An additional problem occurs in maintaining the nominal zero rebalance torquing level sufficiently close to zero. Systems with transistor switches in the configuration shown are most typical. Unbalanced transistor leakage current in the three-way switch mechanization is the primary source of unwanted gyro torques during the nominally zero torquing level periods. A generalized equation describing the pulse-on-demand mechanization will be derived.

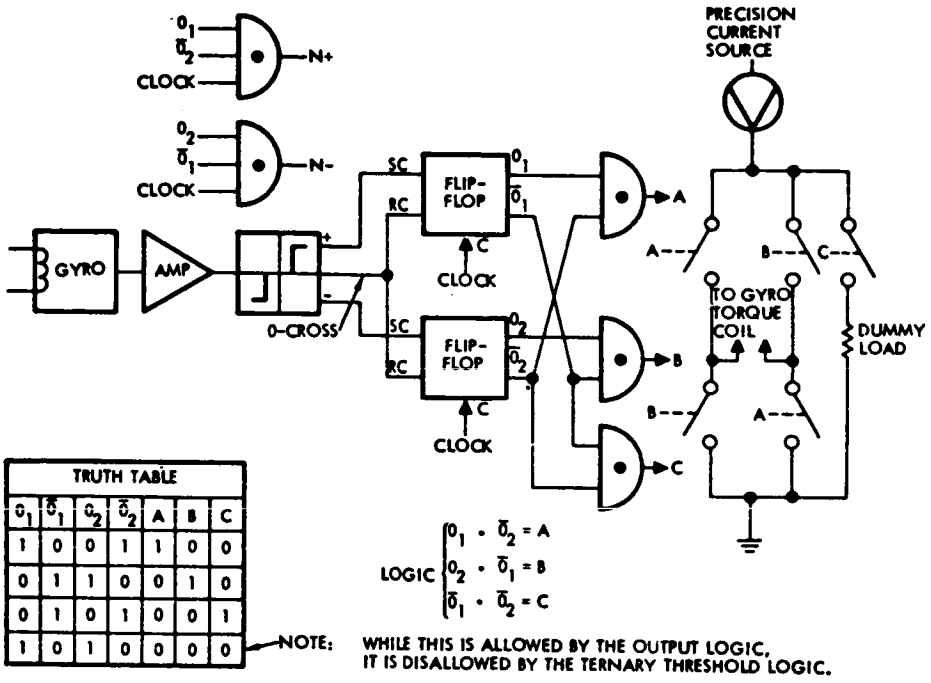

TRUTH TABLE

σ_1	$\bar{\sigma}_1$	σ_2	$\bar{\sigma}_2$	A	B	C
1	0	0	1	1	0	0
0	1	1	0	0	1	0
0	1	0	1	0	0	1
1	0	1	0	0	0	0

LOGIC $\begin{cases} \sigma_1 \cdot \bar{\sigma}_2 = A \\ \sigma_2 \cdot \bar{\sigma}_1 = B \\ \bar{\sigma}_1 \cdot \bar{\sigma}_2 = C \end{cases}$

Figure A-2. Variable Power (Pulse on Demand) Pulse-Torque Representation

Note that in this mechanization, once the gyro gimbal is within its null dead band, and there are no input rates to the gyro, no pulses will be called up or applied to the gyro except as required to rebalance extraneous gimbal torques. The expression shown in Equation (A-2) describes the error resulting from both the pulse-weight variation the leakage current during the no-pulse time.

$$E_R = \left\{ \left[1 - \frac{\Delta_1 - \Delta_3}{A} \right] \frac{H}{A} \int_0^T \omega^+ dt + \left[1 - \frac{\Delta_2 + \Delta_3}{A} \right] \frac{H}{A} \int_0^T \omega^- dt - \frac{CT\Delta_3}{A} \right\}_{\text{Indicated}} - \left\{ \frac{H}{A} \int_0^T \omega dt \right\}_{\text{Actual}} \quad \text{(A-2)}$$

where

Δ_3 - error introduced by the leakage current through the torquer

ω^+ - input rate in positive direction

ω^- - input rate in negative direction

The output count, N, will be equal to the algebraic sum of the integral of positive input rate times its scale factor, the integral of negative input rate times its scale factor and a bias term. The scale-factor nonlinearity (discontinuity at zero) is caused by positive and negative pulse unbalance, the bias term is caused by unbalanced leakage currents occurring during the nominal zero pulse state and deviations of the scale-factor slope from its nominal value, H/A, are influenced both by pulse-amplitude variations and the off-state leakage currents.

It is instructive to write Equation (A-2) in another form.

$$N = \frac{H}{A}\int_0^T \omega dt - \frac{H}{A}\left[\frac{\Delta_1}{A}\int_0^T \omega^+ dt + \frac{\Delta_2}{A}\int_0^T \omega^- dt + \frac{\Delta_3}{A}\frac{H}{A}\int_0^T |\omega| dt - CT\right]$$

where N is the summation of pulses.

The first term is the ideal relationship. The other two terms represent errors which are dependent upon circuitry parameters and mission profile. It is significant to note that both error terms kinematically rectify alternating input angular rates, so that drift rate will be critically a function of vehicle limit cycling. The second term, which results from pulse unbalance, will grow as the limit cycle ω's increase, while the third term, which comes about due to the pulse off-state leakage, will decrease as ω increases.

Once the distinction has been made between the constant and variable power system categories of pulse-torquing logic may be discussed. Figure A-3 presents some rather broad types of loops that are discussed here.

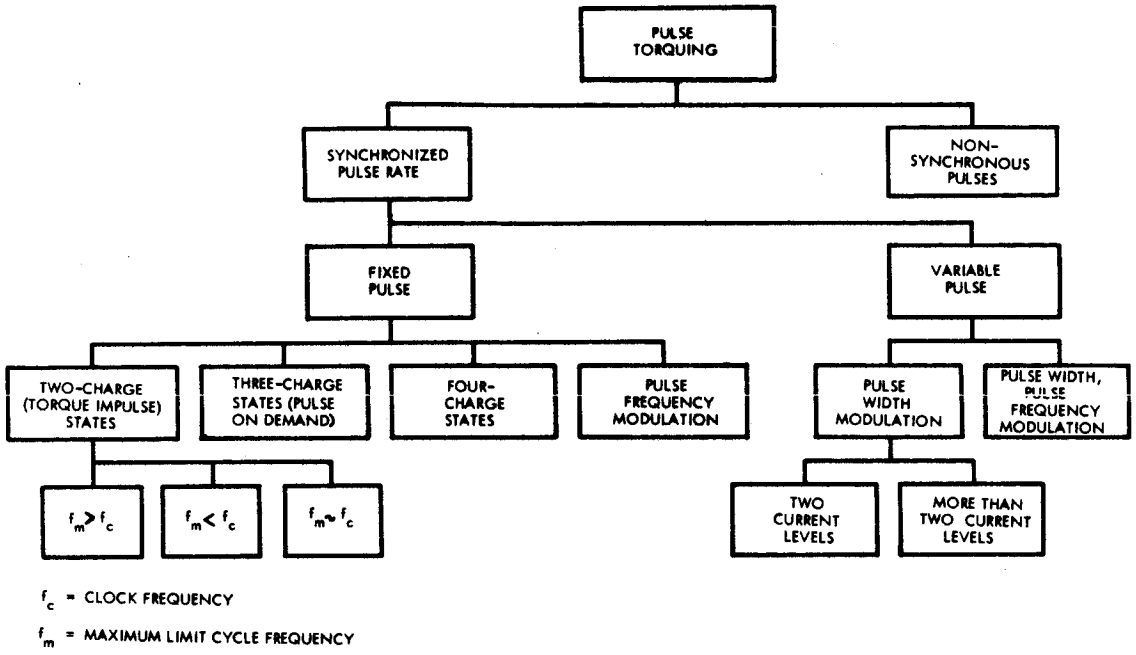

Figure A-3. Types of Pulse Torquing

3. CATEGORIES OF PULSE-TORQUING LOGIC

3.1 SYNCHRONIZED PULSE RATE (PERIOD T_s): FIXED PULSE

3.1.1 Two-Charge State

The two-charge state system is defined by the following equations:

$$\text{Pulse off time}/\ T_s = C$$

$$\text{Pulse on time}/\ T_s = 1 - C$$

where C is a constant, $0 < C < 1$. When C = zero the system has two current levels with the pulse time equal to T_s. When zero $< C < 1$, the system has three current levels. However, the charge or torque impulse produced during each clock period is one of two states. These states are positive maximum or negative maximum.

This system dissipates a constant energy per pulse in the sensor torquer by applying torquing pulses to the torquer at a fixed rate, regardless of the sensor pickoff position. Three types of two-charge state systems are discussed below. Their characteristics vary depending on

the relative frequency of the clock, f_c, and the dynamics of the sensor. The dynamics of the sensor can be discussed in terms of f_m, the maximum limit cycle frequency, which is defined as follows: given a fixed energy torquing pulse, f_m is the maximum clock frequency for which a 1 to 1 moding of the system is possible, if closed-loop operation for zero input consists of alternating positive and negative pulses.

If f_c is substantially less than f_m, the polarity of the amplified pick-off signal from the inertial sensor controls the torque polarity of the next pulse; however, the switching time is constrained to occur only at the time of a clock pulse. Typically, in this case, the clock period and torque pulse width are identical. Since f_c is much less than f_m, it is possible with no input to force the gyro gimbal to move synchronously with 1/2 f. Under these conditions, the sensor would be operating in a 1 to 1 mode. Typical operating curves at zero input are shown in Figure A-4. If the sensor experienced an input, the mode would change accordingly. For example, the mode may be 1 to 1 for a while then change to 1 to 2, and so on. In other words, the mode will vary as a function of inputs. In this system, instantaneous inputs are not obtainable, and only integrated results are of any value. This is the case for practically all pulse torquing systems due to their fundamental characteristic of storing information in the float angle.

Now if f_c is much greater than f_m, a torque pulse (the width of one-torque pulse is usually adjusted to be equal to the period of f_c) is not sufficient to produce a phase reversal of the sensor pickoff signal prior to the arrival of the next clock pulse. The result is that the float motion no longer moves at the same f_c but at some other frequency dictated by f_m and the inertial sensor's input. In this case, stable limit cycles other than 1 to 1 can be achieved and, in fact, will be. For example, the limit cycle may be 10 to 10 in which 10 clock pulses occur each one-half cycle of the float oscillating period, provided zero input is applied. (For $f_c > f_m$, see Figure A-5.)

When the value of f_c is close to that of f_m, the limit cycle cannot be predicted unless some form of compensation is applied to stabilize the limit cycle (e.g., to a 1 to 1 system).

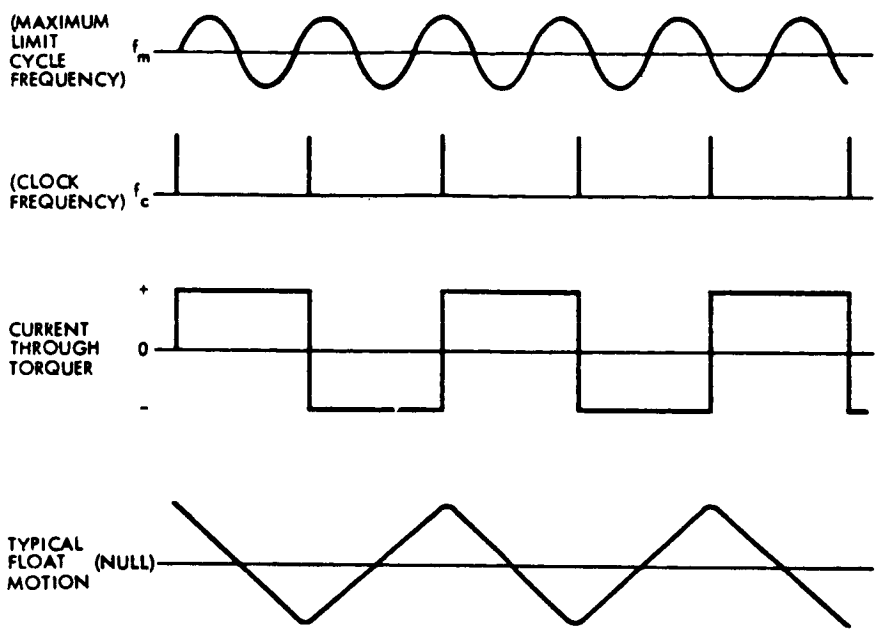

NOTE: SYSTEM IS SHOWN WITH ZERO INPUT

Figure A-4. Synchronized Pulse Rate, Fixed Pulse Width, Two-Charge State System ($f_m > f_c$)

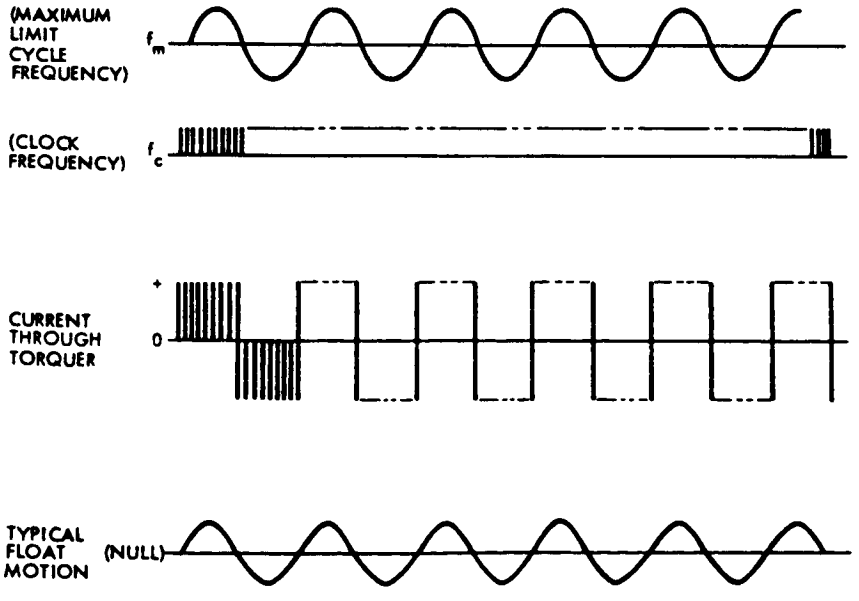

NOTE: SYSTEM IS SHOWN WITH ZERO INPUT

Figure A-5. Synchronized Pulse Rate, Fixed Pulse Width, Two-Charge State System ($f_c > f_m$)

3.1.2 Three-Charge State or Pulse-on-Demand

The three-charge state or pulse-on-demand system uses three torquer current states and has a deadband associated with the sensor pickoff signal. The three-charge states are:

1) Full scale positive

2) Zero

3) Full scale negative

When the pickoff signal is outside the deadband, a pulse of the appropriate polarity is applied to the torquer coil.

Typically, the pulse energy is selected in design to be equivalent to the information stored in the sensor (a Δ velocity or a Δ angle) when the sensor pickoff is at the edge of the deadband. When the pickoff is within the deadband, no current is applied to the torquer.† The algebraic sum of the pulses through the torquer as a function of time corresponds to the change in angle rotation or velocity experienced by the inertial sensor during that time period.

3.1.3 Four-Charge State

The charge as a function of gimbal angle is illustrated by Figure A-6. The values of the torquing rates

$$\left(\frac{Q_1}{T_s} \text{ and } \frac{Q_2}{T_s}\right)$$

depend on the system requirements.

This system's advantage is that throughout the major portion of the mission the torquing requirement will be less than the level corresponding to Q_1; therefore, the torquer will be receiving a continuous power input. However, a large level pulse is available for the maximum vehicle rate to be considered during the mission.

---

†If it is desired to have constant power dissipated in the sensor torquer, the torquing pulses might be switched through a noninductively wound resistor in the torquer when the sensor pickoff is within the deadband.

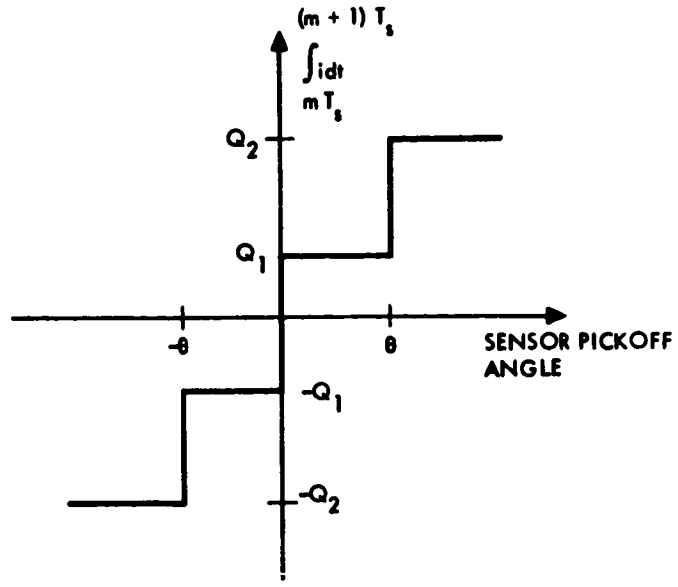

Figure A-6. Four-Charge State System

3.1.4 Pulse-Frequency Modulation

In pulse-frequency modulation systems, the pulse width is fixed and the pulse frequency is made proportional to some function of the sensor pickoff angle.

3.2 SYNCHRONIZED PULSE RATE (PERIOD T_s): VARIABLE PULSE

3.2.1 Pulse-Width Modulated Systems, Two or More Current Levels

Pulse width is modulated to within T_s/N, where N is an integer. Many techniques are available, only one of which will be discussed here. This system employs two clock signals, f_{c1}, and f_{c2}, which are derived from the same source. A low-frequency clock, f_{c2}, is used to switch the logic circuits so that a particular polarity of torque is applied regardless of the sensor float position. A signal derived from the float position in conjunction with a high frequency clock signal, f_{c1}, is used to determine the precise time of the torque reversal, which always occurs in synchronism with the f_{c1} pulse train. By this means a pulse modulation system is achieved (see Figure A-7.) The relative widths of the torquing pulses may be measured by using the logic circuits to gate the high-frequency clock pulse, F_{c1}, to a counter.

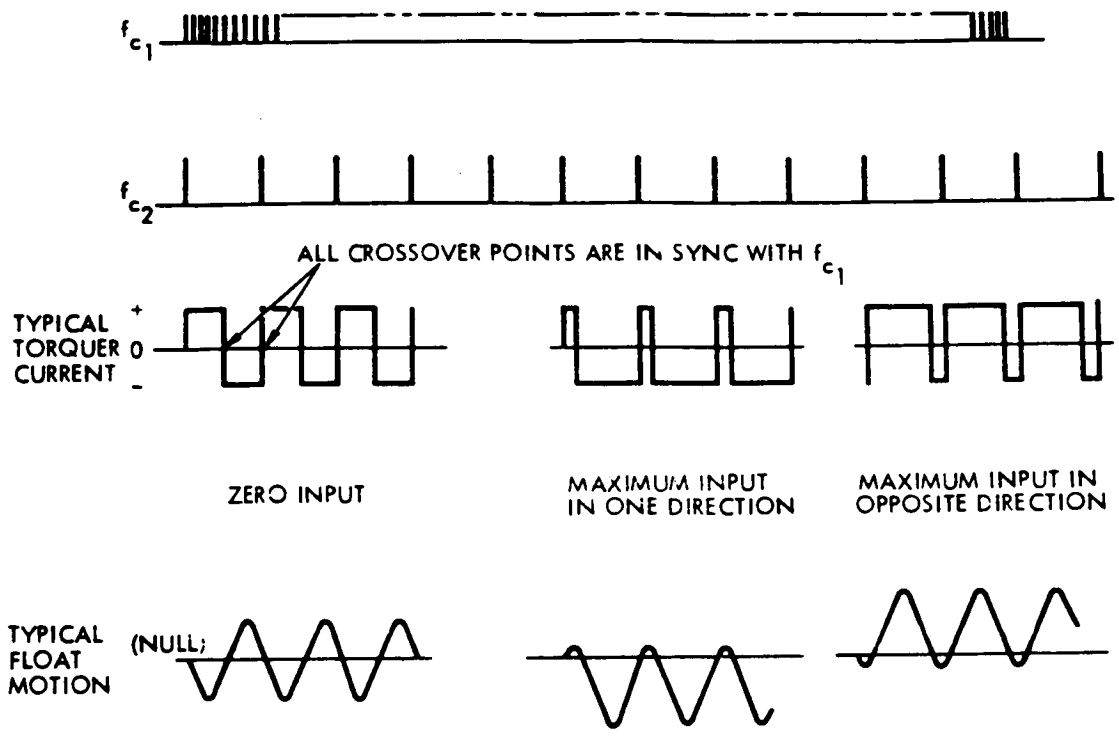

Figure A-7. Pulse Width Modulated, Two-Current Level System

3.2.2 Nonsynchronous Pulses

There appears to be little advantage to fixed pulse width, nonsynchronous systems. The most desirable of the nonsynchronous approaches appears to be a nonfixed pulse width system wherein the total energy of each pulse is accurately measured. (Of course, the concept of measuring the pulse energy to improve accuracy is applicable to all the systems discussed so far and, in fact, is often implicitly used.) Nonsynchronous systems, if desired, could be subdivided into systems similar to synchronous systems. As an example, consider a two-charge state, bang-bang, nonsynchronous system. The torquing signal would have two states, full positive or full negative. A negative signal from the sensor pickoff would turn on the full positive torquing current (this current would continue until the sensor pickoff was generating a positive signal. Then the torquing current would be switched to negative until the sensor pickoff signal changed state. Finally, a measurement of the applied pulse width and pulse area would have to be made.

APPENDIX B

STRAPDOWN GUIDANCE SYSTEM DYNAMIC PERFORMANCE

Strapdown and gimbaled inertial guidance systems, because of their physical differences, perform differently in the operational environment. The strapdown guidance system performance is more susceptible to vibration environment and computational errors than the gimbaled system, but is less sensitive to some of the error sources that affect gimbaled systems. This appendix has been included to identify the error effects which are important to the functioning of the strapdown guidance system in the operational environment, so that strapdown system performance can be compared with the more familiar and widely analyzed gimbaled system performance.

1. STRAPDOWN GUIDANCE SYSTEM PERFORMANCE FORMULATION

Strapdown system synthesis and system performance evaluation involves the properties of the inertial instruments, the associated instrument control electronics, the digital computer, and the software programmed into the computer. Rebalance instrument loop designs must be achieved which meet performance criteria under vibrational environments and large vehicle motions. The properties of the digital computer such as the errors associated with computer algorithms, the computer sampling errors, and round-off errors must be considered jointly with the properties of the instrument loops.

The system synthesis process logically starts with the establishment of the environment in which the system must operate. The most significant environmental inputs which must be defined are linear vibrations, angular vibrations, vehicle control motions such as limit cycles and body-bending mode rotations, the maximum input levels of acceleration and angular rate, and gross vehicle reorientation requirements associated with the particular trajectory. In establishing the input environment under which the strapdown system must operate, any local mechanical resonances associated with the system supporting structure or any internal resonance must be considered.

Based on the environment specification under which the system must operate, a preliminary design for the instrument and rebalance loops is accomplished. Of course, fundamental to any system design is the choice of appropriate inertial sensors and specification of required performance and functional properties. The synthesis of instrument rebalance loops requires that the loop designs must first meet relatively conventional criteria such as dynamic stability, dc bias stability, and ability to operate without saturation under the maximum specified input environments. Also of fundamental importance to rebalance loop design are the phenomena such as vibration rectification errors, gyro float excursion under large angular rates, and accelerometer pendulous mass excursion under input accelerations, all effects to which strapdown systems are particularly sensitive.

The dynamic errors which result from vibrational inputs as well as vehicle limit cycle motions are discussed in greater detail below, and expressions for these error sources are given. The next logical step in the design process is to accomplish a worst-case analysis of each of these error sources individually. In order to perform such a worst-case analysis, each error source is assumed to be excited by an environment in a manner such as to maximize each error source individually. Also, tolerances on loop parameters that affect these error sources are assumed to be in worst-case conditions. The objective of such a worst-case analysis is to ensure that no single error source can exceed some reasonable performance criteria based on the assumed environment and on the overall mission requirements. Based on the above worst-case analysis, design iterations are accomplished as required.

The above type of worst-case analysis, although highly useful in ensuring that the error sources are bounded, is nevertheless a highly conservative method of estimating system errors. In order to be useful as inputs to an overall system error model, realistic input environments must be assumed. In worst-case error analysis, the environment is assumed to always act in a direction such as to maximize a particular error source. In a real vehicle environment, this is generally not the case. The direction of a particular form of environment can be expected

generally to vary with time. Also, over the mission duration, the magnitude of a particular environment will vary with time and discrete events; for instance, the staging or maximum mach number regions will generally result in significantly higher environment than in the intervening periods of time. Hence, these factors must be included in the development of an overall system error analysis by appropriate judgment as well as utilization of existing and previously acquired data from other vehicles.

The errors which are identified in the next sections and which must be evaluated for inclusion in the overall system error model can generally be grouped into two categories. The first category of error sources is one in which the errors manifest themselves as disturbance torques in the instruments. Such errors include spin input rectification, vibropendulous error, anisoinertia, etc. These errors either arise internally within the instruments or are due to the combined performance of the instrument and its individual rebalance loop and are essentially independent of the digital computer. The second category of error sources, which includes coning, fictitious coning, and sculling errors, must be evaluated by considering the instrument loop and the digital computer properties jointly. The first category of errors are generally analyzed by techniques that make use of digital computer simulation programs developed at TRW. The second category of errors, which include such effects as computer-sampling errors as well as algorithm errors, can be estimated by these simulation programs and by linear analytical techniques, but generally require the use of different, more specialized, digital computer simulation programs to accurately evaluate their magnitudes.

These two categories of errors will be separated into sensor-induced rectification and computer-induced errors for the ensuing discussion in this appendix.

2. RECTIFICATION AND DIRECTION COSINE ERROR

The inertial components (gyros and accelerometers) of a strapdown guidance system are usually mounted directly to the spacecraft without benefit of vibration-absorbing material. Therefore, these gyros and accelerometers are subjected to the same vibration environment as that of the mounting surface. For reliable prediction of system performance,

an accurate estimation of inertial component errors due to vibration must be made. In addition, the accuracy of solution of the strapdown system equations is critical to the proper performance of the system. If the computer errors for the attitude reference, velocity integration, and alignment equations are made sufficiently small by the selection of the proper equations, word size, and iteration rate, it will follow that the errors made by the same computer on the other computations can be made negligible. Only the most important of these, the direction cosine errors, will be discussed here.

The types of errors to be discussed herein are usually divided into two groups that are commonly referred to as

1) Rectification errors (includes the following):

   Spin-input rectification
   Spin-output rectification
   Accelerometer vibropendulosity
   Fictitious coning

2) Direction cosine errors (classified by the following effects):

   Drift errors
   Orthogonality errors.

The rectification errors are related to the inertial reference unit (IRU) as opposed to the direction cosine errors which are associated primarily with the digital computer and software.

Fictitious coning is given special consideration in the ensuing rectification error discussion since it is also affected by lack of perfect computer computations. Each of the effects listed under direction cosine errors is discussed with regard to their causes to define clearly their cause-effect relationships.

The effects of vibrations on the attitude reference are quite complex and usually not negligible. A closed-form equation for the errors of the gyroscope/computer system when subjected to arbitrary inputs is neither available now, nor is it likely to be. Digital simulation does provide a convenient and meaningful analysis of the system errors.

Certain results are available which, although they fall short of the complete analysis required, are nonetheless instructive in that they give an insight into the problem and, in addition, furnish approximate and convenient estimates of the system errors. These techniques are discussed in detail in the references of this report and some of the results obtained are abstracted herein.

3. RECTIFICATION ERRORS

The process by which each of the above rectification errors occurs is explainable by similar phenomena, i.e., in each case, two separate vibrational inputs propagate through different inertial sensor servo paths and combine in time domain multiplication (TDM). The average value of this TDM constitutes the rectification error. A mathematical model of the rectification phenomenon is shown in Figure B-1.

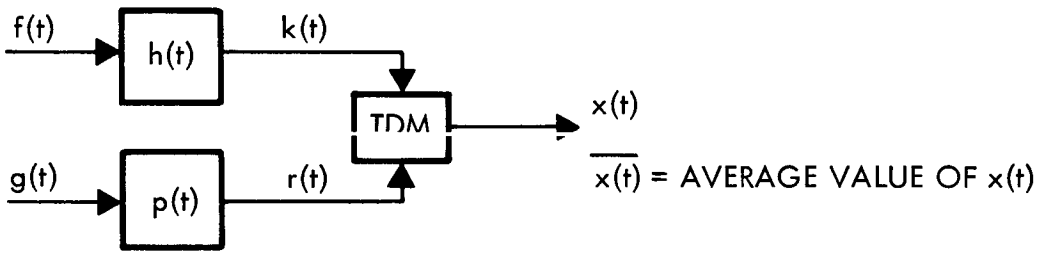

Figure B-1. Rectification Model†

†Note that h(t) and p(t) are merely time domain counterparts of sensor loop transfer functions.

The vibrational inputs, f(t) and g(t), in Figure B-1, are considered to be excitations acting along (translation) or about (rotation) spacecraft fixed axes. The impulse responses, h(t) and p(t), are the responses of linearized sensor servo loop paths associated with these axes. The prediction of rectification errors, as presented here, is contingent upon two factors. First, the sensor loops must be representable by a linear model. Second, and most important, an accurate description of the excitations, either deterministic or statistical, must be known.

If these inputs can be described deterministically (sinusoidal, constant, etc.) then the output, x(t), can be predicted exactly as a function of time. However, when the inputs are nondeterministic or random in nature, then no exact solution can be found. Instead, only statistical means can be employed to demonstrate a most probable value for x(t). This most probable value, or mean, will be denoted by $\overline{x(t)}$.

Several forms of a general solution for this average error have been derived. One form is a time domain solution to random excitations,

$$\overline{x(t)} = \int_{-\infty}^{\infty} R_{fg}(\beta) \left[\int_{-\infty}^{\infty} h(\beta+\gamma)\, p(\gamma)\, d\gamma \right] d\beta \qquad \text{(B-1)}$$

and the alternate frequency domain solution is

$$\overline{x(t)} = \frac{1}{\pi}\int_{o}^{\infty} \left|P(j\omega)\right|\left|H(j\omega)\right| R_e\left[\Phi_{fg}(\omega)\right] \cos(\theta_P - \theta_H)\, d\omega$$

$$-\frac{1}{\pi}\int_{o}^{\infty} \left|P(j\omega)\right|\left|H(j\omega)\right| I_m\left[\Phi_{fg}(\omega)\right] \sin(\theta_P - \theta_H)\, d\omega \qquad \text{(B-2)}$$

The symbols R_{fg} and Φ_{fg} indicate correlation and power spectral density representations of the general environments, f(t) and g(t).

Equivalent forms of these equations can be derived pertaining to a sinusoidal environment.

3.1 Gyro-Accelerometer Model

To demonstrate how each of the rectification errors is related to the mathematical model above, a basic IRU configuration is assumed. This IRU contains three single-degree-of-freedom, rate-integrating gyros and three damped pendulum accelerometers. Each of the six instruments operates in conjunction with an electrical rebalance loop. As can be shown, certain of the error sources considered are functionally related to the dynamic response characteristics of the closed instrument loops.

Hence, certain closed-loop relationships can be developed from which the dynamic errors can be derived. In the ensuing analysis because of the similarity between the gyro and accelerometer closed loops, a single derivation was accomplished in sufficiently general form to allow its use in the analysis of either instrument. That is, a basic gyro instrument model was used for the derivation, but the equations that were developed also assumed the existence of a pendulous mass attached to the gyro float. Hence, the resulting expressions apply to a gyro loop if the pendulosity is taken to be zero and apply to an accelerometer loop if the wheel momentum is taken as zero. The instrument model is represented by Figure B-2.

The general equation resulting from the derivation is

$$I_y \ddot{\theta} + C\dot{\theta} = L_a + H_r \omega_X - m\ell\, a_X + L_e - I_y \dot{\omega}_Y \qquad \text{(B-3)}$$

where

$$L_e = L_e' - \omega_X \omega_Z \left(I_x - I_z \right) - H_r \theta \omega_Z + m\ell\, \theta a_Z \qquad \text{(B-4)}$$

L_e' = error torques (biases, scale factor errors. unintentional mass unbalances)

L_a = electrically applied torque by means of the instrument torquer

I_y = float moment of inertia about output axis

C = viscous damping coefficient

H_r = angular momentum of gyro

a_X, a_Z = components of case acceleration relative to inertial space along the case X and Z axes, respectively.

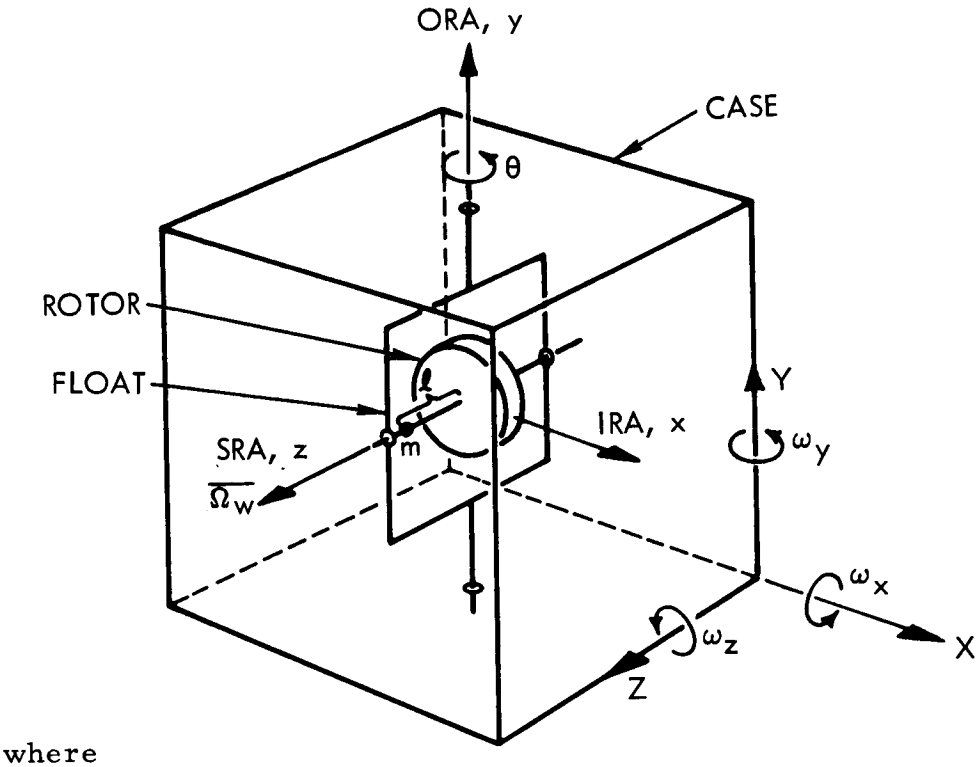

where

X, Y, Z	instrument case fixed axes
x, y, z	axes fixed to inner member
θ	rotation of float relative to case
$\overline{\Omega w}$	angular velocity vector of gyro wheel
m	pendulous mass
ℓ	effective moment arm of pendulous mass
ω_i	angular velocities

Figure B-2. Combined Sensor Model

These equations apply to either type of instrument (gyro or accelerometer) considered in this report. By letting H_r be zero, the equation of a damped pendulum results; and by letting $m\ell$ be zero, a single-axis gyro is represented. It can be shown that the equation may be used to describe the basic instrument rectification errors: spin-input, spin-output, anisoinertia, vibropendulous, anisoelastic, and cylindrical torque rectifications.

Since L_a is defined as a linear function of θ during closed-loop operations, Equations (B-2) and (B-3) are linear but the last three terms in Equation (B-4) are not. The term involving the product of ω_X and ω_Z would not, by itself, preclude the use of linear analysis techniques to obtain the solution of these equations, since it involves only external forcing functions and is not a function of θ, the float angle. Hence, it is only the terms $H_r \theta \omega_Z$ and $m \ell \theta a_Z$ which preclude general linear solutions of Equations (B-3) and (B-4). However, in deriving the expression for dynamic rectification errors, general solutions are not required. Instead, these rectification errors can be defined in terms of the steady-state rectification errors for either sinusoidal or stationary gaussian random inputs.

3.2 Spin-Input Rectification (SIR)

The general equations that were presented above will now be applied to an error phenomena commonly known as Spin-Input Rectification (SIR). This error is caused by vibratory angular excitations acting on a spacecraft simultaneously about the spin and input axes of a gyro. The following discussion demonstrates the mechanism by which SIR occurs in a gyro loop. The parameters used in this demonstration are then related to the appropriate parameters of the general form for x(t).

3.2.1 Gyro Model and SIR

A linearized block diagram that is representative of a typical SDGS gyro loop is shown in Figure B-3. In essence, the operation of the loop is based on nulling the angular float motion by means of a feedback torque. To accomplish this nulling, the gyro pickoff signal is amplified and converted to a current which drives an output axis torquer in a direction opposite to that of the float motion.

The symbol, ω_I (s), represents the angular rate acting on the spacecraft along the gyro input reference axis. The symbol, ω_{IM} (s), indicates the input rate as measured by the gyro loop. Symbol, θ (s), is the gyro float offset angle from null (caused predominantly by ω_I(s) and the gyro dynamics).

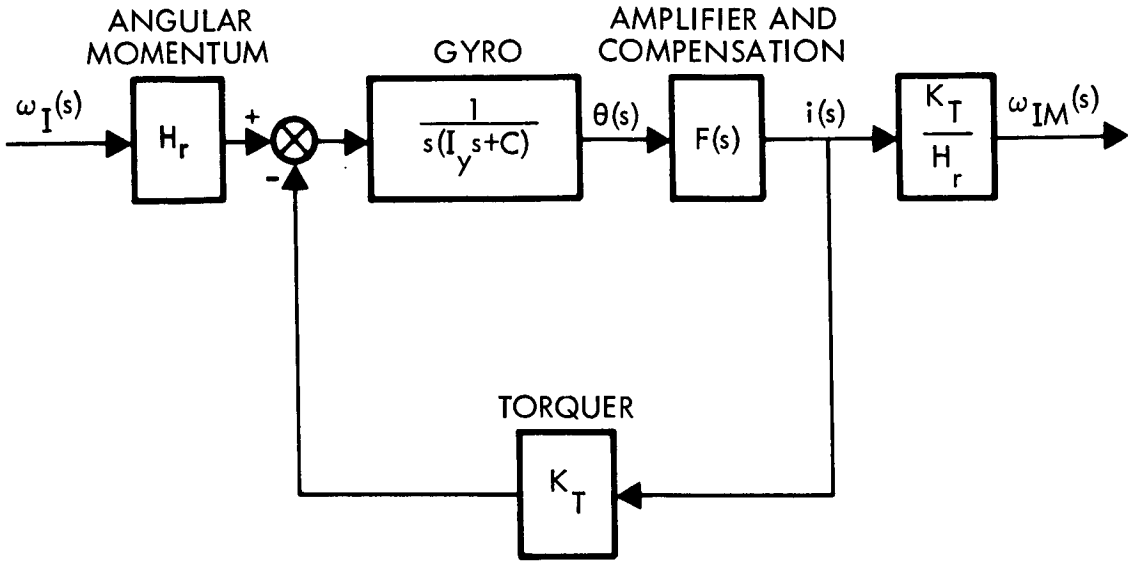

Figure B-3. Linearized Gyro Loop Block Diagram

By reduction of the block diagram to conventional transfer function form, a closed loop expression for $\theta(s)$ is obtained:

$$\theta(s) = \frac{H_r}{s(I_y s + C) + F(s) K_T} \omega_I(s). \qquad \text{(B-5)}$$

If the vehicle also happens to have a component of its angular rate acting about the spin reference axis of the gyro then some of this rate component will couple into the loop when θ is non-zero. This coupling is illustrated in Figure B-4.

Inspection of Figure B-4 shows that for θ non-zero, a component of ω_s, the spin reference axis rate, will fall along the instantaneous input axis. Moreover, for a well-designed gyro loop†, the magnitude of this component will be $\omega_s \theta$. It is this unwanted input that causes SIR. In particular, SIR is defined by

$$\text{SIR} \triangleq \overline{\omega_s(t) \cdot \theta(t),} \qquad \text{(B-6)}$$

†This reliance on good loop design is based on an assurance that θ is always being nulled so as to be a small angle. Therefore, it is justifiable to approximate sin θ by θ.

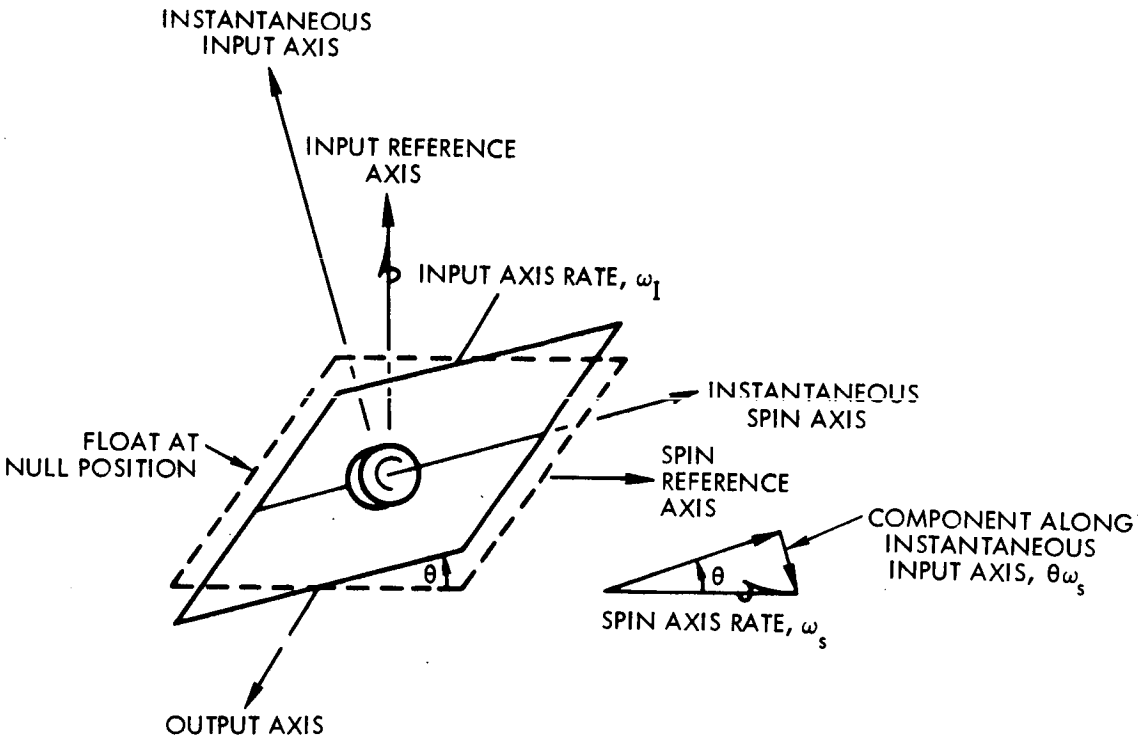

Figure B-4. Pictorial Representation of Gyro Float Motion

where the bar again denotes time averaging. For purposes of identification, SIR will be denoted by $\overline{\Delta(t)}$.

It is appropriate to point out that the introduction of an extraneous input, namely $\omega_s \theta$, into the gyro input would have some effect on θ. Although this is true, since θ is a small angle, it also follows that

$$\omega_I >> \omega_s \theta \qquad \text{(B-7)}$$

Therefore, it is concluded that the additional input furnished by $\omega_s \theta$ has a negligible effect on θ. By this token, the validity of the previously presented expression for θ (Equation B-5) is maintained.

To evaluate SIR as given by Equation (B-6), the following facts are reiterated:

1) By Equation (B-6) SIR, $\overline{\Delta(t)}$, is the time average of $\omega_s(t) \cdot \theta(t)$.

2) $\theta(t)$ is excited only by $\omega_I(t)$. In frequency domain form, this condition is given by Equation (B-5).

3) Both $\omega_I(t)$ and $\omega_s(t)$ are assumed to be given random processes that are both stationary and ergodic.

It is convenient to present a block diagram representation of SIR phenomena. This diagram, Figure B-5, assists in relating the above facts to the general conditions of Figure B-1.

A direct comparison, element-by-element, of Figures B-1 and B-5 clearly establishes the following relationships:

Figure B-1 Elements	Figure B-5 Elements
$f(t)$	$\omega_I(t)$
$g(t)$	$\omega_s(t)$
$h(t)$	$L^{-1}\left[\frac{\theta}{\omega_I}(s)\right]$
$p(t)$	$L^{-1}[1]$
$k(t)$	$\theta(t)$
$r(t)$	$\omega_s(t)$
$\overline{x(t)}$	$\overline{\theta(t)\cdot\omega_s(t)}$

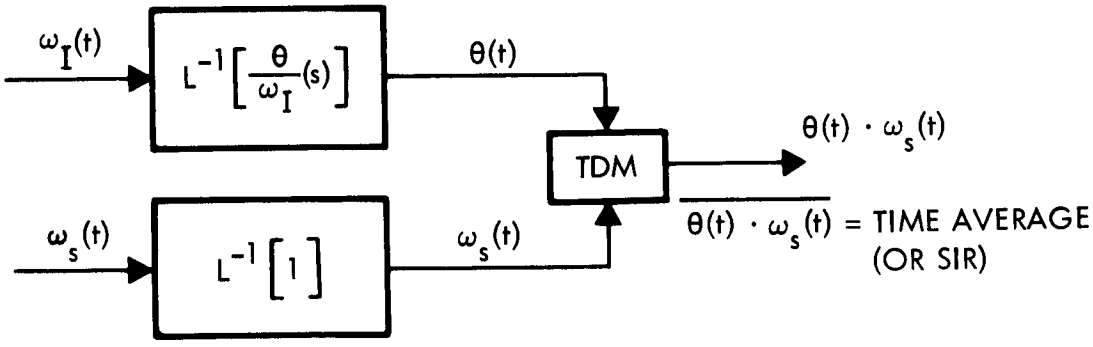

Figure B-5. Spin-Input Rectification Error Model

Therefore, it can be concluded that SIR phenomena do belong in the category of errors described by Equations (B-1) and (B-2).

If the SIR error is expressed in the general frequency domain form indicated by Equation (B-2), it appears as

$$\overline{\theta(t) \cdot \omega_s(t)} = \frac{1}{\pi}\int_0^\infty \left|\frac{\theta}{\omega_I}(j\omega)\right| R_e\left[\Phi_{IS}(\omega)\right] \cos\left\{\angle\frac{\theta}{\omega_I}(j\omega)\right\} d\omega$$

$$+ \frac{1}{\pi}\int_0^\infty \left|\frac{\theta}{\omega_I}(j\omega)\right| I_m\left[\Phi_{IS}(\omega)\right] \sin\left\{\angle\frac{\theta}{\omega_I}(j\omega)\right\} d\omega \qquad \text{(B-8)}$$

where $\Phi_{IS}(\omega)$ is the cross power spectral density function of the assumed random time variables $\omega_I(t)$ and $\omega_s(t)$.

3.3 Rectification Error Characteristics

It follows by similar processes that the other rectification errors can be evaluated under random inputs. The derivations are not presented here, but the results are summarized in Table B-I which shows the relationships between the variables of Figure B-1 and the rectification error variables.

Of particular note in Table B-I are the latter two gyro rectification errors being considered in this discussion. These are due to anisoelastic and cylindrical torque errors. Both of these error sources generate torques about the float because of components of linear acceleration along the spin and input axes and may be represented (refer to Equation (B-4)) by torques comprising the term L_e'. A detailed description of the basic mechanism giving rise to these torques will not be given here because they are well documented in available unclassified literature, and because such errors are not peculiar to strapdown systems. Instead, the final drift rate expressions associated with each and a brief description of the terms involved are presented. These error torques are generated within the instrument, are essentially independent of the parameters of the gyro rebalance loop for a strapdown configuration, and are dependent only on the accelerations to which the gyro is subjected.

Table B-I. Identification of Rectification Symbols (Frequency Domain Solution)

Error Term	f(t)	g(t)	$\lvert H(j\omega)\rvert$	$\lvert P(j\omega)\rvert$	θ_H	θ_P
Spin-Input Rectification	$\omega_I(t)$	$\omega_S(t)$	$\left\lvert \frac{\theta}{\omega_I}(j\omega) \right\rvert$	1	$\angle \frac{\theta}{\omega_I}(j\omega)$	0
Spin-Output Rectification	$\omega_o(t)$	$\omega_S(t)$	$\left\lvert \frac{\theta}{\omega_o}(j\omega) \right\rvert$	1	$\angle \frac{\theta}{\omega_o}(j\omega)$	0
Anisoinertia	$\omega_I(t)$	$\omega_S(t)$	$I_x - I_z$	$\frac{1}{H_r}$	0	0
Anisoelastic Rectification	$a_I(t)$	$a_S(t)$	$\lvert G_4(j\omega) \rvert$	$\frac{1}{H_r}$	$\angle G_4(j\omega)$	0
Cylindrical Torque Rectification	$a_I(t)$	$a_S(t)$	$\lvert G_5(j\omega) \rvert$	$\frac{1}{H_r}$	$\angle G_5(j\omega) + \frac{\pi}{2}$	0
Accelerometer Anisoinertia	$\omega_I(t)$	$\omega_p(t)$	$I_x - I_z$	$\frac{1}{m\ell}$	0	0
Accelerometer Vibropendulosity	$a_I(t)$	$a_p(t)$	$\left\lvert \frac{\theta}{a_I}(j\omega) \right\rvert$	1	$\angle \frac{\theta}{a_I}(j\omega)$	0
Untitled in Literature	$\omega_o(t)$	$a_p(t)$	$\left\lvert \frac{\theta}{\omega_o}(j\omega) \right\rvert$	1	$\angle \frac{\theta}{\omega_o}(j\omega)$	0

NOTE: Subscripts o and p refer to output and pendulous axes, respectively. Symbols G_4 and G_5 are frequency-sensitive coefficients pertaining to the particular drift effect.

3.4 Coning Errors

The evaluation of coning motions under random environments has not been included in Table B-I since this error source requires special treatment. That is, the basic equations describing coning errors are not directly analogous to the equations for the other error sources. Some preliminary steps are required to express the coning error terms in a form to which Figure B-1 can be applied.

Coning errors presented here are basically IRU related but are affected by the computational errors experienced under coning motion. To this end, it will be useful to represent pictorially (Figure B-6) the angular information flow from the IRU to the digital computer. The signal flow elements left of the dotted line represent the approximate form of small angular motions assumed to be acting.

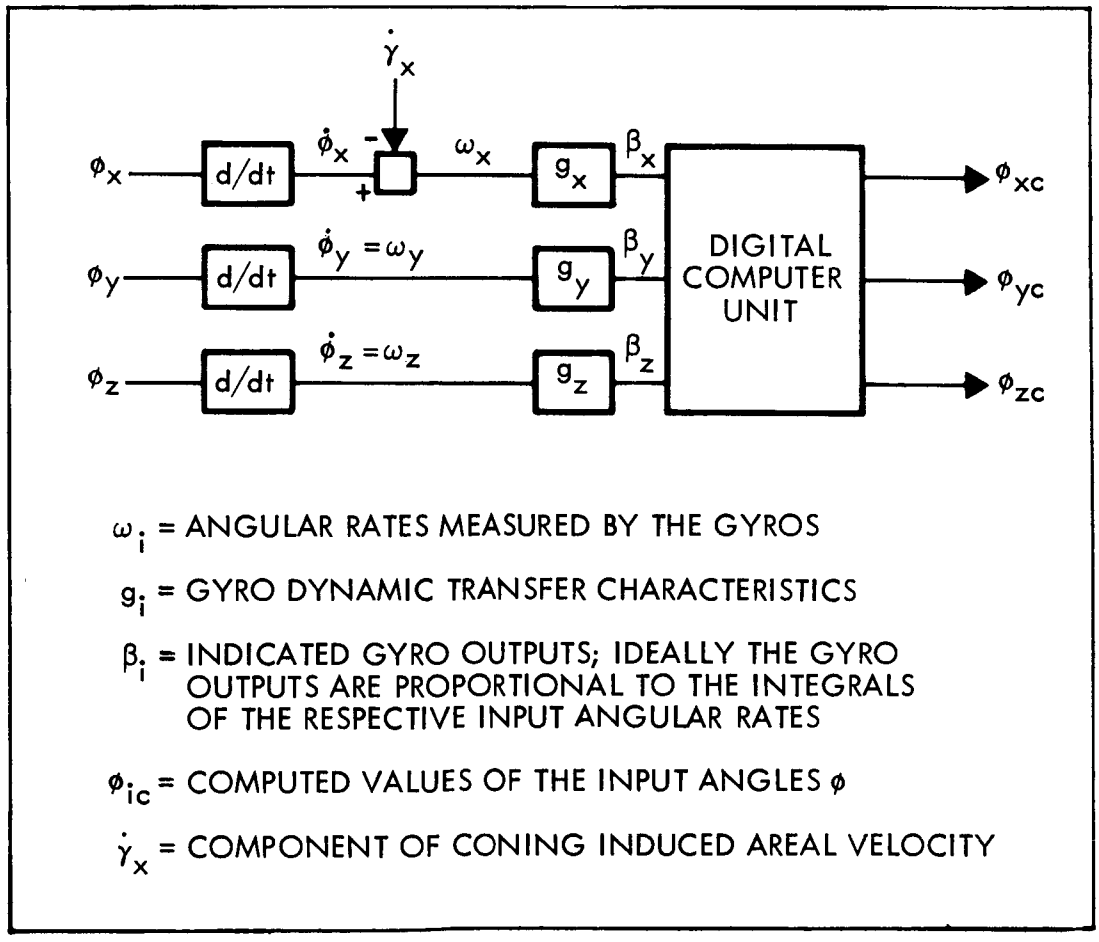

Figure B-6. Information from IRU to Computer

Referring to Figure B-6, consider the motion of the rigid body to be such that the angles ϕ_1 (assumed to be small) can be characterized by random time functions. Furthermore, assume $\omega_x = 0$, $\phi_x \ll \phi_y$, and $\phi_x \ll \phi_z$. In a real environment, these assumptions would not generally be true. However, the use of such assumptions essentially reduces the problem to one of analyzing coning drift rate about a single axis and results in significant simplification of the algebra. In the general case where the restriction on the relative amplitudes of the three components of rotation is not applied, it can be shown that coning drift rates are predicted about each axis. The magnitude of each drift rate is then given by the results for the single axis case.

For the single axis case, the true vehicle coning about z axis may be expressed as

$$\dot{\phi}_x(t) = 1/2\ (\phi_y\dot{\phi}_z - \phi_z\dot{\phi}_y) \tag{B-9}$$

For the case of an idealized digital computer, the computed values of the single-axis coning drift rate are given by

$$\dot{\phi}_{x_c}(t) = 1/2\ (\beta_y\dot{\beta}_z - \beta_z\dot{\beta}_y) \tag{B-10}$$

It should be noted that the above equation for the assumed case of an ideal computer includes no functional parameter that is associated with computer sampling effects. Due to such sampling, random input noise components above the sampling frequency are "folded down" and contribute to the output noise content below the sampling frequency. A rigorous treatment of the case of sampling has been accomplished for specific inputs only. However, evaluation of the error for the specific random input is rather laborious and the form of the resulting expression is such that it gives no insight into the mechanism of error propagation nor into the sensitivity of the result to changes in assumed parameters. Use of the concept of an ideal computer allows a relatively simple analytical treatment and in fact can result in a reasonably good approximation. The effects of a non-ideal computer are treated in the following discussion. Hence, the error in computed coning drift is defined as the difference

between the actual and computed values. Mathematically, the difference appears as

$$\epsilon\dot{\phi}_x = \dot{\phi}_x - \dot{\phi}_{xc} \tag{B-11}$$

or, after expanding in frequency domain parameters,

$$\overline{\epsilon\dot{\phi}_x} = -\frac{1}{\pi}\int_0^\infty \omega\, I_m\{\Phi_{yz}\}\left[1 - |G_y|\cdot|G_z|\cos\{\angle G_y - \angle G_z\}\right] d\omega$$

$$-\frac{1}{\pi}\int_0^\infty \omega\,|G_y|\cdot|G_z|\, R_e\{\Phi_{yz}\}\sin\{\angle G_y - \angle G_z\}\, d\omega \tag{B-12}$$

where the gyro transfer functions, G: are defined by the Laplace transforms as

$$\frac{\dot{\beta}_i}{\omega_i}(S) \equiv G_i(S) \tag{B-13}$$

3.4.1 Environment Characteristics

A highly significant fact which may be observed by inspection of Equations (B-2) and (B-12) is that, in order to completely evaluate these rectification errors, as well as others applicable to a strapdown system, it is necessary to completely define the power spectrum of the input environments in terms of both the real and imaginary parts. An equivalent statement may be made after referring to Equation (B-1). That equation demonstrates a fundamental relationship from which time domain expressions for rectification errors may be derived. That relationship implies that the environment should ideally be defined in a manner so as to show the true correlation between orthogonal components, such as by cross-correlation functions.

However, this ideal is at present not generally realizable, primarily because of the lack of adequate test data from existing or previously developed vehicles. In order to allow such definition, the test data should be instrumented over sufficiently wide bandwidths along three orthogonal axes, and cross-spectral analyses performed. The realization of such a goal could be accomplished in a relatively straightforward manner once the requirements were established.

The presently used alternative is to base system accuracy predictions on only the estimated magnitude of the environment. Additional conservatism is also applied by evaluating worst-case errors obtained through application of the environment in a direction relative to the IRU reference axis so as to maximize each individual error source. Figure B-7 illustrates this as a visual interpretation of this concept.

In Figure B-7 the axes of $\eta(t)$ and $\xi(t)$ represent the axes along which data is taken to evaluate the environment. The axes along which the system inputs are measured correspond to those of f(t) and g(t). The angle between these two sets of axes is denoted as ϕ.

Only the simple two-dimensional case will be considered here. It is assumed that the axes of $\eta(t)$ and $\xi(t)$ are normal to each other and that the axes of f(t) and g(t) are also perpendicular.

It can be shown that the average error associated with this condition is

$$\overline{k(t)} \cdot \overline{r(t)} = \frac{C - D}{2} + \frac{(A - B)}{2} \sin 2\phi + \frac{(C + D)}{2} \cos 2\phi \qquad \text{(B-14)}$$

where

$$A = \frac{1}{2\pi} \int_{-\infty}^{\infty} P(j\omega)\, H(-j\omega)\, \Phi_{\xi\xi}(\omega)\, d\omega \qquad \text{(B-15a)}$$

$$B = \frac{1}{2\pi} \int_{-\infty}^{\infty} P(j\omega)\, H(-j\omega)\, \Phi_{\eta\eta}(\omega)\, d\omega \qquad \text{(B-15b)}$$

$$C = \frac{1}{2\pi} \int_{-\infty}^{\infty} P(j\omega)\, H(-j\omega)\, \Phi_{\xi\eta}(\omega)\, d\omega \qquad \text{(B-15c)}$$

and

$$D = \frac{1}{2\pi} \int_{-\infty}^{\infty} P(j\omega)\, H(-j\omega)\, \Phi_{\eta\xi}(\omega)\, d\omega \qquad \text{(B-15d)}$$

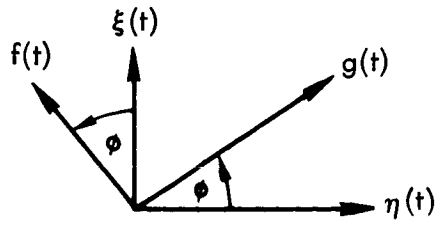

Figure B-7. Nonparallel Instrument/Data Axes

Equation (B-14) was derived in order to illustrate the dependence of rectification errors on IRU orientation. The terms involving the integrals C and D contain the cross-correlation information between orthogonal axes. Without knowledge of the specific functional form of the environmental cross-spectral density functions, which are implicit in these two integrals, it is not possible to make any general statements regarding their relative importance. Obviously, it is also not possible to evaluate these terms. With regard to the term containing the integrals A and B, it may be observed that its maximum absolute magnitude occurs when Φ is 45 deg and when the assumed difference between the two integrals is maximized.

From the definition of these integrals, Equations (B-15a) and (B-15b), it may be observed that they are of the same sign since power spectral density functions are real and positive. Hence, this term is largest when either integral is assumed zero, resulting in a worst-case condition.

3.5 Analytical Computation of Rectification Errors

Subsections 3.1 through 3.4 present the general solution for the drift rate caused by rectification errors in a strapdown IMU subjected to random vibrations. A computer program exists for performing the necessary integrations. This section presents a solution for the special case of a single input where both the transfer functions and input power spectral density are rational functions of frequency. A particularly simple result is obtained when the spectrum is that of a first order Gauss-Markov process. The answer is obtained without the necessity for numerical integration.

3.5.1 Derivation

Consider the situation shown in the following block diagram:

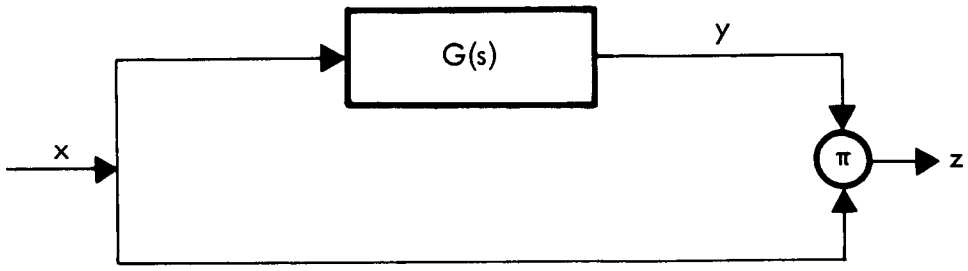

Figure B-8. Mathematical Block Diagram

We are required to find the mean value of z given the power spectral density of x.

$$\bar{z} = \overline{xy} \tag{B-16}$$

where the bar represents a time average. By definition, the cross correlation function of x and y is

$$\phi_{xy}(\tau) = \overline{x(t)y(t+\tau)} \tag{B-17}$$

provided x is stationary and ergodic. Therefore

$$\bar{z} = \phi_{xy}(o) \tag{B-18}$$

The cross correlation function of x and y is the inverse transform of the cross power spectral density.

$$\phi_{xy}(\tau) = \frac{1}{2\pi j} \int_{-j\infty}^{j\infty} \Phi_{xy}(s)\, e^{s\tau}\, ds \tag{B-19}$$

therefore

$$\bar{z} = \frac{1}{2\pi j} \int_{-j\infty}^{j\infty} \Phi_{xy}(s)\, ds \tag{B-20}$$

By the residue theorem,

$$\overline{z} = -\Sigma \text{Res}\,(a_k) \tag{B-21}$$

Where a_k are the poles of $\Phi_{xy}(s)$ in the right half plane. If $\Phi_{xx}(s)$ is the power spectral density of x then

$$\Phi_{xy}(s) = G(s)\,\Phi_{xx}(s) \tag{B-22}$$

For a stable transfer function, G(s) will have no poles in the right half plane.

3.5.2 Simplified Case

For the simplified case where the power spectral density of x is a first order Gauss-Markov process

$$\Phi_{xx}(s) = \frac{2\omega_0\sigma^2}{(s+\omega_0)(-s+\omega_0)} \tag{B-23}$$

and

$$\Phi_{xy}(s) = G(s)\,\frac{2\omega_0\sigma^2}{(s+\omega_0)(-s+\omega_0)} \tag{B-24}$$

For this case there is only one pole in the right half plane, at $s = \omega_0$. Therefore

$$\overline{z} = \sigma^2\,G(\omega_0) \tag{B-25}$$

3.5.3 Example - Spectrum Approximation

An angular rate spectrum is given in a straight line plot in Figure B-9 where this spectrum approximates that of Paragraph 4.4.4, Figure 4-6. It may be approximated as follows:

$$\lambda_{\omega\omega}(f) = \frac{.025}{1+\left(\frac{f}{2}\right)^2} \tag{B-26}$$

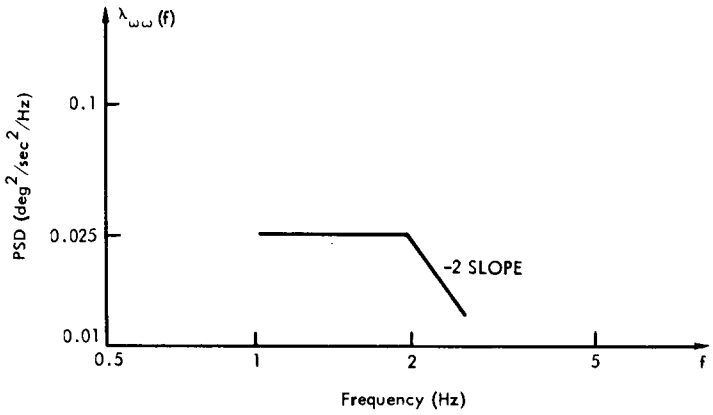

Figure B-9. Power Spectral Density (Log Scales)

The standard deviation is given by

$$\sigma^2 = \int_0^\infty \frac{.025}{1 + \left(\frac{f}{2}\right)^2} d_f = .0785 \left(\frac{\text{deg}}{\text{sec}}\right)^2 \qquad \text{(B-27)}$$

Conversion from degrees to radians lets us express the spectrum as in Equation (B-23).

$$\Phi_{\omega\omega} = \frac{2\omega_0 \sigma^2}{(s + \omega_0)(-s + \omega_0)} \qquad \text{(B-28)}$$

where

$$\sigma^2 = 2.4 \times 10^{-5} \text{ (rad/sec)}^2 \qquad \text{(B-29)}$$

$$\omega_0 = 2\pi \cdot 2 = 12.56 \text{ rad/sec}$$

3.5.4 Example - Spin - Input Rectification

The rate described by the above spectrum is applied about an axis in the plane of the gyro input and spin axes at an angle ψ from the input axis. As is well known, the spin-input rectification drift computation for this situation may be approximated by the block diagram on the following page.

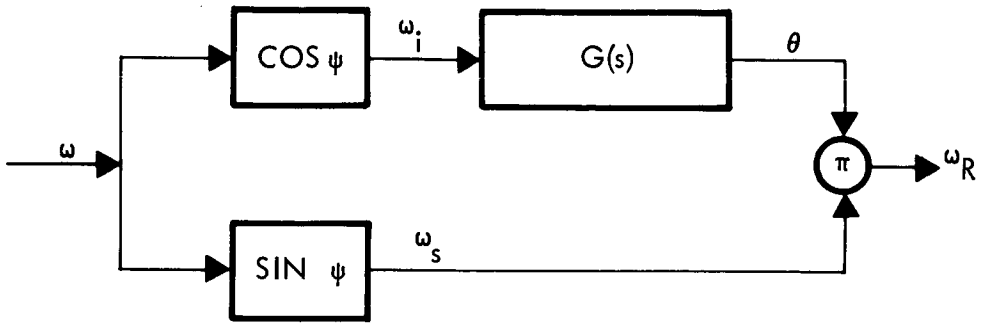

Figure B-10. Spin-Input Rectification Block Diagram

Where

ω_i, ω_s are the input and spin axis rates

θ is the float angle

G (s) is the transfer function from input axis rate to float angle

From the derivation above we have the mean drift rate

$$\bar{\omega}_R = \sigma^2 \sin\psi \cos\psi \, G(\omega_0)$$

Suppose ψ = 45 deg

$$G(s) = \frac{5 \times 10^{-5} \left(\frac{s}{240} + 1\right)}{\left(\frac{s}{404+j417} + 1\right)\left(\frac{s}{404-j417} + 1\right)\left(\frac{s}{2384} + 1\right)\left(\frac{s}{10,256} + 1\right)} \quad \text{(B-30)}^{\dagger}$$

Then $\bar{\omega}_R = 6.10 \times 10^{-10}$ rad/sec = 0.000127 deg/hr.

3.5.5 Example - Fictitious Coning

The case of fictitious coning is more complex than spin-input rectification. However, it is shown in Subsection 3.6 that fictitious coning may be put in the form of Figure B-10 if

$$G(s) = \frac{1}{s}\left[G_1(s) - G_2(s)\right] \qquad \text{(B-31)}$$

---

†Eq (B-30) gives the transfer function for a pulse rebalance loop developed at TRW Systems (Ref B-1). It is considered to be reasonably typical.

Where G_1 (s) and G_2 (s) are the transfer functions from input rate to output rate of gyros 1 and 2 and the rate is applied about an axis in the plane of their input axes at an angle ψ from the gyro 2 input axis. Therefore, we have

$$\bar{\omega}_F = \sigma^2 \sin\psi \cos\psi \frac{1}{\omega_0} [G_1(\omega_0) - G_2(\omega_0)] \qquad \text{(B-32)}$$

It should be noted that Equation (B-31) may not be infinite at s = 0. Therefore

$$G_1(0) - G_2(0) = 0 \qquad \text{(B-33)}$$

must hold. This is the normal case for properly designed systems. Now let ψ = 45 deg as before and

$$G_1(s) = \frac{\left(\frac{s}{100}+1\right)\left(\frac{s}{570}+1\right)}{\left(\frac{s}{547+j458}+1\right)\left(\frac{s}{547-j458}+1\right)\left(\frac{s}{106}+1\right)\left(\frac{s}{2159}+1\right)\left(\frac{s}{10212}+1\right)} \qquad \text{(B-34)}$$

$$G_2(s) = \frac{\left(\frac{s}{100}+1\right)\left(\frac{s}{570}+1\right)}{\left(\frac{s}{311+j362}+1\right)\left(\frac{s}{311-j362}+1\right)\left(\frac{s}{111}+1\right)\left(\frac{s}{2565}+1\right)\left(\frac{s}{10,297}+1\right)} \qquad \text{(B-35)}$$

Then $\bar{\omega}_F = 1.658 \times 10^{-9}$ rad/sec = 0.000342 deg/hr.

3.6 Fictitious Coning

A coordinate system can be changed from any orientation to any other by a single rotation about an axis fixed in space. Let θ_0 be the amount of the rotation. Construct a line segment of length θ_0 along the positive direction of the axis of rotation. Let the projection of θ_0 on the i th axis of the coordinate system be θ_i. Then the θ_i define the final orientation of the coordinate system with respect to the initial orientation. The θ_i satisfy the relationship

$$\theta_0 = \left(\theta_1^2 + \theta_2^2 + \theta_3^2\right)^{1/2} \qquad \text{(B-36)}$$

Let the quaternion that defines the final orientation with respect to the initial orientation be ρ. Then

$$\rho = (\theta_1 i + \theta_2 j + \theta_3 k)\frac{1}{\theta_0}\sin\frac{\theta_0}{2} + \cos\frac{\theta_0}{2} \qquad \text{(B-37)}$$

The differential equation defining ρ in terms of the quaternion of the angular velocity of the coordinate system, ω, is

$$\dot{\rho} = \rho\frac{\omega}{2} \qquad \text{(B-38)}$$

If all terms of higher than first order in the θ_i in Equation (B-37) are discarded and the result is substituted in Equation (B-38), differential equations for the θ_i are obtained which are valid for small changes in orientation.

$$\begin{aligned}
\dot{\theta}_1 &= \omega_1 + \tfrac{1}{2}(\theta_2\omega_3 - \theta_3\omega_2) \\
\dot{\theta}_2 &= \omega_2 + \tfrac{1}{2}(\theta_3\omega_1 - \theta_1\omega_3) \qquad \text{(B-39)} \\
\dot{\theta}_3 &= \omega_3 + \tfrac{1}{2}(\theta_1\omega_2 - \theta_2\omega_1)
\end{aligned}$$

For small θ_i, the major contribution to $\dot{\theta}_i$ comes from the left hand terms on the right hand sides of Equation (B-39). Let

$$\dot{\phi}_i = \omega_i \qquad i = 1, 2, 3 \qquad \text{(B-40)}$$

Then Equation (B-39) may be approximated by

$$\begin{aligned}
\dot{\theta}_1 &= \omega_1 + \tfrac{1}{2}(\phi_2\omega_3 - \phi_3\omega_2) \\
\dot{\theta}_2 &= \omega_2 + \tfrac{1}{2}(\phi_3\omega_1 - \phi_1\omega_3) \qquad \text{(B-41)} \\
\dot{\theta}_3 &= \omega_3 + \tfrac{1}{2}(\phi_1\omega_2 - \phi_2\omega_1)
\end{aligned}$$

Now let ω_i' be the outputs of the gyros

$$\omega_i' = G_i(s)\,\omega_i \qquad i = 1, 2, 3 \qquad \text{(B-42)}$$

and let

$$\dot{\phi}_i' = \omega_i' \qquad i = 1, 2, 3 \qquad \text{(B-43)}$$

The computer, attempting to perform Equation (B-41), will actually perform

$$\begin{aligned}
\dot{\theta}_1' &= \omega_1' + \frac{1}{2}(\phi_2' \omega_3' - \phi_3' \omega_2') \\
\dot{\theta}_2' &= \omega_2' + \frac{1}{2}(\phi_3' \omega_1' - \phi_1' \omega_3') \\
\dot{\theta}_3' &= \omega_3' + \frac{1}{2}(\phi_1' \omega_2' - \phi_2' \omega_1')
\end{aligned} \tag{B-44}$$

Now let the error rate be

$$\Delta\dot{\theta}_i = \dot{\theta}_i' - \dot{\theta}_i \tag{B-45}$$

and let

$$\begin{aligned}
\omega_i' &= \omega_i + \Delta\omega_i \\
\phi_i' &= \phi_i + \Delta\phi_i
\end{aligned} \tag{B-46}$$

Now by substituting Equations (B-46) in (B-44) and the result and (B-41) in (B-45), discarding second order terms in $\Delta\omega$ and $\Delta\phi$, we obtain

$$\begin{aligned}
\Delta\dot{\theta}_1 &= \Delta\omega_1 + \frac{1}{2}(\phi_2\Delta\omega_3 + \Delta\phi_2\omega_3 - \phi_3\Delta\omega_2 - \Delta\phi_3\omega_2) \\
\Delta\dot{\theta}_2 &= \Delta\omega_2 + \frac{1}{2}(\phi_3\Delta\omega_1 + \Delta\phi_3\omega_1 - \phi_1\Delta\omega_3 - \Delta\phi_1\omega_3) \\
\Delta\dot{\theta}_3 &= \Delta\omega_3 + \frac{1}{2}(\phi_1\Delta\omega_2 + \Delta\phi_1\omega_2 + \phi_2\Delta\omega_1 - \Delta\phi_2\omega_1)
\end{aligned} \tag{B-47}$$

The mean drift rates are

$$\begin{aligned}
\overline{\Delta\dot{\theta}_1} &= \frac{1}{2}(\overline{\phi_2\Delta\omega_3} + \overline{\Delta\phi_2\omega_3} - \overline{\phi_3\Delta\omega_2} - \overline{\Delta\phi_3\omega_2}) \\
\overline{\Delta\dot{\theta}_2} &= \frac{1}{2}(\overline{\phi_3\Delta\omega_1} + \overline{\Delta\phi_3\omega_1} - \overline{\phi_1\Delta\omega_3} - \overline{\Delta\phi_1\omega_3}) \\
\overline{\Delta\dot{\theta}_3} &= \frac{1}{2}(\overline{\phi_1\Delta\omega_2} + \overline{\Delta\phi_1\omega_2} - \overline{\phi_2\Delta\omega_1} - \overline{\Delta\phi_2\omega_1})
\end{aligned} \tag{B-48}$$

since the $\Delta\omega$ are assumed to have zero mean. Now suppose that the input rate ω is applied about an axis in the plane of the input axes of gyros 1 and 2 at an angle ψ from the gyro 2 input axis. Then

$$\omega_1 = \omega \sin \psi$$

$$\omega_2 = \omega \cos \psi \qquad \text{(B-49)}$$

$$\omega_3 = 0$$

From Equations (B-42) and (B-46) we have

$$\Delta\omega_i = [G_i(s) - 1]\,\omega_i \qquad i = 1, 2, 3 \qquad \text{(B-50)}$$

and from (B-40) and (B-50)

$$\phi_i = \frac{1}{s}\omega_i \qquad i = 1, 2, 3 \qquad \text{(B-51)}$$

$$\Delta\phi_i = \frac{1}{s}[G_i(s) - 1]\,\omega_i$$

From (B-48)

$$\overline{\Delta\dot{\theta}_1} = \overline{\Delta\dot{\theta}_2} = 0 \qquad \text{(B-52)}$$

$$\overline{\Delta\dot{\theta}_3} = \frac{1}{2}\left(\overline{\phi_1\,\Delta\omega_2} + \overline{\Delta\phi_1\,\omega_2} - \overline{\phi_2\,\Delta\omega_1} - \overline{\Delta\phi_2\,\omega_1}\right)$$

Each term of (B-52) may be evaluated separately. The block diagram of the first term is

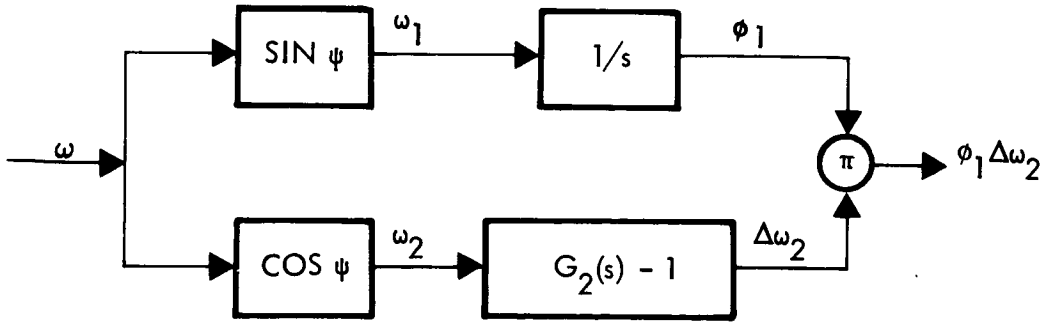

Therefore

$$\Phi\phi_1\,\Delta\omega_2(s) = \left(\frac{1}{-s}\right)[G_2(s) - 1]\,\sin\psi\,\cos\psi\,\Phi_{\omega\omega}(s) \qquad \text{(B-53)}$$

The block diagram for the second term is

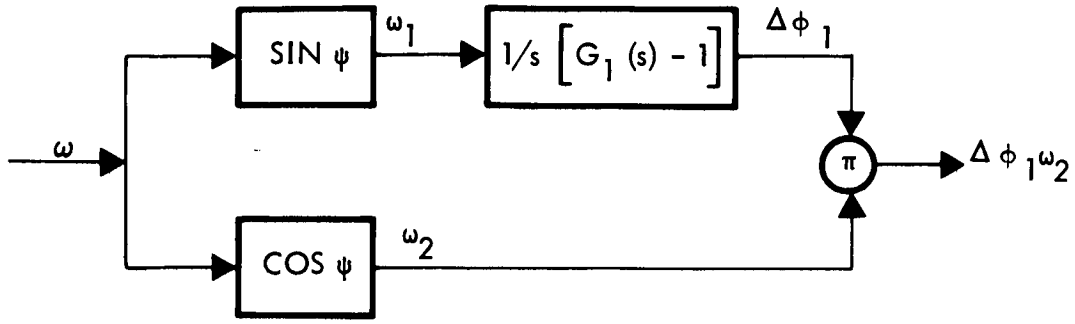

Therefore

$$\Phi_{\omega_2 \Delta\phi_1}(s) = \frac{1}{s}[G_1(s) - 1] \sin\psi \cos\psi \, \Phi_{\omega\omega}(s) \qquad \text{(B-54)}$$

The block diagram for the third term is

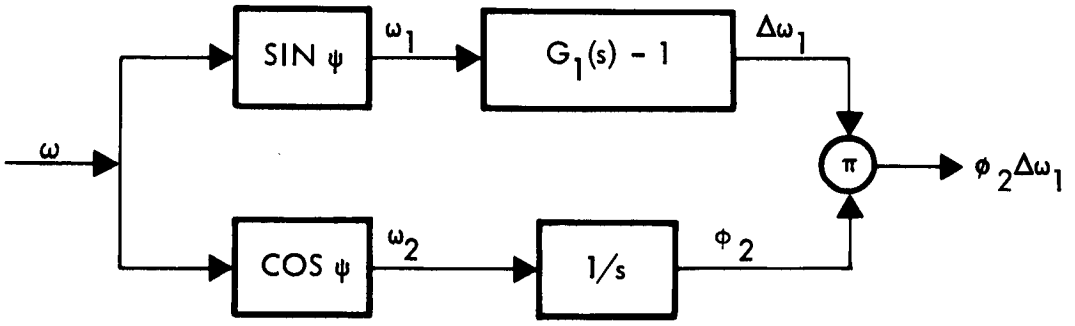

Therefore

$$\Phi_{\phi_2 \Delta\omega_1}(s) = \left(\frac{1}{-s}\right)[G_1(s) - 1] \sin\psi \cos\psi \, \Phi_{\omega\omega}(s) \qquad \text{(B-55)}$$

The block diagram for the fourth term is

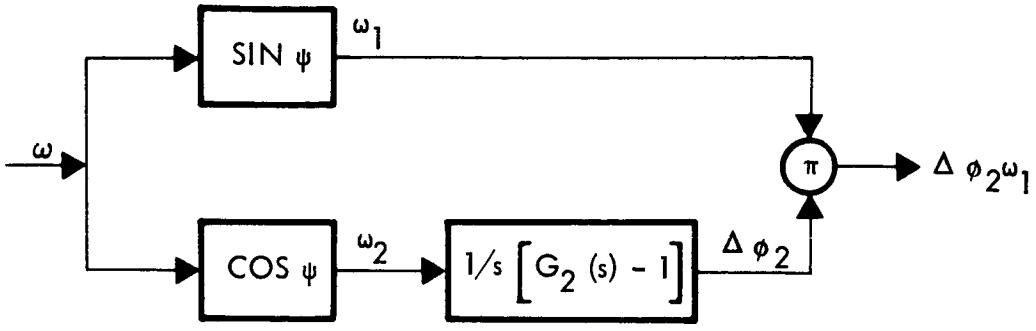

Therefore

$$\Phi_{\omega_1 \Delta\phi_2}(s) = \frac{1}{s}[G_2(s) - 1] \sin\psi \cos\psi \, \Phi_{\omega\omega}(s) \qquad \text{(B-56)}$$

From Equation (B-20)

$$\overline{\Delta\dot{\theta}_3} = \frac{1}{2\pi j} \int_{-j\infty}^{j\infty} \frac{1}{2}\left[\Phi_{\phi_1 \Delta\omega_2} + \Phi_{\omega_2 \Delta\phi_1} - \Phi_{\phi_2 \Delta\omega_1} - \Phi_{\omega_1 \Delta\phi_2}\right] ds \qquad \text{(B-57)}$$

From Equations (B-53) - (B-57) we obtain

$$\overline{\Delta\dot{\theta}_3} = \frac{1}{2\pi j} \int_{-j\infty}^{j\infty} \frac{1}{s}[G_1(s) - G_2(s)] \sin\psi \cos\psi \, \Phi_{\omega\omega}(s) \, ds \qquad \text{(B-58)}$$

If $\Phi_{\omega\omega}(s)$ is given by Equation (B-28) then, by the residue theorem

$$\overline{\Delta\dot{\theta}_3} = \sigma^2 \frac{1}{\omega_0}[G_1(\omega_0) - G_2(\omega_0)] \sin\psi \cos\psi \qquad \text{(B-59)}$$

If we define

$$G(s) = \frac{1}{s}[G_1(s) - G_2(s)] \qquad \text{(B-60)}$$

then fictitious coning may be put in the form of Figure B-3.

4. DIRECTION COSINE ERRORS

The strapdown system components are subjected to an angular rate environment considerably more severe than that which occurs on a stable platform. These angular rates have several effects, including the fact that the linear acceleration is measured in a rotating coordinate system. This effect can be made negligible. Another effect on the linear acceleration measurements is the error which occurs if all three accelerometers are not located at exactly the same point. This error is generally negligible, and if not, it can be readily compensated for by the flight computer. In this Section the effects of the angular rates on the direction cosine matrix will be considered. The errors of the direction cosine matrix may be classified as follows:

Drift errors
Orthogonality errors
  Scale errors
  Skew errors

They also may be classified by source as follows:

Commutativity errors
Quantization errors
Truncation errors
Roundoff errors

The cause-effect relationship is symbolized in the following Table where the presence of an "X" means that the indicated cause can result in the indicated effect:

Table B-II. Cause/Effect Relationships of Direction Cosine Errors

Cause	Effect	
	Drift Error	Orthogonality Error
Commutativity	X	
Quantization	X	
Truncation	X	X
Roundoff	X	X

These relationships may be described in the following manner.

Consider an orthogonal triad of unit vectors. Let them each be transformed by the direction cosine matrix and examine the resulting errors.

4.1 Drift Errors

The transformed vectors may be rotated as a group from a set of vectors transformed by an ideal direction cosine matrix. The rotation may be described by three small angles, the drift errors.

4.2 Scale Errors

The lengths of the transformed vectors may differ from unity. The three differences are the scale errors.

4.3 Skew Errors

The angles between each of the three pairs of vectors may differ from right angles. The differences are the skew errors. Scale and skew errors cannot exist if the direction cosine matrix is orthogonal, and are therefore referred to as orthogonality errors.

4.4 Commutativity Errors

The existence of commutativity errors in a strapdown attitude reference comes about not from any fundamental principle, but from the way in which most strapdown gyroscopic sensors are implemented. That is, the components of angular velocity are individually integrated, sampled, and quantized, and the resulting increments of angle are all that is available to the algorithm that determines attitude. The information as to the variations of the direction of the angular velocity vector during the sampling period, contained in the unmodified components of angular velocity, has been lost. The typical algorithm assumes that the direction of the angular velocity vector is unchanging during the sampling period. Whenever the assumption differs from the actuality, commutativity errors occur.

An appropriate test case for commutativity errors is a circular coning motion. For such a motion the vehicle angular velocity is

$$\omega = \begin{Bmatrix} 0 \\ \Omega \tan \alpha \cos \Omega t \\ \Omega \tan \alpha \sin \Omega t \end{Bmatrix} \qquad \text{(B-61)}$$

where

α = the coning half-angle (rad)

Ω = angular frequency (rad/sec)

ω = angular velocity (rad/sec)

t = time (sec)

It has been shown that (Ref B-2) for $\alpha < 10$ deg and for sampling rates greater than about 2 samples per coning cycle, the drift rate due to commutativity error is approximately

$$\omega_D \cong \frac{\Omega^3 T^2 \alpha^2}{12} \qquad \text{(B-62)}$$

where

T = the sampling period (sec)

ω_D = the drift rate (rad/sec)

For sampling rates which are slow compared to the coning rate, the drift rate is approximately the geometric coning error

$$\omega_D \cong \Omega(1 - \cos \alpha) \qquad \text{(B-63)}$$

Algorithms exist for reducing commutativity errors by attempting to recover some of the lost information by suitable derivative filters. The degree to which this procedure can be made successful is limited by the presence of quantization errors.

4.5 Quantization Errors

Quantization errors arise when the analog gyro information is converted to digital information for input to the computer. This process may occur in an analog-to-digital (A/D) converter following an analog-torqued rate gyro, in the torquing loop of a pulse-torqued rate gyro, or in a code wheel on the output shaft of a single axis platform. The resulting quantization errors have the property that they are "remembered" from one

sampling instant to the next; in the integrator of the A/D converter, in the float of the pulse-torqued gyro, or in the code wheel of the single axis platform. Thus, the first order direction cosine drift errors resulting do not grow with time, but have a constant standard deviation equal to $Q/\sqrt{12}$ where Q is the quantum size. Second order errors due to quantization induced commutativity errors do grow with time, but are quite small in most applications.

4.6 Truncation Errors

If it is assumed that the direction of the angular velocity vector is constant during a sampling period, then the exact solution for the new direction cosine matrix is

$$[A_n] = e^{[\theta]}[A_{n-1}] \tag{B-63a}$$

where

$$[\theta] = \begin{bmatrix} 0 & \theta_3 & -\theta_2 \\ -\theta_3 & 0 & \theta_1 \\ \theta_2 & -\theta_1 & 0 \end{bmatrix} \tag{B-64}$$

and the θ_i are the integral of the angular velocity components over the sampling period. This transcendental result must be approximated for use in a digital computer.

One set of approximations consists of truncating the Taylor series for $e^{[\theta]}$ after a chosen number of terms. The errors for one sampling period of the first four such approximations are given in the Table on the following page.

Here

$$\theta_o = \left(\theta_1^{\,2} + \theta_2^{\,2} + \theta_3^{\,2}\right)^{1/2} \tag{B-65}$$

and,

when i =	1,	j =	2,	and k =	3
	2		3		1
	3		1		2.

Table B-III. Taylor Series Approximations

Order	Drift	Skew	Scale
1	$-\theta_i \theta_o^2/3$	$-\theta_j \theta_k$	$\left(\theta_j^2 + \theta_k^2\right)/2$
2	$\theta_i \theta_o^2/6$	$-\theta_j \theta_k \theta_o^2/4$	$\left(\theta_j^2 + \theta_k^2\right) \theta_o^2/8$
3	$\theta_i \theta_o^4/30$	$\theta_j \theta_k \theta_o^2/12$	$-\left(\theta_j^2 + \theta_k^2\right) \theta_o^2/24$
4	$-\theta_i \theta_o^4/120$	$\theta_j \theta_k \theta_o^4/72$	$-\left(\theta_j^2 + \theta_k^2\right) \theta_o^4/144$

These algorithms may be modified further by the use of orthogonality corrections. Other algorithms have been formulated such as Backwards Differencing and Algorithm A (a Runge-Kutta technique modified to improve accuracy). The latter two algorithms and the first and second order Taylor series algorithms have been compared for accuracy when subjected to coning motion of the vehicle. The results are summarized in the graph of Figure B-11, which is an empirically obtained normalized curve from which the drift error resulting from an input of two orthogonal sinusoidal rates of equal amplitude and 90-deg phase shift can be calculated. The error of any of the four algorithms for any limit cycle amplitude, frequency, and computer sampling interval may be found as follows:

1) Normalize the computer sampling interval with respect to the limit cycle period. For example, the normalized sampling interval for a 0.5-cps signal and a 20-msec sampling interval is $0.02T/2.0 = 0.01T$.

2) Obtain the percent error from the normalized graph. For instance, the percent error for the Taylor's series is 0.1 percent for the 0.5-cps signal and a 20-msec sampling interval.

3) Calculate the correct vehicle coning rate in the desired units. For a 0.5-cps signal with an amplitude of 0.1 rad, the vehicle coning rate is

$$\omega' = (0.01)^2 (\pi) (0.5) = 1.5708 \times 10^{-4} \text{ rad/sec}$$

$$\omega' = 0.5655 \text{ rad/hr} = 32.403 \text{ deg/hr}$$

4) The coning error is 0.1 percent of 32.4 deg/hr or an equivalent drift of 0.034 deg/hr.

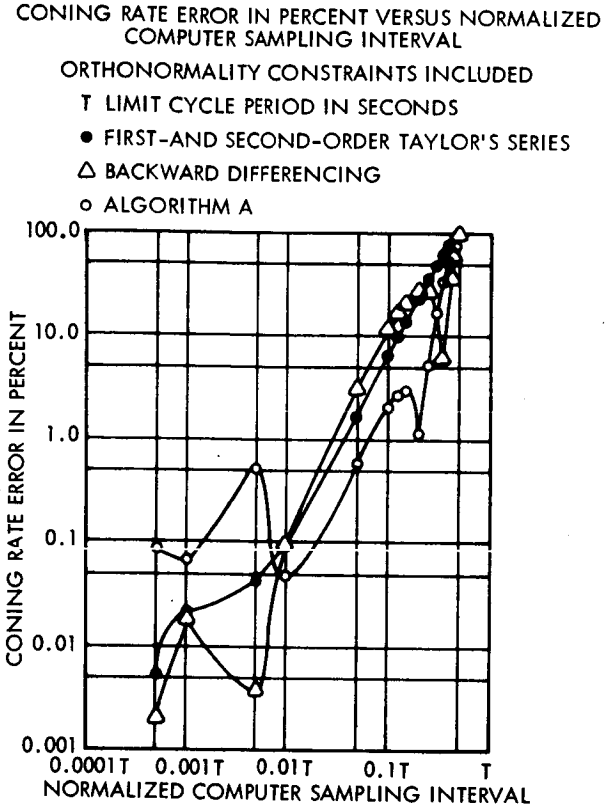

Figure B-11. Coning Study Results

The results of Figure B-11 and the relative complexity of the computer equations generally leads to a clear choice of the Taylor's series expansion for maintenance of the attitude reference.

An analysis of the errors made when the vehicle turns at a constant rate about one axis (termed slewing) has also been made (Ref B-3) and B-7) and analytical error terms derived. The results of that analysis are summarized in Table B-IV. The incremental angle is designated Δ. The second-order Taylor's series' primary advantage is the reduction of the scale factor error. The choice of first or second order is a tradeoff between the available computer space, maximum available computation rate, and the required accuracy.

In Table B-V, the errors for both algorithms are tabulated for four different sampling rates subject to angular environments which can be considered severe steady-state conditions for a boost vehicle. From the Table, it appears that the first-order Taylor's series meets a drift criterion of 0.01 deg/hr if sampled faster than every 8.5 msec.

Table B-IV. Direction Cosine Slewing Errors

	Single Axis Slew		Three Axis Slew	
	Scale Factor Error	Per Cycle Angle Error	Scale Factor Error	Per Cycle Angle Error
First-order Taylor's series	$\sqrt{1 + \Delta^2}$	$-\frac{\Delta^3}{3}$	$\sqrt{1 + 3\Delta^2}$	$-\Delta^3$
Second-order Taylor's series	$\sqrt{1 + \Delta^4/4}$	$-\Delta^3/6$	$\sqrt{1 + 9\Delta^4/4}$	$-\frac{\Delta^3}{2}$

Roundoff Errors. During a 1000-sec booster powered flight, the second-order Taylor's series would update the direction cosines 100,000 times. Suppose it is desired to keep the roundoff error less than (arbitrarily) 13 arc sec. An unjustifiably conservative approach would assume additive roundoff and yield a requirement of

$$\frac{13 \text{ arc sec} \times 4.85 \times 10^{-6}}{\times 10^{5}} \text{ rad/arc sec} \doteq 6.31 \times 10^{-10} \text{ rad}$$

which would require 31 bits.

A much more realistic approach is to assume that the roundoff error is uncorrelated from one computation to the next. Assuming a uniform probability distribution, and assuming that the central limit theorem holds would result in an error of $\epsilon \times \sqrt{n/12}$ where ϵ is the minimum bit size and n is the number of computations. Thus for the 100,000 computations,

$$\Delta\theta = \frac{\sqrt{12} \times 13 \times 4.85 \times 10^{-6}}{\sqrt{10^5}} 7 \times 10^{-7}$$

which is equivalent to a word length of 21 bits.

Table B-V. Results of Attitude Reference Error Studies

	Drift Errors of the First-Order Taylor's Series (10^{-2} deg/hr)					Drift Errors of the Second-Order Taylor's Series (10^{-2} deg/hr)				
Computer Sampling Rate in msec	15	10	7.5	5	2	15	10	7.5	5	2
Slewing Errors (maximum rate = 6 deg/sec)	5.37	2.3	1.34	0.6	0.0956	2.69	1.15	0.67	0.3	0.033
Coning Errors (0.05 deg at 3 cps)	2.07	1.0	0.044	0.028	0.0081	2.07	1.0	0.044	0.028	0.0081
RSS 3σ	5.76	2.51	1.34	0.6	0.096	3.39	1.52	0.67	0.3	0.033

REFERENCES FOR APPENDIX B

B1 Curby, R. D., "Analysis of a Two-Level, Binary Pulse-Torqued Gyro Rebalance Loop," TRW IOC 7223.2-132, 24 March 1967.

B2 Wilcox, J.C., "Whole Number Computer Algorithm to Reduce Commutatively Errors," TRW IOC 7223.2-18, 21 September 1966.

APPENDIX C

EARTH HORIZON SENSOR PERFORMANCE

1. INTRODUCTION

The most obvious optical reference for an earth-orbiting spacecraft is the earth itself. The angular position of the center of the earth is a readily measured parameter for use in control or monitoring of spacecraft attitude as well as in orbital navigation. The measurement of the angular position can be done either actively or passively and in any one of several bands of the electromagnetic spectrum. Since past experience, both analytically and operationally, has led to nearly exclusive use of passive infrared methods, only instruments of this type are considered herein.

In this appendix, the nature of the earth's infrared radiation is first considered. The elements of a horizon sensor and various possible mechanizations are described, briefly analyzed with respect to performance, and compared. A bibliography is given containing those references which directly relate to the problem of horizon sensor design.

2. EARTH RADIANCE MODEL

The radiation from the earth when viewed from outside the earth's atmosphere consists primarily of two parts: reflected solar radiation, and radiation emitted by the earth and its atmosphere due to their temperatures. Because the reflected solar radiation can be used to sense the horizon only during the day, horizon sensors are normally designed to utilize the earth's self-emitted radiation.

The earth is at a temperature of approximately 280°K and can be called a graybody, i.e., the radiation can be described by Planck's law for blackbody radiation modified by the earth's emissivity. However, when viewed from outside the atmosphere, this graybody radiation is modified by the atmosphere. Water vapor, carbon dioxide, and ozone absorb radiation in specific wavelength bands. The absorptance depends upon the wavelength of the radiation and the temperature and pressure of the absorbing gas. These gases in turn radiate energy in wavelength bands dependent to a large extent on atmospheric conditions.

In addition, radiation is scattered by dust particles, aerosols, and to some extent by molecules in the infrared. Another effect due to viewing the earth's horizon from near the earth is refraction caused by the path length of the radiation through an atmosphere with varying indexes of pressure and temperature.

In order to determine the appearance of the earth from outside the atmosphere so that design criteria for horizon sensors can be generated, mathematical models describing the radiation have been formulated. The earliest models considered the earth to be a sphere at a temperature of approximately 280°K with an emissivity of one. This results in blackbody radiation with peak output at a wavelength of about 10 μ. The atmosphere was assumed to be perfectly transparent in the wavelength interval of 8 to 13 μ and opaque elsewhere. On the basis of this model, the earliest horizon sensors were designed. With the advent of the Tiros satellite more attention was paid to the earth's radiation, and more complex models were constructed. The early efforts described the earth as a sphere with concentric spheres representing the atmosphere. Temperatures, based on balloon and rocket soundings, were assigned to the spherical atmospheric shells for radiation calculations. As the demand for more detail grew, the number of concentric spheres describing the atmosphere was increased and the effects of latitude and season were added. The most recent models of the earth's radiation are based on a spherical earth with continuous atmospheric pressure, temperatures, and gas concentrations for several model atmospheres which are based on latitude and season. These models also include some cloud variations. Wark (Ref 1) has evaluated the effects of refraction when viewing the horizon. The results of these analytical models show clearly that in order to minimize gradients of radiance across the earth and to define the sharpest apparent horizon, the 15-μ CO_2 band and the water vapor rotational bands beyond 21 μ are superior to the other wavelength intervals considered. In these regions local atmospheric anomalies such as storm fronts apparently cause little disturbance in the radiance.

The atmospheric radiance computations of Wark and his associates are the most accurate currently available in that they are predicated upon a true spherical atmospheric shell, they are carried through at

narrow spectral intervals, and they are based upon meteorological profiles representing undercast as well as the usual clear weather conditions. Figure C-1 shows the results obtained by Wark in terms of relative earth radiance versus the tangent ray height for several significant atmospheric absorption bands using the ARDC standard atmosphere. The tangent ray height (Z_o') is defined as the distance from the surface of the earth to the orthogonal intersection of a satellite ray and an earth radial line. In this figure, the several radiance curves have been normalized to their value at Z_o' = -6371 km, corresponding to the satellite subpoint. The curves illustrate some general properties of the absorption bands such as the fact that uniform mixing of CO_2 in the atmosphere leads to a relatively high and abrupt apparent edge, the severe discontinuity in the O_3 curve at the maximum ozone concentration region (stratopause) and the transparency of the atmosphere in the 10.5-to 11-μ region resulting in an apparent horizon at the tropopause.

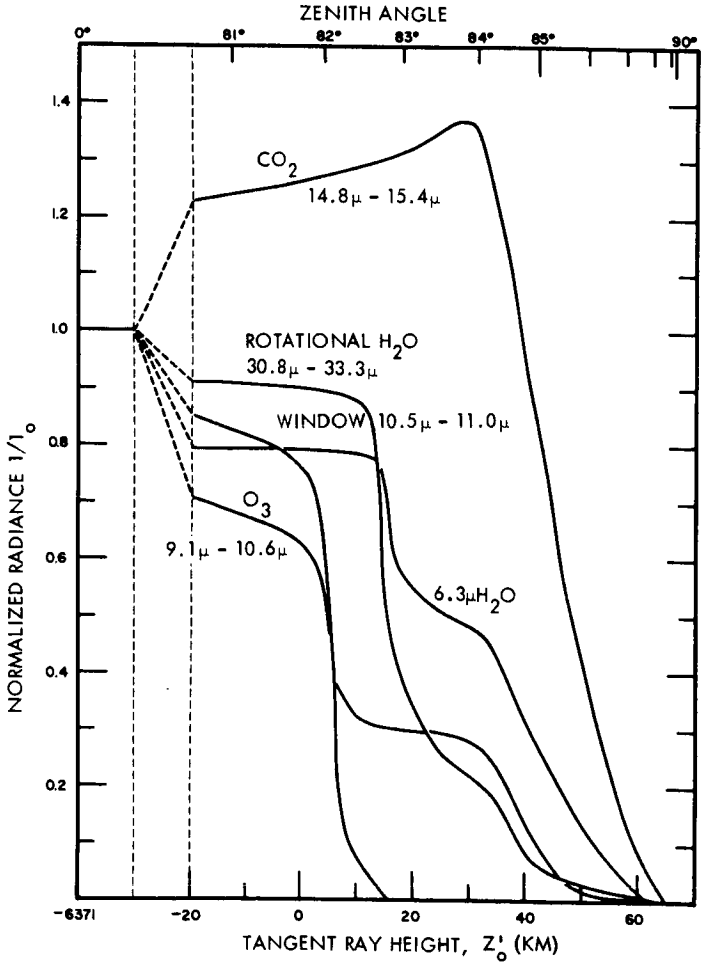

Figure C-1. Variation of the Radiance, Normalized to the Value at Z'_o = 6371 km, for Five Spectral Intervals. (The ARDC Model is Used.)

Figures C-2, C-3, and C-4 show atmospheric radiance profiles for three of these bands, the 15-μ CO_2 absorption band and the H_2O rotation band, which are both appropriate for horizon sensing and the absorption-free "window" region between 10.6 and 11 μ. Figure C-5 shows the filters used to generate the absorption band curves. The window region curves are for an ideal "rectangular" band. The lettered labeling of the curves indicates the meterological profile used for computation, i.e.,

A ARDC Standard Clear Atmosphere, 1959

B Albuquerque, Clear, July

C Ponape, Caroline Islands, Undercast, May

D Resolute, North West Territory, Undercast, December

The radiance curves computed from these four meteorological profiles are indicative of the range of inputs a satellite-borne horizon sensor might experience during a given mission.

Inspection of Figures C-2 through C-4 reveals the desirability of viewing the earth's atmosphere in a strong absorption band rather than a window. In the window region a strong contribution of radiance at the sensor is received from the region near the earth which is subject to extreme meteorological change. From Figure C-4, it is noted that there is a ratio of 13:1 between the extreme horizon radiance curves. In the strong absorption regions, only radiance from the upper portion of the atmosphere is transmitted to the sensor. Meteorological conditions are more stable in these regions, which is demonstrated by the equivalent ratios in the CO_2 and H_2O bands which are 1.55 and 1.35, respectively. The desirability of using the latter spectral ranges for accurate horizon sensing is apparent.

Several significant computational programs other than that of Wark have been dedicated to the horizon-sensing problem. McArthur (Ref 2) has prepared a statistical model of the horizon radiance in the 14- through 16-μ band with both time and distance as parameters. Hanel, Conrath, and Bandeen (Ref 3, 4) preceded Wark with a computation of radiance from a curved earth and atmosphere. Burn (Ref 5)

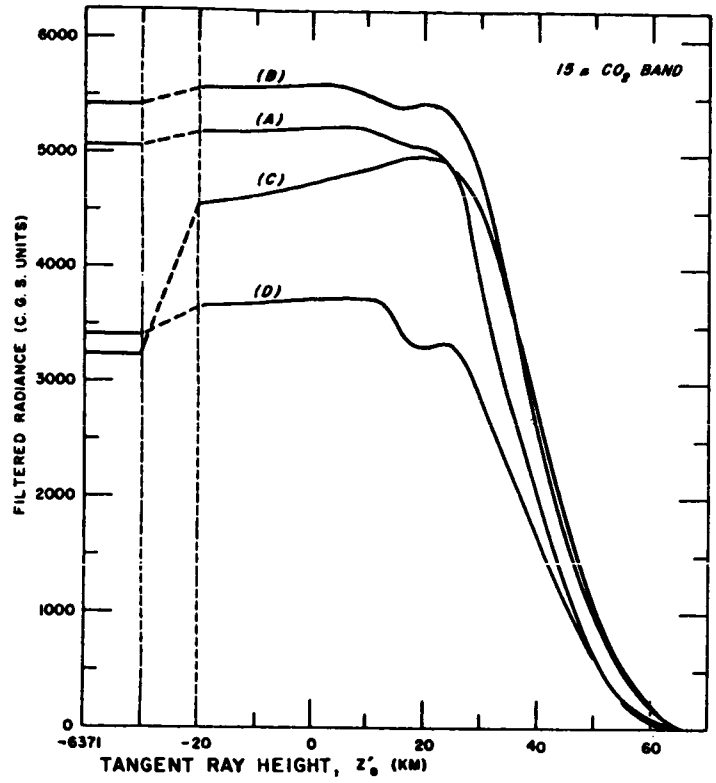

Figure C-2. Variation of the Radiance with Z'_o Atmospheric Models in the Carbon Dioxide Band (Filter response is shown in Figure C-5)

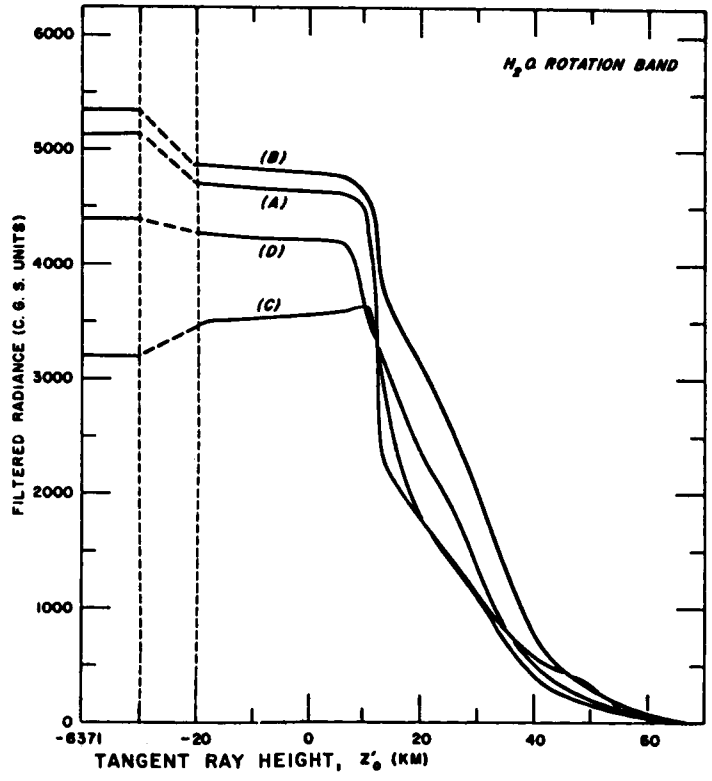

Figure C-3. Variation of the Radiance with Z'_o for Four Atmospheric Models in the Water Vapor Rotation Band. (Filter response is shown in Figure C-5.)

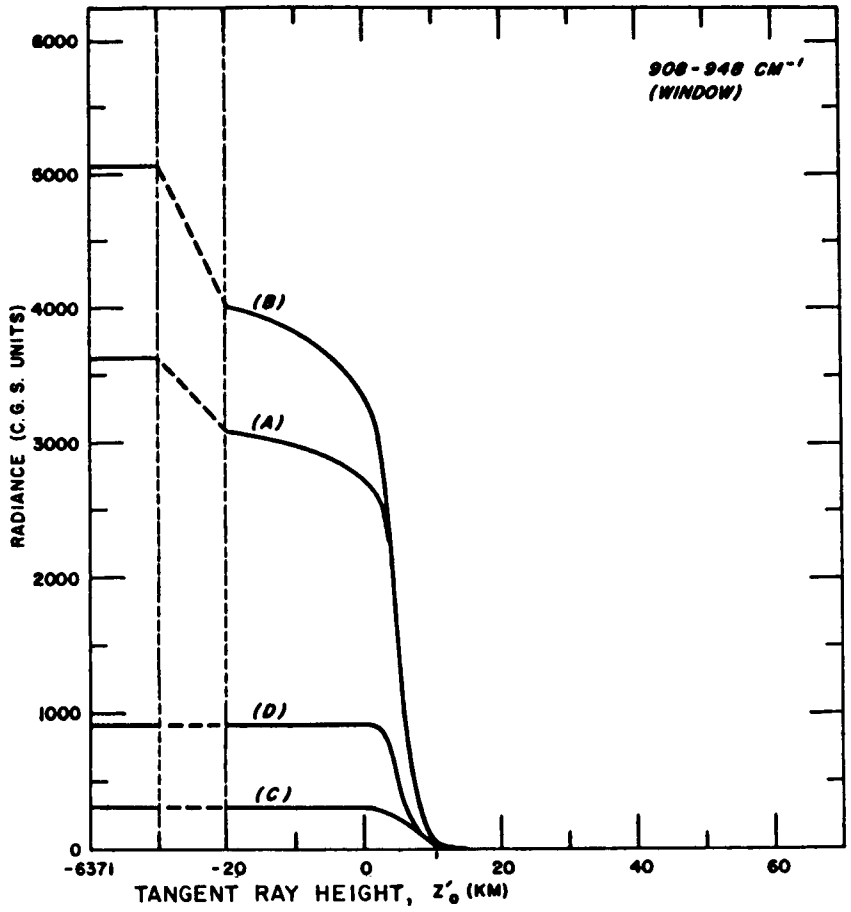

Figure C-4. Variation of Radiance with Z'_o for Four Atmospheric Models in the 908-948 cm^{-1} Interval in the "Window." The radiance for the vertical beam (Z'_o = 6371 km) is shown at the left; the radiance near the limb is shown to the right of the dashed lines.

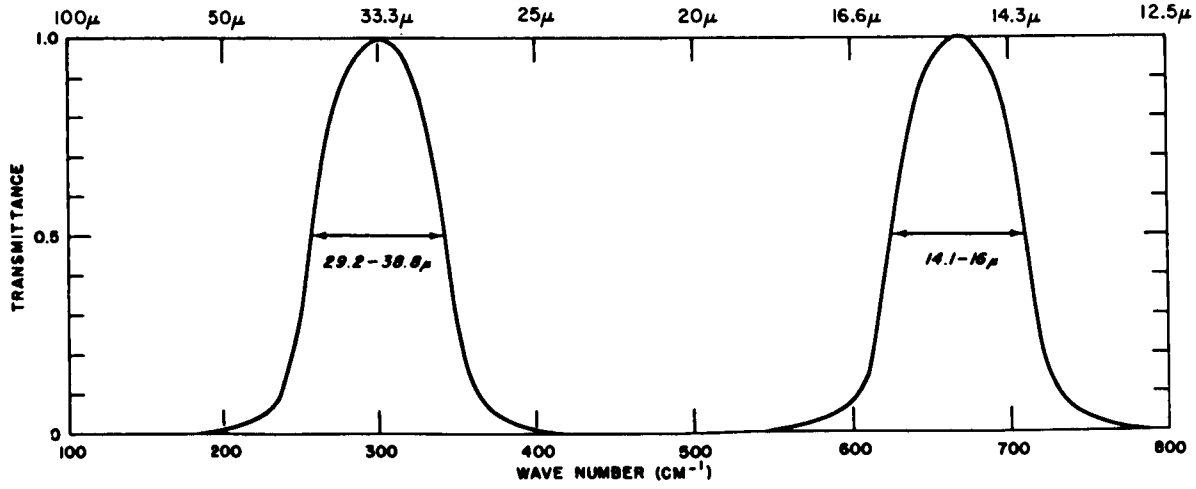

Figure C-5. Transmittance of Hypothetical Filters in the 15-Micron Carbon Dioxide Band and in the Rotational Water Vapor Band, Normalized to Unity at the Maxima.

has demonstrated theoretically that the 15-μ band is optimal for rejection of "cold clouds" in the atmosphere. Other programs of this general type are referenced in the bibliography of this section.

In addition to "fallout" data from such scientific programs as Tiros, horizon data have been obtained on programs carried out specifically for that purpose. In particular, orbital test programs were performed by Lockheed and by Kodak in 1962 (Ref 6, 7). In these programs, operational and experimental horizon scanners operating in several spectral bands were flown, and the outputs of their preamplifiers monitored. The data collected in all cases verify theoretical expectations of radiance levels in the various bands and permit some statistical analysis of the likelihood of a given reading. The significant limitation to this data is a lack of precision attitude reference. No data are available to make a precise correspondence between the orientation of the line of sight in geocentric coordinates and a given radiance reading. Therefore, exact determination of the radiance profile of the horizon is not possible from this data.

NASA has undertaken a program under the title project Scanner, which will overcome these objections by means of a precision celestial reference (Ref 8). The first phase of this program, involving a 12-min ballistic flight of the celestial reference along with horizon radiometers has been carried out. The resulting data are being reduced and published at the time of writing and the second phase of the program, an orbital flight, has not yet been carried out. The scanner radiometers are sensitive in the CO_2 and H_2O rotational absorption bands of the atmosphere.

3. MECHANIZATION

The elements of a horizon sensor system; the modulation technique, the detector, the electronic processing, and optics are treated individually in this section. The discussion is as general as is practical with the previously stated restriction to passive infrared devices.

3.1 Modulation Techniques

The sensing of the discontinuity between the apparent earth horizon and space by sensing the earth and earth atmosphere radiation can be done in many ways. The general techniques can be broken into three categories: a) nonscanning methods, b) conical scan, and c) edge scan.

3.1.1 Nonscanning Methods

The radiation from the earth is projected onto several detection elements, and the difference in radiation on the different detectors is sensed and an error signal is developed. In the simplest form this type of system would consist of four detectors with the earth image focused on the detectors as shown in Figure C-6.

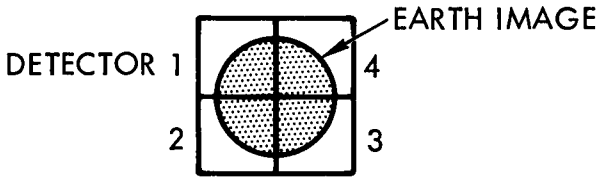

Figure C-6. Radiation Balance Detector

Against a perfect spherical target this system would have the planetary disc divided equally onto the four detectors when the optical axis of the system is pointed at the center of the disc. Through simple differencing of opposite detector outputs this system develops an error signal in two axes.

3.1.2 Conical Scan

In this method a small instantaneous field of view is made to scan in a cone with an apex angle dependent upon the distance to the earth and the geometry involved. Figure C-7 shows this scanning motion across the earth. Note that two scanning motions are necessary to determine the direction to the earth's center in two axes. The information from a scan is derived by using the change in irradiance at the scanner when the instantaneous field of view sweeps across the horizon. The angle half way between the two irradiance discontinuities represents the coordinates of the earth's center in one axis of the scanner coordinates. The scan cone may be degenerated to a plane when the apparent planet angle is small.

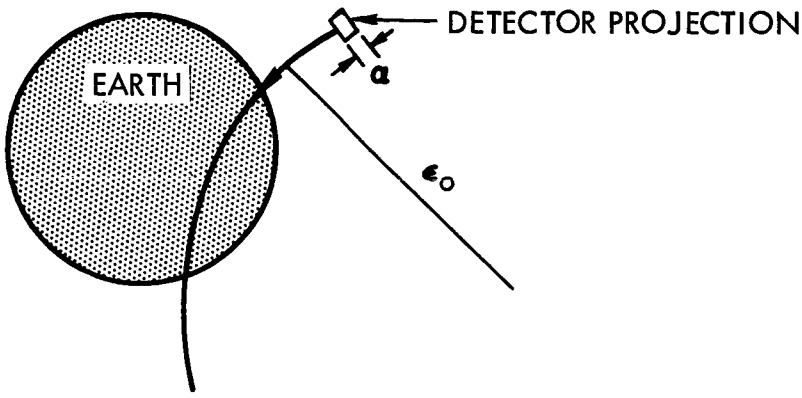

Figure C-7. Conical Scanning of Earth Horizon

3.1.3 Edge Scan

This method of scanning moves the instantaneous field of view in a relatively small angle back and forth across the earth's horizon. A scan of this type is shown in Figure C-8. Note that three separate paths must be scanned to determine the center of the earth's disc. The edge scanner must go through a wider scan search mode to find the horizon initially.

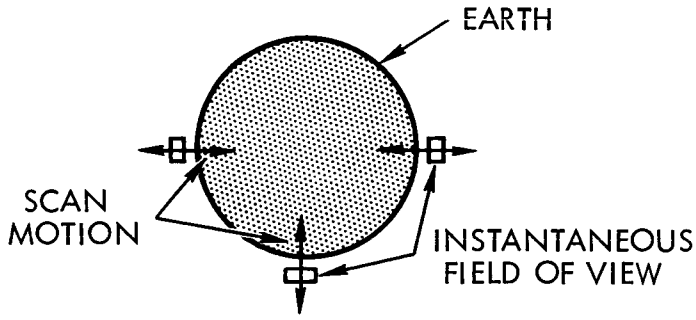

Figure C-8. Edge Scanning of Earth Horizon

Combinations of conical and edge scan techniques can be used. See Figure C-9. Two scanning motions are imparted simultaneously; one is a conical scan with an apex angle equal to the earth's subtense at the scanner, and the other is a motion perpendicular to this scan motion and at a different rate. This method can be modified so that the scan motion is a rosette, etc. This type of scan must go through an initial search mode just as with the edge scanner. The apex angle of the conical part of the scan can be adjusted from the error information to compensate for varying altitude.

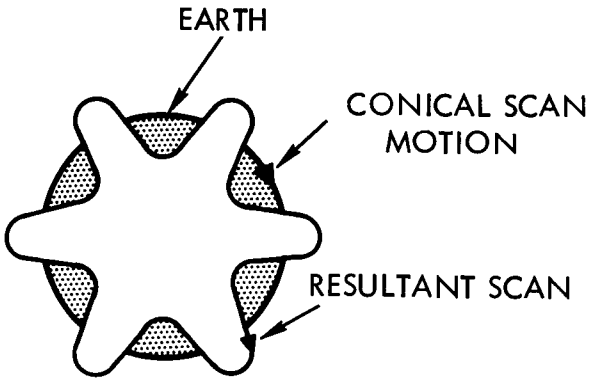

Figure C-9. Combination of Edge and Conical Scan

3.2 Detectors

Detectors suitable for use in the detection of infrared radiation can be divided into two main categories depending upon the nature of detection. The two categories are (1) quantum detectors and (2) thermal detectors. The first class depends upon photon-electron interaction to change the electrical properties of the detector whereas the second class absorbs radiation and transforms it into heat which in turn affects the detector electrical properties.

This section will be devoted almost exclusively to the discussion of thermal detectors since all operational (or proposed) earth horizon sensors utilize this type. Figure C-10 illustrates why this is the case. The spectral detectivity† of representative quantum detectors and a thermistor bolometer detector are shown along with the spectral region of typical absorption band horizon scanning devices. The quantum

† Detectivity is a convenient, if approximate, figure-of-merit for electro-optical detectors. It is defined as:

$$D^* = \sqrt{A\Delta f}/P_n$$

where

A = effective detector receiving area, cm^2
Δf = measurement noise bandwidth, cps
P_n = incident power required to produce an rms signal equal to detector rms noise, watts

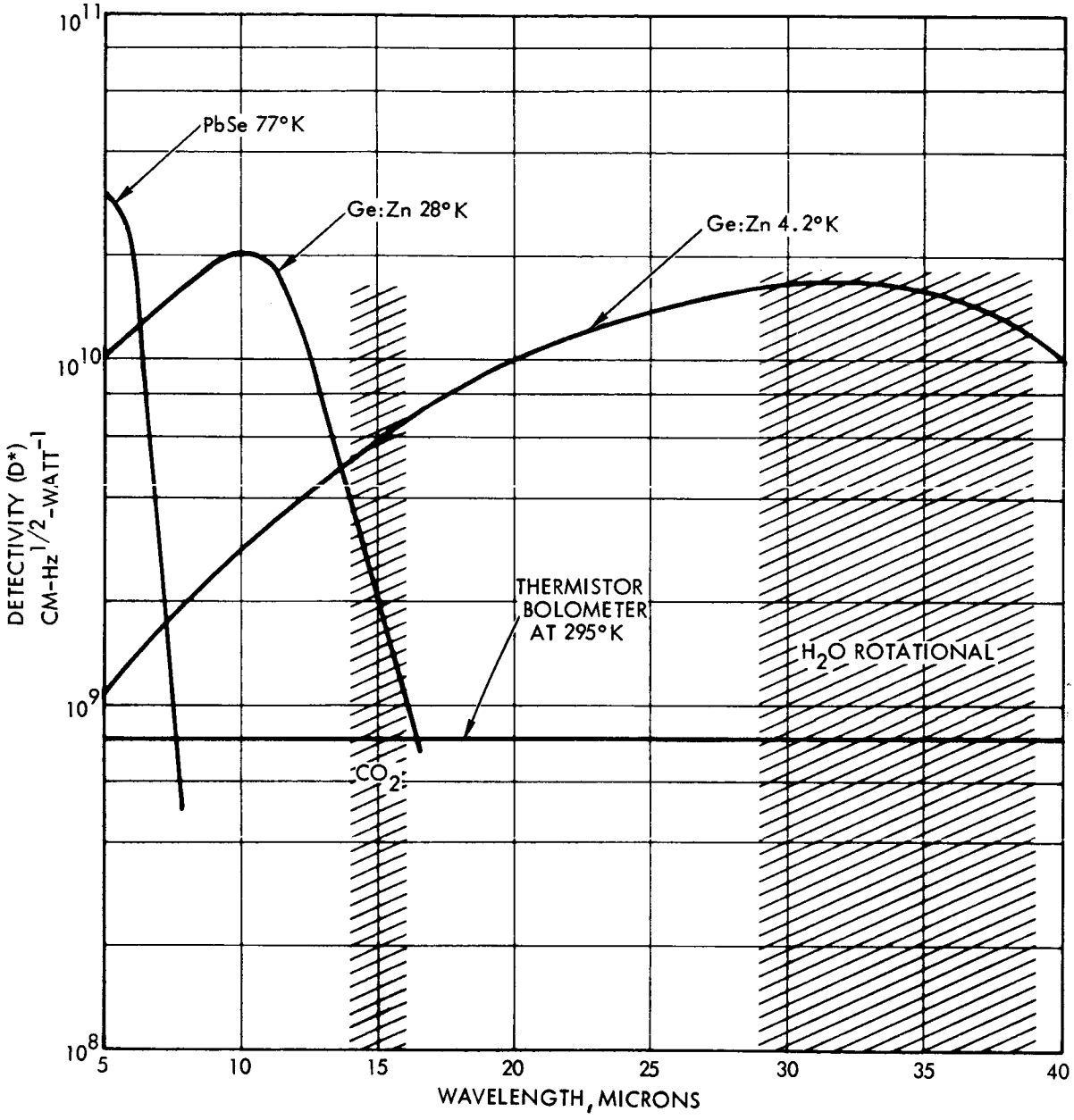

Figure C-10. Spectral Detectivity of Quantum and Thermistor Bolometer Detectors

detectors shown represent the extreme state-of-the-art for long wavelength detection. Note that the zinc-doped germanium and mercury-doped photoconductors, operated at 4.2°K and 28°K, respectively, are superior in detectivity to the thermistor bolometer operated at 295°K. It is the unfortunate characteristic of photoconductive detectors, however, that they must be cooled to extremely low temperatures to extend their spectral response to the desired horizon-sensing bands. Since

cryogenic support equipment of the sophistication required to operate at these levels for extended periods is not available for orbital use, the quantum detector is not covered further in this report.

3.2.1 Thermocouples

These detectors consist of two dissimilar materials of different thermoelectric power which are in electrical contact. Because of the different thermoelectric powers there is a contact potential difference whose amplitude is dependent upon the temperature of the junction of the two materials.

The materials with the greatest difference in thermoelectric power have been found to be various semiconductors, and most applications of radiation thermocouples now utilize semiconductor materials. Metal radiation thermocouples are only used where the better long-term stability is important.

The resistance of thermocouples is quite low ($\sim$ 10 ohms) so that a transformer coupling is usually employed. This results in a sensitivity limited by the Johnson noise of the thermocouple. Because the output of a thermocouple is quite low, several are often connected in series to form a thermopile. The time constant for a thermopile is, however, quite long and for this reason it is seldom used as an ac device.

Because thermocouples do not depend upon the quantum nature of radiation, there is no cutoff wavelength. The wavelength response is determined by windows in front of the thermocouple and by the wavelength dependence of the absorptivity of the heat absorbing element.

In general, thermocouples are good detectors for infrared radiation in applications where an uncooled detector is desired; however, they are usually quite delicate and are very difficult to ruggedize for shock and vibration environments.

3.2.2 Thermistor Bolometer

Thermistors are semiconductor elements of very small mass which have large negative temperature coefficients of resistance. The absorption

of radiation raises the temperature of the thermistor flake and the resulting resistance change is sensed. Because of the temperature dependence, these detectors change resistance with ambient temperature as well as with radiation. Because of this, they are generally used in pairs connected in a bridge circuit with radiation incident on only one element. Ambient temperature effects are balanced out over reasonable temperature ranges by this technique. Detectors used in this manner are called bolometers.

Thermistors and thermistor bolometers do not require cooling, and respond to wavelength regions determined in the same way as thermocouples. These detectors can be quite rugged and can be immersed or placed in direct contact with a lens. The immersion increases the radiation density that is incident on the detector by an amount equal to the index of refraction of the lens material for a hemispherical immersion lens.

Other thermal detectors such as metal film bolometers have been used to sense infrared radiation under conditions where long-term stability is of major importance. Thermistor bolometers have much higher responsivities than metal bolometers but do show hysteresis effects which are not present in metal bolometers.

The type of detector which appears to be the best for precision horizon scanner application by virtue of the high responsivity is the immersed thermistor bolometer. This detector can be immersed in germanium, increasing the output by approximately four times, is quite rugged and requires no cooling to low temperatures.

3.2.3 Specification of Detector Parameters

The impact of detector parameters upon sensor system performance is described in some detail elsewhere. It is useful, however, to describe the parameters at this point and indicate those which must be carefully specified when considering the design of a new sensor. Parameters of primary significance are detailed in the following list.

a) Responsivity. The voltage measured across the detector flake when it is exposed to a calibrated radiation source must be specified. Responsivity should be specified as a function of bias voltage, wavelength of incident monochromatic radiation, detector temperature (over the expected range of ambient operating temperatures) and of source intensity (i.e., linearity).

b) Time Constant. The time constant is best represented by a specification of responsivity versus source modulation frequency. Such a curve permits a calculation of time constant and also the specification of multiple time constant effects when they occur. The time constant measurement should be made as a function of detector operating temperature.

c) Detector noise. The power spectral density of the noise voltage appearing across the detector must be known. This power spectrum should be known as a function of temperature and of bias voltage. The low frequency limit of the noise power spectral density measurement must be such that the contribution passed by the sensor electronics at this low frequency limit is negligible.

d) Miscellaneous. Other parameters which have a secondary impact upon sensor performance are impedance and its functional dependence upon temperature and environmental resistance such as the immunity of contacts to vibration. Detector performance degradation with shelf and operating lifetime is an important and little known parameter. Currently the design of earth sensors for long life missions is based upon very limited experimental data of questionable statistical validity.

3.2.4 Electronic Circuitry

The electronic circuitry associated with a horizon sensor must serve the following functions:

a) Detector bias supply

b) Detector signal preamplification

c) Noise filtering

d) Radiance variation compensation

e) Signal amplification

f) Signal demodulation

g) Generate modulator drive signal.

Most of these functions are common to many electronic applications and the frequency response, stability requirements, etc., are well within the state-of-the-art. The areas of electronic design which require particular attention in the horizon sensing application are compensation for component value drifts with life and temperature, careful optimization of the frequency response in terms of the signal and noise spectrum, and the incorporation of some form of compensation for earth radiance variations in the case of thresholding devices.

3.2.5 Optics

The detection of radiation from the earth requires the collection of a sufficient or "detectable" amount of radiation and delivery of that energy to a detector. In an infrared system this function is often performed by a telescope, similar to those used in visible systems.

In general, optical systems can be broken into three categories: reflective, refractive, and catadioptric. Reflective systems utilize reflective elements (mirrors), refractive systems utilize refractive elements (lenses), and catadioptric systems utilize both types of elements. Many infrared systems have been designed to cover large wavelength intervals, say 2 through 14 μ, which is 30 times the entire visible wavelength region. These systems are commonly reflective because mirrors do not have color aberration, although they do possess all the other simple aberrations found in lenses. For relatively narrow wavelength regions and wider wavelength intervals where high resolution is not important, refractive or catadioptric systems may be used. Horizon sensors normally fall into this last category. The detector size usually decides the maximum resolution obtainable in a system, and since it is large with respect to the blur from almost any optical system, the types of elements are usually determined by weight and size considerations, and by the availability of materials for lenses. This last item imposes a much more severe restriction in the infrared region than it does in the visible region where many types of glass with various indexes of refraction exist. Some materials which transmit infrared radiation are unsuitable for optical elements in most applications because of undesirable characteristics such as extreme softness, hygroscopic behavior, tendency to cold flow, etc.

In addition to the optical elements considered above, it is necessary to incorporate into the design a spectral filter to define the wavelength band of sensitivity. These filters are, in general, either absorptive, reflective, or operate by selective scattering. Filters operating by selective scattering, called Christiansen filters, pass energy in narrow spectral bands. These filters are prepared by mixing a dielectric powder in a fluid and placing the mixture between plane, parallel plates. There is a small spectral band in which the fluid and the dielectric have the same index of refraction, and in this band energy will be transmitted. At all other wavelength the indexes differ and the energy is scattered.

Absorption filters can be either of the gelatin type which are primarily restricted to use in the visible region, or semiconductors which show sharp absorption edges. The semiconductor type is useful when a material with an absorptive edge at the proper wavelength is available. Absorptive filters re-emit radiation in the absorbed wavelengths as graybodies at the filter temperature. Because of this, in some systems, they must be cooled or otherwise temperature controlled.

Reflective filters can be of several types but the most important from the standpoint of applicability to horizon sensors are interference filters. Interference filters are prepared by depositing thin films of dielectric material on a semiconductor substrate. By proper selection of the thickness and index of refraction of the dielectric films and the number of films, these filters can be designed to transmit energy over any nominal spectral region where a transmitting substrate can be found. The major limitation is in finding dielectric materials with the desired index of refraction.

In general, even though they are relatively expensive, interference filters are most useful in infrared systems because of the variety of transmission properties available.

Another type of reflective filter, the reststrahlen filter, may be useful for systems operating in the water vapor rotational bands. These filters are constructed of materials with ionic bonding which show very sharp cut-on wavelength edges for reflection in the infrared.

Many materials with reststrahlen wavelength peaks greater than 20 μ are available.

The third horizon scanner optical element is the scanning mechanism. In most horizon scanners a small field of view is scanned in space. This may be done mechanically or electronically. In mechanical scanning techniques some part of the optical-detector system is moved. This might be done by rotating a plane mirror about some axis as in Figure C-11. Another method of generating a scanning motion similar to the rotating plane mirror is a rotating prism. In similar ways other scan motions

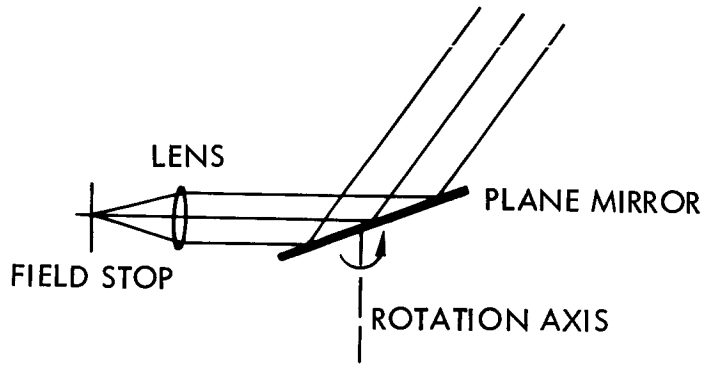

Figure C-11. Rotary Scan of Optical Field of View

could be generated, e.g., rotation through part of an arc and back by a plane mirror as in Figure C-12. Many other scanning motions are possible by movement of elements in the optical system. Many techniques can be developed to move the optical elements utilizing almost any method of generating a force.

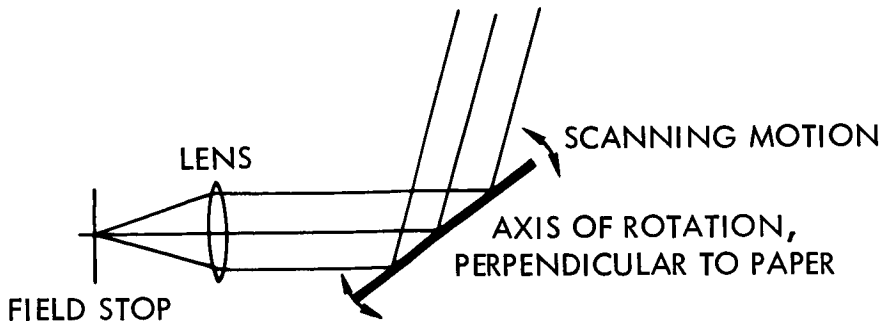

Figure C-12. Oscillating Scan of Optical Field of View

A small instantaneous field of view may also be scanned by electronic techniques. This may take the form of switching the input to the pre-amplifier between several detectors each of which "sees" a different space volume. This method requires many detectors if a small instantaneous field of view and a large total field of view are desired. Another type of electronic scan is that used in TV pickup tubes such as the vidicon or orthicon. In these devices the total field of view is projected on an extended detector area and an electron beam scanning this area "reads out" the information in one small element of the detector at a time. In the current state of development, infrared vidicon image tubes are not appropriate for earth sensing.

4. HORIZON SENSOR PERFORMANCE

This section describes the performance of a horizon sensor under operational circumstances in relation to accuracy and reliability. The predicted performance is discussed in some detail and then a summary is given of data pertaining to the actual performance of operational devices.

4.1 Accuracy

There are two general types of error involved in measuring spacecraft attitude with a horizon sensor system. These are:

a) Errors instrinsic to the horizon sensor such as uncertainties in angular information due to noise, bias errors due to time lags in the signal processing and angle transducer readout errors.

b) Errors connected with the earth as a target, such as a non-abrupt horizon in a given spectral region, a non-uniform horizon, oblateness of the earth, etc.

4.1.1 Errors Intrinsic to the Horizon Sensor

These errors can be broken down into noise effects, and offset or bias error induced by detector-preamplifier time lags and by the difference in radiance from the various sections of the earth's disc.

Noise Effects. A certain signal-to-noise level is necessary to maintain lock-on to the horizon gradient. The minimum signal-to-noise level necessary for a reasonably small rms angle error depends upon the particular mechanization of the scanner and is usually experimentally determined. In order to roughly evaluate the effects of signal-to-noise ratio, a simplified horizon scanner will be analyzed qualitatively.

Example Problem

Assume a conical scan with apex angle ϵ_o, a detector of angular width which determines the field of view, and a perfect spherical earth with uniform radiance. In the object plane of the scanning telescope the projection of the detector forms a square which intersects the earth as in Figure C-13.

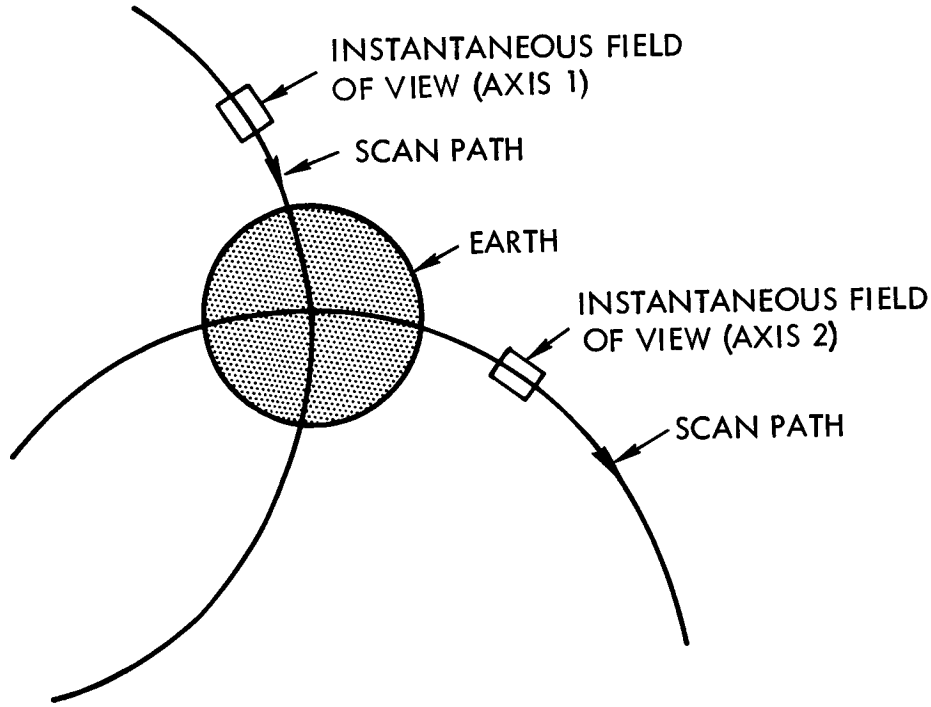

Figure C-13. Intercept of Conical Scan with Earth

If the detector and preamplifier have an optimized time constant, the output signal appears as shown in Figure C-14b, when the detector projection is swept across the horizon (the image of the horizon is swept across the detector in image space). The detector signals returns to zero by capacitive coupling. The actual signal in the presence of noise will look more like Figure C-14c.

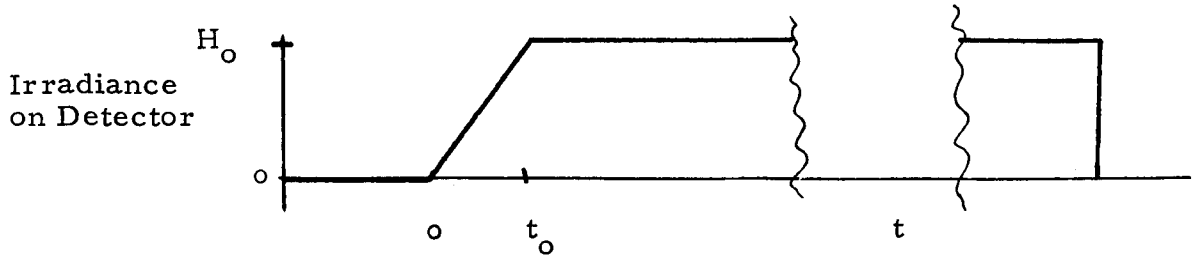

Figure C-14a. Irradiance on the Detector

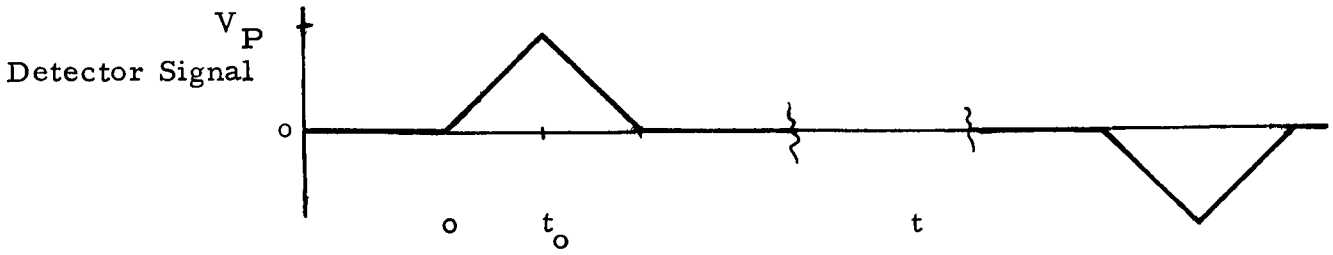

Figure C-14b. Detector Response

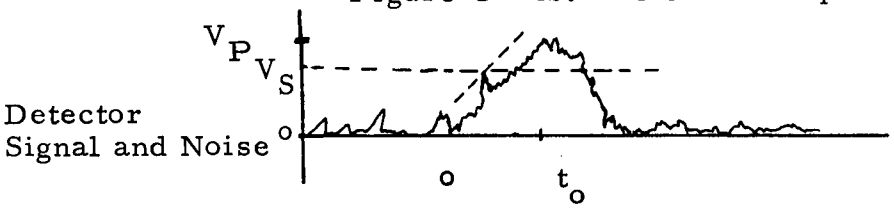

Figure C-14c. Detector Response with Noise

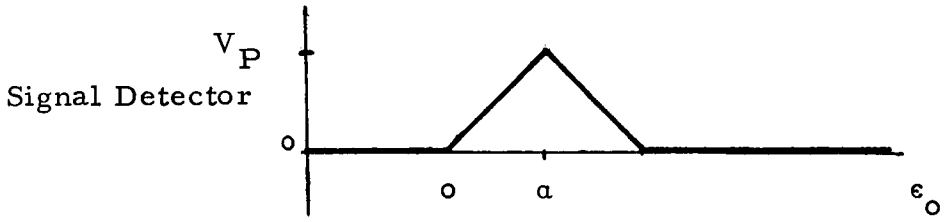

Figure C-14d. Detector Response as a Function of Scan Angle

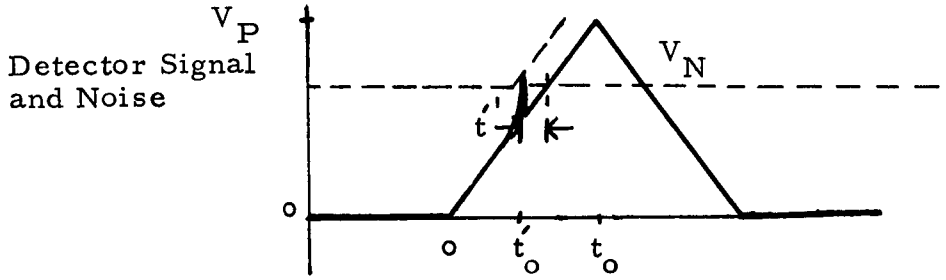

Figure C-14e. Expanded Time Scale

Figure C-14. Signal Amplitude Versus Angle of Scan

Let

V_p = peak signal output

V_s = threshold level

V_n = rms noise

$x = V_p/V_n$ and $y = V_s/V_n$.

In this simple system it is assumed that the signal position is determined by the signal exceeding a predetermined threshold level V_s. The signal is then demodulated in a demodulator with a period of $1/f$ where f is the frequency of the conical scan.

The position of the horizon in terms of the scan angle is determined by sensing the time of maximum signal t_o with reference to some arbitrary time. The rest of the determination of the coordinate of the earth's center is done by similiarly acting on the pulse when the detector projection sweeps off the earth and into space.

The analysis of the angle noise has now to be broken into two parts: high signal-to-noise where $V_s \gg V_n$ so that the only noise pulses which cause error are on the leading edge of the signal pulse, and the low signal-to-noise case where interpulse noise adds to the error. A perfect target is assumed so that effects due to variation in signal strength will be ignored here.

(1) $V_s \gg V_n$

The error is caused when a noise pulse causes the signal plus noise to exceed the threshold too early.

$t' = t_o - t'_o$ is the time error; the equivalent angular error is e. The signal is plotted in terms of the angle in Figure C-14d to indicate the equivalence of time and angular position.

From similar triangles (see expanded scale Figure C-14e).

$$\frac{t'}{t_o} = \frac{V_n}{V_p} \text{ also } \frac{t'}{t_o} = \frac{e}{a}$$

Assuming narrowband gaussian noise, the variance of the time is:

$$\sigma_t^2 = t'^2$$

and the variance of angle is

$$\sigma_\epsilon^2 = \epsilon^2.$$

then,

$$\frac{\sigma_t^2}{t_o^2} = \frac{\sigma_\epsilon^2}{\alpha^2} = \left(\frac{V_n}{V_p}\right)^2 = \frac{1}{x^2}$$

After demodulation, the angle noise density at zero frequency is given by

$$W_n(o) = \frac{2}{f}\sigma_\epsilon^2 = \frac{2}{f}\frac{\alpha^2}{x^2}$$

and the rms angle noise by

$$\sqrt{W_n(o)} = \sqrt{\frac{2}{f}}\frac{\alpha}{x}$$

(2) The analysis of the interpulse noise case is more complex than the first case and no general analysis exists. An approximate solution can be found by considering the zero crossings of the noise; but since the analysis is quite involved, only the result will be stated here.

$$\sqrt{W_n(o)} \approx \epsilon_o^{3/2}\sqrt{\frac{\pi}{\alpha f}}\frac{e^{-(y/2)^2}}{\frac{1}{2\pi}\int_{-(x-y)}^{\infty} e^{-u^2/2}\,du}$$

Figure C-15 is a plot of the angle noise density for a particular set of typical parameters. The parameters chosen for this plot were:

$$\alpha = 0.035 \text{ rad}$$

$$\epsilon_o = 0.96 \text{ rad}$$

$$f = 30 \text{ scans/sec}$$

$$Y = 5.4$$

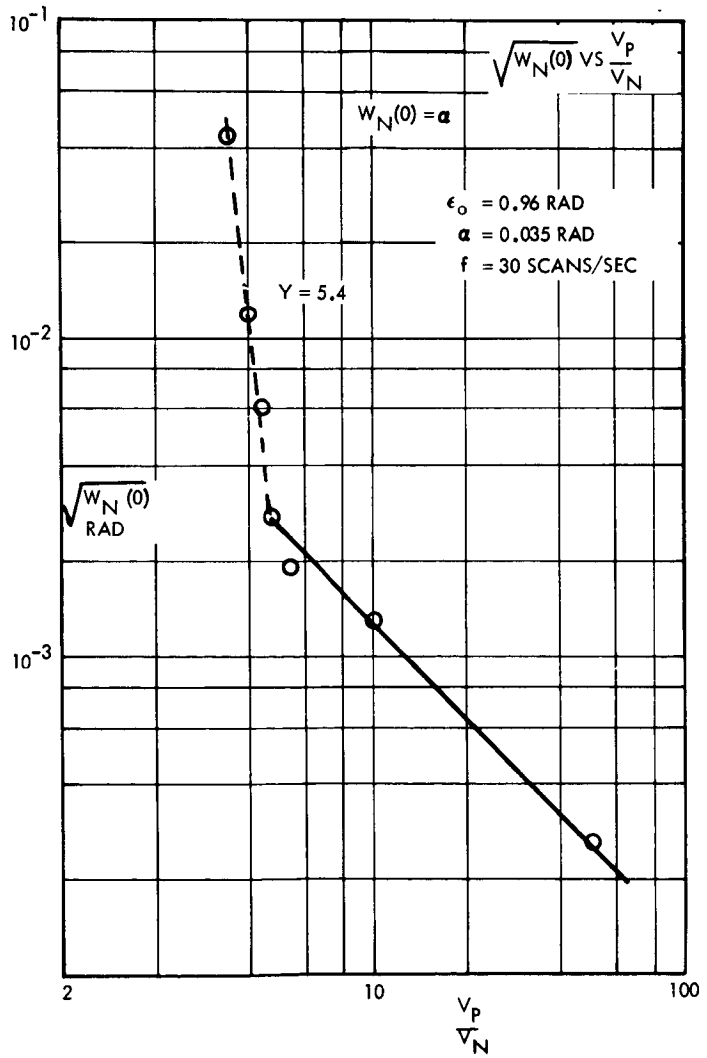

Figure C-15. Angular Noise Density

Since the total angle noise depends upon sensing two pulses, the pulse formed when the image of the earth sweeps onto the detector and the pulse formed when the image sweeps off the detector, the noise contribution of the second pulse must also be considered. Assuming that the noise is random (noncorrelated), the noise contributions will add rms - wise and the rms angle noise will be $\sqrt{2}$ times the values found from the above equations. From this plot it can be seen that with the simplified scanner and the parameters given here, a signal-to-noise ratio of approximately 5 is necessary to maintain the rms angle noise at about 1/10 the instantaneous field of view. The angle noise can be larger than calculated above if care is not taken to insure that other sources of noise do not occur in the signal processing after the preamplifier.

Offset Error. For a horizon scanner utilizing a threshold level such as the example considered above, there is an offset or bias error induced by a difference in temperature of the two limbs of the earth. Figure C-16 indicates this type of error. From the figure it can be seen that the time difference is $t_2 - t_1$, indicating that the earth's radiance width is not the same as $t'_2 - t'_1$ which is the sensed parameter, by an amount Δt which depends upon the radiance difference of the two limbs, the threshold chosen, and the system parameters. This error can be

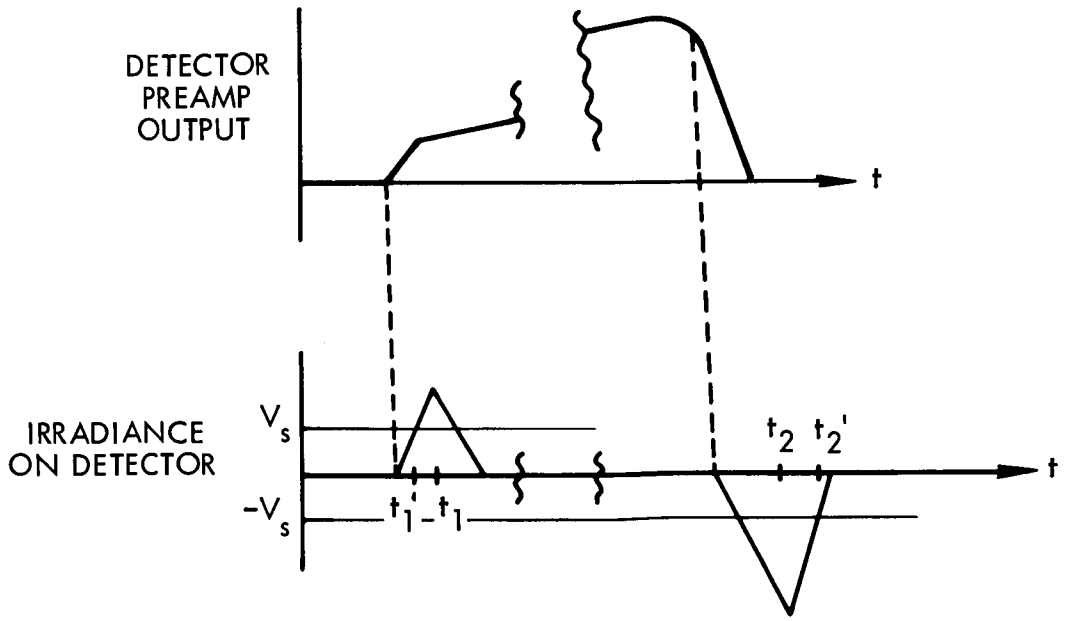

Figure C-16. Bias Error Due to Earth Limb Temperature Differential

minimized by raising the threshold, but at the expense of more susceptibility to gradients within the earth's radiant disc which could be very large errors.

Another offset error occurs in the example because of the time constant of the detector preamplifier combination. This time constant causes a lag in the signal and a consequent lag in the apparent angles to the horizon. If the radiances of the two limbs are equal, the phase lag due to the time constant could be compensated for in the signal processing circuitry. However, if the radiance is different at the two limbs, the lag will be different at the two limbs, and a fixed compensation will not eliminate this error completely.

Errors in Alignment and Transducer Readout. Alignment errors consist of initial alignment errors between the horizon scanner and the spacecraft reference, nonlinearities and drifts in the transducer readouts of the horizon scanner. Initial alignment accuracy is determined by alignment methods, and with sufficient finesse can be made negligibly small in comparison with angle readout errors. Readout errors can usually be held to quite small values over small angular ranges where linearities are good. Often the equipment can be designed so that operation is restricted to these linear, relatively high accuracy areas. Random errors in the readout devices are also a cause of error; however, they are usually small in comparison to other sources.

4.1.2 Earth Effect Errors

The error sources due to the earth can be divided into:

- Gradients within the earth's radiant disc
- Differences in radiance and altitude of the apparent horizon due to latitude and season
- Oblateness of the earth
- Atmospheric anomalies such as storm fronts.

Radiance Differences. From the discussion of the earth's radiance, it can be seen that the errors due to gradients in radiation and altitude variations in the apparent horizon can be minimized by proper selection of the operating spectral region. These errors can also be minimized by

optimizing the signal processing methods. If approximate orientation and sub-satellite latitude information were available, errors due to latitude effects in the radiance of the horizon could be calculated and partially eliminated. In a like way, the season effect could be calculated and eliminated.

Oblateness. The errors due to the earth's oblateness could also be computed and compensated for. An estimate of the effects of oblateness can be made by assuming that the true earth shape is an ellipsoid and calculating the error in determination of local vertical from this effect.† The deviation of the measured center of the earth's disc from the geocenter for a spacecraft with no roll or pitch error is given approximately by (see Ref 9):

$$\Delta\theta = \epsilon^2 \frac{\alpha^2}{\rho^2} \sin\lambda \cos\lambda \sin\phi$$

where

ϵ = eccentricity of ellipsoid, 0.082

α = equatorial earth radius

ρ = radial distance, geocenter to satellite

λ = latitude of satellite subpoint

ϕ = azimuth of sensor measurement plane about vertical measured from line parallel to the earth's major axis

This error is quite small at synchronous altitudes, being less than 0.01 deg when there is no pitch-or-roll offset. The error becomes more significant at low-altitude orbits.

Atmospheric Anomalies. The effects of atmospheric anomalies can be reduced by sensing many points around the horizon and averaging the results. If the effects of storm fronts, etc., are localized, this method of averaging will greatly reduce the error.

---

†Variations in the earth's atmosphere dependent on latitude (as measured on the oblate earth).

Conversations with John Duncan at the Institute of Science and Technology, the University of Michigan, indicate that his studies of the effect of weather conditions on the 14-through 16-μ CO_2 radiance band show only small effects which are highly correlated over large viewing areas. This result indicates that, if the 14- through 16-μ region is used, there is no advantage in averaging over many points on the horizon and a simpler scanner may offer the same accuracy.

4.2 Accuracy Comparison, Conical Scan Versus Edge Tracker

Although both conical scan and edge scan systems have the same angle noise for equivalent signal-to-noise ratios from the preamplifier and equivalent signal processing, the smaller scan angle of the edge scanner results in much higher signal-to-noise ratios and subsequently less angle noise than the conical scanner. This difference can be expressed in terms of the size of the collecting optics required for the two types for equivalent signal-to-noise ratio. As an example of this difference, consider a conical scanner with

scan angle = $110^{o} = 2\theta_{o}$

detector size: $1^{o} \times 1^{o}$, $\Omega = 6.91 \times 10^{-4}$ rad = instantaneous field-of-view

optical collection area = A_{o}

scan frequency: $f = 30$ scans/sec

detector responsivity: $R = 300$ v/w

noise due to amplifier (limiting noise): $v = 0.5\ \mu v/(cps)^{1/2}$

and an edge tracker with scan angle = 5 deg and all other parameters the same as the conical scanner.

4.2.1 Conical Scanner

The horizon cross over time τ_{C} for the conical scanner is given by

$$\tau_{C} = \frac{\alpha}{2\pi\theta_{o} f}$$

where α = detector width. τ_C for the conical scan is $\tau_c = 9.63 \times 10^{-5}$ sec. In order to pass the information contained in this pulse, we assign a bandwidth

$$\Delta f = \frac{1}{2\tau_c} = 5.19 \times 10^{3} \text{ cps.}$$

If the radiance from the earth is taken to be $N = 3.5 \text{ w/m}^2$ - ster, and the optical transmission is taken to be 0.65 we can calculate the required A_o for any signal-to-noise (S/N) ratio. For S/N = 10, the noise is assumed to be entirely from the preamp and is

$$V_N = V(\Delta f)^{1/2} = 3.6 \times 10^{-5} \text{ v}$$

The signal must then be $V_s = 10V_n = 3.6 \times 10^{-4}$ v. The total power on the detector, W, necessary to produce this signal is given by

$$W = \frac{Vs}{R} = 1.2 \times 10^{-6} \text{ w}$$

The necessary optical collection area can then be derived from

$$W = NA_o \Omega T$$

or

$$A_o = \frac{W}{N\Omega T} = 7.62 \text{ cm}^2$$

4.2.2 Edge Scanner

For the edge scanner the horizon crossover time is

$$\tau_c = 3.33 \times 10^{-3} \text{ sec}$$

and,

$$\Delta f = \frac{1}{2\tau_c} = 150 \text{ cps}$$

The noise is

$$V_N = V(\Delta f)^{1/2} = 6.13 \times 10^{-6} \text{ v}$$

$$V_s = 10\, V_n = 61.3 \times 10^{-6} \text{ v}$$

for a signal-to-noise ratio of 10. The total power is then

$$W = \frac{Vs}{R} = 0.204 \times 10^{-6} \text{ w}$$

and the optical collection area is

$$A_o = \frac{W}{N\Omega T} = 1.3 \text{ cm}^2$$

With presently available thermal detectors, the difference in the required collecting area is even greater because the detector time constant causes a decrease in the high frequency response, but the preamplifier noise remains essentially constant with frequency. From this respect, the edge scanner appears to offer more accurate information for a given size of optics. From a weight tradeoff standpoint, the smaller collection area of the edge scanner is partly offset by the requirements of three edge trackers and only two conical scanners, although the requirements for rotating parts in the conical scan tend to increase the weight of the conical scanner.

4.3 Reliability

It is difficult to obtain horizon sensor information in a form that allows easy comparison between different systems. This is partly because of the difference in the missions for which these sensors were designed. It is often difficult to determine whether a reliability number represents a design goal or an experimentally derived result. Extensive experience with the OGO horizon sensor has indicated that with four sensors which provide a degree of redundancy, and with projected parts failure rate data, the reliability is 0.992 for one year. Because of complex independence of reliability on specific design, it is not possible

to use the OGO sensor reliability to easily predict reliability of other sensors. It is probable, however, that the Gemini and Agena horizon sensors will have roughly the same reliability as the OGO sensor because of similarities, although different numbers of parts are involved in each sensor. However, the Gemini and Agena sensors have a rotating part with lubricated bearings which affects reliability.

5. OPERATIONAL SENSORS

A survey has been performed as part of the present study in order to gather data concerning current earth sensing systems. The findings of this survey are presented in Volume III (Part I). It is the purpose of this section to indicate those sensors which have actually been operated in the orbital environment and to supply comments regarding their performance as available. It is important that the slight operational accuracy data which have been obtained are classified and, therefore, not presented here. The information is summarized in Table C-I.

Table C-I. Summary of Flight Proven Scanning Horizon Sensors

Vehicle	Horizon Sensor Type	Comment
Mercury	Conical scan	Wide spectral band resulting in much earth effect error. Short duration mission
Gemini	Peripheral edge tracker	Considerable earth effect errors, short term missions
Agena	Conical scan	Original version did not function to specification, experimental flights led to changed spectral band.
Saturn	Edge track	Used during ballistic portion of flight
OGO	Edge track	Original version suffered from cold cloud problems spectral band change required and implemented in "AOGO" horizon scanner system.

This table does not include the "pipper" type of horizon sensor which has been used on spinning spacecraft such as Tiros. These devices are essentially narrow-field infrared radiometers and are not applicable for missions requiring full stabilization. Two major conclusions may be drawn from flight experience with scanning horizon sensors.

(1) Earth radiance in the 1.8-μ to 12-μ band is highly variable and unsuitable for generation of attitude data.

2) Little or no experience has been gained with infrared horizon scanners operating over long mission periods. Of the devices listed in Table C-I, only the OGO sensor system was designed for long life. To date, the earth stabilized mode of OGO flights has not lasted significantly longer than Agena or manned missions.

Several devices have been designed and tested which operate in the "optimal" 14-μ through 16-μ band and/or designed for extremely long orbital life. These sensors have not yet been proven, however, in the control system of a fully stabilized earth-orbiting spacecraft.

REFERENCES FOR APPENDIX C

1. Wark, D. W., J. Alishouse, et al., "Calculations of the Earth's Spectral Radiance for Large Zenith Angles," Meteorological Satellite Laboratory Report No. 21, U. S. Department of Commerce, Washington, D. C., October 1963.

2. McArthur, William G., "Horizon Sensor Navigation Errors Resulting from Statistical Variations in the CO_2 14-16 Micron Radiation Band," Transactions of the 9th Symposium on Ballistic Missile and Space Technology, Vol. 1, 12-14, August 1964.

3. Hanel, R. A., W. R. Bandeen, et al., "The Infrared Horizon of the Planet Earth," Journal of the Atmospheric Sciences, Vol. 20, March 1963.

4. Bandeen, W. R., B. J. Conrath, et al., "Experimental Confirmation from the TIROS VII Meterological Satellite of the Theoretically Calculated Radiance of the Earth Within the 15-Micron Band of Carbon Dioxide," Journal of the Atmospheric Sciences, Vol. 20, No. 6, November 1963, pp. 609-614.

5. Burn, J. W., "The Application of the Spectral and Spatial Characteristics of the Earth's Infrared Horizon to Horizon Scanners," IEEE Transactions on Aerospace-- Support Conference Procedures, p. 1115.

6. Bradfield, L., "Horizon Sensor Infra-Red Flight Test Program, Summary Report," Lockheed Missiles and Space Co. Report No. A064189, 19 October 1962.

7. Collinge, J., W. Haynie, "Measurement of 15 Micron Horizon Radiance from a Satellite," Eastman Kodak Co. Report Z-3112, 1 March 1963.

8. Dodgen, J., Howard J. Curfman, "Summary of Horizon Definition Studies Being Undertaken by Langley Research Center," in Proceedings of the First Symposium on Infrared Sensors for Spacecraft Guidance and Control, Barnes Engineering Co., 12, 13 and 26, 27 May 1965.

9. Duncan, J., W. Wolfe, et al., "IRIA State-of-the-Art Report, Infrared Horizon Sensors," Institute of Science and Technology, University of Michigan, April 1965.

APPENDIX D

ANALYTICAL TECHNIQUES USED FOR TRACKING AND NAVIGATION ERROR ANALYSIS STUDIES

1. INTRODUCTION

The tracking and navigation error analysis studies carried out as part of the Radio/Optical/Strapdown Inertial Guidance Study were conducted using TRW's SVEAD† computer program. This appendix contains a brief description of the SVEAD program and a detailed description of the subroutines developed and supplied to SVEAD for performing this study.

Briefly, this study was concerned with the comparative performance of DSIF tracking (earth based Doppler) and onboard optical navigation. Optical instruments considered were: star tracker, planet tracker, sun sensor, and planet subtense angle tracker (range measurement). Major error sources considered were: slowly drifting biases in the optical equipment, uncertainty in the planet diameter, Doppler bias error (slowly drifting), planet ephemeris errors, and uncertainty in the dynamic model of the solar system (that is, errors in solar wind, gravitational constants, planet oblateness, etc.).

2. STATE VARIABLE ESTIMATION AND ACCURACY DETERMINATION (SVEAD) PROGRAM

This Section describes the State Variable Estimation And Accuracy Determination (SVEAD) program. SVEAD is a general purpose Kalman filtering program, developed in the System Analysis and Software Department of the Guidance and Navigation Laboratory at TRW Systems. It is used to analyze problems in which parameters (the state vector) must be estimated from noisy measurements. SVEAD has been successfully used for many types of applications, including the following: orbit determination (both near earth and deep space); powered flight tracking (in the earth-moon gravity field); on-board satellite navigation (earth, moon, and

---

†State Variable Estimation and Accuracy Determination Program. For detailed information on the basic SVEAD program, the reader is referred to the SVEAD Users Manual, TRW Document No. 7221.1-10, W.M. Lear, 28 April 1967.

deep space); ground station location; navigation of ships and planes; radar altimeter map matcher; estimation of the earth's gravitational potential; satellite attitude determination; inertial platform alignment and calibration; fire control problems; and estimation of rocket motor parameters.

In general, SVEAD is useful in analyzing any problem in which

a) A state vector (list of unknowns) can be defined.

b) A system of differential equations, governing the action of the state vector, can be written. Note that coefficients in the differential equations may themselves be part of the state vector. Also the differential equations need not be linear.

c) A series of inaccurate (noisy) measurements, which are functions of the state variables, are made.

d) An estimate of the noise statistics is available.

Then the SVEAD program can be used to

a) Determine how accurately the state vector could be estimated if measurements were available (but not actually available). This is the error analysis mode.

b) Determine how accurately the state vector could be estimated by simplified, nonoptimum filters, or determine how accurately estimation could be performed if the statistical knowledge necessary to construct an optimum filter was not known. This is the suboptimal error analysis mode.

c) Process actual measurements to form an actual estimate of the state vector.

d) Simulate the processing of measurements to form a simulation estimate of the state vector.

The program also has several other minor options. Some of these are: "trajectory" generator, transition matrix generator, and error covariance matrix propagator (in the absence of measurements).

SVEAD utilizes a Kalman filter. The Kalman filter is a minimum variance type of filter. If the quantity x_n is a state variable, and the quantity $\hat{x}_n$ is an estimate of x_n, then a minimum variance filter is one that, among other things, minimizes $E\left[(x_n - \hat{x}_n)^2\right]$ for all n (all the state variables). In addition, it can be shown that a minimum variance filter also minimizes $E\left[(y_m - \hat{y}_m)^2\right]$, where the y_m are elements of the measurement vector. A conventional least squares estimator will minimize

$\sum_m (y_m^\dagger - \hat{y}_m)^2$, where the $y_m^\dagger$ are the actual noise corrupted measurements. Thus it can be said that a minimum variance estimator attempts to make a fit to exact values, while a least squares estimator makes a fit to noise corrupted measurements.

The Kalman filter has several advantages over the conventional least squares program, including the following:

a) No difficult inversion of an ill-conditioned N x N matrix, where N is the number of state variables, is required when using a Kalman filter.

b) The Kalman filter can easily handle time correlated measurement noise, thus allowing more realistic modeling of measurement error statistics.

c) Perhaps the most important advantage of the Kalman filter is its ability to handle "state noise". Examples of sources of state noise are random gyro drift, accelerometer noise, random solar winds, drifting instrument biases, and unmodeled forces such as higher order harmonics in the earth's gravity field. Also the filter, in some instances, may be "told" that there is state noise acting on the system as an engineering "trick". This can be done when a simple mathematical model of the system is used in place of the more complex (and often unknown) model of the system. This addition of state noise prevents the filter from becoming overconfident of its estimate of the state variables, and in effect represents the unmodeled part of the real world. Also the concept of state noise is generally necessary if tracker or navigator dynamics are modeled.

d) The Kalman filter generally estimates the current state of the system, as opposed to estimating the state at some fixed epoch time. However, it can be set up to directly estimate the state at some epoch time, but when this is done, state noise can not be handled.

e) The Kalman filter readily lends itself to on-line or real time filtering problems. Thus SVEAD is useful for studies which may lead to such applications.

f) The Kalman filter gives an estimate of the state variables after each measurement is processed, thus giving a time history of the estimated state and its accuracy. If such a time history is desired using a least squares program, it must be rerun for each point on the curve.

g) Both the Kalman filter and the conventional least squares program contain linearity assumptions. The Kalman filter, however, improves its linearity assumption (that is, it relinearizes itself) after each measurement is processed. The conventional least squares program must wait until all the measurements are processed before it can improve its linearity assumption. At this time it relinearizes itself about the new estimate and repeats the processing of all the measurements to obtain another improved estimate of the state, about which it again relinearizes. Generally, the least squares program requires about four or more such iterations to process satellite tracking data.

h) The standard deviations of the state estimation errors, using a minimum variance estimator, are always less than or equal to the standard deviations of the state estimation errors using a least squares estimator.

In summary, SVEAD provides a modern method of studying state variable estimation problems. An implicit feature of this program is the built-in experience gained from a large number of previous studies.† For example, built-in diagnostic dumps and the printout of correlation coefficient matrices (in arbitrary coordinates) are conveniences which are the products of experience. Various devices have been employed to obtain rapid cycle times and control machine roundoff errors. Also the program is designed to easily facilitate changes in a specific problem being studied. Due to the completely variable in size matrices and vectors, state variables may be added or deleted with no modification of the main program. Due to variable size matrices and vectors, SVEAD will handle large or small problems as though the program had been specifically written for that problem. Through its ability to handle state noise and time correlated measurement noise, the Kalman filter used by SVEAD can implement a more realistic model of the real world than can conventional least squares programs.

3. MATHEMATICAL MODEL OF THE OPTICAL MEASUREMENTS

The principal purpose of the optical measurements is to locate the position of the planet (Mars) relative to the spacecraft. The lines of

---

†At the time of writing, about 50 previous studies have been done. Included in these is the first space application of the Kalman filter, used in the Ranger and Mariner guidance equations in 1963.

sight to two known stars may be used to provide a known coordinate system, in which the planet may be located. For this study, one star is taken to be Canopus, and the other is taken to be the Sun. Mars is then located by a cone angle Ψ and a clock angle θ, as shown in Figure D-1. The angle ϕ, shown in Figure D-1, is the Sun-Canopus angle. For this study, the directions to the Sun and Canopus are assumed to be known quantities. Strictly speaking, this assumption is only true if the Sun and Canopus were infinitely far away. Near Mars encounter, the Sun is about $0.2 \cdot 10^9$ km away. A 500-km position error causes a 0.5-arc sec angular error in the position of the sun. This error is negligible compared to the other optical errors.

The optical system which measures the cone and clock angles includes a Canopus tracker, a Sun tracker, and a Mars tracker. Associated with each of these devices are angular errors which cause the measured lines of sight to deviate from their true directions. It is assumed

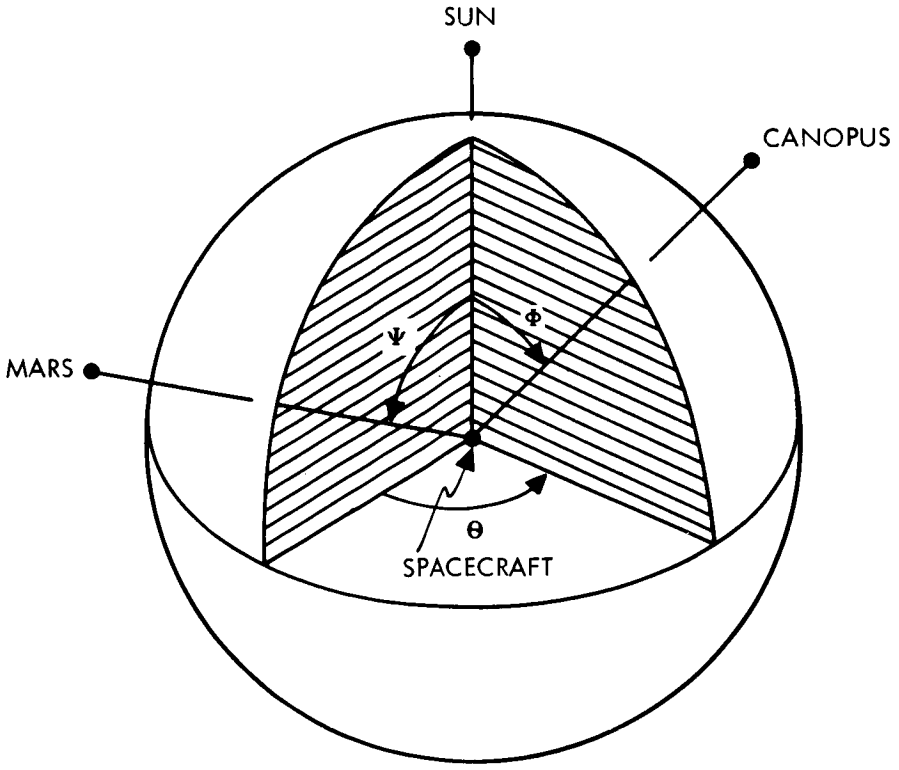

Figure D-1. Measurement Geometry

in this study that each tracker has two sensitive axes which are at right angles to each other as shown in Figure D-2. It is further assumed that the errors along the various axes are all independent of each other.

Let $\underline{i}_s$, $\underline{i}_m$, and $\underline{i}_c$ be unit vectors along the line of sight from the vehicle to the Sun, Mars, and Canopus respectively. The orientations of the displacement error vectors, $\underline{\epsilon}$, are defined by

$\underline{\epsilon}_{s1}$ is in the Sun-Mars plane, normal to $\underline{i}_s$.
$\underline{\epsilon}_{s2}$ completes the right-hand set, $(\underline{\epsilon}_{s1}, \underline{\epsilon}_{s2}, \underline{i}_s)$.

$\underline{\epsilon}_{m1}$ is in the Sun-Mars plane, normal to $\underline{i}_m$.
$\underline{\epsilon}_{m2}$ completes the right-hand set, $(\underline{\epsilon}_{m1}, \underline{\epsilon}_{m2}, \underline{i}_m)$.

$\underline{\epsilon}_{c1}$ is in the Sun-Canopus plane, normal to $\underline{i}_c$.
$\underline{\epsilon}_{c2}$ completes the right-hand set, $(\underline{\epsilon}_{c1}, \underline{\epsilon}_{c2}, \underline{i}_c)$.

Assuming small values of $\underline{\epsilon}$, the cone angle measurement is seen to be

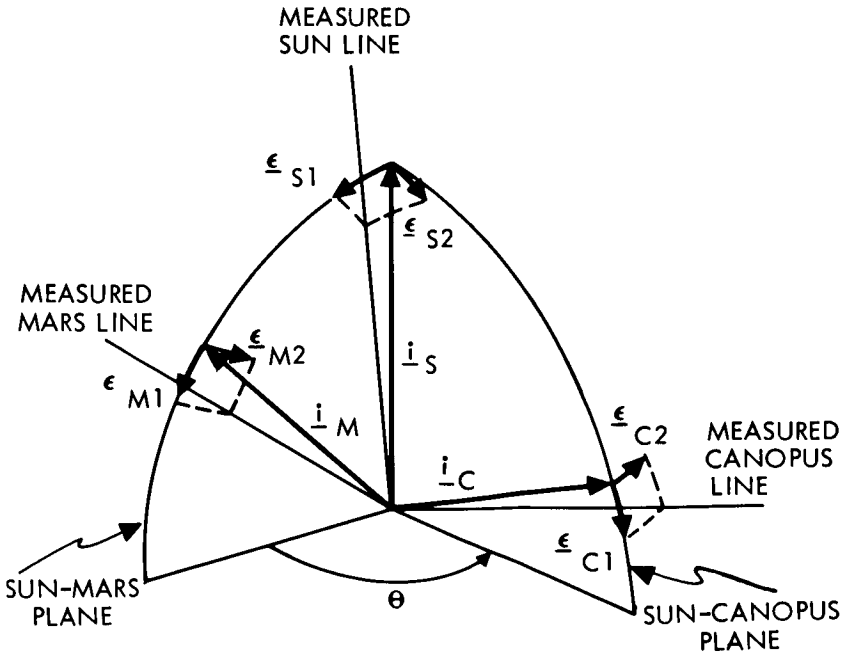

Figure D-2. Tracker Errors

$$y_1 = \psi + \epsilon_{m1} - \epsilon_{s1} \tag{D-1}$$

and the clock angle measurement is

$$y_2 = \theta - \epsilon_{m2}/\sin\psi + \epsilon_{c2}/\sin\phi \tag{D 2}$$

Let ϵ_ψ and ϵ_θ be defined by

$$\boxed{\epsilon_\psi = \epsilon_{m1} - \epsilon_{s1}} \tag{D-3}$$

$$\boxed{\epsilon_\theta = -\epsilon_{m2}/\sin\psi + \epsilon_{c2}/\sin\phi} \tag{D-4}$$

Then the cone and clock angle measurements are

$$\boxed{y_1 = \psi + \epsilon_\phi} \tag{D-5}$$

$$\boxed{y_2 = \theta + \epsilon_\theta} \tag{D-6}$$

Note that, from Equations (D-3) and (D-4), the angular errors, ϵ_ψ and ϵ_θ, are uncorrelated. Their variances are given by

$$\boxed{\sigma^2_{\epsilon\psi} = \sigma^2_{\epsilon m1} + \sigma^2_{\epsilon s1}} \tag{D-7}$$

$$\boxed{\sigma^2_{\epsilon\theta} = \sigma^2_{\epsilon m2}/\sin^2\psi + \sigma^2_{\epsilon c2}/\sin^2\phi} \tag{D-8}$$

The cone and clock angles, ψ and θ, are given by

$$\boxed{\cos\psi = \underline{i}_s \cdot \underline{i}_m} \tag{D-9}$$

$$\boxed{\cos\theta = \frac{\underline{i}_s \times \underline{i}_c}{|\underline{i}_s \times \underline{i}_c|} \cdot \frac{\underline{i}_s \times \underline{i}_m}{|\underline{i}_s \times \underline{i}_m|}} \tag{D-10}$$

It is remembered that $\underline{i}_s$ and $\underline{i}_c$ are assumed to be known and the equation relating $\underline{i}_m$ to the state vector is

$$\underline{i}_m = \underline{R}_m/R_m \tag{D-11}$$

where $\underline{R}_m$ is the position of Mars with respect to the spacecraft.

Let $\underline{i}_{ms}$ be a unit vector in the Sun-Mars plane, normal to $\underline{i}_m$ and in the direction of increasing ψ. Thus it easily checked that

$$\underline{i}_{ms} = \frac{\cos \psi}{\sin \psi} \underline{i}_m - \frac{1}{\sin \psi} \underline{i}_s \tag{D-12}$$

Let $\underline{u}_{ms}$ be a unit vector normal to the Sun-Mars plane, in the direction of increasing θ. Thus

$$\underline{u}_{ms} = \frac{\underline{i}_s \times \underline{i}_m}{|\underline{i}_s \times \underline{i}_m|} \tag{D-13}$$

It is now easily seen, from geometric considerations, that

$$\boxed{\delta\psi = \frac{1}{R_m} \underline{i}_{ms} \cdot \delta \underline{R}_m} \tag{D-14}$$

$$\boxed{\delta\theta = -\frac{1}{R_m \sin \psi} \underline{u}_{ms} \cdot \delta \underline{R}_m} \tag{D-15}$$

These two equations give the partial derivatives of the cone and clock angles with respect to x_m, y_m, z_m. These partial derivatives are needed by SVEAD to form the elements of the first two rows of the measurement matrix.

The third optical measurement to be considered is the apparent angular diameter of Mars. If the radius of Mars is denoted by r, then the angle to be measured, also known as the subtense angle, is given by

$$\alpha = 2 \sin^{-1} (r/R_m)$$

The third optical measurement is then taken as

$$\boxed{y_3 = 2 \sin^{-1} \frac{r_N + \epsilon_r}{R_m} + \epsilon_\alpha} \tag{D-16}$$

where r_N is a nominal radius of Mars, ϵ_r is the error in the radius of Mars, and ϵ_α is the measurement error.

The partial derivatives of y_3 with respect to elements of the state vector are conveniently expressed by

$$\boxed{\delta y_3 = \frac{-2r}{R_m^2 \cos(\alpha/2)} \underline{i}_m \cdot \delta \underline{R}_m + \frac{2}{R_m \cos(\alpha/2)} \delta \epsilon_r + \delta \epsilon_\alpha} \quad \text{(D-17)}$$

4. MATHEMATICAL MODEL OF THE DOPPLER MEASUREMENTS

As the spacecraft moves away from the Earth, toward Mars, the measurement geometry is little affected by ground tracking station location. The major geometric effect is that the earth is changing its location along its orbit, not that the tracking station is located on the surface of a rotating body. Therefore, as a matter of convenience for error analysis purposes, a single ground station will be assumed to be located at the center of the earth. Further, for error analysis purposes, it will be sufficient to assume that the Doppler measurements are line-of-sight rate (range-rate) measurements. Thus the fourth measurement to be considered for this study is

$$\boxed{y_4 = \underline{i}_E \cdot \dot{\underline{R}}_E + \epsilon_{\dot{R}}} \quad \text{(D-18)}$$

where $\underline{R}_E$ is the position vector of the earth's center with respect to the vehicle, $\epsilon_{\dot{R}}$ is the error in the measurement, and $\underline{i}_E = \underline{R}_E / R_E$. The partial derivatives of y_4 with respect to elements of the state vector are conveniently expressed by

$$\boxed{\delta y_4 = \frac{1}{R_E} [\dot{\underline{R}}_E - (\underline{i}_E \cdot \dot{\underline{R}}_E) \underline{i}_E] \cdot \delta \underline{R}_E + \underline{i}_E \cdot \delta \dot{\underline{R}}_E + \delta \epsilon_{\dot{R}}} \quad \text{(D-19)}$$

5. SECOND PARTITION DYNAMICS

The state vector is partitioned into two parts. The elements of the second partition are:

ϵ_{ax} = xx2(1), random acceleration in x direction, acting on vehicle.

ϵ_{ay} = xx2(2), random acceleration in y direction, acting on vehicle.

ϵ_{az} = xx2(3), random acceleration in z direction, acting on vehicle.

ϵ_{y1} = xx2(4), "bias" adding to first measurement (cone angle).

ϵ_{y2} = xx2(5), "bias" adding to second measurement (clock angle).

ϵ_{y3} = xx2(6), "bias" adding to third measurement (subtense angle).

ϵ_{y4} = xx2(7), "bias" adding to fourth measurement (range-rate).

ϵ_{r} = xx2(8), error adding to the radius of Mars.

All state variables in the second partition are assumed to be exponentially correlated (in time) random variables. Thus, by adjusting their time constants, they may range all the way from uncorrelated noise to constant biases.

The updating of exponentially correlated random variables, from time t_i to t_{i+1}, is given by

$$xx2(I)_{i+1} = a_I\, xx2(I)_i + \sigma_I \sqrt{1 - a_I^2}\, w_{I,i} \qquad \text{(D-20)}$$

where $w_{I,i}$ is unit variance, zero mean, uncorrelated in time, noise; σ_I^2 is the variance of xx2(I); and a_I is given by

$$a_I = e^{-|\Delta T/T_I|} \qquad \text{(D-21)}$$

where T_I is the time constant associated with xx2(I).

The three random acceleration components ϵ_{ax}, ϵ_{ay}, ϵ_{az} are used to model uncertainties in the gravity fields, uncertainties in the solar wind, and software approximations (e.g., deletion of higher order harmonics in the martian gravity field).

In a gravity free environment, the effect of the ϵ_{ax} component of random acceleration is to produce a random position and velocity error, ϵ_{px} and ϵ_{vx} respectively, in the x direction. For time, $T >> T_{\epsilon ax} = T_1 >> \Delta T$, it can be shown that

$$E\left[\epsilon_{px}^2\right] = \frac{2}{3} T^3 T_{\epsilon ax} \sigma_{\epsilon ax}^2 \quad \text{(variance of position error)} \qquad \text{(D-22)}$$

$$E\left[\epsilon_{vx}^2\right] = 2 T T_{\epsilon ax} \sigma_{\epsilon ax}^2 \quad \text{(variance of velocity error)} \qquad \text{(D-23)}$$

$$E\left[\epsilon_{px} \epsilon_{vx}\right] = T^2 T_{\epsilon ax} \sigma_{\epsilon ax}^2 \quad \text{(correlation coeff} = \sqrt{0.75}\text{)} \qquad \text{(D-24)}$$

For this study, the nominal flight time from Earth to Mars is $0.1523 \cdot 10^8$ sec. Taking T to be this value and arbitrarily letting $T_{\epsilon ax}$ be one week ($0.6048 \cdot 10^6$ sec), then the position and velocity standard deviations are given by

$$\sigma_{px} = 3.77 \cdot 10^{13} \sigma_{\epsilon ax} \qquad \text{(D-25)}$$

and

$$\sigma_{vx} = 4.29 \cdot 10^6 \sigma_{\epsilon ax} \qquad \text{(D-26)}$$

Arbitrarily choosing the position error, σ_{px}, to have a value of 200 km, gives a random acceleration of

$$\sigma_{\epsilon ax} = .531 \cdot 10^{-11} \text{ km/sec}^2 \qquad \text{(D-27)}$$

$$= 1.74 \cdot 10^{-8} \text{ ft/sec}^2$$

This uncertainty in acceleration is approximately the same size as the acceleration due to the uncertainty in the suns gravitational constant.

It should be mentioned here that the rate bias error, ϵ_{y4}, adding to the range-rate measurement, had a time constant of 1/3 day associated with it. This is about the maximum time that any station could continuously track the vehicle. Also, a time constant of this value allowed the rate bias errors at Goldstone, Madrid, and Woomera to be modeled as a single state variable for this error analysis study.

6. FIRST PARTITION DYNAMICS

The first partition of the state vector contains the following elements:

$$\left.\begin{aligned} x_E &= x_1 = xx1\ (1) \\ y_E &= y_1 = xx1\ (2) \\ z_E &= z_1 = xx1\ (3) \end{aligned}\right\} = \underline{R}_1, \text{ position of earth with respect to the vehicle.}$$

$$\left.\begin{aligned} x_M &= x_2 = xx1\ (4) \\ y_M &= y_2 = xx1\ (5) \\ z_M &= z_2 = xx1\ (6) \end{aligned}\right\} = \underline{R}_2, \text{ position of Mars with respect to the vehicle.}$$

$$\left.\begin{aligned} \dot{x}_E &= \dot{x}_1 = xx1\ (7) \\ \dot{y}_E &= \dot{y}_1 = xx1\ (8) \\ \dot{z}_E &= \dot{z}_1 = xx1\ (9) \end{aligned}\right\} = \dot{\underline{R}}_1, \text{ velocity of earth with respect to the vehicle.}$$

$$\left.\begin{aligned} \dot{x}_M &= \dot{x}_2 = xx1\ (10) \\ \dot{y}_M &= \dot{y}_2 = xx1\ (11) \\ \dot{z}_M &= \dot{z}_2 = xx1\ (12) \end{aligned}\right\} = \dot{\underline{R}}_2, \text{ velocity of Mars with respect to the vehicle.}$$

In addition to these positions and velocities, there are the following known positions and velocities:

$$\left.\begin{aligned} x_s &= x_3 \\ y_s &= y_3 \\ z_s &= z_3 \end{aligned}\right\} = \underline{R}_3, \text{ position of sun with respect to the vehicle.}$$

$$\left.\begin{aligned} x_4 \\ y_4 \\ z_4 \end{aligned}\right\} = \underline{R}_4, \text{ position of arbitrary, fourth gravitational body with respect to the spacecraft.}$$

$$\left.\begin{aligned} \dot{x}_s &= \dot{x}_3 \\ \dot{y}_s &= \dot{y}_3 \\ \dot{z}_s &= \dot{z}_3 \end{aligned}\right\} = \dot{\underline{R}}_3$$

$$\left.\begin{matrix}\dot{x}_4 \\ \dot{y}_4 \\ \dot{z}_4\end{matrix}\right\} = \dot{\underline{R}}_4$$

Let $\underline{R}_{i/j}$ be and $\underline{i}_{i/j}$ be defined by

$$\underline{R}_{i/j} = \underline{R}_i - \underline{R}_j \quad \text{and} \quad \underline{i}_{i/j} = \frac{1}{R_{i/j}} \underline{R}_{i/j}$$

And let the gravitational constants for the four bodies be designated by μ_1, μ_2, μ_3, and μ_4. Then the equations of motion of the vehicle, in a four body gravitational field; are

$$\ddot{\underline{R}}_1 = -\frac{\mu_1}{R_1^3}\underline{R}_1 - \frac{\mu_2}{R_2^3}\underline{R}_2 - \frac{\mu_3}{R_3^3}\underline{R}_3 - \frac{\mu_4}{R_4^3}\underline{R}_4 + \frac{\mu_2}{R_{2/1}^3}\underline{R}_{2/1} + \frac{\mu_3}{R_{3/1}^3}\underline{R}_{3/1} + \frac{\mu_4}{R_{4/1}^3}\underline{R}_{4/1} \tag{D-28}$$

$$\ddot{\underline{R}}_2 = -\frac{\mu_1}{R_1^3}\underline{R}_1 - \frac{\mu_2}{R_2^3}\underline{R}_2 - \frac{\mu_3}{R_3^3}\underline{R}_3 - \frac{\mu_4}{R_4^3}\underline{R}_4 + \frac{\mu_1}{R_{1/2}^3}\underline{R}_{1/2} + \frac{\mu_3}{R_{3/2}^3}\underline{R}_{3/2} + \frac{\mu_4}{R_{4/2}^3}\underline{R}_4 \tag{D-29}$$

$$\ddot{\underline{R}}_3 = -\frac{\mu_1}{R_1^3}\underline{R}_1 - \frac{\mu_2}{R_2^3}\underline{R}_2 - \frac{\mu_3}{R_3^3}\underline{R}_3 - \frac{\mu_4}{R_4^3}\underline{R}_4 + \frac{\mu_1}{R_{1/3}^3}\underline{R}_{1/3} + \frac{\mu_2}{R_{2/3}^3}\underline{R}_{2/3} + \frac{\mu_4}{R_{4/3}^3}\underline{R}_{4/3} \tag{D-30}$$

$$\ddot{\underline{R}}_4 = -\frac{\mu_1}{R_1^3}\underline{R}_1 - \frac{\mu_2}{R_2^3}\underline{R}_2 - \frac{\mu_3}{R_3^3}\underline{R}_3 - \frac{\mu_4}{R_4^3}\underline{R}_4 + \frac{\mu_1}{R_{1/4}^3}\underline{R}_{1/4} + \frac{\mu_2}{R_{2/4}^3}\underline{R}_{2/4} + \frac{\mu_3}{R_{3/4}^3}\underline{R}_{3/4} \tag{D-31}$$

The partial derivatives of $\ddot{\underline{R}}_1$ and $\ddot{\underline{R}}_2$ with respect to elements of the state vector are needed to generate the updating (or transition) matrix. These partial derivatives are given by (D-32)

$$\delta\ddot{\underline{R}}_1 = \left[-\left(\frac{\mu_1}{R_1^3} + \frac{\mu_2}{R_{2/1}^3} + \frac{\mu_3}{R_{3/1}^3} + \frac{\mu_4}{R_{4/1}^3}\right) I + 3\frac{\mu_1}{R_1^3}\underline{i}_1\underline{i}_1^T + 3\frac{\mu_2}{R_{2/1}^3}\underline{i}_{2/1}\underline{i}_{2/1}^T + 3\frac{\mu_3}{R_{3/1}^3}\underline{i}_{3/1}\underline{i}_{3/1}^T + 3\frac{\mu_4}{R_{4/1}^3}\underline{i}_{4/1}\underline{i}_{4/1}^T\right]\delta\underline{R}_1$$

$$+ \left[\left(-\frac{\mu_2}{R_2^3} + \frac{\mu_2}{R_{2/1}^3}\right)I + 3\frac{\mu_2}{R_2^3}\underline{i}_2\underline{i}_2^T - 3\frac{\mu_2}{R_{2/1}^3}\underline{i}_{2/1}\underline{i}_{2/1}^T\right]\delta\underline{R}_2$$

$$\delta\ddot{\underline{R}}_2 = \left[\left(-\frac{\mu_1}{R_1^3} + \frac{\mu_1}{R_{1/2}^3}\right)I + 3\frac{\mu_1}{R_1^3}\underline{i}_1\underline{i}_1^T - 3\frac{\mu_1}{R_{1/2}^3}\underline{i}_{1/2}\underline{i}_{1/2}^T\right]\delta\underline{R}_1$$

$$+ \left[-\left(\frac{\mu_1}{R_{1/2}^3} + \frac{\mu_2}{R_2^3} + \frac{\mu_3}{R_{3/2}^3} + \frac{\mu_4}{R_{4/2}^3}\right)I + 3\frac{\mu_1}{R_{1/2}^3}\underline{i}_{1/2}\underline{i}_{1/2}^T + 3\frac{\mu_2}{R_2^3}\underline{i}_2\underline{i}_2^T + 3\frac{\mu_3}{R_{3/2}^3}\underline{i}_{3/2}\underline{i}_{3/2}^T + 3\frac{\mu_4}{R_{4/2}^3}\underline{i}_{4/2}\underline{i}_{4/2}^T\right]\delta\underline{R}_2$$

(D-33)

7. THE TRAJECTORY INTEGRATOR

Let the $\underline{z}$ vector be composed of the following 24 elements: x_1, y_1, z_1, x_2, y_2, z_2, x_3, y_3, z_3, x_4, y_4, z_4, $\dot{x}_1$, $\dot{y}_1$, $\dot{z}_1$, $\dot{x}_2$, $\dot{y}_2$, $\dot{z}_2$, $\dot{x}_3$, $\dot{y}_3$, $\dot{z}_3$, $\dot{x}_4$, $\dot{y}_4$, $\dot{z}_4$. Then the equations of motion, given by Equations (D-28) through (D-31), can be written in the following form,

$$\dot{\underline{z}} = \underline{f}(\underline{z}) \qquad \text{(D-34)}$$

Let $\Delta T = t_{i+1} - t_i$. Then Equation (D-34) can be integrated by

$$\underline{z}_{i+1} = \underline{z}_i + \alpha_1\underline{k}_1 + \alpha_2\underline{k}_2 + \alpha_3\underline{k}_3 + \alpha_4\underline{k}_4 + 0(\Delta T^5) \qquad \text{(D-35)}$$

where

$$\underline{k}_1 = \Delta T\, \underline{f}(\underline{z}_i)$$

$$\underline{k}_2 = \Delta T\, \underline{f}(\underline{z}_i + a_1\underline{k}_1)$$

$$\underline{k}_3 = \Delta T\, \underline{f}(\underline{z}_i + b_1 \underline{k}_1 + b_2 \underline{k}_2)$$

$$\underline{k}_4 = \Delta T\, \underline{f}(\underline{z}_i + c_1 \underline{k}_1 + c_2 \underline{k}_2 + c_3 \underline{k}_3)$$

A suggested set of integration constants is

$$a_1 = \frac{1}{2} \qquad b_1 = \frac{1}{2} - b_2 \qquad b_2 = \frac{1}{6\alpha_3} \qquad c_1 = 0$$

$$c_2 = 1 - c_3 \qquad c_3 = 3\alpha_3 \qquad \alpha_1 = \alpha_4 = \frac{1}{6} \qquad \alpha_2 = \frac{2}{3} - \alpha_3$$

α_3 may be chosen so as to minimize the truncation error in Equation (D-35). $\alpha_3 = 1/3$ gives the conventional fourth order Runge-Kutta integrator. A value of $\alpha_3 = 0.436$ was used for this study, which gives an order of magnitude improvement in accuracy over the conventional constants.

8. ESTIMATION OF INTEGRATOR ERROR

One of the input parameters in a tracking and navigation error analysis study is the data sample-rate. Rather than squarely face the problem of how often to sample the data, it was decided to let the computer program pick its own sample rate. This was done by inputing a position accuracy requirement to the trajectory integrator equations. The integrator then chose ΔT to give this accuracy. Thus the program chose a small ΔT during times of rapid changes in the trajectory, and chose a large ΔT when the character of the trajectory was slowly changing. The equations which implement the automatic adjustment of integration step size, for an n^{th} order integrator are shown below.

In order to integrate from time t_i to t_{i+1}, assume that three integrations are made: one integration from t_i to $t_{i+.5}$; the result being integrated from $t_{i+.5}$ to t_{i+1}; and one integration from t_i to t_{i+1} directly.

Integration from t_i to $t_{i+.5}$, for an n^{th} order integrator, may be represented by

$$\hat{\underline{z}}_{i+.5} = \underline{g}(\underline{z}_i) + \underline{e}\left(\frac{\Delta T}{2}\right)^{n+1} \triangleq \underline{z}_{i+.5} + \underline{e}\left(\frac{\Delta T}{2}\right)^{n+1} \qquad \text{(D-36)}$$

where $\Delta T = t_{i+1} - t_i$, and where $\underline{e}\,(\Delta T/2)^{n+1}$ is the truncation error associated with the particular integration scheme being used.

Integration from $t_{i+.5}$ to t_{i+1} is given by

$$\hat{\hat{\underline{z}}}_{i+1} = \underline{g}\left[\underline{z}_{i+.5} + \underline{e}\,(\Delta T/2)^{n+1}\right] + \underline{e}\left(\frac{\Delta T}{2}\right)^{n+1}$$

or

$$\hat{\hat{\underline{z}}}_{i+1} = \underline{z}_{i+1} + \frac{\partial \underline{g}}{\partial \underline{z}}\,\underline{e}\left(\frac{\Delta T}{2}\right)^{n+1} + \underline{e}\left(\frac{\Delta T}{2}\right)^{n+1} \qquad \text{(D-37)}$$

A single integration from t_i to t_{i+1} would yield

$$\hat{\underline{z}}_{i+1} = \underline{z}_i + \underline{e}\,\Delta T^{n+1} \qquad \text{(D-38)}$$

Subtracting Equation (D-37) from (D-38) will give

$$\left(\frac{\Delta T}{2}\right)^{n+1}\left[(2^{n+1}-1)\,I - \frac{\partial \underline{g}}{\partial \underline{z}}\right]\underline{e} = \hat{\underline{z}}_{i+1} - \hat{\hat{\underline{z}}}_{i+1}$$

Thus

$$\underline{e} = \left(\frac{2}{\Delta T}\right)^{n+1}\left[(2^{n+1}-1)\,I - \frac{\partial \underline{g}}{\partial \underline{z}}\right]^{-1}\left(\hat{\underline{z}}_{i+1} - \hat{\hat{\underline{z}}}_{i+1}\right) \qquad \text{(D-39)}$$

As a first approximation, $\partial \underline{g}/\partial \underline{z} \approx I$, so

$$\underline{e} \approx \frac{1}{2^{n+1}-2}\left(\frac{2}{\Delta T}\right)^{n+1}\left(\hat{\underline{z}}_{i+1} - \hat{\hat{\underline{z}}}_{i+1}\right) \qquad \text{(D-40)}$$

For $\partial \underline{g}/\partial \underline{z} \approx I$

In situations where $\underline{z} = \begin{bmatrix} \underline{z}_1 \\ \dot{\underline{z}}_1 \end{bmatrix}^T$, a better approximation is

$$\frac{\partial \underline{g}}{\partial \underline{z}} = \begin{bmatrix} I & I\frac{\Delta T}{2} \\ 0 & I \end{bmatrix}$$

In this case

$$\underline{e} \approx \frac{1}{2^{n+1}-2}\left(\frac{2}{\Delta T}\right)^{n+1}\begin{bmatrix} I & I\,\dfrac{\Delta T}{2(2^{n+1}-2)} \\ 0 & I \end{bmatrix}\left(\hat{\underline{z}}_{i+1} - \hat{\hat{\underline{z}}}_{i+2}\right) \qquad \text{(D-41)}$$

For $\underline{z} = \begin{bmatrix} \underline{z}_1 \\ \dot{\underline{z}}_1 \end{bmatrix}^T$ only.

Knowing $\underline{e}$, and assuming $\underline{e}$ remains relatively constant from one cycle to the next, a value of ΔT for the next cycle may be picked to give any desired integration error. Equation (D-40) was used for this study, and found to be entirely satisfactory for controlling ΔT.

For example suppose that $\underline{z} = [z_1\ \dot{z}_1]^T$ and the error in $\hat{\hat{z}}_1$ (the position error) is to be controlled. From Equation (D-37), the position error in the next cycle is (for $\partial \underline{g}/\partial \underline{z} = I$)

$$2\,\underline{e}_1\left(\frac{\Delta T_{i+1}}{2}\right)^{n+1}$$

Let the magnitude of the allowable position error vector be

$$\delta_p \ \frac{\text{kilometers}}{\text{seconds of integration}}$$

Then

$$\delta_p\,\Delta T_{i+1} = 2|e_1|\left(\frac{\Delta T_{i+1}}{2}\right)^{n+1}$$

Substituting Equation (D-40) into the above, and solving for ΔT_{i+1} gives

$$\Delta T_{i+1} = \left[\frac{(2^n-1)\,\delta_p\,\Delta T_i}{|\hat{\underline{z}}_1 - \hat{\hat{\underline{z}}}_1|}\right]^{\frac{1}{n}}\Delta T_i \qquad \text{(D-42)}$$

Equation (D-42), with $n = 4$ and $\delta_p = 0.695 \cdot 10^{-10}$ km/sec, was used for this study. This gave an integration step size of $\Delta T \approx 6$ sec in the vicinity of the earth; $\Delta T \approx 12$ hr in deep space; and $\Delta T \approx 111$ sec at Mars perifocus.

Caution! When operating with very small values of δ_p (and small integration step sizes), there is a very large loss of significant figures in the quantity $\hat{\underline{z}} - \hat{\hat{\underline{z}}}$. Generally, integrator equations can be written in the form

$$\underline{z}_{i+1} = \underline{z}_i + \Delta\underline{z}_i$$

Thus the loss of significant figures is diminished if we let $\hat{\underline{z}} - \hat{\hat{\underline{z}}} = \Delta\hat{\underline{z}} - \Delta\hat{\hat{\underline{z}}}$.

9. GENERATING THE UPDATING MATRIX

Briefly reviewing, the equations of motion are given by

$$\dot{\underline{z}} = \underline{f}(\underline{z}) \tag{D-43}$$

Integration of this vector differential equation is accomplished by

$$\underline{z}_{i+1} = \underline{z}_i + \alpha_1 \underline{k}_1 + \alpha_2 \underline{k}_2 + \alpha_3 \underline{k}_3 + \alpha_4 \underline{k}_4 + 0\,(\Delta T^5) \tag{D-44}$$

Where

$$\underline{k}_1 = \Delta T\, \underline{f}(\underline{z}_i) \qquad \Delta T = t_{i+1} - t_i \tag{D-45}$$

$$\underline{k}_2 = \Delta T\, \underline{f}(\underline{z}_i + a_1 \underline{k}_1) \tag{D-46}$$

$$\underline{k}_3 = \Delta T\, \underline{f}(\underline{z}_i + b_1 \underline{k}_1 + b_2 \underline{k}_2) \tag{D-47}$$

$$\underline{k}_4 = \Delta T\, \underline{f}(\underline{z}_i + c_1 \underline{k}_1 + c_2 \underline{k}_2 + c_3 \underline{k}_3) \tag{D-48}$$

A suggested set of integration constants is

$$a_1 = \frac{1}{2} \qquad b_1 = \frac{1}{2} - b_2 \qquad b_2 = \frac{1}{6\alpha_3} \qquad c_1 = 0$$

$$c_2 = 1 - c_3 \qquad c_3 = 3\alpha_3 \qquad \alpha_1 = \alpha_4 = \frac{1}{6} \qquad \alpha_2 = \frac{2}{3} - \alpha_3$$

where α_3 is chosen to minimize $0\,(\Delta T^5)$.

Let $\underline{x}$ be the state vector of unknowns, and let $\underline{x}$ be a subset of $\underline{z}$. It is seen that Equation (D-44) is of the form

$$\underline{x}_{i+1} = \underline{g}(\underline{x}_i) \tag{D-49}$$

The updating matrix, U, is defined by

$$U \triangleq \frac{\partial \underline{g}}{\partial \underline{x}_i} = \frac{\partial \underline{x}_{i+1}}{\partial \underline{x}_i} \tag{D-50}$$

Thus, from Equations (D-44) through (D-48), it is seen that

$$U = I + \alpha_1 \frac{\partial \underline{k}_1}{\partial \underline{x}_i} + \alpha_2 \frac{\partial \underline{k}_2}{\partial \underline{x}_i} + \alpha_3 \frac{\partial \underline{k}_3}{\partial \underline{x}_i} + \alpha_4 \frac{\partial \underline{k}_4}{\partial \underline{x}_i} \tag{D-51}$$

where

$$\frac{\partial \underline{k}_1}{\partial \underline{x}_i} = \Delta T \left. \frac{\partial \underline{f}}{\partial \underline{x}} \right|_{\text{evaluated at } \underline{z}_i} \tag{D-52}$$

$$\frac{\partial \underline{k}_2}{\partial \underline{x}_i} = \Delta T \left. \frac{\partial \underline{f}}{\partial \underline{x}} \right|_{\underline{z}_i + a_1 \underline{k}_1} \left[I + a_1 \frac{\partial \underline{k}_1}{\partial \underline{x}_i} \right] \tag{D-53}$$

$$\frac{\partial \underline{k}_3}{\partial \underline{x}_i} = \Delta T \left. \frac{\partial \underline{f}}{\partial \underline{x}} \right|_{\underline{z}_i + b_1 \underline{k}_1 + b_2 \underline{k}_2} \left[I + b_1 \frac{\partial \underline{k}_1}{\partial \underline{x}_i} + b_2 \frac{\partial \underline{k}_2}{\partial \underline{x}_i} \right] \tag{D-54}$$

$$\frac{\partial \underline{k}_4}{\partial \underline{x}_i} = \Delta T \left. \frac{\partial \underline{f}}{\partial \underline{x}} \right|_{\underline{z}_i + c_1 \underline{k}_1 + c_2 \underline{k}_2 + c_3 \underline{k}_3} \left[I + c_1 \frac{\partial \underline{k}_1}{\partial \underline{x}_i} + c_2 \frac{\partial \underline{k}_2}{\partial \underline{x}_i} + c_3 \frac{\partial \underline{k}_3}{\partial \underline{x}_i} \right] \tag{D-55}$$

An alternate, and more common, method of obtaining the U matrix is to solve the matrix differential equation

$$\dot{U} = V(t)\, U \quad \text{where} \quad V = \frac{\partial \underline{f}}{\partial \underline{x}} \quad \text{and} \quad U_i = I \tag{D-56}$$

The suggested set of integration constants may be used to integrate the above equation. However, it can be shown that the solution is independent of the value of α_3. Therefore, we will choose the convenient value of $\alpha_3 = 1/3$. Then

where

$$U = I + \frac{1}{6} H_1 + \frac{1}{3} H_2 + \frac{1}{3} H_3 + \frac{1}{6} H_4 \qquad \text{(D-57)}$$

$$H_1 = \Delta T \, V_i \qquad V_i = \left.\frac{\partial \underline{f}}{\partial \underline{x}}\right|_{t_i} \qquad \text{(D-58)}$$

$$H_2 = \Delta T \, V_{i+.5} \left[I + \frac{1}{2} H_1\right] \qquad V_{i+.5} = \left.\frac{\partial \underline{f}}{\partial \underline{x}}\right|_{t_{i+.5}} \qquad \text{(D-59)}$$

$$H_3 = \Delta T \, V_{i+.5} \left[I + \frac{1}{2} H_2\right] \qquad \text{(D-60)}$$

$$H_4 = \Delta T \, V_{i+1} \left[I + H_3\right] \qquad V_{i+1} = \left.\frac{\partial \underline{f}}{\partial \underline{x}}\right|_{t_{i+1}} \qquad \text{(D-61)}$$

This method of solving for the updating matrix has the advantage of needing only three evaluations of $\partial \underline{f}/\partial \underline{x}$ as compared with four evaluations of $\partial \underline{f}/\partial \underline{x}$ for the first method [Equation (D-51)]. And these three evaluations may be reduced to two, for error analysis studies, by saving the last cycle's last value of $\partial \underline{f}/\partial \underline{x}$, to be used as the current cycle's first value of $\partial \underline{f}/\partial \underline{x}$. An advantage of the first method is that the accuracy of the U matrix is directly related to the accuracy of the trajectory integrator, whose accuracy is controlled by choosing a suitable value of α_3. Also, in the first method, the evaluation of $\partial \underline{f}/\partial \underline{x}$ may be done concurrently with the evaluation of $\underline{f}$. Since both of these quantities have many variables in common, $\partial \underline{f}/\partial \underline{x}$ is more quickly evaluated in method 1.

If Equation (D-57) is used to obtain U, then a value of $\underline{z}$ at time $t_{i+.5}$ is needed to evaluate $V_{i+.5}$. If $\underline{z}_{i+1}$ is obtained from Equation (D-44), then $\underline{z}_{i+.5}$ may be conveniently calculated from

$$\underline{z}_{i+.5} = \underline{z}_i + \beta_1 \underline{k}_1 + \beta_2 \underline{k}_2 + \beta_3 \underline{k}_3 + \beta_4 \underline{k}_4 + 0(\Delta T^4) \qquad \text{(D-62)}$$

where the $\underline{k}$'s are given by Equations (D-45) through (D-48), and where (using the suggested integration constants)

$$\beta_1 = \frac{5}{24} \qquad \beta_2 = \frac{1}{3} - \beta_3 \qquad \beta_3 = \frac{1}{2} \alpha_3 \qquad \beta_4 = -\frac{1}{24}$$

Both methods of obtaining U; for a 6000 sec, circular, xy plane, earth orbit; were tried. The theoretical value of the product of all the U's, for one orbit, i.e., $\partial \underline{x}_{6000} / \partial \underline{x}_0$, is

1	0	0	0	0	0
-18.84 9556	1	0	0	-18,000	0
0	0	1	0	0	0
.01973 9209	0	0	1	18.84 9556	0
0	0	0	0	1	0
0	0	0	0	0	1

Theoretical Value of $\partial \underline{x}_{6000} / \partial \underline{x}_0$

Using $\Delta T = 100$ sec and $a_3 = 0.436$, method 1 gave the following value of $\partial \underline{x}_{6000} / \partial \underline{x}_0$:

0.99981	$-0.47 \cdot 10^{-4}$	0	-0.066	-0.17	0
-18.8491	1.00008	0	.17	-17999.6	0
0	0	0.9999997	0	0	-0.0055
0.0197386	$-0.88 \cdot 10^{-7}$	0	0.99981	18.8491	0
$0.88 \cdot 10^{-7}$	$0.38 \cdot 10^{-7}$	0	$0.47 \cdot 10^{-4}$	1.00008	0
0	0	$0.6 \cdot 10^{-8}$	0	0	0.9999998

Value of $\partial \underline{x}_{6000} / \partial \underline{x}_0$ Using Method 1

Direct integration of $\dot{U} = V(t)\,U$, using $\Delta T = 100$ sec, gave the following value of $\partial \underline{x}_{6000}/\partial \underline{x}_0$:

1.6	0.12	0	184	580.5	0
-20	0.715	0	-577	-18,954	0
0	0	0.9999995	0	0	$-0.61 \cdot 10^{-2}$
0.021	0.0003	0	1.6	20	0
-0.0003	$-0.9 \cdot 10^{-4}$	0	-0.12	0.715	0
0	0	$0.7 \cdot 10^{-8}$	0	0	0.9999994

Value of $\partial \underline{x}_{6000}/\partial \underline{x}_0$ Using Method 2

It is clearly seen that method 1 is much more accurate than method 2. Thus, method 1 was used for this study.

The method 1 equations [Equations (D-51) through (D-55)] were used to generate the U_1 updating matrix for the first partition of the state vector (see Section 6). The form of the matrix V, for the first partition elements is

$$V = \begin{bmatrix} 0 & I \\ A & 0 \end{bmatrix} \tag{D-63}$$

where all submatrices are 6x6, and the elements of A are given by Equations (D-32) and (D-33). Substituting this V into Equations (D-51) through (D-55), and using the suggested integration constants, will yield

$$U_1 = \left[\begin{array}{c|c} I + (2-3\alpha_3)\frac{\Delta T^2}{6} A_2 + \alpha_3 \frac{\Delta T^2}{2} A_3 + \frac{\Delta T^2}{6} A_1 + \frac{\Delta T^4}{24} A_3 A_1 & \left[(2-3\alpha_3)\frac{\Delta T}{3} A_2 + \alpha_3 \Delta T A_3\right]\frac{\Delta T^2}{4} + I\,\Delta T \\ \hline (2-3\alpha_3)\frac{\Delta T}{3} A_2 + \alpha_3 \Delta T A_3 + \frac{\Delta T}{6} A_1 + \frac{\Delta T}{6} A_4 + \frac{\Delta T^3}{12} A_3 A_1 + \frac{\Delta T^3}{12} A_4 A_2 & I + (2-3\alpha_3)\frac{\Delta T^2}{6} A_2 + \alpha_3 \frac{\Delta T^2}{2} A_3 + \frac{\Delta T^2}{6} A_4 + \frac{\Delta T^4}{24} A_4 A_2 \end{array}\right] \tag{D-64}$$

where A_1 is evaluated at $\underline{z}_i$

A_2 is evaluated at $\underline{z}_i + \frac{1}{2}\underline{k}_1$

A_3 is evaluated at $\underline{z}_i + b_1\underline{k}_1 + b_2\underline{k}_2$

A_4 is evaluated at $\underline{z}_i + c_2\underline{k}_2 + c_3\underline{k}_3$

$$b_1 = \frac{1}{2} - b_2 \quad b_2 = \frac{1}{6\alpha_3} \quad c_2 = 1 - c_3 \quad c_3 = 3\alpha_3$$

Use of Equation (D-64) substantially reduces computing time and storage requirements.

The U_1 matrix is $\partial \underline{xx1}_{i+1}/\partial \underline{xx1}_i$. The U_2 matrix is $\partial \underline{xx1}_{i+1}/\partial \underline{xx2}_i$. Nonzero elements of the U_2 matrix are due to the random acceleration components; ϵ_{ax}, ϵ_{ay}, ϵ_{az}, (see Section 5). These components are assumed to be constant across the integration interval. Thus

$$U_2 = \begin{bmatrix} \Delta T^2/2 & 0 & 0 & 0 & 0 & 0 & 0 & 0 \\ 0 & \Delta T^2/2 & 0 & 0 & 0 & 0 & 0 & 0 \\ 0 & 0 & \Delta T^2/2 & 0 & 0 & 0 & 0 & 0 \\ \Delta T^2/2 & 0 & 0 & 0 & 0 & 0 & 0 & 0 \\ 0 & \Delta T^2/2 & 0 & 0 & 0 & 0 & 0 & 0 \\ 0 & 0 & \Delta T^2/2 & 0 & 0 & 0 & 0 & 0 \\ \Delta T & 0 & 0 & 0 & 0 & 0 & 0 & 0 \\ 0 & \Delta T & 0 & 0 & 0 & 0 & 0 & 0 \\ 0 & 0 & \Delta T & 0 & 0 & 0 & 0 & 0 \\ \Delta T & 0 & 0 & 0 & 0 & 0 & 0 & 0 \\ 0 & \Delta T & 0 & 0 & 0 & 0 & 0 & 0 \\ 0 & 0 & \Delta T & 0 & 0 & 0 & 0 & 0 \end{bmatrix} \quad \text{(D-65)}$$

U_3 is $\partial \underline{xx2}_{i+1} / \partial \underline{xx1}_i$. U_3 is zero. U_4 is $\partial \underline{xx2}_{i+1} / \partial \underline{xx2}_i$. From Equation (D-20) it is seen that

$$U_4(I, J) = 0 \quad \text{for } I \neq J \tag{D-66}$$

$$U_4(I, I) = \exp \left| \Delta T / T_I \right| \tag{D-67}$$

where T_I is the time constant associated with the I th state variable in the second partition of the state vector.

SVEAD has no provision to take advantage of diagonal U_4 matrix. To save machine time, the PF(15) flag will be set to 1. This is the option for an identity U_4 matrix in the block 30 equations.

$$\begin{bmatrix} J_1 & J_3^T \\ J_3 & J_4 \end{bmatrix} = \begin{bmatrix} U_1 & U_2 \\ 0 & U_4 \end{bmatrix} \begin{bmatrix} J_1 & J_3^T \\ J_3 & J_4 \end{bmatrix} \begin{bmatrix} U_1^T & 0 \\ U_2^T & U_4^T \end{bmatrix} \tag{D-68}$$

The J matrix will now be corrected for a diagonal U_4 matrix in block 31, by means of the equations

$$J_3 = U_4 J_3 = U_4(I, I)\ J3(I, K) \quad I=1, 8 \quad K=1, 12 \tag{D-69}$$

and

$$J_4 = U_4 J_4 U_4 = U_4(I, I)\ J_4(I, K)\ U_4(K, K) \tag{D-70}$$

where I = 1, 8 and K = 1, 8

10. THE STATE NOISE

From Equation (D-20) it is seen that the state noise vector is

$$\underline{r} = \begin{bmatrix} 0 \\ 0 \\ \cdot \\ \cdot \\ \cdot \\ 0 \\ \sigma_1 \sqrt{1 - a_1^2}\, w_{1,i} \\ \sigma_2 \sqrt{1 - a_2^2}\, w_{2,i} \\ \cdot \\ \cdot \\ \cdot \\ \sigma_8 \sqrt{1 - a_8^2}\, w_{8,i} \end{bmatrix} \left.\begin{matrix} \\ \\ \\ \\ \\ \\ \\ \\ \\ \\ \\ \\ \end{matrix}\right\} 12 \text{ zeros} \qquad \text{(D-71)}$$

where $w_{I,i}$ is uncorrelated, unit variance, zero mean noise; a_I is $\exp(\Delta T / T_I) = U_4(I,I)$; and σ_I^2 is the steady state variance of the Ith element of the second partition of the state vector when no measurements are being processed. The state noise covariance matrix is defined by

$$R \triangleq E[\underline{r}^T \underline{r}] = \begin{bmatrix} R_1 & R_2 \\ R_3 & R_4 \end{bmatrix} \qquad \text{(D-72)}$$

Thus, from Equation (D-71), it is seen that

$$R_1 = R_2 = R_3 = 0 \qquad \text{(D-73)}$$

$$R_4(I,J) = 0 \quad \text{for} \quad I \neq J \qquad \text{(D-74)}$$

$$R_4(I,I) = \sigma_I^2 \left[1 - U_4(I,I)^2 \right] \qquad \text{(D-75)}$$

The R matrix is added to the state error covariance matrix, J, in block 31 of SVEAD. Since SVEAD has no R matrix defined, block 31 equations will be of the form

$$J4(I,I) = J4(I,I) + \sigma_I^2[1 - U4(I,I)^2] \qquad \text{(D-76)}$$

$$\text{for } I = 1, 2, \ldots, 8$$

11. BLOCK 405 COORDINATE TRANSFORMATION

The coordinate transformation matrix, generated in block 405 of SVEAD, will transform the state error covariance matrix from x, y, z coordinates to up, downrange, crossrange coordinates for printout purposes. The u axis (vertical) will be the line of sight from the spacecraft to Mars. The v axis (downrange) will be in the plane formed by u and velocity vector of Mars with respect to the vehicle. w (crossrange) will be taken so as to complete the right-handed coordinate system u, v, w.

The position and velocity of Mars with respect to the vehicle are x_2, y_2, z_2, $\dot{x}_2$, $\dot{y}_2$, $\dot{z}_2$. Then x, y, z coordinates are transformed to u, v, w coordinates by

$$\begin{bmatrix} u \\ v \\ w \end{bmatrix} = \begin{bmatrix} E_1 & E_2 & E_3 \\ E_4 & E_5 & E_6 \\ E_7 & E_8 & E_9 \end{bmatrix} \begin{bmatrix} x \\ y \\ z \end{bmatrix} \qquad \text{(D-77)}$$

and

$$\begin{bmatrix} \dot{u} \\ \dot{v} \\ \dot{w} \end{bmatrix} = \begin{bmatrix} E_1 & E_2 & E_3 \\ E_4 & E_5 & E_6 \\ E_7 & E_8 & E_9 \end{bmatrix} \begin{bmatrix} \dot{x} \\ \dot{y} \\ \dot{z} \end{bmatrix} \qquad \text{(D-78)}$$

where

$$E_{10} = \sqrt{x_2^2 + y_2^2 + z_2^2}$$

$$E_{11} = (x_2\dot{x}_2 + y_2\dot{y}_2 + z_2\dot{z}_2)/E_{10}$$

$$E_{12} = \sqrt{\dot{x}_2^2 + \dot{y}_2^2 + \dot{z}_2^2 - E_{11}^2}$$

$$E_1 = x_2 / E_{10}$$

$$E_2 = y_2 / E_{10}$$

$$E_3 = z_2 / E_{10}$$

$$E_4 = (\dot{x}_2 - E_{11}\, E_1) / E_{12}$$

$$E_5 = (\dot{y}_2 - E_{11}\, E_2) / E_{12}$$

$$E_6 = (\dot{z}_2 - E_{11}\, E_3) / E_{12}$$

$$E_7 = (E_2\, \dot{z}_2 - E_3\, \dot{y}_2) / E_{12}$$

$$E_8 = (E_3\, \dot{x}_2 - E_1\, \dot{z}_2) / E_{12}$$

$$E_9 = (E_1\, \dot{y}_2 - E_2\, \dot{x}_2) / E_{12}$$

The T3, coordinate transformation matrix, in block 405 is given by

T3(1, J) = E(J)	T3(2, J) = E(J+3)	T3(3, J) = E(J+6)
T3(4, J+3) = E(J)	T3(5, J+3) = E(J+3)	T3(6, J+3) = E(J+6)
T3(7, J+6) = E(J)	T3(8, J+6) = E(J+3)	T3(9, J+6) = E(J+6)
T3(10, J+9) = E(J)	T3(11, J+9) = E(J+3)	T3(12, J+9) = E(J+6)

J = 1, 2, 3

12. TABLE OF P'S AND OTHER INPUT QUANTITIES

The bridge, or link, between the engineering equations developed in the previous sections, and the SVEAD programming instructions, is given by the table of P's and the table of E's (next section). The P cells in SVEAD are permanent storage and input constant cells. A list of the P cells, together with suggested input values for an Earth-Mars error analysis study, is shown below.

P(1) = ΔT for the first cycle. Program sets ΔT thereafter. A suggested value is ΔT = 6 sec.

P(2) = time interval between printouts. Suggested value = 3600 sec.

P(3) = end of case time. Suggested value = $.1522827 \cdot 10^8$ sec, which is about the time of Mars perifocus.

P(4) = time of the next printout. Set by the program.

P(5) = a_1

P(6) = b_1

P(7) = b_2

P(8) = c_1

P(9) = c_2

P(10) = c_3

P(11) = α_1

P(12) = α_2

P(13) = α_3

P(14) = α_4

Integrator constants. A suggested set is

$a_1 = \frac{1}{2}$ $\quad b_1 = \frac{1}{2} - b_2$ $\quad b_2 = \frac{1}{6\alpha_3}$ $\quad c_1 = 0$

$c_2 = 1 - c_3$ $\quad c_3 = 3\alpha_3$ $\quad \alpha_1 = \alpha_4 = 1/6$ $\quad \alpha_2 = \frac{2}{3} - \alpha_3$

The above set must be used when generating an updating matrix. A suggested value for α_3 is 0.436.

P(15) = allowable vehicle position error/(sec of integration). A suggested value is $0.695 \cdot 10^{-10}$ km/sec.

P(16) = maximum allowable ΔT. Suggested value 10^8 sec.

P(17) = ΔT used by the trajectory integrator. Set by the program.

P(18) = last cycle's value of ΔT. Set by the program.

P(19) = x position of earth with respect to the vehicle.

P(20) = y position of earth with respect to the vehicle.

P(21) = z position of earth with respect to the vehicle.

P(22) = x position of Mars with respect to the vehicle.

P(23) = y position of Mars with respect to the vehicle.

P(24) = z position of Mars with respect to the vehicle.

P(25) = x position of sun with respect to the vehicle.

P(26) = y position of sun with respect to the vehicle.

P(27) = z position of sun with respect to the vehicle.

P(28) = x position of arbitrary body with respect to the vehicle.

P(29) = y position of arbitrary body with respect to the vehicle.

P(30) = z position of arbitrary body with respect to the vehicle.

P(31) = $\dot{x}$ velocity of earth with respect to the vehicle.

P(32) = $\dot{y}$ velocity of earth with respect to the vehicle.

P(33) = $\dot{z}$ velocity of earth with respect to the vehicle.

P(34) = $\dot{x}$ velocity of Mars with respect to the vehicle.

P(35) = $\dot{y}$ velocity of Mars with respect to the vehicle.

P(36) = $\dot{z}$ velocity of Mars with respect to the vehicle.

P(37) = $\dot{x}$ velocity of sun with respect to the vehicle.

P(38) = $\dot{y}$ velocity of sun with respect to the vehicle.

P(39) = $\dot{z}$ velocity of sun with respect to the vehicle.

P(40) = $\dot{x}$ velocity of arbitrary body with respect to the vehicle.

P(41) = $\dot{y}$ velocity of arbitrary body with respect to the vehicle.

P(42) = $\dot{z}$ velocity of arbitrary body with respect to the vehicle.

Other designations of the above P's, with suggested input values, are

$P(19) = x_1 = x_E = xx1(1) = .6264\ 2296 \cdot 10^4$ km
$P(20) = y_1 = y_E = xx1(2) = .1278\ 1681 \cdot 10^4$
$P(21) = z_1 = z_E = xx1(3) = -.1635\ 1867 \cdot 10^4$
} $\underline{R}_1$

$P(22) = x_2 = x_M = xx1(4) = .6840\ 2704 \cdot 10^8$
$P(23) = y_2 = y_M = xx1(5) = -.9263\ 8206 \cdot 10^8$
$P(24) = z_2 = z_M = xx1(6) = -.4439\ 9169 \cdot 10^8$
} $\underline{R}_2$

$P(25) = x_3 = x_S = .9755\ 8797 \cdot 10^8$
$P(26) = y_3 = y_S = .1058\ 4733 \cdot 10^9$
$P(27) = z_3 = z_S = .4590\ 0069 \cdot 10^8$
} $\underline{R}_3$

$P(28) = x_4 = .1267\ 1489 \cdot 10^9$

$P(29) = y_4 = .3043\ 32866 \cdot 10^9$

$P(30) = z_4 = .1361\ 99307 \cdot 10^9$

} $\underline{R}_4$, at the antipode of Mars to prevent divisions by zero on non-IBM equipment.

$P(31) = \dot{x}_1 = \dot{x}_E = xx1(7) = .3164\ 3128 \cdot 10^{-1}$ km/sec

$P(32) = \dot{y}_1 = \dot{y}_E = xx1(8) = .9655\ 8893 \cdot 10^1$

$P(33) = \dot{z}_1 = \dot{z}_E = xx1(9) = .6063\ 0606 \cdot 10^1$

} $\dot{\underline{R}}_1$

$P(34) = \dot{x}_2 = \dot{x}_M = xx1(10) = .2733\ 1554 \cdot 10^1$

$P(35) = \dot{y}_2 = \dot{y}_M = xx1(11) = .2660\ 0217 \cdot 10^2$

$P(36) = \dot{z}_2 = \dot{z}_M = xx1(12) = .1271\ 8872 \cdot 10^2$

} $\dot{\underline{R}}_2$

$P(37) = \dot{x}_3 = \dot{x}_S = -.2221\ 8499 \cdot 10^2$

$P(38) = \dot{y}_3 = \dot{y}_S = .2739\ 5139 \cdot 10^2$

$P(39) = \dot{z}_3 = \dot{z}_S = .1375\ 6207 \cdot 10^2$

} $\dot{\underline{R}}_3$

$P(40) = \dot{x}_4 = -47.17\ 01534$

$P(41) = \dot{y}_4 = 28.19\ 0061$

$P(42) = \dot{z}_4 = 14.79\ 3542$

} $\dot{\underline{R}}_4$

$P(43) = \mu_1 = \mu_E = \mu_{earth} = .3986\ 032 \cdot 10^6$ km^3/sec^2

$P(44) = \mu_2 = \mu_M = \mu_{Mars} = .4297\ 78 \cdot 10^5$

$P(45) = \mu_3 = \mu_S = \mu_{sun} = .1327\ 15445 \cdot 10^{12}$

$P(46) = \mu_4 = 0$

P(47) = x direction cosine of star (Canopus) = -.06102 7528

P(48) = y direction cosine of star (Canopus) = .6032 5508

P(49) = z direction cosine of star (Canopus) = -.79521

P(50) = r_N, nominal radius of Mars = 3410 km.

P(51), multiplies first row of measurement matrix = 0 or 1.

P(52), multiplies second row of measurement matrix = 0 or 1.

P(53), multiplies third row of measurement matrix = 0 or 1.

P(54), multiplies fourth row of measurement matrix = 0 or 1.

Set zero to delete measurement.

P(55) = $T_{\epsilon ax} = T_1$, time constant of random x acceleration.

P(56) = $T_{\epsilon ay} = T_2$, time constant of random y acceleration.

P(57) = $T_{\epsilon az} = T_3$, time constant of random z acceleration.

Suggested values are $.6048 \cdot 10^6$ sec = 1 week.

P(58) = $T_{\epsilon y1} = T_4$ = time constant of "bias" adding to first measurement.

P(59) = $T_{\epsilon y2} = T_5$ = time constant of "bias" adding to second measurement.

P(60) = $T_{\epsilon y3} = T_6$ = time constant of "bias" adding to third measurement.

Suggested values are $0.3024 \cdot 10^6$ sec = 1/2 week.

P(61) = $T_{\epsilon y4} = T_7$ = time constant of "bias" adding to fourth measurement.

Suggested value = $.288 \cdot 10^5$ seconds = 1/3 day.

P(62) = $T_{\epsilon r} = T_8$ = time constant of error adding to nominal radius of Mars.
Suggested value is $.864 \cdot 10^5$ sec = 1 day, to account for changing error due to oblateness simplifications, etc. in the software.

P(63) = $\sigma^2_{\epsilon ax}$ = variance of random x acceleration.

P(64) = $\sigma^2_{\epsilon ay}$ = variance of random y acceleration.

P(65) = $\sigma^2_{\epsilon az}$ = variance of random z acceleration.

Suggested values are $(.531 \cdot 10^{-11}$ km/ sec$^2)^2$ which give position errors of about 200 km in 176 days.

P(66) = $\sigma^2_{\epsilon y1} = \sigma^2_{\epsilon \psi} = \sigma^2_{\epsilon M1} + \sigma^2_{\epsilon S1}$, Equation (D-7). Variance of "bias" error adding to first measurement (cone angle). Suggested value = $(1.921 \cdot 10^{-3})^2 + (1.746 \cdot 10^{-3})^2 = (2.597 \cdot 10^{-3}$ rad$)^2$. For improved optics, $\sigma^2_{\epsilon y1} = (.391 \cdot 10^{-3})^2 + (0.407 \cdot 10^{-3})^2 = (0.5645 \cdot 10^{-3}$ rad$)^2$.

P(67) = $\sigma^2_{\epsilon y2} = \sigma^2_{\epsilon \theta}$ = variance of "bias" error adding to clock angle. Calculated by the program in block 31 from Equation (D-8), P(67) = P(75) P(71) + P(76) P(72).

P(68) = $\sigma^2_{\epsilon y3}$ = variance of "bias" error adding to the subtense angle. Calculated by the program in block 31 by P(68) = P(78) + [P(79) P(77)/ 100]^2.

P(69) = $\sigma^2_{\epsilon y4} = \sigma^2_{\epsilon \dot{R}}$ = variance of "bias" error adding to the range-rate measurement. Suggested value = $(10^{-5}$ km/ sec$)^2$. Note, 10^{-5} km/ sec = .0328 ft/ sec.

P(70) = $\sigma^2_{\epsilon r}$ = variance of error adding to nominal radius of Mars. Suggested value = (20 km)^2.

P(71) = $\sigma^2_{\epsilon M2}$ = variance of Mars clock angle "bias" error, see Figure 2. Suggested value = $(1.921 \cdot 10^{-3}$ rad$)^2$. For improved optics, $\sigma^2_{\epsilon M2} = (.391 \cdot 10^{-3}$ rad$)^2$.

P(72) = $\sigma^2_{\epsilon c2}$ = variance of Canopus clock angle "bias" error, see Figure 2. Suggested value = $(.873 \cdot 10^{-3}$ rad$)^2$. For improved optics, $\sigma^2_{\epsilon c2} = (.391 \cdot 10^{-3}$ rad$)^2$.

P(73) = variance of clock angle uncorrelated noise due to Mars sensor. Suggested value = $(0.349 \cdot 10^{-4}$ rad$)^2$, equivalent to $0.1746 \cdot 10^{-3}$ rad errors averaged over 25 measurements.

P(74) = variance of clock angle uncorrelated noise due to Canopus sensor. Suggested value = $(0.1746 \cdot 10^{-4}$ rad$)^2$, equivalent to $0.873 \cdot 10^{-4}$ rad errors averaged over 25 measurements.

P(75) = $1/\sin^2\psi$, ψ is the cone angle.

P(76) = $1/\sin^2\phi$, ϕ is the Sun-Canopus angle.

P(77) = α, the subtense angle in rad.

} Calculated by the program in block 24.

P(78) = lower limit of subtense angle bias error variance. Suggested value = $(.873 \cdot 10^{-3}$ rad$)^2$. For improved optics, P(78) = $(.485 \cdot 10^{-4}$ rad$)^2$.

P(79) = percent of subtense angle contributing to subtense "bias" error standard deviation. Suggested value = 1. For improved optics, P(79) = 0.

The uncorrelated measurement noise statistics are given to the filter by means of the W matrix, the measurement noise covariance matrix. Suggested input values are shown below.

W(1, 1) = variance of uncorrelated measurement noise adding to the first measurement (the cone angle ψ). Suggested value = $(0.4935 \cdot 10^{-4}$ rad$)^2$, equivalent to $0.247 \cdot 10^{-3}$ rad errors averaged over 25 measurements.

W(2, 2) = variance of uncorrelated measurement noise adding to the second measurement (the clock angle θ). Calculated by the program in block 24 by W(2, 2) = P(71) P(75) + P(72) P(76), see Equation (D-8).

W(3, 3) = variance of uncorrelated measurement noise adding to the third measurement (the subtense angle α). Suggested value is $(.1745 \cdot 10^{-4}$ rad$)^2$, equivalent to $0.873 \cdot 10^{-4}$ rad errors averaged over 25 measurements.

W(4, 4) = variance of uncorrelated measurement noise adding to the fourth measurement (range-rate). Suggested value = $(0.732 \cdot 10^{-5}$ km/sec$)^2$, equivalent to 0.12 ft/sec per 1 sec sample, 25 samples averaged.

Suggested values of the initial state error covariance matrix, for the first partition, are shown below.

J1(1, 1) = (2 km)^2, initial uncertainty in x_E.

J1(2, 2) = (2 km)^2, initial uncertainty in y_E.

J1(3, 3) = (2 km)^2, initial uncertainty in z_E.

J1(4, 4) = (220 km)^2, initial uncertainty in x_M.

J1(5, 5) = (220 km)^2, initial uncertainty in y_M.

J1(6, 6) = (220 km)^2, initial uncertainty in z_M.

Due to periodic terms in the state transition matrix, these 220 km initial position errors grow to about 500 km in 170 days (a quarter of a Mars orbit). 500 km is felt to be a reasonable uncertainty in the Mars ephemeris, at least at the present time.

J1(7, 7) = $(2 \cdot 10^{-3}$ km/sec$)^2$, uncertainty in $\dot{x}_E$.

J1(8, 8) = $(2 \cdot 10^{-3}$ km/sec$)^2$, uncertainty in $\dot{y}_E$.

J1(9, 9) = $(2 \cdot 10^{-3}$ km/sec$)^2$, uncertainty in $\dot{z}_E$.

J1(10, 10) = $0.40025 \cdot 10^{-5}$ (km/sec)^2, variance of $\dot{x}_M$ error.

J1(11, 11) = $0.40025 \cdot 10^{-5}$ (km/sec)^2, variance of $\dot{y}_M$ error.

J1(12, 12) = $0.40025 \cdot 10^{-5}$ (km/sec)^2, variance of $\dot{z}_M$ error.

J1(10, 10) was obtained in the following manner. Let

$\dot{\epsilon}_{M/v}$ = velocity error of Mars with respect to the vehicle.

$\dot{\epsilon}_{M/E}$ = velocity error of Mars with respect to the Earth.

$\dot{\epsilon}_{E/v}$ = velocity error of earth with respect to the vehicle.

Then

$$\dot{\epsilon}_{M/v} = \dot{\epsilon}_{M/E} + \dot{\epsilon}_{E/v} \tag{D-79}$$

and

$$E[\dot{\epsilon}^2_{M/v}] = E[\dot{\epsilon}^2_{M/E}] + E[\dot{\epsilon}^2_{E/v}] \tag{D-80}$$

Based on experience, it has been found that velocity errors, of objects in circular orbits, are related to position errors by the approximate equation

$$E[\dot{\epsilon}^2_{M/E}] \approx \left(\frac{\text{velocity of Mars}}{\text{Sun-Mars distance}}\right)^2 E[\epsilon^2_{M/E}]$$

$$\approx 10^{-14} \cdot 500^2$$

Thus Equation (D-80) becomes

$$J1(10, 10) = E[\dot{\epsilon}^2_{M/v}] = 500^2 \cdot 10^{-14} + J1(7, 7)$$

$$= .40025 \cdot 10^{-5} \text{ (km/sec)}^2$$

Likewise for J1(11, 11) and J1(12, 12).

Off-diagonal terms appear in the error covariance matrix in the following way.

$$J1(7, 10) = E[\dot{\epsilon}_{M/v} \dot{\epsilon}_{E/v}]$$

But from Equation (D-79), it is seen that

$$J1(7, 10) = E[\dot{\epsilon}^2_{E/v}] = .4 \cdot 10^{-5} \text{ (km/sec)}^2$$

Thus

$$J1(7,10) = .4 \cdot 10^{-5} \text{ (km/sec)}^2$$

$$J1(8,11) = .4 \cdot 10^{-5}$$

$$J1(9,12) = .4 \cdot 10^{-5}$$

$$J1(10,7) = .4 \cdot 10^{-5}$$

$$J1(11,8) = .4 \cdot 10^{-5}$$

$$J1(12,9) = .4 \cdot 10^{-5}$$

Suggested values for the initial state error covariance matrix, for the second partition, are shown below.

$$J4(1,1) = 0.282 \cdot 10^{-22} \text{ (km/sec}^2\text{)}^2 = \sigma^2_{\epsilon ax} = P(63)$$

$$J4(2,2) = 0.282 \cdot 10^{-22} \text{ (km/sec}^2\text{)}^2 = \sigma^2_{\epsilon ay} = P(64)$$

$$J4(3,3) = 0.282 \cdot 10^{-22} \text{ (km/sec}^2\text{)}^2 = \sigma^2_{\epsilon az} = P(65)$$

$$J4(4,4) = 0.673 \cdot 10^{-5} \text{ rad}^2 = \sigma^2_{\epsilon y1} = P(66)$$

$$J4(5,5) = 0.5 \cdot 10^{-5} \text{ rad}^2 = \sigma^2_{\epsilon y2} = P(67)$$

$$J4(6,6) = 0.7615 \cdot 10^{-6} \text{ rad}^2 = \sigma^2_{\epsilon y3} = P(68)$$

} near earth only

$$J4(7,7) = 10^{-10} \text{ (km/sec)}^2 = \sigma^2_{\epsilon y4} = P(69)$$

$$J4(8,8) = 400 \text{ km}^2 = \sigma^2_{\epsilon r} = P(70)$$

Other inputs to SVEAD are the input dimension numbers

PD1 = 12 PD2 = 8 PD3 = 4 PD4 = 100 PD5 = 400

PD6 = 12 PD7 = 8 PD10 = 8 PD12 = 12

and the input control flags

PF(15) = 1 PF(19) = 1 PF(23) = 1 PF(27) = 1

The material presented in this section contains the necessary information to run the ERC radio/optical tracking and navigation error analysis study. Thus this section may be thought of as a user's manual for this particular SVEAD error analysis study.

13. TABLE OF E'S

The SVEAD subroutine equations are written in terms of P's and E's, where the P's are permanent storage cells and the E's are temporary or working storage. The definitions of the E's used for the dynamics is as follows:

$E_1 = x_1$ $E_2 = y_1$ $E_3 = z_1$ $E_4 = x_2$ $E_5 = y_2$ $E_6 = z_2$

$E_7 = x_3$ $E_8 = y_3$ $E_9 = z_3$ $E_{10} = x_4$ $E_{11} = y_4$ $E_{12} = z_4$

$E_{13} = x_2 - x_1$ $E_{14} = y_2 - y_1$ $E_{15} = z_2 - z_1$

$E_{16} = x_3 - x_1$ $E_{17} = y_3 - y_1$ $E_{18} = z_3 - z_1$

$E_{19} = x_4 - x_1$ $E_{20} = y_4 - y_1$ $E_{21} = z_4 - z_1$

$E_{22} = x_3 - x_2$ $E_{23} = y_3 - y_2$ $E_{24} = z_3 - z_2$

$E_{25} = x_4 - x_2$ $E_{26} = y_4 - y_2$ $E_{27} = z_4 - z_2$

$E_{28} = x_4 - x_3$ $E_{29} = y_4 - y_3$ $E_{30} = z_4 - z_3$

$E_{31} = R_1^2$ $E_{32} = R_2^2$ $E_{33} = R_3^2$ $E_{34} = R_4^2$

$E_{35} = |\underline{R}_2 - \underline{R}_1|^2$ $E_{36} = |\underline{R}_3 - \underline{R}_1|^2$ $E_{37} = |\underline{R}_4 - \underline{R}_1|^2$

$E_{38} = |\underline{R}_3 - \underline{R}_2|^2$ $E_{39} = |\underline{R}_4 - \underline{R}_2|^2$ $E_{40} = |\underline{R}_4 - \underline{R}_3|^2$

$E_{41} = R_1$ $E_{42} = R_2$ $E_{43} = R_3$ $E_{44} = R_4$

$E_{45} = |\underline{R}_2 - \underline{R}_1|$ $E_{46} = |\underline{R}_3 - \underline{R}_1|$ $E_{47} = |\underline{R}_4 - \underline{R}_1|$

$E_{48} = |\underline{R}_3 - \underline{R}_2|$ $E_{49} = |\underline{R}_4 - \underline{R}_2|$ $E_{50} = |\underline{R}_4 - \underline{R}_3|$

$E_{51} = \mu_1/R_1^3$ $E_{52} = \mu_2/R_2^3$ $E_{53} = \mu_3/R_3^3$ $E_{54} = \mu_4/R_4^3$

$$E_{55} = \frac{\mu_1}{|\underline{R}_2 - \underline{R}_1|^3} \qquad E_{56} = \frac{\mu_1}{|\underline{R}_3 - \underline{R}_1|^3} \qquad E_{57} = \frac{\mu_1}{|\underline{R}_4 - \underline{R}_1|^3}$$

$$E_{58} = \frac{\mu_2}{|\underline{R}_2 - \underline{R}_1|^3} \qquad E_{59} = \frac{\mu_3}{|\underline{R}_3 - \underline{R}_1|^3} \qquad E_{60} = \frac{\mu_4}{|\underline{R}_4 - \underline{R}_1|^3}$$

$$E_{61} = \frac{\mu_2}{|\underline{R}_3 - \underline{R}_2|^3} \qquad E_{62} = \frac{\mu_2}{|\underline{R}_4 - \underline{R}_2|^3} \qquad E_{63} = \frac{\mu_3}{|\underline{R}_3 - \underline{R}_2|^3}$$

$$E_{64} = \frac{\mu_4}{|\underline{R}_4 - \underline{R}_2|^3} \qquad E_{65} = \frac{\mu_3}{|\underline{R}_4 - \underline{R}_3|^3} \qquad E_{66} = \frac{\mu_4}{|\underline{R}_4 - \underline{R}_3|^3}$$

$$E_{67} = \frac{\mu_1}{R_1^3} x_1 + \frac{\mu_2}{R_2^3} x_2 + \frac{\mu_3}{R_3^3} x_3 + \frac{\mu_4}{R_4^3} x_4$$

$$E_{68} = \frac{\mu_1}{R_1^3} y_1 + \frac{\mu_2}{R_2^3} y_2 + \frac{\mu_3}{R_3^3} y_3 + \frac{\mu_4}{R_4^3} y_4$$

$$E_{69} = \frac{\mu_1}{R_1^3} z_1 + \frac{\mu_2}{R_2^3} z_2 + \frac{\mu_3}{R_3^3} z_3 + \frac{\mu_3}{R_3^3} z_4$$

These are all the E's needed to calculate the acceleration vector. The following E's are needed for the acceleration partial derivatives.

$$E_{70} = \frac{x_1}{R_1} \quad E_{71} = \frac{y_1}{R_1} \quad E_{72} = \frac{z_1}{R_1} \quad E_{73} = \frac{x_2}{R_2} \quad E_{74} = \frac{y_2}{R_2} \quad E_{75} = \frac{z_2}{R_2}$$

$$E_{76} = \frac{x_2 - x_1}{|\underline{R}_2 - \underline{R}_1|} \qquad E_{77} = \frac{y_2 - y_1}{|\underline{R}_2 - \underline{R}_1|} \qquad E_{78} = \frac{z_2 - z_1}{|\underline{R}_2 - \underline{R}_1|}$$

$$E_{79} = \frac{x_3 - x_1}{|\underline{R}_3 - \underline{R}_1|} \qquad E_{80} = \frac{y_3 - y_1}{|\underline{R}_3 - \underline{R}_1|} \qquad E_{81} = \frac{z_3 - z_1}{|\underline{R}_3 - \underline{R}_1|}$$

$$E_{82} = \frac{x_4 - x_1}{|\underline{R}_4 - \underline{R}_1|} \qquad E_{83} = \frac{y_4 - y_1}{|\underline{R}_4 - \underline{R}_1|} \qquad E_{84} = \frac{z_4 - z_1}{|\underline{R}_4 - \underline{R}_1|}$$

$$E_{85} = \frac{x_3 - x_2}{|\underline{R}_3 - \underline{R}_2|} \qquad E_{86} = \frac{y_3 - y_2}{|\underline{R}_3 - \underline{R}_2|} \qquad E_{87} = \frac{z_3 - z_2}{|\underline{R}_3 - \underline{R}_2|}$$

$$E_{88} = \frac{x_4 - x_2}{|\underline{R}_4 - \underline{R}_2|} \qquad E_{89} = \frac{y_4 - y_2}{|\underline{R}_4 - \underline{R}_2|} \qquad E_{90} = \frac{z_4 - z_2}{|\underline{R}_4 - \underline{R}_2|}$$

$$E_{91} = \frac{\mu_2}{|\underline{R}_2 - \underline{R}_1|^3} \frac{x_2 - x_1}{|\underline{R}_2 - \underline{R}_1|} \qquad E_{92} = \frac{\mu_3}{|\underline{R}_3 - \underline{R}_1|^3} \frac{x_3 - x_1}{|\underline{R}_3 - \underline{R}_1|}$$

$$E_{93} = \frac{\mu_4}{|\underline{R}_4 - \underline{R}_1|^3} \frac{x_4 - x_1}{|\underline{R}_4 - \underline{R}_1|} \qquad E_{94} = \frac{\mu_1}{R_1^3} \frac{x_1}{R_1}$$

$$E_{95} = \frac{\mu_2}{R_2^3} \frac{x_2}{R_2} \qquad E_{96} = \frac{\mu_3}{|\underline{R}_3 - \underline{R}_2|^3} \frac{x_3 - x_2}{|\underline{R}_3 - \underline{R}_2|}$$

$$E_{97} = \frac{\mu_4}{|\underline{R}_4 - \underline{R}_2|^3} \frac{x_4 - x_2}{|\underline{R}_4 - \underline{R}_2|} \qquad E_{98} = \frac{\mu_1}{|\underline{R}_2 - \underline{R}_1|^3} \frac{x_2 - x_1}{|\underline{R}_2 - \underline{R}_1|}$$

$$E_{99} = \frac{\mu_2}{|\underline{R}_2 - \underline{R}_1|^3} \frac{y_2 - y_1}{|\underline{R}_2 - \underline{R}_1|} \qquad E_{100} = \frac{\mu_3}{|\underline{R}_3 - \underline{R}_1|^3} \frac{y_3 - y_1}{|\underline{R}_3 - \underline{R}_1|}$$

$$E_{101} = \frac{\mu_4}{|\underline{R}_4 - \underline{R}_1|^3} \frac{y_4 - y_1}{|\underline{R}_4 - \underline{R}_1|} \qquad E_{102} = \frac{\mu_1}{R_1^3} \frac{y_1}{R_1}$$

$$E_{103} = \frac{\mu_2}{R_2^3} \frac{y_2}{R_2} \qquad E_{104} = \frac{\mu_3}{|\underline{R}_3 - \underline{R}_2|^3} \frac{y_3 - y_2}{|\underline{R}_3 - \underline{R}_2|}$$

$$E_{105} = \frac{\mu_4}{|\underline{R}_4 - \underline{R}_2|^3} \frac{y_4 - y_2}{|\underline{R}_4 - \underline{R}_2|} \qquad E_{106} = \frac{\mu_1}{|\underline{R}_2 - \underline{R}_1|^3} \frac{y_2 - y_1}{|\underline{R}_2 - \underline{R}_1|}$$

$$E_{107} = \frac{\mu_1}{R_1^3} + \frac{\mu_2}{|\underline{R}_2 - \underline{R}_1|^3} + \frac{\mu_3}{|\underline{R}_3 - \underline{R}_1|^3} + \frac{\mu_4}{|\underline{R}_4 - \underline{R}_1|^3}$$

$$E_{108} = \frac{\mu_2}{R_2^3} - \frac{\mu_2}{|\underline{R}_2 - \underline{R}_1|^3} \qquad E_{109} = \frac{\mu_1}{R_1^3} - \frac{\mu_1}{|\underline{R}_2 - \underline{R}_1|^3}$$

$$E_{110} = \frac{\mu_2}{R_2^3} + \frac{\mu_1}{|\underline{R}_2 - \underline{R}_1|^3} + \frac{\mu_3}{|\underline{R}_3 - \underline{R}_2|^3} + \frac{\mu_4}{|\underline{R}_4 - \underline{R}_2|^3}$$

The following E's are needed for the trajectory integrator (see Section 7). I = 1, 2, ... , 24.

E(I + 110) = last cycle's value of the 24 element state vector, $\underline{z}$.

E(I + 134) = next value of $\underline{z}$ from a single integration.

E(I + 158) = temporary storage for $\underline{z}$.

E(I + 182) = $\dot{\underline{z}}$

E(I + 206) = $\underline{k}_1$

E(I + 230) = $\underline{k}_2$

E(I + 254) = $\underline{k}_3$

E(I + 278) = $\underline{k}_4$

$$E(J + 302) = \alpha_1 \hat{\underline{k}}_1 + \alpha_2 \hat{\underline{k}}_2 + \alpha_3 \hat{\underline{k}}_3 + \alpha_4 \hat{\underline{k}}_4 - \left(\alpha_1 \hat{\hat{\underline{k}}}_1 + \alpha_2 \hat{\hat{\underline{k}}}_2 + \alpha_3 \hat{\hat{\underline{k}}}_3 + \alpha_4 \hat{\hat{\underline{k}}}_4\right)$$

J = 1, 2, ... , 12

The following E's are used in block 24 to generate the measurement matrix, M (I, J).

$$E_1 = |\underline{R}_m| = |\underline{R}_2| \qquad E_2 = |\underline{R}_s| = |\underline{R}_3|$$

$$(E_3\ E_4\ E_5) = \underline{i}_m \qquad (E_6\ E_7\ E_8) = \underline{i}_s$$

$$E_9 = \cos\psi \qquad E_{10} = \cos\phi \qquad E_{11} = \sin\psi \qquad E_{12} = \sin\phi$$

$$(E_{13}\ E_{14}\ E_{15}) = \underline{i}_s \times \underline{i}_c \qquad (E_{16}\ E_{17}\ E_{18}) = \underline{i}_s \times \underline{i}_m$$

$$E_{19} = |\underline{i}_s \times \underline{i}_c| \qquad E_{20} = |\underline{i}_s \times \underline{i}_m|$$

$$(E_{21}\ E_{22}\ E_{23}) = \frac{\underline{i}_s \times \underline{i}_c}{|\underline{i}_s \times \underline{i}_c|} \qquad (E_{24}\ E_{25}\ E_{26}) = \frac{\underline{i}_s \times \underline{i}_m}{|\underline{i}_s \times \underline{i}_m|} = \underline{u}_{ms}$$

$$E_{27} = \cos\theta \qquad E_{28} = \sin\theta \qquad E_{29} = R_m \sin\psi \qquad E_{30} = \sin\frac{\alpha}{2}$$

$$E_{31} = \cos\frac{\alpha}{2} \qquad E_{32} = R_m \cos\frac{\alpha}{2} \qquad E_{33} = -\frac{r_N^2}{R_m^2 \cos(\alpha/2)}$$

$$E_{34} = |\underline{R}_E| \qquad (E_{35}\ E_{36}\ E_{37}) = \underline{i}_e \qquad E_{38} = \underline{i}_e \cdot \dot{\underline{R}}_E$$

$E_{39} = \psi$, cone angle (deg).

$E_{40} = \theta$, clock angle (deg).

$E_{41} = \phi$, Sun-Canopus angle (deg).

$E_{42} = \alpha$, subtense angle (deg).

14. E-EQUATIONS FOR ACCELERATION COMPONENTS

The acceleration equations of Section 5 are given in terms of the E's by

$$\ddot{x}_1 = -E_{67} + E_{58}E_{13} + E_{59}E_{16} + E_{60}E_{19}$$
$$\ddot{y}_1 = -E_{68} + E_{58}E_{14} + E_{59}E_{17} + E_{60}E_{20}$$
$$\ddot{z}_1 = -E_{69} + E_{58}E_{15} + E_{59}E_{18} + E_{60}E_{21}$$

$$\ddot{x}_2 = -E_{67} - E_{55}E_{13} + E_{63}E_{22} + E_{64}E_{25}$$
$$\ddot{y}_2 = -E_{68} - E_{55}E_{14} + E_{63}E_{23} + E_{64}E_{26}$$
$$\ddot{z}_2 = -E_{69} - E_{55}E_{15} + E_{63}E_{24} + E_{64}E_{27}$$

$$\ddot{x}_3 = -E_{67} - E_{56}E_{16} - E_{61}E_{22} + E_{66}E_{28}$$
$$\ddot{y}_3 = -E_{68} - E_{56}E_{17} - E_{61}E_{23} + E_{66}E_{29}$$
$$\ddot{z}_3 = -E_{69} - E_{56}E_{18} - E_{61}E_{24} + E_{66}E_{30}$$

$$\ddot{x}_4 = -E_{67} - E_{57}E_{19} - E_{62}E_{25} - E_{65}E_{28}$$
$$\ddot{y}_4 = -E_{68} - E_{57}E_{20} - E_{62}E_{26} - E_{65}E_{29}$$
$$\ddot{z}_4 = -E_{69} - E_{57}E_{21} - E_{62}E_{27} - E_{65}E_{30}$$

15. E-EQUATIONS FOR ACCELERATION PARTIALS

The equations of the partial derivatives of the acceleration vector (see Section 6) are given in terms of the E's by

$$\partial \ddot{x}_1/\partial x_1 = 3(E_{94} E_{70} + E_{91} E_{76} + E_{92} E_{79} + E_{93} E_{82}) - E_{107}$$

$$\partial \ddot{x}_1/\partial y_1 = 3(E_{94} E_{71} + E_{91} E_{77} + E_{92} E_{80} + E_{93} E_{83})$$

$$\partial \ddot{x}_1/\partial z_1 = 3(E_{94} E_{72} + E_{91} E_{78} + E_{92} E_{81} + E_{93} E_{84})$$

$$\partial \ddot{x}_1/\partial x_2 = 3(E_{95} E_{73} - E_{91} E_{76}) - E_{108}$$

$$\partial \ddot{x}_1/\partial y_2 = 3(E_{95} E_{74} - E_{91} E_{77})$$

$$\partial \ddot{x}_1/\partial z_2 = 3(E_{95} E_{75} - E_{91} E_{78})$$

$$\partial \ddot{y}_1/\partial x_1 = \partial \ddot{x}_1/\partial y_1$$

$$\partial \ddot{y}_1/\partial y_1 = 3(E_{102} E_{71} + E_{99} E_{77} + E_{100} E_{80} + E_{101} E_{83}) - E_{107}$$

$$\partial \ddot{y}_1/\partial z_1 = 3(E_{102} E_{72} + E_{99} E_{78} + E_{100} E_{81} + E_{101} E_{84})$$

$$\partial \ddot{y}_1/\partial x_2 = \partial \ddot{x}_1/\partial y_2$$

$$\partial \ddot{y}_1/\partial y_2 = 3(E_{103} E_{74} - E_{99} E_{77}) - E_{108}$$

$$\partial \ddot{y}_1/\partial z_2 = 3(E_{103} E_{75} - E_{99} E_{78})$$

$$\partial \ddot{z}_1/\partial x_1 = \partial \ddot{x}_1/\partial z_1$$

$$\partial \ddot{z}_1/\partial y_1 = \partial \ddot{y}_1/\partial z_1$$

$$\partial \ddot{z}_1/\partial z_1 = -\partial \ddot{x}_1/\partial x_1 - \partial \ddot{y}_1/\partial y_1$$

$$\partial \ddot{z}_1/\partial x_2 = \partial \ddot{x}_1/\partial z_2$$

$$\partial \ddot{z}_1/\partial y_2 = \partial \ddot{y}_1/\partial z_2$$

$$\partial \ddot{z}_1/\partial z_2 = -\partial \ddot{x}_1/\partial x_2 - \partial \ddot{y}_1/\partial y_2$$

$$\partial \ddot{x}_2/\partial x_1 = 3(E_{94}\,E_{70} - E_{98}\,E_{76}) - E_{109}$$

$$\partial \ddot{x}_2/\partial y_1 = 3(E_{94}\,E_{71} - E_{98}\,E_{77})$$

$$\partial \ddot{x}_2/\partial z_1 = 3(E_{94}\,E_{72} - E_{98}\,E_{78})$$

$$\partial \ddot{x}_2/\partial x_2 = 3(E_{95}\,E_{73} + E_{98}\,E_{76} + E_{96}\,E_{85} + E_{97}\,E_{88}) - E_{110}$$

$$\partial \ddot{x}_2/\partial y_2 = 3(E_{95}\,E_{74} + E_{98}\,E_{77} + E_{96}\,E_{86} + E_{97}\,E_{89})$$

$$\partial \ddot{x}_2/\partial z_2 = 3(E_{95}\,E_{75} + E_{98}\,E_{78} + E_{96}\,E_{87} + E_{97}\,E_{90})$$

$$\partial \ddot{y}_2/\partial x_1 = \partial \ddot{x}_2/\partial y_1$$

$$\partial \ddot{y}_2/\partial y_1 = 3(E_{102}\,E_{71} - E_{106}\,E_{77}) - E_{109}$$

$$\partial \ddot{y}_2/\partial z_1 = 3(E_{102}\,E_{72} - E_{106}\,E_{78})$$

$$\partial \ddot{y}_2/\partial x_2 = \partial \ddot{x}_2/\partial y_2$$

$$\partial \ddot{y}_2/\partial y_2 = 3(E_{103}\,E_{74} + E_{106}\,E_{77} + E_{104}\,E_{86} + E_{105}\,E_{89}) - E_{110}$$

$$\partial \ddot{y}_2/\partial z_2 = 3(E_{103}\,E_{75} + E_{106}\,E_{78} + E_{104}\,E_{87} + E_{105}\,E_{90})$$

$$\partial \ddot{z}_2/\partial x_1 = \partial \ddot{x}_2/\partial z_1$$

$$\partial \ddot{z}_2/\partial y_1 = \partial \ddot{y}_2/\partial z_1$$

$$\partial \ddot{z}_2/\partial z_1 = -\partial \ddot{x}_2/\partial x_1 - \partial \ddot{y}_2/\partial y_1$$

$$\partial \ddot{z}_2/\partial x_2 = \partial \ddot{x}_2/\partial z_2$$

$$\partial \ddot{z}_2/\partial y_2 = \partial \ddot{y}_2/\partial z_2$$

$$\partial \ddot{z}_2/\partial z_2 = -\partial \ddot{x}_2/\partial x_2 - \partial \ddot{y}_2/\partial y_2$$

The above partials will be stored in the lower right hand corner of the A1 matrix in the PRLTS 2 subroutine, Section 17.

16. SUBROUTINE TRAJ2

This subroutine integrates the $\underline{z}$ state vector (24 elements) ahead P(17) sec. When PF(9) = 0, it also stores the acceleration partial derivatives in

$$\left.\begin{array}{l} \text{A1(I, J) for } \underline{z} = \underline{z}_i \\ \text{A1(I, J+6) for } \underline{z} = \underline{z}_i + \frac{1}{2}\underline{k}_1 \\ \text{A1(I+6, J) for } \underline{z} = \underline{z}_i + b_1\underline{k}_1 + b_2\underline{k}_2 \\ \text{A1(I+6, J+6) for } \underline{z} = \underline{z}_i + c_2\underline{k}_2 + c_3\underline{k}_3 \end{array}\right\} \begin{array}{l} I = 1, 2, \ldots, 6 \\ J = 1, 2, \ldots, 6 \end{array}$$

The integrator implemented here is the one discussed in Section 7. The programming instructions for the TRAJ2 subroutine are shown below.

```
          DO  a   I = 1, 24
      a)  E(I+158) = P(I+18)
          DO  i   J = 1, 4
comment   START DERIVATIVE CALCULATION
          DO  j   I = 1, 12
          E(I) = P(I+18)
      j)  E(I+182) = P(I+30)
          DO  k   I = 1, 3
          E(I+12) = E(I+3) - E(I)
          E(I+15) = E(I+6) - E(I)
          E(I+18) = E(I+9) - E(I)
          E(I+21) = E(I+6) - E(I+3)
          E(I+24) = E(I+9) - E(I+3)
      k)  E(I+27) = E(I+9) - E(I+6)
          DO  ℓ   I = 1, 10
          K = 3*I - 2
          E(I+30) = E(K)**2 + E(K+1)**2 + E(K+2)**2
```

```
l)  E(I+40) = DSQRT (E(I+30))
    E(51) = (P(43)/E(31))/E(41)
    DO  m  I = 1, 3
    E(I+51) = (P(I+43)/E(I+31))/E(I+41)
    E(I+54) = (P(43)/E(I+34))/E(I+44)
m)  E(I+57) = (P(I+43)/E(I+34))/E(I+44)
    DO  n  I = 1, 2
    E(I+60) = (P(44)/E(I+37))/E(I+47)
    E(I+62) = (P(I+44)/E(I+37))/E(I+47)
n)  E(I+64) = (P(I+44)/E(40))/E(50)
    DO  o  I = 1, 3
    E(I+66) = E(51)*E(I) + E(52)*E(I+3) + E(53)*E(I+6)
              + E(54)*E(I+9)
    E(I+194) = - E(I+66) + E(58)*E(I+12) + E(59)*E(I+15)
               + E(60)*E(I+18)
    E(I+197) = - E(I+66) - E(55)*E(I+12) + E(63)*E(I+21)
               + E(64)*E(I+24)
    E(I+200) = - E(I+66) - E(56)*E(I+15) - E(61)*E(I+21)
               + E(66)*E(I+27)
o)  E(I+203) = - E(I+66) - E(57)*E(I+18) - E(62)*E(I+24)
               - E(65)*E(I+27)
comment  END DERIVATIVE CALCULATION
    L = (J*(J-1))/2 + 4
    IF  P(1) ≠ P(17)  GO TO h
```

```
      IF PF(9) = 1   GO TO h
      CALL PRTLS2          (see next section)
      GO TO (b, d, f, h), J
b)    DO   c   I = 1, 6
      DO   c   K = 1, 6
c)    A1(I, K) = A1(I+6, K+6)
      GO TO h
d)    DO   e   I = 1, 6
      DO   e   K = 1, 6
e)    A1(I, K+6) = A1(I+6, K+6)
      GO TO h
      DO   g   I = 1, 6
      DO   g   K = 1, 6
g)    A1(I+6, K) = A1(I+6, K+6)
h)    DO   i   I = 1, 24
      M = I + 182 + 24*J
      E(M) = P(17) * E(I+182)
      P(I+18) = E(I+158)
      DO   i   K = 1, J
      LK = L + K
      N = I + 182 + 24*K
i)    P(I+18) = P(I+18) + P(LK)*E(N)
      RETURN
```

17. SUBROUTINE PRLTS 2

This subroutine calculates the 36 acceleration partial derivatives (see Sections 6 and 15) and stores them in A1 (I + 6, J + 6) where I = 1, 2, ..., 6 and J = 1, 2, ..., 6. The programming instructions are

```
      DOa I = 1, 3
      DOa K = 1, 5
      IK = 3 * K + I + 9
a)    E(IK + 63) = E(IK)/E(K + 44)
      DO b I = 1, 3
      K = 3 * I + 73
      E(I + 69) = E(I)/E(41)
      E(I + 72) = E(I + 3)/E(42)
      E(I + 90) = E(I + 57) * E(K)
b)    E(I + 98) = E(I + 57) * E(K + 1)
      DO c I = 1, 2
      K = 8 * I
      E(K + 86) = E(51) * E(I + 69)
      E(K + 87) = E(52) * E(I + 72)
      E(K + 88) = E(63) * E(I + 84)
      E(K + 89) = E(64) * E(I + 87)
c)    E(K + 90) = E(55) * E(I + 75)
      E(107) = E(51) + E(58) + E(59) + E(60)
      E(108) = E(52) - E(58)
      E(109) = E(51) - E(55)
      E(110) = E(52) + E(55) + E(63) + E(64)
      DO d K = 1, 2
      M = -K + 4
      KK = 8 * K
      DO d I = 1, M
      IK = I + K
```

```
A1 (K + 6, IK + 5) = 3.D0 * (E(KK + 86) * E(IK + 68)
   + E(KK + 83) * E(IK + 74)   + E(KK + 84) * E(IK + 77)
   + E(KK + 85) * E(IK + 80))

A1 (K + 6, IK + 8) = 3.D0 * (E(KK + 87) * E(IK + 71)
   - E(KK + 83) * E(IK + 74))

A1 (K + 9, IK + 5) = 3.D0 * (E(KK + 86) * E(IK + 68)
   - E(KK + 90) * E(IK + 74))

A1 (K + 9, IK + 8) = 3.D0 * (E(KK + 87) * E(IK + 71)
   + E(KK + 90) * E(IK + 74)   + E(KK + 88) * E(IK + 83)
   + E(KK + 89) * E(IK + 86))
```

d)
```
DO e K = 1, 2
L = 3 * K
DO e I = 1, 2
IL = I + L + 3
IML = I - L + 12
A1 (IL, IL) = A1 (IL, IL) - E(L + 104)
```

e)
```
A1 (IL, IML) = A1 (IL, IML) - E(K + 107)
DO f I = 3, 6, 3
DO f K = 3, 6, 3
A1 (K + 5, I + 4) = A1 (K + 4, I + 5)
A1 (K + 6, I + 4) = A1 (K + 4, I + 6)
A1 (K + 6, I + 5) = A1 (K + 5, I + 6)
```

f)
```
A1 (K + 6, I + 6) = - A1 (K + 4, I + 4) - A1 (K + 5, I + 5)
RETURN
```

18. BLOCK 28 PROGRAMMING INSTRUCTIONS

Block 28 equations are used to integrate the trajectory ahead ΔT sec, and to estimate the integrator error. The equations of Section 8 are used to estimate the integrator error, and to adjust ΔT, for the next cycle, to give the required integration accuracy. The programming instructions are

```
P(17) = P(1)
P(18) + P(1)
```

```
      CALL TRAJ2
      DO a I = 1, 12
a)    E(I + 302) = P(11) * E(I + 206) + P(12) * E(I + 230)
                 + P(13) * E(I + 254) + P(14) * E(I + 278)
      DO b I = 1, 24
      E(I + 134) = P(I + 18)
      E(I + 110) = E(I + 158)
b)    P(I + 18) = E(I + 158)
      P(17) = P(1)/2.D0
      CALL TRAJ2
      DO c I = 1, 12
c)    E(I + 302) = E(I + 302) - P(11) * E(I + 206)
                 - P(12) * E(I + 230) - P(13) * E(I + 254)
                 - P(14) * E(I + 278)
      CALL TRAJ2
      P(17) = 0.D0
      DO d I = 1, 12
      E(I + 302) = E(I + 302) - P(11) * E(I + 206)
                 - P(12) * E(I + 230) - P(13) * E(I + 254)
                 - P(14) * E(I + 278)
d)    P(17) = P(17) + E(I + 302) ** 2
      P(17) = DSQRT (P(17))
      P(1) = P(1) * (((15.D0 * P(15) * P(1))/P(17)) ** .25)
      IF P(1) ≤ P(16) GO TO e
      P(1) = P(16)
e)    IF PF(2) = 0 RETURN
      Print T, P(1), P(I + 18) I = 1, 24
      RETURN
```

Note the nonstandard SVEAD printout of time, next ΔT, and the 24 elements of the state vector.

19. BLOCK 291 PROGRAMMING INSTRUCTIONS

The equations in this block generate the elements of the 12 x 12 U1 updating matrix by the method suggested in Section 9. Also generated here are the elements of the 12 x 8 U2 matrix, and 8 x 8 U4 matrix (U3 is zero). The programming instructions are

```
      K = PD1/2
      E(1) = 2.D0 - 3.D0 * P(13)
      E(2) = P(18) **2
      E(3) = P(18)/6.D0
      E(4) = P(13) * P(18)
      E(5) = E(1) * P(18)/3.D0
      E(6) = E(2)/6.D0
      E(7) = E(2)/4.D0
      E(8) = P(13) * E(2)/2.D0
      E(9) = E(1) * E(6)
      E(10) = E(6) * P(18)/2.D0
      E(11) = E(6) * E(7)
      DO b I = 1, K
      DO a J = 1, K
a)    U1 (I, J) = E(9) * A1 (I, J + K) + E(8) * A1 (I + K, J)
b)    U1 (I, I) = U1 (I, I) + 1.D0
      DO c I = 1, K
      DO c J = 1, K
      U1 (I + K, J + K) = U1 (I, J)
      U1 (I, J + K) = 0.D0
c)    U1 (I +K, J) = 0.D0
      DO d I = 1, K
      DO d J = 1, K
      DO d L = 1, K
      U1 (I, J + K) = U1 (I, J + K) + A1(I + K, L)
                    *A1 (L, J)
d)    U1 (I + K, J) = U1 (I + K, J) + A1 (I + K, L + K)
                    *A1 (L, J + K)
```

```
      DO f I = 1, K
      DO e J = 1, K
      U1 (I, J) = U1 (I, J) + E (6) *A1 (I, J) + E (11)
                  *U1 (I, J + K)
      U1 (I + K, J + K) = U1 (I + K, J + K) + E (6) *A1 (I + K,
                          J + K) + E (11) * U1 (I + K, J)
      U1 (I + K, J) = E (10) *(U1 (I + K, J) + U1 (I, J + K))
                      + E (3) (A1 (I, J) + A1 (I + K, J + K))
      A1 (I, J) = E (5) *A1 (I, J + K) + E (4) *A1 (I + K, J)
      U1 (I + K, J) = U1 (I + K, J) + A1 (I, J)
e)    U1 (I, J + K) = E (7) *A1 (I, J)
f)    U1 (I, I + K) = U1 (I, I + K) + P (18)
      DO g I = 1, PD2
g)    U4 (I, I) = DEXP (-DABS (P (18)/P (I + 54)))
      U2 (1, 1) = .5 D0 *P (18) *P (18)
      DO h I = 1, 3
      U2 (I, I) = U2 (1, 1)
      U2 (I + 3, I) = U2 (1, 1)
      U2 (I + 6, I) = P (18)
h)    U2 (I + 9, I) = P (18)
```

20. BLOCK 31 PROGRAMMING INSTRUCTIONS

SVEAD has no provision to take advantage of a diagonal U4 matrix other than U4 = I. To save machine time, the PF (15) flag will be set to 1 for the runs. This is the option of an identity U4 matrix in block 30. The J matrix will then be corrected in block 31 for a diagonal U4 matrix by means of the equations

$$J3 = U4\ J3$$

$$J4 = U4\ J4\ U4$$

The programing instructions for these equations are

```
      DO a I = 1, PD1
      DO a J = 1, PD2
```

```
a)  J3 (I, J) = U4 (I, I) * J3 (I, J)
    DO  b  I = 1, PD2
    DO  b  J = 1, PD2

b)  J4 (I, J) = U4 (I, I) *J4 (I, J) *U4 (J, J)
```

The state noise covariance matrix, discussed in Section 10, is added to the J matrix by means of the equations

```
    P (67) = P (75) *P (71) + P (76) *P (72)
    P (68) = P (78) + (P (79) * P(77)/100. D0) **2
    DO  c  I = 1, PD2

c)  J4 (I, I) = J4 (I, I) + P (I + 62) *(1. D0 - U4 (I, I) **2)
```

21. BLOCK 24 PROGRAMMING INSTRUCTIONS

This block implements the equations of the measurement partials developed in Sections 3 and 4. The programming instructions are

```
    DO  a  J = 1, 2
    K = 3 *J

a)  E (J) = DSQRT (P (K + 19) **2 + P (K + 20) **2
              + P (K + 21) **2)
    DO  b  J = 1, 3
    E (J + 2) = P (J + 21)/E (1)

b)  E (J + 5) = P (J + 24)/E (2)
    E (9) = E (6) *E (3) + E (7) *E (4) + E (8) *E (5)
    E (10) = E (6) *P (47) + E (7) *P (48) + E (8) *P (49)
    DO  c  J = 9, 10

c)  E (J + 2) = DSQRT (1. D0 - E (J) **2)
    E (13) = E (7) *P (49) - E (8) *P (48)
    E (14) = E (8) *P (47) - E (6) *P (49)
    E (15) = E (6) *P (48) - E (7) *P (47)
    E (16) = E (7) *E (5) - E (8) *E (4)
    E (17) = E (8) *E (3) - E (6) *E (5)
    E (18) = E (6) *E (4) - E (7) *E (3)
    E (19) = DSQRT (E (13) **2 + E (14) **2 + E (15) **2)
    E (20) = DSQRT (E (16) **2 + E (17) **2 + E (18) **2)
```

```
      DO  d J = 1, 3
      E (J + 20) = E (J + 12)/E (19)
d)    E (J + 23) = E(J+ 15)/E (20)
      E (27) = E (24) *E (21) + E (25) *E (22) + E (26) *E (23)
      E (28) = (E (25) *E (23) - E (26) *E (22)) *E (6)
        + (E (26) *E (21) - E (24) *E (23)) *E (7)
        + (E (24) *E (22) - E (25) *E (21)) *E (8)
      E (29) = E (1) *E (11)
      E (30) = P (50)/E (1)
      E (31) = DSQRT (1.D0 - E (30) **2)
      DO  e J = 1, 3
      M1 (1, J + 3) = P (51) * (E (9) *E (J + 2) - E (J + 5))/E (29)
e)    M1 (2, J + 3) = -P (52) *E (J + 23)/E (29)
      M2 (1, 4) = P (51)
      M2 (2, 5) = P (52)
      P (75) = 1.D0/(E (11) **2)
      P (76) = 1.D0/(E (12) **2)
      W (2, 2) = P (73) *P (75) + P (74) *P (76)
      IF E (30) < .0004363 D0  GO TO j
      E (32) = E (1) *E (31)
      E (33) = -2.D0 *P (50)/(E (1) *E (32))
      DO  k J = 1, 3
k)    M1 (3, J + 3) = P (53) *E (33) *E (J + 2)
      M2 (3, 6) = P (53)
      M2 (3, 8) = 2.D0 *P (53)/E (32)
j)    IF P (54) = 0.D0  GO TO  f
      E (34) = DSQRT (P (19) **2 + P (20) **2 + P (21) **2)
      DO  g J = 1, 3
g)    E (J + 34) = P (J + 18)/E (34)
      E (38) = E (35) *P (31) + E (36) *P (32) + E (37) *P (33)
f)    DO  h J = 1, 3
      M1 (4, J) = P (54) * (P (J + 30) - E (38) *E (J + 34))/E (34)
```

```
h)  M1 (4, J + 6) = P (54) *E (J + 34)
    M2 (4, 7) = P (54)
    E (39) = 57.3 D0 *DATAN 2 (E (11), E (9))
    E (40) = 57.3 D0 *DATAN 2 (E (28), E (27))
    IF E (40) ≥ 0. D0 GO TO i
    E (40) = 360. D0 + E (40)

i)  E (41) = 57.3 D0 *DATAN 2 (E (12), E (10))
    P (77) = 2. D0 *DATAN 2 (E (30), E (31))
    E (42) = 57.3 D0 *P (77)
    IF PF (2) = 0 RETURN
    Print E (39), E (40), E (41), E (42).
```

Note the nonstandard SVEAD printout:

E (39) = ψ, cone angle (deg)
E (40) = θ, clock angle (deg)
E (41) = φ, Sun-Canopus angle (deg)
E (42) = α, subtense angle (deg)

22. BLOCK 405 PROGRAMMING INSTRUCTIONS

These programming instructions are to implement the equations discussed in Section 11.

```
    E (10) = DSQRT (P (22) **2 + P (23) **2 + (P 24) **2)
    E (11) = (P (22) *P (34) + P (23) *P (35)
             + P (24) *P (36))/ E (10)
    E (12) = DSQRT (P (34) **2 + P (35) **2
             + P (36) **2 - E (11) **2)
    DO  a I = 1, 3
    E (I) = P (I + 21)/ E (10)

a)  E (I + 3) = (P (I + 33) - E (11) *E (I))/ E (12)
    E (7) = (E (2) *P (36) - E (3) *P (35))/ E (12)
    E (8) = (E (3) *P (34) - E (1) *P (36))/ E (12)
    E (9) = (E (1) *P (35) - E (2) *P (34))/ E (12)
    DO  b J = 1, 3
    DO  b K = 1, 3
    N = J + 3 *K - 3
```

```
      DO  b I = 1, 10, 3
      L = I - 1 + K
      M = J - 1 + I
b)    T3 (L, M) = E (N)
```